



# DEVELOPMENT OF A TEMPLATE-FREE MICROWAVE-ASSISTED METAL SULFIDE NANOPARTICLES SYNTHESIS METHOD AND FILM DEPOSITION WITH FORMULATED INKS

DAVID MAGALHÃES SOUSA  
Master in Materials Engineering

DOCTORATE IN MATERIALS SCIENCE AND ENGINEERING

NOVA University Lisbon  
February, 2023





# DEVELOPMENT OF A TEMPLATE-FREE MICROWAVE-ASSISTED METAL SULFIDE NANOPARTICLES SYNTHESIS METHOD AND FILM DEPOSITION WITH FORMULATED INKS

DAVID MAGALHÃES SOUSA  
Master in Materials Engineering

DOCTORATE IN MATERIALS SCIENCE AND ENGINEERING

NOVA University Lisbon  
February, 2023







# DEVELOPMENT OF A TEMPLATE-FREE MICROWAVE-ASSISTED METAL SULFIDE NANOPARTICLES SYNTHESIS METHOD AND FILM DEPOSITION WITH FORMULATED INKS

**DAVID MAGALHÃES SOUSA**

Master in Materials Engineering

**Adviser:** Isabel Maria das Mercês Ferreira  
*Associate Professor with Aggregation, Faculty of Sciences and Technology, NOVA University Lisbon*

**Co-adviser:** João Carlos dos Santos Silva e Pereira de Lima  
*Associate Professor with Aggregation, Faculty of Sciences and Technology, NOVA University Lisbon*

## Examination Committee

**Chair:** Rodrigo Ferrão de Paiva Martins  
*Full Professor, Faculty of Sciences and Technology, NOVA University Lisbon*

**Rapporteurs:** Tito da Silva Trindade  
*Full Professor, Department of Chemistry, University of Aveiro*

Eulália Fernanda Alves de Carvalho Pereira  
*Associate Professor with Habilitation, Department of Chemistry and Biochemistry, University of Porto*

**Adviser:** Isabel Maria das Mercês Ferreira  
*Associate Professor with Aggregation, Faculty of Sciences and Technology, NOVA University Lisbon*

**Members:** Maria de Jesus Matos Gomes  
*Full Professor, Department of Physics, University of Minho*

João Miguel Ribeiro Avó  
*Postdoctoral Researcher, Instituto Superior Técnico, University of Lisbon*

Ana Catarina Bernardino Baptista  
*Postdoctoral Researcher, Faculty of Sciences and Technology, NOVA University Lisbon*



## **Development of a Template-Free Microwave-Assisted Metal Sulfide Nanoparticles Synthesis Method and Film Deposition with Formulated Inks**

Copyright © David Magalhães Sousa, NOVA School of Science and Technology, NOVA University Lisbon.

The NOVA School of Science and Technology and the NOVA University Lisbon have the right, perpetual and without geographical boundaries, to file and publish this dissertation through printed copies reproduced on paper or on digital form, or by any other means known or that may be invented, and to disseminate through scientific repositories and admit its copying and distribution for non-commercial, educational or research purposes, as long as credit is given to the author and editor.

---

“Sometimes the hardest prisons to break out of, are the ones without locks.”  
*Abed Nadir*

## Acknowledgments

Agradeço à Fundação para a Ciência e Tecnologia o suporte financeiro através da bolsa de doutoramento SFRH/BD/135948/2018 e também à European Research Council pelo suporte através do projecto ChapTerPV (647596). Agradeço também às instituições de acolhimento CENIMAT e LAQV por me terem aceite e fornecido as condições para executar este trabalho. Agradeço também ao secretariado pela ajuda nos processos administrativos.

Um especial obrigado aos meus orientadores Isabel e João que me ensinaram a fazer ciência, a crescer enquanto pessoa e me apoiaram em todos os bons e maus momentos do meu percurso.

Agradeço também a todos os co-autores que participaram mais directamente no trabalho. Sem eles não poderia ter ido longe.

A todos os meus colegas e amigos do laboratório de fotoquímica do departamento de química e do departamento de materiais, um obrigado profundo por me terem ajudado e acompanhado ao longo destes anos.

Fico feliz por ter amigos que me apoiaram e aturaram durante este período e agradeço-lhes por isso. Por último, quero agradecer à minha mãe, o meu pai, Flip, Maria, Samuel e Raul todo o suporte, amor e paciência.



# Abstract

Developing efficient and green materials for solar cells is of the utmost importance. In the pursuit of attempting to harvest all of the solar spectrum energy, from the ultra-violet to the near-infrared, metal sulfide nanoparticles were deemed as the most promising materials, due to their low toxicity, low cost, chemical stability, and band gap tunability, compared to the oxide, selenide and telluride counterparts.

A microwave-assisted sustainable synthesis protocol was developed to obtain metal sulfide nanoparticles. Using solely 1-dodecanethiol as the sulfur source, solvent, and particle stabilizer, coupled with a metal salt precursor systematically, binary and ternary metal sulfide nanoparticles were synthesized using relatively abundant elements from group 2 to group 15 of the periodic table. Pure ternary alloys were obtained, but syntheses performed with some elements instead resulted in the binary sulfides, influenced by the final phase of each other. Quaternary metal sulfide syntheses were also attempted. Control of the synthesis was attained through video recording and post-analysis of the color profiles, crossed with the temperature and pressure profile, to pinpoint relevant transformations, such as the sulfide formation. The influence of reaction time, temperature, precursors type and concentration, and the presence of light on the size, morphology, material phase, and optical properties of the nanoparticles were evaluated. Changing the concentration of the precursor resulted in the same phase of the metal sulfide but using a higher concentration required less energy input to achieve the same temperature since the thiol weakly absorbs the microwave radiation. In contrast, the salts absorb it more efficiently. Two temperature control modes were tested, one automated and another at constant power. The automated temperature mode was chosen since the temperature profiles were more reproducible between syntheses, but the constant power mode allowed to see if a particular reaction was exothermic. A lower synthesis temperature usually resulted in a metal-thiol complex, while a higher temperature resulted in metal sulfide. The synthesis time was directly correlated to the size of the particles; for example, zinc sulfide particles with an average length of 3 nm with a 5-minute synthesis at 300 °C, up to 8 nm with a synthesis time of 25 minutes. The presence of light paired with light-sensitive precursors, such as silver salts, results in smaller particles. In the dark bigger particles were obtained when silver nitrate was used. When the synthesis was performed with silver oxide, both the metal sulfide and metallic silver were obtained in the dark, while metallic silver was the primary product in the presence of light. Precursors not sensitive to light, such as zinc acetate, revealed no changes in the final material with or without light.

A library of metal sulfide nanomaterials was obtained with band gaps of 0.51 eV (copper iron sulfide) that absorbs infrared photons, to 2.56 (indium sulfide) to absorb visible photons, and to 3.54 eV (zinc sulfide) to absorb ultra-violet photons, as well a metallic-like material (NbS<sub>2</sub>).

Stable inks were formulated with the synthesized nanoparticles in isopropanol, with no additives. Slot-die coating and spray deposition methods were tested. Like the synthesis protocol, a simple spray method was developed using a relatively low deposition temperature. As a result, the inks could be used throughout the whole deposition with minimal sedimentation. Thin films of zinc sulfide, tin sulfide, and copper iron sulfide were obtained with the desired optical properties to use in solar cells. The possibility to choose between 2D nanoparticles shape, controllable structure modification with temperature and luminescence properties make this work an important source of metal sulfides nanoparticles syntheses for a vast range of applications from solar cells, batteries,

---

capacitors, photonic devices, and other not yet discovered applications.

**Keywords:** metal sulfide, synthesis, microwave, nanoparticle, film, spray deposition, band gap

---



## Resumo

Desenvolver materiais eficientes e verdes para as células solares é da maior importância. Na tentativa de captar toda a energia do espectro solar, do ultra-violeta ao infravermelho, as nanopartículas de sulfureto de metal foram consideradas como os materiais mais promissores, devido à sua baixa toxicidade, baixo custo, estabilidade química e possibilidade de afinar a banda proibida, conhecida em inglês como *band gap*, em comparação com os homólogos óxido, selenieto e telureto.

Foi desenvolvido um protocolo de síntese sustentável com assistência de microondas para obter nanopartículas de sulfureto de metal. Usando sistematicamente apenas 1-dodecanotiol como fonte de enxofre, solvente, e estabilizador de partículas, associado a um precursor de sal de metal, as nanopartículas binárias e ternárias de sulfureto de metal foram sintetizadas usando elementos relativamente abundantes do grupo 2 ao grupo 15 da tabela periódica. Foram obtidas ligas ternárias puras, mas as sínteses realizadas com alguns elementos resultaram nos sulfuretos binários, influenciados pela fase final uns dos outros. Foram também tentadas sínteses de sulfuretos metálicos quaternários. O controle da síntese foi alcançado através de gravação vídeo e análise posterior dos perfis de cor, cruzados com o perfil de temperatura e pressão, para identificar transformações relevantes, tais como a formação de sulfuretos. A influência do tempo de reação, temperatura, tipo e concentração dos precursores, e a presença de luz no tamanho, morfologia, fase material, e propriedades ópticas das nanopartículas foi avaliada. A alteração da concentração do precursor resultou na mesma fase do sulfureto de metal mas a utilização de uma concentração mais elevada requereu menos energia para atingir a mesma temperatura uma vez que o tiol absorve menos a radiação de microondas. Em contraste, os sais absorvem-na de forma mais eficiente. Dois modos de controle de temperatura foram testados, um automático e outro com potência constante. O modo de temperatura automatizado foi escolhido porque os perfis de temperatura eram mais reprodutíveis entre sínteses, mas o modo de potência constante permitiu ver se uma determinada reação era exotérmica. Uma temperatura de síntese mais baixa geralmente resultou num complexo metal-tiol, enquanto que uma temperatura mais alta resultou num sulfureto de metal. O tempo de síntese foi directamente correlacionado com o tamanho das partículas; por exemplo, foram obtidas partículas de sulfureto de zinco com um tamanho médio de 3 nm com uma síntese de 5 minutos a 300 °C, até 8 nm com um tempo de síntese de 25 minutos. Finalmente, a presença de luz em conjunto com precursores sensíveis à luz, tais como sais de prata, resulta em partículas mais pequenas. No escuro, foram obtidas partículas maiores quando se utilizou nitrato de prata. Quando a síntese foi realizada com óxido de prata, foram obtidos tanto o sulfureto de prata como a prata metálica na ausência de luz e maioritariamente o metal na presença de luz. Precursores não sensíveis à luz, tais como o acetato de zinco, não revelaram alterações no material final com ou sem luz.

Uma biblioteca de nanomateriais de sulfureto de metal foi obtida com *band gaps* de 0,51 eV (sulfureto de ferro de cobre) que absorve fotões infravermelhos, a 2,56 (sulfureto de índio) para absorver fotões visíveis, e a 3,54 eV (sulfureto de zinco) para absorver fotões ultra-violetas, bem como um material semelhante ao metal (NbS<sub>2</sub>).

Foram formuladas tintas estáveis com as nanopartículas sintetizadas em isopropanol, sem aditivos. Os métodos de deposição revestimento por extrusão de matriz e pulverização foram testados. Tal como o protocolo de síntese, foi desenvolvido um método simples de pulverização usando uma temperatura de deposição relativamente baixa. As tintas foram usadas durante toda a deposição

---

com o mínimo de sedimentação. Foram obtidas filmes finos de sulfureto de zinco, sulfureto de estanho e sulfureto de ferro de cobre com as propriedades ópticas desejadas para uso em células solares.

A possibilidade de escolher entre forma de nanopartículas 2D, modificação da estrutura controlável com propriedades de temperatura e luminescência fazem deste trabalho uma importante fonte de síntese de nanopartículas de sulfuretos metálicos para uma vasta gama de aplicações desde células solares, baterias, condensadores, dispositivos fotônicos, e outras aplicações ainda não descobertas.

**Palavras-chave:** sulfureto de metal, síntese, microondas (micro-ondas), nanopartícula, filme, deposição por pulverização, *band gap* (banda proibida)

---

# Contents

<b>List of Figures</b>	<b>xv</b>
<b>List of Tables</b>	<b>xxiii</b>
<b>Acronyms</b>	<b>xxv</b>
<b>1 Outline</b>	<b>1</b>
<b>2 Introduction</b>	<b>3</b>
2.1 Motivation and Objectives . . . . .	3
2.2 Review of Concepts . . . . .	5
2.3 Synthesis Methods . . . . .	18
2.3.1 Conduction and Convection Heating . . . . .	19
2.3.2 Microwave-assisted Heating . . . . .	20
2.3.3 Template-free . . . . .	24
2.3.4 Sulfur and Metal Sources . . . . .	24
2.4 Ink Formulation . . . . .	27
2.5 Ink Deposition Methods . . . . .	31
<b>3 Metal Sulfide Nanoparticle Syntheses</b>	<b>35</b>
3.1 Methods . . . . .	35
3.1.1 Synthesis Protocol . . . . .	35
3.1.2 Image Recording: Reproducibility . . . . .	35
3.1.3 Materials Characterization Methods . . . . .	39
3.2 Binary Metal Sulfides . . . . .	46
3.2.1 Group 4: Ti, Zr, Hf . . . . .	46
3.2.2 Group 5: V, Nb, Ta . . . . .	50
3.2.3 Group 6: Cr, Mo, W . . . . .	55
3.2.4 Group 7: Mn . . . . .	59
3.2.5 Group 8: Fe . . . . .	60
3.2.6 Group 9: Co . . . . .	61
3.2.7 Group 10: Ni . . . . .	63
3.2.8 Group 11: Cu, Ag . . . . .	64
3.2.9 Group 12: Zn, Cd . . . . .	69
3.2.10 Group 13: In . . . . .	74
3.2.11 Group 14: Sn . . . . .	76
3.2.12 Group 15: Bi . . . . .	78
3.2.13 Resume . . . . .	80
3.3 Multinary Metal Sulfide . . . . .	84
3.3.1 Ternary . . . . .	85
3.3.1.1 Cu, Fe . . . . .	85

3.3.1.2	Cu, In . . . . .	87
3.3.1.3	In, Sn . . . . .	89
3.3.1.4	Zn, In . . . . .	91
3.3.1.5	Zn, Sn . . . . .	92
3.3.1.6	Ba, Zr . . . . .	95
3.3.2	Quaternary . . . . .	98
3.3.2.1	Cu, In, Sn . . . . .	98
3.3.2.2	Cu, Ag, In . . . . .	100
3.3.2.3	Zn, In, Sn . . . . .	101
3.3.3	Resume . . . . .	105
3.4	Input Parameters and Impact on the Synthesis . . . . .	106
3.4.1	Electric Arcs . . . . .	106
3.4.2	Temperature and Time . . . . .	108
3.4.3	Concentration . . . . .	114
3.4.4	Reagents . . . . .	116
3.4.5	Light . . . . .	120
3.5	Sustainability . . . . .	124
<b>4</b>	<b>Metal Sulfide Nanoparticle Inks</b>	<b>129</b>
4.1	Formulation . . . . .	129
4.2	Deposition . . . . .	131
4.2.1	Slot die . . . . .	131
4.2.2	Spray . . . . .	133
4.2.2.1	Method . . . . .	134
4.2.2.2	Tin Sulfide Film . . . . .	135
4.2.2.3	Zinc Sulfide Film . . . . .	137
4.2.2.4	Niobium Sulfide Film . . . . .	139
4.2.2.5	Copper Iron Sulfide Film . . . . .	141
4.2.3	Resume . . . . .	145
<b>5</b>	<b>Conclusions and Future Perspectives</b>	<b>147</b>
<b>6</b>	<b>Research Impact</b>	<b>149</b>
6.1	Main Publications . . . . .	149
6.2	Other Publications . . . . .	149
6.3	Oral Presentation . . . . .	150
6.4	Posters . . . . .	151
	<b>Bibliography</b>	<b>153</b>
<b>A</b>	<b>Auxiliary Data</b>	<b>185</b>
A.1	Binary Metal Sulfides . . . . .	185
A.1.1	Group 2: Be, Mg, Sr, Ba . . . . .	185
A.1.2	Group 3: Sc, Y . . . . .	192
A.1.3	Group 4: Ti, Zr, Hf . . . . .	195
A.1.4	Group 5: V, Nb, Ta . . . . .	197
A.1.5	Group 6: Cr, Mo, W . . . . .	199

A.1.6	Group 7: Mn . . . . .	201
A.1.7	Group 8: Fe . . . . .	202
A.1.8	Group 9: Co . . . . .	203
A.1.9	Group 10: Ni . . . . .	204
A.1.10	Group 11: Cu, Ag . . . . .	205
A.1.11	Group 12: Zn, Cd . . . . .	206
A.1.12	Group 13: Al, Ga, In . . . . .	207
A.1.13	Group 14: Si, Ge, Sn . . . . .	212
A.1.14	Group 15: Bi . . . . .	216
A.2	Multinary Metal Sulfides . . . . .	217
A.2.1	Ternary . . . . .	217
A.2.2	Quaternary . . . . .	220
A.3	Input Parameters and Impact on the Synthesis . . . . .	224
A.4	Metal Sulfide Nanoparticle Inks . . . . .	227
A.4.1	Tin Sulfide Film . . . . .	227
A.4.2	Zinc Sulfide Film . . . . .	228
A.4.3	Niobium Sulfide Film . . . . .	229
A.4.4	Copper Iron Sulfide Film . . . . .	230
A.5	Reagents . . . . .	231
<b>B</b>	<b>Python Scripts</b>	<b>233</b>
B.1	Interpolation . . . . .	233
B.2	Band Gap Determination . . . . .	235
B.3	X-ray Diffraction Pattern Identification . . . . .	250
B.4	Selected Area Electron Diffraction Pattern Identification . . . . .	263
B.5	Auxiliary Python 3 Scripts . . . . .	266



## List of Figures

2.1	Irradiance spectrum of the sun at sea level, a picture of the sun, the fraction of the sun's spectrum currently captured by silicon and perovskite solar cells, and their efficiencies. . . . .	4
2.2	Energy band diagram of the electronic states of a metal, a semimetal, a semiconductor, and an insulator. The bands' width represents the density of states at a certain energy. The gray shades in the energy bands represent the distribution of the electrons, with black as filled and white as empty states. . . . .	5
2.3	Schematic of the quantum confinement effect on the energy bands and band gaps of a material with a successive shorter dimension, from bulk to a quantum dot. . . . .	6
2.4	Scheme with the price and availability of the native elements oxygen, sulfur, selenium and tellurium. . . . .	9
2.5	Scatter plot of the elements, with the background related with their availability, with their position dependent on price and abundance. . . . .	9
2.6	Generic representation of a Jablonski diagram with energy levels. . . . .	11
2.7	Diagram representing a Förster and a Dexter energy transfer process. . . . .	12
2.8	Example of the absorption spectra (full lines) of a solar cell composed of three layers and the emission spectrum (dashed lines) of the lowest and the topmost layer. . . . .	13
2.9	Example of an absorbance (green), excitation (magenta), and emission (blue) spectra, illustrating the Stokes shift (red). . . . .	14
2.10	Jablonski diagram of the singlet fission mechanism. . . . .	14
2.11	Jablonski diagram of the triplet-to-triplet annihilation mechanism involving two annihilators (A and B) pre-sensitized by a sensitizer. . . . .	16
2.12	Schematic of a deposition performed by physical vapor deposition. . . . .	18
2.13	Schematic of heating mantle. . . . .	20
2.14	Schematic of a microwave reactor. . . . .	21
2.15	Periodic table with an overview of the number of articles and citations regarding the microwave-assisted synthesis of metal sulfides. . . . .	23
2.16	Reaction diagrams comprising the possible combinations regarding the metal and metal sulfide as either kinetic or thermodynamic products. . . . .	25
2.17	Two pictures of the same copper sulfide synthesis with visible . . . . .	26
2.18	Schematics of a substrate with emphasis on two types of surface functionalization (A), hydrophilic and hydrophobic, and their interaction with hydrophobic ink, (I) and (II) respectively. Two types of surface traps, surface roughness, and dangling bonds, that can interfere with the ink deposition are shown in (B). . . . .	29
2.19	Schematics of the various non-scalable and scalable ink deposition methods. . . . .	31
3.1	Color profile, with the average red, green and blue pixel values for each picture, and the temperature, pressure and microwave generating magnetron input power profiles of a tin sulfide microwave-assisted synthesis. . . . .	36
3.2	Pictures taken from the video of a silver sulfide synthesis, using a mobile phone camera (A) and corresponding color profiles (B). . . . .	37
3.3	X-ray diffraction patterns of a synthesized tin sulfide powder sample and the red bar plots are references taken from Materials Project database[128][129]. . . . .	39

3.4	Procedure to obtain the d-spacing values from a selected area electron diffraction pattern. A gold reference pattern was used to calibrate the transmission electron microscope (Hitachi H-8100) equipment used in this work (1). The sequence of the procedure is from 1 to 8. In step 8, the value of the Rau argument, which is the value of $R_{Au}$ , must be determined previously by the user after calibrating. . . . .	42
3.5	Schematic of the python script steps to obtain a band gap from a diffuse reflectance spectrum. . . . .	44
3.6	Color, temperature, and pressure profiles (A) of the syntheses starting from titanium(IV) isopropoxide, TEM image (B), a SAED pattern as an inset, and the XRD pattern (C) of the synthesized powder and a reference pattern of an amorphous $TiS_2$ (C). . . . .	47
3.7	Color, temperature, and pressure profiles (A) of the syntheses starting from zirconium(IV) chloride, TEM image (B), a SAED pattern as an inset, and the XRD pattern (C) of the synthesized powder and a reference pattern of an amorphous $TiS_2$ (C). . . . .	48
3.8	Color, temperature, and pressure profiles (A) and the resulting powder's XRD pattern (B) of synthesis starting from $HfCl_4$ . . . . .	49
3.9	Color, temperature, and pressure profiles (A) and the resulting powder's XRD pattern (B) of synthesis starting from $VO_2$ . . . . .	50
3.10	Color, temperature, and pressure profiles (A) and the resulting powder's XRD pattern (B), with a TEM image (1) and SAED pattern (2) as insets, of synthesis starting from triisopropoxyvanadium(V) oxide. . . . .	51
3.11	Color, temperature, and pressure profile (A) of the synthesis starting from 1-dodecanethiol and $NbCl_5$ and an amplification (B) of the initial part of the profile. . . . .	52
3.12	X-ray diffraction pattern (A) and transmission electron microscopy (TEM) image (B), including an amplified region with measurements of a particle as an inset and the hexagonal crystal structure $2H-NbS_2$ adapted from reference [159], of the synthesized powder starting from $NbCl_5$ . . . . .	53
3.13	Color, temperature, and pressure profiles (A) and the resulting powders' XRD pattern (B) of two syntheses starting from $TaCl_5$ , one performed under temperature control and the other in constant power (20 W) mode. . . . .	54
3.14	Color, temperature, and pressure profiles of the syntheses starting from $Cr(acac)_3$ (A) or $CrCl_3 \cdot 6H_2O$ (C), pictures of both syntheses (B), and the XRD pattern from the powder starting with $CrCl_3 \cdot 6H_2O$ (D). . . . .	56
3.15	Color, temperature, and pressure profiles of the syntheses starting from $MoO_2$ (A), the resulting powder's and reagent's XRD patterns (B). Starting from $MoCl_5$ , a TEM image (C), with a SAED pattern as an inset, and the XRD pattern (D). . . . .	57
3.16	Color, temperature, and pressure profiles of the syntheses starting from $WO_2$ (A) or $WCl_6$ (C), and the respective XRD patterns (B) and (D), the latter with a TEM image and SAED pattern as insets. . . . .	58
3.17	Color, temperature, and pressure profiles (A) of the synthesis starting from $Mn(CH_3CO_2)_2 \cdot 4H_2O$ and the obtained powder's XRD pattern (B). . . . .	59
3.18	Color, temperature, and pressure profiles (A) of the syntheses starting from $FeCl_3 \cdot 6H_2O$ or $FeSO_4 \cdot 7H_2O$ and the XRD pattern from the synthesis with $FeSO_4 \cdot 7H_2O$ (B). . . . .	61
3.19	Color, temperature, and pressure profiles of the synthesis starting from iron(III) acetylacetonate with three color transitions marked at (1), (2), and (3). . . . .	61



3.20	Color, temperature, and pressure profiles of the synthesis starting from $\text{CoCl}_2 \cdot 6 \text{H}_2\text{O}$ with three color transitions marked at (1), (2), (3), and (4), the XRD pattern of the obtained powder with the reference for $\text{Co}_9\text{S}_8$ , a TEM image as an inset with amplification as a sub-inset (B), the diffuse reflectance spectrum of the powder (C) and the corresponding Tauc plot (D).	62
3.21	Color, temperature, and pressure profiles (A) of the synthesis starting from $\text{Ni}(\text{CH}_3\text{CO}_2)_2 \cdot 4 \text{H}_2\text{O}$ with four transition moments marked from (1) to (4), the obtained powder's XRD pattern (B), and three TEM images with (2) and (3) as zooms from (1).	64
3.22	Color, temperature, and pressure profiles (A) of the synthesis starting from $\text{CuO}$ and XRD pattern (B).	65
3.23	Transmission electron microscopy images (1, 3, and 4) and the particle size distribution (2) from measurements from (1) of the synthesized $\text{Cu}_2\text{S}$ particles starting from $\text{CuO}$ .	66
3.24	Color, temperature, and pressure profiles (A) of the synthesis starting from $\text{Cu}_2\text{O}$ and XRD pattern (B).	67
3.25	Tauc plot obtained from the diffuse reflectance spectrum of the powder obtained from the synthesis starting from $\text{Cu}_2\text{O}$ .	67
3.26	Color, temperature, and pressure profiles (A) and the XRD pattern (B), with a TEM image and the particle size distribution as an inset, of the synthesized powder starting from $\text{AgNO}_3$ .	68
3.27	Tauc plot calculated from the diffuse reflectance spectrum of a powder from a synthesis starting from $\text{Ag}_2\text{O}$ .	69
3.28	Color, temperature, and pressure profiles (A), TEM image (B), with the particle size histogram as an inset, X-ray diffraction pattern (C) and an SEM image (D) of synthesis starting from zinc(II) acetate dihydrate.	70
3.29	Raman spectrum of the powder obtained from the synthesis starting from 1-dodecanethiol and zinc(II) acetate dihydrate.	71
3.30	Emission and diffuse reflectance spectrum (A) and Tauc plot calculated from the diffuse reflectance spectrum (B) of a powder from a synthesis starting from zinc(II) acetate dihydrate and manganese(II) acetate tetrahydrate as the dopant.	72
3.31	Color, temperature, and pressure profiles (A) of the synthesis starting from cadmium(II) acetate, with two color changes marked as (1) and (2), and the XRD pattern (B) with a TEM image as an inset.	73
3.32	Color, temperature, and pressure profiles (A) of syntheses starting from $\text{InCl}_3$ , with maximum temperatures of $300 \text{ }^\circ\text{C}$ (T300) and $215 \text{ }^\circ\text{C}$ (T215) for 25 minutes, the XRD patterns from each synthesis (B), and a TEM image (C), with a SAED pattern as an inset, and an SEM image (D) of the (T300) synthesis.	75
3.33	Raman spectrum and Tauc plot of the powder obtained from the synthesis starting from 1-dodecanethiol and indium(III) chloride.	76
3.34	Color, temperature, and pressure profile (A) of the synthesis starting from tin(II) 2-ethylhexanoate and the resulting powder's XRD pattern (B), TEM image (C) with a SAED pattern as an inset and an SEM image (D).	77
3.35	Raman spectrum (A) and Tauc plot (B) calculated from the diffuse reflectance spectrum of the powder obtained from the synthesis starting from tin(II) 2-ethylhexanoate.	78
3.36	Bismuth sulfide microwave-assisted synthesis attempt color, temperature, and pressure profiles (A) and two TEM images (B) starting from bismuth(III) nitrate pentahydrate.	79
3.37	Bismuth sulfide microwave-assisted synthesis attempt Color, temperature, and pressure profiles (A) and the XRD of the obtained powder (B).	80

3.38	Color, temperature, and pressure profiles of the microwave-assisted synthesis of $\text{CuFeS}_2$ (A) and photos of the reaction vessel taken at certain moments (B). . . . .	85
3.39	X-ray diffraction pattern (A) of the synthesized $\text{CuFeS}_2$ powder, with reference patterns below, and TEM image as inset showing large particles, and a TEM image with the corresponding particle size distribution below (B). . . . .	87
3.40	Color, temperature, and pressure profiles (A) and XRD patterns (B) of two synthesis replicas, with the particles washed with either ethanol or chloroform. . . . .	88
3.41	Transmission electron microscopy images (A) and the size distribution of particles (B) of $\text{CuInS}_2$ particles washed with ethanol. . . . .	89
3.42	Color and temperature profiles (A) of syntheses starting from 1-dodecanethiol and either indium(III) chloride (In-S), tin(II) 2-ethylhexanoate (Sn-S) or both (In-Sn-S) and the resulting XRD patterns (B) with SEM images as insets. . . . .	90
3.43	Diffuse reflectance spectrum (A) of the powder from the product of the synthesis starting from 1-dodecanethiol, indium(III) chloride and tin(II) 2-ethylhexanoate and the corresponding Tauc plots (B). . . . .	90
3.44	Color and temperature profiles (A) of syntheses starting from 1-dodecanethiol and either zinc(II) acetate dihydrate (Zn-S), or indium(III) chloride (In-S) or both (Zn-In-S) and the resulting powders' XRD patterns (B) with the SEM images as insets. . . . .	92
3.45	Diffuse reflectance spectrum of the powder from the product of the synthesis starting from 1-dodecanethiol, zinc(II) acetate dihydrate and indium(III) chloride. . . . .	92
3.46	Color profiles (A) of syntheses starting from 1-dodecanethiol and either zinc(II) acetate dihydrate (Zn-S), tin(II) 2-ethylhexanoate (Sn-S), or both (Zn-Sn-S) and the resulting XRD patterns (B) with SEM images as insets. . . . .	93
3.47	Raman spectra of the powders from the syntheses involving 1-dodecanethiol with either tin(II) 2-ethylhexanoate (Sn-S), zinc(II) acetate dihydrate (Zn-S) or both (Zn-Sn-S). . . . .	94
3.48	Tauc plots (A) and (B) calculated from the same diffuse reflectance spectrum of the powder from the product of the synthesis starting from 1-dodecanethiol, zinc(II) acetate dihydrate and tin(II) 2-ethylhexanoate. . . . .	95
3.49	Color, temperature, and pressure profiles of a synthesis in 1-dodecanethiol, involving either $\text{ZrCl}_4$ (A), barium triflate (B), both reagents (C), and $\text{Ba}(\text{NO}_3)_2$ and $\text{ZrCl}_4$ (D). . . . .	96
3.50	X-ray diffraction pattern of the resulting washed and dried powder from the synthesis attempt to obtain $\text{BaZrS}_3$ . . . . .	97
3.51	Color, temperature, and pressure profiles (A) of the syntheses (A1) and (A2) starting from $\text{CuI}$ , $\text{InCl}_3$ and tin(II) 2-ethylhexanoate and the XRD patterns of the powders resulting from the respective synthesis (B). . . . .	98
3.52	Normalized red color profile plotted against the heating rate of the two syntheses (A1), high temperature $300\text{ }^\circ\text{C}$ and short duration, and (A2), lower temperature ( $225\text{ }^\circ\text{C}$ ) and longer duration, according to Figure 3.51. . . . .	99
3.53	Color, temperature, and pressure profiles (A) of the synthesis starting from $\text{CuI}$ , $\text{AgNO}_3$ , and $\text{InCl}_3$ and the XRD pattern of the resulting powder (B). . . . .	101
3.54	Color profiles (A) of syntheses starting from 1-dodecanethiol and either zinc(II) acetate dihydrate (Zn-S) and the powder obtained from the synthesis shown in Section 3.3.1.4 (Zn-In-S), indium(III) chloride (In-S), tin(II) 2-ethylhexanoate (Sn-S) or the three precursors (Zn-In-Sn-S) and the resulting XRD patterns (B) with SEM images as insets. . . . .	102
3.55	Raman spectra of the powders from the syntheses involving 1-dodecanethiol with either indium(III) chloride (In-S), tin(II) 2-ethylhexanoate (Sn-S), zinc(II) acetate dihydrate or the three (Zn-In-Sn-S). . . . .	103

3.56	Diffuse reflectance spectrum (A) of the powder from the product of the synthesis starting from 1-dodecanethiol, zinc(II) acetate dihydrate indium(III) chloride and tin(II) 2-ethylhexanoate and the corresponding Tauc plots (B). . . . .	103
3.57	Pictures of synthesis performed starting from $\text{Cu}(\text{NO}_3)_2$ , $\text{NbCl}_5$ , nickel(II) acetate, and $\text{RuCl}_3 \cdot x\text{H}_2\text{O}$ . . . . .	106
3.58	Temperature profiles versus time and energy fed to the microwave reactor's magnetron and the red color values plotted against time of synthesis involving 1-dodecanethiol and $\text{AgNO}_3$ , performed using the automated temperature control mode or the constant power mode at 20 W, 30 W or 40 W. . . . .	109
3.59	Temperature profiles of a microwave-assisted synthesis involving 1-dodecanethiol and $\text{AgNO}_3$ , with readings performed by an infrared sensor and ruby thermometer (A), the difference between the readings from the infrared sensor and the ruby thermometer (B), the infrared sensor readings between two equivalent synthesis (C) and their red pixel values profiles (D). . . . .	110
3.60	Red color value profiles plotted against the energy (A) and time (B) and temperature profiles against the energy (C) and time (D). . . . .	112
3.61	X-ray diffraction patterns patterns of syntheses at different maximum temperatures, starting from either zinc(II) acetate dihydrate, 300 °C (Zn300) and 100 °C (Zn100), or silver(I) nitrate, 300 °C (Ag300), 190 °C (Ag190), or 135 °C (Ag135). . . . .	113
3.62	Transmission electron microscopy images of powders obtained from syntheses starting from zinc(II) acetate and kept at 300 °C for different times at 300 °C, 5 minutes (A), 15 minutes (B), and 25 minutes (C). . . . .	113
3.63	Color, temperature, and pressure profiles (A) of two syntheses (R1 and R0.1) starting from tin(II) 2-ethylhexanoate and the resulting powders' XRD patterns (B). . . . .	114
3.64	Red color profile (A) or temperature (B) plotted against the energy supplied to microwave magnetron, starting from tin(II) 2-ethylhexanoate. . . . .	115
3.65	Red color and temperature profiles plotted against the energy supplied to microwave magnetron, for the syntheses involving the precursors containing the elements Zn, Nb and a mixture of Cu and Fe. . . . .	116
3.66	X-ray diffraction pattern of silver thiolate with the representation of the complex as an in-set. . . . .	116
3.67	Color, temperature, and pressure profiles (A) and XRD patterns (B) of various microwave-assisted synthesis starting from 1-dodecanethiol and copper precursors. . . . .	118
3.68	Comparison between the XRD patterns of four synthesis, starting from either $\text{Ag}_2\text{O}$ or $\text{AgNO}_3$ , performed in the dark or with illumination from the microwave reactor's internal lamp (light). . . . .	121
3.69	Comparison between the XRD patterns (A) and TEM images (B) of two zinc sulfide synthesis, starting from zinc(II) acetate dihydrate, with one performed under irradiation from the microwave reactor's internal lamp (light) and the other in the (dark). . . . .	122
3.70	Scheme representing the three syntheses with consecutive reutilization of the previously used 1-dodecanethiol (A), color and temperature profiles (B) and red pixel value and temperature profiles plotted against the energy (C) of each three syntheses. . . . .	124
3.71	X-ray diffraction patterns of the three powders obtained after reusing the thiol from synthesis 1 in 2, and from 2 in synthesis 3. . . . .	125
3.72	Temperature profile against the energy supplied to the microwave reactor's magnetron of syntheses starting from 1-dodecanethiol and either zinc(II) acetate dihydrate or zinc(II) acetylacetonate monohydrate. . . . .	126
4.1	Absorbance and transmittance spectra measured at 1000 nm over time of a suspension of SnS. . . . .	130

4.2	Photograph (A) and two microscope images (B) and (C) of the SnS film deposited by slot-die coating. . . . .	132
4.3	Schematic of the preliminary spray setup to deposit the synthesized SnS nanoparticles (A) and results including a microscope image (B), the particle size distribution and relevant statistical data from the microscope image (C) and transmittance and total reflectance spectra (D). . . . .	133
4.4	Schematic of the setup used to manually spray the metal sulfide inks onto a 75x25 mm Corning glass substrate. . . . .	134
4.5	Photograph of the film of tin sulfide deposited by spray (A1), microscopy image (A2), a particle size histogram (A3) taken from (A2), transmittance and diffuse reflectance spectra (B1), and Tauc plot (B2). . . . .	136
4.6	Raman spectrum (A) and two microscope images, one focused on the substrate's surface (B1) and another on the film's surface (B2), of the film obtained by spray from the tin sulfide ink. . . . .	137
4.7	Photograph of the film of zinc sulfide deposited by spray (A1), microscopy image (A2), transmittance and diffuse reflectance spectra (B1), and Tauc plot (B2). . . . .	138
4.8	Raman spectrum (A) and two microscope images, one focused on the substrate's surface (B1) and another on the film's surface (B2), of the film obtained by spray from the zinc sulfide ink. . . . .	139
4.9	Photograph of the film of niobium sulfide deposited by spray (A1), microscopy image (A2), transmittance and diffuse reflectance spectra (B1), and Tauc plot (B2). . . . .	140
4.10	Raman spectrum (A) and two microscope images, one focused on the substrate's surface (B1) and another on the film's surface (B2), of the film obtained by spray from the niobium sulfide ink. . . . .	141
4.11	Photograph of the film of copper iron sulfide deposited by spray (A1), microscopy image (A2), transmittance and diffuse reflectance spectra (B1), and Tauc plots estimated from the diffuse reflectance spectrum (B2) and the transmittance spectrum (B3). . . . .	142
4.12	Raman spectrum (A) and two microscope images, one focused on the substrate's surface (B1) and another on the film's surface (B2), of the film obtained by spray from the copper iron sulfide ink. . . . .	143
A.1	Color, temperature and pressure profiles (A) of the synthesis attempt, starting from BeO, to obtain a beryllium sulfide and the XRD pattern (B) of the obtained product. . . . .	185
A.2	Color, temperature and pressure profiles of the synthesis attempt to obtain MgS starting from magnesium stearate and three pictures of the vial at different synthesis times. . . . .	187
A.3	X-ray diffraction pattern of the resulting powder from the synthesis attempt to obtain MgS (A) and an amplification of the pattern (B). . . . .	188
A.4	Color, temperature and pressure profiles (A) and XRD pattern (B) of the synthesis starting from SrCl <sub>2</sub> . . . . .	189
A.5	Color, temperature and pressure profiles of the synthesis starting from barium(II) triflate. . . . .	190
A.6	Color, temperature and pressure profiles (A) of the syntheses starting from scandium(III) acetate hydrate, TEM images (B), with a SAED pattern as an inset, another TEM image (C), with the particle size histogram, and the XRD patterns (D) of the synthesized powder and the reagent. . . . .	192
A.7	Color, temperature, and pressure profiles (A) of the syntheses starting from yttrium(III) carbonate and the XRD pattern from the obtained powder (B). . . . .	194
A.8	Color, temperature and pressure profiles (A) and TEM image (B), with a SAED pattern as an inset, of the syntheses starting from aluminum(III) acetylacetonate. . . . .	207

A.9	Absorbance (A) and emission (B) spectra of a few drops in chloroform of the obtained mixture from the synthesis starting from aluminum(III) acetylacetonate and 1-dodecanethiol. . . . .	208
A.10	Color, temperature and pressure profiles of the syntheses starting from gallium(III) isopropoxide. . . . .	210
A.11	Color, temperature and pressure profiles (A) of the syntheses starting from tetramethoxysilane and a TEM image with a SAED pattern as an inset (B). . . . .	212
A.12	Color, temperature and pressure profiles of the syntheses starting from GeI <sub>4</sub> . . . . .	214
A.13	D-spacing plot calculated from the SAED pattern obtained from the synthesis starting from bismuth(III) nitrate pentahydrate, according to the procedure found in Section B.4. . . . .	216
A.14	Color, temperature, and pressure profiles (A) and stacked temperature and red color profiles (B) of two replica syntheses, 1 and 2, to attempt to produce the alloy between the elements Zn, Sn, In. . . . .	221
A.15	Color, temperature, and pressure profiles of two sequential syntheses, according to the ordered addition of precursors: Sn → In → Zn (A1) and Zn → In → Sn (A2), and their resulting powders' Raman spectra and XRD patterns, respectively (B1) and (B2). . . . .	222
A.16	Segments of periodic tables showing which precursors developed electric arcs during the synthesis, marked by the element background; red - formed electric arcs, blue - no arcs. Each segment belongs to an anion: chlorides, oxides, or nitrates. . . . .	224
A.17	Segments of periodic tables showing which precursors developed electric arcs during the synthesis, marked by the element background; red - formed electric arcs, blue - no arcs. Each segment belongs to an anion: acetates, acetylacetonates, or others. . . . .	225
A.18	Total reflectance spectra (TR) and absorption spectrum of the copper iron sulfide film deposited by spray. . . . .	230



## List of Tables

3.1	Comparison of some direct band gaps calculated by GapExtractor v1.0 software and the python script developed in this work. . . . .	45
3.2	Metal element used in the metal sulfide binary synthesis, the corresponding periodic table group and its section. . . . .	46
3.3	Compilation of all successful (A) attempted to obtain binary metal sulfide nanoparticles of various elements, with the identification of the obtained product, crystal type, the particle size, measured and reference band gap, and comments with the temperature at which the metal sulfide formed ( $T_{formed}$ ). The unsuccessful (B) syntheses, with the precursor used and comments are also shown. . . . .	81
3.4	Compilation of all successful (A) attempted to obtain multinary metal sulfide nanoparticles of various elements, with the identification of the obtained product, crystal type, the particle or [crystallite] size, measured and reference band gap, and the temperature at which the metal sulfide formed ( $T_{formed}$ ) and unsuccessful (B) syntheses, with the obtained product, the expected product, measured and reference band gap, and $T_{formed}$ . . . . .	105
3.5	A table containing the particle size of each copper sulfide phase, their temperature of formation, and if during the synthesis electric arcs formed for each reagent used in the microwave-assisted synthesis with 1-dodecanethiol. . . . .	119
A.1	Reagents and solvents name, brand, and purity. . . . .	231





## Acronyms

**ALD** atomic layer deposition.

**CB** conduction band.

**CVD** chemical vapor deposition.

**DBP** dibenzotetraphenylperiflanthen.

**FRET** Förster resonant energy transfer.

**HOMO** highest occupied molecular orbital.

**IB** intermediate band.

**ISC** intersystem crossing.

**LUMO** lowest unoccupied molecular orbital.

**NIR** near-infrared.

**P3HT** poly(3-hexylthiophene-2,5-diyl).

**PVD** physical vapor deposition.

**RGB** red, green and blue.

**SAED** selected area electron diffraction.

**SEM** scanning electron microscopy.

**SF** singlet fission.

**TEM** transmission electron microscopy.

**TPA** two-photon absorption.

**TTA** triplet-triplet annihilation.

**VB** valence band.

**XRD** X-ray diffraction.



## Outline

**Chapter 1** is the current chapter which contains the structure of the document and a brief summary of the contents from each chapter.

**Chapter 2** comprises the motivation, objectives, a brief explanation of basic concepts, such as the definition of semiconductor, band gap, nanoparticle, and photophysical process of the light energy conversion. The nanoparticle synthesis, comparing various synthesis methods, and ink formulation and deposition methods are also explored in this chapter.

**Chapter 3** is dedicated to the metal sulfide nanoparticle synthesis method developed, control attempt, and characterization methods. The results of the synthesized materials are discussed, with a section dedicated to the binary metal sulfides which is organized by periodic table groups, followed by a section dedicated to the multinary metal sulfides synthesis. The influence of the synthesis parameters on the properties of the obtained materials and the sustainability of the syntheses were also discussed.

**Chapter 4** includes the results regarding ink formulations and film depositions and their characterization.

**Chapter 5** is a wind-up of the principal aspects of each chapter and a presentation of future uses of the results obtained.

The **Chapter 6** contains the published articles, presentations, and posters that resulted from this work and some indirectly related.

The **Appendix A** holds all the auxiliary data, plots, and information that was deemed important to support the discussion from the syntheses and inks chapters.

The **Appendix B** contains the raw Python 3 scripts used in this work.



# Introduction

The motivation that led to this work and the proposal of the approach used to achieve the goals are shown in this introductory chapter in the first two sections. Understanding the importance of semiconductor nanoparticles in today's technology requires some basic concepts that will be explored in the following sections. The final sections were dedicated to understanding ink formulation with the metal sulfide nanoparticles synthesized and their application in uniform and homogeneous thin films.

## 2.1 Motivation and Objectives

Developing efficient and green materials for solar cells is of the utmost importance. Enhancing their properties can further increase the efficiency of the solar cells contributing to new developments in the energy generation sector. Consequently, it may reduce carbon emissions due to energy production from fossil fuels and augment the energy harvested from the sun while becoming cheaper. Current silicon solar cells efficiently absorb the spectrum's ultraviolet, visible, and near-infrared parts but due to physical and design limitations, such as quantum, optical, thermal and resistance losses, only less than 30% of the captured energy can be converted to electricity (Figure 2.1). Silicon solar cells have been the most studied and applied, but lead-based perovskite solar cells have recently gained attention. To overcome the referred limitations of silicon, lead-based perovskites in tandem with silicon solar cells have been developed and achieved an energy conversion efficiency of around 29%, which should soon go beyond the 30% limit.[1] Although silicon is the most abundant element in the Earth's crust, the process to obtain pure silicon is energy-demanding, complex, and costly. More importantly, the drawbacks of using lead-based perovskites are the use of the toxic metal element lead and their poor resistance to ambient conditions, requiring advanced encapsulation to prevent their degradation and leaching to the environment. A group of materials called metal sulfides, especially those containing abundant, available, and non-toxic metal elements, are promising alternatives due to their optical and electrical properties. The range of band gaps is extensive, similar to the metal selenides and tellurides, from the ultraviolet to the near-infrared spectrum region, unlike the metal oxides that are restricted to the visible and ultraviolet. Although their efficiency in solar cells is not yet comparable with silicon-based or perovskite-based cells, by developing a simple and cheap synthesis and deposition method, this work strives to manipulate their properties and obtain a library of materials capable of absorbing the sun's full spectrum. The main goal of this work was to develop a simple, fast, reproducible, and sustainable synthesis method to obtain metal sulfide nanoparticles using environment-friendly reagents. This work is also integrated into the work plan of a European research grant, ERC-CoG: 647596 CapTherPV, where metal sulfide

nanoparticles, either as single compounds, alloys, or core-shell composites, were chosen as prime materials for the production of solar cells.

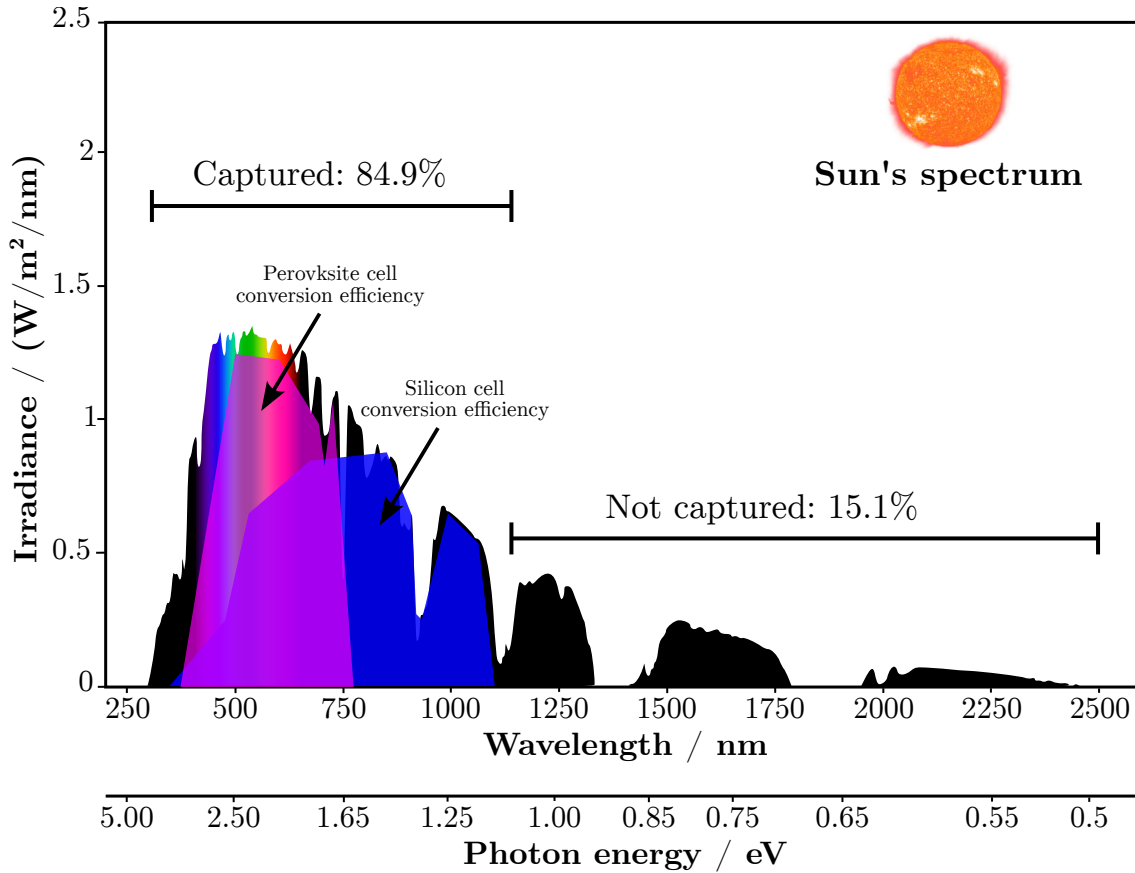


Figure 2.1: Irradiance spectrum of the sun at sea level, a picture of the sun, the fraction of the sun's spectrum currently captured by silicon and perovskite solar cells, and their efficiencies. The solar spectrum was adapted from [https://en.wikipedia.org/wiki/Sunlight#/media/File:Solar\\_spectrum\\_en.svg](https://en.wikipedia.org/wiki/Sunlight#/media/File:Solar_spectrum_en.svg); original by Robert A. Rohde; license CC BY-SA 3.0. and the efficiencies from <https://qdsolarinc.com/technology/>

The nanoparticles have been produced by solvothermal template-free microwave-assisted synthesis. The obtained materials were deposited as films by cast techniques, such as spray, slot-die cast, or physical evaporation. A final evaluation of the sustainability of the synthesis was accessed by attempting to recover the synthesis solvent and reusing it in subsequent syntheses. To achieve these goals, the work plan addressed the following studies:

1. Synthesis protocol definition to obtain single element and core-shell or multinary metal sulfide nanoparticles by determining the influence of synthesis time, temperature, and precursors on the size, morphology, material phase, and optical properties of the nanoparticles;
2. Recovery of the unreacted sulfur source to achieve reasonable sustainability and characterization of the obtained material with the reused source;
3. Optimization of the metal sulfide nanoparticle ink formulations and production and optical characterization of films.

The introduction contains a review of some concepts to understand better the materials and synthesis method chosen.

## 2.2 Review of Concepts

### Semiconductors

Semiconductors are materials used in every electronic device, such as computers, mobile phones, televisions, batteries, solar cells, etc. They accounted for an average annual profit of 335 billion dollars in profit[2] and are the basis of the digital era.[3] The most important property of semiconductors is their ability to serve as switches that can either be activated by light, temperature, or an electric potential difference, letting electricity flow or blocking it. Around 1834, Michael Faraday discovered that when a material with a low band gap is heated, such as silver sulfide, the gap is closed, and the electric conductivity increases as if it became a metal.[4] Five years later, the first evidence of the photovoltaic effect was observed by Alexandre Becquerel in a junction between a semiconductor and an electrolyte. The photoconductivity was discovered by Willoughby Smith in 1873 when he measured the resistance of Se and observed a dramatic decrease when light irradiated the cable. The first systematic studies on the photoconductivity of semiconductors were made in metal sulfides such as  $\text{Ag}_2\text{S}$  and  $\text{Cu}_2\text{S}$ . [5] Later, in 1883, Charles Fritts constructed the first solar cell consisting of a metal plate covered with a thin layer of Se with a gold layer on top, raising 1% efficiency.[6] The photovoltaic effect is possible since semiconductors contain electronic states; the valence and conduction bands are separated by an energy gap called the band gap. In bulk metals, the conduction and valence electronic states are close in energy, and the electrons navigate freely. On the other hand, insulators have the conduction and valence states far apart, and the electrons are confined to the lower states. The semiconductor materials are unique due to a band gap with energy that enables the excitation of electrons from the valence band and conduction band with light and temperature. A representation of the energy bands of the different types of materials described before, metals, semimetals, semiconductors, and insulators, are found in Figure 2.2.

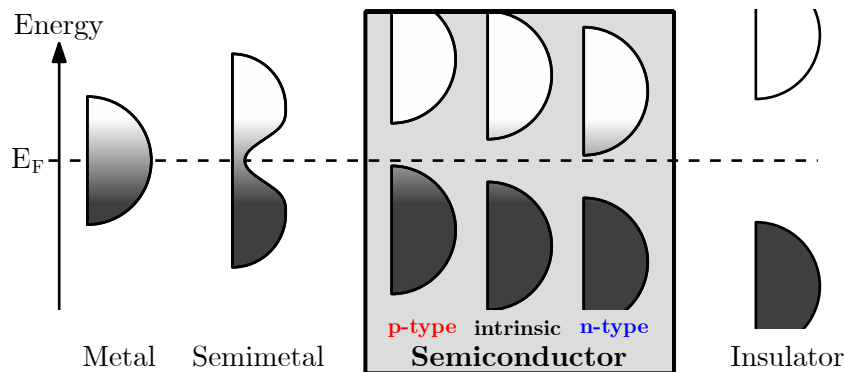


Figure 2.2: Energy band diagram of the electronic states of a metal, a semimetal, a semiconductor, and an insulator. The bands' width represents the density of states at a certain energy. The gray shades in the energy bands represent the distribution of the electrons, with black as filled and white as empty states. The maximum energy level where the electrons rest at 0 kelvin, known as the Fermi level, is represented by  $E_F$  and the dashed line.

Shinning light with equal or higher energy than the semiconductor's band gap will promote the

transition of electrons from the valence band to the conduction band. Free electrons are then created in the conduction band, and an equal number of holes are left in the valence band. This effect is behind critical applications of semiconductors in solid-state devices such as light sensors, solar cells, and light-emitting diodes. For example, solar cells can deliver electric energy to a load upon illumination of the p-type and n-type (pn) junction, in which the presence of an electric field is responsible for the charge separation to the respective electrodes.

## Band gap Tuning

The band gap is a characteristic that depends on its structure and chemical bonding. It can be tuned by modifying the material's composition or size. When the size is decreased to the nanoscale, quantum confinement is responsible for an increase in band gap (Figure 2.3).

A nanomaterial is any material with at least one dimension lower than 1000 nm or, in some scientific areas, strictly lower than 100 nm.[7] Nonetheless, these materials are extremely small and differ from their bulk counterparts since their properties depend highly on the material's size. The possibility to decrease the size of devices enabled the development of chips with enhanced functionality per unit area allowing computers with higher processing efficiencies and power. Photovoltaic cells gained boosted properties with nanomaterials. Nanomaterials have been successfully applied in efficient contacts for batteries and capacitors due to higher surface areas, and biomedical applications such as cancer treatment or diagnostics.

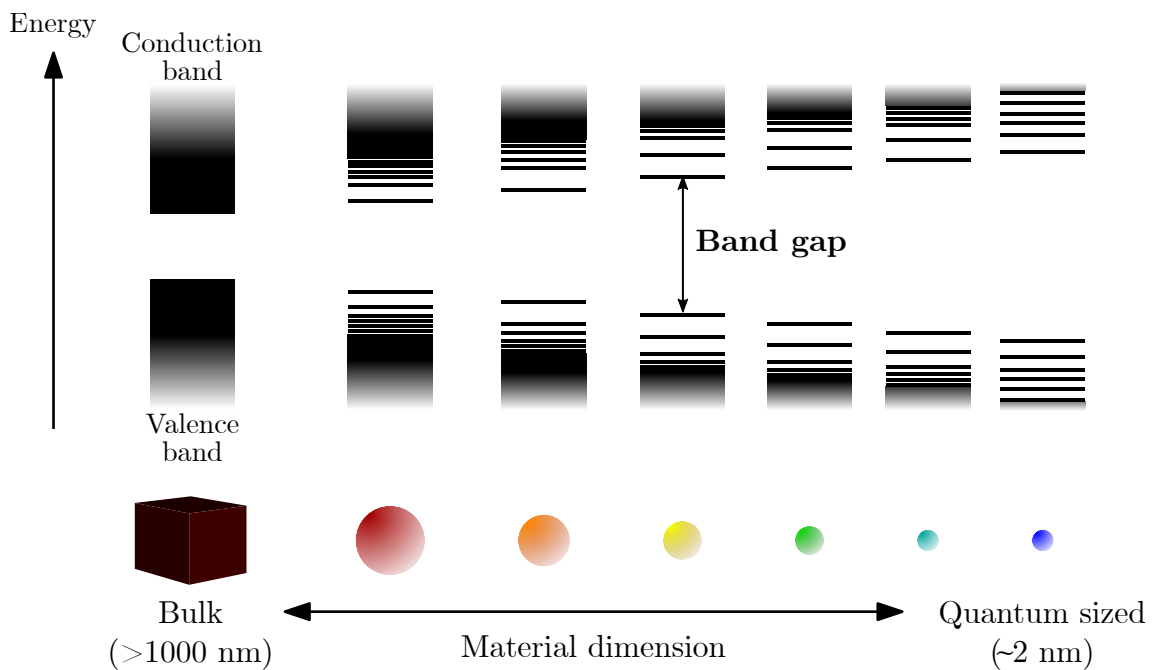


Figure 2.3: Schematic of the quantum confinement effect on the energy bands and band gaps of a material with a successive shorter dimension, from bulk to a quantum dot. The schematic was adapted from reference [8].

The ability to change a material's optical and electric properties by merely changing its size is a tremendous advantage since it can capture a broad range of photons with different energies with



the same material. Furthermore, nanomaterials also fulfill the requirement for the production of thin films by solution process allowing simultaneously the control of thicknesses below a micrometer and large area production using easy and cheap deposition processes.

Nano-sized materials are currently in significant demand for photovoltaics, photonics, thermoelectrics, and energy storage devices, such as batteries and capacitors. In particular, nanostructured metal sulfide materials have been paving their way into technology due to their outstanding properties compared to metal oxides. In gas sensing devices, sulfides of cadmium and tin require less power input and have higher selectivity.[9] Electrodes can also benefit from the intrinsic properties of metal sulfide materials.[10] The sulfides of iron, copper, cobalt, tin, and other elements, with a varied amount of metal to sulfur ratios, are good candidates for supercapacitors showing a relatively high capacitance and moderate stability, coupled with the de- and lithiation process.[10] Nanoscale lithium sulfide is surging as an attractive cathode electrode with high theoretical capacitance. Still, reports on the synthesis of this material are limited.[11] Light-emitting diodes (LEDs) require good quality electroluminescent hosts. The first phosphorescent material to be reported was doped barium sulfide, followed by calcium sulfide and zinc sulfide, which was recognized as an excellent host for other ions.[12] Luminescence properties from zinc sulfide, doped with manganese (orange emission), copper (blue emission), terbium (green emission), samarium (red emission), and holmium (white emission), are ideal for electroluminescent devices.[12] Metal sulfides have an adequate band gap, ranging from the ultraviolet to the near-infrared, when compared to metal oxides, serving as light absorbing materials for photovoltaics.[13] Photons emitted by the sun can be harvested by these nano-sized materials. For example, infrared photons can be captured with lead sulfide, an infra-red light absorber whose band gap can be tuned from 0.8 eV to 1.5 eV by changing the particles' size from 80 nm to 35 nm[14], visible photons with copper-indium sulfide with a tunable band gap from 1.65 eV to 1.95 eV with particle sizes from 7 nm to 3 nm[15] and ultra-violet photons with zinc sulfide tunable from 3.6 eV to 3.7 eV with particle sizes from 10 nm to 2 nm.[16].

The band gap can be tuned by mixing elements. Alloys that have combined properties can be obtained according to the percentage of each of its constituents. Using a specific example, the semiconductor  $\text{AgInS}_2$  was a promising material for hydrogen gas generation by splitting water. Still, the conduction band was not at the correct energy level. An adequate current density was obtained by alloying the material with the element Ga to enhance the water splitting efficiency.[17] Concerning solar cell application, silicon, one of the most abundant and environmentally friendly materials, dominates the semiconductor and photovoltaic industry. Current commercially available silicon solar cells attain 90% of the market share[18], have an efficiency of 24%, theoretically limited to 29%.[19] The development of alternative materials that enable higher conversion efficiencies has been pursued by researchers for a long time. The ultimate efficiency was achieved with tandem solar cells composed of different layers, typically III-V type semiconductors (e.g.,  $\text{InGaAs}$  and  $\text{GaInNAs}$ ), capture photons with different energies, reaching a broader spectral absorption and an efficiency of 44,7%, under concentrated light.[20] However, these compounds are scarce or environmental hazards, mainly due to the presence of arsenic. They may leach

into the underground water and soil, contaminate drinking water, and are dangerous to flora and fauna. Mining arsenic is also an unadvisable practice since it endangers workers.[21] Given that the previously mentioned compounds cannot be deposited by solution casting, an emerging technology based on the perovskite material structure has been considered suitable to fulfill those roles. The current top efficiency of lead-based perovskite solar cells is around 23%[22] but several aspects, such as long-term stability, are currently being addressed by Kobayashi et al. with the achievement of 20-year stability[23], and lead leaching problems are still under development.[24] An alternative to the mentioned materials is the metal chalcogenide group. They are less prone to chemical instability, relatively less toxic than lead-based perovskites and arsenides, and, as opposed to silicon, easily synthesized by sustainable wet chemical routes which permit their deposition using low-cost cast techniques. The elements present in group 16 of the periodic table are chalcogens, which include oxygen, sulfur, selenium, tellurium, and the radioactive element polonium. When reacted with metals, the product is known as metal chalcogenide. Metal sulfides, selenides, and tellurides are intrinsically less stable than metal oxides in ambient air. Given the high oxygen atmospheric concentration and more stable bonds with metals, sulfides, selenides, and tellurides will gradually convert to oxides. When metal sulfides are protected from oxygen, their extended properties can be used. The greater range of band gaps, lying between 0.3 eV and 5.5 eV[25][17], and conductivity available from metal sulfides, arise from differences in ion radii. Sulfide ions are softer, i.e., larger ion radius and more polarizable than the oxide ions. The metal-sulfide bond is more covalent or less ionic and can be easily distorted.[26] The stoichiometry in metal sulfides can be, therefore, different from the oxides. In metal sulfide compounds the possibility of formation of S–S can result in non-stoichiometric materials, yielding for example the nickel sulfides  $\text{Ni}_3\text{S}_2$ ,  $\text{Ni}_7\text{S}_6$ ,  $\text{NiS}$ ,  $\text{Ni}_3\text{S}_4$  and  $\text{NiS}_2$ , each with different properties. In contrast, the only stable oxide is  $\text{NiO}$ . [27] Further below in group 16 are selenium and tellurium, which yield promising materials when combined with transition metals. Metal selenides generally have a higher conductivity than metal sulfides, leading to higher efficiencies in hydrogen production[28], for example, and a band gap range from 0.3 eV to 5.6 eV.[29][17] Metal tellurides tend to yield a lower thermal and higher electric conductivities, requisites to obtain efficient thermoelectric devices[30] and their band gaps go from 0.5 eV to 3.5 eV[31].[17] The availability of selenium and tellurium is far lower than that of sulfur and oxygen, and prices are also higher. Based on sustainability and affordable materials, sulfur was chosen in this work as the chalcogen to produce semiconductor nanoparticles. These properties are summarized in Figure 2.4, with the prices of each element considered on the date of December of 2021 and with the references according to the following: oxygen[32], sulfur[33][34], selenium[35][36] and tellurium[37].

The choice of metal elements for synthesizing metal sulfide nanoparticles was made not only based on their properties but also on the elements' availability, both in the earth's crust and in terms of geopolitical affairs and price, as presented in Figure 2.5. Data regarding the abundance and price of the elements were taken from Wikipedia[38], and the availability was adapted from an edited version of a periodic table that depicts the current (2021) availability of the elements and their prospect.[39]

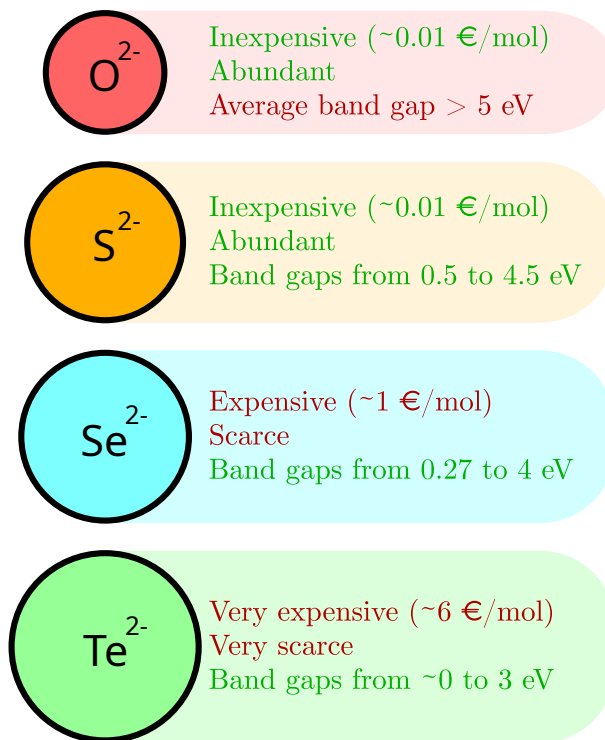


Figure 2.4: Scheme with the price and availability of the native elements oxygen, sulfur, selenium and tellurium and average band gap of the metal chalcogenides formed by them.

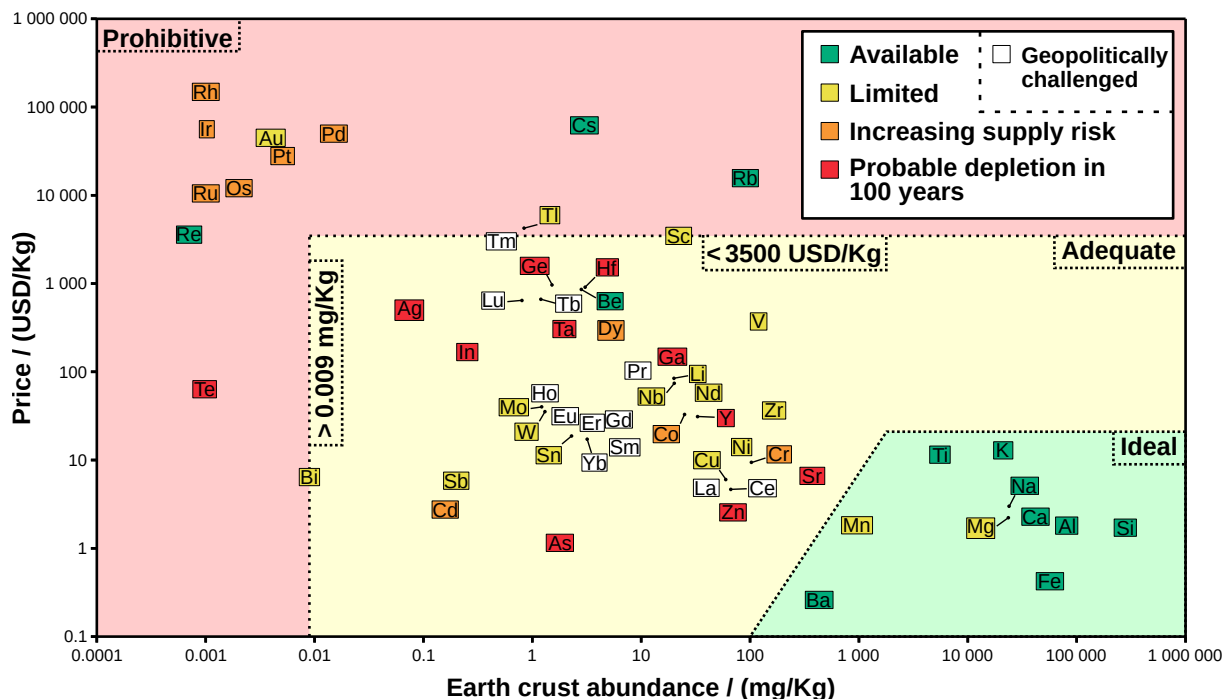


Figure 2.5: Scatter plot of the elements, with the background related with their availability, with their position dependent on price and abundance. The background color of each element reflects its availability and the prospect of future depletion based on its current use. The faint colored regions delimit ideal elements (green), adequate (yellow), and prohibitive (red).

Some elements were excluded from the synthesis scope, such as the noble gases, the prohibitively expensive such as the noble metals from groups 7 to 10 and periods 5 and 6, rubidium, cesium,

thallium, and tellurium, or due to geopolitical issues regarding availability, such as the lanthanide elements, or for being radioactive. Hydrogen, carbon, nitrogen, oxygen, phosphorous, and halogens (period 17) were also excluded due to the formation of liquids, gases, or explosives. Bismuth, the last non-radioactive element, was used as the threshold in terms of abundance, and scandium as the threshold for the price. Technetium (Tc) and promethium (Pm) were also excluded due to practically only existing synthesized elements, and mercury (Hg) and lead (Pb) were excluded due to being hazardous. Note that a high abundance does not necessarily mean the element is available for use. For example, the elements found over the ideal green region in Figure 2.5 are all rock-forming elements, except barium, which heavily contributes to their availability.

Some of the sulfides that contain very abundant and available elements from the green region in Figure 2.5 are not environmentally stable (e.g.,  $\text{TiS}_2$ ) and require the presence of another element, forming a more stable multinary sulfide. One example is  $\text{BaS}$  which is used as an emitter in electronic displays but is highly soluble in water[40], which leads to the same instability as lead-based perovskites. However, barium-based multinary sulfides such as the perovskite  $\text{BaZrS}_3$  which has a band gap between 1.8 eV and 1.9 eV[41], and  $\text{Ba}_2\text{TiS}_4$  with an estimated band gap of  $\sim 2.1$  eV[42] and non-perovskite  $\text{BaTiS}_3$  (0.3 eV)[43] are promising candidates to substitute the lead perovskite materials, due to their spectral coverage and environmental stability. Very recently, the alloy  $\text{NaBiS}_2$  was synthesized and revealed to have outstanding photonic and electronic properties, with a band gap of 1.4 eV, a substantial absorption coefficient, and long-lived charge carriers.[44] Although sodium is one of the ideal elements, bismuth is unfortunately borderline inadequate. Some alloys containing the abundant element Fe are also interesting, such as  $\text{CuFeS}_2$  which is known to be adequate for thermoelectric devices[45] and has a band gap of 0.5 eV[46]. Regarding the abundant lower weight alkaline metals Na, Mg, K, and Ca, these elements tend to form soluble sulfides but, like barium sulfide, when combined with other elements, they can be used in batteries. Due to their ionic features, such as the case of in  $\text{NaTiS}_2$ , they tend to be intercalated between layers of the other element's sulfide, which is ideal for electrodes.[47] Aluminum sulfide is also reactive towards humidity but combined with barium, for example, the compound formula is stable and has a band gap above 3.95 eV.[48] Finally, the most abundant and available element, Si, forms what are known as thiosilicates which are easily attacked by water, but some multinary sulfides have interesting properties. For example,  $\text{Mg}_2\text{SiS}_4$  can be used as a host for rare-earth elements such as europium  $\text{Mg}_2\text{SiS}_4$ , which serves as a light source. Details on the inclusion of dopants in hosts are discussed in the following sections.

## Photon Conversion

The focus of semiconductor research applied to photovoltaics has been pursuing materials with a band gap optimized to harvest the entire solar light spectrum. The limitation of using one semiconductor for that purpose is that the spectral quantum efficiency of the material is limited to its band gap.

To better understand this section, Jablonski diagrams[49], such as the generic one found in Figure 2.6, will be used to represent energy levels.

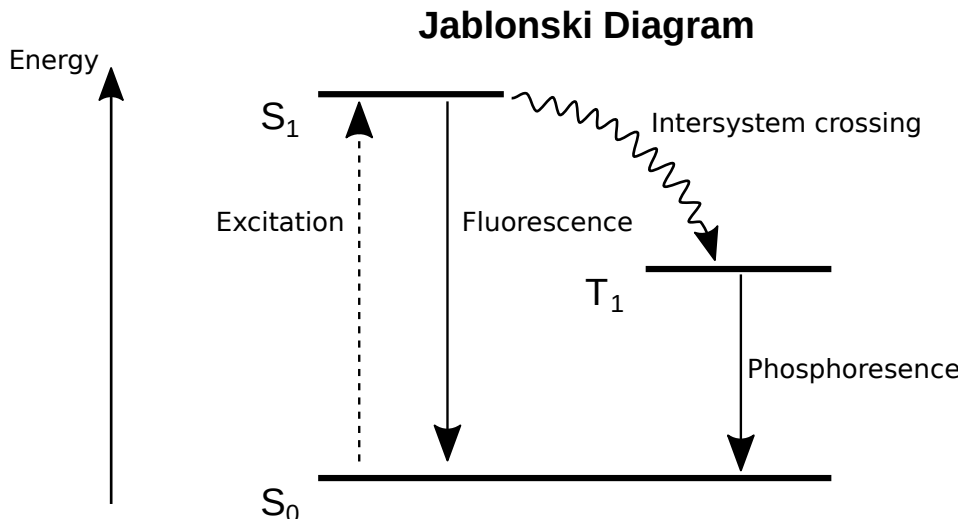


Figure 2.6: Generic representation of a Jablonski diagram with energy levels. Intersystem crossing (wavy curved arrow), excitation (up arrow), fluorescence and phosphorescence (down arrows), and energy level denominations are also represented. The S and T stand for singlet and triplet, respectively, while the subscript is the energy level relative number.

Molecular orbitals theory says that when two atoms bond, for example, two hydrogen atoms, their atomic orbitals combine and form two new states: a higher energy antibonding orbital and a lower energy bonding. When more atoms are put together, new states arise, and in that collection of states, the lowest energy level with no electrons and the one with the highest energy level occupied with electrons are called lowest unoccupied molecular orbital (LUMO) and highest occupied molecular orbital (HOMO), respectively. This energy level description is relatively simple to evaluate for molecules that contain a small number of atoms. Oversimplistically stating, inorganic materials, which are usually groups of thousands, millions, etc., atoms bonded together, have too many energy levels to be described. They are instead treated as two bands: the conduction band (CB), which is the lowest energy band with no electrons, and the valence band (VB), which is the highest energy band occupied with electrons. The separation between these two bands, as explained previously, is the band gap. For simplicity's sake, in the following concept explanations, one can consider the pairs (CB and LUMO) and (VB and HOMO) equivalents.

Several processes can occur upon the absorption of a photon by an atom or a molecule. After the exciting an electron from the fundamental state  $S_0$  (VB or HOMO) to  $S_1$  (CB or LUMO), the electron can either decay back to  $S_0$  (fluorescence) or transition, losing some energy, to a

forbidden triplet state  $T_1$  intersystem crossing (ISC) and decaying back to  $S_0$  (phosphorescence). All these processes can happen in an individual atom or molecule. When another substance is in immediacy, the energy from an excited state of a substance may be transferred radiatively to another in the form of a photon or via dipole-dipole coupling, known as Förster resonant energy transfer (FRET), which is a long-range process. However, the efficiency of a FRET is inversely proportional to the distance, with an exponential factor of 6.[50]

A close-range process can also occur under a different mechanism known as Dexter electron transfer.[51] It differs from FRET since the energy transfer involves the relay of an electron from the donor to the acceptor, while the distance between them must be below 1 nm, as represented in Figure 2.7, and ideally chemically bonded.[52]

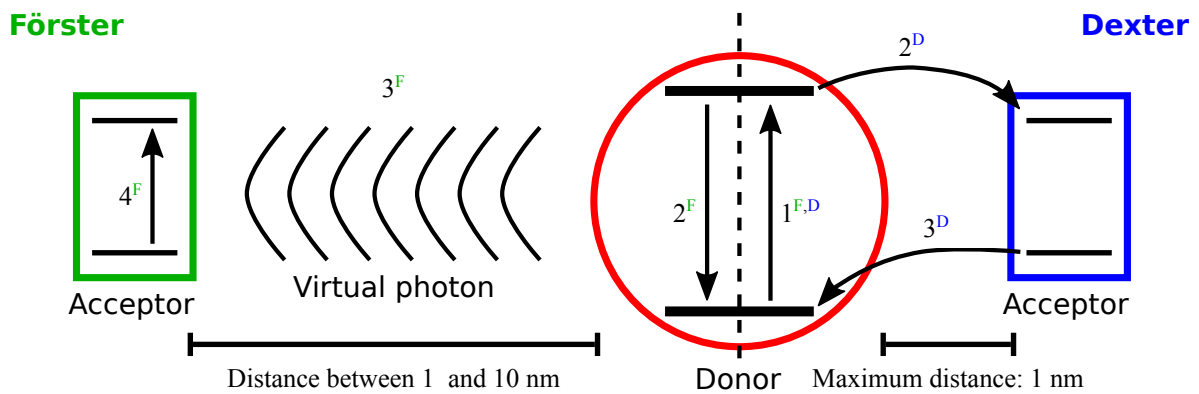


Figure 2.7: Diagram representing a Förster and a Dexter energy transfer process, starting from the excitation of an electron from the ground level to the next one ( $1^{F,D}$ ). Dexter: transfer of the excited electron from the donor to the acceptor ( $2^D$ ), with the simultaneous electron transfer from the acceptor's ground level to the donor's. Förster: the decay of the excited electron in the acceptor to the ground level ( $2^F$ ), followed by the emission of a virtual photon ( $3^F$ ), which the acceptor absorbs, exciting the electron in its ground level to a higher state ( $4^F$ ).

Attempts to construct solar cells able to capture and convert all the radiation of the solar spectrum have been pursued. Solar cells composed of various stacked thin layers of semiconductors are a possible solution, but the current supplied by the device is limited to the lowest yield from one of the layers in the stack. Instead of relying on a single or a stack of materials, an interesting approach that relies on photon interconversion is using three materials. The first layer, i.e., the first to face the light source, captures the most energetic ultraviolet photons and lets the remaining lower energy photons pass. The higher energy photons are then converted to visible and passed to the middle layer, which captures only the visible photons. Finally, the near-infrared photons traverse both upper layers and are absorbed by the final layer, converted to visible photons, and transmitted to the middle layer. Figure 2.8 shows an example of an absorption spectrum of a device composed of three layers of semiconducting materials, accompanied by the emission of the topmost and lowest layer, which lies in the absorption region of the middle layer.

Regarding the two main interconversion processes of interest, downconversion and upconversion, both processes can take place by a series of possible mechanisms. They have been studied for decades but are only recently being unraveled and detailed. Contrary to the typical photo-

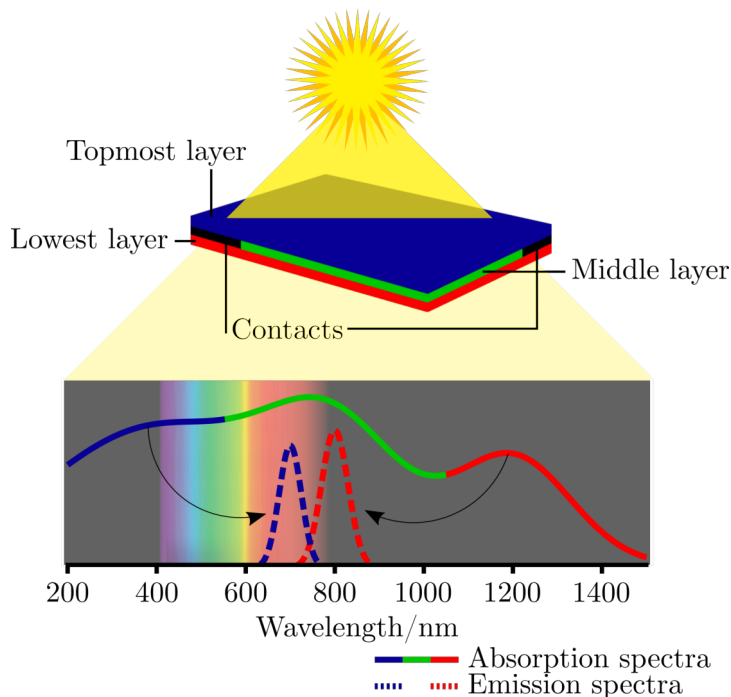


Figure 2.8: Example of the absorption spectra (full lines) of a solar cell composed of three layers and the emission spectrum (dashed lines) of the lowest and the topmost layer, according to the solar cell structure in the inset. The arrows represent the conversion of low and high-energy photons to the absorption region of the middle layer. The color of the lines in the spectra matches the color of the layers in the device.

electronic (spectroscopic) analysis used to study the conversion mechanisms, Seiler et al.[53] used femtosecond electron diffraction techniques, combined with real-time time-dependent density-functional theory and molecular dynamics simulations, to observe the molecular and atomic changes that occur during the conversion events. Furthermore, by using pentacene, one of the most studied and most efficient singlet fission (SF) molecules, they showed that to evaluate SF correctly and probably triplet-triplet annihilation (TTA), one must consider long-range intermolecular dynamics.

An overview of both downconversion and upconversion mechanisms is presented in the following sections.

### Downconversion

Downconversion is the most common process since it naturally happens when matter absorbs a photon and re-emits another with lower energy due to vibrational relaxation, leading to an effect known as the Stokes shift.[54] This effect is illustrated in Figure 2.9. The figure represents an example of an absorbance spectrum (green) with scattering effects typically observed in colloidal suspensions,[55] two absorption bands (A and B), an excitation spectrum (magenta) corresponding to the absorption band B, which is a representation of the luminescence intensity at the peak of the emission spectrum (blue) plotted against the excitation energy. The excitation spectrum is usually similar to the absorbance spectrum, but not all absorbance bands lead to an emission

upon excitation.

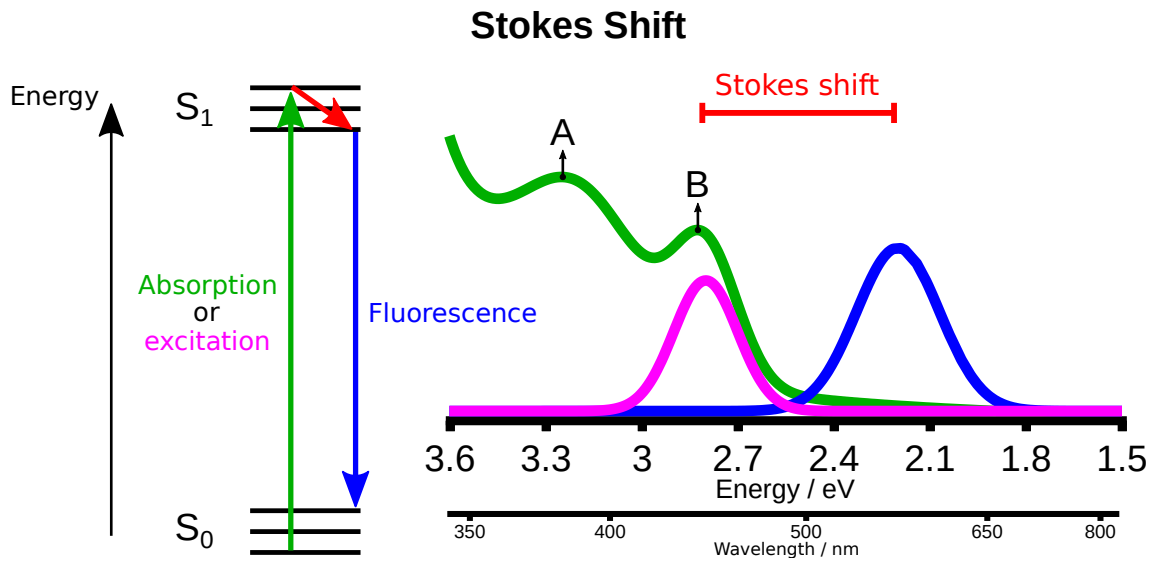


Figure 2.9: Example of an absorbance (green), excitation (magenta), and emission (blue) spectra, illustrating the Stokes shift (red). A Jablonski diagram of vibrational energy levels of a conduction band ( $S_0$ ) and a valence band ( $S_1$ ) is shown to the left, in parallel to the corresponding spectra to the right, with an example of an absorption, excitation spectra corresponding to the absorption band B and no emission from absorption band A, vibrational relaxation (Stokes shift) and the emission band.

The downconversion mechanisms mentioned before lead to significant energy losses due to the emission of phonons - as heat. A more efficient alternative downconversion mechanism is called SF, depicted in Figure 2.10. A given substance A1 absorbs a high energy photon, exciting the electron from ground state  $S_0$  to a higher level  $S_1$ , followed by a radiative decay to its triplet state  $T_1$ . The previous decay is enough to excite another substance, A2, from  $S_0$  to  $T_1$ .

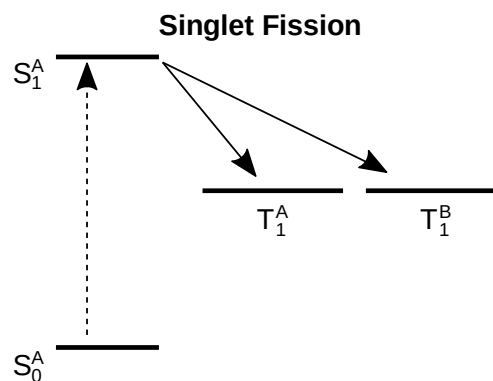


Figure 2.10: Jablonski diagram of the singlet fission mechanism. Substance A is excited by a high-energy photon. After the electron decays to the triplet, the energy radiated is used by substance B to excite an electron to its triplet state. The decay of both triplets yields two photons, and the energy of both is not higher than that of the singlet of A.

After step 1 in Figure 2.10, the transient state with both triplets spatially separated and spin correlated generates two distinct and uncorrelated triplets.[53] A high-energy photon is split into two photons, naturally yielding a photon conversion quantum efficiency of 2. However, as



stated in a review on singlet fission by Smith and Michl[56], there are four conditions to consider regarding SF efficiency. The first aspect is the impossibility of SF happening on a single molecule with only one chromophore since it cannot accommodate two excited triplet states. Nevertheless, singlet fission can be observed if small chromophores - molecules with one or more light-absorbing chemical groups - are in a solid-state phase, such as rubrene[57], which is typically seen in the literature as an upconverter. The second condition entails the energy match between the singlet and the two triplets. For instance, the sum of the energy of the triplets should not exceed the energy of the singlet. Thirdly, if the coupling between two chromophores is too strong, the system behaves as a single chromophore. The same happens when the two chromophores are covalently linked, but a crystal of the same chromophore will yield SF at a higher efficiency. The last condition pertains to the diffusion of the formed triplets after the SF takes place. Molecular solids and conjugated polymers rapidly diffuse the excited triplets, preventing the reverse of SF: the triplet-to-triplet annihilation described in section 2.2.

### Upconversion

An exhaustive review by Zhou et al. on upconversion materials and applications can be found in reference [58]. There are two main approaches to upconversion systems: the lanthanide energy ladder-like phosphors and the triplet-to-triplet annihilation mechanism. Both mechanisms usually have the same structure involving a sensitizer and the upconverter. The system with lanthanide elements requires a host to prevent nonradiative decays, such as heat, which is essential to sustain a useful upconversion efficiency. The host must have a low lattice phonon energy typical of heavier atoms to achieve this. The most used host is  $\text{NaYF}_4$ , doped with lanthanides such as  $\text{Yb}^{3+}$  coupled with  $\text{Er}^{3+}$ ,  $\text{Tm}^{3+}$  or  $\text{Ho}^{3+}$ .

Rare-earth elements have inherent problems related to availability and toxicity. It was shown that lanthanides tend to accumulate in the body of rats and interfere with calcium and proteins.[59] Regarding the availability, world distribution of these elements are mostly confined to China, which originates from political imbalance[60], and there is still much development to be done in terms of sustainable extraction and recycling.[61] Taking into account that for two-photon absorption (TPA) is relatively inefficient[58], TTA is a better alternative. A TTA system comprises a sensitizer that absorbs lower energy light, such as lead sulfide, and an annihilator, such as rubrene, that upconverts low energy to high energy photons; in this particular case, near-infrared (NIR) to visible.[62] The sensitizer absorbs the lower energy photons, followed by ISC to its triplet. After the triplets from two annihilators are excited with the energy from the sensitizer and when the two annihilators collide, the energy is transferred to one of the annihilator's higher energy triplets followed by ISC to the singlet, which can then decay yielding a high energy photon, as shown in Figure 2.11.

Recently, a TTA system comprising a lanthanide complex sensitizer and rubrene as the annihilator was reported with an efficiency of less than 0.01. The advantage of using the complex resides in its longer triplet lifetime and absence of absorption in the range of upconverted light emission

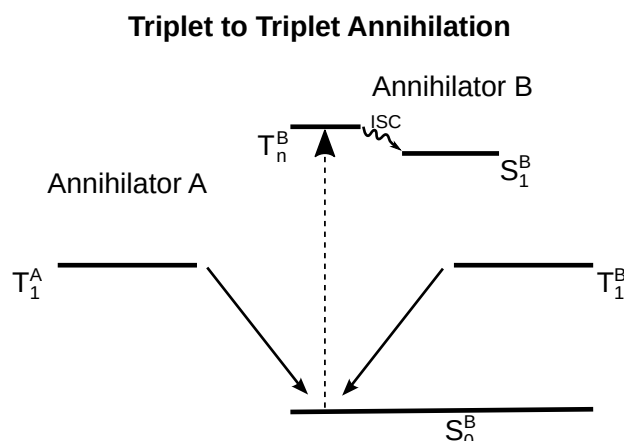


Figure 2.11: Jablonski diagram of the triplet-to-triplet annihilation mechanism involving two annihilators (A and B) pre-sensitized by a sensitizer. The energy from the triples of both A and B is converted to a singlet with an energy no higher than the sum of the triplets' energy.

(re-absorption). [63] Nonetheless, alternatives to these heavy metals should be considered, even at the loss of some of the advantages stated before.

There are many organic molecules capable of TTA. These molecules are usually polycyclic aromatic or heterocyclic compounds.[58] Rubrene is one of them and has a fluorescence quantum yield of 98% in toluene[64] but degrades in air, forming a discolored endoperoxide.[58] However, a solar cell of any kind should be isolated and the degradation of its components minimal. There is a report that a crystal of rubrene, in the absence of a sensitizer, can upconvert NIR to visible light, albeit with only 0.0019[65] of upconversion efficiency compared to the 0.012[66] obtained with a solid-state PbS and rubrene mixture. Even though it has a fluorescence quantum yield close to unity, the efficiency of converting two triplets to a singlet is only around 0.15. While attempting to increase the overall upconversion efficiency, Radiunas et al. synthesized a modified rubrene with tert-butyl groups to increase its solubility and, consequently, its concentration. However, this resulted in a further decreased probability of conversion from two triplets to a singlet.[67] Given the ability of rubrene to also serve as a SF agent, most of the TTA is hindered. Using a second compound such as dibenzotetraphenylperiflanthen (DBP) forces the singlet exciton in rubrene, formed by TTA, to be transferred to itself, preventing the reverse and raising the upconversion.[66], [68]

Another possible contribution to lowering upconversion efficiencies is the fact that TTA occurs solely by the Dexter energy transfer mechanism since the dipole-dipole coupling FRET is restricted to spin-permitted transfers.[52] It is paramount that the distance between the donor and acceptor is below 1 nm. The similarity between the dependence of Dexter energy transfer efficiency and that of FRET towards the distance could help in adopting some strategies used in the past to minimize the distance between the donor and acceptor. In 2017, Morgner et al. created a contactless pressure measurement system based on the variation of the FRET efficiency.[69] The authors do not explicitly say that FRET efficiency could increase with pressure applied to the system. However, it is implicit that the densification, through applied pressure, could decrease the contact

distance between the donors and acceptors, such as the case where applying pressure during the fabrication of perovskite solar cells enhances its efficiency due to void suppression and increased contact between all components.[70] Another approach was made by Melle et al., in which they surrounded donor lanthanide containing  $\text{NaYF}_4$  with a silica shell, functionalized with  $(-\text{NH}_2)$  positive groups. The  $(-\text{COOH})$  negative groups attached to the acceptor CdSe nanoparticles tethered to the positive groups, guaranteeing proximity between both donor and acceptor. The authors concluded that the thinner the silica shell was, the higher FRET efficiency.[71]

A less toxic and cheaper alternative to rare-earth-containing systems is the copper indium sulfide semiconductor which is currently being commercially implemented in windows by UbiQD as light capturing material that re-emits, trapping the light between the two glasses and redirecting the light to solar cells in the window frame, achieving a conversion efficiency of 0.036.[72] Upconversion has also been demonstrated for zinc sulfide nanoparticles doped with manganese, from 1.3 eV to 2.1 eV.[73] Tin sulfide has been doped with copper to control the band-gap[74] and copper sulfide with cobalt to enhance light absorption and shift the band-gap from 2.0 eV to 2.1 eV.[75] Playing with these single metal sulfide properties and attempting to produce an alloy composed of the singular modified sulfides is an interesting way to cover the entire solar spectrum. Core-shell structures with metal sulfide shells and metallic cores contribute to the absorption efficiency of the nanocomposites due to the plasmon resonance enhancement, where the collective oscillation of the metal electrons with strong oscillating electric fields at the surface between metal and the semiconductor leads to higher absorption and emission of the nanocomposites.[76] This core-shell combination can further enhance a device's power conversion efficiencies. Using the alloy CZTS, Zhang et al. managed to synthesize gold nanoparticles with a CZTS shell (CZTS@Au), resulting in enhanced light absorption due to the plasmon resonance energy transference from the Au core to the CZTS shell.[77]

## 2.3 Synthesis Methods

The most common synthesis methods employed to fabricate metal sulfide nanoparticles are presented in this section. For a more complete overview of the various methods used to produce metal sulfide nanomaterials, refer to the review published by Chandrasekaran et al. in 2019.[78] The alternatives to microwave-assisted synthesis are shown in the following sections to demonstrate their advantages and disadvantages, regarding the synthesis of metal sulfide nanoparticles.

Traditionally, high-quality semiconductor thin films are produced using either physical vapor deposition (PVD) or chemical vapor deposition (CVD). Unlike the other methods presented in this chapter, these vapor deposition methods are, naturally, not a wet process but they are the most used production methods in microelectronics and the energy sector. Figure 2.12 A and B, respectively, show schematics of the PVD and CVD processes.

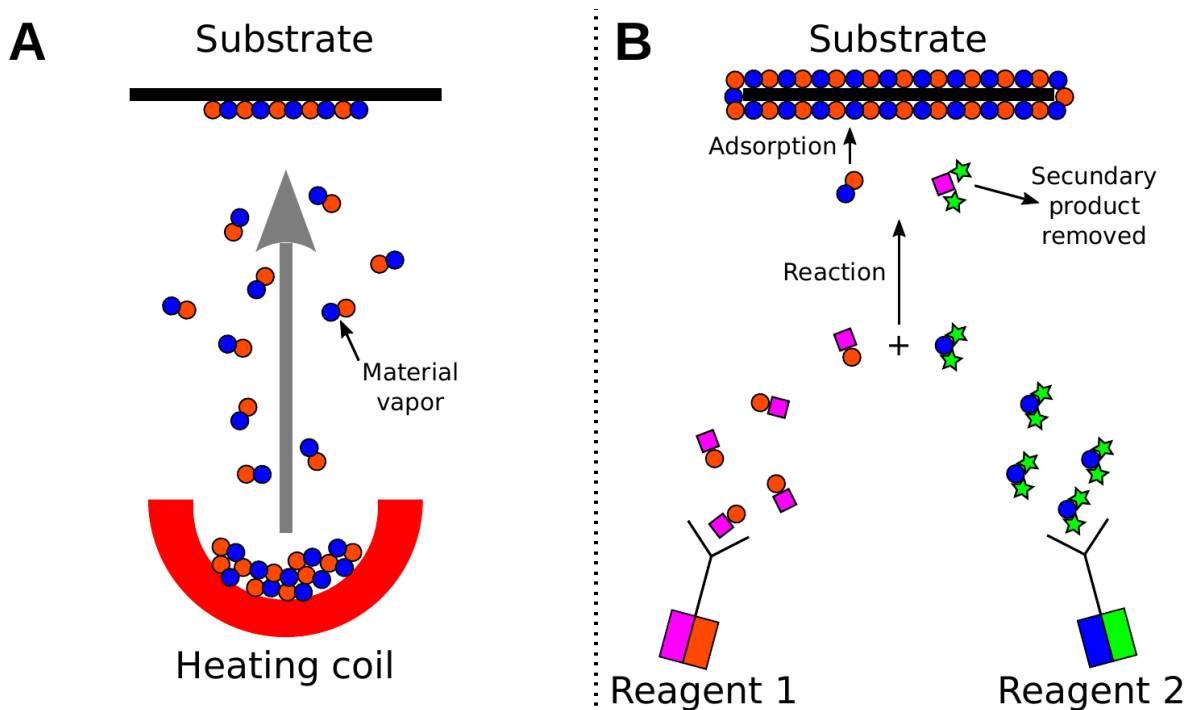


Figure 2.12: Schematic of a deposition performed by physical vapor deposition (A), with the material first heated to be vaporized and then condensing on the substrate, or by chemical vapor deposition (B), where two reactants produce the desired material, which is subsequently deposited on a substrate.

The main difference between both vapor deposition methods is that to obtain the desired material with CVD a chemical reaction occurs, whereas in the PVD the material itself is evaporated, under vacuum, directly to the substrate by thermal evaporation or by sputtering, i.e. by etching a target formed with the material using a plasma of a non-reactive gas. One advantage of CVD over PVD is the substrate coverage, which in the physical process is determined by the line-of-sight from the source to the substrate, while in the chemical process the vapor interacts with all of the available surfaces on the substrate. The most promising deposition method is a sub-class of CVD, called atomic layer deposition (ALD), which allows the production of materials at the atomic level,

consisting of coverage of any complex surface. It allows fabricating layers of semiconductors oxides, nitrides, and sulfides including elements such as Cu, Zn, Cd, In, and Sn. With this method, it is possible to control the thickness of the films with atomic resolution. Briefly, instead of obtaining the product in the gaseous phase, the first reagent is pumped into the chamber and left to adsorb onto the substrate, forming a monolayer, followed by the insertion of a second reagent which reacts with the first. The chamber is purged, to remove the secondary products and the cycle is repeated until the desired thickness is achieved. Production of ternary and quaternary alloys is also possible but suffers from difficulty to predict the non-linear relation between the input ratio between reagents and the actual alloy composition. In terms of production output, the process is slow (up to 3600 nm/h) and the equipment is expensive and not trivial to handle.[79]

Electric explosion wire is also a very promising and very high throughput method to produce fine nanoparticles, with relatively homogeneous sizes ranging from tens of nanometers to micrometers. Equally a non-wet process like the PVD and CVD methods it should be presented given its outstanding advantages. The method consists of heating a metal wire inside a reactor chamber, with the aid of an electric circuit with a capacitor that discharges a very high current. The metal reaches a very high temperature, liquefying, followed by an explosion that releases a plume of metal gas, composed of very small particles that react with the chosen atmosphere.[80] Metal sulfide nanoparticles can be produced in high quantities, up to hundreds of grams per exploded wire, with the electric explosion wire method.

Mechanochemical synthesis is a process where the reagents, typically in the solid state, are crushed together by ceramic balls in a grinding mill. The products are formed whilst the mechanical energy is transferred to the reagents.[81]

Still, in the domain of the mechanical and phonon-assisted synthesis methods, ultrasound-assisted or sonochemical synthesis method consists of injecting high-frequency sound waves into the reaction medium. The liquid vaporizes and forms tiny bubbles that, upon reaching a critical size, violently implode and create a hot spot with enough energy for the reagents to react and form the product.

The collapse of the bubbles also participates in the etching of the material present in the medium, leading to smaller particles.[82]

### **2.3.1 Conduction and Convection Heating**

Conduction and convection heating is the most classic and conventional form of synthesizing compounds. Heat is transferred from a hotter surface, such as heating mantle and oil baths, or a more direct heat source such as a flame, to the reactor containing reagents. Figure 2.13 shows a simplified schematic of a reactor heated by a mantle and the temperature gradient developed.

Through conduction and convection, heat travels throughout the reactor which slowly achieves temperature homogeneity. Achieving fast heating rates is not possible and when the solvent reaches its boiling temperature and evaporates, assuming an open reactor, the energy that was targeted at the reactants is trapped in the gaseous phase and is not in contact with them. Most

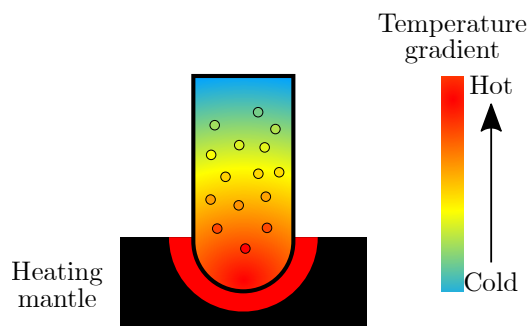


Figure 2.13: Schematic of heating mantle, where heat is only transferred due to phonon energy transference or mass effects such as convection and agitation. A qualitative temperature scale is shown to demonstrate the temperature gradient.

of the energy in the form of heat easily dissipates away from the target, making this method one of the least efficient. Some of the heat is also wasted heating the air surrounding the reactor. As the oldest method of heating a mixture, there is a multitude of results published in the literature regarding the synthesis of metal sulfide nanoparticles.

### 2.3.2 Microwave-assisted Heating

Given the numerous synthesis methods available to obtain nanoparticles, the microwave-assisted solvothermal synthesis method was chosen as the most convenient. High temperatures and pressures are achieved faster than the conventional heating method[83], leading to lower particle size, size dispersion, and higher crystallinity.[84] Figure 2.14 shows an example of a vessel, containing the reaction medium which partially absorbs the microwaves, and the reagent represented by small red circles, intensively absorbing the radiation and heating up preferentially. The vessel, which is usually made of quartz or borosilicate, is significantly more transparent to the radiation and stays relatively cooler than the medium inside. Microwave radiation frequency lies in the  $10^2$  GHz region; the photon has neither the energy to excite an electron, nor to induce a chemical reaction by itself and only couples with the rotational modes.[85] The reactions occur due to the formation of high-temperature heat spots that have enough energy to break chemical bonds, which also depends on the microwave absorption cross-section of the components; the capability of a compound to absorb a determined microwave frequency.

Regarding industrial scale production of the metal sulfide nanomaterials, except for the explosive wire method which can achieve gram product quantities and both mechanochemical and ultrasound-assisted methods which also achieve high amounts of product, the microwave-assisted synthesis method using one static reactor is not suitable. The construction of a big microwave reactor would require a bigger magnetron, which is a potential hazard due to the higher currents needed to produce microwave light. The microwave light penetration depth is no more than a few centimeters which further limits the volume of the reactor's chamber. Two solutions that can solve the previous problems are the use of many smaller microwave reactors in parallel or the use

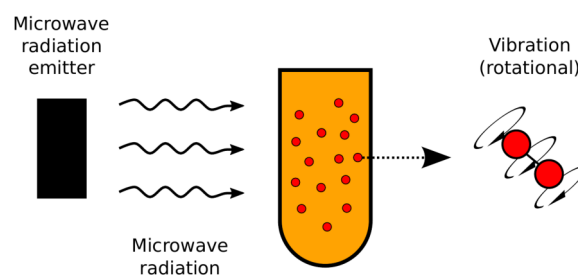


Figure 2.14: Schematic of a microwave reactor, where heating is a consequence of the absorption of microwave radiation. The orange (mildly hot) and red (very hot) colors illustrate the difference in temperature between the reaction medium and the reactants (small circles), respectively.

of a continuous flow microwave reactor, where the solution containing the reagents flows through the chamber, targeted by the microwave radiation, continuously forming the product and leaving the chamber.[86]

Microwave-assisted synthesis has some inherent problems when compared with the conventional synthesis using a heating mantle apparatus. The frequency of the light source used in a common kitchen microwave, or even most advanced microwave reactors, is 2.45 GHz. This is a limitation that was established to prevent interference with radio communications as well as due to being the optimal frequency to heat water and some organic and inorganic compounds.[87] Not all materials absorb that frequency and there is no special impediment, other than the cost of the equipment, to use a variable frequency microwave reactor. One of the characteristics that distinguish microwave-assisted heating from the conventional mantle is localized heating, as mentioned before. This is only possible if the microwave light is absorbed selectively by the target compounds. If the vessel, solvent, and surrounding air are also heated, unwanted effects might arise such as solvent decomposition and overall system overheating. Studying the absorption spectrum in the microwave region, previously to the synthesis experiment, could benefit the product yield and quality. Another factor that weighs heavily against fixed frequency microwave heating is the formation of electric arcs. The standing wave produced by the reactor will eventually build up a charge if a metal is present, such as copper nanoparticles. arcing develops into and both pressure and temperature rise abruptly, leading to vessel rupture and dangerous chemical runaway or explosion. The solution found by Antonio et al. was to sweep between various microwave frequencies, to prevent a lasting standing wave.[88] This technology is, however, still not commonly found in microwave reactors due to higher cost.

Another factor to weigh in during synthesis is the temperature measurement method employed. The standard is the infrared sensor that measures a lower temperature than the real one, which is more accurately measured by an internal fiber-optic probe constituted by a ruby thermometer that measures temperature as a function of the luminescence decay time, or with a diode in reverse where the maximum voltage that can be applied changes practically linearly with temperature.[89] Stirring the mixture at 1200 RPM homogenizes the temperature in the vial and both the infrared

sensor and the probes share the same readings.[90]

A literature review on template-free, term explained in Section 2.3.3 of this chapter, microwave-assisted wet synthesis of single metal sulfide nanoparticles was done to verify the availability of a synthesis method and evaluate qualitatively the interest in each element, in terms of articles versus citations. The keywords and syntax <sup>1</sup> used in the search for published articles on the microwave-assisted synthesis of metal sulfide nanoparticles, resulted in an overview of the published articles and corresponding citations, shown in Figure 2.15. Queries were done using Web of Science, all databases except the Engineering Section, Chemical Section, and Electrical and Electronic Section, until the end of 2020.

A large amount of microwave-assisted synthesis methods exist for zinc sulfide and cadmium sulfide nanoparticles and, to a less extent, for copper and silver sulfides nanoparticles. Heavier element sulfides synthesis, like lead and tin, are also well studied, as well as bismuth sulfides to a lesser extent. Reports on the synthesis of other sulfides such as iron, cobalt, and nickel, which are more directed to electrode development, or even manganese, gallium, and indium, found as dopants or in alloy nanoparticles applied in photovoltaic devices, up to the end of 2020 are scarce or non-existing.

---

<sup>1</sup>Example for lithium sulfide: TI = ( ( ("microwave\*" OR "micro-wave\*") AND ("synthesis" OR "production" OR "preparation") ) AND (" Li\$S" OR "lithium \*sul\*ide" ) NOT "Li\*Se")



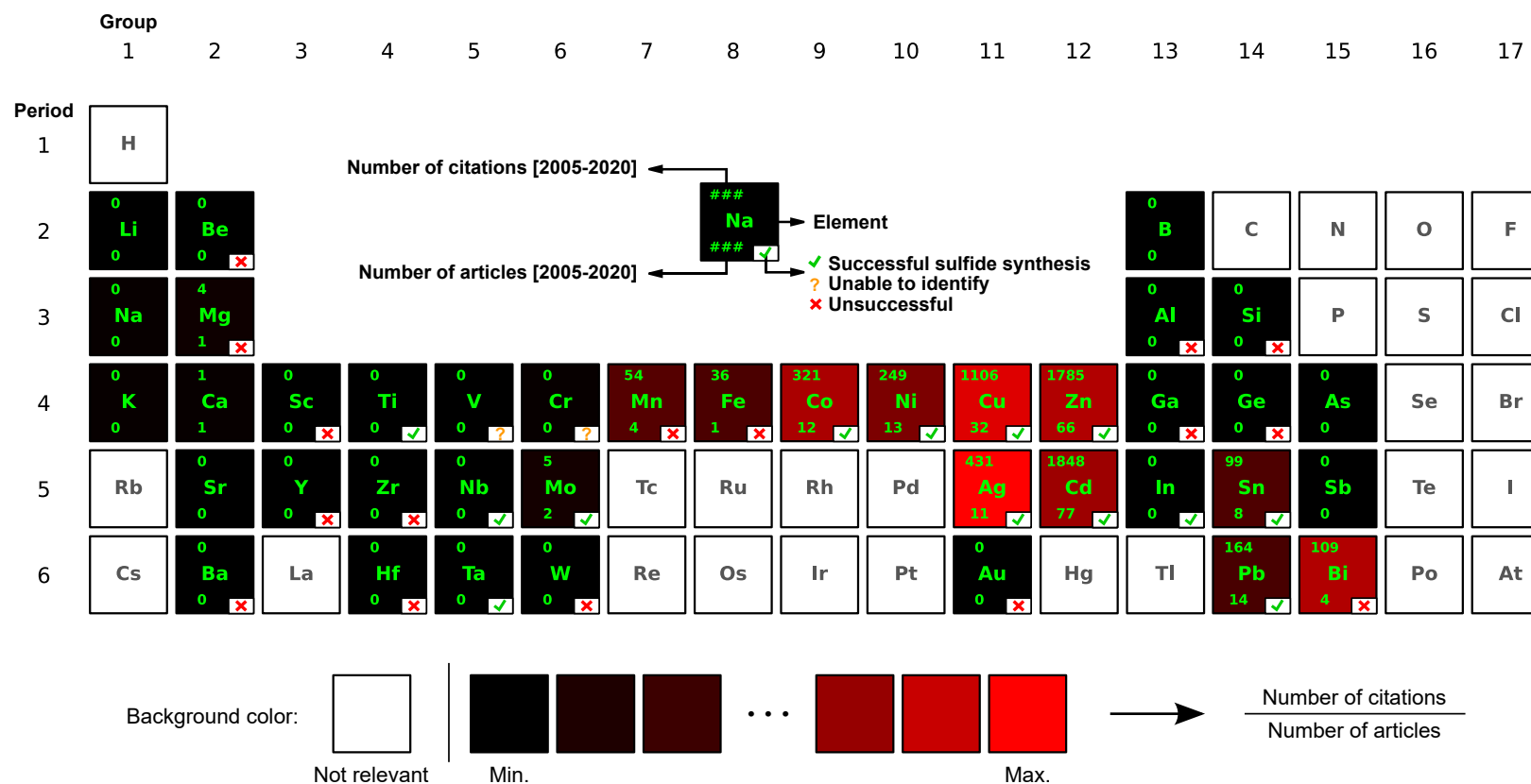


Figure 2.15: Periodic table with an overview of the number of articles and citations regarding the microwave-assisted synthesis of metal sulfides published between 2015 and 2020, with the number of articles published on the bottom of each element and the number of citations on the top. The background color of each element, spanning from black (lowest number) to red, indicates the ratio between the number of citations and articles. The symbol at the bottom right indicates if the synthesis was successful, unsuccessful or the material's composition was unidentifiable. Data taken from queries from Web of Science v.5.27.2, all databases included, until the end of 2020.

### 2.3.3 Template-free

It is important to refer that all of the syntheses performed in this work involved 1-dodecanethiol as the sulfur source and, when it forms a complex with some of the metal salts, it creates ordered structures that are classified as soft templates.[91] The metal salt precursor dissolves in the thiol as temperature rises, before the sulfide is formed, resulting in metal-dodecanethiol complexes such as zinc[92], copper[93], tin[94], bismuth[94] and silver[95] thiolates, which are intermediate species in the metal sulfide synthesis and form ordered structures with periodic patterns.[95] In the case of silver sulfide, alkyl thiols tend to freeze the morphology of the particles and protect them from corrosion by halide atoms.[96]

Although the formation of these structures is considered soft templates, the term template-free was meant to exclude hard templates such as graphene oxide layers, typically used in the synthesis of vanadium sulfide[97], [98], which end up being a composite that has interesting properties for the production of electrodes for capacitors but is hard to separate to obtain the sulfide alone. The advantage of using zeolites, polymer spheres, and others as templates enables a fine morphology control of the nanomaterials, to obtain a myriad of forms. The basis for the template-free choice was the absence of steps required to remove the template after the synthesis and deposition, which in the presence of impurities can leave pin-holes and other defects.

### 2.3.4 Sulfur and Metal Sources

Pertaining the sulfur source, 1-dodecanethiol was chosen due to its relatively high decomposition temperature, which simulates a hot-injection synthesis. Hot-injection method is an advantageous way to quickly expose a reagent to high temperatures, where nucleation is favored instead of the particle growth phase.[83] At the temperature where the thiol starts to decompose, nucleation becomes dominant and growth of the newly formed particles is minimized. Small nanoparticles with a low size distribution are therefore achievable in these conditions.[92] This alkyl-thiol also has the advantage of being a liquid at room temperature and having a high boiling point. It serves as a solvent with low microwave absorption, guaranteeing that the metal salt precursor absorbs most of the radiation and is activated.[99] The thiol can form a metal-thiolate complex which can be considered a single-source precursor. This type of reagent contains both the metal and the sulfur part, which upon heating forms the sulfide. This concept was discovered by Paul O'Brien, a professor at the University of Manchester, who unfortunately passed away in 2018, but left a legacy of a wholesome publication collection of around 70 articles and inspired materials scientists with the introduction of the extremely important concept of producing CdSe from a single reagent.[100] This served as the basis for the now very common and generalized method of a single precursor for the fabrication of nanomaterials, including metal sulfides.[101]–[103] During the synthesis, further heating of the intermediary metal-dodecanethiolate complex, or the metal precursor if no complex is formed, can result in either the metal or the metal sulfide product, as shown in the reaction diagrams in Figure 2.16.

Diagram (A) in Figure 2.16 represent a reaction where only a small amount of energy is required

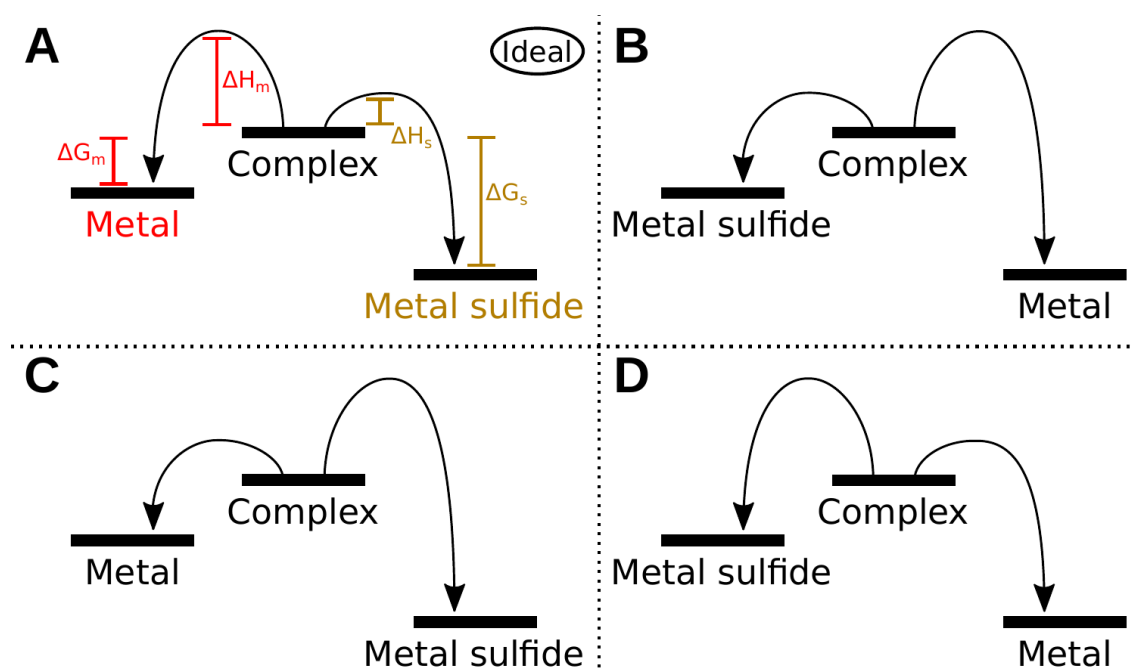


Figure 2.16: Reaction diagrams comprising the possible combinations regarding the metal and metal sulfide as either kinetic or thermodynamic products, starting from a metal-thiolate complex, and the corresponding enthalpy ( $\Delta H_x$ ) and Gibbs ( $\Delta G_x$ ) energies for the formation of the metal ( $x = m$ ) or the metal sulfide ( $x = s$ ).

to pass the activation barrier ( $\Delta H_s$  is less than  $\Delta H_m$ ) to form the metal sulfide product. Even if the reaction is prolonged in time, since  $\Delta G_s$  is greater than  $\Delta G_m$ , the majority of the product is the metal sulfide which is the ideal situation. In this instance, a fixed-wavelength microwave reactor does not pose a hazard since the metal product is unlikely to form. If the metal sulfide activation barrier is smaller but the material itself is less stable than the metal, diagram (B), the reaction has to be shorter to guarantee the absence of the metal product. The two last diagrams (C) and (D) are suboptimal situations, where the metal forms preferably. Diagram (D) corresponds to the most hazardous possibility, where the metal is both thermodynamic and kinetic product. The latter two reaction pathways, (C) and (D), can only be pursued if the metal does not interact with the 2.45 GHz radiation if the final product to be achieved is the metal sulfide. Kinetic control can be achieved with heating rate, which is one of the main advantages of using microwave radiation; very high heating rates can be easily achieved. There are two types of chemical composition profiles: isomeric inversion and induced selectivity. In the isomeric inversion profile, under low heating rates, one of two products is obtained as the main one, while at higher heating rates (5 °C per second) the second product is obtained preferentially. As for the induced selectivity, both products are obtained in similar quantities at low heating rates, while at higher rates, only one of them is obtained.[85]

As stated in Section 2.2, metal sulfides can have different stoichiometries which can create some difficulty in controlling the composition. To complicate even more, thiols are mildly reducing agents and can, for some metal elements, reduce them to the metallic state. This limits, to some extent, the possibility of synthesizing metal sulfides such as ones derived from copper, silver, gold,

and other metals with a higher reduction potential.

The composition of the counter ion in the metal salt is also detrimental to controlling the formation of either the metal sulfide, the metal, or neither. The formation of silver and silver sulfide, for example, can be controlled by changing the reaction temperature or sulfur source availability[104] and the anion from the starting silver salt. The oxidative strength of the conjugate acid of the anion relative to metallic silver can dictate the equilibrium between the metal and the sulfide form. It is known that  $\text{Ag}^0$  quickly dissolves in nitric acid, while  $\text{Cu}^0$  is slower.[105] During the synthesis of silver sulfide and copper sulfide in this work, starting from the  $\text{AgNO}_3$  and  $\text{Cu}(\text{NO}_3)_2$ , the characteristically orange gas nitrogen dioxide was released when the mixture reached high temperatures. Since metallic copper does not dissolve as fast as silver, at a higher temperature when copper sulfide and metallic copper are formed, develops as can be seen in Figure 2.17 depicted by the red circles.

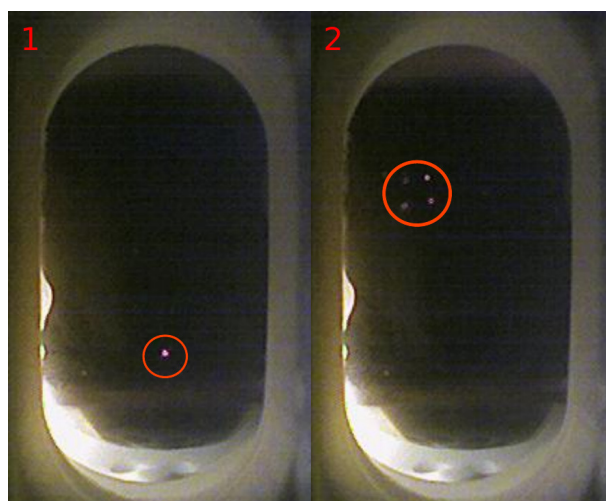


Figure 2.17: Two pictures of the same copper sulfide synthesis with visible occurring possibly due to the formation of metallic copper structures due to the microwave irradiation, marked by circles.

It is unsafe for a synthesis to proceed if is observed at any moment, as it might lead to a thermal runaway and consequent vessel rupture or explosion. In the silver sulfide synthesis, although the formation of  $\text{Ag}^0$  exists, no was observed when nitrate is the anion. The synthesis can proceed at high temperatures indefinitely without danger. However, starting from silver oxide, the synthesis progressed with casual . The possible formation of is one of the biggest problems in microwave-assisted synthesis and can severely limit the options, regarding the anion, cation, and solvent choices.

## 2.4 Ink Formulation

The role of semiconductors in today's economy is indisputable since they are the core of any electronic device, and energy production and storage. The production of solar cells, batteries, capacitors, etc. is usually realized with non-wet methods such as physical evaporation and or chemical vapor deposition. These methods, without discarding the excellent properties of the produced thin films as discussed in previous sections, require expensive facilities, highly trained and qualified labor and the throughput is relatively low. The production of large area electronics such as solar cells has been facing different approaches to reduce costs while increasing efficiency. New materials have been developed and attempts have been made to lower production costs, both by reducing equipment costs and energy consumption costs. Formulation of inks appears as a viable alternative to PVD and CVD classical techniques of thin film production. For instance, the lead-based perovskite solar cell development achieved high solar cell efficiencies with a simple drop-cast of a perovskite ink on a substrate, without special or expensive facilities.[106] All of this was possible due to the formulation of inks that can be deposited on a surface and carry the materials needed to fabricate a device. The formulation itself, however, is not trivial and its principles are presented in the following sections, including the deposition of the inks. For an in-depth review of said principles, including ink rheology, deposition, and future developments, please refer to the excellent review written by Zeng and Zhang.[107]

### Nanoparticle Colloidal Stability

To achieve useful nanoparticle ink, the first requirement is that the solid phase of the colloid is suspended and stable. Nanoparticle colloidal stability, not to be confused with chemical stability which is the resistance of the material to chemical change over time, is achieved when nanoparticles or nanoparticle clusters remain in suspension for a very prolonged time, preferably weeks to months. Several physical and chemical aspects contribute to the stability of colloids. The most basic physical phenomenon known as buoyancy is characterized by the force exerted by an object in a medium that contraries gravity, which depends on the density of the medium, the volume displaced by the object, and the force of gravity. When the weight of the object surpasses the buoyancy force, the object sinks. Naturally, all metal sulfides have a density higher than most solvents and will therefore sediment. To counter this effect, there are two possible approaches or a combination of both. One is to passivate (or cap) the nanoparticles with a shell of molecules that interacts well with the solvent and also contributes to particles repelling each other. The second approach is to increase the viscosity of the medium, normally with the addition of polymers, to create enough drag such that the particles will move slower.

A second problem that usually affects colloidal stability is the aggregation of nanoparticles. Given that with decreasing particle size, the van der Waals interaction, or the weak electrostatic attraction forces, between particles increases[108], guaranteeing their separation can only be achieved by manipulating their surface chemistry. Attaching molecules to the surface of the

particles can promote repulsive behaviors, such as charge-based repulsion or simple steric repulsion. The latter is usually achieved using either polymers or molecules containing long chain alkyl groups or preferably branched alkyl chains which increase the entropic barrier between functionalized particles. The barrier is increased, as explained by Robert Zwanzig[109], due to an increase in the complexity of the environment, fomented by the branching. When two particles are in a collision trajectory, if their surfaces contain linear alkyl chains, the difficulty for the particles to traverse the shell is less hindered compared to if the shell was composed of an intricate mesh. A mixture of linear molecules has also proven to be an effective way to achieve stable suspensions, as was demonstrated for the case of CdSe nanoparticles functionalized with myristate and docosanoate, which are carboxylic acids with alkyl chains respectively with 13 and 21 carbons.[108]

Choosing the correct ligand is detrimental since the functionalization can have negative effects such as poisoning, the term associated with ligands strongly binding to active sites of the nanoparticle, and degrading the properties of the material. Such is the case of 1-dodecanethiol, a typically used thiol capping agent, which poisons the catalytic centers of the metallic nanoparticles, due to strong binding effects and the formation of sulfides. Given that one of the objectives of this work is to produce metal sulfide nanoparticles, this side effect is an advantage. Long-chain ligands carry the disadvantages of having low volatility and leaving carbonaceous residues, which can be avoided by performing a ligand exchange with short-chain ligands.[110], [111] Another disadvantage of using 1-dodecanethiol is that it leads to a high amount of agglomerates. Even after washing and under high intensity and prolonged ultra-sounds, a stable suspension cannot be obtained. As stated by Tang et al.[104], 1-dodecanethiol easily binds to the metal sulfide nanocrystal surfaces but also forms stable interactions with itself. Nonetheless, removal of excess 1-dodecanethiol can be achieved by heating to 143 °C at a pressure of 0.02 bar[112] or by performing a ligand exchange.

Instead of relying on the ligand used during the synthesis to produce the ink, it is possible to perform a ligand exchange afterwards. Guo et al.[113] synthesized copper-indium-gallium sulfide nanoparticles using oleylamine as the ligand. After removing said ligand and drying the particles in an Argon stream, they were able to obtain ink by dispersing the particles in hexanethiol and achieved a very high particle concentration of 200 mg/mL. After depositing the nanoparticle ink by blade coating, selenizing the metal sulfide film, and depositing the rest of the layers, the photovoltaic device achieved a 7.7% efficiency. Many other ligands can be used to fabricate nanoparticle inks. A special class of ligands is called perfluorocarbon molecules, which are alkyl chains with the hydrogen atoms partially or fully substituted by halogen fluorine. A stable ink with copper sulfide nanoparticles with 1H,1H,2H,2H-perfluorodecanethiol as a ligand has been previously used in medical diagnostic applications.[114] The halogen atoms enhance the stability of the particles in suspension, due to strong repulsive forces from the negative charges and due to the rigidity conferred to the ligand shell around the particles[115] that prevents the exposure of colliding particles' raw surfaces, while the thiol group anchors the ligand to the nanoparticles' surface.

## Substrate Affinity

Substrate affinity to the ink is of the utmost importance to obtain a high-quality film. As depicted in Figure 2.18 (A-I), when the substrate's surface is contaminated with hydrophilic molecules or contains dangling bonds, which are atoms on the surface that are not bonded, the hydrophobic ink's contact angle can be too high, forming islands instead of a film. If the surface is functionalized with a molecule that matches the polarity of the ink, the droplets will be able to spread (Figure 2.18 (B-II)). An uneven surface due to roughness and surface traps (Figure 2.18 (C)), such as dangling bonds, will inevitably accumulate particles, leading to a heterogeneous film.

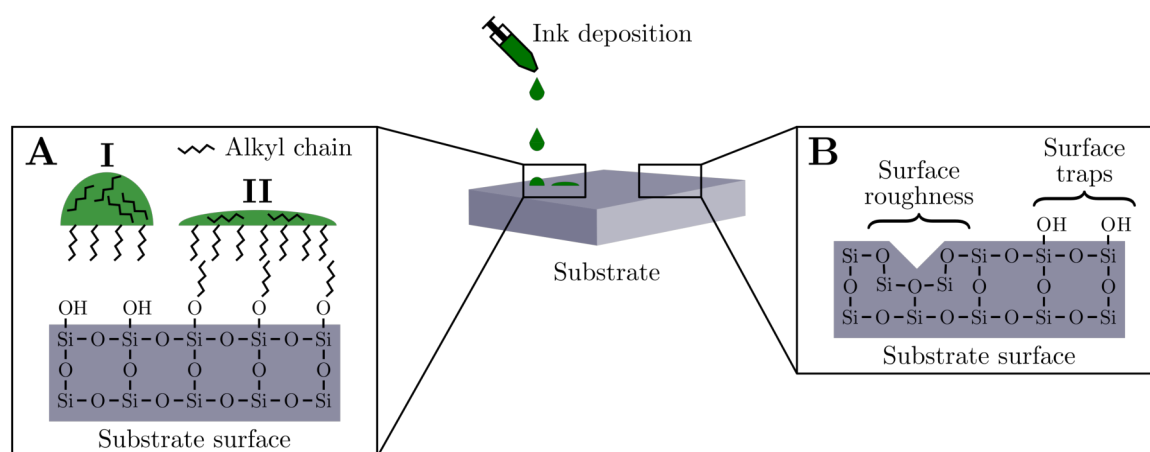


Figure 2.18: Schematics of a substrate with emphasis on two types of surface functionalization (A), hydrophilic and hydrophobic, and their interaction with hydrophobic ink, (I) and (II) respectively. Two types of surface traps, surface roughness, and dangling bonds, that can interfere with the ink deposition are shown in (B).

Surface functionalization is the usual approach to make nanoparticle ink deposition possible since it is relatively easy to select a compound that chemically matches both the substrate's surface, the ink's solvent, and the suspended particles' surface. The typical molecules used to passivate the surface of a glass substrate containing a group with Si-X - with X as any halogen element or oxygen - bonds that link to the glass surface and, on the other end, either a hydrophilic or hydrophobic group, depending on the polarity of the ink. Deposition of inks containing nanoparticles of a metal sulfide is dependent not only on the properties of the ink and the substrate's surface but, also, on the particles' surface chemistry. As an example, PbS synthesized from lead(II) oleate and hexamethyldisilathiane (sulfur source), suspended in dimethylformamide is less compatible with raw glass surfaces. A device produced with the former ink resulted in poor electronic properties. Meng et al.[116] tested the functionalization of a silica surface of a silicon substrate with either octadecyltrichlorosilane, which contains an alkyl group and another containing Si-Cl bonds, or the ammonium chloride salt. The substrate was first treated with plasma to remove any organic contamination and increase the number of polar groups at the surface, promoting a better adherence of the functionalizing groups. Since the solvent of the ink containing the PbS nanoparticles was dimethylformamide, the nitrogen part of the solvent's

molecule interfaced better with the chlorine-containing molecules used to functionalize the surface. A lower contact angle between the ink and the substrate was obtained, with the successful wetting leading to a more homogeneous PbS film and, consequently, better device properties.



## 2.5 Ink Deposition Methods

The development of ink usually is the hardest part of the device development. Once the ink is stable, its deposition can be done using a variety of methods such as spraying, blade coating, simple drop-cast, spin-coating, roll-to-roll, etc. All of these methods require determined ink properties that can be adjusted during the ink formulation, for example, the ink's viscosity, the solvent's polarity, boiling point, vapor pressure, etc. A final aspect of the deposition that should also be taken into account is the substrate's affinity toward the ink being deposited.

Some of the most common ink deposition methods are shown in Figure 2.19, which are divided into two groups, non-scalable and scalable methods for depositions over very large areas. All of the methods exhibited here are electroless (without the aid of electricity to guide the particles to the surface) since the materials were already formed previously and the use of electric potential is known to induce the formation of undesired phases in the case of metal sulfide alloys.[117]

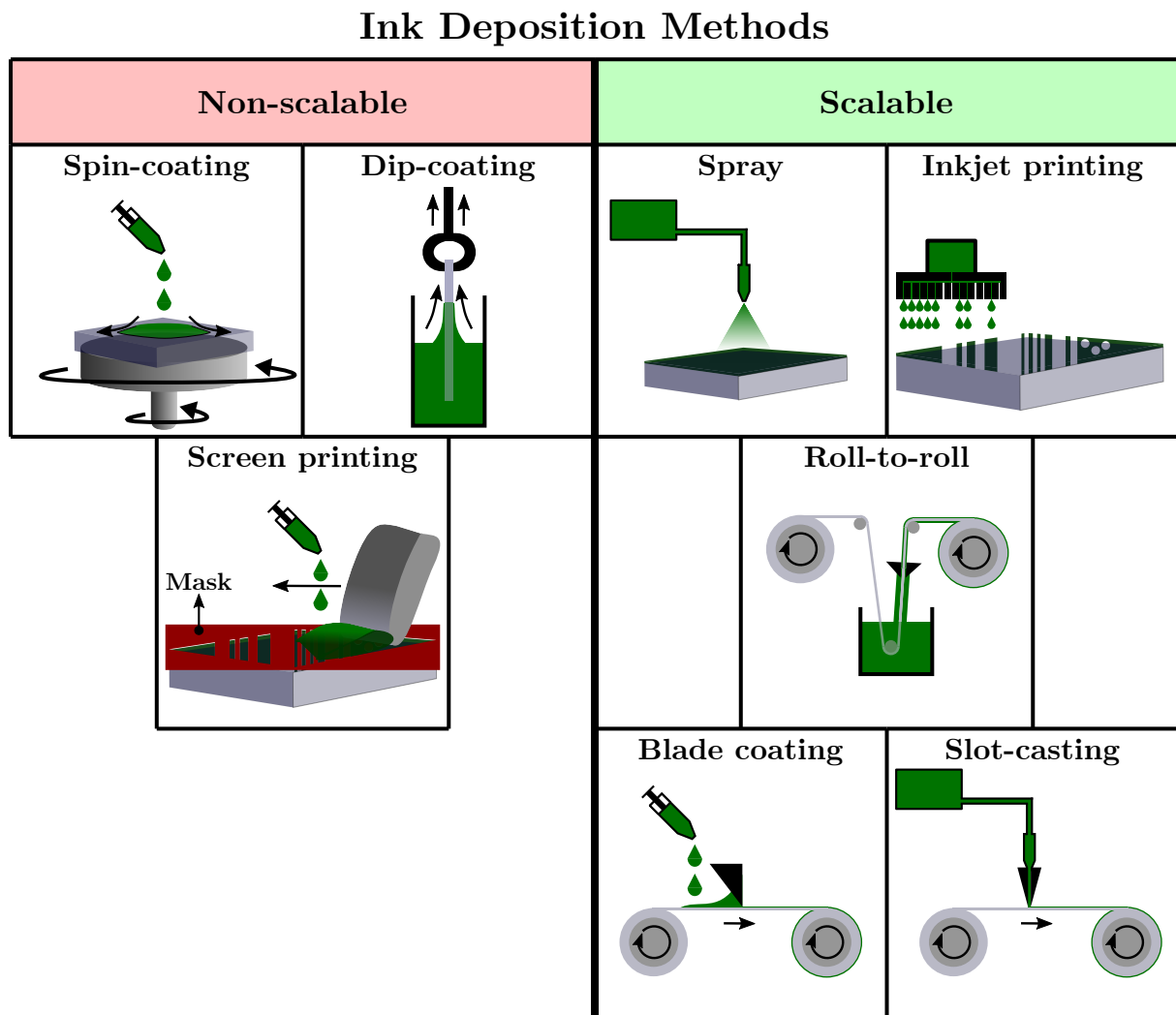


Figure 2.19: Schematics of the various non-scalable and scalable ink deposition methods, with the non-scalable including spin-coating, dip-coating, and screen printing and the scalable methods including spray, roll-to-roll, blade coating, slot-casting and inkjet printing.

One of the most used and quickest methods to deposit layers of materials fabricated on a laboratory scale is the spin-coating method. This method relies on the simple steps beginning with the deposition, spin-up, spin-off, and evaporation stage. Although each step can be explained with relatively complex physical models, a brief explanation of the process is as follows: the ink is dripped onto the rotating substrate, covering it, followed by a quick spin-up with an abrupt acceleration, forcing the bulk of the ink that was near the substrate edge to be expelled. When the rotation speed stabilizes, the film starts thinning, sometimes forming a heterogeneous pattern known as spinning-off, and the final stage begins when the solvent evaporates, further helping the densification of the thin film. This method is inherently not scalable since spinning a very big substrate constitutes a hazard and only up to 2% of the ink is effectively used, with the rest being flung away.[118]

Dip-coating consists of submerging a substrate in an ink tank and then removing it at a constant rate. This process can be repeated several times to obtain thicker films or various films with different compositions. There is less waste of ink when compared to spin-coating since the ink remains in the reservoir and can be recovered after. The process can be fully automated, enabling the reproducibility of the process and the obtained films. The properties of the film can be predicted, so long as the ink behaves as a Newtonian liquid, based on the substrate affinity to the solvent and particles, the ink's viscosity, particle concentration, and surface tension, and controllable parameters such as the dipping and withdrawal rates, soaking time and temperature.[119] Although this process is used industrially for several coating industries, the maximum size can be a limitation for large area solar cells application.

Screen printing requires a mask (or mesh) with holes that form the desired film pattern. The mask is laid on top of the substrate, the ink is spread in front of a squeegee that spreads and presses the ink. The holes in the mask let the ink pass and the film is formed. Intuitively, it seems the main factor that influences the properties of the film is the amount of fluid that is permitted to pass by the mask. However, as simulated by Kapur et al.[120] and demonstrated by Pott et al.[121], it is the amount of ink that is pulled out of the substrate by the mask and the ink's free surface that determines the amount of ink transferred. This method has the interesting advantage of being able to accommodate inks with a wide range of viscosities. Regarding high throughput production, this method was included in the non-scalable class since the method produces some degree of ink waste and the need to clean the mask for continuous use creates an economic and environmental problem.

The scalable methods present better options in terms of economical and environmental aspects. Achieving a higher throughput, using lower quantities of material and recycling is fundamental to avoiding waste, preserving the environment, and generating more profit. The first two methods shown in the scalable group in Figure 2.19, spray and inkjet printing, are more appropriate for the production of patterned thin films. The spray method consists of two main parts: the ink deposit and the spray nozzle. The basic principle of this technique is the production of droplets, through various means such as pressurized gas that forces the liquid through a small aperture in the nozzle or with the aid of an ultrasonic piezo transducer that can be either located in

the nozzle or the ink deposit an aerosol. The latter is composed of a fine plume of the mist of particles that can have dimensions lower than 100 nm and a narrow size distribution.[122][123] This method requires a mask to obtain a patterned film, unless the deposition resolution is low, in other words, the pattern lines and spots are bigger than the spray spot. So long as there is ink to be deposited, small or vast areas can be sprayed to produce uniform thin films.

The second element of the scalable methods, inkjet printing, works the same as a household printer. The system is composed of a cartridge with a head containing a piezoelectric element, which ejects droplets or a continuous thin flow of ink[124], at a targeted location with very good accuracy. The droplets' size is typically 20 to 30 $\mu$ m and depends on the nozzle's aperture and the ink's viscosity and surface tension.[125] The advantage of depositing the droplets at a precise position, removes the need for a mask. Compared to other techniques, inkjet printing is practically waste-free, setting the method as one of the most promising.

The remainder three scalable methods seen in Figure 2.19 are very similar between themselves and the root principle is set on the roll-to-roll process. The latter is configured by two rolls, one defined as the start containing a flexible substrate that unrolls to the end roll. In between the travel, the substrate is submerged in an ink and when the substrate reemerges the excess ink is removed by blades near the surface of the substrate. Both blade coating and slot-casting differ from the previous only in the way the ink is dispensed on the substrate. The blade coating method does not involve submerging the substrate in the ink but rather dropping the ink on one side of the substrate. While the substrate travels to the other roll, the excess ink is removed with a blade. Similarly, in slot-casting, or slot die coating, the ink is deposited by the slot-die head by forcing the ink through a thin horizontal gap, as close to the substrate as needed to achieve the desired wet thickness, which is around half the distance between the substrate's surface and the slot-die head gap.[126] These methods, although patternless, have the highest throughput rate of all the mentioned methods, achieving several meters per second of thin film production, with little waste.



## Metal Sulfide Nanoparticle Syntheses

This chapter includes the description of the method used for all the metal sulfide nanoparticle syntheses, detailing the procedure to control the syntheses' reproducibility, and main characterizations performed. The results from the binary metal sulfide syntheses are presented sequentially and were ordered according to the periodic table's groups. The multinary metal sulfide syntheses are not presented in any particular order but copper based alloys were grouped together, as well as the zinc based ones.

### 3.1 Methods

#### 3.1.1 Synthesis Protocol

A systematic approach was used to attempt to synthesize the metal sulfide nanomaterials. The following method was used in all syntheses unless a modification is clearly stated in each step. Table A.1, with the suppliers and purity for all reagents used in the synthesis, can be found in Section A.5 of Appendix A. To obtain the sulfide, 1-dodecanethiol was used as the sulfur source, solvent, and as a ligand to stabilize the morphology of the particles. The amount of thiol used was kept constant at 5 g and was mixed with 1 mmol of metal precursor in an Anton Paar G30 proprietary reaction vial with a polytetrafluoroethylene-covered Cowie stirring magnets with a size of 10 mm by 3 mm. The mixture was purged for 15 min with either industrial grade nitrogen gas, or argon, ALPHAGAZ 1 with a purity of 99.999%. The vial was capped with the proprietary polytetrafluoroethylene-covered silicon sealing cap and immediately inserted into the Anton Paar Monowave 400 microwave reactor's cavity. Under constant steering at 1200 RPM, the temperature was raised to 300 °C in 10 min, held at that temperature for 5 min, 10 min or 25 min, and then automatically cooled to 50 °C, with the aid of a compressed air jet.

The suspension was then divided into three 2 mL microcentrifuge tubes, centrifuged at 9000 RPM (9146 *g*), the supernatant discarded, followed by the addition of either ethanol or chloroform up to the 2 mL mark. With the aid of a vortex, the tubes were shaken until all of the pellets were resuspended and the suspensions were centrifuged again. This process was repeated two more times. After discarding the supernatant, the pellet was vacuum dried for 1 h by perforating the microcentrifuge cap with a needle to create a hole for the air and solvent to pass.

#### 3.1.2 Image Recording: Reproducibility

Monitoring is essential in any given experiment, mainly when synthesizing nanoparticles whose particle size and structures strongly depend on the synthesis parameters. Therefore, reproducibility was a significant concern in this work, and a procedure was developed to control it. A script was

created to extract color data from images captured from any camera. It was applied not only to the synthesis performed in this work but also to show the applicability to generic synthesis. The script and the results are available in a scientific journal publication [127]. The images obtained from the camera are processed, and the average values from red, green, and blue color channels are used to generate a color profile plotted against time. Different color or color shade changes can be better visualized with this data. For example, a compound's isolation can be pursued by fixing the temperature at which its color is stable. The intent of the published article was also to supply the script to the chemistry community that lacks computational expertise and shows the potential of such a simple script with a simple explanation of how to use it.

The script developed transforms captured images from any recording media and outputs the average red, green and blue (RGB) values from each picture. These values can then be plotted against synthesis time. When accompanied by other synthesis data, such as temperature, pressure, and the microwave generating magnetron input power, a quick analysis can determine when and at what temperature a dissolution, reaction, or precipitation occurred. An example of the plot is shown in Figure 3.1, with three pictures taken during the synthesis of tin sulfide as examples.

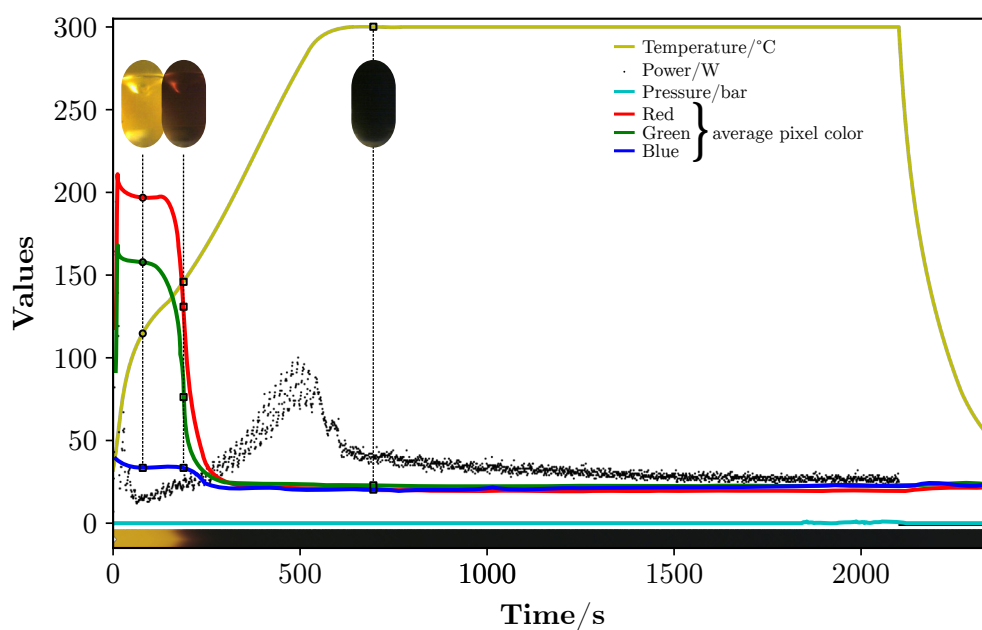


Figure 3.1: Color profile, with the average red, green and blue pixel values for each picture, and the temperature, pressure and microwave generating magnetron input power profiles of a tin sulfide microwave-assisted synthesis. Three representative pictures of the synthesis are shown to depict the different observed stages of the synthesis.

The limitation of image recording is mostly regarding the illumination setting and the recording device. Light variations over time can create artifacts in the color profile and if the resolution of the recording device is too low, valuable information can be lost, such as a slight color variation due to precipitation.

Naturally, the script is useful for any kind of experiment where a video or sequence of images is recorded. In the article, a color profile of an example of a Briggs-Rauscher oscillating reaction (iodine-starch clock) is shown. The cycle duration of both the amber-colored suspension and the

dark one can be extracted from the color profile, which enables the direct correlation with other analyses such as the iodine concentration.

A follow-up experiment with a hue-changeable lamp clearly shows the limitations of the method described in the article. Apart from the microwave-assisted synthesis performed in the microwave reactor, an experiment was attempted by mixing silver nitrate with 1-dodecanethiol and heating the mixture on a hotplate. The experiment was recorded using a cellphone camera and the setup was illuminated with a hue-changeable lamp. Over 57 minutes of recording, the light was either switched off or the hue was changed randomly. In Figure 3.2 lies a plot representing both the color of the suspension and the color of the hotplate, which was chosen because it is semi-white and would reflect the light hue changes. Instead of representing the color hue as RGB values, bars with the color hue as their background were chosen to better perceive the actual color difference.

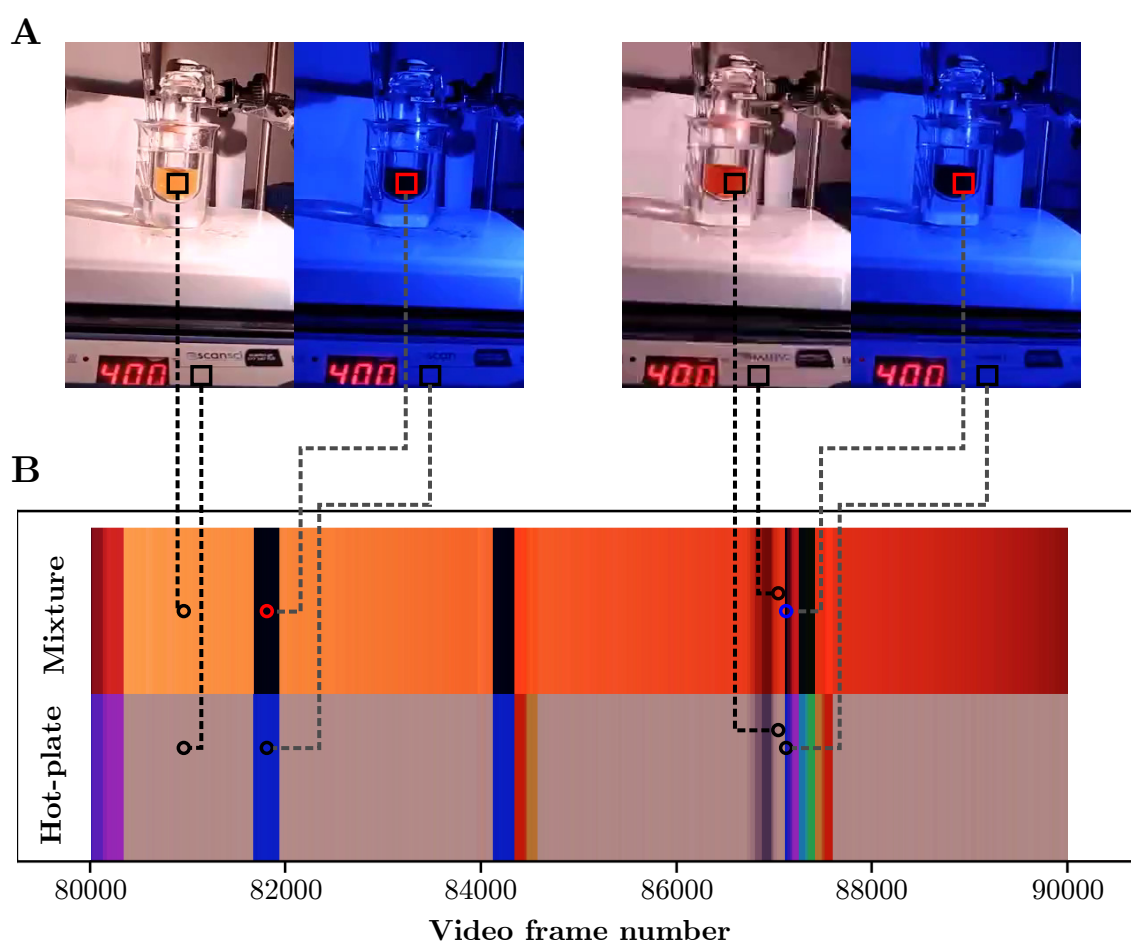


Figure 3.2: Pictures taken from the video of a silver sulfide synthesis, using a mobile phone camera (A) and corresponding color profiles (B), processed from the marked square spots in the pictures, of the mixture inside the flask and a semi-white-surface from the hotplate. Over the recording period, the light hue was changed periodically or turned off.

A compound that is yellow (Figure 3.2 A), while illuminated by white light, appears to be black under blue light (Figure 3.2 B). The change of color observed in the mixture over time from yellow to orange, is seen with white light. When the blue light is switched on, the same transition cannot be observed; the two pictures show a dark mixture with no outstanding differences. In most cases,

the setup should be illuminated with white light. Another factor to weigh in while analyzing the color profile is the light intensity. The dimmer the light is, the darker the compound will appear to be and changes in color are therefore harder to see, due to the low contrast between colors and color shades.

Some special cases could benefit from a different illumination source. The synthesis of manganese doped zinc sulfide is known to yield, under the right conditions, luminescent nanoparticles that emit orange light. Changing the light setup from the microwave reactor to a UV lamp and taking the color profile from the latter synthesis, would probably result in a dark profile at the beginning, followed by the appearance of an orange profile, indicating that the doped nanoparticles had formed. It would also be interesting to evaluate the relation between the growth of the nanoparticles and the relative intensity of the emitted orange light from the UV excitation.



### 3.1.3 Materials Characterization Methods

#### X-Ray Diffraction: Pattern Identification and Average Crystallite Size

The synthesized products were characterized by X-ray diffraction in a PANalytical X'Pert PRO MPD equipped with a PW3050/60 goniometer (minimum step size of  $2\theta$   $0.001^\circ$ ), PW3071/xx Bracket stage and using a mixture ratio of 1:1 of two Cu K- $\alpha$  sources at the X-ray wavelengths of  $1.540598 \text{ \AA}$  and  $1.544426 \text{ \AA}$ , with an average step time of 33.02 s or 74.93 s, depending if the signal was too low, with a  $2\theta$  collection from  $10^\circ$  to  $90^\circ$ .

The Python 3 script used to obtain the reference patterns from Materials Project database[128][129] can be found in my GitHub page <https://github.com/DavidMSou/Scientific-Tools>.

As an example, using the Python function `XRD_PLOTTER`<sup>1</sup> from the X-Ray Diffraction.py file in my GitHub, starting from a comma separated values file ("SnS.csv"), yields a column of plots (Figure 3.3) with all the experimentally confirmed ("**theoretical**": **False**) X-ray diffraction patterns of materials containing ["Sn", "S"] elements, limited to a  $2\theta$  range of [10, 90] and including all the crystal systems available `crystals=["all"]`.

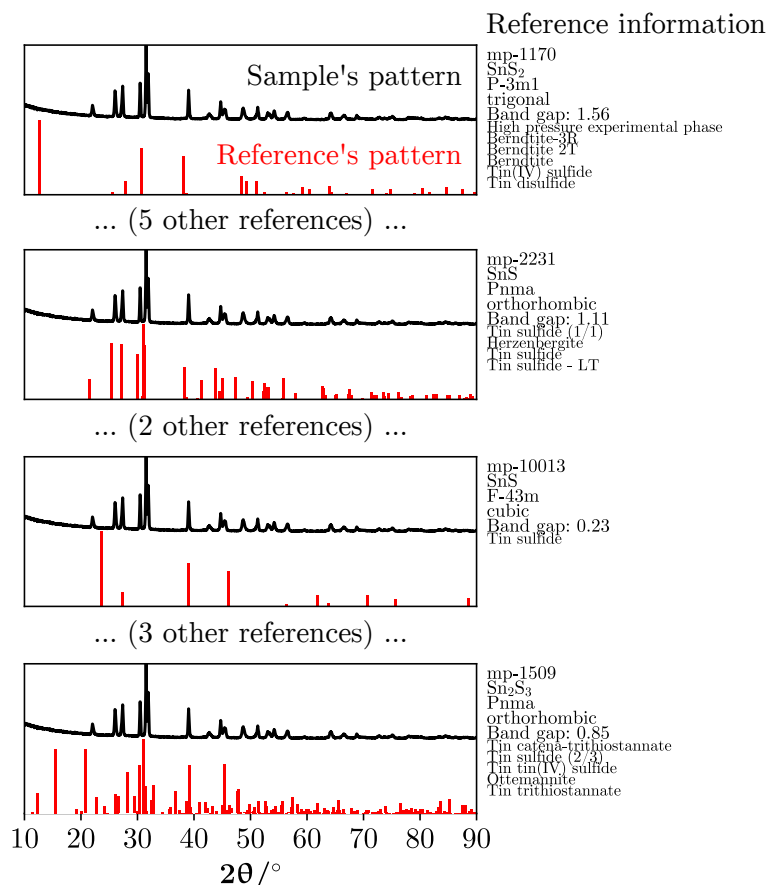


Figure 3.3: X-ray diffraction patterns of a synthesized tin sulfide powder sample and the red bar plots are references taken from Materials Project database[128][129]. Some reference patterns were omitted since there are 14 patterns available.

<sup>1</sup>`XRD_PLOTTER(['SnS.csv'], element_criteria = ["Sn", "S"], xlim = [10, 90], criteria_add = "theoretical": False, crystals = ["all"])`

In this example, the XRD pattern of the synthesized tin sulfide powder can be visually matched the reference pattern with the ID mp-2231, which corresponds to the orthorhombic phase (Pnma) of SnS, also known as Herzenbergite, with a calculated band gap of 1.1 eV, as per the database. All intensities are normalized and the axis title and values, henceforth, are omitted to avoid visual clutter. In some rare occasions, the experimentally confirmed reference data might not be available and the argument ("**theoretical**": **False**) has to be removed, to include the predicted patterns. In the tin sulfide case, if all the reference data was included, a total of 16 patterns would be returned.

The average crystallite size of the particles were determined from the X-ray diffraction patterns, using the Scherrer equation as described in reference [130]. The well known equation is shown in equation 3.1, with  $L$  as the size of the crystallite in nanometers,  $K$  is a numerical constant that was assumed as 0.94,  $\lambda$  is the X-ray beam wavelength in nanometers,  $B$  is the full width at half maximum of the chosen diffraction peak and the diffraction angle  $\theta$  is the half of  $2\theta$ .

$$L = \frac{K \times \lambda}{B \times \cos(\theta)} \quad (3.1)$$

The value of the full width at half maximum (B) was determined by fitting a Lorentzian curve, after subtracting the baseline from the pattern. The baseline function was adapted from Castanho et al.[55] work, where they present a function that can be used to remove the light scattering effect from colloidal suspensions, during absorbance measurements. The function is presented in equation 3.2, with  $b$  as the linear baseline, and the following parameters have no physical meaning and served only to achieve a good fit:  $a$ , and  $2\theta_0$ . The dependent variable  $Y$  corresponds to the intensity of the XRD signal and  $2\theta$  is the angle.

$$Y = b + a \times 2\theta^9 \quad (3.2)$$

The error function used was also customized. A penalty was established that increased the error if any point from the fit was higher than the experimental data. The error was simply the sum of absolute value of the differences between the experimental data and the fit, plus the sum of points, powered to the 10, where the fit was higher than the experimental.

### Imaging: Particle Size and Geometry

The transmission microscopy images were obtained in a Hitachi H- 8100 II with a 200 kV electron beam, using Formvar and carbon coated 200 mesh copper grids that were previously dipped in an ethanol (97% purity) suspension containing the synthesized powders.

The scanning electron microscopy images were acquired in a field emission gun scanning electron microscopy (SEM) JEOL 7001F with an Oxford light elements EDS detector and an EBSD detector, with the samples previously mounted on a sample holder and coated with a thin layer of Au and Pd in a Polaron Quorum Technologies sputter coater and evaporator.

### Selected Area Electron Diffraction Pattern: D-spacing

The SAED patterns were acquired in a Hitachi H- 8100 II and a gold sample was used previously as the reference to determine the d-spacing values.

ImageJ software is required for the procedure of extracting the data from a pattern image file, as well as the plugin Radial Profile Extended from Philippe Carl, available on <http://questpharma.u-strasbg.fr/html/radial-profile-ext.html>, based on the plugin Radial Profile from Philippe Carl. A SAED pattern (image) of a reference pattern like the one in Figure 3.4 (1), usually gold, is also required to obtain the d-spacing values. The calibration was performed in this work using a photograph of the pattern with a resolution of 1376 by 1032 pixels. The calibration procedure, as well as the procedure to obtain the d-spacing values from an experimental SAED pattern, are described in Figure 3.4 and its caption.

The macro used in (5) in ImageJ to obtain the gray pixel color values, each value at a certain distance from the chosen center and at a certain angle, is found below.

---

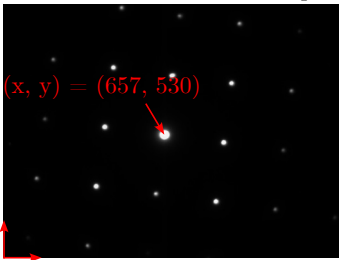
```
/mnt/Fast/Github/Scientific-Tools/Diffraction/Selected Area Electron  
Diffraction (ImageJ Macro).ijm
```

---

The  $R_{Au}$  distance represented in (B) can be of any units since the calibration equation 3.3, used to obtain the d-spacing for each (hkl) plane which is represented by  $d_{hkl(sample)}$  from each spot or ring from an experimental SAED pattern, is a ratio that cancels both  $R_{Au}$  and  $R_{Sample}$  units. The unit for the d-spacing of the sample comes from the already known d-spacing for the (002) plane of Au ( $d_{002(Au)}$ ) which is 2.039 Å.

$$d_{hkl(sample)} = \frac{R_{Au} \times d_{002(Au)}}{R_{Sample}} \quad (3.3)$$

While selecting the pixel from the center of the pattern after calibrating, for example in the case of the Au SAED pattern, if the user chooses a pixel that is slightly away from the optimal, (652, 531) instead of (657, 530), the value of  $d_{002(Au)}$  which is 2.039 Å is now wrongly estimated as 2.056 Å. Although the difference is not very large, care should be taken when choosing the pixel at the center of the pattern.

- 1 In ImageJ, find the pixel that corresponds to the middle of the center spot.
 

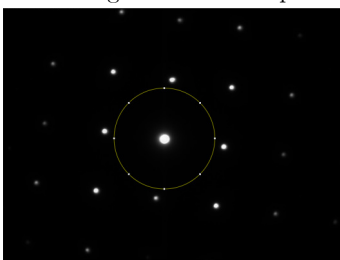
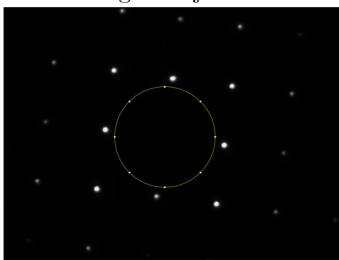

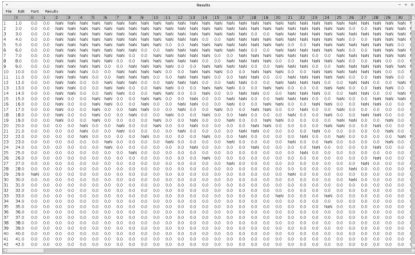
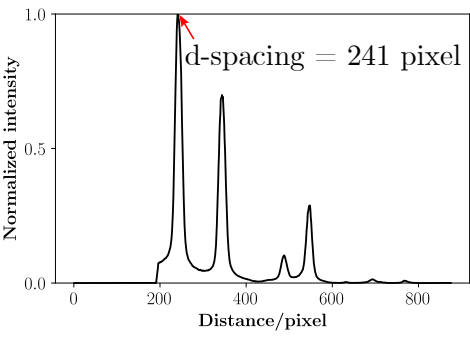
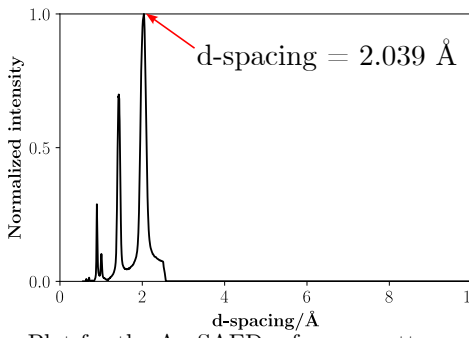
Au SAED pattern
- 2 Use Select (Oval), put the cursor on top of the previous pixel and expand the circle to the edges of the next spots.
 
- 3 Press Delete or go to Edit > Clear. Optional: Image > Adjust > Threshold
 
- 4 Select (Rectangle) the pixel in the middle of the center spot.
 
- 5 Run the macro supplied in this section to obtain this table of Results.
 
- 6 Copy all of the data from the Results; Edit > Select All Edit > Copy  
  
Run the script: "Selected Area Electron Diffraction.py"  
  
Run the function: data = get\_data()
- 7 Run the function: pixels = plot\_data(data) With the variable "pixels", find the d-spacing value in pixels for the first peak.
 
- 8 Rau can now be defined as 241 pixel. To obtain the d-spacing in Å for another pattern, repeat steps from 1 to 6, then: d = plot\_data(data, Rau = 241)  
  
Plot for the Au SAED reference pattern, following the procedure described here.
 

Figure 3.4: Procedure to obtain the d-spacing values from a selected area electron diffraction pattern. A gold reference pattern was used to calibrate the transmission electron microscope (Hitachi H-8100) equipment used in this work (1). The sequence of the procedure is from 1 to 8. In step 8, the value of the Rau argument, which is the value of  $R_{Au}$ , must be determined previously by the user after calibrating.

### Optical Spectra: Band Gap and Raman

Transmittance spectra were acquired in a simple film holder and diffuse reflectance spectra in a 60 mm integrating sphere (ISN-923), both in a JASCO V-770. The powders were mounted between two glass plates and the films obtained by spray with the material directly on the sphere's window. The spectra were acquired after performing a baseline with a barium sulfate reference.

Band gaps were determined from the diffuse reflectance spectra of the obtained powders, according to reference [131]. First, the diffuse reflectance spectrum ( $R_\infty$ ), with values from 0 to 100, was transformed into a pseudo absorption spectrum using the following equation 3.4:

$$F(R_\infty) = \frac{(1 - R_\infty)^2}{2R_\infty} \quad (3.4)$$

For the determination of a direct band gap, the relation between  $(F(R_\infty) \times eV)^2$  and the photon energy  $eV$  were used to create a Tauc plot. The value of the band gap was calculated by the photon energy value of the intersection between two linear regressions: one on the semi-linear steep slope at higher photon energies and another at the Urbach tail at lower energies (treated as the baseline). An example of the determination of a band gap from the diffuse reflectance spectrum of SnS is shown in Figure 3.5, with an estimated average direct band gap of 1.25 eV. Using the same method but for the indirect band gap, the value obtained is 1.19 eV. The first step requires the user to slice the spectrum, to focus on the region where the band gap is to be determined. As described in the caption of Figure 3.5, the only manual step is where the user inputs the points where the baseline and absorption slope are estimated to be. The Python 3 script can be found in my GitHub page <https://github.com/DavidMSou/Scientific-Tools>.

There is an excellent free software called GapExtractor v1.0, although closed source, available to automatically determine the band gap from a diffused reflectance spectrum of a solid material, with an article associated explaining the method and validity, by Escobedo-Morales et al.[132]. The software is available in the link shown in this page's footnote <sup>2</sup> and can be referred to in the DOI database by 10.17632/j9ypzmdx5n.1. A comparison between the described Python script and GapExtractor for some of the band gaps of the materials synthesized in this work is shown in Table 3.1. Both the Python script and the GapExtractor software yielded similar band gaps for the Ag<sub>2</sub>S and SnS powders. However, for the determination of the band gaps of the Co<sub>9</sub>S<sub>8</sub>, In<sub>x</sub>S<sub>y</sub> and ZnS powders, GapExtractor was unable to reliably determine the values, even after changing the parameters in the software. Using the Python script, adjusting the window of the available data facilitated the extraction of the band gaps. Spectra that were acquired with bigger steps have a very little amount of points to be considered during the linear regressions and can compromise the determination of the band gap. A 0.5 nm step appears to be enough to correctly determine the band gap, as seems to be the SnS case, or for band gaps determined in the infrared part of the spectrum.

A spectrum should be acquired with a step of 0.2 nm, ideally 0.1 nm to avoid errors in the script due to lack of data points, with the minimum noise possible, to determine band gaps in the

<sup>2</sup><https://data.mendeley.com/datasets/j9ypzmdx5n/1>

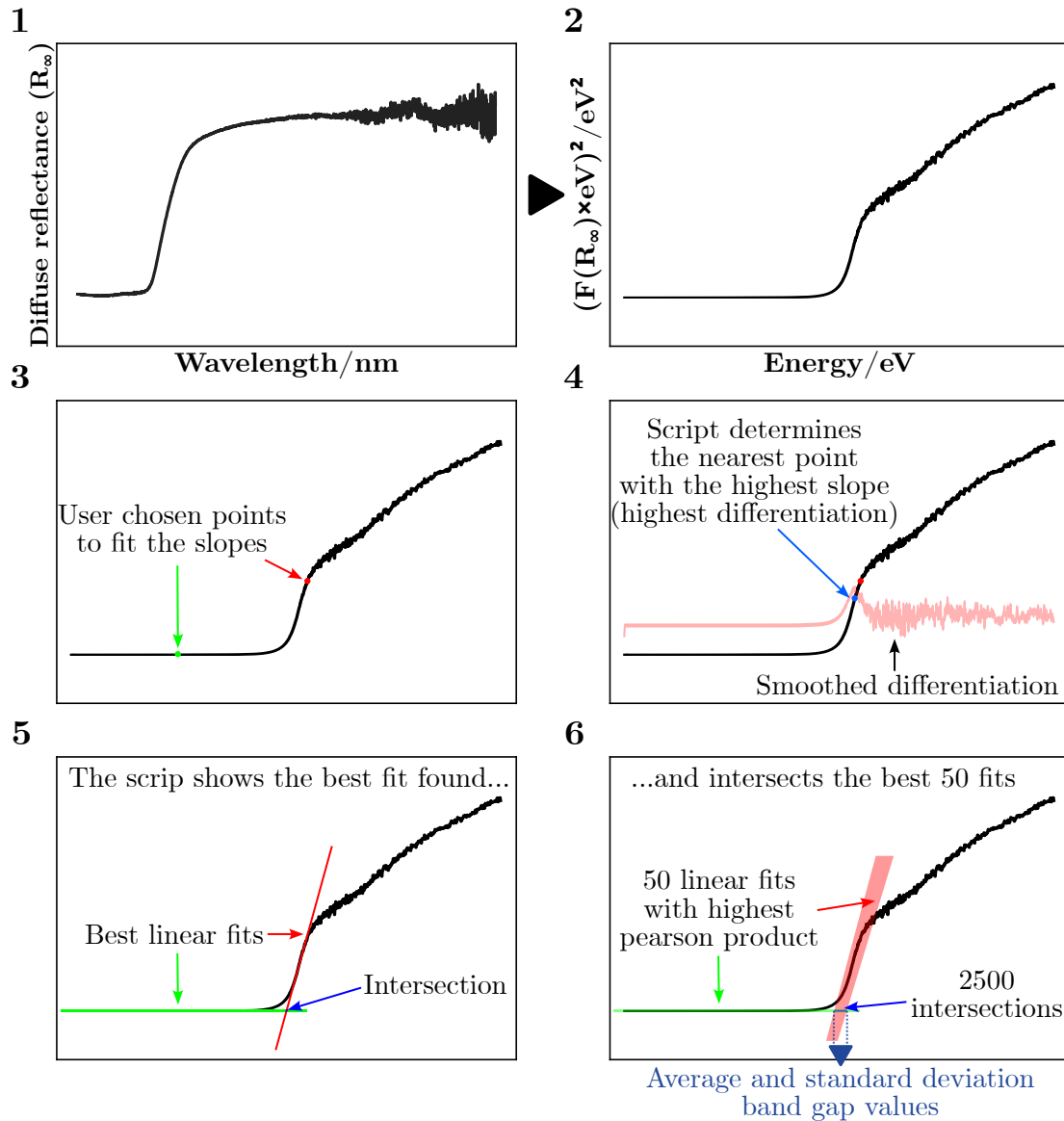


Figure 3.5: Schematic of the python script steps to obtain a band gap from a diffuse reflectance spectrum of a synthesized SnS powder (1) as an example, the corresponding Tauc plot (2), user inputs the estimation of where the baseline and absorption slopes are (3), the script determines where the highest slope is, through differentiation of the Tauc plot (4). The script then shows the best fit for the baseline and for the absorption slopes (5), followed by the intersection between the slopes' best 50 linear fits to obtain an average band gap and its standard deviation (6).

visible and ultraviolet regions. The script contains a function that can interpolate the spectrum values, as explained in Section B.1, to help the user artificially fabricate more data points without changing the shape of the spectrum.

Raman spectra were measured in a WITec alpha300 R Raman spectrometer, using a 532 nm laser with a controllable power intensity. A rough measurement of the films thickness was performed using the focal property of the Raman equipment's microscope. This was done by keeping the focus unchanged while the motor of the stabilizing table, responsible for its vertical movement, was used to focus on the substrate's surface and then to focus on the film. The distance that was traveled by the motor was registered as the film's thickness.

Table 3.1: Comparison of some direct band gaps calculated by GapExtractor v1.0 software and the python script developed in this work. The asterisks (\*) mark the spectra with a data interval equal or above 1nm, which created some difficulties for both methods to determine the band gap. STD stands for standard deviation and n/a for not available - unable to calculate.

Direct band gaps	Python script/eV			GapExtractor/eV	
	Material	Best fit	Average	STD	Value
Ag <sub>2</sub> S	1.03	1.15	0.10	1.03	0.00
Co <sub>9</sub> S <sub>8</sub> *	1.59	1.59	0.00	n/a	n/a
In <sub>x</sub> S <sub>y</sub>	2.56	2.56	0.00	n/a	n/a
SnS	1.18	1.18	0.00	1.25	0.02
ZnS*	3.44	3.44	0.00	3.15	0.77

### Emission and Quantum Yield

Emission spectroscopy of the silver sulfide powders was performed in a Bruker Vertex 80v Fourier transform infrared spectrometer, equipped with a Hyperion microscope unit. The excitation source was a laser with a wavelength of 532 nm, the power was measured at the front of the spectrometer window and varied from 5 to 150 mW. The samples' temperature was kept at 67 K during measurements.

To estimate the quantum yield of the zinc sulfide nanoparticles, the emission and absorbance spectra of ~1 mg of the particles suspended in 100 mL chloroform were measured respectively in a Perkin Elmer Lambda 35 UV-Vis and a Perkin Elmer LS45. The excitation wavelength was 280 nm, using a cutoff filter of 360 nm and a neutral density filter of 1 Abs, and the reference was 7-diethylamino-4-methylcoumarin in ethanol (quantum yield of 0.73).

## 3.2 Binary Metal Sulfides

The results obtained from the microwave-assisted synthesis of various metal sulfide nanoparticles are presented in the following sections. In addition, binary metal sulfide microwave-assisted syntheses that were not reported as of 2020, according to Figure 2.15, have also been attempted as a demonstration of the generalizability of the synthesis method developed in this work. The sections were divided into periodic table groups, where each element's sulfide synthesis attempt is described and the results are discussed, as described in Table 3.2. The synthesis details can be found at the end of each section dedicated to the element in the Appendix A. Some of the syntheses that either did not form a metal sulfide or had incomplete characterizations can also be found in the Appendix A. A resume of the results is presented in Table 3.3. Details on the reagents used during the syntheses are presented in Table A.1.

Table 3.2: Metal element used in the metal sulfide binary synthesis, the corresponding periodic table group and its section.

Metal	Group	Section	Metal	Group	Section
Be	2	A.1.1.1	Fe	8	3.2.5.1
Mg		A.1.1.2	Co	9	3.2.6.1
Sc	3	A.1.2.1	Ni	10	3.2.7.1
Y		A.1.2.2	Cu	11	3.2.8.1
Ti	4	3.2.1.1	Ag		3.2.8.2
Zr		3.2.1.2	Zn	12	3.2.9.1
Hf		3.2.1.3	Cd		3.2.9.2
V		3.2.2.1	Al	A.1.12.1	
Nb	5	3.2.2.2	Ga	13	A.1.12.2
Ta		3.2.2.3	In		3.2.10.1
Cr	6	3.2.3.1	Si	A.1.13.1	
Mo		3.2.3.2	Ge	14	A.1.13.2
W		3.2.3.3	Sn		3.2.11.1
Mn		3.2.4.1	Bi	15	3.2.12.1

### 3.2.1 Group 4: Ti, Zr, Hf

#### 3.2.1.1 Titanium

Titanium sulfide ( $\text{TiS}_2$ ) has been recently used as an electrode in batteries[133], [134], in thermoelectrics[135] and in photonics[136]. According to Greenaway and Nitsche,  $\text{TiS}_2$  is a semiconductor with an optical band gap between 0.8 eV and 1.2 eV. However, the material's color is yellow, which matches the reported bonding and anti-bonding energy difference of 3.35 eV.[137]

Nanosheets of hexagonal  $\text{TiS}_2$  have been previously synthesized by solvothermal reaction between  $\text{TiCl}_4$  and sulfur[138] or by the reaction between  $\text{TiCl}_4$  and  $\text{CS}_2$  in oleylamine at 300 °C for 15 min[139].

The synthesis of  $\text{TiS}_2$  was attempted starting from titanium(IV) isopropoxide and is detailed in Section A.1.3.1. The color, temperature, and pressure profiles, and the resulting powder's XRD



pattern and TEM image can be found in Figure 3.6.

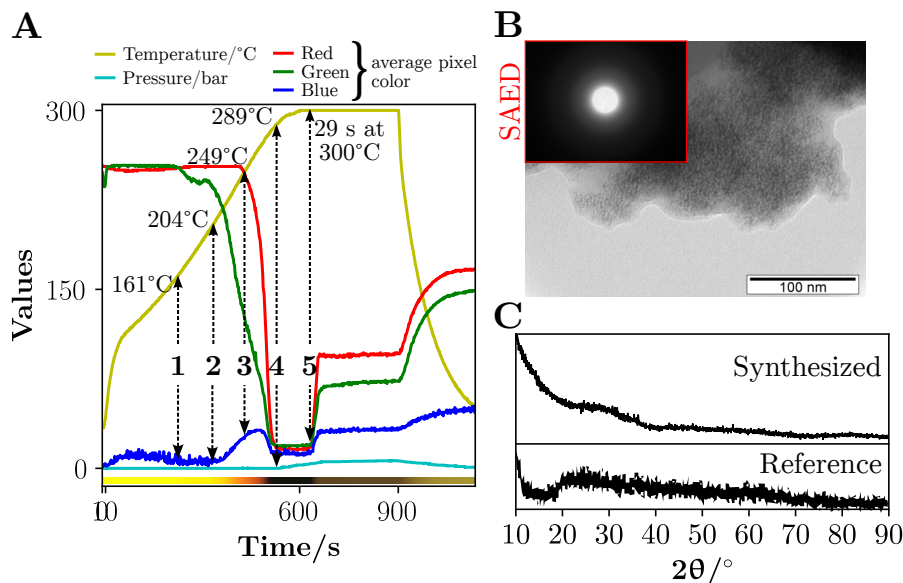


Figure 3.6: Color, temperature, and pressure profiles (A) of the syntheses starting from titanium(IV) isopropoxide, TEM image (B), a SAED pattern as an inset, and the XRD pattern (C) of the synthesized powder and a reference pattern of an amorphous  $\text{TiS}_2$  (C). Five events are marked from (1) to (5) in the profiles. The scale bar is 100 nm in (B).

The color profile in Figure 3.6 shows a change in the green channel at 161 °C (1) and another at 204 °C (2), the latter accompanied by an increase in the blue channel value. A sudden color change from orange/red to a deep black color can be seen at around 249 °C (3), which could be related to the black  $\text{TiO}_2$  nanoparticles reported in a review by Chen et al.[140]. This transformation to a black suspension was also observed by Plashnitsa et al.[141] during the synthesis of  $\text{TiS}_2$ , accompanied by the same pressure rise at 289 °C (4) seen in this work. Around 29 seconds after the temperature reached 300 °C (5), a dark yellow suspension formed, signaling the precipitation of  $\text{TiS}_2$ , which is yellow[142]. The TEM image (B) appears to have tiny - not easily measurable - particles and the selected area electron diffraction (SAED) corroborates the amorphous phase seen in the XRD pattern (C) that has no appreciable peak to determine crystallite size. It resembles the pattern of the  $\text{TiS}_2$  product that was not annealed found in reference [138], where the same reagent was reacted with  $\text{H}_2\text{S}$ . The yellow powder collected after the synthesis became white after 2-3 months, revealing the instability of the sulfide that transformed into  $\text{TiO}_2$ . An attempt to isolate the black suspension that forms at 289 °C should be done in a future synthesis and to improve the crystallinity of the obtained yellow powder, the synthesis should be prolonged to 25 minutes at 300 °C or by annealing.

### 3.2.1.2 Zirconium

Zirconium sulfide ( $\text{ZrS}_2$ ) forms 2D materials which is ideal for electronics[143] and energy storage as anode in batteries[144]. It also has a direct band gap of 2.1 eV.[145]

Similarly to the solvothermal synthesis found for  $\text{TiS}_2$  using  $\text{CS}_2$  as the sulfur source,  $\text{ZrS}_2$  nanoparticles have been synthesized previously, starting from  $\text{ZrCl}_4$  and reacting for 3 hours at

300 °C.[139] Another report on the hydrothermal synthesis of  $\text{ZrS}_2$  performed at 180 °C for 2 hours is found in reference [146], which uses a complex mixture of toxic reagents[146].

The synthesis of  $\text{ZrS}_2$  was attempted starting from zirconium(IV) chloride and is detailed in Section A.1.3.2. The color, temperature, and pressure profiles, the XRD pattern, and a TEM image of the  $\text{ZrS}_2$  synthesis attempt can be found in Figure 3.7.

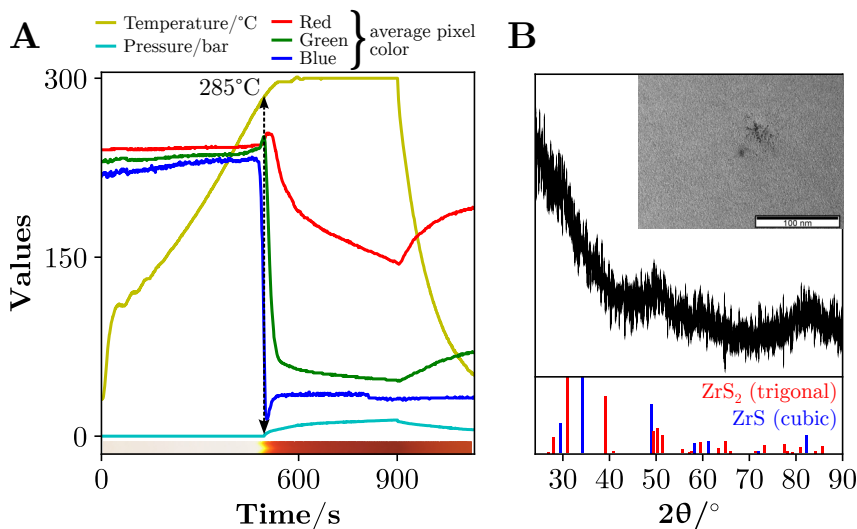


Figure 3.7: Color, temperature, and pressure profiles (A) of the syntheses starting from zirconium(IV) chloride, TEM image (B), a SAED pattern as an inset, and the XRD pattern (C) of the synthesized powder and a reference pattern of an amorphous  $\text{TiS}_2$  (C). Five events are marked from (1) to (5) in the profiles. The scale bar is 100 nm in (B).

The color profile (A) shows a color transition, where the white suspension suddenly turns yellow, pressure rises, and turns orange/red immediately after. These transitions are similar to the ones from the synthesis of  $\text{TiS}_2$  in the previous Section 3.2.1.1, but it appears that only a zirconium thiolate complex formed since  $\text{ZrS}_2$  is black. There was, however, a very small darkening of the suspension at 300 °C near the cooling phase which could be related to the formation of the sulfide. The XRD pattern (B) does not match any of the phases seen in reference [147], although the bumps seen could tentatively be attributed to either amorphous or ultra-small particles of either  $\text{ZrS}_2$  or  $\text{ZrS}$ . Small black spots can be seen in the TEM images. However, they started to vanish after a short exposure to the electron beam, indicating that the material is probably a zirconium thiolate complex.

Although the XRD pattern resembles the shape of the patterns from the trigonal  $\text{ZrS}_2$  and the cubic  $\text{ZrS}$ , the noise and extremely broad peaks indicate that there was not enough material to acquire a cleaner signal and that the crystallites are very small. Although the synthesis of zirconium sulfide could be considered successful, for the application in photovoltaic devices, the material should have a higher quality, such as a higher crystallinity and yield. Extending the synthesis to 25 minutes at 300 °C is a potential solution to enhance the final product and obtain a higher yield. A heat treatment in a sulfiding atmosphere and an even higher temperature could

also result in a more crystalline product.

### 3.2.1.3 Hafnium

Like, titanium and zirconium, studies regarding hafnium sulfide  $\text{HfS}_2$  are uncommon, even though its properties have been praised and used in photonics[148], [149], with a predicted direct band gap of 1.2 eV.[150]

Hafnium sulfide is typically synthesized by chemical vapor transport, followed by exfoliation[151], or by chemical vapor deposition (CVD)[152]. The method involving  $\text{CS}_2$  as the sulfur source to obtain  $\text{HfS}_2$  has also been reported[139], starting from  $\text{HfCl}_4$  and reacting for 12 hours at 300 °C.

The synthesis of hafnium sulfide was attempted starting from hafnium(IV) chloride and is detailed in Section A.1.3.3. The color, temperature, and pressure profiles, and the XRD pattern of the resulting powder from the  $\text{Hf}_x\text{S}_y$  synthesis attempt are shown in Figure 3.8.

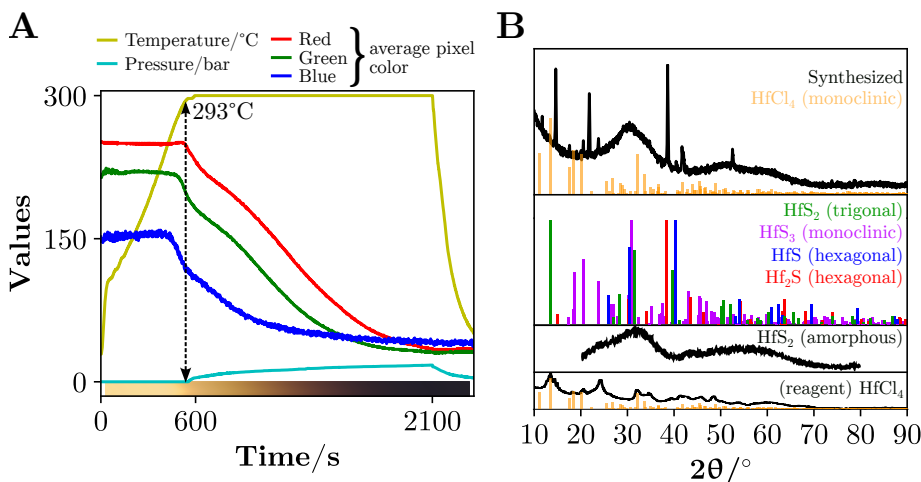


Figure 3.8: Color, temperature, and pressure profiles (A) and the resulting powder’s XRD pattern (B) of synthesis starting from  $\text{HfCl}_4$ . The XRD pattern of the reagent  $\text{HfCl}_4$  used was measured and is shown, the patterns taken from Materials Project[128][129], such as the monoclinic  $\text{HfCl}_4$  (mp-29422), trigonal  $\text{HfS}_2$  (mp-985829), monoclinic  $\text{HfS}_3$  (mp-9922), hexagonal  $\text{HfS}$  (mp-1206743), trigonal  $\text{Hf}_2\text{S}$  (mp-10000) and an adaption from the pattern of an amorphous phase of hafnium disulfide ( $\text{HfS}_2$ ) with reduced graphene oxide from reference [153].

A color transition is seen in the color profile (A) at 293 °C, accompanied by a pressure increase, and the suspension darkens progressively until the end of the synthesis. The bumps seen in the XRD pattern (B) match the ones adapted from the  $\text{HfS}_2$  pattern published by Meganathan et al.[153], which was synthesized from the reaction between  $\text{HfCl}_4$  and  $\text{Na}_2\text{S}$  for 24 hours at 200 °C. The sharper peaks appear to be slightly shifted from the presented references of the multiple hafnium sulfides. This suggests that the final product is a mixture of the hafnium sulfides.

Control of stoichiometry using this method must be studied in detail to understand the reproducibility, since the color profile shows a very slow transition to black at the maximum temperature allowed by the reactor, which is also limited to 25 minutes at that temperature.

### 3.2.2 Group 5: V, Nb, Ta

#### 3.2.2.1 Vanadium

The sulfides of the element Vanadium, comprise many phases, such as  $V_3S$ ,  $VS$ ,  $V_2S_3$ ,  $VS_2$ ,  $V_2S_5$ ,  $VS_4$  and  $VS_6$ . As stated in a review written by Liu et al.[154] the most interesting phases are  $VS_2$  and  $VS_4$ . The element's oxidation states, ranging from +2 to +5, make it an interesting element for energy storage solutions. Vanadium disulfide,  $VS_2$ , owing to its 2D layered geometry is a potential candidate for cathodes in batteries.[155] As for  $VS_4$ , it is also predicted to be a useful material for electrodes in batteries. A report by Dey et al., suggests that this sulfide could be used in Mg-based batteries, which are not prone to the formation of dendrites like the Li-based ones.[156]

Most of the reported hydrothermal or solvothermal syntheses of  $VS_2$  and  $VS_4$  take at least 6 hours to form the material.[154] A solvothermal method using  $CS_2$  as the sulfur source, starting from  $VCl_4$  and reacting for 6 h at 300 °C was found in the literature.[139]

The synthesis of vanadium sulfide was attempted starting from  $VO_2$  and is detailed in Section A.1.4.1. The color, temperature, and pressure profiles and the XRD pattern of the synthesis (Synthesis 1) of  $V_xS_y$  attempt are found in Figure 3.9.

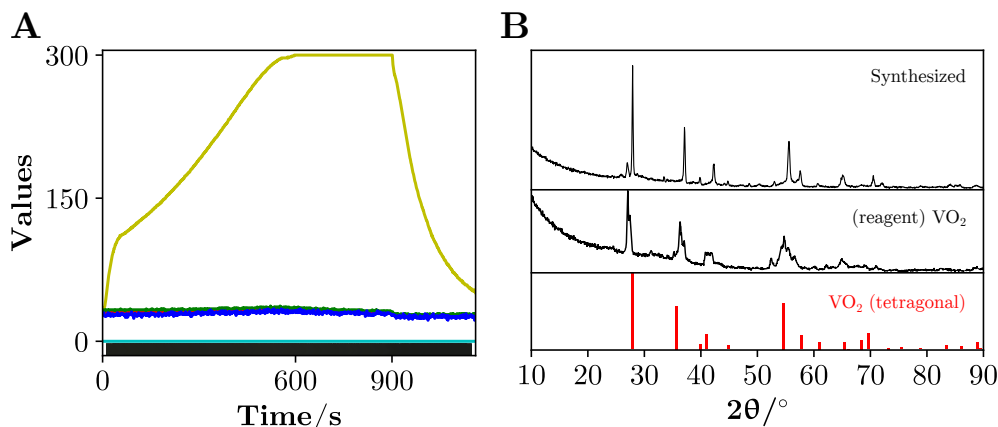


Figure 3.9: Color, temperature, and pressure profiles (A) and the resulting powder's XRD pattern (B) of synthesis starting from  $VO_2$ . The XRD pattern of the reagent  $VO_2$  used was measured and is shown, as well as the pattern from the tetragonal phase of  $VO_2$  (mp-19094), taken from Materials Project[128][129].

The color profile (A) remained flat, with no color change throughout the synthesis. The XRD pattern (B) shows that no reaction occurred since the obtained powder's pattern matches the reagent's. Oxides are known to be generally more stable than sulfides. A second synthesis (Synthesis 2) was performed starting from a vanadium alkoxide.

Another synthesis was attempted starting from triisopropoxyvanadium(V) oxide and is also detailed in Section A.1.4.1. The color, temperature profiles, the XRD pattern, and a TEM image can be found in Figure 3.10.

No significant color changes are observed in the color profile (A), except for the dissolution of the

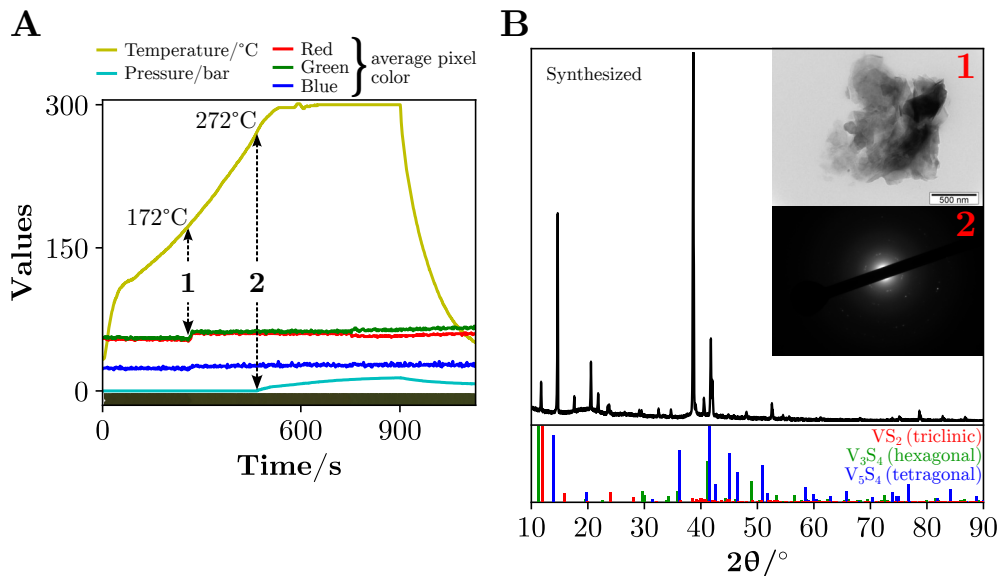


Figure 3.10: Color, temperature, and pressure profiles (A) and the resulting powder's XRD pattern (B), with a TEM image (1) and SAED pattern (2) as insets, of synthesis starting from triisopropoxyvanadium(V) oxide. The pattern from the tetragonal phase of  $\text{VS}_2$  (mp-849080),  $\text{V}_3\text{S}_4$  (mp-799), and  $\text{V}_5\text{S}_4$  (mp-1133) were taken from Materials Project[128][129]. The scale bar is 500 nm in (B).

reagent in dodecanethiol at 172 °C. However, pressure started to rise at 272 °C which could be attributed to the formation of the unknown material, yet crystalline as per the XRD peaks (B). None of the most similar vanadium sulfide reference patterns matched the obtained one. The observed sheets in the TEM image (B) (1) are considerably large, around 500 nm, and the SAED (2) indicates, like the XRD pattern, that the material is crystalline.

Vanadium sulfide was not obtained starting from either  $\text{VO}_2$  or triisopropoxyvanadium(V) oxide, with the first yielding the reagent itself and the second resulting in a crystalline but unidentified powder. As suggested in the literature, future synthesis should be attempted starting from  $\text{VCl}_4$ .

### 3.2.2.2 Niobium

Like Vanadium, Niobium can also adopt several oxidation numbers. From the group of niobium sulfides,  $\text{NbS}_2$  stands out as a promising material for hydrogen evolution from electrochemical water splitting[157] and in batteries[158].

Niobium sulfide,  $\text{NbS}_2$ , has been previously synthesized by mixing  $\text{CS}_2$  with  $\text{NbCl}_5$  at 300 °C for 3 h[139], as well as its trigonal prismatic phase by heating a mixture of  $\text{NbCl}_5$  and 1-dodecanethiol in oleylamine.[158]

The synthesis of niobium sulfide was attempted starting from  $\text{NbCl}_5$  and is detailed in Section A.1.4.2. The color, temperature, and pressure profiles of the  $\text{Nb}_x\text{S}_y$  synthesis attempt are shown in Figure 3.11 (A).

After the addition of the niobium precursor to the thiol, a yellow suspension formed as can be seen in the amplification (B). Heating this suspension to 93 °C quickly formed an orange suspension. Both the yellow and orange suspensions are presumed to be niobium thiolate. The formation of

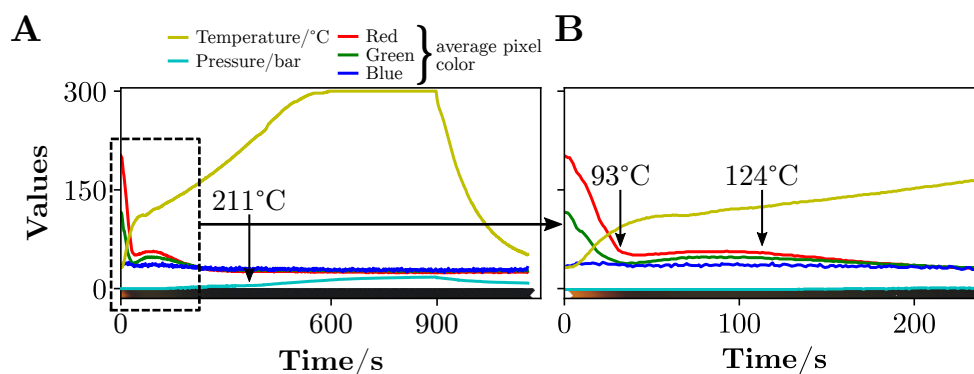


Figure 3.11: Color, temperature, and pressure profile (A) of the synthesis starting from 1-dodecanethiol and  $\text{NbCl}_5$  and an amplification (B) of the initial part of the profile and emphasis on a pressure rise seen in (A) at 211 °C two color changes in (B) at 93 °C and 124 °C.

the black suspension occurs at a very low temperature (124 °C), compared to the other synthesis from this work. Pressure started rising at 232 °C, which could be attributed to the formation of a niobium sulfide.

The synthesized powder XRD powder was revealed to be a mixture of phases and compositions, namely of  $\text{NbS}_2$  and  $\text{NbS}_3$ , as seen in Figure 3.12 (A).

Peaks from 2H- $\text{NbS}_2$  (hexagonal), 3R- $\text{NbS}_2$  (trigonal), and the monoclinic phase of  $\text{NbS}_3$  can be found in the XRD pattern. The precursor used had an oxidation state of 5+ and the products had an oxidation state of 4+;  $\text{NbS}_3$  is in fact  $\text{Nb}(\text{S}_2)\text{S}$ .<sup>[162]</sup> The presence of a weak reducer like 1-dodecanethiol aggravates the variation of niobium's oxidation state. The 2H- $\text{NbS}_2$  phase identified in the pattern, according to Leroux et al.<sup>[163]</sup>, is only stable when quenched from a temperature of around 623 °C. Since the synthesis was performed at a much lower temperature, this method can yield a usually unstable phase of niobium disulfide, although mixed with other phases. The TEM image in (B) shows an amalgam of particles that appear amorphous and some needles. Since it was not possible to do SAED singularly on the needles or on the material surrounding the needles, during the TEM image acquisition, distinguishing the phases was not possible. The following analysis is based on the assumption that the peak found in  $2\theta 14.7^\circ$  and  $34.3^\circ$  correspond to the respective Miller indices (002) and (102) of the double layer hexagonal  $\text{NbS}_2$  (2H- $\text{NbS}_2$ ). As shown in Figure 3.12 (B), the size of an observed needle is 30 nm in length and 6 nm in width, which matches the sizes calculated from the XRD pattern.

A mixture of hexagonal phase of  $\text{NbS}_2$ , trigonal phase of  $\text{NbS}_2$ , and monoclinic phase of  $\text{NbS}_3$  was obtained.

### 3.2.2.3 Tantalum

Quantum dots of Tantalum sulfide ( $\text{TaS}_2$ ) have been reported as a potential candidate for photovoltaic or photonic applications, with a band gap of  $\sim 3.7$  eV and an emission at  $\sim 3.1$  eV (400 nm) with a quantum yield of 0.46.<sup>[164]</sup> It has also been predicted as a stable and active material for hydrogen production<sup>[165]</sup>, similarly to the elements from the same group.

Tantalum sulfide,  $\text{TaS}_2$ , nanoparticles have been previously synthesized by exfoliation of bulk

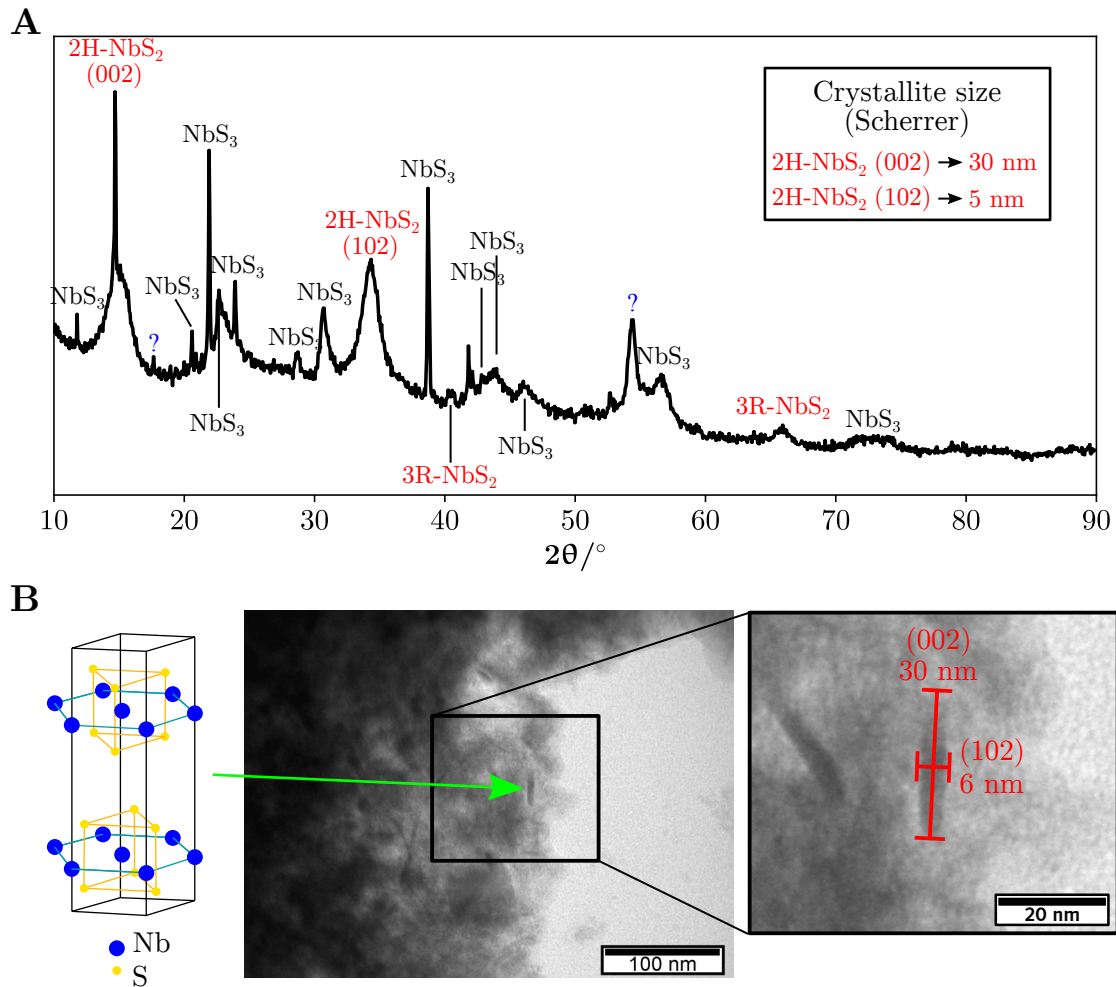


Figure 3.12: X-ray diffraction pattern (A) and transmission electron microscopy (TEM) image (B), including an amplified region with measurements of a particle as an in set and the hexagonal crystal structure 2H-NbS<sub>2</sub> adapted from reference [159], of the synthesized powder starting from NbCl<sub>5</sub>. The peaks corresponding to the hexagonal (2H-NbS<sub>2</sub>) and trigonal (3R-NbS<sub>2</sub>) phases were adapted from reference [160] and the monoclinic phase of NbS<sub>3</sub> from reference [161]. The symbols (?) mark two unidentified peaks. The scale bar is 100 nm in (B) and 20 in the inset.

TaS<sub>2</sub> by ultrasound, a top-down method, which produced quantum dots with sizes around 3 nm[164] or nano flakes[166], or by the reaction between Ta and S at high temperatures in a furnace.[167] A solvothermal TaS<sub>2</sub> synthesis method was found in the literature, using CS<sub>2</sub> as the sulfur source, TaCl<sub>5</sub> as the starting reagent and reacting for 1.5 hours at 300 °C.[139]

Two synthesis attempts were performed starting from TaCl<sub>5</sub>, detailed in Section A.1.4.3, one using the typical temperature-controlled mode, which resulted in the formation of violent electric arcs, and another using the constant microwave power mode to remove the bursts of microwave power supplied in the temperature-controlled mode. However, both developed violent electric arcs and had to be interrupted to prevent a thermal runaway. The synthesis performed under constant power developed fewer electric arcs throughout the synthesis, compared to the temperature-controlled one. However, at a later stage, the arcs were too intense to allow the synthesis to continue.



The color, temperature, and pressure profiles, and XRD patterns from both syntheses' attempts are shown in Figure 3.13.

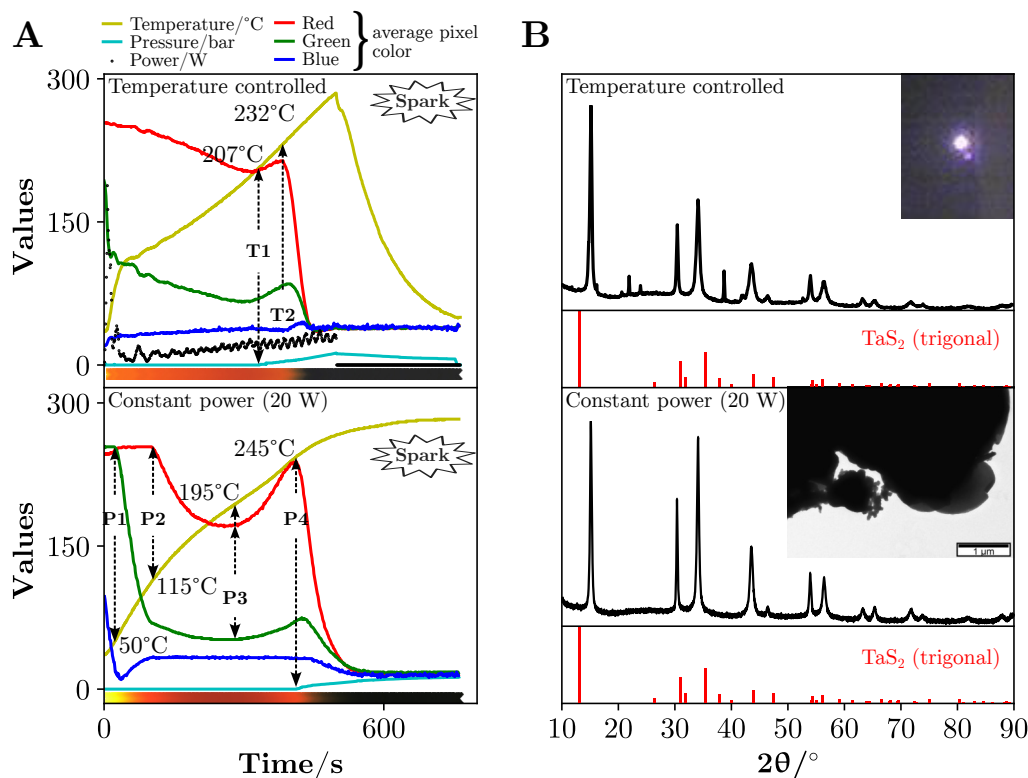


Figure 3.13: Color, temperature, and pressure profiles (A) and the resulting powders' XRD pattern (B) of two syntheses starting from  $\text{TaCl}_5$ , one performed under temperature control and the other in constant power (20 W) mode. The XRD pattern of the synthesis performed under temperature control contains a picture as an inset of an electric spark that occurred during the synthesis and under constant power a TEM image. The reference pattern from the trigonal phase of  $\text{TaS}_2$  (mp-555037) was taken from Materials Project[128][129]. The scale bar is 1  $\mu\text{m}$  in (B).

Both syntheses begin with the dissolution of the tantalum(V) chloride. However, in the temperature-controlled mode, it happens at an earlier stage, since the microwave reactor injects a greater amount of power. In the constant power one, the formation of the orange complex occurs at 50 °C (P1) with a decrease in the green and blue color channels. The color transformations in the constant power mode are much more well defined than in the temperature control mode. As the temperature increases more homogeneously in the constant power mode, the orange complex begins to darken at 115 °C (2P), while in the temperature mode it is unclear where the transition begins. In the temperature mode, the dark orange begins to lighten at 207 °C (T1) and the pressure rises at the same moment, shortly followed by the precipitation of the  $\text{TaS}_2$  at 232 °C (T2). The synthesis had to be interrupted due to the electric arcs seen in the inset in (B) (1). The constant power's color profile behaved slightly differently. When the dark orange began to lighten at 195 °C (P3), no pressure had developed yet. Between (P3) and (P4) the temperature rose slightly above the expected constant curvature, indicating that an exothermic reaction began. In this moment (P4) at 245 °C,  $\text{TaS}_2$  precipitated and pressure rose simultaneously. After the formation of the black sulfide, very small electric arcs were seen near the stirring magnet



and, although it was safe to proceed with the synthesis, it was interrupted. At the time it was not possible to judge the safety. The resulting powders were washed and their XRD patterns revealed the pure phase of trigonal TaS<sub>2</sub>, according to the pattern from Materials Project and both references [168] and [169]. However, the powder obtained from the temperature-controlled mode contained extra peaks that could not be identified. Therefore, the constant power mode yielded a purer powder. The TEM image contains flakes with several micrometers as well as smaller nano-sized particles. In future experiments and using the constant power mode, to obtain smaller particles the synthesis should be interrupted as soon as the black suspension forms; after 10 minutes at 20 W of microwave power.

### 3.2.3 Group 6: Cr, Mo, W

#### 3.2.3.1 Chromium

There is almost no literature regarding the applications of chromium sulfide nanomaterials, except a work that demonstrates the properties of Cr<sub>2</sub>S<sub>3</sub> applied to water remediation[170] and another that proposes the material for data storage, due to its magnetic properties[171]. The reported band gap for Cr<sub>2</sub>S<sub>3</sub> is 3.91 eV[172] which is unusually high for a metal sulfide. As stated by Kulkarni et al.[173], there are not many solvothermal or hydrothermal syntheses described in the literature. The authors developed a hydrothermal synthesis by heating egg yolk with CrO<sub>3</sub> at 80 °C and then calcining the resulting powder at 400 °C, obtaining monoclinic CrS. Previous reports state that Cr<sub>2</sub>S<sub>3</sub> can be synthesized by refluxing CrCl<sub>3</sub> · 6 H<sub>2</sub>O, thiourea and triethylamine in acetone[170] or from CrCl<sub>2</sub> and sulfur vapors in a tube furnace at 830 °C.

Two syntheses were attempted to produce Cr<sub>x</sub>S<sub>y</sub>, detailed in Section A.1.8.1, starting from two different chromium precursors: chromium(III) acetylacetonate (Cr(acac)<sub>3</sub> and chromium(III) chloride hexahydrate (CrCl<sub>3</sub> · 6 H<sub>2</sub>O). The color, temperature, and pressure profiles and pictures of the vials taken during both syntheses, and the XRD of the powder resulting from the synthesis with CrCl<sub>3</sub> · 6 H<sub>2</sub>O are shown in Figure 3.14.

Throughout the synthesis starting from the acetylacetonate, there were no significant changes to the color (A) of the suspension. The expected sulfide Cr<sub>2</sub>S<sub>3</sub>, being a white semiconductor due to its high band gap, did not form. The first event (A1) is marked by an increase in pressure, around the boiling point of 1-dodecanethiol. Knowing that Cr(acac)<sub>3</sub> sublimates around 110 °C[174], the rise in pressure was expected to happen at this temperature. However, the vial pictures show that above the liquid medium, the vial walls that were previously clear (B) (A1) were covered with a dark substance (B) (A2), presumably Cr(acac)<sub>3</sub>, 430 seconds at 300 °C. The resulting material was lost after centrifugation and washing with ethanol, suggesting that the final powder was the starting reagent, which is relatively soluble in ethanol. Starting from another reagent (CrCl<sub>3</sub> · 6 H<sub>2</sub>O), the profiles show that the reagent never dissolves in the thiol during the synthesis and, in the beginning, progressively turns more white until at 172 °C pressure begins to rise (C1). The color then stabilizes until the temperature reaches 279 °C and the material that was previously at the bottom of the vial (B) (C2-C3) partially suspends in the thiol. The three color

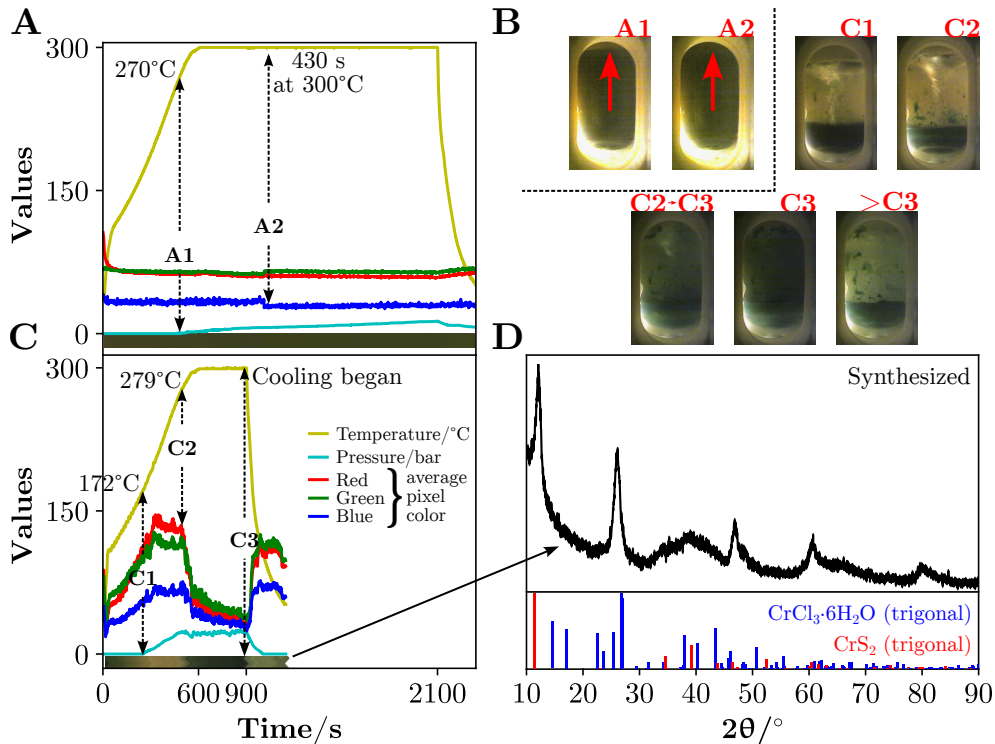


Figure 3.14: Color, temperature, and pressure profiles of the syntheses starting from  $\text{Cr}(\text{acac})_3$  (A) or  $\text{CrCl}_3 \cdot 6\text{H}_2\text{O}$  (C), pictures of both syntheses (B), and the XRD pattern from the powder starting with  $\text{CrCl}_3 \cdot 6\text{H}_2\text{O}$  (D). Certain moments were marked in the profiles of each synthesis as (A1) and (A2) and from (C1), (C2), and (C3). The reference patterns of the trigonal phases of  $\text{CrCl}_3 \cdot 6\text{H}_2\text{O}$  and  $\text{CrS}_2$  were taken from Materials Project[128][129] with the respective IDs: mp-745175 and mp-13555.

channels decrease until the automated cooling begins (C3) and the suspended material sinks (>C3). The XRD pattern mainly matches the  $\text{CrCl}_3 \cdot 6\text{H}_2\text{O}$  reference pattern. The only peak that could be attributed to  $\text{CrS}_2$  is at a  $2\theta$  of  $12.8^\circ$  but it is insufficient to declare the phase presence. With these starting compounds, it was not possible to obtain pure chromium sulfides. As an alternative, chromium(III) alkoxides, such as the ethoxide, should be considered for future syntheses, since the oxidation state of  $3+$  is known to form sulfides.

### 3.2.3.2 Molybdenum

Molybdenum sulfide,  $\text{MoS}_2$ , as many metal sulfide materials that adopt a 2D structure, is used in hydrogen production[175], lubricant[176], in electronics, such as transistors[177], and in supercapacitors[178].

Two  $\text{MoS}_2$  microwave-assisted syntheses are available in the literature. A hydrothermal synthesis was proposed by Thi Xuyen et al.[179], starting from hydrated sodium molybdate  $\text{Na}_2\text{MoO}_4 \cdot 2\text{H}_2\text{O}$ , oxalic acid, and thiourea, heated to  $220^\circ\text{C}$  for 30 min. The second is a solvothermal synthesis proposed by Barrera et al.[180], where  $\text{MoCl}_3$  was mixed with sulfur in oleylamine and 1,2-hexadecanediol and heated to  $280^\circ\text{C}$  for 15 min.

Two syntheses were attempted to produce  $\text{Mo}_x\text{S}_y$ , detailed in Section A.1.5.2, starting from two different precursors:  $\text{MoO}_2$  and  $\text{MoCl}_5$ . The color, temperature, and pressure profiles and

the resulting powder's XRD pattern from the synthesis performed with  $\text{MoO}_2$  are shown in Figure 3.15 (A) and (B), respectively. In the second synthesis performed starting from  $\text{MoCl}_5$ , the microwave reactor returned an error and erased all of the images that were recorded. Therefore, only the resulting powder's XRD pattern and TEM images are shown in (C) and (D), respectively.

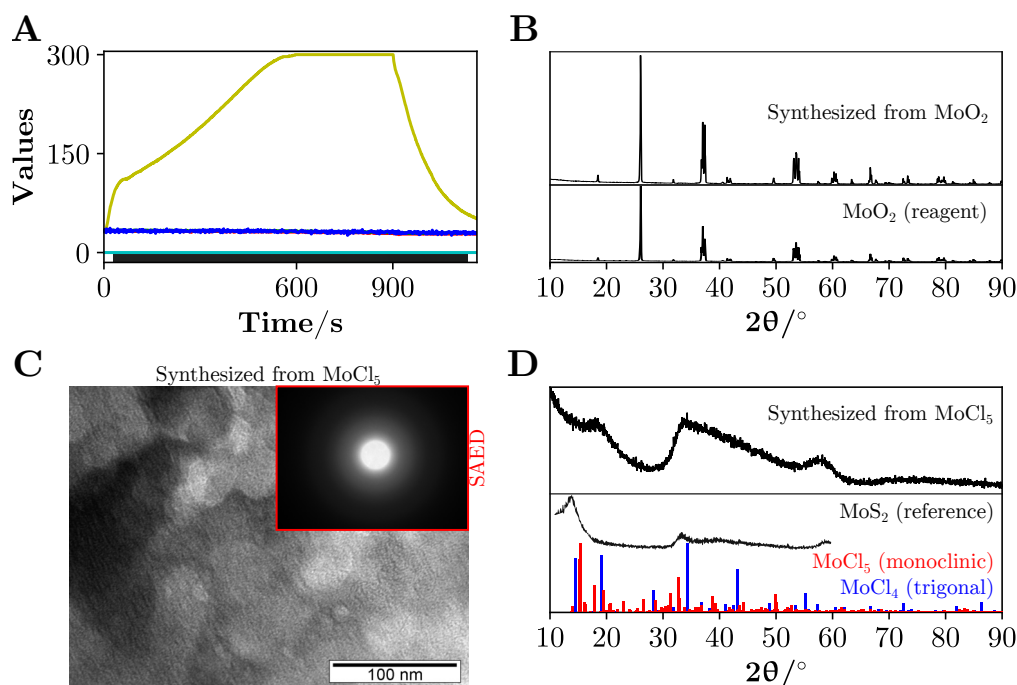


Figure 3.15: Color, temperature, and pressure profiles of the syntheses starting from  $\text{MoO}_2$  (A), the resulting powder's and reagent's XRD patterns (B). Starting from  $\text{MoCl}_5$ , a TEM image (C), with a SAED pattern as an inset, and the XRD pattern (D). The reference pattern of the  $\text{MoS}_2$  was adapted from [181] and the patterns of monoclinic  $\text{MoCl}_5$  (mp-571256) and trigonal  $\text{MoCl}_4$  (mp-1221517) were taken from Materials Project[128][129]. The scale bar is 100 nm in (C).

From the first synthesis starting from  $\text{MoO}_2$ , the profiles (A) reveal no changes and the XRD pattern (B) of the final product matches the pattern of the reagent. There are no visible particles or sheets in the TEM images (C) and the SAED reveals an amorphous structure. The XRD pattern also corresponds to an amorphous material (D) and is very similar to the  $\text{MoS}_2$  pattern adapted from [181]. However, the bump seen below  $2\theta$  of  $20^\circ$  in the synthesized sample coincides more with the peaks from the molybdenum chlorides. It is unclear if molybdenum sulfide was obtained from  $\text{MoCl}_5$  using this method. Molybdenum alkoxides could be an alternative as starting materials to obtain the sulfides in future synthesis.

### 3.2.3.3 Tungsten

Similarly to molybdenum, tungsten sulfide,  $\text{WS}_2$ , is also used as a lubricant[176], for hydrogen production through electrochemical water splitting[182] and in energy storage as an anode[183]. Two simple template-free tungsten sulfide,  $\text{WS}_2$ , synthesis were found in the literature: a hydrothermal, involving  $\text{Na}_2\text{WO}_4$  and  $\text{Na}_2\text{S}$  in an aqueous solution raised to a temperature of  $220^\circ\text{C}$  for 5 h[184] and a solvothermal synthesis starting from  $\text{WCl}_6$  and thioacetamide in a mixture of ethanol and isopropanol heated to  $200^\circ\text{C}$  for 24 h[183]. A microwave-assisted synthesis

proposed to fabricate  $\text{MoS}_2$  was also used to produce  $\text{WS}_2$ [180], starting from  $\text{WCl}_4$  and sulfur in oleylamine and 1,2-hexadecanediol at  $280^\circ\text{C}$  for 15 min.

Two synthesis attempts were performed to obtain  $\text{W}_x\text{S}_y$ , detailed in Section A.1.5.3, starting from either  $\text{WO}_2$  or  $\text{WCl}_6$ . The color, temperature, and pressure profiles and the resulting powders' XRD patterns, from both syntheses, are shown in Figure 3.16.

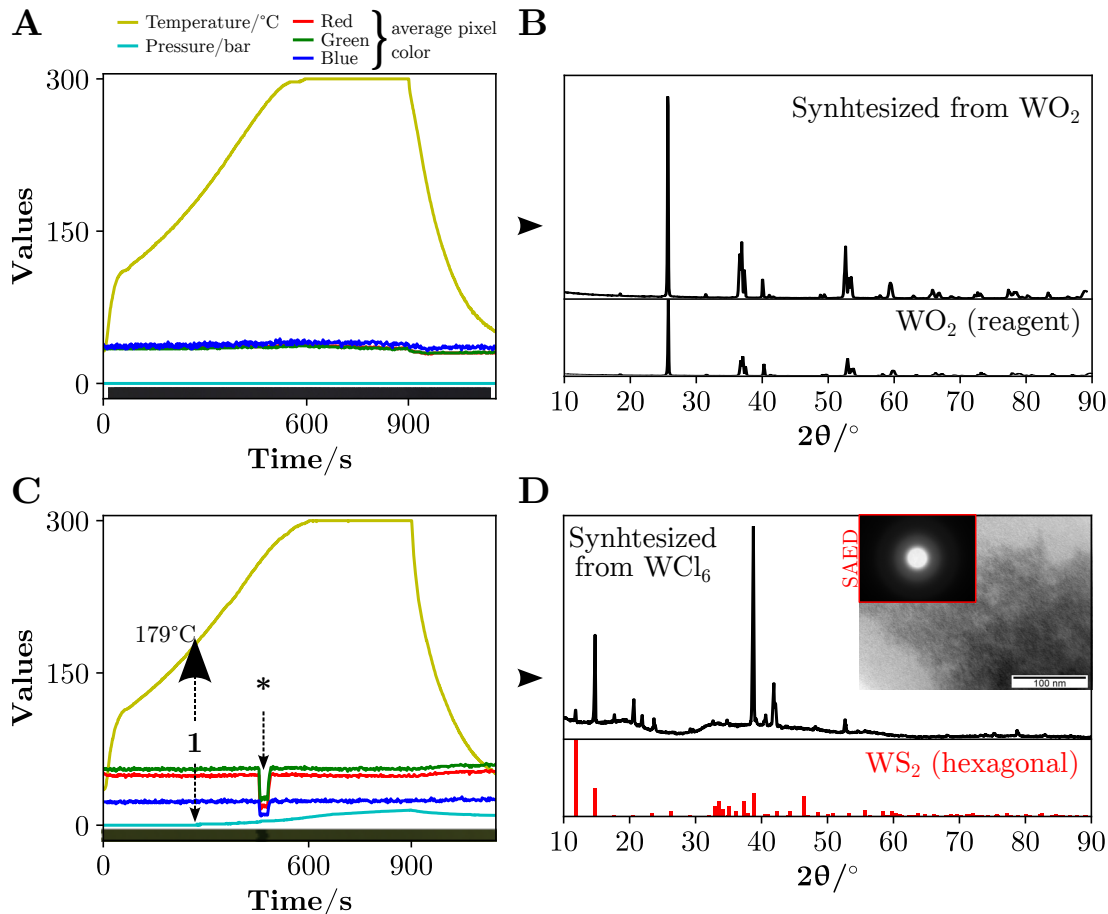


Figure 3.16: Color, temperature, and pressure profiles of the syntheses starting from  $\text{WO}_2$  (A) or  $\text{WCl}_6$  (C), and the respective XRD patterns (B) and (D), the latter with a TEM image and SAED pattern as insets. The moment marked with an \* in (B) corresponds to a purposeful decrease in the lamp's light intensity to check for electric arcs and moment (1) marks a pressure rise. The reference pattern of the hexagonal phase of  $\text{WS}_2$  (mp-1025571) was taken from Materials Project[128][129] and shifted to the right by  $0.573^\circ$ . The scale bar is 100 nm in (D).

As is recurrent with oxide reagents, the color profile (A) from the synthesis starting from  $\text{WO}_2$  shows no significant changes and the resulting powder's XRD pattern (B) matches that of the reagent. Regarding the synthesis starting from  $\text{WCl}_6$ , a pressure rise is seen at  $179^\circ\text{C}$  in the color profile (C), indicating a possible reaction. It was not possible to identify the peaks in the XRD pattern (D) from the resulting product, since they do not match any specie from the tungsten sulfide family, tungsten chlorides or tungsten chloro-sulfide complexes from Materials Project[128][129] database. Some of the peaks from the synthesized powder's pattern could tentatively be matched with  $\text{WS}_2$  if the reference pattern is shifted by  $0.573^\circ$ , as was done in (D). This implies that the metal was reduced from the original 6+ oxidation state to 4+. Although

the powder appears to be crystalline, due to the sharp XRD peaks, at least part of the product is amorphous, according to the SAED.

It was not possible to synthesize tungsten sulfide starting from  $\text{WO}_2$ . The XRD pattern from the powder obtained starting from  $\text{WCl}_6$  appears to match the pattern of the hexagonal phase of  $\text{WS}_2$  but is not clear enough. In future synthesis, tungsten(VI) ethoxide should be considered due to its high reactivity.

### 3.2.4 Group 7: Mn

#### 3.2.4.1 Manganese

Manganese sulfide is currently not used alone but is mainly found in doped systems, such as Pd modified MnS nanoparticles for the photoreduction of  $\text{CO}_2$ [185], in core-shell structures for supercapacitors, such as  $\text{CoMn}_2\text{O}_4@\text{MnS}$ [186],  $\text{Ni}_3\text{S}_2@\text{MnS}$ [187] and  $\text{MnS}@\text{Mn}_3\text{O}_4$ [188], and graphene-MnS[189], [190] composites as anodes for batteries. It has a wide band gap of 3.23 eV.[191]

A review on the synthesis and applications of manganese sulfide presented by Ferretti et al.[192] states that zero-dimensional MnS nanoparticles are mainly synthesized by the solvothermal route. Nanoparticles of the three polymorphs can be obtained by the reaction of  $\text{MnCl}_2$  with thioacetamide to obtain the cubic (rock-salt) structure, while the cubic (zinc blende) and hexagonal structures are usually obtained as a mixture. A cation exchange synthesis starting from  $\text{Cu}_2\text{S}$  nanoparticles can be performed to obtain hexagonal MnS nanoparticles.

The synthesis of MnS was attempted starting from manganese(II) acetate tetrahydrate and is detailed in Section A.1.6.1. The color, temperature, and pressure profiles and the resulting powder's XRD pattern are shown in Figure 3.17.

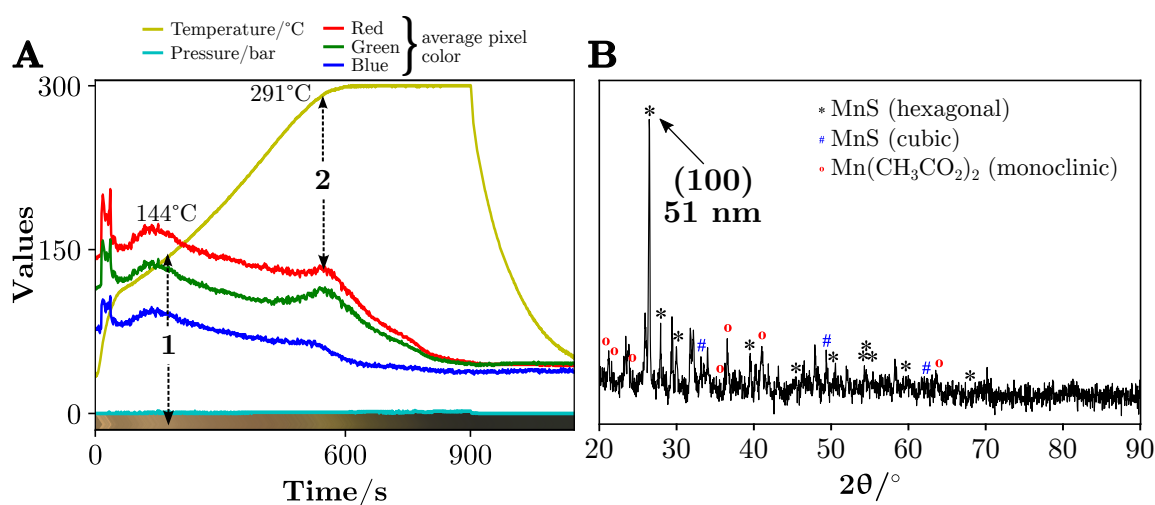


Figure 3.17: Color, temperature, and pressure profiles (A) of the synthesis starting from  $\text{Mn}(\text{CH}_3\text{CO}_2)_2 \cdot 4\text{H}_2\text{O}$  and the obtained powder's XRD pattern (B). The reference pattern marks of the hexagonal (\*) and cubic (rock-salt) (#) phases of MnS, and monoclinic phase of manganese(II) acetate (°) were adapted from reference [193].

The color profile (A) shows a transformation at 150 °C, associated with the dissolution of the reagent, followed by an overall darkening of the suspension at 275 °C, probably corresponding to the formation of MnS. According to reference [193], the peaks found in the XRD pattern (B) of the obtained powder correspond mainly to the hexagonal of MnS, the cubic (rock-salt), and monoclinic manganese(II) acetate, the reagent used in this synthesis. From the most intense peak at  $2\theta$  of 26°, the crystallite size of the hexagonal phase (100) is estimated to be 51 nm. However, obtaining the pure hexagonal phase of MnS was impossible, as some residual manganese precursor and the sulfide's cubic phase remained. Furthermore, heating at 300 °C for a longer time might result in a mixture of both the hexagonal and cubic phases in future synthesis.

### 3.2.5 Group 8: Fe

#### 3.2.5.1 Iron

Iron sulfide, namely FeS and FeS<sub>2</sub> has been recently used for water and soil remediation.[194]–[197] Pyrite (FeS<sub>2</sub>) can also be found in supercapacitors' electrodes[198] and FeS in batteries' electrodes[199].

Pyrite (cubic FeS<sub>2</sub>) has been synthesized by Kim and Batchelor[200] by microwave-assisted heating of FeCl<sub>3</sub> · 6 H<sub>2</sub>O and NaHS · xH<sub>2</sub>O in water but the temperature of the synthesis was not measured. Phase-controlled syntheses of FeS<sub>2</sub>, Fe<sub>3</sub>S<sub>4</sub> and Fe<sub>7</sub>S<sub>8</sub> were performed using a variety of organic sulfides and disulfides by Rhodes et al.[201]. The phase control they achieved is interesting, but they did not experiment using a long chain and saturated alkyl thiol. The thiol most similar to 1-dodecanethiol they used was tert-butylthiol and the reaction with anhydrous FeCl<sub>2</sub> led to the formation of monoclinic (with some hexagonal polytypes) Fe<sub>1-x</sub>S, with x from 0 to 0.2.

Synthesis of iron sulfide was attempted starting from FeSO<sub>4</sub> · 7 H<sub>2</sub>O and is detailed in Section A.1.7.1. The color, temperature, and pressure profiles, from both syntheses, and the resulting powder's XRD pattern, are shown in Figure 3.18.

As shown in Figure 3.18 (A), the color profile appears (A) to begin to darken at around 206 °C (1) in both syntheses, but the transition on the synthesis with FeCl<sub>3</sub> · 6 H<sub>2</sub>O is sharper, probably due to the reduction of Fe<sup>3+</sup> to Fe<sup>2+</sup>. The synthesis starting from FeSO<sub>4</sub> · 7 H<sub>2</sub>O yielded iron(II) sulfate monohydrate (Szomolnokite) and the heptahydrate (Melanterite), according to the XRD pattern (B). On the other hand, the synthesis starting from FeCl<sub>3</sub> · 6 H<sub>2</sub>O appears to have formed the sulfide after 207 seconds at 300 °C (2), given the relatively sharp color transition to black. The yield was too low to be able to obtain an XRD pattern.

Another reagent, iron(III) acetylacetonate, was used to attempt to produce an iron sulfide with a higher yield, as detailed in Section A.1.7.1. The color, temperature, and pressure profiles (Figure 3.19) show three color transitions. The first is associated with the dissolution of the reagent in the thiol at 120 °C (1), and the second event corresponds to a darkening of the suspension at 194 °C (2), probably corresponding to the simultaneous reduction of Fe<sup>3+</sup> to Fe<sup>2+</sup> and the formation of iron sulfide. The third corresponds to the stabilization of the color at 216 °C

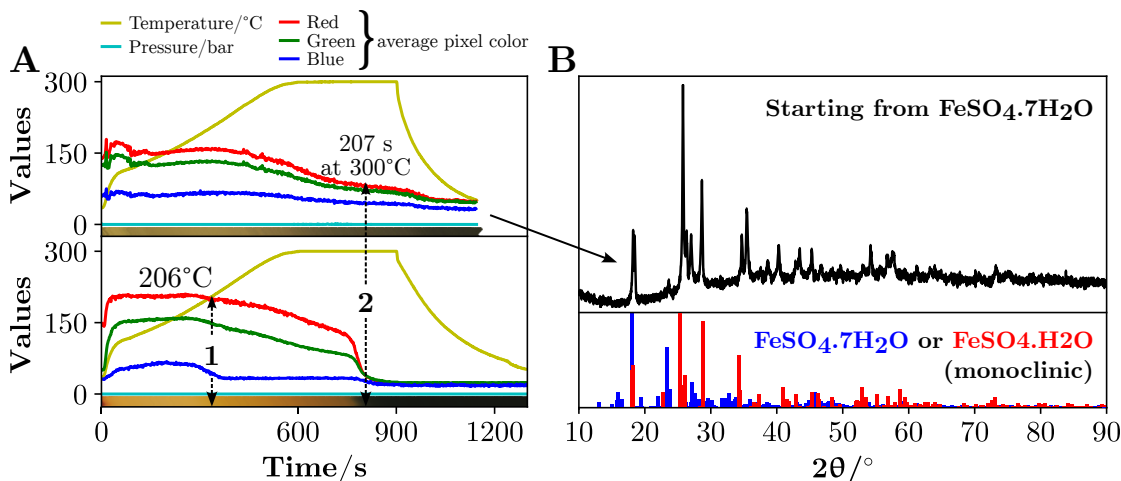


Figure 3.18: Color, temperature, and pressure profiles (A) of the syntheses starting from  $\text{FeCl}_3 \cdot 6\text{H}_2\text{O}$  or  $\text{FeSO}_4 \cdot 7\text{H}_2\text{O}$  and the XRD pattern from the synthesis with  $\text{FeSO}_4 \cdot 7\text{H}_2\text{O}$  (B). Two moments were marked in the profiles. The reference patterns of the monoclinic phases of  $\text{FeSO}_4 \cdot \text{H}_2\text{O}$  and  $\text{FeSO}_4 \cdot 7\text{H}_2\text{O}$  were taken from Materials Project[128][129] with the respective IDs: mp-643564 and mp-1198559.

(3). The reaction developed electric arcs after the third event and had to be interrupted.

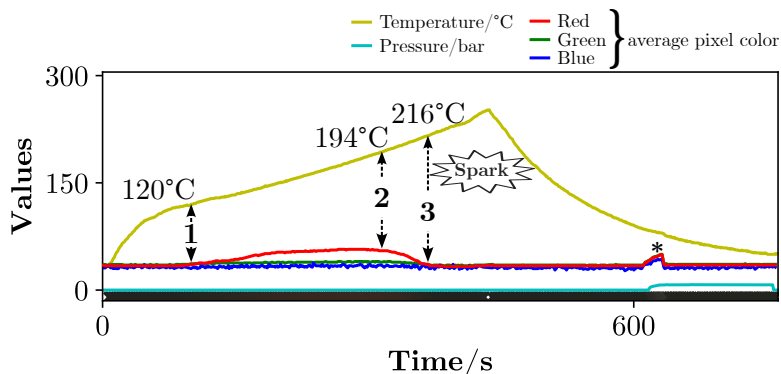


Figure 3.19: Color, temperature, and pressure profiles of the synthesis starting from iron(III) acetylacetonate with three color transitions marked at (1), (2), and (3). The asterisk marks a moment when the reactor's piston malfunctioned and lifted the vial.

### 3.2.6 Group 9: Co

#### 3.2.6.1 Cobalt

Cobalt sulfides are used in supercapacitors and batteries with other elements.[202]–[204] Besides their supercapacity properties, hollow structures of the various cobalt sulfides have been reported as excellent materials, specially  $\text{CoS}_2$ , for the production of  $\text{H}_2$ [205] and  $\text{O}_2$ [206] via electrolysis. When used in pair with  $\text{CdIn}_2\text{S}_4$ ,  $\text{Co}_9\text{S}_8$  enhances the photocatalytic production of  $\text{H}_2$  under visible light irradiation.[207] Synthesis without control over the cobalt sulfide phase has been previously attained by Srouji et al.[208], using a single-source cobalt-sulfur precursor and generating the sulfides by chemical vapor deposition. More recently, it has been shown that microwave-assisted

synthesis of  $\text{Co}_9\text{S}_8$  produces nanoparticles with better efficiency at water splitting[209] compared to traditional conduction and convection heating.

The synthesis of cobalt sulfide was attempted starting from  $\text{CoCl}_2 \cdot 6\text{H}_2\text{O}$  and is detailed in Section A.1.8.1. The color, temperature, and pressure profiles of the  $\text{Co}_x\text{S}_y$  synthesis attempt are shown in Figure 3.20 (A).

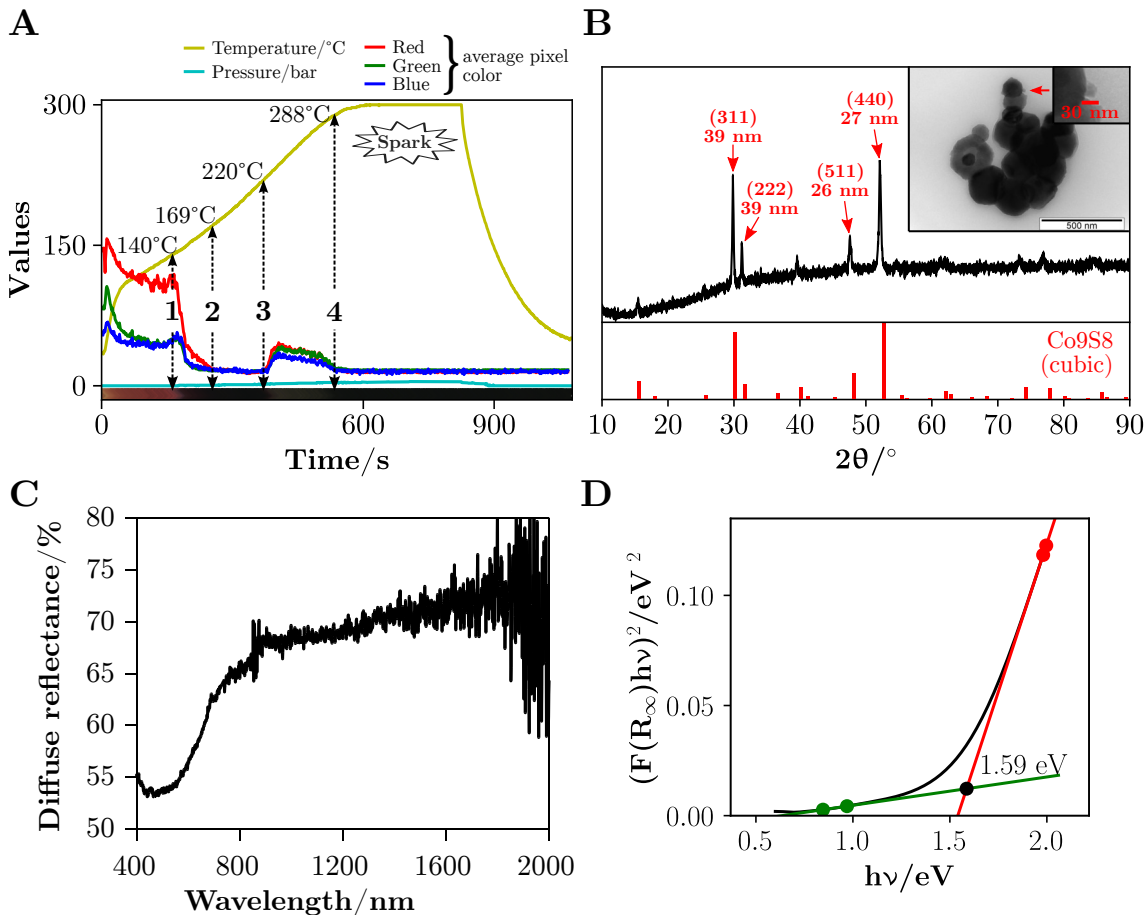


Figure 3.20: Color, temperature, and pressure profiles of the synthesis starting from  $\text{CoCl}_2 \cdot 6\text{H}_2\text{O}$  with three color transitions marked at (1), (2), (3), and (4), the XRD pattern of the obtained powder with the reference for  $\text{Co}_9\text{S}_8$ , a TEM image as an inset with amplification as a sub-inset (B), the diffuse reflectance spectrum of the powder (C) and the corresponding Tauc plot (D). The cubic phase of  $\text{Co}_9\text{S}_8$  was taken from Materials Project[128][129] and corresponds to the ID mp-1513. The scale bar is 500 nm in (B).

There are four color changes in the color profile (A). The first is at 140 °C (1) where the salt has already dissolved in the thiol, the suspension abruptly darkens, and the pressure begins to rise. This could be the formation of the sulfide. The second moment (2) at 169 °C is when the color stabilizes but is followed by the third change (3) at 220 °C with the formation of dark gray material. This change of color was unexpected since a sulfide was most probably already formed unless it is a phase change from one form to another. The same can be said about the fourth color change (4) as the suspension reverts to black again at 288 °C. During the synthesis, electric arcs formed and future synthesis should be performed with another cobalt precursor. This final black powder obtained was the pure cubic phase of  $\text{Co}_9\text{S}_8$ , according to the XRD pattern



in (B), and the crystallite size is consistently on average 30 nm. The TEM image, however, shows agglomerates that are not made of cubic particles but, the amplification does show a smaller material that matches the size obtained from the XRD pattern (B), between 27 nm and 39 nm. The aggregates appear to form hollow structures, similar to the ones reported by Sun et al.[206] as well as microwave-assisted synthesized  $\text{Co}_9\text{S}_8$  flower-like structures obtained by Yin et al.[210]. The presence of cobalt ions appear to heavily interfere on the shape of some materials, for example, when  $\text{Nb}_2\text{O}_5$  is synthesized in its presence, sphere shaped particles are obtained.[211] The band gap of the obtained powder was determined by measuring the diffuse reflectance spectrum (C), which was transformed into a Tauc plot (D) using the Kubelka-Munk method[131] and as described in Section 3.1.3, and has a value of 1.59 eV, which is on pair with the literature (1.6 eV).[212]

### 3.2.7 Group 10: Ni

#### 3.2.7.1 Nickel

Nickel sulfide can be found in supercapacitors in the phase NiS[213], [214], and  $\text{Ni}_3\text{S}_2$ [215]. Nanoparticles of NiS have also been used for hydrogen production[216] and both  $\text{NiS}_2$ [217] and NiS[218] as electrodes for dye-sensitized solar cells.

Hexagonal nickel sulfide (NiS) has been previously synthesized in a microwave reactor, starting from nickel(II) acetate tetrahydrate and thiourea in ethylene glycol. The mixture was irradiated with microwaves for 3 minutes and then annealed at 550 °C for 3 hours.[219] Another mixture was used by Salavati-Niasari et al.[220] composed of a complex between nickel(II) and 2-hydroxyacetophenone, and thioacetamide in ethylene glycol. The mixture was then irradiated with microwaves for five cycles of on and off. The authors did not calculate the particle size from their XRD pattern but the broad peaks indicate that the material probably had nano-sized crystallites.

The synthesis of nickel sulfide was attempted starting from nickel(II) acetate tetrahydrate ( $\text{Ni}(\text{CH}_3\text{CO}_2)_2 \cdot 4\text{H}_2\text{O}$ ) and is detailed in Section A.1.9.1. The synthesis began to develop electric arcs and was interrupted when it reached around 300 °C. The color, temperature, and pressure profiles, the XRD pattern, and TEM images of the  $\text{Ni}_x\text{S}_y$  synthesis attempt are shown in Figure 3.21.

From the color profile (A) it is possible to observe the almost instantaneous conversion of the yellow suspension to a dark brown suspension (1), as soon as the synthesis starts and is slightly above room temperature. According to an image shown in a report published by Urgunde et al.[221], who synthesized nickel(II) alkyl thiolates at around 70 °C using an alkyl thiol such as 1-dodecanethiol, these nickel complexes are dark brown. Soon after, the color stabilizes until a temperature of 126 °C is reached (2) and darkens slightly after, probably corresponding to the formation of one of the phases of NiS. At 217 °C (3) pressure starts to rise, with no visible color change, but at 259 °C (4) the overall color of the suspension becomes grayer, which probably indicates the formation of the phase. The synthesis was interrupted due to the formation of

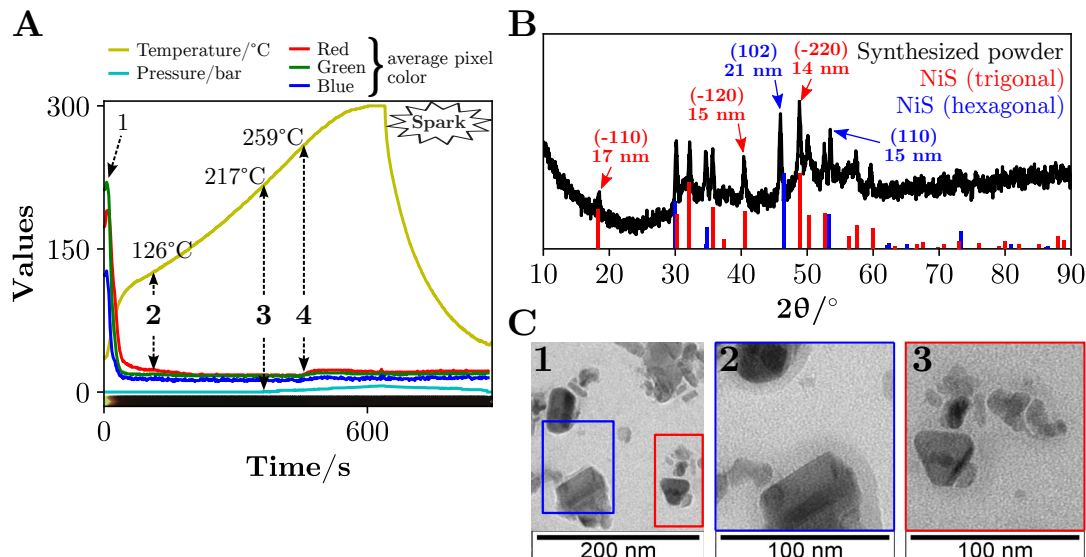


Figure 3.21: Color, temperature, and pressure profiles (A) of the synthesis starting from  $\text{Ni}(\text{CH}_3\text{CO}_2)_2 \cdot 4\text{H}_2\text{O}$  with four transition moments marked from (1) to (4), the obtained powder's XRD pattern (B), and three TEM images with (2) and (3) as zooms from (1). The reference patterns of the trigonal and hexagonal phases of NiS were taken from Materials Project[128][129] with the respective IDs: mp-1547 and mp-594. The scale bar is 200 nm in (C-1), 100 nm in (C-2) and (C-3).

electric arcs. The peaks in the XRD pattern (B) reveal a mixture of two nickel sulfide phases: the trigonal and hexagonal phases of NiS. The TEM image (C1) shows particles with different shapes and sizes, but it is possible to distinguish a hexagonal particle in (C2) and a trigonal in (C3). The TEM images show particles with different sizes ranging from some nanometers to almost a hundred. The peaks of interest, found in the XRD pattern, corresponding planes such as (001) from both phases would allow us to estimate the hexagonal and trigonal faces' lengths and compare them with the sizes seen in the TEM images ( $\sim 40$  nm). However, the peaks are too convoluted. Some needle-like particles can be seen in the images and their thickness are similar to the values obtained from the XRD pattern. Phase and size control of NiS was not achieved by heating the mixture to  $300^\circ\text{C}$  in 1-dodecanethiol. Microwave-assisted synthesis using thiourea is still the better choice when targeting a pure trigonal phase NiS.[220] In future syntheses, the temperature should be kept below  $259^\circ\text{C}$  to prevent electric arc formations and attempt to obtain a single phase of NiS.

### 3.2.8 Group 11: Cu, Ag

#### 3.2.8.1 Copper

Copper(II) sulfide CuS is used in optoelectronics, with a band gap of 2.51 eV[222] or 2 eV[223], in supercapacitors and sensitized solar cells[224] and in water remediation[225], [226]. Copper(I) sulfide  $\text{Cu}_2\text{S}$  can be used in thermoelectric[227] and has a lower band gap than CuS. The band gaps of  $\text{Cu}_{2-x}\text{S}$  with  $x$  from 0 to 1, are presented within a wide range of values in the literature. It depends heavily on the composition, size, and crystal type. Bulk hexagonal  $\text{Cu}_2\text{S}$  has a band gap

between 1.2 eV and 1.22 eV, while for the same stoichiometry, the orthorhombic phase presents a 2.48 eV band gap. Copper sulfides with a lower content of the metal have lower band gaps, such as the tetragonal  $\text{Cu}_{1.96}\text{S}$  with a band gap of 1.4 eV, an unreported phase of  $\text{Cu}_{1.8}\text{S}$  (digenite) with 1.5-1.55 eV, and the cubic  $\text{Cu}_{1.76}\text{S}$  exception with a larger band gap of 2.11 eV.[223], [228] Wang et al.[229] have demonstrated that the use of 1-dodecanethiol in a mixture of toluene and water, starting from copper(II) sulfate, and heating in a microwave reactor at 190 °C for 4 hours produced small-sized nanoparticles. They also found a direct correlation between the amount of thiol used and the particles' average size. By increasing the amount of dodecanethiol, the particles' size decreased to 3 nm, while a lower amount of thiol increased the size to 8 nm.

The synthesis of copper sulfide was attempted starting from CuO and is detailed in Section A.1.10.1. The color, temperature, and pressure profiles and the resulting powder's XRD pattern are shown in Figure 3.22.

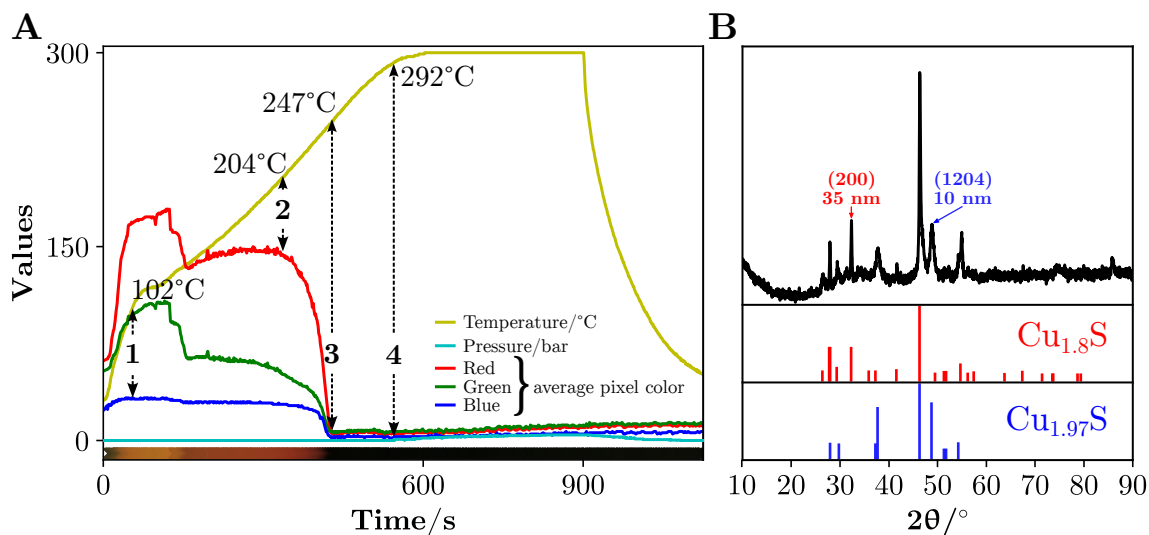


Figure 3.22: Color, temperature, and pressure profiles (A) of the synthesis starting from CuO and XRD pattern (B), with the corresponding hexagonal  $\text{Cu}_{1.8}\text{S}$  and orthorhombic  $\text{Cu}_{1.97}\text{S}$  reference patterns respectively adapted from JCPDS standards 47-1748 and 20-0365, from reference [223].

A series of color transformations can be seen in the color profile (A), ranging from the dissolution of the oxide (1) in the thiol to the formation of the copper-thiolate complex (2) that changes color with the increasing temperature. At 204 °C the suspension begins darkening black, stabilizing the color (3) at 247 °C and at 292 °C pressure starts to rise (4). According to the X-ray diffraction (B) obtained from the cleaned synthesized powder a mixture of two phases of  $\text{Cu}_2\text{S}$  were obtained: hexagonal  $\text{Cu}_{1.8}\text{S}$  and orthorhombic  $\text{Cu}_{1.97}\text{S}$ , according to reference.[223]

Attempting to synthesize CuS by starting from a reagent with copper in the same oxidation state (CuO) resulted in a copper sulfide with a lower oxidation state. As suggested by Smith et al.[230], after the  $\text{Cu}^{2+}$  forms a colored complex with the thiol, the copper is reduced to Cu(I) and 1-dodecanethiol oxidizes to the radical  $\text{RS}\cdot$ . Both the  $\text{Cu}^+$  and the radical, upon reacting with other 1-dodecanethiol that is present in excess, form a  $\text{Cu}^+$ -dodecanethiolate and a didodecane disulfide. At a higher temperature, the bond S–R is broken and a non-stoichiometric  $\text{Cu}_2\text{S}$  is

formed.

The synthesized powder's TEM images are shown in Figure 3.23.

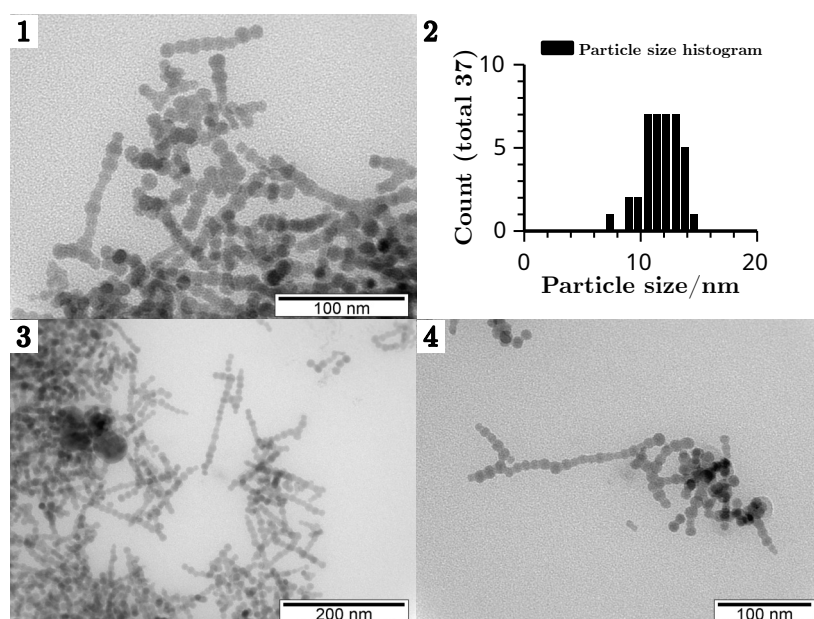


Figure 3.23: Transmission electron microscopy images (1, 3, and 4) and the particle size distribution (2) from measurements from (1) of the synthesized  $\text{Cu}_2\text{S}$  particles starting from  $\text{CuO}$ . The scale bar is 100 nm in (1), 200 nm in (3), and 100 nm in (4).

The average particle size extracted from the TEM image (1) is 12 nm, while from the XRD pattern in Figure 3.22 (B) the average crystallite size of  $\text{Cu}_{1.97}\text{S}$  is 10 nm from the peak with a  $2\theta$  of  $49^\circ$  (miller index 1204[231]) and 35 nm for  $\text{Cu}_{1.8}\text{S}$  from the peak with a  $2\theta$  of  $32^\circ$  (miller index 200). Notice that TEM image (3) contains some bigger particles which have an approximate size of 40 nm, similar to the size estimated for  $\text{Cu}_{1.8}\text{S}$  from the XRD pattern. Therefore, a mixture of two phases with distinct sizes was obtained starting from  $\text{CuO}$ . Comparatively to Wang et al.[229], the synthesis was performed using solely 1-dodecanethiol and is equivalent to their synthesis using a maximum concentration, which predicatively produces bigger particles. The attribution of phases should be taken with a grain of salt, as stated by Zhao et al.[223] since the amount of stoichiometries that can be obtained in the copper sulfides is unusually large and it is not trivial to pinpoint one.

Given that the synthesis starting from  $\text{CuO}$  inevitably forms a mixture of phases of the less oxidized, albeit non-stoichiometric,  $\text{Cu}_2\text{S}$ , the synthesis was attempted starting directly from the dark red  $\text{Cu}_2\text{O}$ , instead as detailed in Section A.1.10.1. During the synthesis, electric sparks formed casually but they were deemed safe enough until the end. The color, temperature, and pressure profiles (A), as well as the X-ray diffraction pattern (B), are shown in Figure 3.24.

Notice that the color profile of the synthesis starting from  $\text{Cu}_2\text{O}$  is similar to the one starting from  $\text{CuO}$ , with the reagent dissolving at around  $102^\circ\text{C}$  (1), then begins to darken comparatively at a slightly higher temperature of  $223^\circ\text{C}$  (2), also reaching a stable black color at a higher temperature of  $252^\circ\text{C}$  (3), and the pressure rises more or less at the same temperature. The similarity of the transformation temperatures between the two syntheses suggests that the same

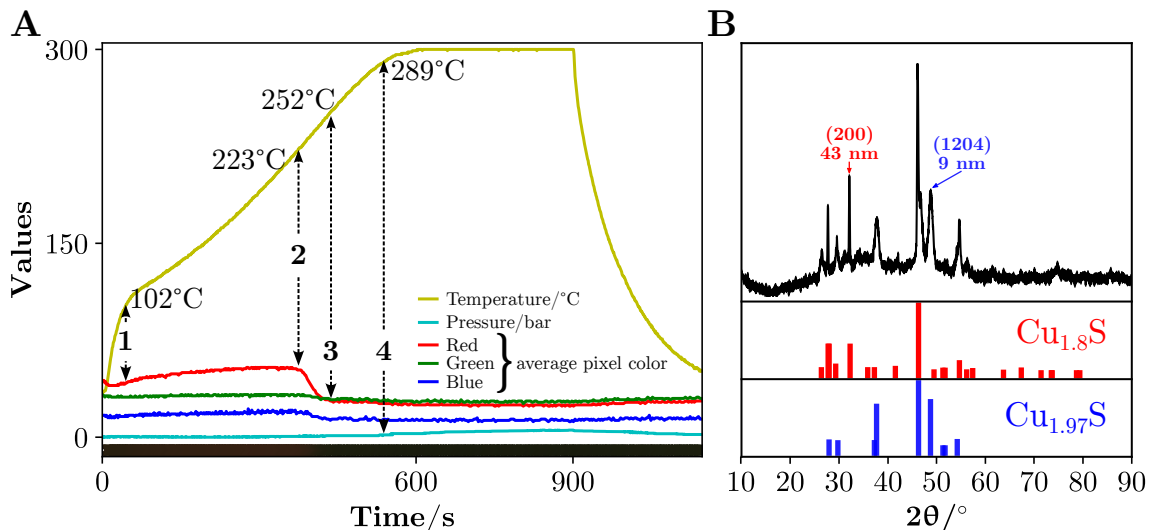


Figure 3.24: Color, temperature, and pressure profiles (A) of the synthesis starting from  $\text{Cu}_2\text{O}$  and XRD pattern (B), with the corresponding hexagonal  $\text{Cu}_{1.8}\text{S}$  and orthorhombic  $\text{Cu}_{1.97}\text{S}$  reference patterns respectively adapted from JCPDS standards 47-1748 and 20-0365, from reference [223].

reactions are occurring, except for the reduction of the copper reagent which only occurs for  $\text{CuO}$ . The color transition from orange/yellow to red seen in Figure 3.22 between moments 1 and 2, could probably be attributed to the reduction of  $\text{Cu}^{2+}$  to  $\text{Cu}^+$ .

The band gap of the powder obtained from  $\text{Cu}_2\text{O}$  was estimated from the Tauc plot, calculated from the Kubelka-Munk transformation of the diffuse reflectance spectrum, shown in Figure 3.25

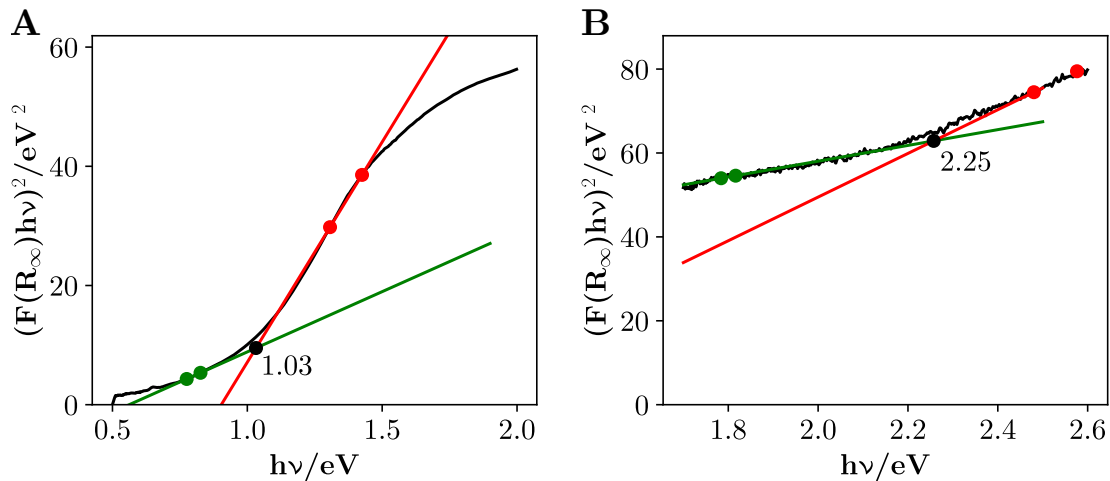


Figure 3.25: Tauc plot obtained from the diffuse reflectance spectrum of the powder obtained from the synthesis starting from  $\text{Cu}_2\text{O}$ . The black dots indicate the estimated band gap value. The remainder scatter dots show the limits that were used to fit the linear regressions.

The estimated band gap was 1.03 eV in (A), expected for a lower stoichiometry such as the identified hexagonal  $\text{Cu}_{1.8}\text{S}$ , and a band gap of 2.25 eV was determined from (B) stoichiometry of  $\text{Cu}_{1.97}\text{S}$  in the orthorhombic phase, which is near the one reported for  $\text{Cu}_{1.95}\text{S}$ . [232]

### 3.2.8.2 Silver

Silver sulfide ( $\text{Ag}_2\text{S}$ ) usually finds applications in biomedicine, due to the optical property of

near-infrared (NIR) emission that easily trespasses skin tissue and enables imaging[233], [234], as well as in near-infrared detectors[235], due to its band gap between 0.9 eV and 1.1 eV.[236]

Silver sulfide has been previously synthesized in a microwave reactor, with  $\text{Ag}_2\text{CO}_3$  as the metal source and thioacetamide.[237] The authors noted that  $\text{Ag}_2\text{CO}_3$  under microwave irradiation can decompose and form metallic silver. As for synthesis involving 1-dodecanethiol, Tang et al.[104] synthesized  $\text{Ag}_2\text{S}$  and Ag by controlling the temperature and amount of thiol. They proposed that a lower temperature (190 °C) and amount of thiol, with 1-octadecene as the solvent, only Ag was produced. In the absence of 1-octadecene - using the thiol as the solvent - and at 200 °C, only the sulfide was obtained. A similar synthesis was performed by Tian et al.[95] and they reached the same conclusion, this time without 1-octadecene, that a lower temperature (180 °C) and a shorter synthesis (4 hours) time led to the formation of metallic silver. A higher temperature (200 °C) and longer time (5 hours) resulted in pure  $\text{Ag}_2\text{S}$ .

The synthesis of  $\text{Ag}_2\text{S}$  was attempted starting from  $\text{AgNO}_3$  and is detailed in Section A.1.10.2. The color, temperature, and pressure profiles, the XRD pattern, and a TEM image of the resulting powder are shown in Figure 3.26.

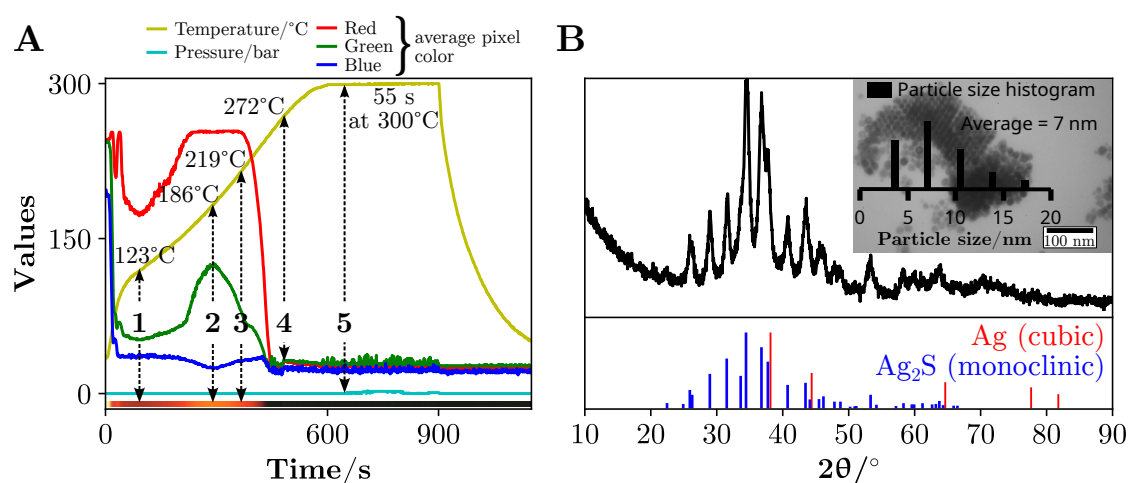


Figure 3.26: Color, temperature, and pressure profiles (A) and the XRD pattern (B), with a TEM image and the particle size distribution as an inset, of the synthesized powder starting from  $\text{AgNO}_3$ . Five distinct moments were marked in the profiles. The reference pattern of the cubic metallic silver was adapted from reference [238] and the monoclinic phase of  $\text{Ag}_2\text{S}$  from [239]. The scale bar is 100 nm in (B).

The synthesis started with the dissolution of the reagent in the thiol, forming a dark orange complex as shown in the color profiles (A), until the temperature reached 123 °C (1). As the temperature rose, the complex started to turn yellow until the moment (2) at 186 °C and soon after began to darken at 219 °C (3), which was attributed to the formation of the silver sulfide. When a temperature of 272 °C (4) was reached, a tenuous silvery mirror developed on the vial's wall, probably associated with the formation of metallic silver. Then, after 55 seconds at 300 °C (5), pressure rose slightly. When the synthesis was over and the vial's cap was removed, an orange gas evolved from within, seemingly appearing from thin air. The orange gas was easily recognized as  $\text{NO}_2$ , which then condensed as a yellow liquid on the upper parts of the vial. The pressure

developed during the synthesis was most probably due to the release of NO, which entered in contact with O<sub>2</sub> when the vial was opened and formed NO<sub>2</sub>. A more detailed explanation of the reactions leading to the formation of NO can be found in Section 3.4.5.

The XRD pattern (B) reveals that pure monoclinic Ag<sub>2</sub>S was obtained, with no Ag contamination. An average particle size of 7 nm was estimated from the TEM image.

Another synthesis was performed starting from Ag<sub>2</sub>O, which is detailed in Section 3.4.5, and with the microwave reactor's lamp turned off. It resulted in pure monoclinic Ag<sub>2</sub>S like the synthesis starting from AgNO<sub>3</sub> and the Tauc plot calculated from the diffuse reflectance spectrum is shown in Figure 3.27.

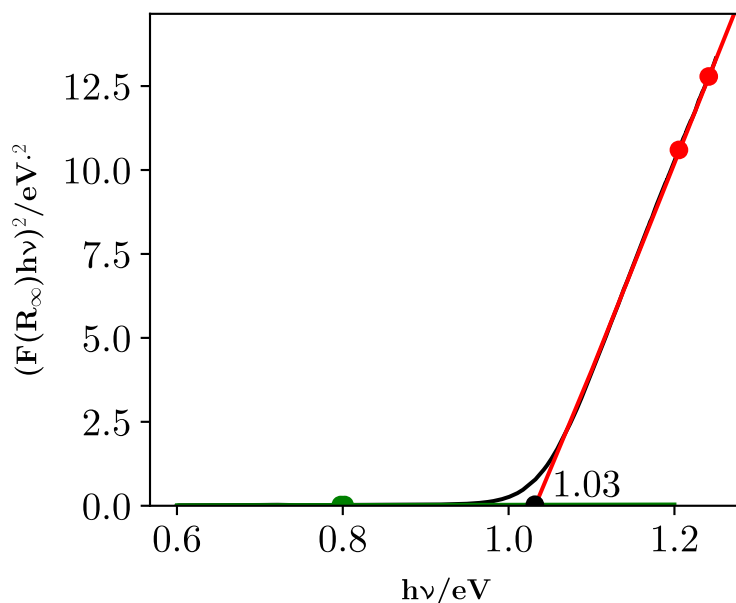


Figure 3.27: Tauc plot calculated from the diffuse reflectance spectrum of a powder from a synthesis starting from Ag<sub>2</sub>O.

The calculated band gap is 1.03 eV, which is within the expected range of 0.9 eV and 1.1 eV, according to the literature. Silver compounds' light sensitivity has been known for more than a century since photography was developed. Since the video recording of all of the syntheses performed in this work required the presence of light, the question if the light would influence the product arose. Details regarding the light's influence on the synthesis of silver sulfide can be found in Section 3.4.5.

Pure monoclinic silver sulfide Ag<sub>2</sub>S was obtained with a particle size around 7 nm and a band gap of 1.03 eV.

### 3.2.9 Group 12: Zn, Cd

#### 3.2.9.1 Zinc

Zinc sulfide (ZnS) is a versatile sulfide, especially when doped with manganese. The doped material can be found in optoelectronics, namely in organic photovoltaics by protecting the organic layer from UV radiation and downconverting it to yellow/orange photons.[240]



Previous use of 1-dodecanethiol on the fabrication of zinc sulfide, stabilized by oleylamine and heating with a mantle, led to nanoparticles with a size of 4.7 nm.[241] Zinc sulfide has also been synthesized by a microwave-assisted solvothermal method, starting from zinc(II) 2-ethylhexanoate and thiourea in a mixture of methanol and water, heated to 150 °C for an unknown amount of time.[242]

The synthesis of ZnS was attempted starting from zinc(II) acetate dihydrate and is detailed in Section A.1.11.1. The color, temperature, and pressure profiles, the XRD pattern, and the TEM and SEM images of the resulting powder can be found in Figure 3.28.

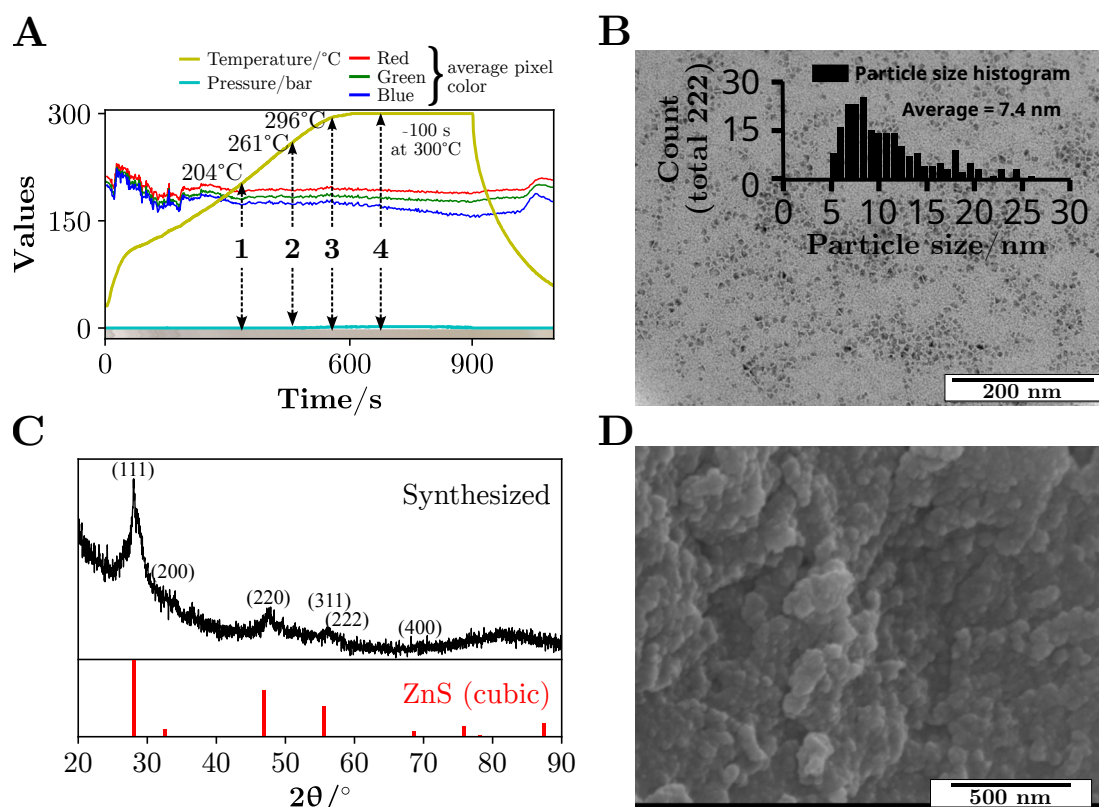


Figure 3.28: Color, temperature, and pressure profiles (A), TEM image (B), with the particle size histogram as an inset, X-ray diffraction pattern (C) and an SEM image (D) of synthesis starting from zinc(II) acetate dihydrate. Four moments were marked in the profiles from (1) to (4). The reference patterns of the cubic phase of ZnS (mp-10695) was taken from Materials Project[128][129]. The scale bar is 200 nm in (B) and 500 nm in (D). The scale bar is 200 nm in (B) and 500 nm in (D).

After the complete dissolution of the reagent in the thiol at 204 °C (A) (1), at 261 °C (2) pressure started rising, probably due to the vapor from the dehydration of the salt and acetic acid released from the zinc precursor. Slight precipitation occurs at 296 °C (3), followed by more pronounced precipitation of zinc sulfide after around 100 seconds at 300 °C. Finally, the automated cooling begins and the temperature decreases to 50 °C.

From the TEM image (B) average particle size of 7.4 nm was estimated. From the most intense peak at  $2\theta$  of 29° in the XRD pattern (C), a crystallite size of 5.3 nm was calculated, which roughly corresponds to the size estimated from the TEM image. The phase of ZnS corresponds



to the face-centered cubic (JCPDS 65-1691)[243], known as zinc blende, and the zinc ions occupy the tetrahedral sites. The quality of the SEM image (D) was too low to determine the aggregates' sizes but the blobs, which are assumed to be agglomerates of the particles seen in the TEM image, are no bigger than  $\sim 60$  nm.

To further examine if the produced powder contained the hexagonal or cubic phase of ZnS, a Raman spectrum was measured and is shown in Figure 3.29

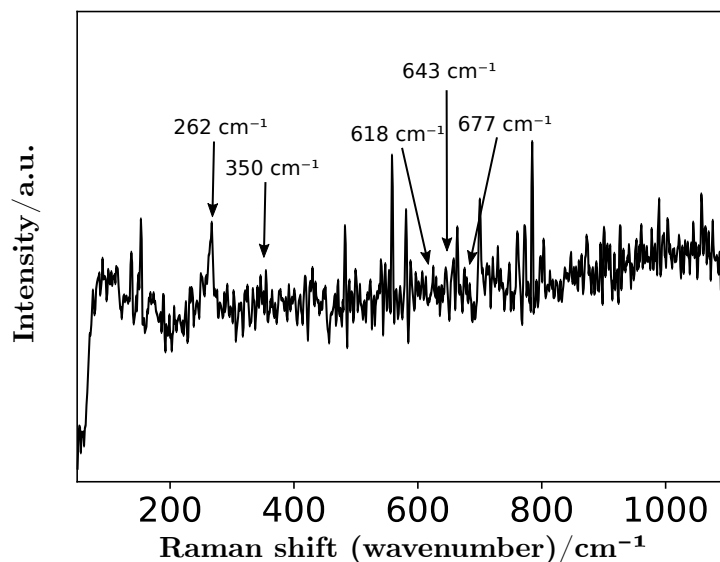


Figure 3.29: Raman spectrum of the powder obtained from the synthesis starting from 1-dodecanethiol and zinc(II) acetate dihydrate. The spectrum was acquired using a laser, with an emission at 532 nm and a power of 0.15 mW. The marked peaks correspond to those found in the literature for reference spectra of ZnS[244]

The ZnS Raman spectrum shows a characteristic peak at  $262\text{ cm}^{-1}$  and the other peaks, that are not visible due to noise, would be at  $350\text{ cm}^{-1}$ ,  $618\text{ cm}^{-1}$ ,  $643\text{ cm}^{-1}$  and  $677\text{ cm}^{-1}$ . The latter peaks were according to the spectra obtained with a laser of 514.5 nm by Cheng et al.[244] for the zinc blende. They also differentiated between the zinc blende phase (cubic) from the wurtzite phase (hexagonal) of ZnS since the cubic phase has a broad band at  $262\text{ cm}^{-1}$  while the hexagonal does not.

Small and pure cubic zinc sulfide nanoparticles were obtained with this method. Given that zinc sulfide is known to be a good host for dopants, manganese ions were added to the following synthesis, to obtain orange emitting nanoparticles. A detailed study on the influence of manganese as a dopant on the optical properties of ZnS was performed and published[245]. A well-known downconversion system was demonstrated, involving zinc sulfide as the host and manganese ion as the dopant, with an intermediate band that serves as a step to downconvert ultra-violet photons to orange.

The reported band gap of bulk zinc blende phase of ZnS is 3.68 eV[246] and according to the band gap determination method in Section 3.1.3, a linear fit to the Urbach tail is required and the band gap is estimated to be equal to the point where both the Tauc fit and the linear fit coincide. All the band gap values fall between the range of 3.54 eV (undoped) to 3.61 eV. The maximum

luminescence brightness was achieved at a manganese final concentration of 0.2% and not 0.1%. Another second synthesis was performed to repeat the diffuse reflectance and emission measurements, this time starting from 0.01 mmol for manganese(II) acetate tetrahydrate as the amount dopant relative to the 1 mmol of zinc(II) acetate dihydrate, heated to 300 °C in 10 minutes as usual, with the temperature kept for 25 minutes, before cooling down to 50 °C. The powder was washed according to the developed protocol. The diffuse reflectance of the powder and the emission spectrum, acquired using a cutoff filter of 335 nm and an excitation wavelength of 310 nm (4 eV), as well as the calculated Tauc plot are shown in Figure 3.30.

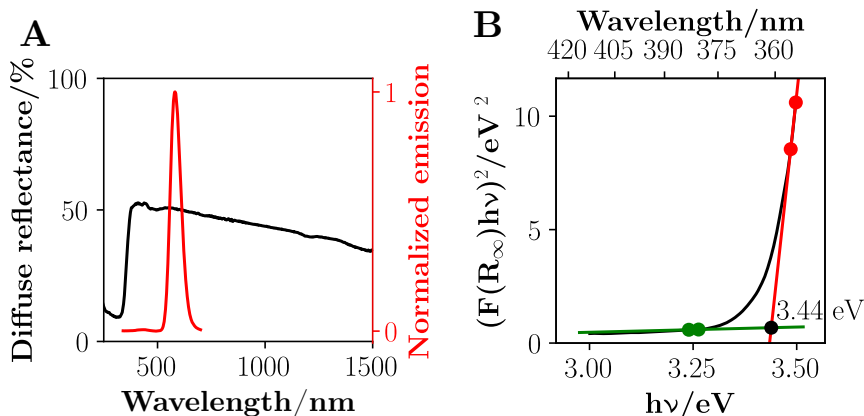


Figure 3.30: Emission and diffuse reflectance spectrum (A) and Tauc plot calculated from the diffuse reflectance spectrum (B) of a powder from a synthesis starting from zinc(II) acetate dihydrate and manganese(II) acetate tetrahydrate as the dopant.

The emission (A) of the doped powder is centered at the typical 590 nm (2.1 eV), the orange region of the visible spectrum, while the sharp absorption seen in the diffuse reflectance spectrum in the ultraviolet region translates to an estimated band gap of 3.44 eV. These values are within the expected for zinc sulfide (3.4 eV).[247] It is lower than the ones obtained in the published article where the average band gap was 3.57 eV, since these were determined in a chloroform suspension and the absorbance spectrum was corrected using Castanho et al.[55] light dispersion correction algorithm. These steps introduce some error and are less direct than simply measuring the diffuse reflectance spectrum of the material's powder alone. Since the particles measured in a chloroform suspension were larger than 5 nm on average and the Bohr radius of ZnS is 2.5 nm[248], corresponding to a diameter of 5 nm, quantum confinement was not responsible for the larger band gap.

The maximum luminescence quantum efficiency reported in the article published and mentioned previously[245], was estimated from the manganese-doped zinc sulfide nanoparticles suspended in chloroform was 0.0097, compared to 7-diethylamino-4-methylcoumarin in ethanol (reference quantum yield of 0.73) and using a cutoff filter of 360 nm and an excitation wavelength of 280 nm. The reported in the literature is also a relatively low 0.03[249], leaving this material as a suboptimal approach for energy downconversion in solar cells. An alternative with a higher quantum efficiency, although not the most economical, neither ecological solution and is from the selenide, is  $\text{Ag}^+$  doped CdSe. This system is characterized by its large Stokes shift (1 eV) to 650

nm, upon irradiation with 400 nm light, and a fluorescence quantum yield of  $\sim 0.5$ . [250] Doping metal sulfides such as  $\text{Nb}_2\text{S}_5$ ,  $\text{MgS}$ ,  $\text{Y}_2\text{S}_3$ ,  $\text{Er}_2\text{S}_3$  and  $\text{ZrS}_2$  with  $\text{Ag}^+$  has been reported as also producing materials that emit in the near-infrared region. However, the quantum efficiency of said materials is not reported. [146]

Cubic zinc sulfide nanoparticles of small size ( $\sim 7$  nm) and a band gap of 3.44 eV were successfully synthesized with and without manganese doping.

### 3.2.9.2 Cadmium

Cadmium sulfide, CdS, is mainly used as a buffer layer in photovoltaics [251] and also in hydrogen production [252], [253], water remediation [254] and optoelectronics such as light-emitting diodes [255].

Nabiyouni et al. [256] have synthesized cubic cadmium sulfide nanoparticles starting from cadmium(II) nitrate and thioacetamide in ethylene glycol, in a microwave reactor. Another report of a microwave-assisted synthesis of cubic CdS involves the use of aqueous solutions of  $\text{CdCl}_2$  and thioacetamide, sodium citrate, and sodium hydroxide to balance the pH to 8. They irradiated the solution with 1650 W microwave power for 60 seconds and obtained particles with an average size of 5 nm. [257]

The synthesis of CdS was attempted starting from cadmium(II) acetate and is detailed in Section A.1.11.2. The color, temperature, and pressure profiles, and XRD pattern of the resulting powder are shown in Figure 3.31 (A).

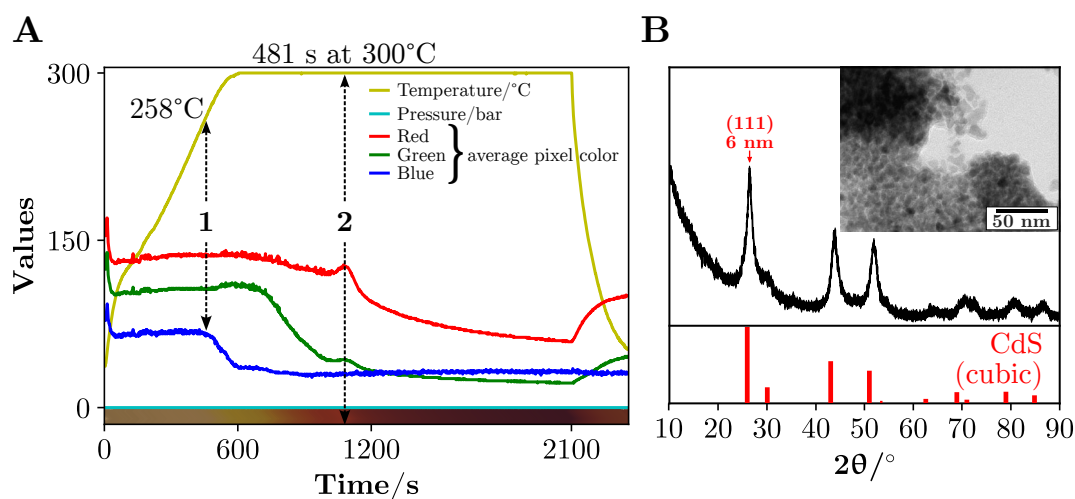


Figure 3.31: Color, temperature, and pressure profiles (A) of the synthesis starting from cadmium(II) acetate, with two color changes marked as (1) and (2), and the XRD pattern (B) with a TEM image as an inset. The cubic CdS reference pattern was taken from Materials Project [128][129] (mp-2469). The scale bar is 50 nm in (B). The scale bar is 50 nm in (B).

The color profile in Figure 3.31 shows a quick dissolution of the reagent in the thiol, followed by a color change from translucent white to yellow ( $258^\circ\text{C}$ ). There is a color change from yellow to orange after 20 seconds at  $300^\circ\text{C}$  and finally to dark brown after around 8 min at  $300^\circ\text{C}$ . Assuming that the CdS forms when the dark brown suspension is formed, the temperature and time required to form cadmium sulfide are very similar to the ones required to form ZnS.

Crystallite size of 6 nm was calculated from the peak at a  $2\theta$  of  $26.5^\circ$  and, like zinc which belongs to the same group as cadmium, the synthesis yielded the zinc blende phase (JCPDS 89-0440)[258] of CdS. The crystallite size for a synthesis performed at  $300^\circ\text{C}$  for 25 min was expected to be around 10 nm, as was obtained for the synthesis of ZnS starting from the acetate salt. According to Dickson and Hu[259], CdS can be obtained using 1-dodecanethiol at a temperature of  $240^\circ\text{C}$  which is near the color change observed in Figure 3.31 A (1). Since CdS is typically a yellow material, the formation of a yellow suspension could be attributed to the appearance of small CdS nanoparticles, that progressively grow with time, which decreases their band gap. The synthesis did not yield enough powder to perform a diffuse reflectance spectrum measurement.

### 3.2.10 Group 13: In

#### 3.2.10.1 Indium

Indium sulfide ( $\text{In}_2\text{S}_3$ ) usually adopts the tetragonal and cubic phases.[260] Indium sulfide has been used for photodegradation of organic dyes[261] and as a buffer layer in solar cells[262], as a promising substitute of the hazardous CdS.

A microwave-assisted synthesis of tetragonal  $\text{In}_2\text{S}_3$  was found outside of the scope of Web of Knowledge (Section 2.3.2, Figure 2.15), which involves the use of  $\text{InCl}_3$  and thiourea in ethylene glycol, but the temperature to which the mixture reached while being irradiated was not reported.[263]

Two syntheses starting from  $\text{InCl}_3$  were attempted and are detailed in Section A.1.12.3. The first was typical, reaching  $300^\circ\text{C}$  in 10 minutes and keeping at that temperature for 25 minutes (T300). Based on the first, the second was set to reach  $215^\circ\text{C}$  in 7 minutes and 10 seconds (T215), corresponding to the same temperature ramp as the previous synthesis. The color, temperature, and pressure profiles and the XRD patterns from the obtained powders from both syntheses attempts are shown in Figure 3.32.

In both syntheses, the first moment (1) observed in the profiles (A) corresponds to the dissolution of the  $\text{InCl}_3$  in the thiol, forming a clear yellow suspension at around  $100^\circ\text{C}$ , and as temperature rises, a second event (2) is seen at around  $215^\circ\text{C}$ , marked by a sharp rise in the three color channels, which signals the formation of a precipitate. From this moment on, the synthesis heating ramps diverged. The first synthesis (T300) followed the method repeated for other elements, with a heating ramp to reach  $300^\circ\text{C}$  in 10 minutes. The second synthesis (T215) was set to stop rising the temperature, to avoid the formation of other stoichiometries. At the third moment (3), the pressure began to rise in both syntheses, at different temperatures but at the same time. Notice that this rise occurs when the blue channel stabilizes, indicating that independently of the temperature, the gas was only released when the color stabilized; possibly an indium sulfide phase. In both syntheses, the colors tend to darken over time; faster on (T300) since it is at a higher temperature. The yielded powders were a bright yellow, typical of indium sulfides[267], albeit the color profiles show a dark brown which was due to the shading provoked by the light scattering. According to the XRD pattern from the synthesized powder (T300), a mixture of compounds was

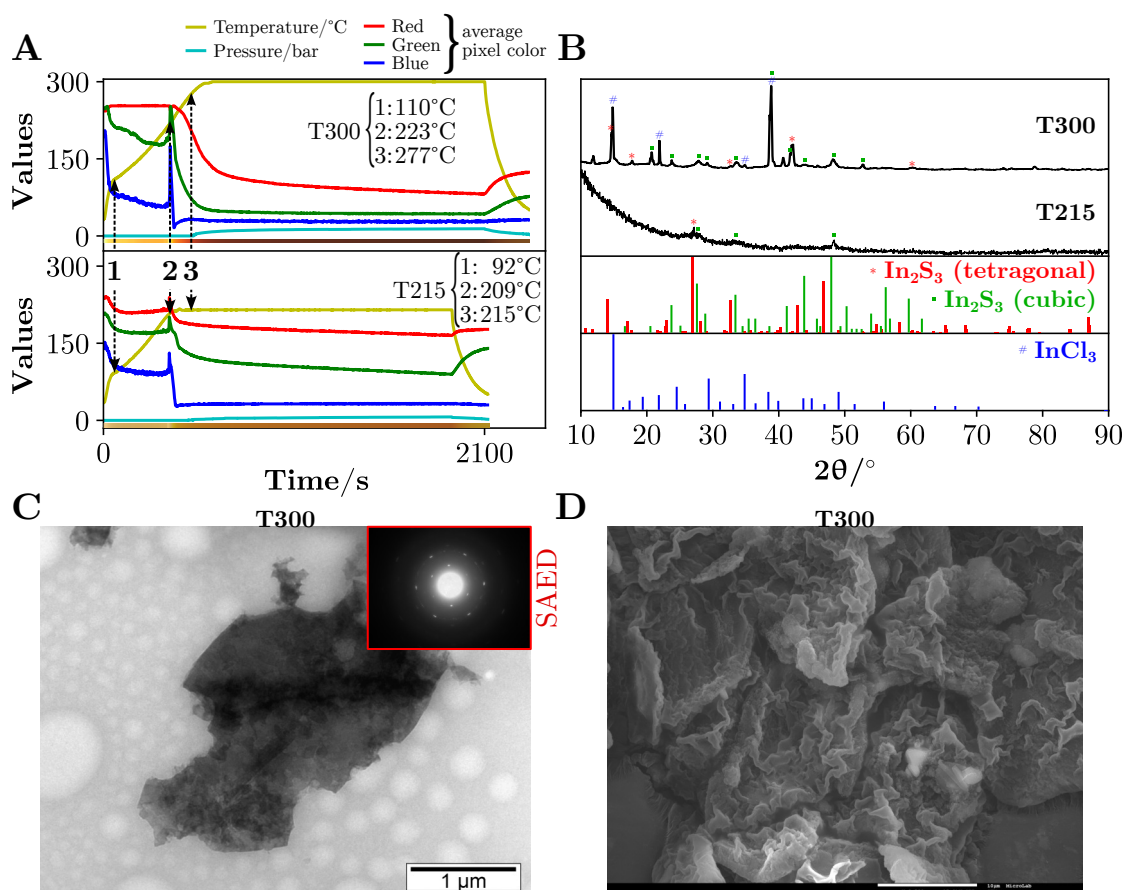


Figure 3.32: Color, temperature, and pressure profiles (A) of syntheses starting from InCl<sub>3</sub>, with maximum temperatures of 300 °C (T300) and 215 °C (T215) for 25 minutes, the XRD patterns from each synthesis (B), and a TEM image (C), with a SAED pattern as an inset, and an SEM image (D) of the (T300) synthesis. Three moments were marked in the profiles. The reference patterns of the tetragonal phase of In<sub>2</sub>S<sub>3</sub> (mp-22216) were taken from Materials Project[128][129], the cubic phase was adapted from reference [264] and [265], and the anhydrous InCl<sub>3</sub> pattern was adapted from reference [266]. The scale bar is 1  $\mu\text{m}$  in (C) and 10  $\mu\text{m}$  in (D). The scale bar is 1  $\mu\text{m}$  in (C) and 10  $\mu\text{m}$  in (D).

obtained, including the unreacted InCl<sub>3</sub>, and the tetragonal and cubic phases of In<sub>2</sub>S<sub>3</sub>[264], [265], [268], [269] and some peaks that did not match the latter phases could not be identified. An estimated crystallite size of 41 nm, obtained from peaks at a  $2\theta$  of 20.7° and the most intense at 38.8°, associated to the cubic phase. This suggests that the micrometer-sized 2D nanosheets seen in the TEM (C) and SEM (D) images are composed of smaller ~40 nm crystallites. The bright spots in the SAED pattern are indicative of a crystalline sample and they appear to coincide with the SAED of the cubic phase of In<sub>2</sub>S<sub>3</sub> reported by Guo et al.[270]. Since no scale indicates the distance in reciprocal space, it was impossible to confirm fully. The 2D layer seen in the TEM image is representative of the overall images seen in the microscope. These 2D structures are ideal for applications that require large, but thin, swathes of material, such as catalysis or batteries. The structures in the SEM image are very similar to those observed by others who obtained the tetragonal phase of In<sub>2</sub>S<sub>3</sub>. [271]

The Raman spectrum and the Tauc plot obtained from the diffuse reflectance spectrum of the

obtained powder were measured and are shown in Figure 3.33.

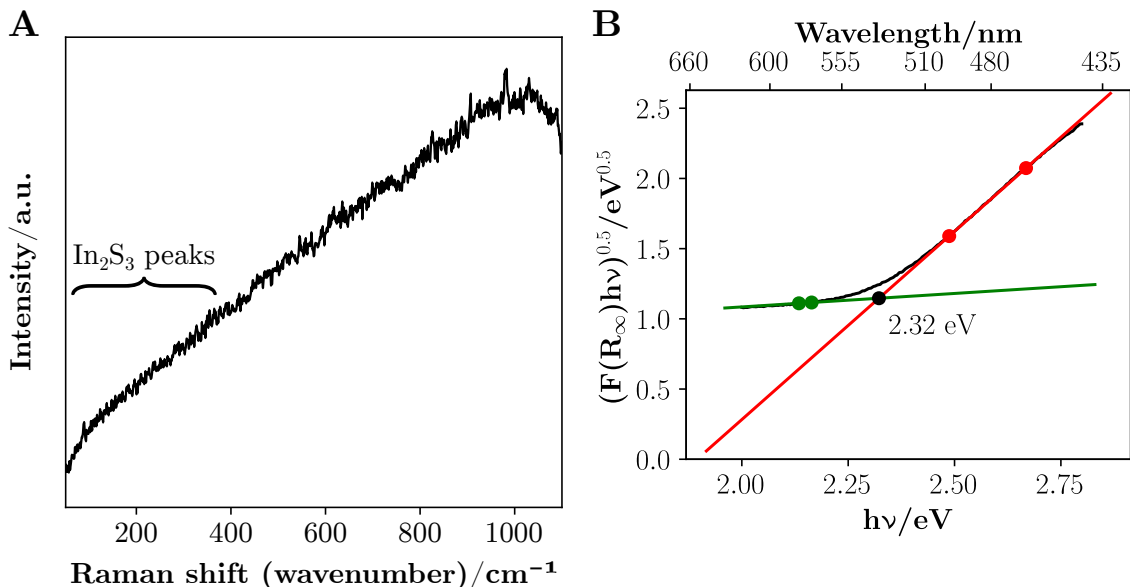


Figure 3.33: Raman spectrum and Tauc plot of the powder obtained from the synthesis starting from 1-dodecanethiol and indium(III) chloride. The peaks where either the tetragonal and trigonal phases of  $\text{In}_2\text{S}_3$  were supposed to be, according to Horani and Lifshitz[260], are marked by the range. The spectrum was acquired using a laser, with emission at 532 nm and a power of 0.15 mW.

Due to the indium sulfide powder's fluorescence, the background seen in Raman spectra (A) did not permit the extraction of any meaningful peak data. According to Horani and Lifshitz[260], the Raman peaks of the tetragonal and trigonal phases of  $\text{In}_2\text{S}_3$  are located between around  $100\text{ cm}^{-1}$  and  $350\text{ cm}^{-1}$ . The band gap of 2.32 eV, obtained from the Tauc plot, matching the 2.3 eV band gap of the cubic phase of  $\text{In}_2\text{S}_3$  obtained by Tulenin et al.[265] and slightly below the characteristic 2.41 eV for the tetragonal phase[272], and explains the powder's yellow color.

The synthesis product analysis was inconclusive since the XRD pattern appears to contain a mixture of the reagent, the tetragonal and cubic phases of  $\text{In}_2\text{S}_3$ . The Raman spectrum is also devoid of any peak that belonging to  $\text{In}_2\text{S}_3$  but the 2.32 eV band gap estimated from the diffuse reflectance spectrum agrees with the reported in the literature for the indium sulfide.[260]

### 3.2.11 Group 14: Sn

#### 3.2.11.1 Tin

Further down group 14, is the element tin. The binary sulfide  $\text{SnS}_2$ , also known as stannic sulfide, is typically used as a photodetector[273] and has an indirect 2.1 eV and a direct 2.8 eV band gap.[274] The uncommon cubic  $\text{SnS}$  has a direct band gap of 1.66 eV[275], near the optimal for photovoltaics[276], while the orthorhombic phase an indirect band gap of 1.1 eV. It can also be used in thermoelectrics[277], batteries, and sensors.[278]

The synthesis of  $\text{SnS}$  was attempted starting from tin(II) 2-ethylhexanoate and is detailed in Section A.1.13.3. The color, temperature, and pressure profiles, the XRD pattern, and TEM and

SEM images from the resulting powder are shown in Figure 3.34.

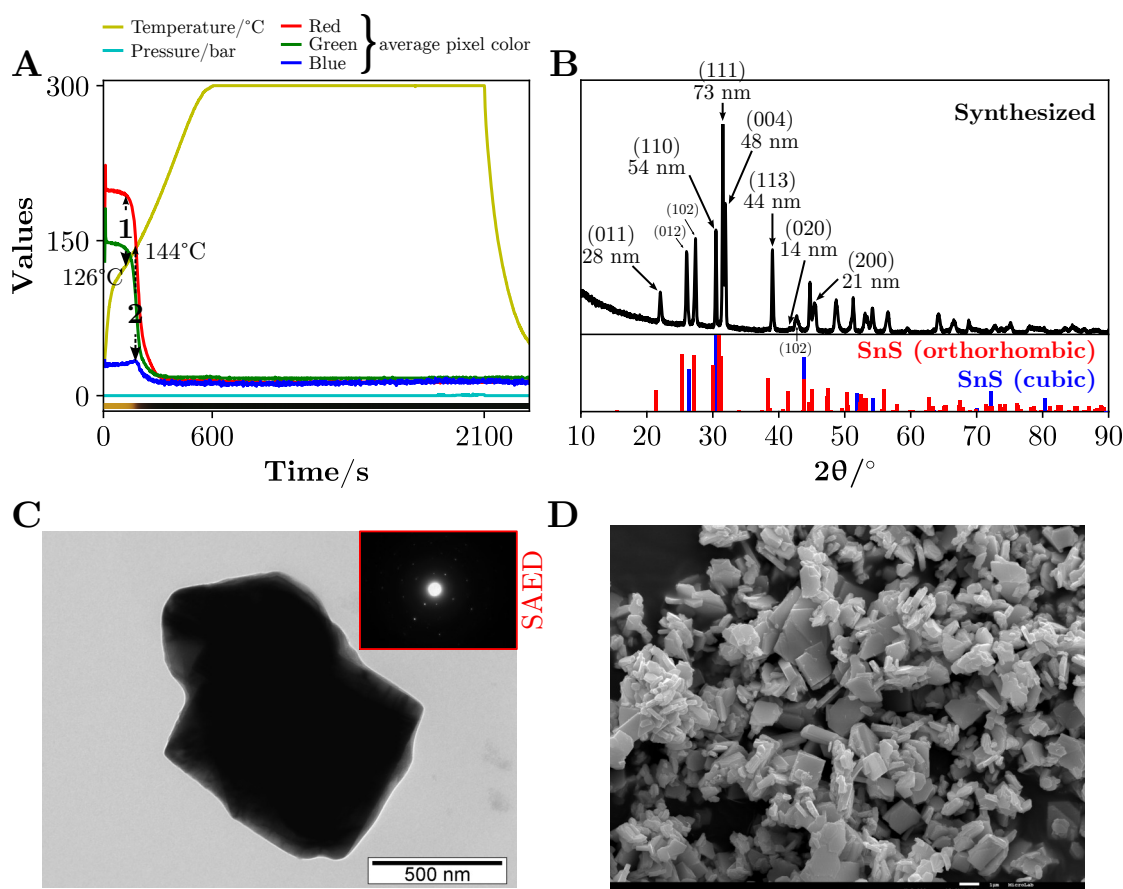


Figure 3.34: Color, temperature, and pressure profile (A) of the synthesis starting from tin(II) 2-ethylhexanoate and the resulting powder's XRD pattern (B), TEM image (C) with a SAED pattern as an inset and an SEM image (D). Two moments were marked in the profiles. The reference patterns of the orthorhombic (including the diffraction planes) and cubic phases of SnS were taken from Materials Project[128][129] with the respective IDs: mp-2231 and mp-1876. The scale bar is 500 nm in (C) and 1 μm in (D).

Before moment (1) in the profiles (A), in the first heating seconds, the milky yellow suspension forms a clear yellow liquid, indicating that the complex that formed between the precursor and the thiol either dissolved and/or melted. As the temperature rises to 126 °C (1), the solution begins to darken progressively, until the formation of the sulfide occurs at the moment (2) at around 144 °C, where the blue color value drops sharply. There were no further significant changes throughout the synthesis. The sulfide formation temperature is much lower than the one reported previously by Brune et al.[274], who used the single-source precursor bis((2,2'-(methylazanediyl)bis(ethane-1-thiolate)) tin(IV) in N-methyl-2-pyrrolidone and heated in a microwave reactor to obtain orthorhombic SnS. According to their thermal analysis, the precursor began to form SnS at around 250 °C, completing the reaction at 300 °C.

The XRD pattern (B) matches that of the orthorhombic phase of SnS, albeit with a deviation of 0.6° from the reference. The large sheets seen in the TEM (C) and SEM (D) images could be explained by the formation mechanism proposed by Patra et al.[279], who stated that after the formation of the SnS clusters, these aggregate preferentially along the (001) plane, leaving the



remainder planes relatively thinner. The main plane of the synthesized SnS particles is (111) with an estimated size of 73 nm but the peaks associated to the planes from the {001}, {101}, {120}, and {021} families are also intense and are associated to the two dimensional growth, which leads to the platelet like grains corroborated by the SEM image (D).

A Raman spectrum was measured and the Tauc plot calculated from the diffuse reflectance spectrum, obtained from the resulting powder, are shown in Figure 3.35.

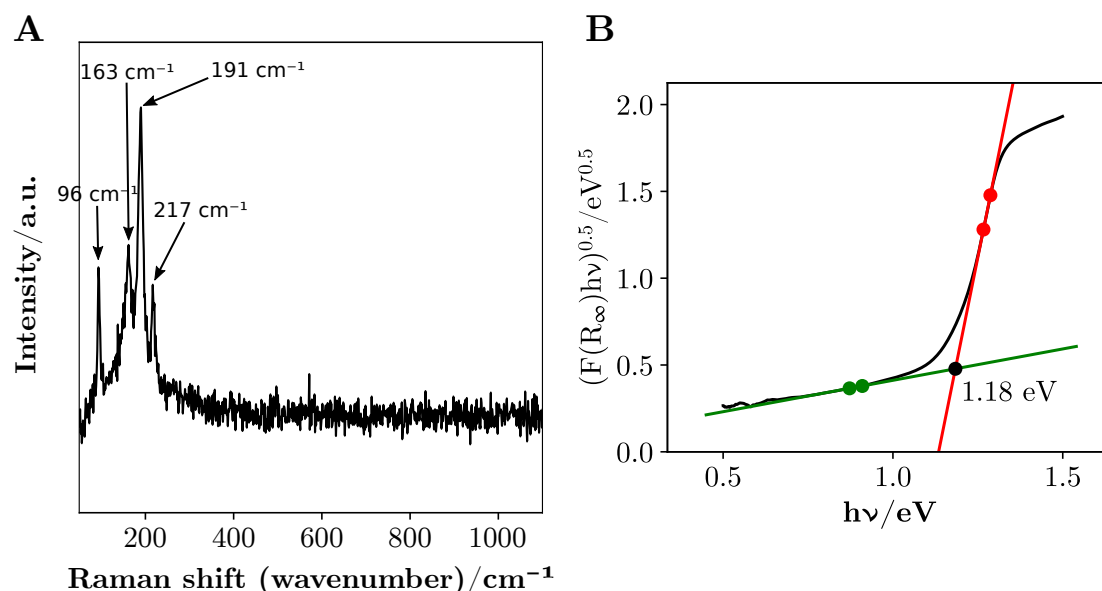


Figure 3.35: Raman spectrum (A) and Tauc plot (B) calculated from the diffuse reflectance spectrum of the powder obtained from the synthesis starting from tin(II) 2-ethylhexanoate. The Raman spectrum was acquired using a laser, with emission at 532 nm and a power of 0.15 mW. The marked peaks indicate the peaks from reference spectra of the orthorhombic phase of SnS[280]

The Raman spectrum (A) of the SnS powder has the five characteristic peaks at  $93.5\text{ cm}^{-1}$ ,  $161.8\text{ cm}^{-1}$ ,  $190\text{ cm}^{-1}$  and  $216.7\text{ cm}^{-1}$ , according to the spectra captured with a laser of 532 nm by Xia et al.[280]. Above the wavenumber region of  $300\text{ cm}^{-1}$  there are no peaks, which indicates that there is no  $\text{Sn}_2\text{S}_3$  ( $\sim 305\text{ cm}^{-1}$ )[281] or  $\text{SnS}_2$  ( $313\text{ cm}^{-1}$ )[282]. The Tauc plot (B) also shows a sharp transition in the near-infrared and it was possible to estimate a 1.18 eV band gap, which is within the expected 1.1 eV for the orthorhombic phase[275].

The pure orthorhombic phase of tin sulfide was obtained, with a particle size in the range of hundreds of nanometers and a large distribution, and a band gap of 1.18 eV.

### 3.2.12 Group 15: Bi

#### 3.2.12.1 Bismuth

As an alternative to lead sulfide, one of the heaviest and most toxic elements, and as the last non-radioactive element, bismuth sulfide finds its use in several applications.[283] From medical applications, such as a contrast agent[284], in supercapacitors[285], in photovoltaic with a reported band gap of 1.3 eV[286] and in water remediation as a composite with other materials[287].



The synthesis of bismuth sulfide was attempted starting from bismuth(III) nitrate pentahydrate and is detailed in Section A.1.14.1. The synthesis was interrupted due to the development of electric arcs. The slurry was instead cleaned with chloroform, as a previous synthesis with ethanol cleaning did not successfully remove the wax that formed. The color, temperature, and pressure profiles and TEM images of the powder obtained are shown in Figure 3.36.

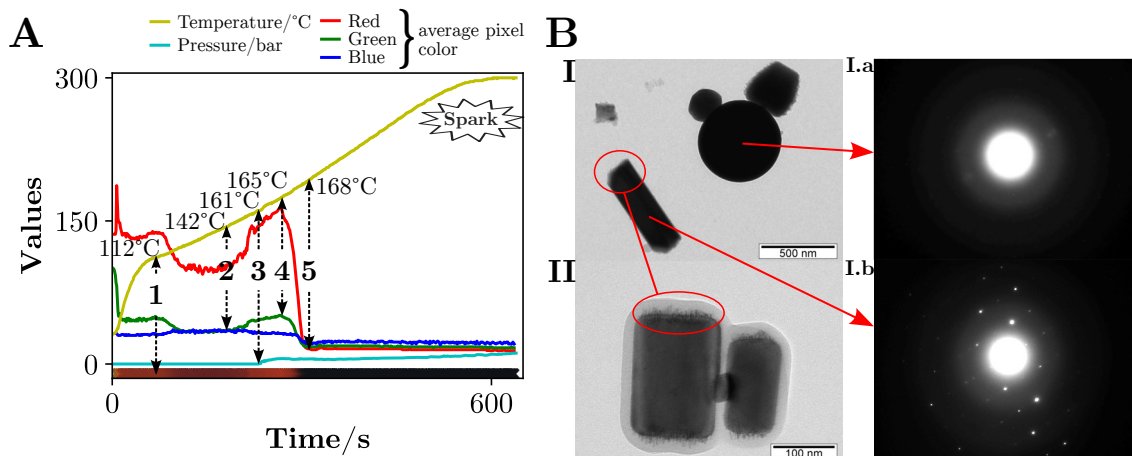


Figure 3.36: Bismuth sulfide microwave-assisted synthesis attempt color, temperature, and pressure profiles (A) and two TEM images (B) starting from bismuth(III) nitrate pentahydrate, with circles pointing to hair-like structures in both images (I) and (II). The arrows point to two distinct SAED patterns (I.a) and (I.b) from two particles in the image (I). The scale bar is 500 nm in (B-I) and 100 nm in (B-II).

The color profile in Figure 3.36 shows an extremely sharp transition from yellow to orange, characterized by a fast dissolution ( $\sim 10$  seconds) of the bismuth(III) nitrate pentahydrate in the thiol, practically as soon as the mixture was irradiated with microwave light. The suspension darkened at  $\sim 140$  °C and then, at  $\sim 150$  °C, an orange precipitate formed, accompanied by an increase in pressure. When the pressure was relatively stable, at 175 °C a black suspension formed and no further color change was observed. The synthesis was interrupted due to the formation of . The SAED images in Figure 3.36 (B-I.a) and (B-I.b) are very distinct. The first (B-I.a) corresponds to an amorphous material and the second (B-I.b) corresponds to crystalline material. It was not possible to match the SAED pattern from the crystalline particles with either Bi or  $\text{Bi}_2\text{S}_3$  SAED patterns from the literature. The estimated d-spacings from (B-I.b) according to the obtained d-spacing plot, shown in Figure A.13 in the Appendix A, are: 0.92 Å, 1.04 Å, 1.18 Å, 1.42 Å, 1.71 Å, 1.84 Å, 2.82 Å, and 2.91 Å using the method described in Section 3.1. It was not possible to match the obtained d-spacing values with those reported in the literature.

Another synthesis was performed using the same 1 mmol (485 mg) of the nitrate precursor and is detailed in Section A.1.14.1. However, the maximum temperature was restricted to 185 °C, reached in 6 minutes and 10 seconds, and kept for 15 minutes, in an attempt to see if the kinetic product was metallic bismuth or its sulfide. This was the temperature at which the precipitation of the black material was observed previously (Figure 3.36). The resulting color, temperature, and pressure profiles and the XRD pattern of the powder are shown in Figure 3.37.

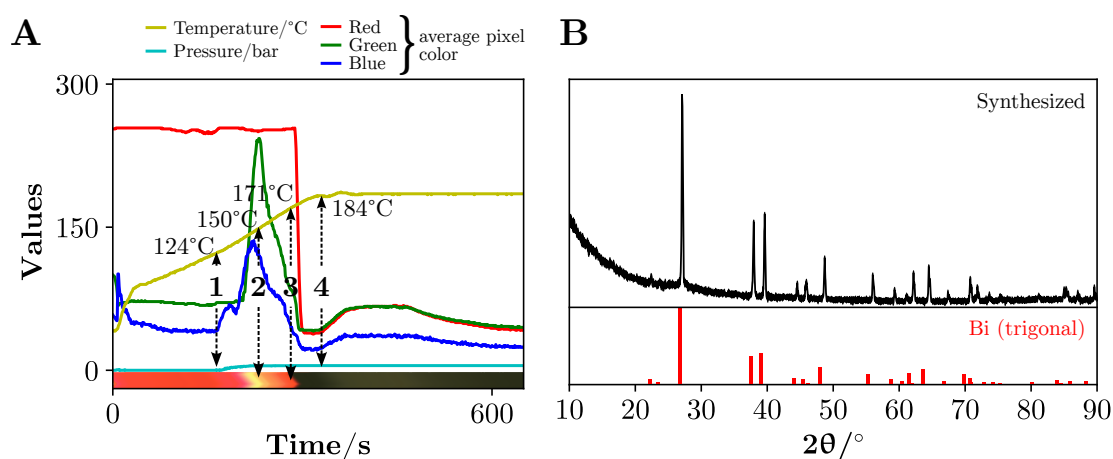


Figure 3.37: Bismuth sulfide microwave-assisted synthesis attempt Color, temperature, and pressure profiles (A) and the XRD of the obtained powder (B). The profiles were truncated as the relevant information is strictly in the region shown. The XRD reference pattern of rhombohedral metallic Bi was taken from Materials Project[128][129] (mp-23152).

The color and pressure changes seen in Figure 3.37 (A) are practically similar to the ones observed in the profiles of synthesis performed at 300 °C (Figure 3.36 (A)). The only differences were attributed to a different image contrast setting that was automatically chosen by the microwave reactor. The continued pressure rise seen in the synthesis performed at 300 °C can be explained by the parallel rise in temperature, as opposed to the constant temperature and pressure in the synthesis performed at 185 °C. There was no during the whole synthesis time. The product of the synthesis was pure metallic bismuth, according to the XRD reference pattern in Figure 3.37 (B). The metallic Bi is therefore the kinetic product while the black sulfide is the thermodynamic product, only accessible at a higher temperature.

Obtaining bismuth sulfide was not possible starting from the nitrate precursor since the first product that is formed is metallic bismuth and when the sulfide is probably formed at a higher temperature, develops and the synthesis cannot proceed.

### 3.2.13 Resume

A compilation of all attempted binary metal sulfide microwave-assisted syntheses is presented in Table 3.3.

The majority of the elements of the successfully synthesized materials (A) belong to the adequate (yellow) region of Figure 2.5. Only  $\text{TiS}_2$ , which belongs to the ideal (green) region, was successfully synthesized but proved to be unstable in air, lasting only up to around 2 months while stored in a closed microcentrifuge tube. The remainder ideal elements listed did not yield a sulfide, as shown in (B). Notice that all of the syntheses performed with the tested elements that belong to groups 2 and 3 of the periodic table were unsuccessful. Following the soft/hard characteristic of the ions from Pearson[296], these cations' hardness and the sulfide's softness justifies the lesser compatibility between them. However, groups 4 and 5 formed the corresponding sulfides, except for vanadium, unexpectedly, since their cations are considered mildly hard. For this reason,

Table 3.3: Compilation of all successful (A) attempted to obtain binary metal sulfide nanoparticles of various elements, with the identification of the obtained product, crystal type, the particle size, measured and reference band gap, and comments with the temperature at which the metal sulfide formed ( $T_{formed}$ ). The unsuccessful (B) syntheses, with the precursor used and comments are also shown. The background color for each metal sulfide represents the metal's availability according to Figure 2.5. The acronym n/a stands for not available. In the Crystal column, a, c, h, m, o, t, and tri respectively correspond to, amorphous, cubic, hexagonal, monoclinic, orthorhombic, and trigonal.

Availability: Ideal Adequate

**A**

	Metal	Product	Crystal	Size/nm	Bandgap/eV		Comments [ $T_{formed}$ ]
					Measured	Reference	
Sulfide	Zn	ZnS	c	6	3.44	3.40 <sup>[247]</sup>	[300 °C]
	Mn	MnS	c, h	n/a	n/a	(c,h)3.23 <sup>[191]</sup>	Very low yield. [275 °C]
	Ti	TiS <sub>2</sub>	a	n/a	n/a	(tri)2.50 <sup>[288]</sup>	Unstable. [300 °C]
	Cd	CdS	c	7	n/a	2.42 <sup>[289]</sup>	Very low yield. [300 °C]
	In	In <sub>2</sub> S <sub>3</sub>	c, t	Microplates	2.32	(t)2.41, (c)2.3 <sup>[265], [273]</sup>	[215 °C]
	Zr	ZrS <sub>2</sub>	tri	n/a	n/a	2.10 <sup>[145]</sup>	Very low yield. [300 °C]
	Co	Co <sub>9</sub> S <sub>8</sub>	c	80	1.59	1.60 <sup>[290]</sup>	[288 °C]
	Cu	Cu <sub>1.8</sub> S, Cu <sub>1.97</sub> S	h, o	11	2.25, 1.03	2.30, 1.30 <sup>[232], [291]</sup>	[247 °C]
	Hf	HfS <sub>2</sub>	a	n/a	n/a	(t)1.20 <sup>[150]</sup>	Very low yield. [293 °C]
	Sn	SnS	o	1130	1.18	1.10 <sup>[275]</sup>	[144 °C]
	Nb	NbS <sub>2</sub> , NbS <sub>3</sub>	h, m	(30, 5), n/a	0.00	0.00, 1.06 <sup>[292], [293]</sup>	[232 °C]
	Ag	Ag <sub>2</sub> S	m	10	1.03	1.00 <sup>[236]</sup>	[219 °C]
	Ni	NiS	tri, h	(49, 10), n/a	n/a	0.55 <sup>[294]</sup>	Very low yield. [259 °C]
	Ta	TaS <sub>2</sub>	tri	Microplates	n/a	0.18 <sup>[295]</sup>	Very low yield. [245 °C]

**B**

	Metal	Precursor	Comments
No sulfide/unclear	Be	BeO	Yielded the precursor.
	Mg	Magnesium(II) stearate	Yielded the precursor.
	Sr	SrCl <sub>2</sub>	Yielded the precursor.
	Ba	Barium(II) triflate	Yielded the precursor (soluble in ethanol).
	Sc	Scandium(III) acetate hydrate	Yielded the precursor.
	Y	Y(CO <sub>3</sub> ) <sub>3</sub>	Yielded the precursor.
	V	VO <sub>2</sub>   Vanadium(V) triisopropoxide oxide	Yielded the precursor.   Unclear XRD pattern.
	Cr	Chromium(III) acetylacetonate	Yielded the precursor.
	Mo	MoO <sub>2</sub>	Yielded the precursor.
	W	WO <sub>2</sub>   WCl <sub>6</sub>	Yielded the precursor.   Unclear XRD pattern.
	Fe	FeSO <sub>4</sub> · 7 H <sub>2</sub> O   FeCl <sub>3</sub> · 6 H <sub>2</sub> O	Yielded the precursor.   Too low yield for XRD.
	Al	Aluminum(III) acetylacetonate	Yielded a luminescent thiol-soluble complex.
	Ga	Gallium(III) isopropoxide	Yielded a soluble complex.
	Si	Tetramethoxysilane	Yielded the precursor.
	Ge	GeI <sub>4</sub>	Unable to centrifuge the black suspension.
Bi	Bi(NO <sub>3</sub> ) <sub>3</sub> · 5 H <sub>2</sub> O	Yielded the metallic bismuth.	

titanium disulfide is converted to titanium dioxide over time, since the oxide is harder. The zirconium and hafnium sulfides were stable since they did not suffer any color change. Both the trigonal zirconium sulfide and amorphous hafnium sulfide powders were insufficient to be optically characterized. From the transition metal groups, only V, Cr, and Fe did not result in a sulfide. Vanadium is known to have a large range of possible oxidation states and, as the XRD pattern revealed, it was not possible to identify an individual vanadium sulfide phase. Niobium sulfide synthesis resulted in a mixture of two stoichiometries, nanoparticles of the hexagonal NbS<sub>2</sub> and

monoclinic  $\text{NbS}_3$ , with the first responsible for the powder's metallic band gap. Chromium(III) was expected to form the corresponding sulfide but the acetylacetonate ion has a stronger affinity to the cation. Manganese(II) is considered a softer cation and a sulfide-forming element, even though the powder was contaminated with the acetate precursor. Iron(II) is also expected to easily form the sulfide but the hydrated sulfate was more stable than the expected iron sulfide. From groups 9 to 12, all of the elements have soft and sulfide-forming cations, with a comparatively lower affinity to oxygen, which is one of the reasons why they easily formed the sulfide, starting from precursors like oxides and acetates. Cobalt sulfide nanoparticles were synthesized and formed peculiar spherical/doughnut clusters of cubic crystallites with a band gap at the transition from visible red to the near-infrared part of the spectrum. Regarding the nickel sulfide nanoparticle synthesis, a mixture of the trigonal and hexagonal phases were obtained but with an insufficient yield to allow for the band gap estimation. Copper sulfide nanoparticles were also obtained as a mixture of two non-stoichiometric phases of  $\text{Cu}_2\text{S}$ , hexagonal and orthorhombic, respectively with band gaps in the visible and near-infrared. Still in group 11, pure monoclinic silver sulfide nanoparticles were obtained with the lowest non-metallic band gap of all the binary metal sulfides obtained and optically characterized. Cubic zinc sulfide and cadmium sulfide small nanoparticles were also obtained with band gaps, respectively, in the ultra-violet and in the visible part of the spectrum. From groups 13 and 14, the elements Al, Ga, and Si, as well as Bi from group 15, failed to generate a sulfide in the presence of 1-dodecanethiol. Their hardness and affinity to oxygen make synthesis of sulfides a difficult challenge, especially in ambient conditions. Germanium (group 14), although it formed a very dark suspension, it was not possible to conclude it was a sulfide. Indium and tin cations are the softest of these two groups and have a considerable affinity for the sulfide anion. A mixture of the tetragonal and cubic phases of indium sulfide ( $\text{In}_2\text{S}_3$ ) microplates were successfully synthesized with a band gap in the visible range of the spectrum. Tin sulfide particles, albeit large, could be easily synthesized and yielded systematically the orthorhombic phase with a low band gap in the near-infrared. Compared to all the binary metal sulfide synthesis successfully performed, tin sulfide formed at the lowest temperature. Bismuth, from group 15, also has a soft cation but due to its affinity toward oxygen, in the presence of triflate, no sulfide was obtained. Switching to the nitrate salt, electric arcs developed during the synthesis, and only metallic bismuth formed. In some syntheses, for example, the ones pertaining Cu, Ag or Bi, at the end of the automated cooling the glass vessel contained a thin layer of metal in the inner wall, where the suspension was. Recalling that the vessel's wall is cooler than the bulk suspension (Section 2.3.2) and that the kinetic product (lower temperature and forms faster) is usually the metallic form, the presence of metal contaminants was expected. Since the cooler part was the vessel's wall and the metallic layer did not dislodge, most of the synthesized products were not contaminated, except bismuth.

Regarding the crystal structures of the obtained metal sulfide powders, there appears to be no significant connection between the crystal structure and the group the metal element belongs to. Zinc and cadmium (group 12) both formed cubic sulfides but in the adjacent group 11, copper formed both hexagonal and orthorhombic structures, while silver formed the monoclinic phase.

Ordering the band gaps revealed that there is an apparent correlation between the crystal family and the band gap. As reported by Roy et al.[297], who synthesized metal-organic framework compounds containing transition metals, those with the most symmetrical crystals (cubic or tetragonal) have the largest band gaps while the least symmetrical (monoclinic and triclinic) have the smallest band gaps. At the time (2015), the authors found no reports on this correlation. The same can be seen in the table for metal sulfide semiconductors, where structures with the lowest symmetry, namely the monoclinic and orthorhombic phases, appear to have smaller band gaps when compared to the cubic phase, which is the structure with the highest symmetry in the crystal family. The remainder, such as the hexagonal - as well as the trigonal which belongs to the hexagonal family, and tetragonal phases were found to not correlate.

As for the formation of electric arcs during the syntheses, since it was heavily dependent on the precursors' anion it is not shown in Table 3.3. The elements from period 6 of the periodic table did, however, tended more to develop arcs during the syntheses than the others. The elements from groups 2 and 3 were not expected to form arcs since the metallic form of the alkaline groups is extremely unstable and unlikely to form in the presence of a sulfide anion. The exception of barium nitrate, during the attempt to produce an alloy with zirconium, was probably due to the nitrate anion which forms gas bubbles - prone to develop electric arcs under microwave radiation. The same was observed in the synthesis involving bismuth nitrate. Only the synthesis involving silver(I) nitrate ran without the formation of electric arcs; even with the formation of gas. Further details on the formation of electric arcs can be found in Section 3.4.1

### 3.3 Multinary Metal Sulfide

Multinary sulfide alloys, a name given to the various groups of multi-metal sulfide alloys such as the ternary, quaternary - etc. - sulfide alloys, have several advantages over the more simple binary. As stated by Stroyuk et al.[298], these alloys can retain their crystal structure even when the stoichiometry is heavily changed, and also retain the quantum confinement observed in the binary sulfides, such as PbS, which allows the modification of the material's band gap by changing its size. They can also be easily doped or alloyed with other elements, such as Se to substitute the S or one of the metals substituted, fully or partially, with another form of the same group. These multinary sulfide alloys show promising properties for solar cells, as absorber materials, and in photocatalysis.

The results obtained from the microwave-assisted metal sulfide nanoparticle synthesis method used to synthesize a variety of metal sulfide alloys will be presented in the following section. First, two copper-based ternary sulfides (Section 3.3.1.1), a well-studied multinary sulfide semiconductor, followed by an attempt to synthesize barium and zirconium based sulfide ( $\text{BaZrS}_3$ ).

The synthesis of alloys attempted and the results are presented in Table 3.3.3 while the synthesis details can be found in Section A.2 of the Appendix A.

### 3.3.1 Ternary

#### 3.3.1.1 Cu, Fe

Chalcopyrite, a readily available, stable and non-toxic sulfide, has been used in thermoelectrics[299], electrode for battery[300], and for photovoltaics given its bulk direct band gap from 0.3 eV to 0.6 eV[301] and if the particles' size is below 3 nm, it can go up to 1.39 eV.[302]

Copper iron sulfide has been recently synthesized by a microwave-assisted solvothermal method, starting from copper(II) acetate, iron(III) chloride, and thiourea in ethylene glycol. The mixture was heated by microwave radiation at a constant power of 400 W for 5 minutes.[303]

The synthesis of copper iron sulfide was attempted starting from copper(I) iodide (CuI) and iron(III) acetylacetonate and is detailed in Section A.2.1.1. The color, temperature, and pressure profiles of the resulting powder are shown in Figure 3.38.

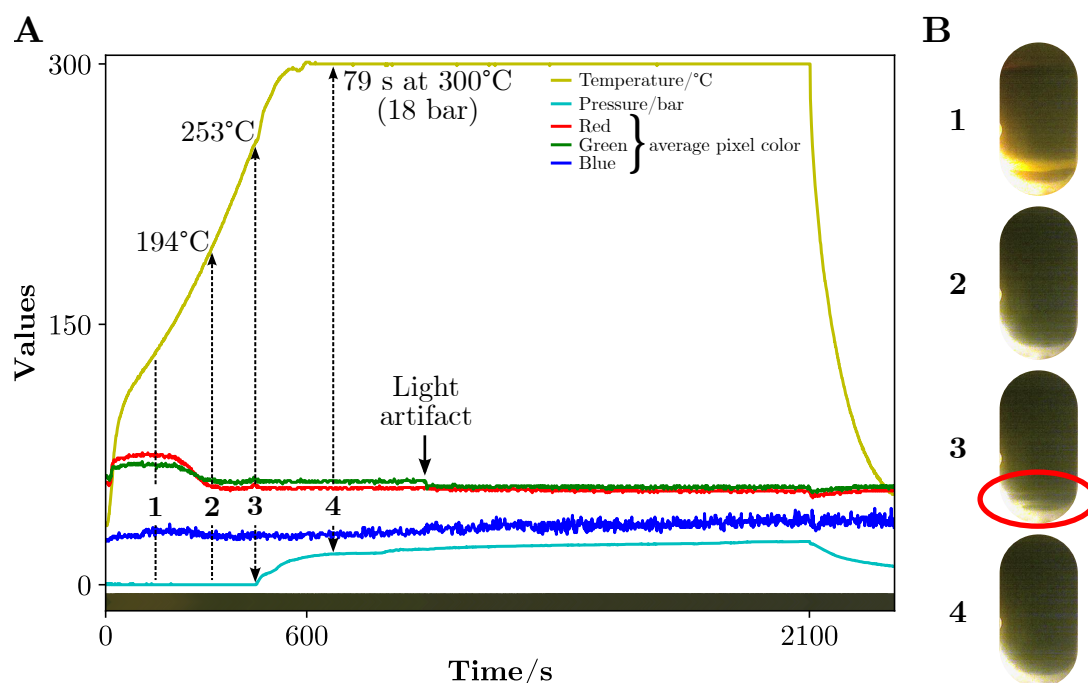


Figure 3.38: Color, temperature, and pressure profiles of the microwave-assisted synthesis of  $\text{CuFeS}_2$  (A) and photos of the reaction vessel taken at certain moments (B). In (B) photo 3, a temporary gas pocket can be seen, marked with a red circle.

Iron(III) acetylacetonate has a deep dark red color that the microwave reactor's camera cannot distinguish from black, which explains the low values for the average pixel colors. The first moment in Figure 3.38 (1) is attributed to the dissolution of the reagents, which occurs at a temperature below 90 °C and it is assumed that the brief yellow color is the same as the one observed by Kumar et al.[303]. Immediately after, the solution darkens with the precipitation of a dark compound at 150 °C. At 194 °C, moment (2), the color of the suspension stabilizes and is kept until the end of the synthesis. An abrupt increase in pressure and a slight increase in temperature (3), which the automated temperature control could not correct to maintain the temperature ramp. It has been previously shown that the hexagonal phase of  $\text{CuFeS}_2$  forms at a temperature

around 140 °C[304][305] and by increasing the temperature to 260 °C the tetragonal phase is obtained.[305] notice that both temperatures correspond to the those of the previously described moments (1) and (3) from Figure 3.38. The exothermic reaction that occurs in (3) probably corresponds to the formation of the tetragonal phase and, if the synthesis was stopped exactly before the moment begins, only the hexagonal phase of  $\text{CuFeS}_2$  would be obtained. According to Vahidshad et al.[305], at 140 °C gas should be released while the solution darkens and the hexagonal  $\text{CuFeS}_2$  forms. However, in this synthesis, the pressure only rose at the temperature where the tetragonal phase forms. Vahidshad et al. synthesis was performed with a heating rate similar to the one from this work and they observed the formation of gas below the temperature seen in Figure 3.38 (3). Either the phenomenon is characteristic of the synthesis conditions they used, starting from  $\text{CuCl}$ ,  $\text{FeCl}_3$ , thiourea, oleylamine, and 1-octadecene (ODE), or since the synthesis was performed using the conventional conduction and convection heating method, the bottom of the flask arrived at 250 °C before thermometer registered this temperature. They also reported that at 310 °C  $\text{CuFeS}_2$  decomposed to  $\text{Cu}_x\text{S}$  but as the X-ray diffraction pattern of the synthesized powder shows (Figure 3.39 A), only the tetragonal phase of  $\text{CuFeS}_2$  was formed, even after keeping the synthesis temperature at 300 °C for 25 minutes. The TEM image of the tetragonal  $\text{CuFeS}_2$  particles in Figure 3.39 B reveals that there are two size populations, one with an average size of 9 nm and another with 18 nm, as per the particles' size distribution shown below. The inset in A shows a TEM image where some bigger particles can be seen. According to the TEM images, this synthesis method yields the pure tetragonal phase of  $\text{CuFeS}_2$  with the majority of the particles with sizes below 18 nm and some casual bigger particles with less than 200 nm.

The average particle size determined from the most intense peak in the XRD pattern and using Scherrer's formula is 34 nm. This value is above both populations observed in the TEM image and is the most representative of the sample since the measurement was done using the whole sample powder. Smaller particles can probably be obtained by stopping the synthesis at a temperature of ~285 °C, after the exothermic reaction occurs, as seen in Figure 3.38 A. There is some similarity between these ordered smaller particles that appear to be fused together and the particles from the synthesized mixture of  $\text{Cu}_{1.8}\text{S}$  and  $\text{Cu}_{1.97}\text{S}$  (Figure 3.23), and from  $\text{Ag}_2\text{S}$  (Figure 3.26) binaries. Were it not for the purity seen in the XRD pattern, added to the abundance of smaller particles seen in the TEM image, and the particles could be assumed to be copper sulfide.

As a side note, the choice of  $\text{CuI}$  for the production of  $\text{CuFeS}_2$  and  $\text{CuInS}_2$ , shown in Section 3.3.1.2, was made purely on the fact that any chosen reagent, except  $\text{CuO}$  and  $\text{CuI}$ , would result in dangerous arc formations at higher temperatures and, after some synthesis trials,  $\text{CuI}$  consistently produced ternary alloys. It was also desirable to avoid any source of oxygen, given that the majority of the elements have a high affinity to it.



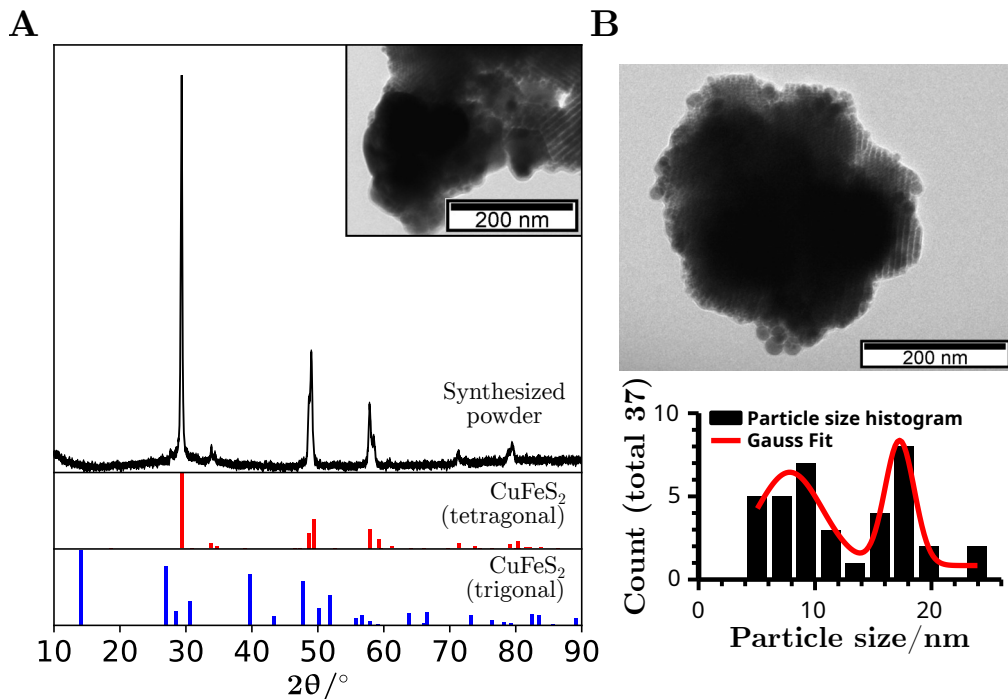


Figure 3.39: X-ray diffraction pattern (A) of the synthesized  $\text{CuFeS}_2$  powder, with reference patterns below, and TEM image as inset showing large particles, and a TEM image with the corresponding particle size distribution below (B). The tetragonal and trigonal reference patterns were taken from Materials Project[128][129] and respectively correspond to mp-3497 and mp-753211. The scale bar is 200 nm in (B).

### 3.3.1.2 Cu, In

Copper indium sulfide nanoparticles are excellent absorbers and are currently being commercially used in the form of quantum dots applied in windows. The dots that are covered by a ZnS shell absorb the incoming light, re-emit it and, through mirror engineering inside the window, the light is trapped and guided to the window frame where it is converted to electricity.[72] The reported band gap for this sulfide is 1.5 eV.[302]

There are some reports in the literature regarding the solvothermal synthesis of the multinary  $\text{CuInS}_2$ . The method most similar to the one used in this work started from a mixture of 1-dodecanethiol, CuI, indium(III) acetate, and zinc(II) stearate, which was heated to  $230^\circ\text{C}$  for 5 minutes, resulting in a tetragonal alloy between  $\text{CuInS}_2$  and ZnS. Hosseinpour-Mashkani et al.[306] developed a more complex microwave-assisted synthesis, where the complex bis(glycinato)copper(II) was first synthesized and then used with  $\text{InCl}_3$  and thiourea in propylene glycol, heated to  $155^\circ\text{C}$ .

Two synthesis were performed to fabricate the multinary metal sulfide  $\text{CuInS}_2$ , both starting from 1-dodecanethiol, CuI and  $\text{InCl}_3$  and are detailed in Section A.2.1.2. However, one of the synthesis products was washed with chloroform, to test if the powder could be suspended after to form an ink, and the other with ethanol. The color, temperature, and pressure profiles and the XRD patterns of both syntheses attempts to obtain  $\text{Cu}_x\text{In}_y\text{S}_z$  are shown in Figure 3.40.

The two synthesis replicas have similar color profiles (A). Both initiate with the dissolution of

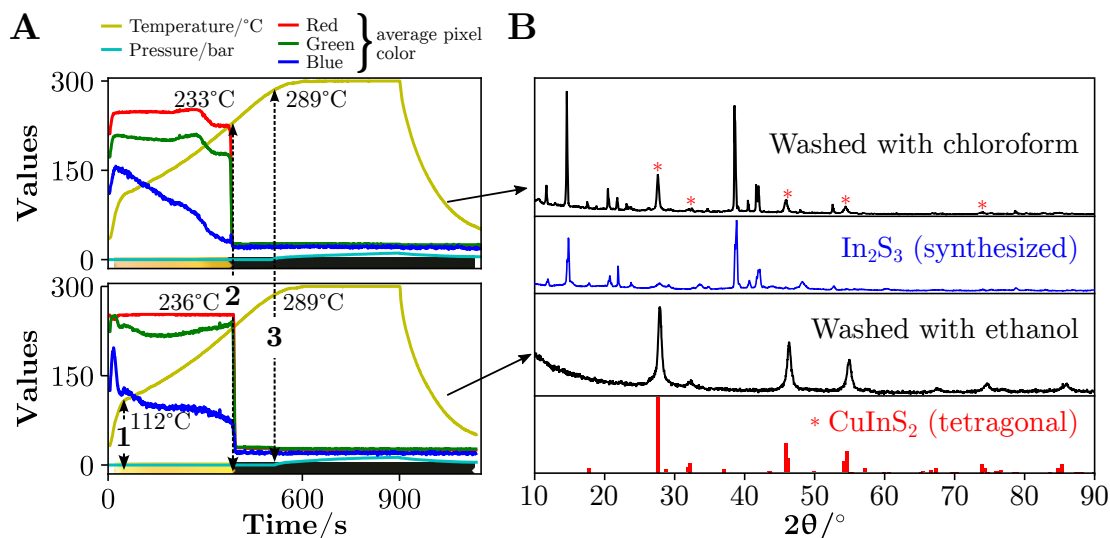


Figure 3.40: Color, temperature, and pressure profiles (A) and XRD patterns (B) of two synthesis replicas, with the particles washed with either ethanol or chloroform. Some events in the profiles were marked from (1) to (3). In (B), the XRD pattern of the synthesized  $\text{In}_2\text{S}_3$  from Section 3.2.10.1 and the reference pattern of the tetragonal phase of  $\text{CuInS}_2$  (mp-22736) taken from Materials Project[128][129].

the reagents and form a complex at around 112 °C (1). The color of the suspension then darkens progressively until a black precipitate is almost instantaneously formed between 233 °C and 236 °C (2), which is most likely the formation of  $\text{CuInS}_2$ , as it is similar to the temperature reported in the literature.[307] The last event is associated with a pressure rise, occurring at 289 °C (3), which could be the evaporation of the thiol.

Using chloroform, instead of ethanol, to wash the powder after the synthesis lead to the inclusion of impurities. The X-ray diffraction (XRD) patterns (B) show that the particles washed with ethanol are composed solely of the tetragonal phase of  $\text{CuInS}_2$ , while the one washed with chloroform contains the tetragonal  $\text{CuInS}_2$  and  $\text{In}_2\text{S}_3$ . This suggests that  $\text{In}_2\text{S}_3$  formed in the presence of copper is suspendable in ethanol, since it was washed away with the solvent during the cleaning procedure.

Applying the Scherrer's formula to the most intense peak at  $2\theta$  of 27.9°, corresponding to the (112) plane, in the XRD pattern of the particles washed with ethanol, an average size of 17 nm was estimated. The particle size distribution obtained from the TEM image in Figure 3.41 is in agreement with the estimated from the XRD pattern. A particle size range from 6 nm to 54 nm, with an average of around 20 nm, was obtained from manual measurement of particle sizes.

The use of 1-dodecanethiol as a sulfur source to produce  $\text{CuInS}_2$  has also been used previously by Zheng et al.[307]. Using oleic acid and 1-octadecene as surface stabilizers, with the latter as the bulk solvent, and a reaction temperature of 235 °C, the obtained particles had sizes in the range of 3 nm, which are much lower than the ones obtained in this work. The presence of the typically used surface stabilizers like oleic acid greatly contributes to the lower particle size. However, it is predictable that interrupting the synthesis at the temperature of ~240 °C, immediately after the black suspension is formed (2), smaller particles could be obtained without the aid of other

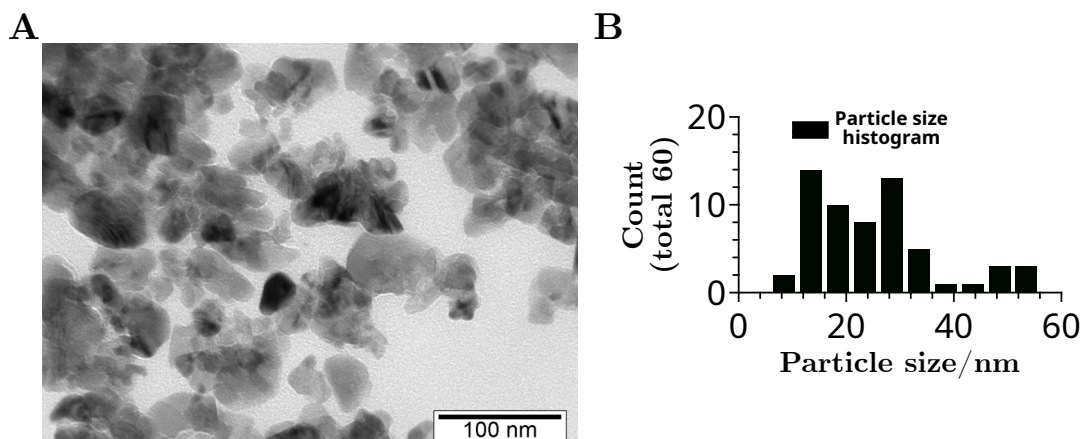


Figure 3.41: Transmission electron microscopy images (A) and the size distribution of particles (B) of  $\text{CuInS}_2$  particles washed with ethanol. Particle sizes were measured manually using the ImageJ software. The scale bar is 100 nm in (A).

stabilizers beside 1-dodecanethiol. Another parameter to take into consideration is the reagent concentration, as mentioned in Section 3.4.3. Zheng et al. used a total volume of 7.825 mL to 0.5 mmol of each of the copper and indium-containing reagents. The total molar concentration, taking into account both reagents, was  $\sim 0.128$  M, which is below the used in this work (0.4 M). Pure tetragonal phase  $\text{CuInS}_2$  nanoparticles were obtained, albeit with a relatively large particle size distribution (6 nm to 54 nm).

### 3.3.1.3 In, Sn

Nanosheets of  $\text{In}_4\text{SnS}_8$  have been used for water remediation of organic dyes using visible light, without the aid of the ultra-violet[308], due to its optical band gap of 2.1 eV, in the visible region.[309]

The alloy has been previously synthesized in an oleylamine solution, with the reaction between indium diethyldithiocarbamate and tin diethyldithiocarbamate, which were previously prepared using sodium diethyldithiocarbamate. The mixture was heating in vacuum to 120 °C and then, under a nitrogen atmosphere, it was further heated to 240 °C for 1 hour.[308] An aqueous-based synthesis was reported by Lei et al.[310], where tin(IV) chloride, L-cysteine and indium(III) chloride tetrahydrate were heated to 160 °C for 24 hours.

The synthesis of indium tin sulfide was attempted starting from indium(III) chloride and tin(II) 2-ethylhexanoate and is detailed in Section A.2.1.3. The color, temperature, and pressure profiles and XRD patterns of the syntheses involving the elements In (Section 3.2.10.1) and Sn (Section 3.2.11.1) and the synthesis involving both elements are shown in Figure 3.42

The profiles of (In-Sn-S) show two distinct events. The first is a color change from dark yellow to black at 197 °C which occurred between the transitions seen in the color profiles of (In-S) and (Sn-S). The second event is a pressure rise at 299 °C, which began at a slightly higher temperature compared to the (In-S) synthesis. The XRD pattern (B) (In-Sn-S) from the obtained powder matches the  $\text{In}_4\text{SnS}_8$  (cubic spline) phase, similar to the one found in reference [309], and using

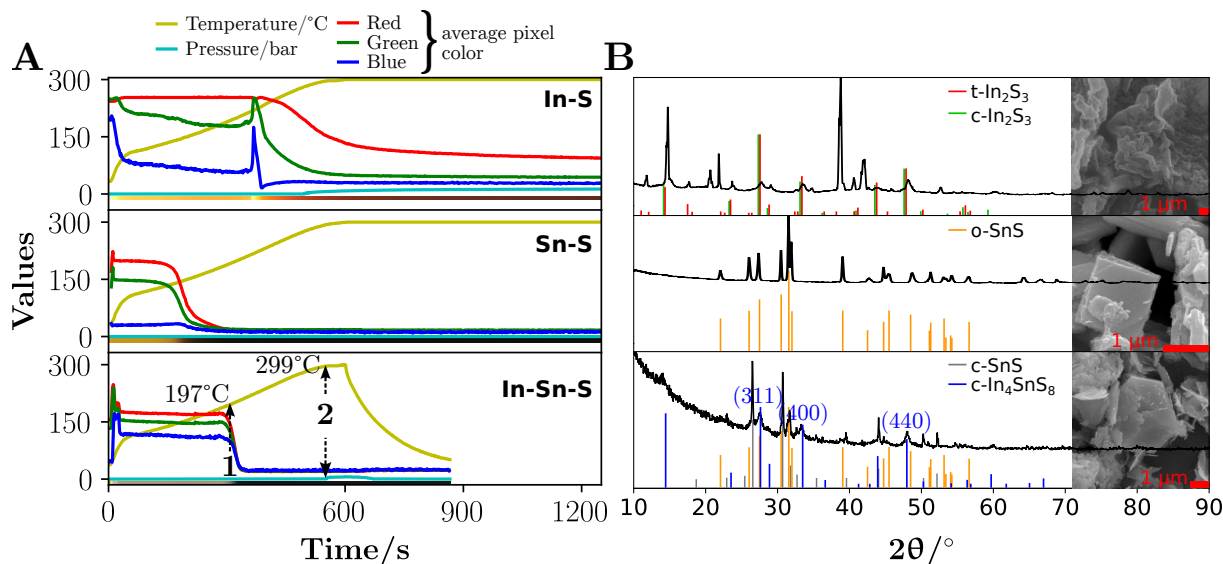


Figure 3.42: Color and temperature profiles (A) of syntheses starting from 1-dodecanethiol and either indium(III) chloride (In-S), tin(II) 2-ethylhexanoate (Sn-S) or both (In-Sn-S) and the resulting XRD patterns (B) with SEM images as insets. Two moments were marked in the profiles of (In-Sn-S). The XRD reference pattern of the orthorhombic (o-SnS) and cubic (c-SnS) phases were adapted from reference[311] and the tetragonal (t-In<sub>2</sub>S<sub>3</sub>), cubic (c-In<sub>2</sub>S<sub>3</sub>) and cubic (c-In<sub>4</sub>Sn<sub>8</sub>) phases were adapted from references [268], [312], and [309], respectively. The scale bars are 1  $\mu\text{m}$  for (In-S), (Sn-S), and (In-Sn-S) in (B).

the most intense peak at  $14.5^\circ$ , a crystallite average size of 80 nm was determined. Since the final powder contains the cubic phase of SnS, the black suspension that formed at a later stage in (In-Sn-S) could be attributed to the formation of the latter compound. The crystallite size obtained from the peak corresponding to the (400) plane of In<sub>4</sub>Sn<sub>8</sub> was estimated to be 10 nm. The SEM image of the (In-Sn-S) sample in (B) reveals micrometer-sized clusters similar to those found in the (Sn-S) sample with flakes presumably of In<sub>4</sub>Sn<sub>8</sub>, since they are dissimilar to the ones found in the SEM image of (In-S).

The diffuse reflectance spectrum of the resulting powder was measured and is shown in Figure 3.43.

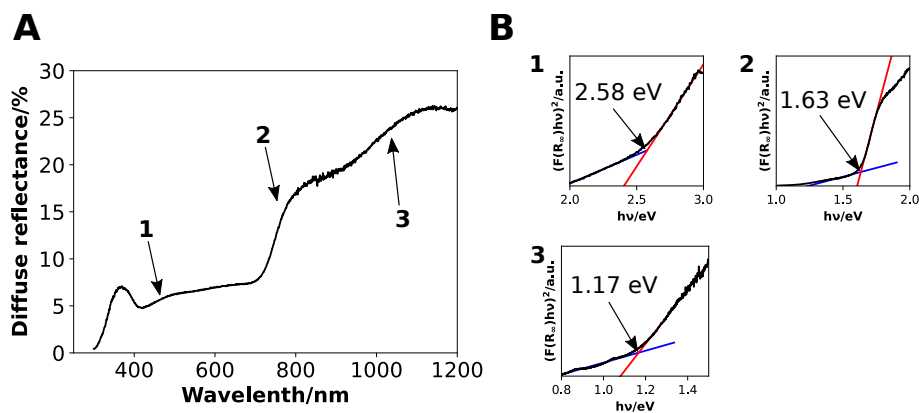


Figure 3.43: Diffuse reflectance spectrum (A) of the powder from the product of the synthesis starting from 1-dodecanethiol, indium(III) chloride and tin(II) 2-ethylhexanoate and the corresponding Tauc plots (B), for each numbered region, with two line regressions and the band gap values.

The diffuse reflectance spectrum (A) contains three slopes. Therefore, the powder is composed of three distinct phases and, unlike the material synthesized with the zinc and tin precursors, slope 2 leads to a band gap of 1.63 eV, near that of the cubic phase of SnS. The presence of cubic  $\text{In}_2\text{S}_3$  favors the formation of cubic SnS, as ZnS did (Section 3.3.1.5). The remainder band gaps (Figure 3.43 (B)) of 1.17 eV and 2.58 eV match the band gaps obtained from the synthesis of orthorhombic SnS and  $\text{In}_2\text{S}_3$ . It was not possible to observe the 2.1 eV band gap of  $\text{In}_4\text{SnS}_8$ .

The XRD pattern points to the existence of a mixture of cubic SnS and  $\text{In}_4\text{SnS}_8$  (10 nm crystallites), while the diffuse reflectance spectrum shows the band gaps of to both the orthorhombic and cubic phases of SnS and that of  $\text{In}_2\text{S}_3$ .

### 3.3.1.4 Zn, In

The multinary sulfide  $\text{ZnIn}_2\text{S}_4$  has interesting thermoelectric (cubic phase) and photonic (hexagonal phase) properties, with a band gap between 2.2 eV and 2.8 eV. Both phases have photocatalytic applications as well.[313]

The cubic and hexagonal phases of the multinary metal sulfide  $\text{ZnIn}_2\text{S}_4$  have been previously synthesized in an aqueous solution by Chen et al.[314] The authors demonstrated that when the chloride precursors were heated to 120 °C for 10 hours with thioacetamide, the cubic phase was obtained while with the nitrates led to the formation of the hexagonal structure. A hot-injection synthesis procedure was proposed by Kempken et al.[313], where zinc(II) acetate and indium(III) acetate were mixed in oleylamine, heated to 280 °C in a nitrogen atmosphere, then tert-dodecanethiol and 1-dodecanethiol were injected and the temperature was kept for 1 hour. The synthesis of zinc indium sulfide was attempted starting from zinc(II) acetate dihydrate and indium(III) chloride and is detailed in Section A.2.1.4. The color, temperature, and pressure profiles and XRD patterns of the syntheses involving the elements Zn (Section 3.2.9.1) and In (Section 3.2.10.1) and the synthesis involving both elements are shown in Figure 3.44

The color profile from the synthesis starting from both the zinc and the indium precursors (Zn-In-S), shows a transition from white/gray to a dark yellow at 275 °C, which occurred after the transition from yellow to dark red (In-S) and before the formation of the zinc sulfide precipitate (Zn-S). The XRD pattern of the resulting powder resembles the one obtained in the zinc sulfide synthesis. However, the first peak from the sample (Zn-In-S) at a  $2\theta$  of 27.9°, matches the most intense peak corresponding to the (102) plane of the hexagonal  $\text{ZnIn}_2\text{S}_4$  reference and with an estimated crystallite size of 2 nm. This crystallite size is justified by the small time the synthesis was allowed to progress after the sulfide formed at 275 °C.

The diffuse reflectance spectrum of the resulting powder was measured and is shown in Figure 3.43. The Tauc plot in the inset reveals that the powder has a band gap of 2.80 eV, which is between the band gaps of indium sulfide (2.56 eV) and zinc sulfide (3.44 eV), and within the expected for  $\text{ZnIn}_2\text{S}_4$ .

From the XRD pattern it was possible to conclude that the ternary metal sulfide  $\text{ZnIn}_2\text{S}_4$  was obtained, but one of the most intense peaks from the hexagonal  $\text{ZnIn}_2\text{S}_4$  near 40° is missing. The

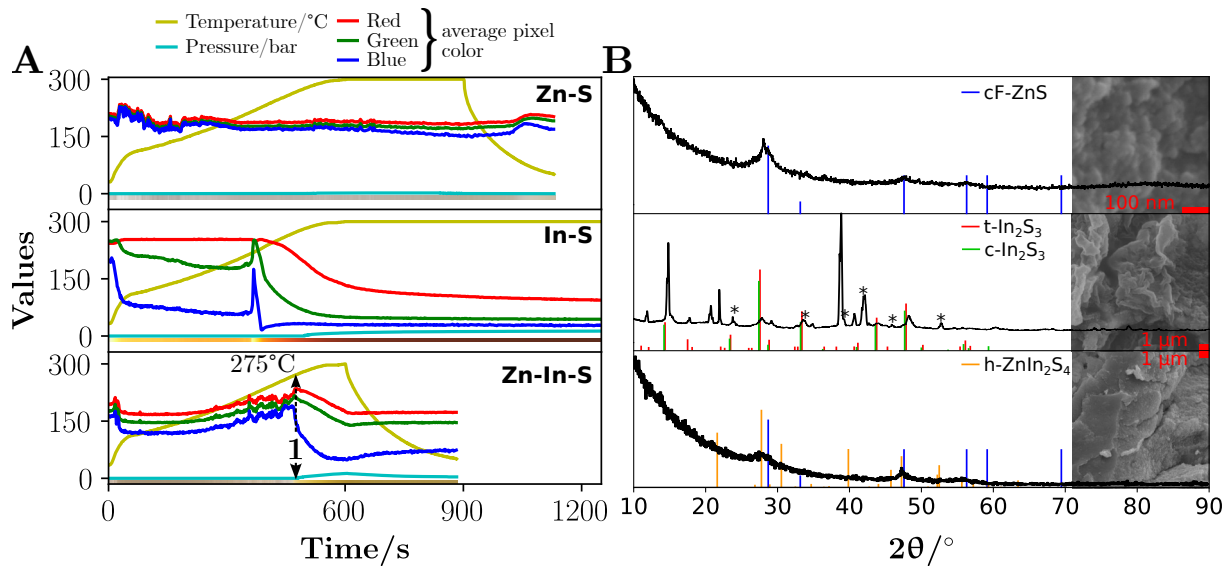


Figure 3.44: Color and temperature profiles (A) of syntheses starting from 1-dodecanethiol and either zinc(II) acetate dihydrate (Zn-S), or indium(III) chloride (In-S) or both (Zn-In-S) and the resulting powders' XRD patterns (B) with the SEM images as insets. One moment was marked in the profiles of (Zn-In-S). The XRD reference pattern of the hexagonal (h-ZnIn<sub>2</sub>S<sub>4</sub>) phase was adapted from reference [313] and the tetragonal (t-In<sub>2</sub>S<sub>3</sub>) and cubic (c-In<sub>2</sub>S<sub>3</sub>) phases of In<sub>2</sub>S<sub>3</sub> were adapted from references [268] and [312], respectively. The scale bars are 100 nm for (Zn-S), and 1 μm for (In-S) and (Zn-In-S) in (B).

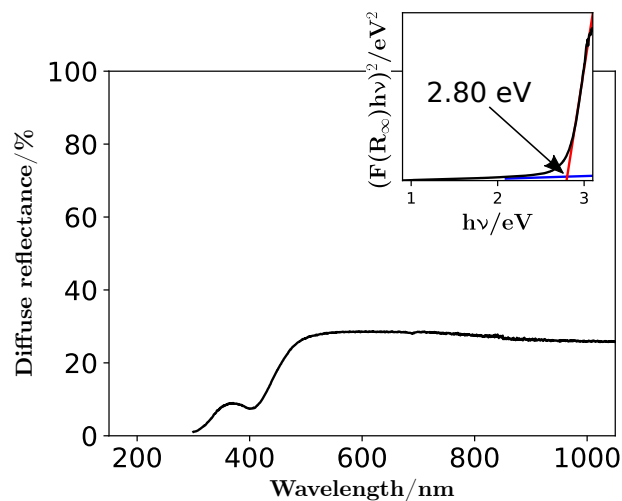


Figure 3.45: Diffuse reflectance spectrum of the powder from the product of the synthesis starting from 1-dodecanethiol, zinc(II) acetate dihydrate and indium(III) chloride, with the corresponding Tauc plot, two line regressions, and the band gap value as inset.

band gap of 2.80 eV does match the one reported for the alloy, further confirming the presence of the multinary sulfide.

### 3.3.1.5 Zn, Sn

The algorithms presented by Saal et al.[315] and Kirklin et al.[316] in The Open Quantum Materials Database, predict the existence of an alloy composed of zinc, tin, and sulfur with the

chemical formula  $\text{Zn}_2\text{SnS}_3$ , a band gap of 0.9 eV and formation energy of -0.594 eV/atom. For comparison, the stable ZnS zinc blende had an experimentally confirmed formation energy of -1.052 eV/atom. In Materials Project database[128][129], the predicted unstable structure is  $\text{ZnSnS}_3$  with a formation energy of -0.682 eV/atom, compared to the -1.063 eV/atom of the cubic ZnS (mp-10695). These lower formation energies are similar to the experimentally confirmed -0.568 eV/atom formation energy of the orthorhombic SnS, which sets the minimum energy limit that provides hope for the possibility of obtaining an alloy between Zn, Sn, and S. The only reference in the literature regarding the alloy with the three elements is of a metal sulfur framework synthesized by Oh et al.[317], comprising a  $\text{Zn}^{2+}$  metal ion and a  $[\text{Sn}_2\text{S}_6]^{-4}$  linker, with a diffraction pattern that does not have discernible peaks.

The synthesis of zinc tin sulfide was attempted starting from zinc(II) acetate dihydrate and tin(II) 2-ethylhexanoate and is detailed in Section A.2.1.5. The color, temperature, and pressure profiles and XRD patterns of the syntheses involving the elements Zn (Section 3.2.9.1) and Sn (Section 3.2.11.1) and the synthesis involving both elements are shown in Figure 3.44.

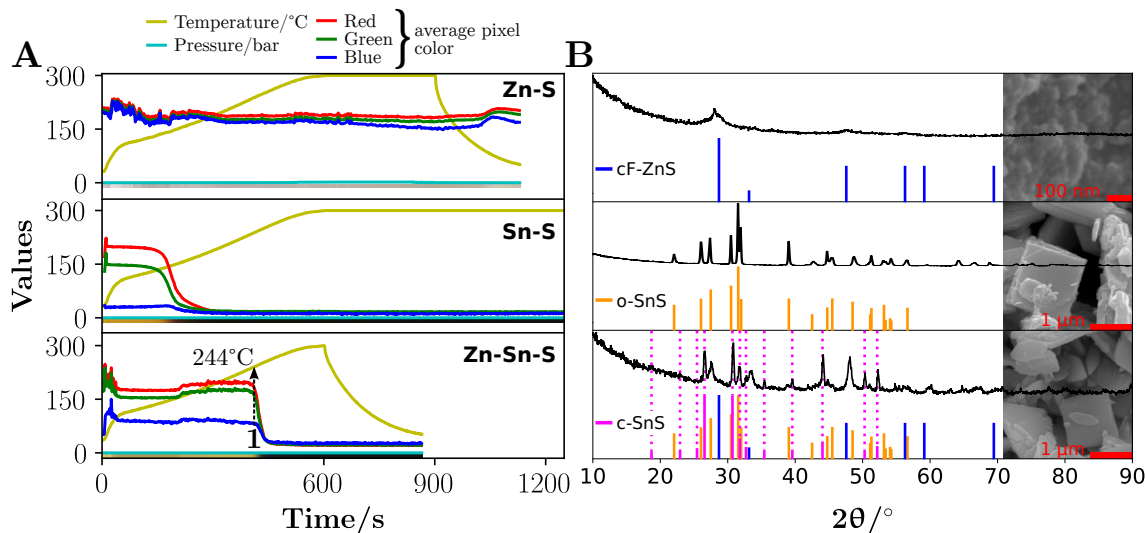


Figure 3.46: Color profiles (A) of syntheses starting from 1-dodecanethiol and either zinc(II) acetate dihydrate (Zn-S), tin(II) 2-ethylhexanoate (Sn-S), or both (Zn-Sn-S) and the resulting XRD patterns (B) with SEM images as insets. One moment was marked in the profiles of (Zn-Sn-S). The XRD reference pattern of ZnS zinc blende face-centered cubic phase (cF-ZnS) was adapted from the JCPDS card 05-0566 [318], and both orthorhombic SnS (o-SnS) and cubic SnS (c-SnS) from reference [311]. The scale bar is 100 nm for (Zn-S), and 1  $\mu\text{m}$  for (Sn-S) and (Zn-Sn-S) in (B).

As can be seen in the profiles (A), the SnS is formed immediately at  $\sim 135^\circ\text{C}$ , while the mixture Zn-Sn-S has a transition at  $\sim 244^\circ\text{C}$ , between the temperatures of formation of both binary metal sulfides (Sn-S) and (Zn-S). According to the XRD patterns in (B), both Zn-S and Sn-S mixtures respectively formed pure zinc blende ZnS and orthorhombic SnS. However, the pattern from Zn-Sn-S, besides the latter two pure phases, contains a third phase that was identified as cubic SnS. This phase has a very specific signature given by a sequence of three peaks with decreasing intensity from 30 to 33, corresponding to the (400), (410), and (411) planes.[319] The presence of



zinc acetate delayed the formation of SnS. It is assumed that the small ZnS particles present in the sol-gel structure, discussed previously in Section 3.2.9.1 and the article[245], served as seeds that forced the formation of cubic SnS. This phase induced constraint has been observed by Kempken et al.[313] in a similar alloy ( $\text{ZnIn}_2\text{S}_4$ ), where they introduced a small amount of copper acetate to force the formation of nanoplates. The micrometer-sized plates seen in (B) for the (Zn-Sn-S) synthesis are probably composed of smaller crystallites of cubic SnS with an estimated size of 35 nm, from the peak at a  $2\theta$  of  $35.5^\circ$ . Another possibility for the color transition delay is the difference in heat capacity between both zinc and tin precursors, presuming that the latter has a lower capacity; zinc acetate absorbs more heat, withholding the energy from the tin precursor. The orthorhombic phase SnS that probably formed at  $\sim 135^\circ\text{C}$  in (Zn-Sn-S) before the sharp transition at  $244^\circ\text{C}$  can be explained by the existence of some free tin precursor.

The absence of a true Zn-Sn-S alloy was further confirmed with Raman spectroscopy, using a 532 nm laser at 0.15 mW power, as seen in Figure 3.47. As a reference, ZnS and SnS Raman spectra from the powders fabricated using the method developed in this work are also shown.

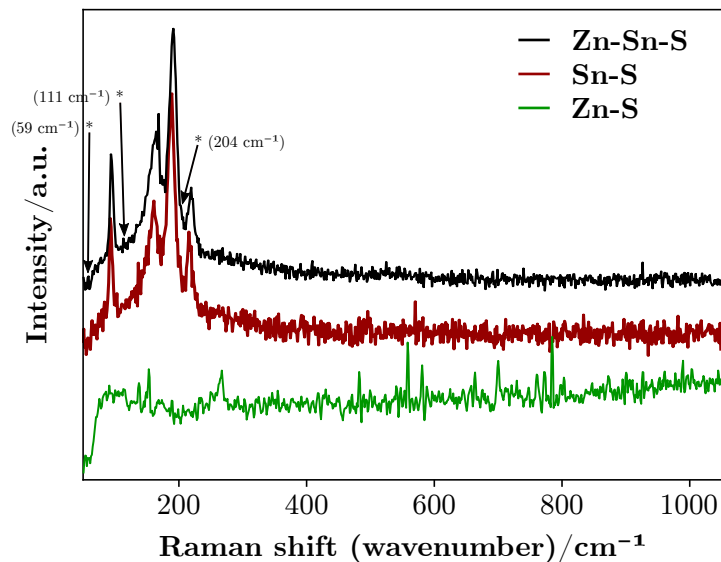


Figure 3.47: Raman spectra of the powders from the syntheses involving 1-dodecanethiol with either tin(II) 2-ethylhexanoate (Sn-S), zinc(II) acetate dihydrate (Zn-S) or both (Zn-Sn-S). The \* marks refer to some of the most intense Raman peaks of the cubic phase of SnS, according to reference [320]. The spectra were acquired using a laser, with emission at 532 nm and a power of 0.15 mW.

The Raman spectrum of the powder from the synthesis performed using both tin(II) 2-ethylhexanoate and zinc(II) acetate dihydrate reveals the presence of the orthorhombic phase of SnS. Contrary to the XRD pattern, the expected Raman peaks from the cubic phase of SnS at  $59\text{ cm}^{-1}$ ,  $111\text{ cm}^{-1}$ , and  $204\text{ cm}^{-1}$ [320] are practically absent. Since the XRD analysis covers a larger amount of powder than the Raman spectroscopy, it is assumed that the majority of the powder is composed of cubic SnS with slight contamination from the orthorhombic phase.

In Figure 3.48 lies the Tauc plots calculated from the diffuse reflectance spectrum of the powder synthesized with the zinc acetate and tin precursors.



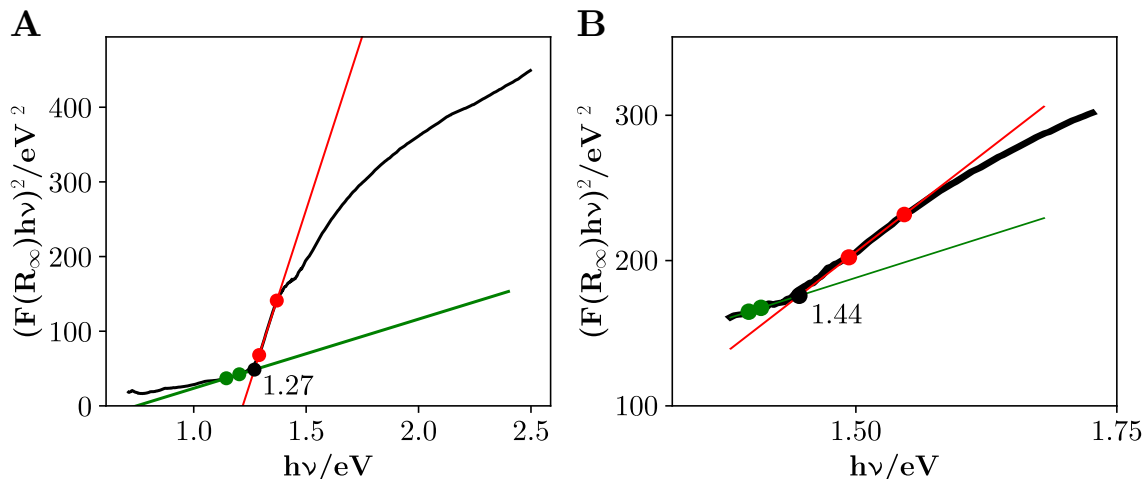


Figure 3.48: Tauc plots (A) and (B) calculated from the same diffuse reflectance spectrum of the powder from the product of the synthesis starting from 1-dodecanethiol, zinc(II) acetate dihydrate and tin(II) 2-ethylhexanoate.

The sharpest transition seen in (A) yielded a band gap of 1.27 eV, near the band gap obtained for the orthorhombic phase of SnS (Section 3.2.11.1), and a much less prominent transition (B) yielded a band gap of 1.44 eV which is near the reported in the literature for the cubic phase between 1.5 eV to 1.7 eV.[311], [321]. The band gaps are consistent with the XRD pattern and Raman spectra, regarding the mixture of phases.

The possibility of obtaining either the orthorhombic or the cubic phase of SnS is very interesting and important, given their different band gaps. However, the objective was to try to obtain an alloy with Zn, Sn, and S, which was not clearly achieved. Since the literature regarding this alloy is scarce, further studies are needed to understand the formation mechanism of the alloy.

### 3.3.1.6 Ba, Zr

As mentioned in section 2.2, lead-based perovskite materials have been on the rise and are an important alternative to silicon, given the advantage of low-temperature processability and the ability to build devices using the roll-to-roll fabrication method. The presence of lead, however, is less ideal when taking the environment and toxicity into account. Although the element is relatively abundant and rather cheap, a recent finding promises to substitute this hazardous component with barium and zirconium. The two elements combined with sulfur form a metal sulfide which adopts a perovskite structure. Proven to be a potential material for perovskite solar cells, due to its 1.7 eV to 1.8 eV band gap[322], light emitting devices and in proton conducting fuel cells[323], most synthetic methods are either physical[324], [325] or chemical vapor deposition and high temperature ( $>500$  °C) solid-state reactions.[326]–[328] Regarding colloidal nanoparticle synthesis, the nearest to  $BaZrS_3$  is a hot-injection synthesis of the similar ternary compound  $BaTiS_3$ , reported by Zilevu et al.[43], using N,N'-diethylthiourea as the sulfur source, oleylamine as a surface stabilizer and the complex with tetrahydrofuran (THF)  $Ba[N(Si(CH_3)_3)_2]_2(THF)_2$  and tetrakis(dimethylamido)-titanium as the metal sources. Since the temperatures used in the

previous synthesis were near 300 °C and titanium is in the same group as zirconium, the formation of BaZrS<sub>3</sub> is expected using the microwave-assisted synthesis method. Also, even though Sadeghi et al. stated that Zr and Hf are "sluggish" in reactions and require high temperatures to form crystalline compounds[41], using the synthesis method from this work, at 300 °C for 25 minutes, to obtain hafnium sulfide resulted in mixture of hafnium sulfides with different stoichiometries and oxidation numbers, according to the XRD pattern in Figure 3.8. This showed that it should be possible to obtain the alloy BaZrS<sub>3</sub>. A clue left by Ravi et al. on the supplementary information of reference [328] states that 1-dodecanethiol is a promising sulfur source since it slowly releases the sulfide ion above 240 °C, which inhibits aggressive nucleation and prevents the segregation of the binary sulfides.

Two attempts to synthesize BaZrS<sub>3</sub> were performed, starting from ZrCl<sub>4</sub> and either Ba(NO<sub>3</sub>)<sub>2</sub> or barium triflate and are detailed in Section A.2.1.6. The color, temperature, and pressure profiles and XRD patterns of the syntheses involving the elements Ba (Section A.1.1.4) and Zr (Section 3.2.1.2) and the synthesis involving both elements are shown in Figure 3.49

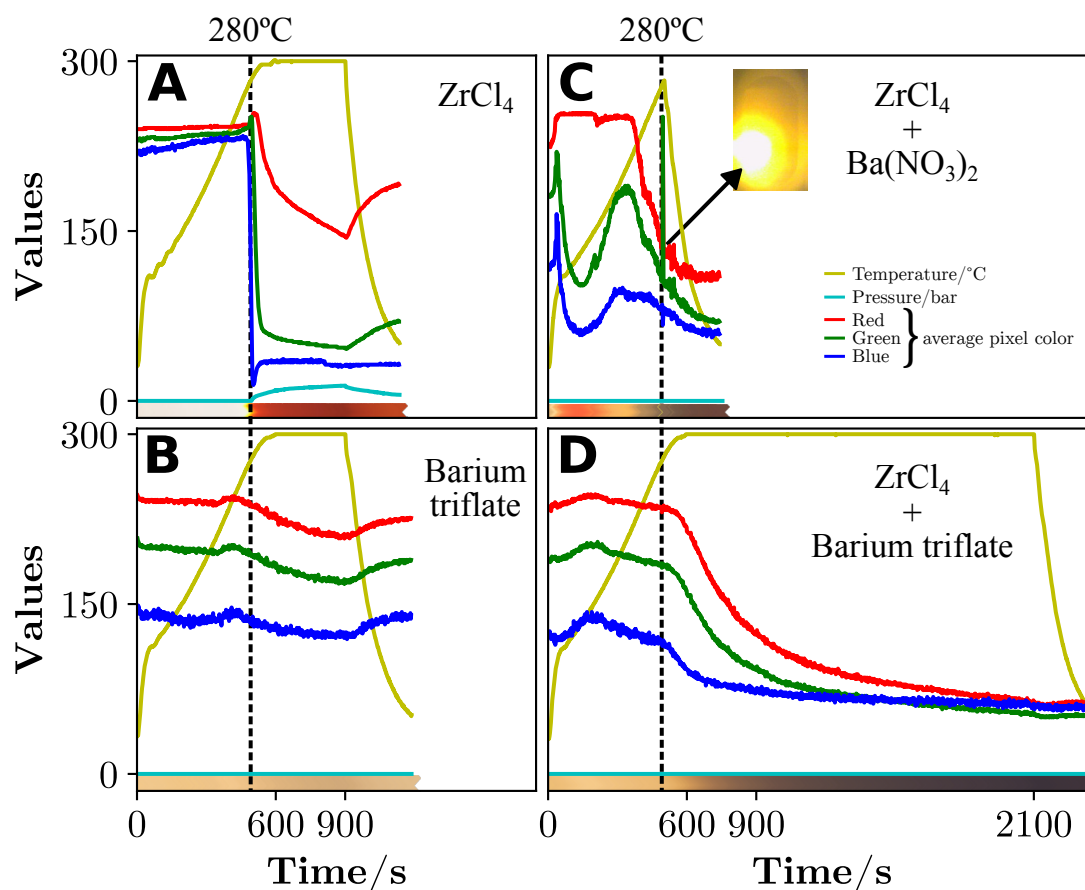


Figure 3.49: Color, temperature, and pressure profiles of a synthesis in 1-dodecanethiol, involving either ZrCl<sub>4</sub> (A), barium triflate (B), both reagents (C), and Ba(NO<sub>3</sub>)<sub>2</sub> and ZrCl<sub>4</sub> (D). The vertical dashed lines mark the moment of the extremely sharp transition that occurs at 280 °C in the synthesis involving ZrCl<sub>4</sub> and Ba(NO<sub>3</sub>)<sub>2</sub> (A). The inset in (C) is a picture of the electric arcing moment.

Starting from Ba(NO<sub>3</sub>)<sub>2</sub> and ZrCl<sub>4</sub> resulted in dangerous electric arcs, with yellow and white

colors as seen in the picture in Figure 3.49 (C), and the synthesis was aborted and discarded. The culprit was the nitrate since a synthesis attempt with barium triflate and  $\text{ZrCl}_4$  proceeded without any arc formation (D). Both the latter reagents were tested individually with 1-dodecanethiol and their profiles are shown in (A) and (B).

The synthesis starting with  $\text{ZrCl}_4$ , shows a sharp transition from a white suspension to a yellow suspension at the same temperature as the previous syntheses transitions: 280 °C. It is accompanied by a pressure rise, followed by a slow color change of the suspension to a deep red. Complexes involving zirconium and thiolates typically have a yellow or orange color.[329] The reagent and the complexes also don't appear to truly dissolve at any temperature. The barium triflate also did not dissolve in 1-dodecanethiol at any temperature and the color profile only presented a slight darkening behavior beginning at 255 °C. When both reagents were combined, the same light dispersion was seen throughout the entirety of the synthesis, but it instead resulted in a dark powder. The XRD pattern of the resulting washed and dried powder, from the synthesis involving both the zirconium and barium precursors, is presented in Figure 3.50.

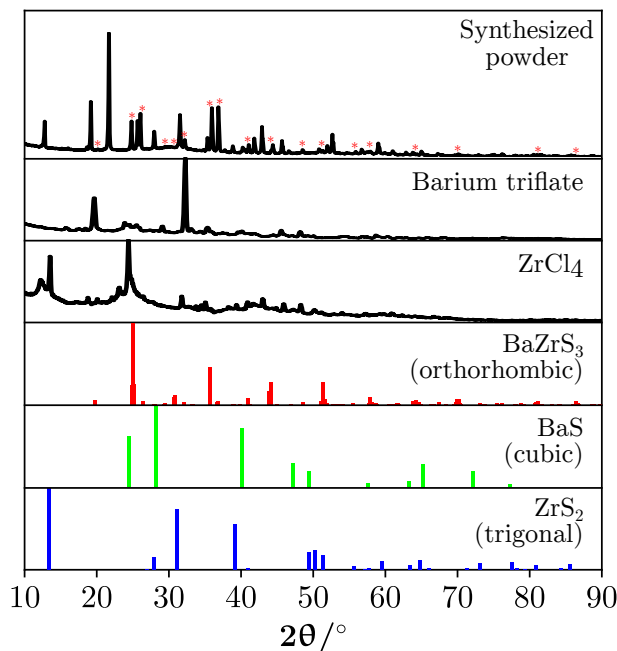


Figure 3.50: X-ray diffraction pattern of the resulting washed and dried powder from the synthesis attempt to obtain  $\text{BaZrS}_3$ . The patterns of barium triflate and  $\text{ZrCl}_4$  were obtained from the reagents that were used. The reference patterns of  $\text{BaZrS}_3$ ,  $\text{BaS}$  and  $\text{ZrS}_2$ , were taken from Materials Project[128][129] and correspond to mp-540771, mp-1500, and mp-1186, respectively. The red asterisks mark where the  $\text{BaZrS}_3$  peaks should be.

Except for the most intense peak at 21.7°, the remainder can be attributed to two or more references. Although all the peaks from the  $\text{BaZrS}_3$  reference appear to be present in the synthesized sample, most are convoluted with peaks from other references. The powder can be considered a mixture of the desired ternary sulfide and the binary sulfides  $\text{BaS}$  and  $\text{ZrS}_2$ .

The synthesis yield was not enough to perform a diffuse reflectance spectrum to extract a band gap.

### 3.3.2 Quaternary

#### 3.3.2.1 Cu, In, Sn

Recent developments regarding the ternary sulfide  $\text{CuInSnS}_4$  suggest that, due to its band gap between 1.3 eV and 1.4 eV, it is a good candidate for solar cell devices, as a light absorber.[330] A solvothermal synthesis method to produce  $\text{CuInSnS}_4$  nanoparticles, with sizes around 10 nm, was presented by Ramasamy et al.[330]. They used 1-dodecanethiol and tert-dodecanethiol to obtain the wurtzite phase and sulfur to obtain the defect chalcopyrite.

Two syntheses attempts to obtain the multinary metal sulfide containing the metal elements Cu, In, and Sn were performed starting from  $\text{CuI}$ ,  $\text{InCl}_3$  and tin(II) 2-ethylhexanoate in 1-dodecanethiol, using different heating ramps and maximum temperatures, which are detailed in Section A.2.2.1. The color, temperature, and pressure profiles and the XRD patterns of the resulting powders are shown in Figure 3.51.

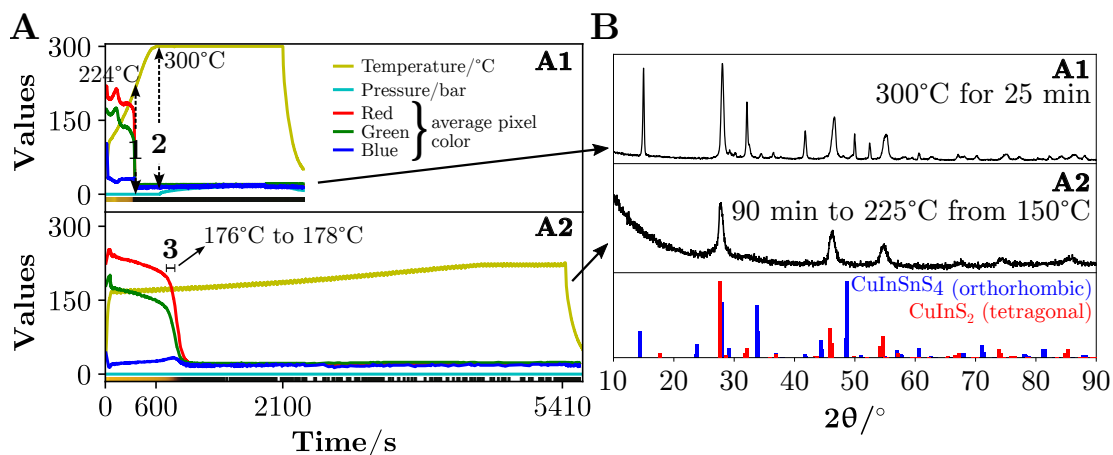


Figure 3.51: Color, temperature, and pressure profiles (A) of the syntheses (A1) and (A2) starting from  $\text{CuI}$ ,  $\text{InCl}_3$  and tin(II) 2-ethylhexanoate and the XRD patterns of the powders resulting from the respective synthesis (B). Two moments were marked in the first synthesis (A1) as (1) and (2) and one moment was marked on the second synthesis (A2) as (3). The reference patterns of the orthorhombic phase of  $\text{CuInSnS}_4$  and the tetragonal  $\text{CuInS}_2$  were taken from Materials Project[128][129] with the respective IDs: mp-1224102 and mp-22736.

The first synthesis (A1) was performed employing the method developed in this work, with the typical heating ramp set to reach 300 °C in 10 minutes and keep that temperature for a certain amount of time; 15 minutes in this experiment. Up to the first moment (1), there is a transition between yellow and dark yellow, which is attributed to the dissolution of the reagents and the formation of a complex. At 224 °C, there is a sharp color transition to black, probably signaling the precipitation of a sulfide. The color is constant until the end but at 300 °C (2) the pressure value begins to rise. The resulting powder appears to have a mixture of orthorhombic  $\text{CuInSnS}_4$  and tetragonal  $\text{CuInS}_2$ , according to its XRD pattern (B) (A1).

The rise in pressure seen in synthesis (A1) could be attributed to the formation of the quaternary sulfide  $\text{CuInSnS}_4$ . A second synthesis (A2) was performed, starting from the same reagents but setting a heating ramp such that the temperature rose to 150 °C in 10 seconds, followed by a

slower increase to 225 °C in 90 minutes. Up to moment (3), the behavior is very similar to (A1), where a bright yellow peak signals the dissolution of the reagents, followed by a progressive darkening. Upon reaching a temperature around 176 °C, the suspension began to slowly become black. As the XRD pattern in (B) (A2) reveals, the composition of the powder obtained is pure tetragonal  $\text{CuInS}_2$ , with no contribution from the Sn element. A slower heating ramp and a lower maximum temperature led to the formation of pure  $\text{CuInS}_2$ . There was no pressure development during the whole synthesis, as opposed to (A1), albeit it only developed at 300 °C. This suggests that the pressure increase (2) could be assigned to a reaction where the Sn is incorporated into the previously formed  $\text{CuInS}_2$  at the moment (1). The reaction was incomplete since there was still  $\text{CuInS}_2$  in the powder. It was unexpected that a synthesis (A2) lasting 1 hour and 30 minutes produced crystallites with sizes ranging from 9 nm to 12 nm, respectively estimated from peaks at  $2\theta$  of 46.2° and 27.7°. The estimation for synthesis (A1), which was shorter and at a higher temperature, at the peak where  $\text{CuInS}_2$  contributes mainly, was 14 nm at  $2\theta$  of 46.6°, while the  $\text{CuInSnS}_4$  peaks at around  $2\theta$  of 15° and 41.8° yielded, respectively, crystallite sizes of 38 nm and 30 nm. These presence of peaks from both  $\text{CuInS}_2$  and  $\text{CuInSnS}_4$  further suggests that the sample is a mixture. The overall heating rates during both syntheses differ significantly, as can be seen in Figure 3.52

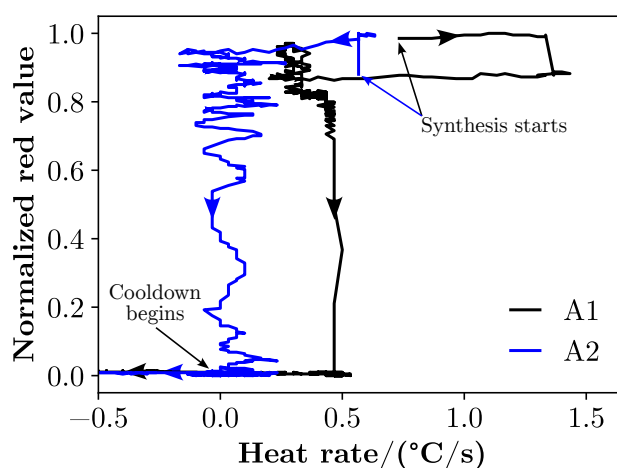


Figure 3.52: Normalized red color profile plotted against the heating rate of the two syntheses (A1), high temperature 300 °C and short duration, and (A2), lower temperature (225 °C) and longer duration, according to Figure 3.51. The arrows on top of the plots indicate the flow of the syntheses time.

Besides the pressure development at 300 °C in (A1), contrary to (A2) where no gas formed, the heating rate was higher in (A1), compared to (A2). Although the colors from the complexes are similar between syntheses, the difference in heating rate could have led to the formation of a different complex in (A1) which involved Sn. The effect of the heating rate was misjudged on these experiments and its influence should be explored in the future. Setting the heating rate to the same as (A1), but limiting the synthesis to 5 minutes at a maximum temperature of 225 °C should be sufficient to understand if it was the heating rate that led to the formation of the quaternary alloy  $\text{CuInSnS}_4$  or the higher temperature of 300 °C. Ramasamy et al.[330]

used tert-dodecanethiol and 1-dodecanethiol and heated to 215 °C to fabricate the alloy. The synthesis process was slightly different since they injected the thiols after heating the mixture of precursors to 150 °C in the presence of oleylamine, as well as starting from tin(IV) instead of tin(II). Although they do not describe the color of the mixture throughout the synthesis, nor the heating rate used to reach 215 °C, this temperature was more similar to the temperature (225 °C) at which the black precipitate formed in (A1). No pressure was also reported by the authors so, presumably, the heating rate is the definitive factor to form the quaternary alloy.

The desired quaternary alloy  $\text{CuInSnS}_4$  was not obtained in a pure form using this method. Instead of changing the reagents, since a faster heating ramp and a higher maximum temperature led to the formation of a mixture of  $\text{CuInSnS}_4$  and  $\text{CuInS}_2$ , while the opposite yielded solely  $\text{CuInS}_2$ , future syntheses should be tried using faster heating ramps.

### 3.3.2.2 Cu, Ag, In

The ternary sulfide alloy  $(\text{Cu, Ag})\text{InS}_2$  has been reported as a promising light absorber, especially when used with ZnO, due to their band gap alignment, in a blend with poly(3-hexylthiophene-2,5-diyl) (P3HT).[331]

An interesting hydrothermal  $(\text{Cu, Ag})\text{InS}_2$  synthesis method was performed by Raevskaya et al.[332], using  $\text{NaS}_2$  as the sulfur source, metal mercaptoacetate complexes as metal sources, and a low-temperature setting of 95 °C for 30 min. The particles were then covered with a ZnS shell to enhance the 2-3 nm particles' photoluminescence properties. Their synthesis method uses a greener approach, by substituting the typical organic solvents with water and using a lower temperature, but the steps are more complex than they allege, due to the several reagent addition steps during the synthesis.

The synthesis of copper silver indium sulfide was attempted starting from CuI,  $\text{AgNO}_3$ , and  $\text{InCl}_3$  and is detailed in Section A.2.2.2. The color, temperature, and pressure profiles and XRD pattern of the resulting powder are shown in Figure 3.53.

Two main events can be seen in the profiles (A). The first corresponds to the formation of a black precipitate at 174 °C (1). According to Dasgupta et al.[333] copper diffusion into  $\text{AgInS}_2$  occurs at 180 °C. Since the ternary sulfides containing Ag and In are usually yellow, it is possible that they are formed before event (1), and then copper begins to incorporate, leading to the formation of either a copper doped  $\text{AgInS}_2$  or the ternary sulfide  $\text{In}_2\text{CuAgS}_4$  (mp-1224138), as predicted in the Materials Project database[128][129]. The second event could be associated with either the evaporation of the thiol or the formation of another sulfide. The final powder appears to be a mixture of both  $\text{CuInS}_2$ , the indium sulfide obtained starting from  $\text{InCl}_3$ , and copper sulfide (B). The most intense peak from the synthesized sample can either be attributed to  $\text{CuInS}_2$  or, as per Raevskaya et al.[332], to the (100) plane of  $\text{AgInS}_2$ , shifted by the copper incorporation.

The XRD pattern of the sample shows that the powder is a mixture of copper indium sulfide, indium sulfide and copper sulfide. To obtain the quaternary metal sulfide, new studies are required.

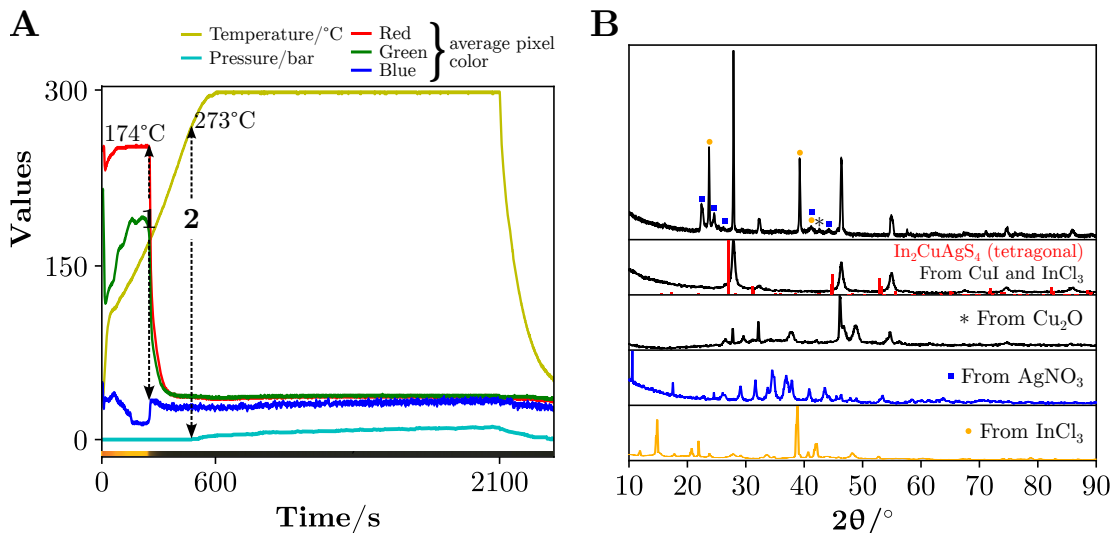


Figure 3.53: Color, temperature, and pressure profiles (A) of the synthesis starting from CuI, AgNO<sub>3</sub>, and InCl<sub>3</sub> and the XRD pattern of the resulting powder (B). Two events were marked in the profiles as (1) and (2). The patterns of the synthesized powders starting from either CuI and InCl<sub>3</sub>, Cu<sub>2</sub>O, AgNO<sub>3</sub>, or InCl<sub>3</sub> were taken respectively from sections 3.3.1.2, 3.2.8.1, 3.2.8.2, and 3.2.10.1. The reference pattern In<sub>2</sub>CuAgS<sub>4</sub> (mp-1224138) was taken from Materials Project[128][129].

### 3.3.2.3 Zn, In, Sn

With a Ga doping of less than 1%, indium zinc tin oxide thin films have been recently fabricated by Bukke and Jang.[334] The authors do not prove the actual structure of an alloy containing indium, zinc, tin, and sulfur, which is not yet predicted, and they did not perform any characterization of the films. Their XRD patterns reveal no peaks and they allege that the structure is amorphous or, as some other publications reveal, the resulting mixture of materials is composed of In<sub>2</sub>O<sub>3</sub>, ZnO, SnO<sub>2</sub> and Zn<sub>2</sub>SnO<sub>4</sub>. [335], [336] Even the equivalent sulfide alloy is yet to be predicted, assuming it can form a stable structure. Without any theoretical prediction, blindly advancing to an attempt is a risk, regarding time and resource consumption. Nonetheless, the path to achieving the quaternary metal sulfide led to the successful fabrication of some of the ternary element combination alloys.

The synthesis of zinc indium tin sulfide was attempted starting from zinc(II) acetate dihydrate, indium(III) chloride, and tin(II) 2-ethylhexanoate and is detailed in Section A.2.2.3. The color temperature, and pressure profiles, XRD patterns and SEM images of the resulting powder are shown in Figure 3.54. The same data for the previously described syntheses of ZnS, In<sub>x</sub>S<sub>y</sub> and SnS are also shown for comparison purposes.

The color profile (A) of (Zn-In-Sn-S) shows a clear delay in the formation of the black suspension that occurs at 249 °C, relative to the (Sn-S). This effect was previously seen in other syntheses involving the Sn elements and either Zn or In. Before the black suspension is formed, the same gelation effect seen in the ZnS synthesis occurs. Although there were time and temperature differences between the quaternary and the binary syntheses, regarding the equivalent color transformations, there were no new color changes in the quaternary synthesis. The XRD pattern



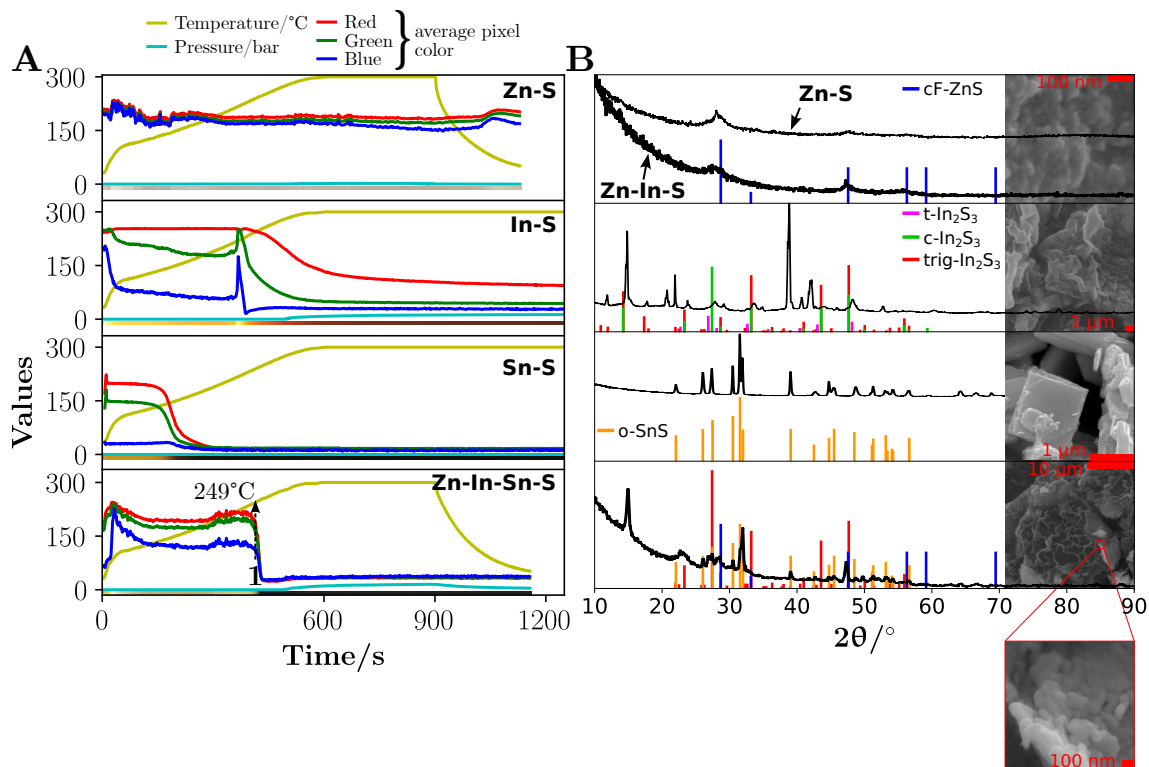


Figure 3.54: Color profiles (A) of syntheses starting from 1-dodecanethiol and either zinc(II) acetate dihydrate (Zn-S) and the powder obtained from the synthesis shown in Section 3.3.1.4 (Zn-In-S), indium(III) chloride (In-S), tin(II) 2-ethylhexanoate (Sn-S) or the three precursors (Zn-In-Sn-S) and the resulting XRD patterns (B) with SEM images as insets. One moment was marked in the profiles of (Zn-Sn-In-S). A zoomed image of the SEM image from the (Zn-In-Sn-S) synthesis is delimited by the red square. The XRD reference pattern of ZnS zinc blende face-centered cubic phase (cF-ZnS) was adapted from the JCPDS card 05-0566[318], both orthorhombic SnS (o-SnS) and cubic SnS (c-SnS) from reference[311] and the tetragonal (t-In<sub>2</sub>S<sub>3</sub>) and cubic (c-In<sub>2</sub>S<sub>3</sub>) phases of In<sub>2</sub>S<sub>3</sub> were adapted from references [268] and [312], respectively. The scale bar is 100 nm for (Zn-S), 1  $\mu$ m for (In-S) and (Sn-S), 10  $\mu$ m for (Zn-In-Sn-S), and 100 nm for the inset in (B).

(B) and the SEM image of the powder appear to be only a mixture of binary sulfides. The flower structure observed in the (Zn-In-Sn-S) synthesis is the same as the one seen in the (In-S) SEM image (Figure 3.32 (D)) but is dotted with either ZnInS<sub>2</sub> or ZnS nanoparticles. This is as per the XRD pattern, which has the zinc indium sulfide, zinc sulfide, indium sulfide and tin sulfide peaks present. The typical micrometer-sized particles of SnS could not be observed in the SEM image. After the synthesis ended and the powder was washed, it was possible to distinguish three different colors, however. A small black spot, presumably tin sulfide, was involved by a faint yellow powder which was probably a mixture of both zinc sulfide and indium sulfide or ZnInS<sub>2</sub>. The Raman spectra of the binary sulfides and a replica of the (Zn-In-Sn-S) sample are shown in Figure 3.55. The synthesis replica was performed since the amount of product from the previous was depleted during the former analysis. The temperature profiles of both the original and the replica syntheses are shown in Figure A.14 in Appendix A, to prove the similarity between the syntheses. The two marked peaks in the Raman spectrum of the (Zn-In-Sn-S) sample correspond



to the expected peaks of ZnS, which were absent in the binary sulfide synthesis. The remainder corresponds to SnS peaks, coupled with the background fluorescence from the indium sulfide.

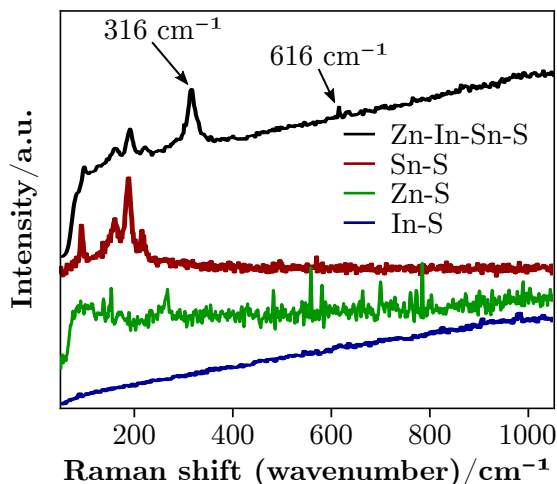


Figure 3.55: Raman spectra of the powders from the syntheses involving 1-dodecanethiol with either indium(III) chloride (In-S), tin(II) 2-ethylhexanoate (Sn-S), zinc(II) acetate dihydrate or the three (Zn-In-Sn-S). The spectra were acquired using a laser, with emission at 532 nm and a power of 0.15 mW.

The band gap of the original sample (Zn-In-Sn-S), now identified as a mixture of the binary sulfides ZnS, SnS and  $\text{In}_2\text{S}_3$ , was determined by diffuse reflectance spectroscopy in powder form. The results are shown in Figure 3.56.

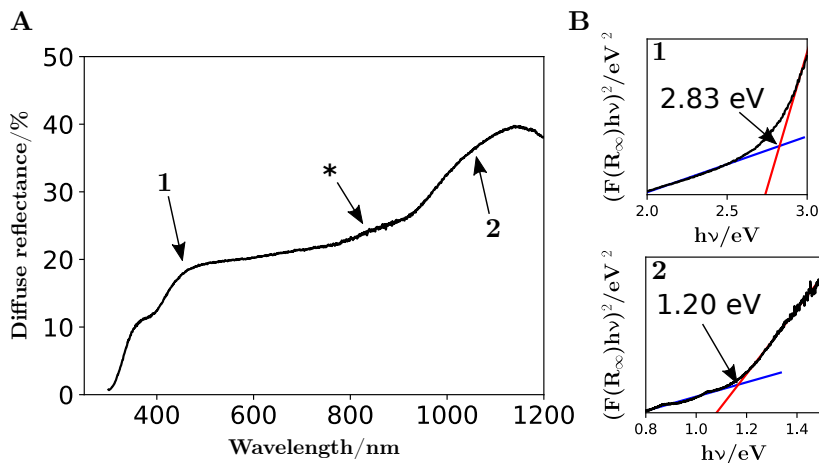


Figure 3.56: Diffuse reflectance spectrum (A) of the powder from the product of the synthesis starting from 1-dodecanethiol, zinc(II) acetate dihydrate indium(III) chloride and tin(II) 2-ethylhexanoate and the corresponding Tauc plots (B), for each numbered region, with two line regressions and the band gap values. The asterisk marks a region of interest.

The tentative slope marked by an asterisk is very similar to the one from the previous synthesis attempt of a ternary alloy containing zinc, tin, and sulfur. The inclusion of a zinc precursor seems to reduce the amount of cubic SnS formed, even in the presence of cubic  $\text{In}_2\text{S}_3$ .

After failing to obtain ternary alloys and the quaternary alloy from the elements Zn, In, Sn, and S, a series of sequential syntheses were performed, i.e. after the synthesis of a binary sulfide finished,

a precursor of another element was added, and when the latter synthesis cooled, the third was added. The addition of the precursors was done immediately after the previous synthesis was cooled to 50 °C and then restarted. This was performed as the first attempt to produce core-shell nanoparticles using the latter elements. The color and temperature profiles of each group with three steps of precursor additions are shown in Figure A.15 in Appendix A, in addition to the XRD patterns and Raman spectra of the resulting powder from the last steps. The procedures for these sequential syntheses are also described at the end of the same section. The first group was performed with a precursor addition sequence of Sn → In → Zn (A1). The color profiles reveal that, after the formation of SnS at ~170 °C, the suspension became completely black, naturally rendering any visible change in the subsequent color profiles impossible. The XRD pattern from the powder formed after the three steps reveals that the major contributions come from the zinc blende phase of ZnS and the orthorhombic phase of SnS. The second group consisted on the sequential addition of Zn → In → Sn. Unlike the former, all of the transitions are visible in the color profiles. Zinc sulfide's precipitation occurred at the expected 2 min mark after reaching 300 °C. In the second step, with the addition of the indium precursor, at around 150 °C the same gel formation behavior developed, similar to the synthesis involving solely the zinc precursor. This suggests that not all of the zinc precursor was consumed in the previous step. Since the average yield of ZnS from a synthesis involving zinc(II) acetate dihydrate is 90% with 25 minutes at 300 °C, a 5-minute synthesis will have a lower yield, leaving more than 10% of unreacted precursor available. At 248 °C, the indium sulfide formed, which is near the temperature expected for the formation of the binary sulfide. Unexpectedly, at the start of the addition of tin(II) 2-ethylhexanoate, which is in the liquid state, a black precipitate started forming at the tip of the pipette. The gas that evolves during the synthesis of In<sub>2</sub>S<sub>3</sub> and raises the pressure up to 14 bar is most probably H<sub>2</sub>S that quickly reacts with the tin precursor. The final step had no visible color changes since the black SnS had already formed. The XRD pattern of the resulting powder shows that the main contribution is from the orthorhombic phase of SnS, while the zinc blende phase of ZnS is almost absent.

The most striking feature of the previous two sequential synthesis is that none of the XRD patterns showed the presence of any phase of In<sub>2</sub>S<sub>3</sub>, even though the color profile from Figure A.15 (A2), in Appendix A, clearly shows a similar color transition seen in the binary synthesis of the indium sulfide at around 215 °C (Figure 3.32).

### 3.3.3 Resume

The results obtained from the syntheses attempts performed to obtain multinary, ternary and quaternary, metal sulfide nanoparticles are shown in Table 3.4

Table 3.4: Compilation of all successful (A) attempted to obtain multinary metal sulfide nanoparticles of various elements, with the identification of the obtained product, crystal type, the particle or [crystallite] size, measured and reference band gap, and the temperature at which the metal sulfide formed ( $T_{formed}$ ) and unsuccessful (B) syntheses, with the obtained product, the expected product, measured and reference band gap, and  $T_{formed}$ . The acronym n/a stands for not available. In the Crystal column, a, c, h, m, o, t, and tri respectively correspond to, amorphous, cubic, hexagonal, monoclinic, orthorhombic, and trigonal.

<b>A</b>					Bandgap/eV		$T_{formed}$
					Measured	Reference	
Metal	Product	Crystal	Size/nm	Measured	Reference	$T_{formed}$	
Multinary sulfide	Cu,Fe	CuFeS <sub>2</sub>	t	9 to 18	n/a	(t)0.5 <sup>[301]</sup>	194 °C
	Cu,In	CuInS <sub>2</sub>	t	8 to 54	n/a	(t)1.5 <sup>[302]</sup>	236 °C
	In,Sn	In <sub>4</sub> SnS <sub>8</sub>	c	[10]	1.2, 1.6, 2.6	(c)2.1 <sup>[309]</sup>	197 °C
	Zn,In	ZnIn <sub>2</sub> S <sub>4</sub>	h	[2]	2.8	(c)2.2, (h) 2.8 <sup>[313]</sup>	275 °C
	BaZr	BaZrS <sub>3</sub>	c	n/a	1.59	1.8 <sup>[322]</sup>	288 °C

<b>B</b>				Bandgap/eV		$T_{formed}$
				Measured	Reference	
Metal	Obtained	Expected	Measured	Reference	$T_{formed}$	
Unclear	Zn,Sn	SnS	Zn <sub>2</sub> SnS <sub>3</sub>	2.3	n/a	244 °C
	Cu,In,Sn	CuInSnS <sub>4</sub> , +++CuInS <sub>2</sub>	CuInSnS <sub>4</sub>	n/a	1.4 <sup>[330]</sup>	194 °C
	Cu,Ag,In	CuInS <sub>2</sub> , In <sub>2</sub> S <sub>3</sub> , Cu <sub>x</sub> S <sub>y</sub>	(Cu, Ag)InS <sub>2</sub>	n/a	2.1 <sup>[331]</sup>	174 °C
	Zn,Sn,In		n/a	1.2, 2.8	n/a	249 °C

From the ternary metal sulfide synthesis attempts, pure CuFeS<sub>2</sub> and CuInS<sub>2</sub> were successfully synthesized. The alloys containing the metal pairs (In, Sn) or (Zn, In) resulted mostly in mixture of the individual binary metal sulfides and, respectively, In<sub>4</sub>SnS<sub>8</sub> and ZnIn<sub>2</sub>S<sub>4</sub>. As for the (Zn, Sn), both the cubic and orthorhombic phases of SnS were obtained. The pair (Ba, Zr) formed the promising perovskite BaZrS<sub>3</sub> but mixed with the binaries BaS and ZrS<sub>2</sub>. Pure ternary copper-based alloys appear to form easily using this method, while the elements Zn, In, and Sn, form the binary sulfides but influence the phase that each other forms.

None of the three tested element combinations, [Cu, In, Sn, S], [Cu, Ag, In, S], and [Zn, In, Sn, S] resulted in the corresponding quaternary alloy. The combination of the elements [Cu, In, Sn, S] resulted in a mixture of orthorhombic CuInSnS<sub>4</sub> with tetragonal CuInS<sub>2</sub>. As for the synthesis involving the elements [Cu, Ag, In, S], the most probable product was a mixture of two ternary sulfides, CuInS<sub>2</sub> and indium sulfide. Finally, the synthesis performed with the elements [Zn, In, Sn, S] did not yield a quaternary sulfide, but instead resulted in the binary metal sulfide of each element. Of the quaternary metal sulfides, Cu, In, Sn, S was the most promising since the alloy is known to be stable and is extensively reported in the literature. Further studies should be done to achieve the pure form.

## 3.4 Input Parameters and Impact on the Synthesis

The previous sections described syntheses where the majority followed a systematic procedure: starting with a constant heat rate, reaching a maximum temperature of 300 °C in 10 minutes, keeping that temperature for a certain time, usually 5, 15, or 25 minutes. There were some exceptions mentioned along the text. Most of the changes however were due to the formation of electric arc during the synthesis. In the following sections, syntheses performed with different conditions that led to the formation electric arc are described. The influence of temperature, synthesis time, precursors used and their concentration, and the presence or absence of light were also the parameters studied for some specific compounds.

### 3.4.1 Electric Arcs

After synthesizing silver sulfide previously without any issues regarding the formation of electric arcs, the copper sulfide synthesis was left unattended. After some time, the vial began to shine dramatically, the microwave reactor did not detect the rise in temperature and pressure soon enough and the glass vial melted with the heat, the suspension spewed to the exterior and ruined the Teflon inner part of the reactor. Due to the importance of this possible and unpredictable hazard, this section was dedicated to microwave-induced electric discharges (electric arcs). As Chen et al.[337] stated, these arcs occur due to many variables such as the materials particle size, solvent dielectric constant, boiling point, composition, etc. They observed that the arcs usually form in the vapor bubbles that evaporate from the solvent, especially at the surface of the hot suspended material. When the surrounding liquid was cold the bubbles collapse, but if the liquid is hot enough and the electric field inside the vapor bubbles is high enough, it ionizes the gas molecules. This leads to the formation of electric arc discharges, the decomposition of the solvent that generates carbonaceous products, and volatile small molecules that increase the pressure.[337] Some examples of electric arcs can be seen in Figure 3.57, including a synthesis that was not shown in this work, involving hydrated ruthenium(III) chloride.

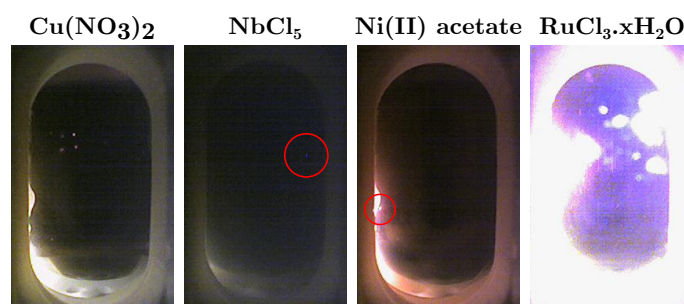


Figure 3.57: Pictures of synthesis performed starting from  $\text{Cu}(\text{NO}_3)_2$ ,  $\text{NbCl}_5$ , nickel(II) acetate, and  $\text{RuCl}_3 \cdot x\text{H}_2\text{O}$ . The red circles point to the spot in the image where the electric arcs can be seen.

Any syntheses performed using a new precursor were conducted under supervision. Some of the syntheses shown in this work developed electric arcs. Figure A.16 and Figure A.17 in Appendix A

include all the attempted syntheses with different precursors, respectively for inorganic and organic anions, and show if for a given cation and anion, electric arcs developed during the synthesis. Each segment of a periodic table in the figures is referent to an anion. Unfortunately, due to the low quality and incapacity of the microwave reactor's camera to record at a higher frame rate, most of the syntheses where electric arcs formed were not recorded. The arcs usually do not linger long enough and it is another hazardous effect, since the user can look away temporarily, miss an arc, and all hell breaks loose with disastrous consequences. Ruthenium and gold are both noble metals and any synthesis attempted with these elements resulted in strong electric arcs, suggesting that with at least 1-dodecanethiol, noble metals should be avoided. Regarding other metal elements, the anion dictated if the synthesis would proceed with or without any electric arcs. It is not clear why some anions lead to the formation of electric arcs when combined with some of the metal cations; for example, barium(II) triflate did not develop arcs, while copper(II) triflate did. Granted that these elements are almost opposed in the periodic table, the nitrate ion serves as a counter-example: both the barium and the copper nitrates formed arcs. The nitrates, however, mostly resulted in the formation of electric arcs. The only nitrate salt that did not form arcs was  $\text{AgNO}_3$ , which was expected to form since copper nitrate formed and the metal belongs to the same group. Recall that the latter two syntheses, involving silver and copper nitrates, generated a thin metal film on the vial's surface. Yet, the silver synthesis proceeded peacefully. Still, in the inorganic anions group (Figure A.16), the oxides of the metal elements mostly did not form electric arcs, except for the copper(I) oxide. These syntheses did not yield the sulfides, except for both copper oxides and silver oxide. As for the organic anions (Figure A.17), from the acetates, only nickel(II)'s developed arcs, and from the acetylacetonates, iron(III) and cobalt(II) also developed arcs. Regarding the other organic anions, none of the alkoxides methoxide, ethoxide, and isopropoxides, the stearates, carbonate, and 2-ethylhexanoate developed arcs during the syntheses. Anions that are bulkier and their acid form have higher boiling points, such as the stearate, tend to evaporate less. This forms fewer gas bubbles, which are known to be one of the causes of the arcs. Also, the lesser the anion is prone to degradation, the least amount of lateral side reactions occur and less volatile products.

Metals, with an oxidation state of zero, are famously the culprits of developing electric arcs under microwave radiation. However, metal sulfides can also develop electric arcs.[338] During the bismuth sulfide synthesis attempt, starting from the nitrate salt, arcs developed quite dramatically but the black suspension had formed before that. Another synthesis was attempted, setting a low enough maximum temperature to form the black precipitate, and no arcs developed. The XRD pattern revealed, however, that the powder was composed solely of metallic bismuth. In some cases, the metal does not develop arcs and the sulfide might. It could also be due to the particles' size.

Another factor to take into account is the concentration of the precursors. For example, a synthesis starting from 1 mmol of  $\text{NbCl}_5$  in 5 g of thiol usually develops some small electric arcs. A synthesis starting from 0.1 mmol of the same precursor in 15 g of thiol did not develop any visible arc. A synthesis that was safely repeated many times with 1 mmol of tin(II) 2-ethylhexanoate in 5

g of thiol, when the amount of precursor was raised to 10 mmol, electric arcs formed. A lower concentration of precursor and a higher volume of solvent can make a synthesis that is dangerous into a safe one.

An attempt was done to correlate the electric arc formation and other variables such as the redox potential of the elements and the acidity constant of the acid of the anion conjugate base, but there was no apparent correlation.

Summarizing, the metals cations that were deemed as the most hazardous belong to the periodic table's groups 5 (Nb and Ta), 8 (Fe and Ru), 9 (Co) and only Cu from group 10. As for the anions, nitrates and chlorides were deemed as the most dangerous, since they usually provoked a rise in pressure. A lower precursor concentration and a large volume of thiol prevent the formation of arcs (iron(II) acetylacetonate was an exception), as well as lowering the maximum temperature, just enough to precipitate the sulfide. Alkoxides and stearates appear to be a safe choice to prevent the formation of arcs too.

Given that the majority of the precursors formed a complex with 1-dodecanethiol, future synthesis should consider the isolation of the metal-thiolate by removing the anion that belonged to the reagent, should prevent the formation of a by-product that leads to the generation of electric arcs. If purifying the metal-thiolate is not possible, the amount of precursor should be kept below 0.1 mmol and the amount of thiol with no less than 15 g.

### 3.4.2 Temperature and Time

Temperature control throughout the synthesis is fundamental to obtaining the correct metal oxidation state, material phase, and particle size. For example, the lower and higher temperatures used in the two syntheses involving bismuth(III) nitrate (Section 3.2.12.1) lead to either pure metallic bismuth or a mixture of the metal and probably the sulfide.

Solvothermal synthesis of metal sulfides usually involves temperatures above 100 °C and the majority of the sulfides synthesized in this work were only obtained at temperatures above 200 °C. To achieve these temperatures, there are two possible modes in a typical microwave reactor: an automated mode where the reactor, through an internal algorithm, can feed the magnetron with the correct power to achieve a determined temperature, and a constant power feed, where the user sets the desired power in each step. A comparison between the automated temperature control and constant power mode was done, using two replicas for each. The data from the automated temperature control replicas were obtained from two syntheses performed in the same conditions as the one shown in Section 3.2.8.2, heating to 300 °C in 10 minutes and kept at that temperature for 5 minutes. For the constant power mode, three sets of synthesis replicas involving 5 g of 1-dodecanethiol and 1 mmol of AgNO<sub>3</sub> were performed. The powers chosen were 20 W, 30 W, and 40 W with a total irradiation time of 900 seconds. The syntheses with 30 W and 40 W were automatically interrupted by the system due to reaching the maximum allowed temperature of 300 °C. The temperature profiles versus time and energy fed to the microwave reactor's magnetron and the red color values plotted against time are shown in Figure 3.58. The

red color profile was chosen since in this particular synthesis the red color channel presents the most prominent changes.

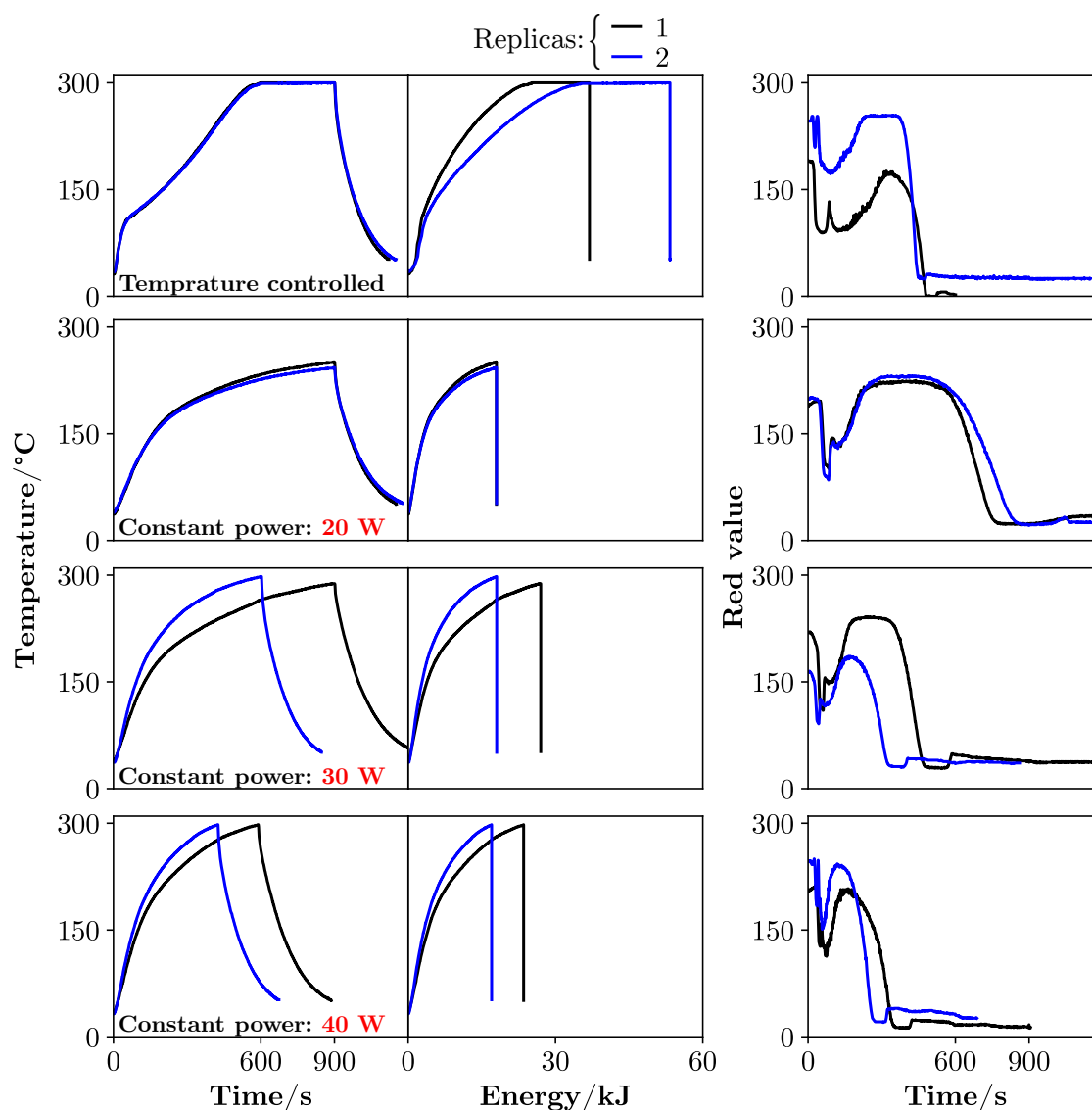


Figure 3.58: Temperature profiles versus time and energy fed to the microwave reactor's magnetron and the red color values plotted against time of synthesis involving 1-dodecanethiol and  $\text{AgNO}_3$ , performed using the automated temperature control mode or the constant power mode at 20 W, 30 W or 40 W, each with two synthesis replicas numbered 1 and 2.

The color and temperature profiles of synthesis performed with a constant power of 30 W and 40 W vary significantly between replicas. On the contrary, at a lower constant power of 20 W both replicas have similar color and temperature profiles. Of the modes tested, fine temperature control was only achieved by the automated temperature control. The temperature profile versus time is the same for both replicas. However, according to the temperature versus energy plot for this mode, a different amount of energy was used by the reactor to maintain similar temperatures. Since the color profiles are also identical, it should not be concerning. Nonetheless, the constant 20 W of power also shows some similarity in-between the red profiles and, since the power is constant, the temperature versus energy is also similar. This constant power appears to be near

the maximum allowed to enable some reproducibility in case of necessity to use the constant power mode.

Regarding the temperature sensor, according to C. Oliver Kappe[90] using a ruby thermometer should be the adequate way to control the reaction temperature, instead of the infrared sensor. Given the exploratory nature of this work, using the ruby thermometer was not advisable. The module contains a ruby crystal that upon periodic excitation with light, the emitted light intensity's decay can be correlated to the temperature of the crystal. Given the unknown behavior of the synthesis medium, the risk of a sudden increase in temperature to several hundreds of degrees Celsius, due to the formation of electric arcs, would easily damage the expensive thermometer. Nonetheless, after knowing in advance that synthesis performed with 1-dodecanethiol and silver(I) nitrate are safe at the temperature range allowed by the microwave system, a synthesis to determine the actual temperature inside the reaction vessel was performed using the ruby thermometer. The results from the latter synthesis and its comparison (ruby controlled) with an equivalent synthesis (infrared controlled) are presented in Figure 3.59.

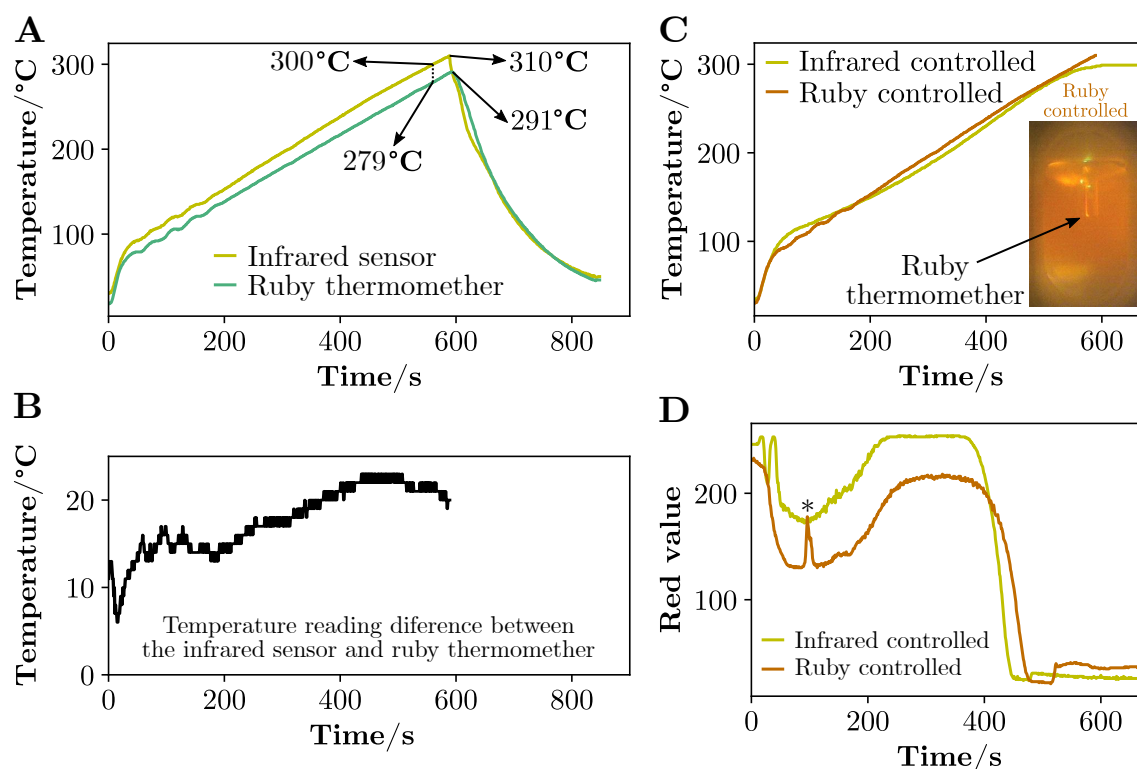


Figure 3.59: Temperature profiles of a microwave-assisted synthesis involving 1-dodecanethiol and  $\text{AgNO}_3$ , with readings performed by an infrared sensor and ruby thermometer (A), the difference between the readings from the infrared sensor and the ruby thermometer (B), the infrared sensor readings between two equivalent synthesis (C) and their red pixel values profiles (D). The inset in (C) is a picture of the synthesis, in which the temperature was controlled by the ruby thermometer. The asterisk in (D) denotes a light artifact.

Two temperature readings from the same synthesis, using an infrared sensor and the ruby thermometer are shown in (A), where the difference between the reading is clear. It should be noted that only the tip of the ruby thermometer was submerged in the solution during



the synthesis, as seen in the ruby-controlled picture example in (C). The average temperature difference between both temperature sensors is shown in (B) and it increases as the temperature readings increase, reaching a difference of up to around 23 °C. The ruby thermometer is more reliable since the sensor is in direct contact with the mixture. However, this sensor only reads the temperature in its immediate surroundings, as opposed to the infrared sensor which covers a higher area, albeit on the vessel's surface. Another variable that was not taken into consideration was the calibration of the infrared sensor before every synthesis. The sensor was only calibrated once every year, since between equivalent syntheses the color profiles were very similar, which indicated reproducibility. Notice that between the two syntheses in (C), one controlled by the infrared sensor and the other by the ruby thermometer, the temperature reading was similar before reaching the maximum temperature at a time of around 600 s. The red pixel color profile below, which has a twin time axis for comparison purposes, reveals that the color transitions occur slightly out of phase, with the last transition from red to black occurring with a temperature reading difference between both sensors of ~16 °C. It appears that for a synthesis controlled by the ruby thermometer, the power feed is lowered since the microwave reactor senses a lower temperature. Under the warrant of speculation, there are three probable reasons for the temperature reading difference between the sensors: a lower absorption of microwaves from the mixture, which leads to a higher temperature on the vessel's surface, and/or the ruby thermometer being too high, delaying the measurement due to heat dissipation.

On account of the temperature limit of 300 °C imposed by the microwave reactor, using the constant power mode, as an alternative to the automated temperature control, would require modulating the predicted temperature achieved during the synthesis for each metal salt. With the limitation of the microwave reactor's inability to accept a continuous power ramp, instead of discrete constant power steps, the modulation was not feasible. A constant power naturally leads to a stable temperature since the system is not isolated.

Given the reproducibility between syntheses, temperature control was performed automatically by the microwave reactor, with the integrated infrared sensor, and the ruby thermometer was not used, to avoid complications. Temperature readings reported in this work are therefore considered uncertain and probably below the actual value by no more than ~13 °C. There was an exception where the constant power mode was a better option, however, as pointed out in Section 3.2.2.3 where the synthesis of trigonal tantalum sulfide was shown. Both modes lead to the formation of the material and originated electric arcs during the synthesis. The constant power mode (20 W) ran with less intense arcs throughout the synthesis. The low constant power of 20 W was enough to produce the desired material, as can be seen in the color transformation in the red color profile plotted against the energy supplied to the microwave reactor's magnetron in Figure 3.60 (A).

Although both syntheses were interrupted after some time, it should be reiterated that the constant power mode formed much less intense electric arcs. Assuming a synthesis yield of 100%, when the suspension's color becomes black and the color stabilizes (A), for both modes and starting from 1 mmol of precursor, the constant power output would be 12.0 kJ/mol (3.3 Wh/mol), against the 9.4 kJ/mol (2.61 Wh/mol) for the temperature control mode. As was

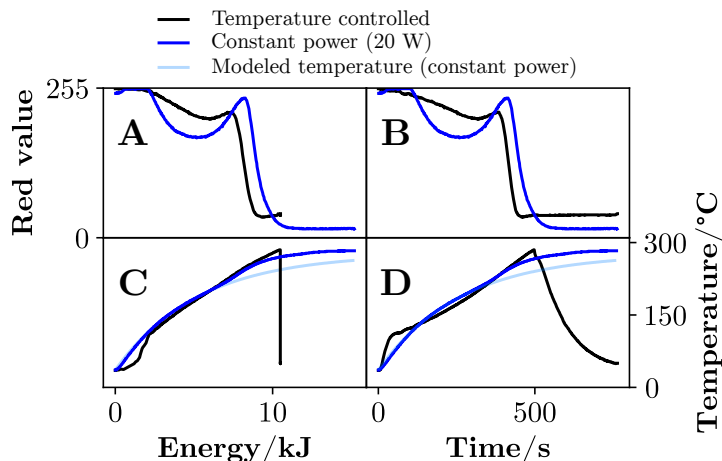


Figure 3.60: Red color value profiles plotted against the energy (A) and time (B) and temperature profiles against the energy (C) and time (D). An adaption of the logistic regression was used to fit a curve to the temperature of the constant power mode in (C) and (D).

mentioned previously in Section 2.3, compared to the conventional heating method, conduction and convection, using a heating plate with a typical power rate of 1200 W, would at least consume 191 Wh/mol, assuming the equivalent temperature of the formation of the black sulfide would be reached in around 573 seconds (B). Another advantage of the constant power mode is that it is possible to see if the precipitation of the sulfide is an exothermic reaction; all of the tested syntheses under constant power were. In (C) and (D), respectively the temperature plotted against the energy or time, an inflection of the blue curve (constant power mode) can be seen before the 500-second mark. This corresponds to the bump seen in the red channel (A) or (B), before the precipitation of the black sulfide. The modeled temperature profile seen in (C) and (D) helps to illustrate this temperature rise. The model was built using an adaption of the logistic regression expression, as shown in Eq. 3.5:

$$T = T_{n=0} + \frac{V + \log_X(W \times (E_{n+1} - E_n)) - T_{n=0}}{1 + e^{\left( Y + \frac{1}{Z \times (E_{n+1} - E_n)^{\frac{3}{4}}} \right) \times \log_e(E_{n+1} - E_n)}} \quad (3.5)$$

where T is temperature, E is energy, n is the data point with 0 as the first point, and V, W, X, Y, and Z are fitting parameters with no physical significance. Here, since it is a constant power situation, time and energy are interchangeable.

Continuing the discussion of the temperature influence on the syntheses products, after choosing the automated temperature control, the effect of the maximum temperature during synthesis was tested. This was evaluated for some of the elements used in this work and in particular, zinc and silver were chosen as examples for the demonstration. Following the same synthesis parameters used for the syntheses of zinc sulfide (Section 3.2.9.1) and silver sulfide (Section 3.2.8.2), two new syntheses were performed with a lower maximum temperature. Figure 3.61 shows the XRD patterns of the low and high-temperature syntheses, starting from either zinc(II) acetate dihydrate

or silver(I) nitrate.

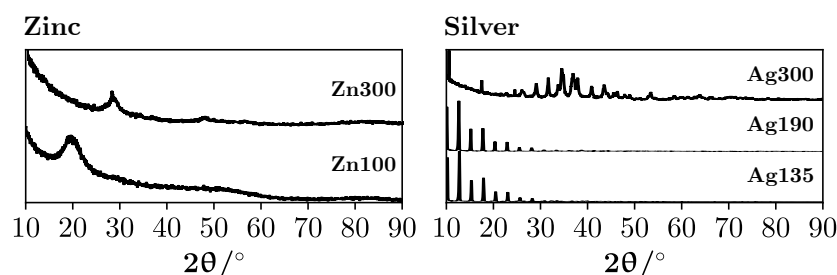


Figure 3.61: X-ray diffraction patterns patterns of syntheses at different maximum temperatures, starting from either zinc(II) acetate dihydrate, 300 °C (Zn300) and 100 °C (Zn100), or silver(I) nitrate, 300 °C (Ag300), 190 °C (Ag190), or 135 °C (Ag135).

The higher syntheses led to the formation of the metal sulfides, but at a lower synthesis temperature, a metal-thiolate formed for both the zinc and the silver examples.

Still using zinc sulfide syntheses as an example, increasing the synthesis time at 300 °C, for example from 5 minutes to 25 min, lead to a significant increase in the particles' size, from 3 nm to 8 nm, as shown in TEM images in Figure 3.62.

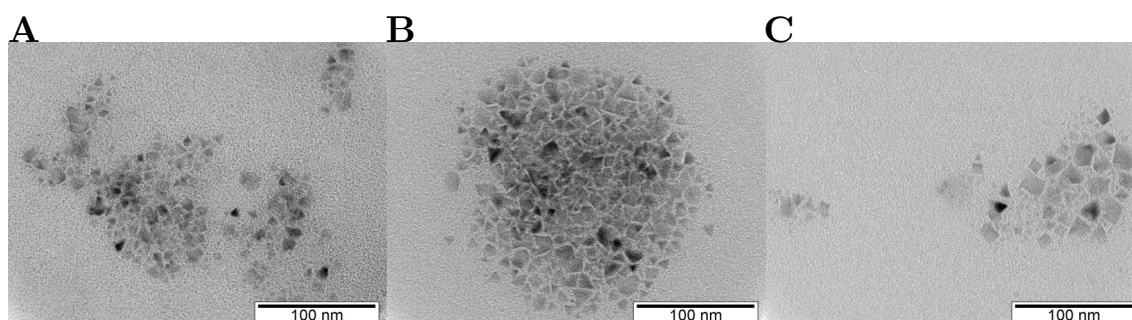


Figure 3.62: Transmission electron microscopy images of powders obtained from syntheses starting from zinc(II) acetate and kept at 300 °C for different times at 300 °C, 5 minutes (A), 15 minutes (B), and 25 minutes (C). The scale bars are 100 nm.

The particles grew proportionally to the synthesis time, although for the zinc sulfide case, the difference of 10 minutes at 300 °C between (B) and (C) is not so marked when compared with the synthesis performed for 5 minutes at the maximum temperature.

To achieve the synthesis temperature control, the automated system was chosen, as it proved to be more reliable and reproducible than using the constant power feed to the microwave reactor's magnetron. The evaluation, if a certain reaction during the synthesis is exothermic or endothermic, can be done by using the constant power mode at a low power of around 20 W. This low power proved to be enough to achieve a high temperature to produce the sulfides and between replicas, the temperature profile is similar. The metal sulfides produced in this work formed above 100 °C, most around 250 °C, and at lower temperatures a complex was usually formed between the thiol and the metal cation. Prolonging the time of the synthesis at a higher temperature led to bigger nanoparticles.

### 3.4.3 Concentration

The effect of different reagent concentrations, as well as the amount of 1-dodecanethiol, on the synthesized products, was evaluated for tin sulfide, zinc sulfide and copper sulfide. Starting with tin sulfide, a synthesis involving 0.1 mmol of tin(II) 2-ethylhexanoate and 15 g of 1-dodecanethiol was performed and is detailed in Section A.3.

The color, temperature, and pressure profiles and the XRD patterns of the latter synthesis and the one described in Section 3.2.11.1, for comparison purposes, are shown in Figure 3.63.

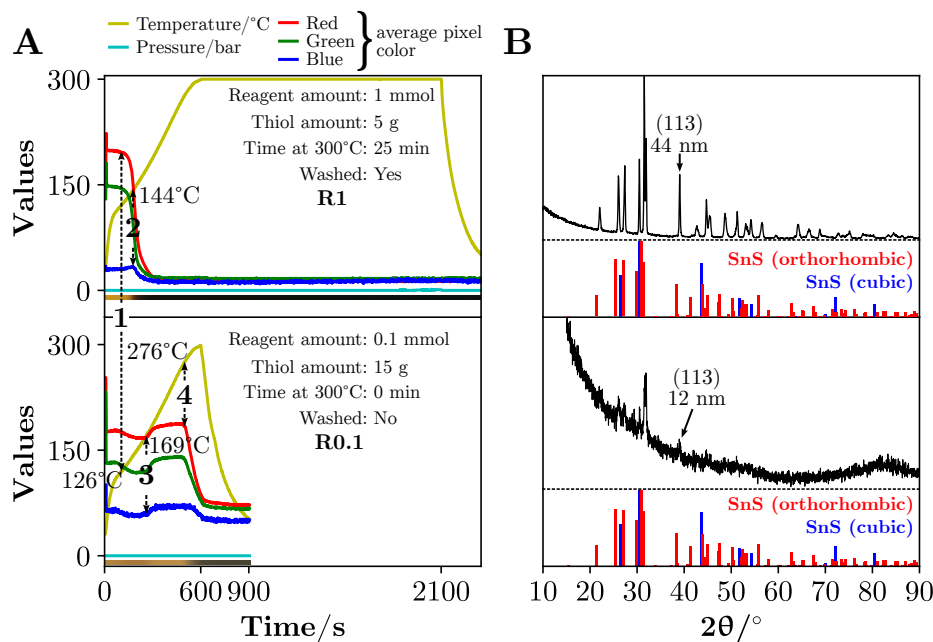


Figure 3.63: Color, temperature, and pressure profiles (A) of two syntheses (R1 and R0.1) starting from tin(II) 2-ethylhexanoate and the resulting powders' XRD patterns (B). The synthesis parameters that differ between syntheses are described in the figure. Four moments were marked in the profiles. The reference patterns of the orthorhombic (including the Miller indices) and cubic phases of SnS were taken from Materials Project [128][129] with the respective IDs: mp-2231 and mp-1876.

The first moment (1) occurs at the same temperature (126 °C) in both syntheses but the one with the lowest concentration (R0.1) only darkened slightly, whereas (R1) began to darken until the suspension was black (2) above 144 °C. At (3) 169 °C, (R0.1) recovered the previous brighter color and only darkened at 276 °C (4). The gray/black color from (R0.1) is not as dark as (R1) as expected, due to the lower concentration. What was unexpected was the fact that the precipitation of the sulfide occurred at a higher temperature when the concentration of the reagent was lower. The amount of energy supplied to the microwave magnetron only matches the first color transformation, as shown in Figure 3.64 (A) marked by moment (1), while the final darkening occurred after supplying the magnetron with a total energy of around 25 kJ.

Notice also that in (B), for (R1) the maximum temperature of 300 °C was reached with less energy required than (R0.1), and much less than (R0) which only contained 1-dodecanethiol; without the tin precursor. The precursor (tin(II) 2-ethylhexanoate) therefore absorbs the microwave radiation

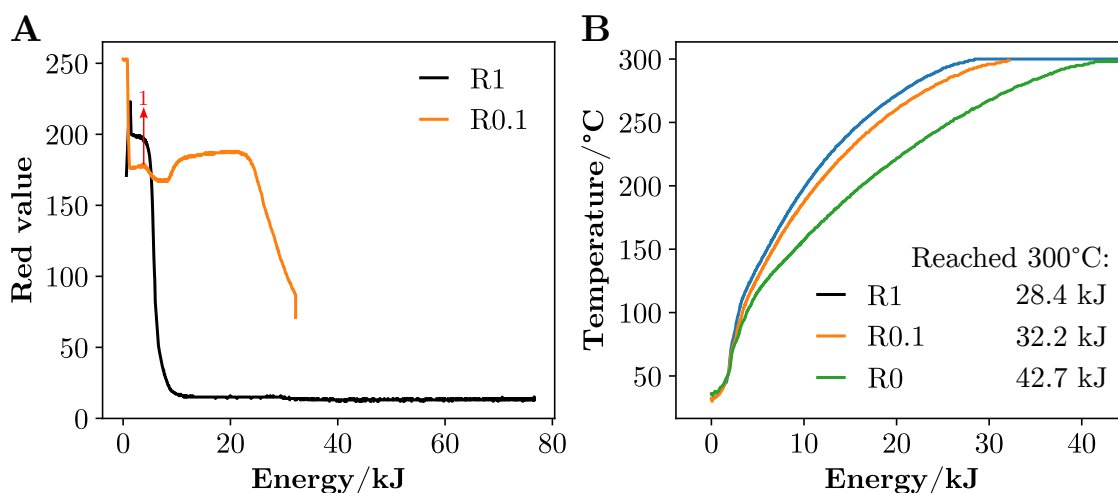


Figure 3.64: Red color profile (A) or temperature (B) plotted against the energy supplied to microwave magnetron, starting from tin(II) 2-ethylhexanoate. One moment was marked in the profile. R1 corresponds to a synthesis starting from 1 mmol of reagent and 5 g of thiol, R0.1 from 0.1 mmol and 15 g, and R0 contains only 5 g of thiol.

much more efficiently than the thiol. This still does not explain why moment (4) from Figure 3.63 (synthesis R0.1) occurred at a much higher temperature, although it required larger energy input. Nonetheless, both syntheses resulted in the same orthorhombic phase of SnS.

Since the color transitions in synthesis performed with 1 mmol of zinc precursor are very weak, using a lower precursor concentration leads to even weaker color changes, as can be seen in the red color profile Figure 3.65 (Zn). The same effect of less energy required to increase the temperature, was seen in the zinc sulfide synthesis temperature versus energy. Zinc(II) acetate dihydrate also poorly absorbs microwave radiation and the temperature profiles are very similar for the two concentrations. Since the color transitions in synthesis performed with 1 mmol of zinc precursor are very weak, using a lower precursor concentration leads to even weaker color changes, as can be seen in the red color profile (Zn). In the niobium sulfide syntheses case, a lower concentration allowed to see the color of the complex formed between niobium and 1-dodecanethiol, while the higher concentration immediately formed the black sulfide. It also formed with a lower energy amount as it appears that niobium(V) chloride absorbs microwave light more efficiently than the other two elements shown in the figure. In the synthesis involving 0.1 mmol of each of the copper and iron precursors (Cu, Fe), contrary to the tin and niobium sulfides syntheses, the red profiles are similar. However, the temperature versus energy profiles reveal that a higher concentration (R1) required more energy to reach the same temperature as the lower concentration synthesis (R0.1). The microwave reactor was unable to keep the temperature ramp with a smooth curve in (R1). It appears that the formation of the ternary copper iron sulfide is endothermic, since the temperature was abnormally low when the black precipitate formed but then it became highly exothermic the moment the pressure started to rise, accompanied by a sharp temperature rise.

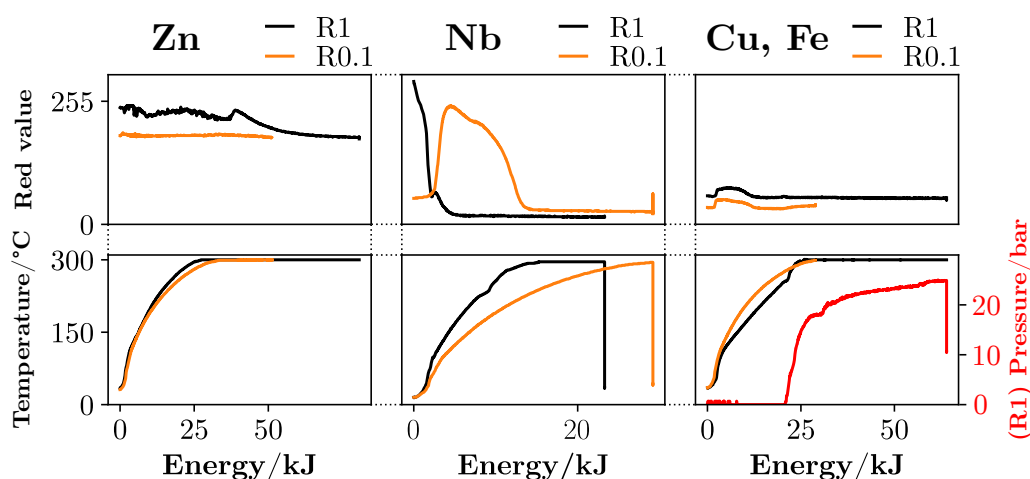


Figure 3.65: Red color and temperature profiles plotted against the energy supplied to microwave magnetron, for the syntheses involving the precursors containing the elements Zn, Nb and a mixture of Cu and Fe. R1 corresponds to a synthesis starting from 1 mmol of reagent and 5 g of thiol, R0.1 from 0.1 mmol and 15 g.

### 3.4.4 Reagents

To synthesize a determined metal sulfide, the choice of the metal is restricted to the metals present in the reagent. The anion bonded to the metal can also dictate if the formation of the sulfide occurs or not, its stoichiometry, and the formation of side products.

Usually, a metal cation forms a metal-thiolate complex with 1-dodecanethiol. The thiol is deprotonated by the anion and the newly-formed thiolate bonds with the metal cation. These complexes sometimes form ordered macro-structures and present sharp signals on their XRD patterns. For example, silver-dodecanethiolate is known to form layered structures[104] and presents a pattern as the one shown in Figure 3.66. The pattern is an example obtained from a synthesis performed at a lower temperature (190 °C) and is similar to the one published by Tian et al.[95]

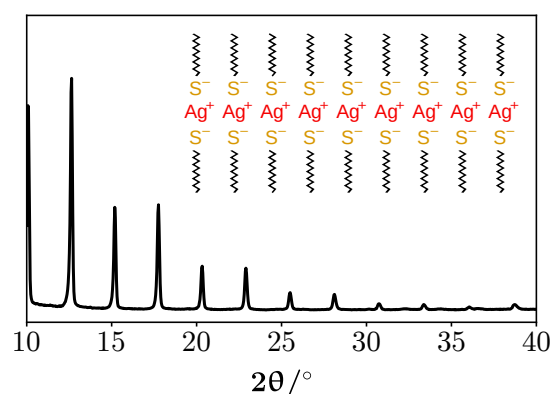


Figure 3.66: X-ray diffraction pattern of silver thiolate with the representation of the complex as an in-set. The compound was obtained by mixing an excess of 1-dodecanethiol with silver nitrate and heating to 190 °C in 1 minute and keeping the temperature for 4 minutes in the microwave reactor.

The advantage of the formation of a metal-thiolate complex is that they are usually soluble

in the thiol. Some thiolates have a relatively low solubility in the thiol, such as the complex formed between tin(II), from tin(II) 2-ethylhexanoate, and 1-dodecanethiolate. However, during the initial heating phase, the easily dissolved in the thiol. Having the complex in solution, instead of a solid floating around during the synthesis, guarantees that the synthesis proceeds in homogeneously throughout the vial and without the formation electric arcs. Another important advantage is that, in the case of the multinary synthesis, the precursors are more randomly distributed and the product's stoichiometry should be the correct one.

Regarding the anion effect, a series of syntheses of copper sulfide were performed, using different copper precursors, to determine the effect of the counter ion on the final product, regarding the material phase and crystallite size. The precursors and quantities used are as follows: 1 mmol (242 mg) of copper(II) nitrate trihydrate ( $\text{Cu}(\text{NO}_3)_2 \cdot 3\text{H}_2\text{O}$ ), 1 mmol (262 mg) of copper(II) acetylacetonate, 1 mmol (362 mg) of copper(II) ditriflate or 1 mmol (191 mg) of copper(I) iodide. The syntheses details can be found in Section A.3.

Except for the diffraction pattern of the powder obtained from the synthesis performed with CuI, the color, temperature, and pressure profiles and the diffraction patterns of all of the syntheses performed are shown in Figure 3.67.

The synthesis performed starting from CuI and the color profile showed a transition from bright yellow to a dark brown suspension at  $\sim 290^\circ\text{C}$  which, although the material was not characterized, is probably a copper sulfide. Over the fear that the sub-product HI, hydrogen iodide, could form, and since it is a very strong acid with a boiling point of  $-35^\circ\text{C}$ , syntheses starting with a metal iodide were postponed to a later stage in this work. There were no electric arcs during the microwave-assisted synthesis, which was expected given the tendency of the iodide to oxidize, which would probably lead to the formation of metallic copper. Oddly, there was also no rise in pressure, as was expected by either the probable formation of the acid,  $\text{I}_2$ , or 1-iodododecane which has a boiling point around  $160^\circ\text{C}$ . Given the overall stability in terms of electric arc formations throughout the synthesis and since the transformation temperature to a dark suspension was higher than with other reagents; metal sulfides tend to form at higher temperatures than the metallic state[95], CuI was chosen as the reagent for the synthesis of copper-based multinary sulfides. Notice that all of the color profiles from each copper precursor used, except for the iodide, show a transition from yellow, to orange, and to black. Copper(I) oxide ( $\text{Cu}_2\text{O}$ ) is dark red and did not form the same colored complex as copper(II) oxide ( $\text{CuO}$ ), which is black. This indicates that  $\text{Cu}_2\text{O}$  is less soluble and the presence of solids during the synthesis is known to lead to the formation of electric arcs. Even the part that did dissolve in the thiol formed a black precipitate at around  $275^\circ\text{C}$ , which was the same temperature in all syntheses, except for the iodide.

A table with a summary of the information extracted from the color profiles and XRD patterns is shown in Table 3.5.

All of the syntheses where the diffraction pattern of powder was obtained yielded a mixture of hexagonal  $\text{Cu}_{1.8}\text{S}$  and orthorhombic  $\text{Cu}_{1.97}\text{S}$ , except for the synthesis performed with the triflate salt, which yielded solely the hexagonal  $\text{Cu}_{1.8}\text{S}$ . The crystallite sizes were determined at a  $2\theta$  of

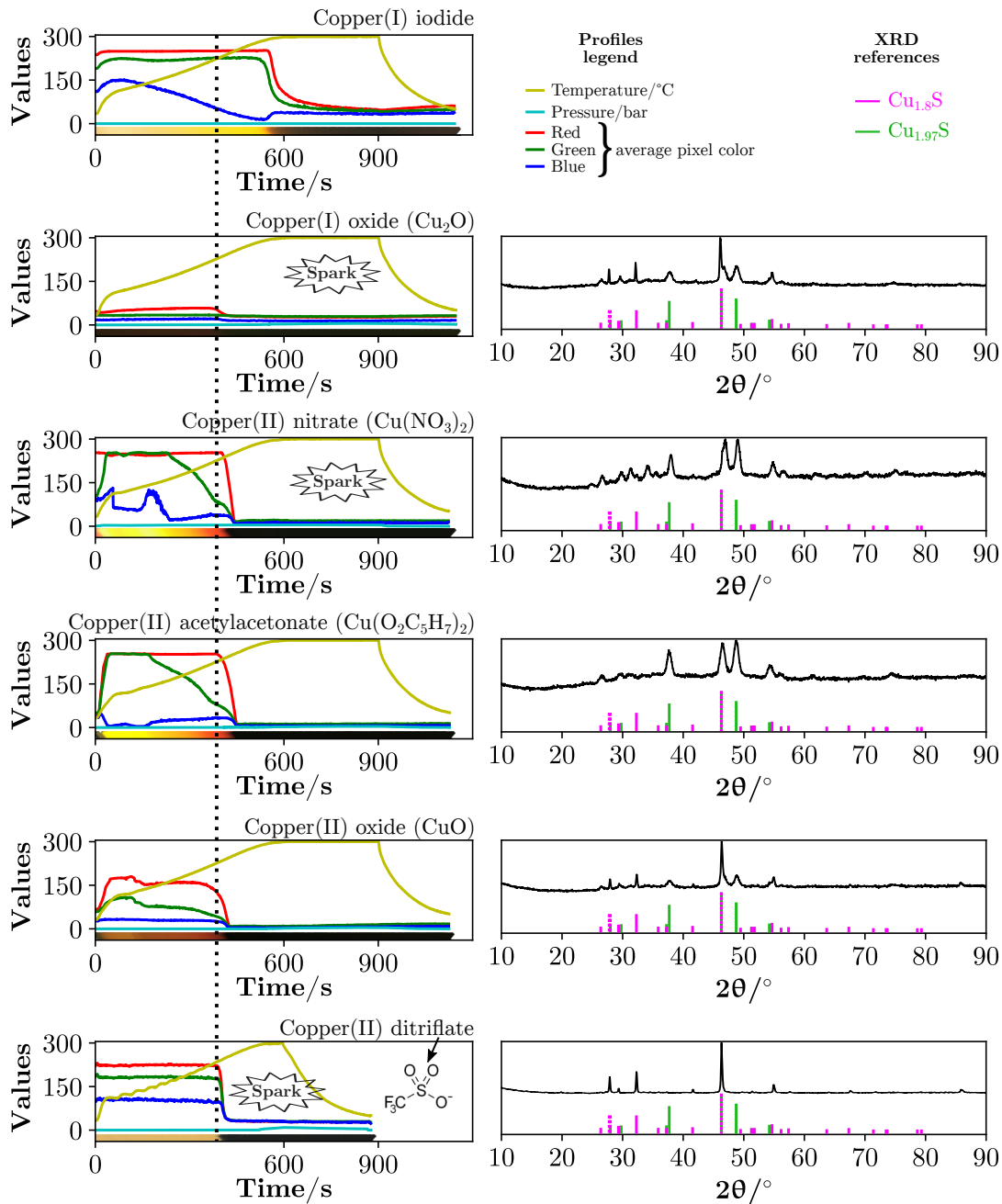


Figure 3.67: Color, temperature, and pressure profiles (A) and XRD patterns (B) of various microwave-assisted synthesis starting from 1-dodecanethiol and copper precursors, such as copper(I) iodide, copper(I) oxide ( $\text{Cu}_2\text{O}$ ), copper(II) nitrate trihydrate, copper(II) acetylacetonate, copper(II) oxide ( $\text{CuO}$ ) and copper(II) triflate. The hexagonal  $\text{Cu}_{1.8}\text{S}$  and orthorhombic  $\text{Cu}_{1.97}\text{S}$  reference patterns were respectively adapted from JCPDS standards 47-1748 and 20-0365.[223]. The dashed line that crosses all profiles denotes the moment that all of the suspensions become dark (around 275 °C), except the  $\text{CuI}$ . Triflate anion's structure is shown since it is an uncommon anion and the profiles that include a "spark" refer to the synthesis where electric arcs formed.

49° (plane (1204)[231]) for  $\text{Cu}_{1.97}\text{S}$  and for  $\text{Cu}_{1.8}\text{S}$  at a  $2\theta$  of 32° (200), due to lower superposition between peaks. There is no clear relation between the anion in the reagent and if a mixture of both the hexagonal  $\text{Cu}_{1.8}\text{S}$  and orthorhombic  $\text{Cu}_{1.97}\text{S}$  phases, or if just one is formed, or their sizes. The particle size for each phase, however, independently of the reagent, is very similar.



Table 3.5: A table containing the particle size of each copper sulfide phase, their temperature of formation, and if during the synthesis electric arcs formed for each reagent used in the microwave-assisted synthesis with 1-dodecanethiol. The size marked with an asterisk carries a lot of uncertainty since the fit was performed on a peak with very low intensity. The absence of data is marked with "n/a" and the absence of a peak to calculate the particle size with "-".

Reagent	Particle size / nm		Temperature/°C	Electric arc
	Cu <sub>1.8</sub> S	Cu <sub>1.97</sub> S		
Copper(I) oxide	43	9	275	yes
Copper(II) oxide	35	10	275	no
Copper(II) acetylacetonate	-	10	275	no
Copper(II) nitrate	14*	12	275	yes
Copper(II) ditriflate	46	-	275	yes
Copper(I) iodide	n/a	n/a	290	no

Although the color profiles seen in Figure 3.67 present similar colors between syntheses, the final product is dissimilar. Phase control can be obtained if the acetylacetonate salt is used to obtain orthorhombic Cu<sub>1.97</sub>S with an average size of 10 nm and it is not possible to safely obtain just the hexagonal Cu<sub>1.8</sub>S phase, starting from the triflate salt, since during the synthesis violent electric arcs will develop.

The same kind of phase control by changing the reagent was not obtained for the ZnS case. The zinc blende (cubic) phase of ZnS was obtained starting starting from the stearate (3 nm, 5 min at 300 °C), acetate (3 nm, 5 min at 300 °C), and acetylacetonate (10 nm, 25 min at 300 °C) salts. The latter sizes were obtained from the XRD patterns at a  $2\theta$  of 28.7°, corresponding to the zinc blende (111) plane. The thiol is limiting the product to the cubic phase since it is possible to obtain the hexagonal phase of ZnS at 150 °C, starting from ZnCl<sub>2</sub> and thiourea in ethylene glycol.[339]

When multiple metal precursors are used to fabricate multinary metal sulfides, if the alloy is not stable, the product is usually a segregated mixture of the sulfides. However, in some cases, the presence of one metal source can influence the crystal structure of the metal sulfide generated by a different metal precursor. An example of this effect is shown in Section 3.3.1.5, where cubic SnS is obtained, as opposed to the orthorhombic phase, when zinc acetate is added. Since the synthesis starting from a zinc precursor in 1-dodecanethiol always yields the zinc blende phase (cubic), when the precursor is added in a synthesis of another metal sulfide, it is as if it serves as a phase template for the other metal sulfide. The opposite effect was seen by Chetty et al.[340], who fabricated nanoparticles of an alloy between CuInS<sub>2</sub> and ZnS with a tetragonal crystal structure. The authors used an Anton-Paar microwave reactor and the same solvent used in this work, 1-dodecanethiol, CuI, indium(III) acetate, and zinc(II) stearate. In this case, since the zinc precursor alloyed with the other precursors, the cubic structure was not forced. The expected CuInS<sub>2</sub> phase using 1-dodecanethiol as the solvent is the tetragonal phase since, in this work, the obtained CuInS<sub>2</sub>, starting from 1-dodecanethiol, CuI, and InCl<sub>3</sub> indeed had a pure tetragonal phase (Section 3.3.1.2). An example where a zinc precursor also does not force the product to have a cubic phase is shown in Section 3.3.1.4, where the final product is the alloy

ZnIn<sub>2</sub>S<sub>4</sub> and has a hexagonal structure.

It is, therefore, possible to modulate the phase of the final product by the addition of another metal precursor, so long as it does not alloy. It is still unclear why the zinc precursor has more "strength" than the other tested metal precursors. We speculate that when two materials (A) and (B) are formed and (A) cannot have the same crystal structures as (B), but (B) can adopt the crystal structure of (A), then (A) will dominate (B). For example, orthorhombic ZnS is not known to exist, so, when put together with a tin precursor to form the sulfides, since the cubic crystal structure of SnS is stable, the zinc precursor will force its existence. Guaranteeing the dissolution of the precursors in the thiol is the correct way to obtain a multinary sulfide and to prevent the formation of electric arcs.

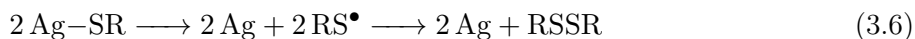
### 3.4.5 Light

The influence of the light in the synthesis of nanoparticles has not been a topic usually mentioned by the scientific community. However, the influence of light on the properties of the nanoparticles can have a drastic impact on the final product, and consequently on their application.

The influence of light on the synthesized product was studied in this work and the material chosen was Ag<sub>2</sub>S, since silver compounds are known to be light sensitive.[341] A set of two syntheses, one with the microwave reactor's light on and another in the dark, starting from either Ag<sub>2</sub>O or AgNO<sub>3</sub> in 1-dodecanethiol, heating to 300 °C in 10 minutes and keeping that temperature for 5 minutes before cooling to 50 °C. The resulting powders' XRD patterns and TEM images are shown in Figure 3.68.

During the synthesis involving silver compounds, if the precursor was AgNO<sub>3</sub>, Ag<sub>2</sub>S was formed independently of light being present or not. Starting from Ag<sub>2</sub>O resulted in a mixture of Ag<sub>2</sub>S and Ag, even if the light was on or off, albeit with the light on there was a larger amount of metallic silver present. A proposed reason for the absence of detectable metallic silver contamination in the syntheses starting from the AgNO<sub>3</sub> is explored below.

As was seen previously in the synthesis of silver sulfide (Section 3.2.8.2), when silver nitrate is heated in the presence of a thiol, a complex is formed. A black precipitate occurs around 260 °C and at 280 °C a silvery tone appears, which is probably contamination of metallic silver. According to Tian et al.[95], the reaction between AgNO<sub>3</sub> and 1-dodecanethiol results in metallic silver Ag, which is the kinetic product formed at a lower temperature and shorter reaction time (180 °C and 4 h), while at higher temperatures and a longer reaction time (200 °C and 5 h) thermodynamic product Ag<sub>2</sub>S is formed. The reaction diagram is equivalent to the one shown in Figure 2.16 C. The formation of metallic silver is assumed to occur with the heterolytic scission of the bond between the metal and the thiolate, as represented in Eq. 3.6 with the group R equal to [−CH<sub>2</sub>(CH<sub>3</sub>)<sub>11</sub>].



In the case of the synthesis starting from AgNO<sub>3</sub>, immediately after the vessel was taken from the

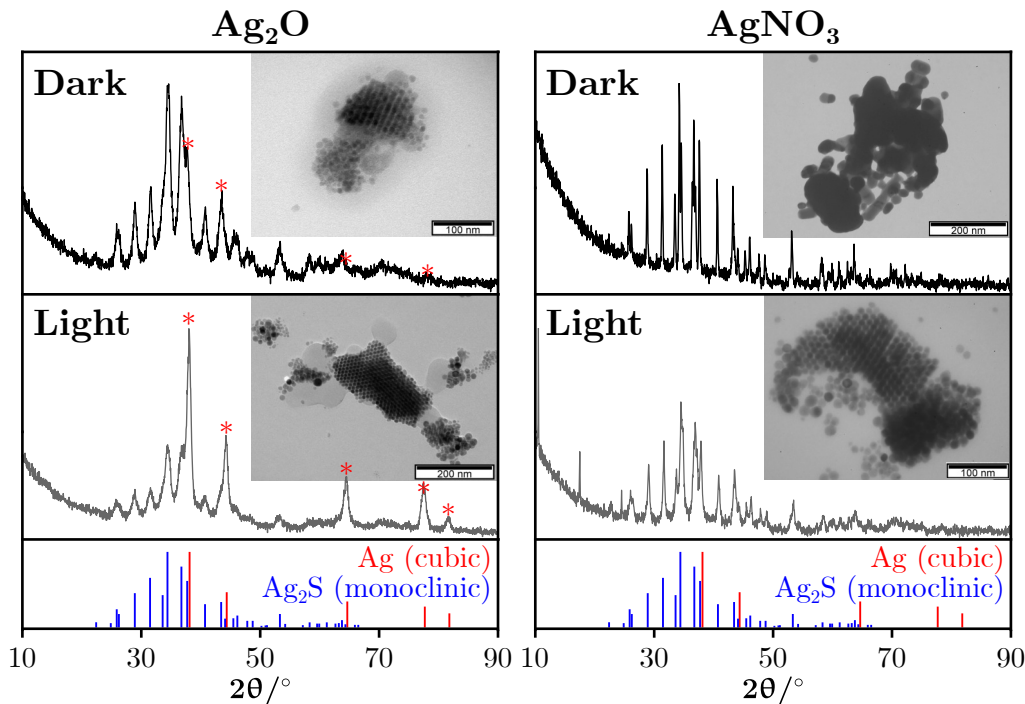
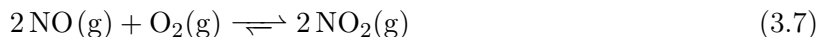


Figure 3.68: Comparison between the XRD patterns of four synthesis, starting from either  $\text{Ag}_2\text{O}$  or  $\text{AgNO}_3$ , performed in the dark or with illumination from the microwave reactor's internal lamp (light). The red asterisk marks the peaks corresponding to the metallic silver. The reference pattern of the cubic metallic silver (Ag) was adapted from reference [238] and the monoclinic phase of  $\text{Ag}_2\text{S}$  from [239]. The scale bars in ( $\text{Ag}_2\text{O}$ ) are 100 nm (Dark) and 200 nm (Light), and in ( $\text{AgNO}_3$ ) are 200nm (Dark) and 100nm (Light).

microwave reactor and opened, an orange gas formed, indicating the formation of the distinctively  $\text{NO}_2$ . This gas can be formed by the reaction of  $\text{NO}$  with the freshly introduced ambient  $\text{O}_2$ [342], as shown in Eq. 3.7.



The release of  $\text{NO}$  could result from previously nitrosated 1-dodecanethiol (RSNO) or from the photolysis of  $\text{NO}_3^-$  (Eq. 3.8).[343] The nitrosated 1-dodecanethiol is formed in the presence of  $\text{NO}_2^-$  ions (Eq. 3.9) in a slightly acidic medium.[342], [344] The source of  $\text{NO}_2^-$  is from the photolysis and thermolysis of  $\text{NO}_3^-$ [343] or the nitric acid, formed from the deprotonation of the thiol.



The nitrosated 1-dodecanethiol is more photoactive than the  $\text{NO}_3^-$  ion and further increases the amount of  $\text{NO}$  released (Eq.3.10). The  $\text{NO}$  reacts with  $\text{NO}_2$  which will only end when either

all of  $\text{NO}_2$  or the thiol is consumed. Another possible parallel reaction is the formation of thiol radicals in the presence of light, as stated by Cao et al.[345]. They could also be formed by the photo-produced  $\text{NO}^\bullet$  radicals. These thiol radicals can digest metallic silver which returns to the solution as a silver-thiolate complex. Since the oxidants  $\text{NO}_2$ ,  $\text{NO}$ , and the thiol radical are presumed to be present during the synthesis starting from  $\text{AgNO}_3$ , any metallic silver that is formed should be immediately consumed. When the light is turned off, the particles stop being digested, suggesting that it is either or both the nitrate and the thiol that are activated by light. This can be seen in Figure 3.68 where the two syntheses starting from  $\text{AgNO}_3$ , under irradiation (light) and in the (dark) respectively resulted in small and larger particles.

As for the synthesis starting from  $\text{Ag}_2\text{O}$ , it is not expected to form strong oxidizing secondary products that digests the particles, but the resulting particles were always small. Contrary to the  $\text{AgNO}_3$  which forms strongly oxidizing by-products and assuming that the secondary product that is formed is the alcohol 1-dodecanol, it is presumed that the constant presence of metallic silver is due to the reduction of  $\text{Ag}^+$  by the alcohol or the thiol, which are both mild reducers.

As in Cao et al.[345] work, the formation of the thiol radical from 1-dodecanethiol has to be evaluated carefully with the electron paramagnetic resonance technique, which uses microwave light pulses in parallel with a magnetic field that detects the presence of unpaired electrons, such as radicals. The above-proposed mechanisms are conjectures and serve as a future reference regarding any metal sulfide syntheses performed with light-sensitive reagents.

Not all metal precursors are light-sensitive.

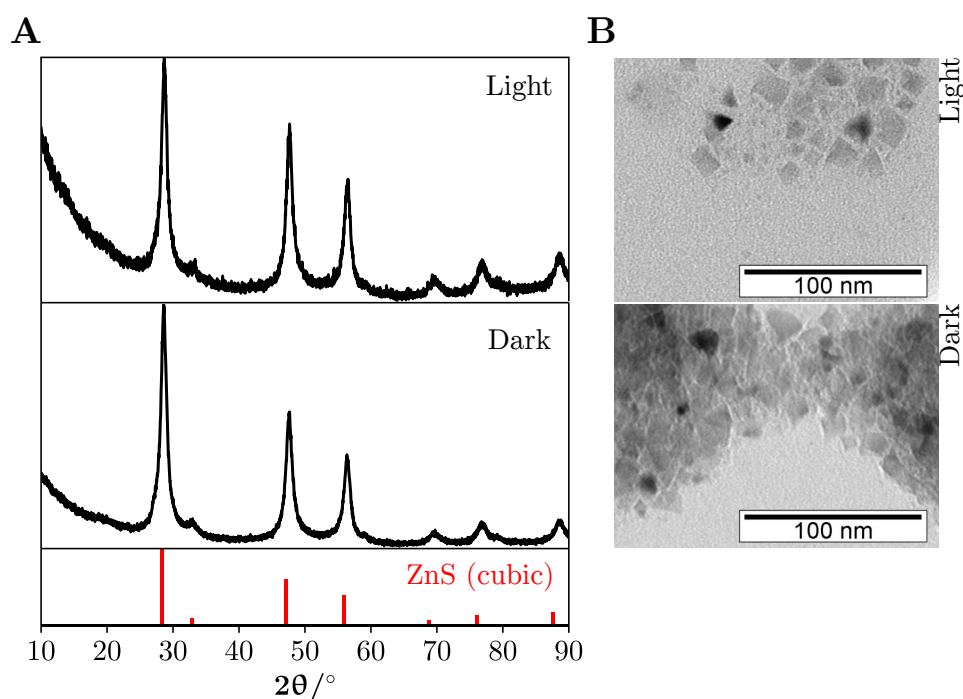


Figure 3.69: Comparison between the XRD patterns (A) and TEM images (B) of two zinc sulfide synthesis, starting from zinc(II) acetate dihydrate, with one performed under irradiation from the microwave reactor's internal lamp (light) and the other in the (dark). The reference patterns of the cubic phase of ZnS (mp-10695) was taken from Materials Project[128][129]. The scale bars are 100 nm.

The products obtained from precursors that are known not to be light sensitive, such as zinc(II) acetate dihydrate, used previously in the synthesis of ZnS (Section 3.2.9.1), are expected to have the same properties when synthesized in the presence of light or darkness. Figure 3.69 includes the XRD patterns and TEM images of two syntheses starting from zinc(II) acetate dihydrate, one in the dark and another irradiated with the microwave reactor's lamp, with a temperature ramp set to reach 300 °C in 10 minutes and staying at that temperature for 25 minutes.

Both syntheses produced cubic ZnS since the XRD patterns (A) are very similar. The nanoparticles also have the same geometry and size.

To summarize, light-sensitive precursors can lead to the formation of materials with other phases or with other oxidation states, while the products resulting from precursors that are not sensitive do not suffer any changes. However, further studies should consider the influence of different light sources - different wavelengths - and intensities.

### 3.5 Sustainability

The decline of the environment through excessive and unsustainable exploitation of resources, demands a shift in the usual methods of material synthesis. Syntheses should be performed with some degree of recyclability and reuseability. For example, Wang et al.[346] synthesized SrS using ethylenediamine as the solvent, they reported that it could be recycled and used in future syntheses.

The recovery of the solvent used was attempted and the results are presented in this section. Tin sulfide synthesis was used as a case study as an illustrative example of the effects of reusing the sulfur source.

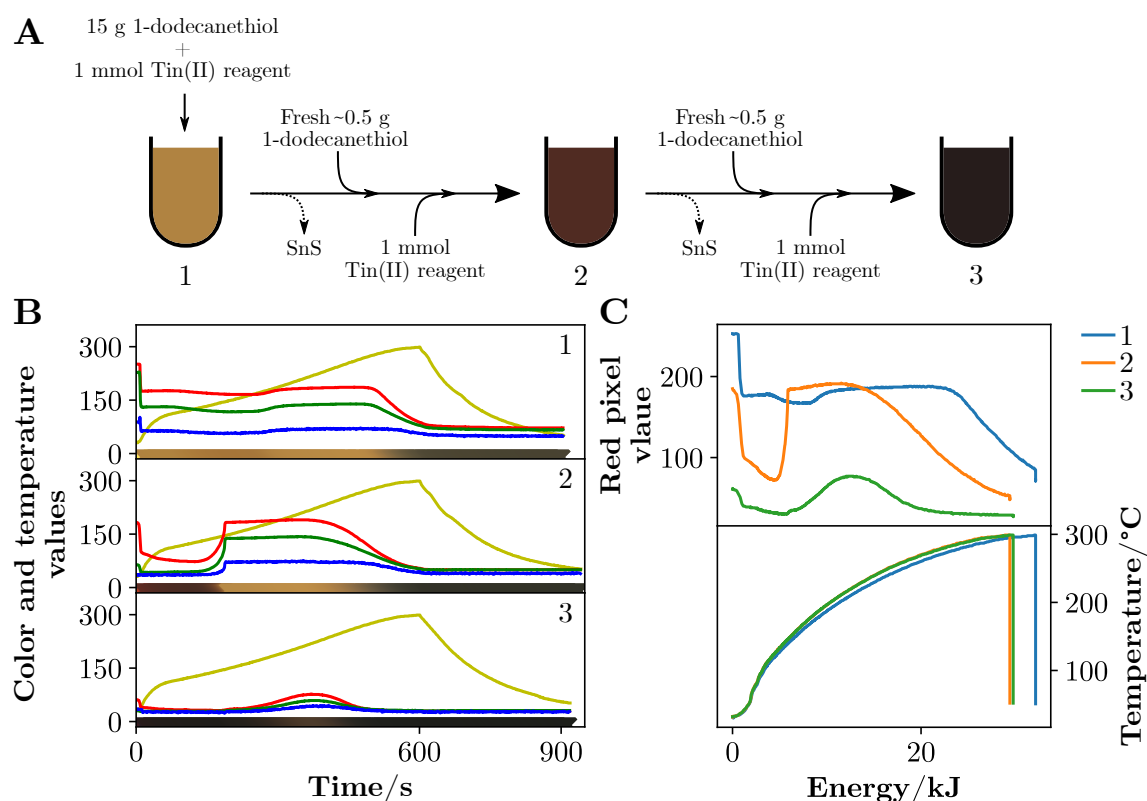


Figure 3.70: Scheme representing the three syntheses with consecutive reutilization of the previously used 1-dodecanethiol (A), color and temperature profiles (B) and red pixel value and temperature profiles plotted against the energy (C) of each three syntheses, with the first synthesis (1) starting from virgin 1-dodecanethiol and the remainder (2) and (3) with the decanted 1-dodecanethiol from each previous synthesis. The Tin(II) reagent used was Tin(II) 2-ethylhexanoate.

Based on the conclusion that the initial concentration of metal reagent should be 0.1 mmol and the adequate volume of 1-dodecanethiol should be 15 g, to obtain sufficiently desaggregated particles and, after, a stable ink, as presented in Section 4.1, the following synthesis was performed taking into account this method alteration. A tin sulfide synthesis was performed starting from 15 g of 1-dodecanethiol and 0.1 mmol of tin(II) 2-ethylhexanoate, purged with nitrogen before heating to 300 °C in 10 min in the microwave reactor and cooling to 50 °C, as shown in the schematic (A) in Figure 3.70. The suspension was centrifuged at 9000 RPM (9146 *g*) and the black pellet was

separated from the liquid, which was stored in another container for the following synthesis. The second synthesis was performed by adding  $\sim 0.5$  g of 1-dodecanethiol to the recovered liquid, to compensate for the loss of the liquid that remained on the reaction vessel and the container's wall. The synthesis process, centrifugation, and liquid recovery and reutilization were repeated two more times. As a side note, when the purge with nitrogen gas was being performed, the mixture with the reused thiol easily formed foaming bubbles. The 1-dodecanethiol reutilization scheme comprises three syntheses where the consequent one used the previous liquid, after removing the resulting black powder (A), the corresponding color and temperature profiles (B) and the red pixel value and temperature profiles plotted against the energy supplied to the reactor's magnetron of the previous 3 syntheses (C) are shown in Figure 3.70.

The typical mixture between tin(II) 2-ethylhexanoate and 1-dodecanethiol yields a yellow suspension but when the recovered liquid from a previous synthesis is used instead, a dark orange suspension is obtained. This is observed in the first moments of the color profiles from synthesis (2) and (3) are much darker than in (1). Synthesis (2) completely recovered the yellow color at  $\sim 150$  °C while synthesis (3) was initially much darker and only recovered partially. The transition to tin sulfide occurs when the yellow suspension darkens again, forming a black suspension at 244 °C for the synthesis with virgin 1-dodecanethiol (1) and at 234 °C for (2) and (3) with the reused thiol.

The resulting powders XRD patterns are shown in Figure 3.71.

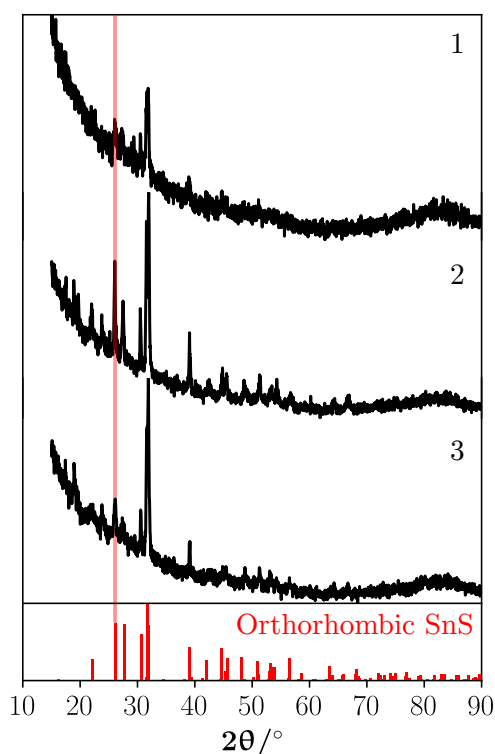


Figure 3.71: X-ray diffraction patterns of the three powders obtained after reusing the thiol from synthesis 1 in 2, and from 2 in synthesis 3. The plane (012) at a  $2\theta$  of  $26.1^\circ$  was marked. The XRD pattern of the orthorhombic phase of SnS (mp-2231) was taken from Materials Project[128][129].

The materials obtained in the three syntheses were the orthorhombic phase of SnS and the size

of the crystallites, estimated from the peak at a  $2\theta$  of  $26.1^\circ$ , were 10 nm, 37 nm, and 20 nm, corresponding respectively to the first synthesis (1), the second (2), and the third (3). Although the same phase was obtained, there was no control over the size of the particles.

Another factor to weight-in is the energy used in the syntheses. The energy supplied to achieve the color transformation to black is lower, comparing (2) and (3) with (1), as seen in Figure 3.70 (C). The energy required to reach  $300^\circ\text{C}$  is also lower in synthesis (2) and (3), compared to the first synthesis (1). Since the 1-dodecanethiol is a poor microwave radiation absorber and the reused solvent is contaminated with by-products and unreacted reagent, this facilitates the absorption of the microwave radiation and decrease the energy required to increase the temperature.

As presented previously in Section 3.4, for some elements, the choice of the starting reagent does not significantly alter the final material's properties, such as the particles' size and crystal phase. However, for two similar syntheses, where the temperature profile, and amount of 1-dodecanethiol (weight) and starting reagent (in number of moles) are the same, the energy supplied to the microwave reactor's magnetron can be quite different. In Figure 3.72, the temperature versus energy profiles of two syntheses starting from 1-dodecanethiol and either zinc(II) acetate dihydrate or zinc(II) acetylacetonate monohydrate are shown to demonstrate that the synthesis starting from the acetate requires more energy to achieve the same temperatures as the synthesis starting from acetylacetonate. The inset serves as proof that the temperature profile is similar between experiments.

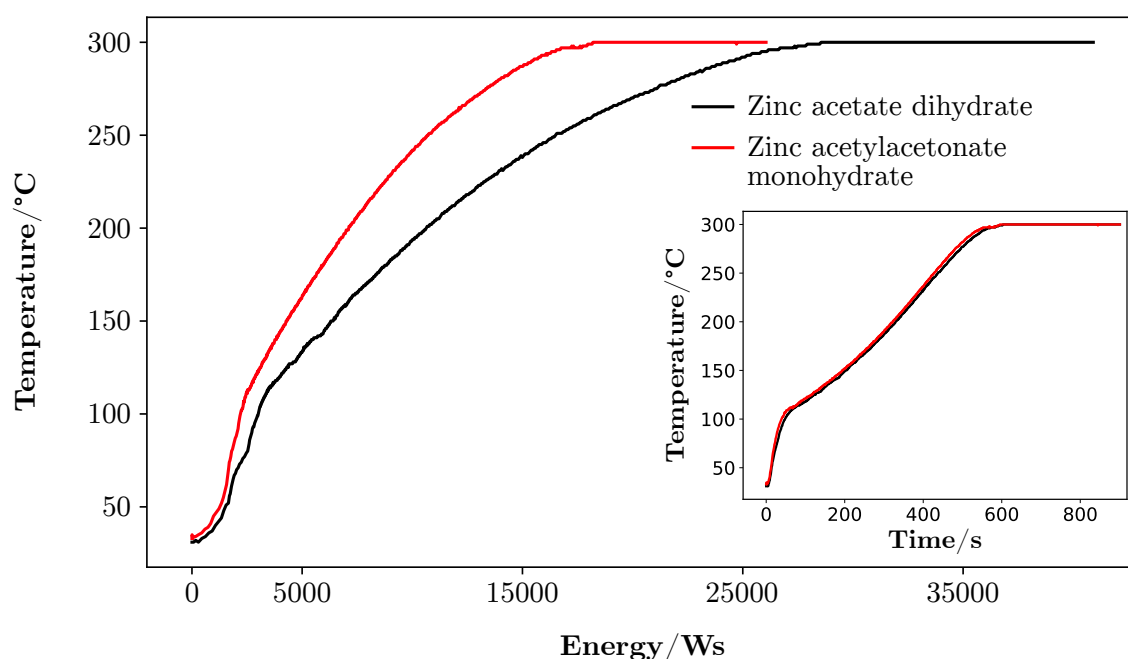


Figure 3.72: Temperature profile against the energy supplied to the microwave reactor's magnetron of syntheses starting from 1-dodecanethiol and either zinc(II) acetate dihydrate or zinc(II) acetylacetonate monohydrate. The inset shows the temperature profile over time for both experiments.

The synthesized materials should also be evaluated from the environmental pollution perspective. In this sense, two metal sulfides, cadmium sulfide and zinc sulfide, were tested in an aquatic



environment with fish, since leaching of nanoparticles from devices to the environment, especially aquatic environments, is a current regarded issue. The synthesized zinc sulfide nanoparticles ( $10\pm 2$  nm), as well as cadmium sulfide nanoparticles ( $8\pm 2$  nm) synthesized under similar conditions to the method developed in this work, were used to evaluate the toxicity effect on Zebrafish (*Danio rerio*). Zinc sulfide and cadmium sulfide particles, both separately and combined, were dispersed in water with concentrations equal to 10  $\mu\text{g/L}$ , 100  $\mu\text{g/L}$ , 1000  $\mu\text{g/L}$ . An evaluation regarding the effect of the nanoparticles on the oxidative stress response was deemed low to moderate and there was no significantly higher mortality, compared to the control. The lower-than-expected toxicity could be explained by the 1-dodecanethiol capping and the tendency to aggregate with increasing particle concentration, leaving fewer particles available to cause damage.[347]



## Metal Sulfide Nanoparticle Inks

This chapter includes the description of the formulation of metal sulfide inks and their deposition by slot-die coating and spray. The films were characterized by optical microscopy to evaluate the size of the aggregates, their transmittance and diffuse reflectance spectra were measured to determine their band gap, and Raman spectroscopy was used to evaluate their composition.

### 4.1 Formulation

Following the protocol defined in Section 3.1.1 for the synthesis of the metal sulfide nanoparticles, the obtained dried powders of any of the attempted syntheses were not easily suspendable in any attempted solvents. The solvents used included acetone, isopropanol, ethanol, chloroform, dichloromethane, *n*-methyl-2-pyrrolidone, toluene, hexane, cyclohexane, 1,6-hexanedithiol, dibutyl disulfide, and carbon disulfide. Even after 5 minutes of sonication in an ultrasound bath, the powder would rapidly sink, and no spectrum could be measured in time. In this work, the synthesis of metal sulfides was performed with an initial metal precursor concentration of 1 mmol in a volume of 5.9 mL (5 g) of 1-dodecanethiol. Some other works used concentrations of 1 mmol per 10 to 40 mL [93], [348]–[350] and all of them used an extra coordinating agent such as oleylamine or trioctylphosphine, coupled with a non-coordinating solvent octadecene, to confer colloidal stability. An exception was found in the literature, where CdS and Ag<sub>2</sub>S were synthesized using only 1-dodecanethiol at a higher concentration of 1 mmol per 6 to 7 mL [351], near the one used in this work. In the latter reported syntheses performed by heating the mixtures on a heating mantle, ethanol was added to the resulting suspensions, which were centrifuged and chloroform was added and removed to purify the nanoparticles further. Finally, the particles were redispersed in chloroform to obtain a stable colloidal suspension but without a clear indication on how the suspension was produced.

Presuming that after several washes, the 1-dodecanethiol left on the powder was insufficient to confer colloidal stability, a SnS synthesis was performed following the same procedure (Section 3.2.11.1) to produce the particles, but the particle cleaning procedure was reduced to simple direct centrifugation at 9000 RPM (9146 *g*) of the mixture after the vial was cooled down. The supernatant was discarded, and the tube was left upside-down for at least 1 hour, so the remaining liquid was drained from the pellet by gravity. A mass of 7.86 g (10 mL) isopropanol was added to the slurry and sonicated in an ultrasound bath, from JP SELECTA ultrasounds H-D, for 5 minutes. Immediately after the sonication, the suspension's transmittance at 1000 nm was measured over time in a quartz cuvette with an optical path of 1 cm, capped with a polytetrafluoroethylene stopper, as shown in Figure 4.1

The wavelength of the test (1000 nm) was chosen since isopropanol does not absorb while the SnS

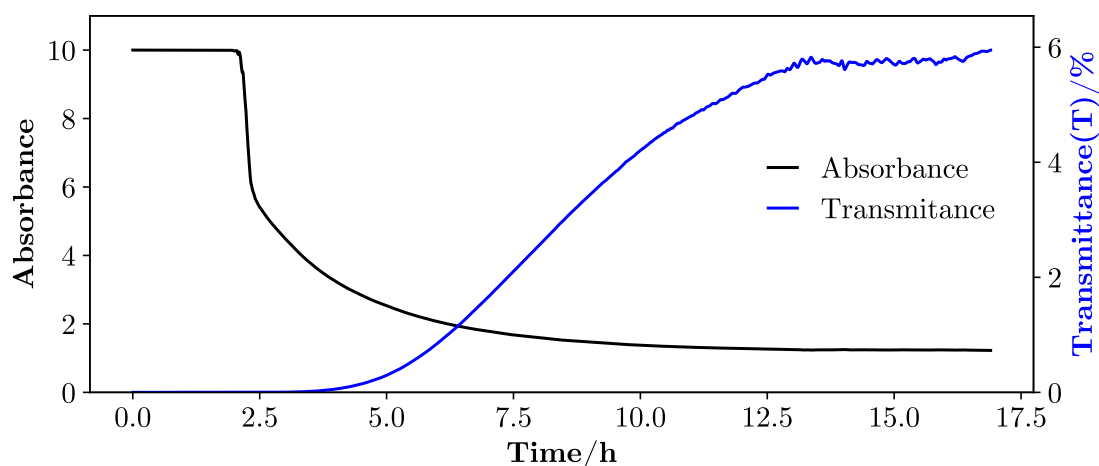


Figure 4.1: Absorbance and transmittance spectra measured at 1000 nm over time of a suspension of SnS.

does. This test aimed to determine the stability of the suspension over time. In the first moments, no detectable light passes the suspension due to a substantial amount of particles blocking the beam from the spectrophotometer. The detector only received enough light around 2 hours later, which indicated that the suspension had enough load for a deposition that lasted up to 2 hours. If the transmittance is considered instead and assuming that the instability is defined as when the transmittance is no longer near zero, the stability lasted 3 hours. Notice that, even after a baseline set with isopropanol, which naturally resulted in zero absorbance when only the solvent was present, after around 13 hours, the absorbance and transmittance stabilized. This plateau could be the concentration at which the SnS particles are truly stable in isopropanol.

After testing the previously prepared suspension in either the slot-die or the airbrush (spray), the load was too high and clogged either equipment's orifices. To prevent clogging, the initial amount of the metal precursor was reduced to 0.1 mmol, the 1-dodecanethiol amount raised to 15 g, and the temperature ramp was the same (300 °C in 10 minutes), but the cooling was initiated after the temperature was reached, to achieve even smaller particles. Tin sulfide was again used as an example in Section 3.4.3, to demonstrate the effect of reducing the precursor reagent, increasing the 1-dodecanethiol, removing the temperature hold after reaching 300 °C and removing the washing steps with ethanol on the particles' properties. The resulting material was shown to be similar in terms of phase, albeit crystallite particles were smaller. The stability was also identical to the ink prepared from the product obtained using 1 mmol of precursor, and the measurement of the transmittance spectrum over time was deemed unnecessary.

## 4.2 Deposition

The formulated ink with isopropanol and SnS was chosen as the model for the slot-die cast and spray deposition experiments. The following sections contain the results regarding said deposition, including optical microscope images and transmittance and reflectance spectra used to evaluate the particles aggregates' size, film density, and optical properties.

### 4.2.1 Slot die

Slot die coating was chosen due to its direct applicability and transferability to the industry. A first approach was performed using the synthesized SnS, according to the modification of the original synthesis protocol, described previously in Section 4.1. Overall, there were only two significant differences between the synthesis procedure used to fabricate the metal sulfide nanoparticles previously in Section 3 and the one employed to obtain the inks: the reduction of time at 300 °C to zero and the washing step consisted solely on the centrifugation of the obtained slurry, followed by simple decantation. To this slurry, 7.86 g (10 mL) of isopropanol was added to obtain distinct concentrations, followed by an ultrasound bath for 5 minutes. A 75x25 mm Corning glass was cleaned with paper previously soaked with isopropanol, dried with compressed air, and the part which was going to be exposed to the spray was submerged in a mixture of nitric and hydrochloric acids (1:1) for 30 minutes at 70 °C. After carefully decanting the acid mixture to another container with a mixture of sodium bicarbonate and water to neutralize it, the substrate was rinsed thoroughly with deionized (Type 2) water (Millipore), followed by rinsing with isopropanol to remove the water, dried with compressed air and left on a covered glass container at 70 °C before using. The slot-die coating was performed on an Ossila Slot-Die Coater, using a 200  $\mu\text{m}$  distance between the die and the substrate and a substrate temperature of 60 °C. The ink was loaded into a 2 mL polypropylene and polyethylene syringe (B Braun Injekt Solo Cone), mounted on the slot-die machine and connected to the polytetrafluoroethylene tube that was attached to the slot-die head, which had an aperture of 100  $\mu\text{m}$ . The piston that pushed the syringe was set to a speed of 0.314 mm/s after setting a syringe diameter of 2 mm, which according to the slot-die software, is equivalent to a dispense rate of 0.522  $\mu\text{L/s}$ . The distance traveled by the stage was set to 25 mm, and 30 depositions were performed sequentially by resetting the stage to the original place and restarting the deposition. Cleaning the slot-die head was performed using paper soaked in isopropanol, including carefully cleaning the orifice until there was no more visible residue on the paper.

The microscope images of the resulting film can be seen in Figure 4.2.

After 30 consecutive depositions, the SnS film presented some visible aggregates (A). The microscope image (B) also reveals aggregates with hundreds of micrometers, although the background is filled with very small aggregates. However, there were many holes between the smaller aggregates (C), and the film did not percolate. Even after several tries, changing the parameters, such as the distance between the slot-die head and the substrate, the temperature of

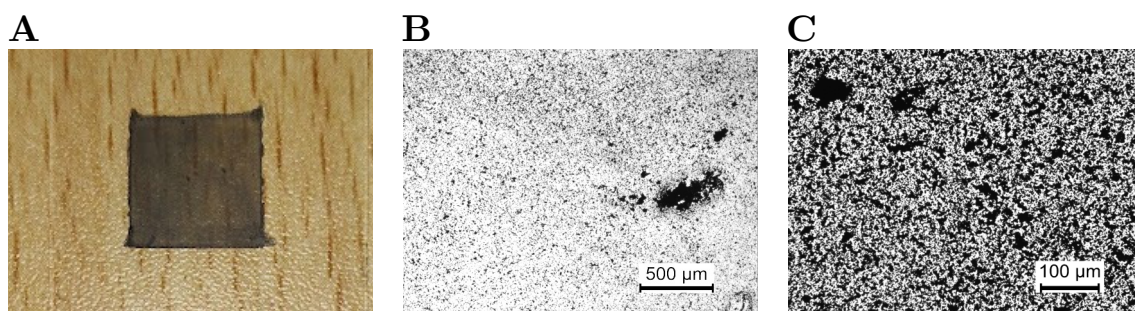


Figure 4.2: Photograph (A) and two microscope images (B) and (C) of the SnS film deposited by slot-die coating. The scale bar is 500  $\mu\text{m}$  in (B) and 100  $\mu\text{m}$  in (D).

the stage/substrate, dispense rate, etc., the films were always non-percolating and similar. The ink was also lacking a higher viscosity for this method and the technique itself was arduous to employ and clean. Since the purpose was to develop an easy method to deposit with a simple ink formulation that contained only volatile solvents to avoid having to remove them later, the slot-die cast deposition method was discarded.

### 4.2.2 Spray

A very complete study of the production of binary and multinary metal sulfide by spray pyrolysis was performed by Murtaza et al.[352] The authors produced films by a three step procedure, starting from the synthesis of a metal N,N-diethyldithiocarbamate complex which was dissolved in tetrahydrofuran to form an ink, followed by its deposition by spray, using argon as the gas medium, onto a hot plate at 200 °C. The precursor film was then heated inside a quartz tube to a temperature between 350 °C and 450 °C, between 30 and 60 minutes. They successfully synthesized a variety of metal sulfides such as ZnS, FeS, MnS, and other binary sulfides, as well as the ternary  $\text{CuFeS}_2$  and quaternary  $\text{Cu}_2\text{ZnSnS}_4$ .

The same tin sulfide ink formulation prepared previously for the slot die coating was used to deposit the nanoparticles by spraying the suspension onto a glass substrate (2.5 cm x 7.5 cm) pre-cleaned from Corning, as shown in Figure 4.3 (A). The substrate was previously heated on a hot plate, set at 200 °C and kept at that temperature throughout the deposition. The tool used to spray the suspension was a simple glass spray bottle, and the spraying was performed at a distance of 10 cm from the substrate. The spray pulses were timed according to the visual drying cue of the isopropanol. After the whole suspension was exhausted, the film was observed under the microscope at the amplification of 20x (Figure 4.3 (B)), and the total reflectance and transmittance spectra of the film were measured (Figure 4.3 (C)).

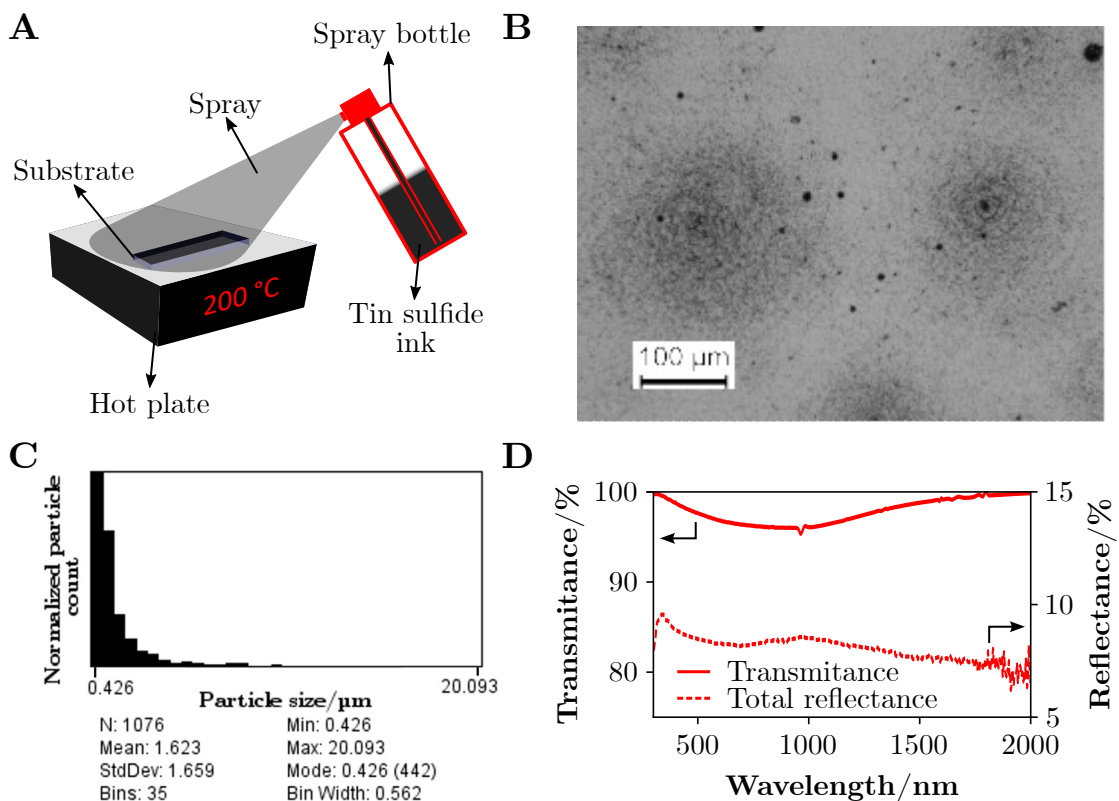


Figure 4.3: Schematic of the preliminary spray setup to deposit the synthesized SnS nanoparticles (A) and results including a microscope image (B), the particle size distribution and relevant statistical data from the microscope image (C) and transmittance and total reflectance spectra (D). The scale bar is 100 μm in (B).

The darker patches in Figure 4.3 (B), where a higher concentration of aggregates is found, indicate that the particle filling is heterogeneous throughout the sample. Using a spray bottle resulted in small aggregates of SnS, with an average diameter of 1.6  $\mu\text{m}$ , even inside the dark patches probably formed by droplets with  $>100 \mu\text{m}$ . Some aggregates with sizes  $>10 \mu\text{m}$  can also be observed, but the overall dimensions are below  $\sim 3.2 \mu\text{m}$ .

After the successful trial using a spray bottle, a more robust setup was mounted to deposit the metal sulfide nanoparticles' inks. The following sections describe the method and results of the deposition of films of tin sulfide, zinc sulfide, niobium sulfide, and copper iron sulfide nanoparticles.

#### 4.2.2.1 Method

An airbrush from Dexter brand equipped with an ink deposit capable of rotating to enable the correct angle adjustment was used. A schematic of the setup can be found in Figure 4.4.

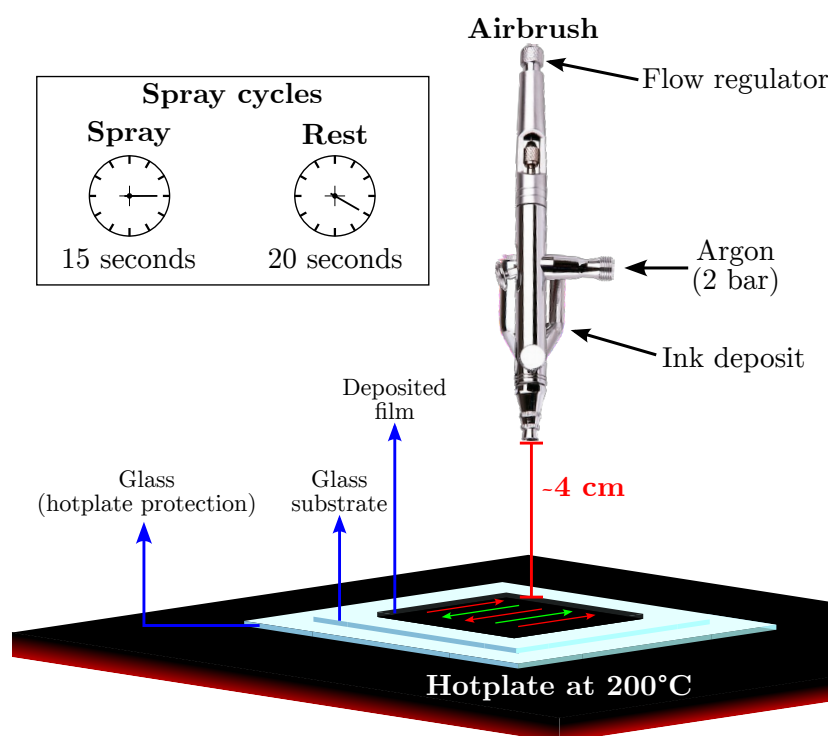


Figure 4.4: Schematic of the setup used to manually spray the metal sulfide inks onto a 75x25 mm Corning glass substrate. Beneath the substrate, a 10x10 cm glass plate was used to protect the hotplate, which was set to 200 °C, controlled by a thermopar on top of the protective glass. The red and green arrow sets represent the movement performed with the airbrush while spraying for 10 seconds at a distance of  $\sim 4$  cm, using an argon inlet at 2 bar, followed by a 20-second resting period.

Before performing the depositions, a 75x25 mm Corning glass was cleaned with paper previously soaked with isopropanol, dried with compressed air, and the part which was going to be exposed to the spray was submerged in a mixture of nitric and hydrochloric acids (1:1) for 30 minutes at 70 °C. After carefully decanting the acid mixture to another container with a mixture of sodium bicarbonate and water to neutralize it, the substrate was rinsed thoroughly with deionized



(Type 2) water (Millipore), followed by rinsing with isopropanol to remove the water, dried with compressed air and left on a covered glass container at 70 °C before using. A mask was made with polyimide (Kapton) tape, leaving a substrate area of 20x20 mm exposed, with part of the tape anchoring the substrate to the glass beneath, protecting the hotplate. The flow regulator of the airbrush was rotated by a quarter of a revolution. Argon gas was used at 2 bar as the compressed gas media to carry the ink to the airbrush's tip and create the aerosol. During the spray cycles, the spray time was set to 15 seconds, where the airbrush continuously released a plum of ink droplets at a distance from the substrate of around 4 cm, following the zigzag motion described in the figure. After the spray time, the spray was stopped for 20 seconds, with the airbrush away from the heat source, to prevent solvent evaporation from the ink deposit. When the ink volume was depleted, the hotplate was turned off, and the film was left to cool down to ambient temperature. To clean the airbrush, the ink deposit was removed and cleaned thoroughly with paper soaked in isopropanol and carefully inserted into the crevices and tubes. The airbrush was submerged in isopropanol in a cup until both the tip and the ink deposit's entrance were submerged. Then the trigger to let the argon gas flow was pressed, refluxing the isopropanol from the tip to the ink tank's entrance for at least 5 seconds. Then, paper soaked in isopropanol was carefully inserted inside the airbrush to clean the residue. This process was repeated until no residue could be seen on the paper.

The following sections contain the methods used to produce tin sulfide, zinc sulfide, niobium sulfide, and the multinary copper iron sulfide films and their respective characterizations by photography, microscopy, and transmittance and diffuse reflectance spectra acquisition, to calculate the Tauc plot and determine their band gaps.

#### 4.2.2.2 Tin Sulfide Film

Both the synthesis, ink preparation, and deposition of a tin sulfide film are detailed in Section A.4.3. The deposition was attempted with a complete turn of the flow regulator and a spray time of 20 seconds, and was confined to an arbitrary 25x11.3 cm. A photograph of the film, a microscope image with the particle count histogram, the transmittance and diffuse reflectance spectra and the Tauc plot are shown in Figure 4.5.

For a manual spray process, areas that are not laterally confined are visually harder to spray homogeneously. In an automated system, the lack of coverage seen in picture (A1) on the top of the black film would not exist, and the film would be uniform. However, since the film was not as dense as the bottom part, it was possible to observe the aggregates separately (A2), such that the mode is 2 micrometers (A3). Through the transmittance spectrum (B1), it is not possible to see the band gap of the material since it appears to begin to absorb light above 2000 nm. It is, in fact, the characteristic reflectivity of the material below its band gap (1.1 eV)[275] that confers the apparent absorption. The film's material band gap was calculated from the diffuse reflectance spectrum, and the value of 1.21 eV was obtained near the powder's band gap (1.18 eV).

The Raman spectrum acquired for this film is represented in Figure 4.6 (A), as well as the pictures

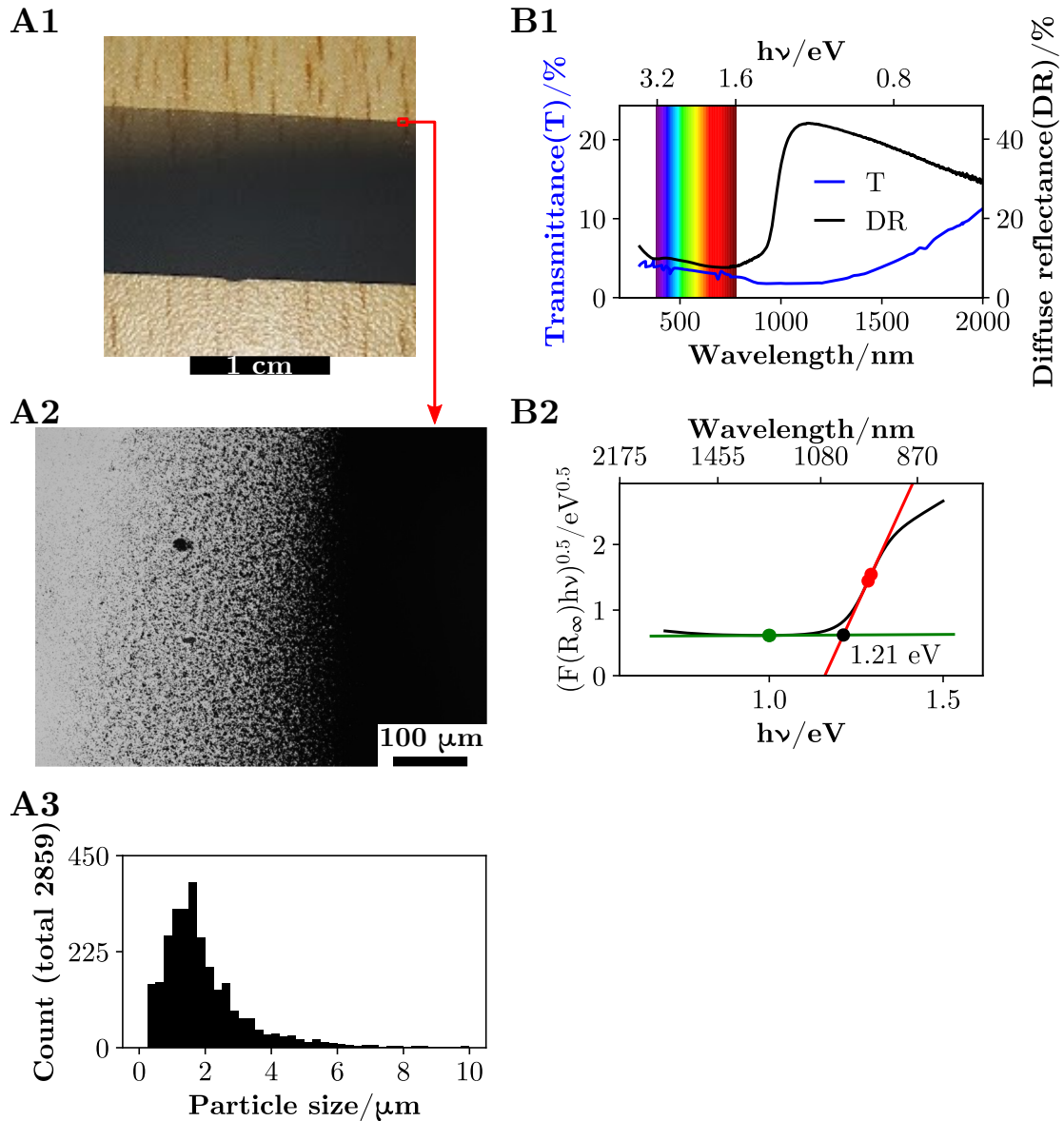


Figure 4.5: Photograph of the film of tin sulfide deposited by spray (A1), microscopy image (A2), a particle size histogram (A3) taken from (A2), transmittance and diffuse reflectance spectra (B1), and Tauc plot (B2). The colored lines on the Tauc plot are the linear regressions used to estimate the band gap (black dot). The colored dots indicate the limits used to perform the regression. The scale bar is 1 cm in (A1) and 100 μm in (A2).

taken to estimate the film's thickness (B).

The Raman spectrum of  $\text{Sn}_2\text{S}_3$  obtained by Güneri et al.[353], prepared at 30 °C for 24 hours by chemical bath deposition of an aqueous solution containing  $\text{SnCl}_2 \cdot 2\text{H}_2\text{O}$ , thioacetamide, and triethanolamine, coincides with the one found in Figure 4.6 (A). The band gap of 2.08 eV the authors reported, unfortunately, is not reported in the articles they cite, which are unrelated. There is another article that reports a band gap of 1.42 eV.[354] The band gap obtained in this work was of 1.21 eV, which coincides with the band gap of SnS. This mismatch between the Raman spectrum and the band gap could result from the fact that the Raman spectrum was acquired on a single spot of the film, while the diffuse reflectance spectrum was captured in a

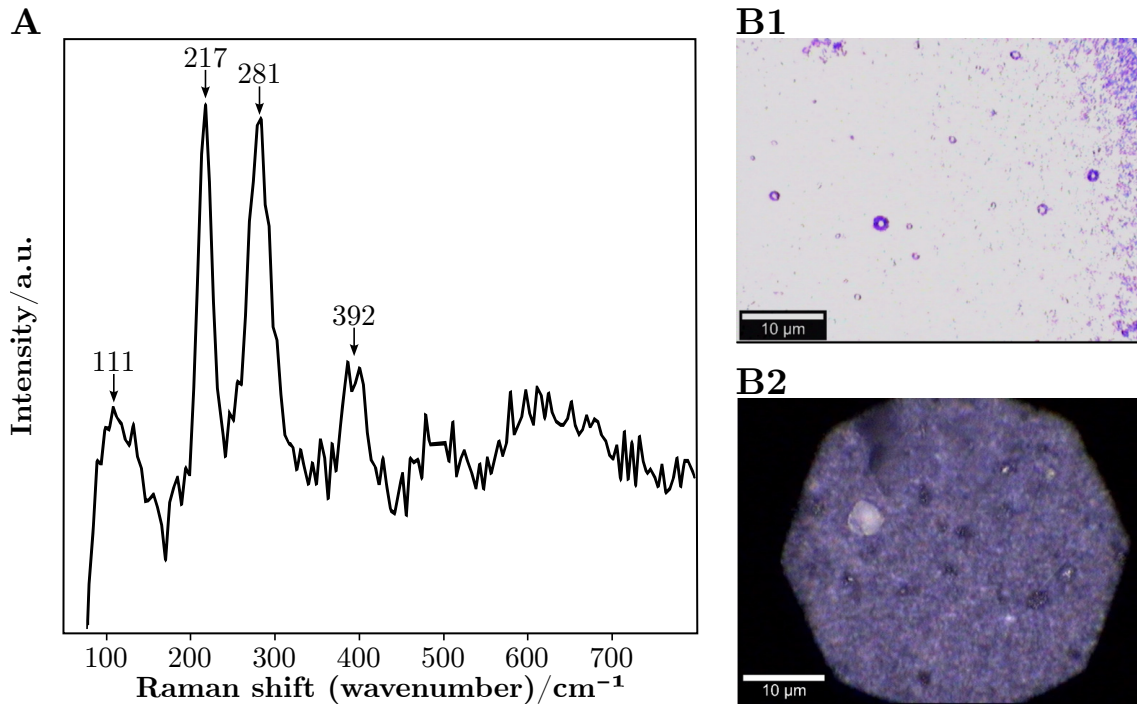


Figure 4.6: Raman spectrum (A) and two microscope images, one focused on the substrate's surface (B1) and another on the film's surface (B2), of the film obtained by spray from the tin sulfide ink. The scale bars are 10  $\mu\text{m}$  in (B1) and (B2).

broad area. Therefore, there is some contamination of  $\text{Sn}_2\text{S}_3$  in the film of  $\text{SnS}$ , that probably formed during the deposition at 200  $^\circ\text{C}$  and while measuring the Raman spectrum, where the laser could have heated the sample.

The conductivity of the  $\sim 9 \mu\text{m}$  film was measured by applying two silver contacts, each approximately with a length 5 mm and both 1 mm apart, and was estimated to be  $1.1 \times 10^{-3} \text{ S/m}$ . The expected conductivity value for a film of  $\text{Sn}_2\text{S}_3$  and  $\text{SnS}$  prepared physical evaporation of both materials at the same time, is  $\sim 500 \text{ S/m}$ .<sup>[354]</sup> The low conductivity obtained can be justified by the lack of annealing. Due to the absence of aggregation between particles, the charges are lost at the interfaces and voids between the grains. The adsorbed air also contributes to the lower conductivity.

A  $\sim 9 \mu\text{m}$  thick tin sulfide nanoparticle film was successfully deposited by spray, presenting a small aggregates (mode of 2  $\mu\text{m}$ ), a band gap of 1.21 eV and a conductivity of  $1.1 \times 10^{-3} \text{ S/m}$ . Part of the film was contaminated with  $\text{Sn}_2\text{S}_3$ , that formed during the deposition.

#### 4.2.2.3 Zinc Sulfide Film

A zinc sulfide film was deposited by spray using the setup described previously in Figure 4.4 and both the synthesis, ink preparation, and deposition are detailed in Section A.4.2. The deposition was confined to an area of 25x25 cm. A photograph of the film, a microscope image, the transmittance and diffuse reflectance spectra and the Tauc plot are shown in Figure 4.7.

The film is practical invisible (A1) since zinc sulfide has a large band gap and, therefore, visible light passes without being absorbed. The film can only be seen, albeit not easily, due to the

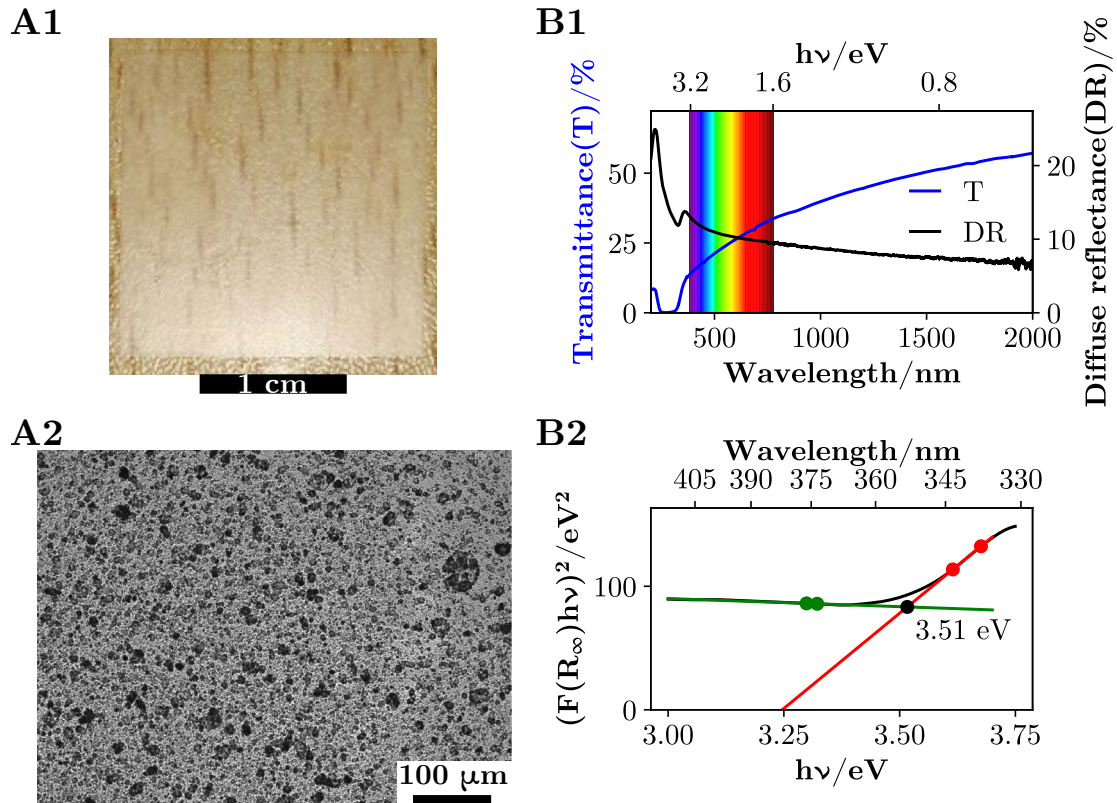


Figure 4.7: Photograph of the film of zinc sulfide deposited by spray (A1), microscopy image (A2), transmittance and diffuse reflectance spectra (B1), and Tauc plot (B2). The colored lines on the Tauc plot are the linear regressions used to estimate the band gap (black dot). The colored dots indicate the limits used to perform the regression. The scale bar is 1 cm in (A1) and 100  $\mu\text{m}$  in (A2).

particle aggregates that disperse light, especially near the light spot from the camera flash at the bottom of the picture. The majority of the aggregates fall into the size range of 2  $\mu\text{m}$  to 9  $\mu\text{m}$ , with another population between 50  $\mu\text{m}$  to 80  $\mu\text{m}$  and some scattered larger aggregates from 200  $\mu\text{m}$  to 400  $\mu\text{m}$  that are composed of the smaller aggregates and resulted from larger droplets. This explains the progressively decreasing transmittance (B1) from the near-infrared to the visible, where it suddenly drops due to the materials band gap of 3.51 eV (353 nm) (B2), which is near the band gap obtained for the powder (3.44 eV). Recall that to correctly estimate the band gap, the film's thickness must be "infinite" and that is not the case. The interference of the Corning glass substrate on the diffuse reflectance measurement is large, since it has a band gap of 4.06 eV (305 nm), which is slightly above that of the zinc sulfide film, leading to an apparent increase in the film's band gap.

The Raman spectrum acquired for this film is represented in Figure 4.8 (A), as well as the pictures taken to estimate the film's thickness (B).

The peaks at 274  $\text{cm}^{-1}$  and 355  $\text{cm}^{-1}$  belong to the cubic ZnS according to Cheng et al.[244] while the other peaks at larger wavenumbers are probably residual thiol, since the Raman spectrum obtained by Gawai et al.[355] does not present any significant peaks up to 800  $\text{cm}^{-1}$ . The large background seen results from the luminescence of the material.

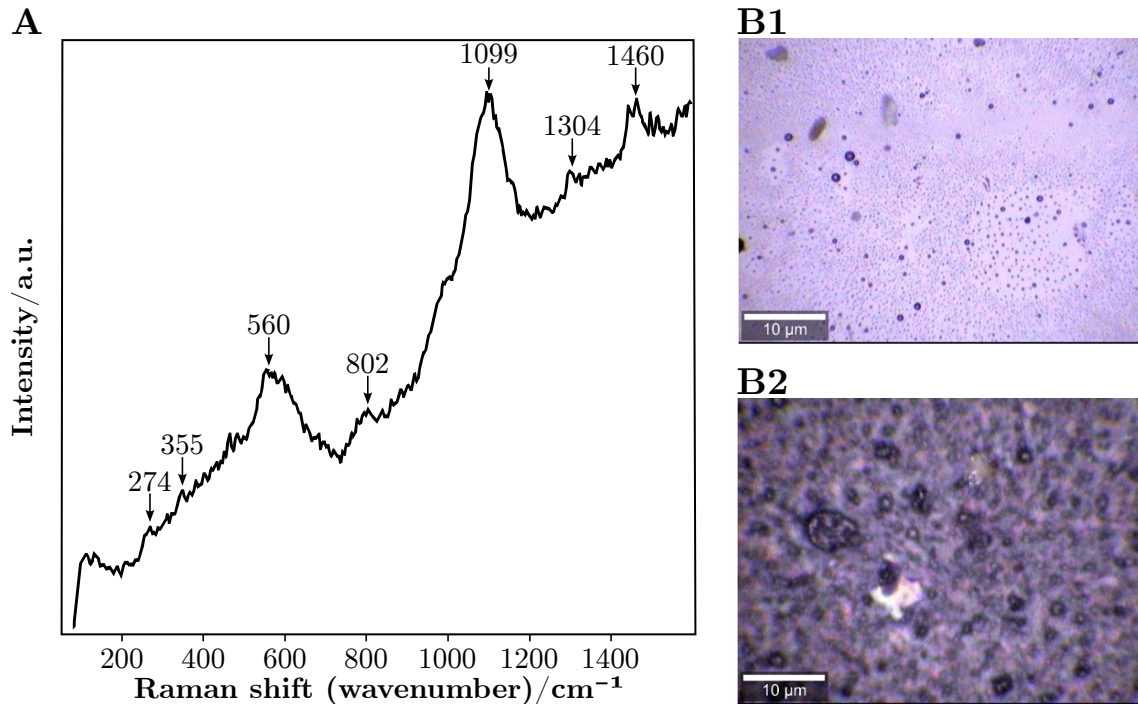


Figure 4.8: Raman spectrum (A) and two microscope images, one focused on the substrate's surface (B1) and another on the film's surface (B2), of the film obtained by spray from the zinc sulfide ink. The scale bars are 10  $\mu\text{m}$  in (B1) and (B2).

The conductivity of the  $\sim 6 \mu\text{m}$  film was measured by applying two silver contacts, each approximately with a length 5 mm and both 1 mm apart, and was estimated to be  $3.1 \times 10^{-6} \text{ S/m}$ . The expected conductivity value for a 6  $\mu\text{m}$  thick film of cubic ZnS prepared at 450  $^{\circ}\text{C}$  by spray pyrolysis of a methanol solution containing  $\text{ZnCl}_2$  and thiourea, is  $\sim 7 \times 10^{-4} \text{ S/m}$ . [356] The latter conductivity is higher since the deposition was performed at 450  $^{\circ}\text{C}$ , much higher than the one used in this work (200  $^{\circ}\text{C}$ ), and could have led to the annealing of the material.

A  $\sim 6 \mu\text{m}$  thick film of zinc sulfide nanoparticles was successfully obtained, with three ranges of aggregate sizes that conferred some light dispersion and an average transmittance of 25% in the visible region, which is not yet ideal for an ultra-violet light absorber upper layer that allows visible and infrared light to pass. After deposition, the material kept the band gap (3.51 eV) characteristic of zinc sulfide, and a conductivity of  $3.1 \times 10^{-6} \text{ S/m}$ .

#### 4.2.2.4 Niobium Sulfide Film

A niobium sulfide film was deposited by spray using the setup described previously in Figure 4.4 and both the synthesis, ink preparation, and deposition are detailed in Section A.4.3. The deposition was confined to an arbitrary 25x25 cm. A photograph, a microscope image with the particle count histogram, the transmittance and diffuse reflectance spectra and the Tauc plot are shown in Figure 4.9.

Some minutes after the deposition and turning off the heating, when the film was gradually cooling down on top of the hotplate, the film changed color from black to white quite rapidly. The picture in (A1) corresponds to the film after said transformation. Unlike the previous depositions,



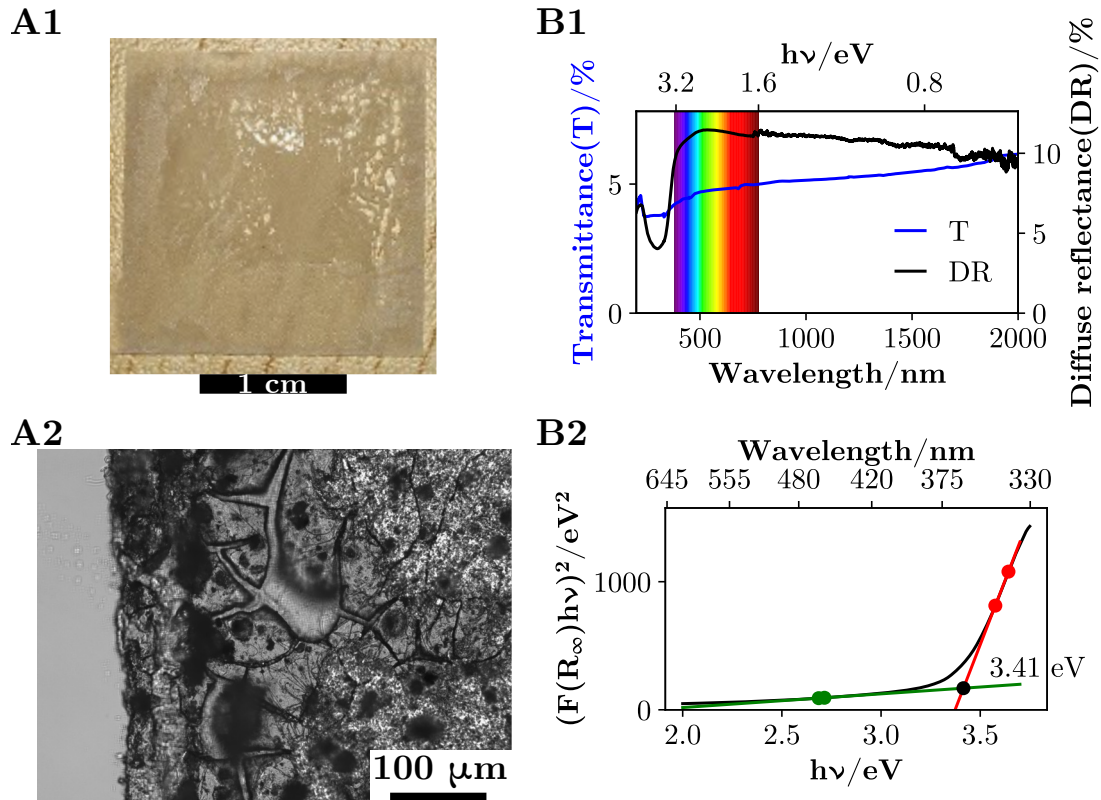


Figure 4.9: Photograph of the film of niobium sulfide deposited by spray (A1), microscopy image (A2), transmittance and diffuse reflectance spectra (B1), and Tauc plot (B2). The colored lines on the Tauc plot are the linear regressions used to estimate the band gap (black dot). The colored dots indicate the limits used to perform the regression. The scale bar is 1 cm in (A1) and 100  $\mu\text{m}$  in (A2).

the cracks in the microscope image (A2) indicate that the film was probably dense immediately after the deposition. But when it reacted with oxygen, due to the difference between the sulfides' (4.4 g/mL) and the oxide's (4.6 g/mL) densities, the rapid reaction led to the film's contraction and formation of cracks. These defects also contributed to the very low transmittance (B1), due to light dispersion, compared with the zinc sulfide film. The estimated band gap (B2) from the diffuse reflectance of the deposited film was 3.41 eV; it absorbs ultra-violet, but neither visible nor near-infrared are absorbed. The expected band gap of the film's material was to be either the hexagonal  $\text{NbS}_2$  or the monoclinic  $\text{NbS}_3$ , respectively 0 eV or 1.06 eV, if it was black. It was, however, within the expected for the white  $\text{Nb}_2\text{O}_5$  semiconductor's band gap, which is between 3.32 eV and 3.47 eV.[357] Like the sulfide of titanium (element from group 4), which slowly reacted with ambient oxygen at room temperature and turned into titanium dioxide, the sulfide of niobium (group 5) also readily reacts with oxygen, albeit it was at a higher temperature. During the deposition, specifically during the spray time, the sulfide was protected by the argon gas used to produce the spray. The rest period at 200 °C was not long enough to let the sulfide visibly transform into oxide. To obtain a niobium sulfide film, the spray deposition and cooling must be performed in a more controlled atmosphere. In this experiment, the deposited film was left cooling in the presence of ambient air and the oxygen oxidized the material, leading to the

formation of niobium oxide.

The Raman spectrum acquired for this film is represented in Figure 4.10 (A), as well as the pictures taken to estimate the film's thickness (B).

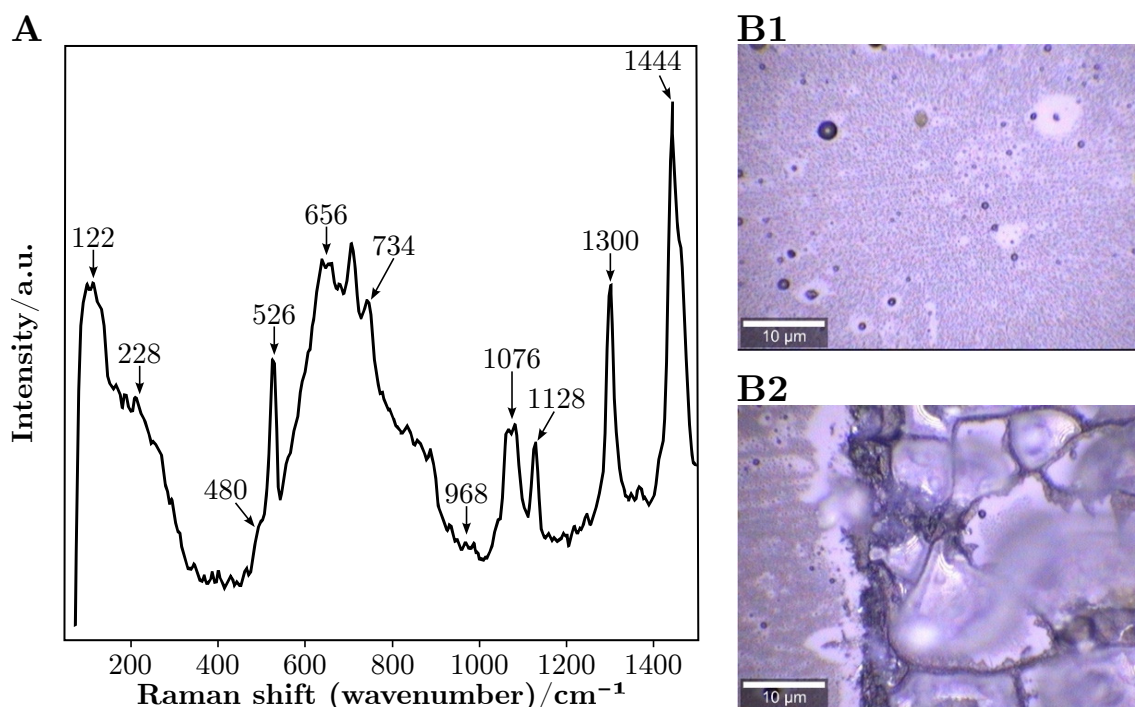


Figure 4.10: Raman spectrum (A) and two microscope images, one focused on the substrate's surface (B1) and another on the film's surface (B2), of the film obtained by spray from the niobium sulfide ink. The scale bars are 10  $\mu\text{m}$  in (B1) and (B2).

The Raman peaks at lower wavenumbers match those reported by Skrodczky et al.[211] for the Nb<sub>2</sub>O<sub>5</sub>. Like the ZnS Raman spectrum at higher wavenumbers, the Nb<sub>2</sub>O<sub>5</sub> film also presents some contamination due to the remaining thiol.

The conductivity of the  $\sim 11 \mu\text{m}$  thick film was measured by applying two silver contacts, each approximately with a length 5 mm and both 1 mm apart, and was estimated to be  $3.1 \times 10^{-6} \text{ S/m}$ . The expected conductivity value for a 450 nm thick film of Nb<sub>2</sub>O<sub>5</sub> prepared at 200 °C by spin-coating, is  $\sim 2 \times 10^{-4} \text{ S/m}$ . [358] The low conductivity can be justified by the lack of annealing and it resulted from a transformation from the sulfide to the oxide, which inevitably forms cracks as the ones seen in Figure 4.9 (A2) and Figure 4.10 (B2).

The niobium sulfide nanoparticle were successfully sprayed onto a glass substrate but the material converted into the oxide Nb<sub>2</sub>O<sub>5</sub> as it cooled down. The final film had a thickness of  $\sim 11 \mu\text{m}$  with a very heterogeneous texture and white color, a band gap of 3.41 eV, and a conductivity of  $3.1 \times 10^{-6} \text{ S/m}$ . Niobium sulfide proved to be less stable than the other deposited metal sulfides.

#### 4.2.2.5 Copper Iron Sulfide Film

A copper iron sulfide film was deposited by spray using the setup described previously in Figure 4.4 and both the synthesis, ink preparation, and deposition are detailed in Section A.4.4. The deposition was confined to an arbitrary 25x25 cm. A photograph, a microscope image with

the particle count histogram, the transmittance and diffuse reflectance spectra and the Tauc plot are shown in Figure 4.11.

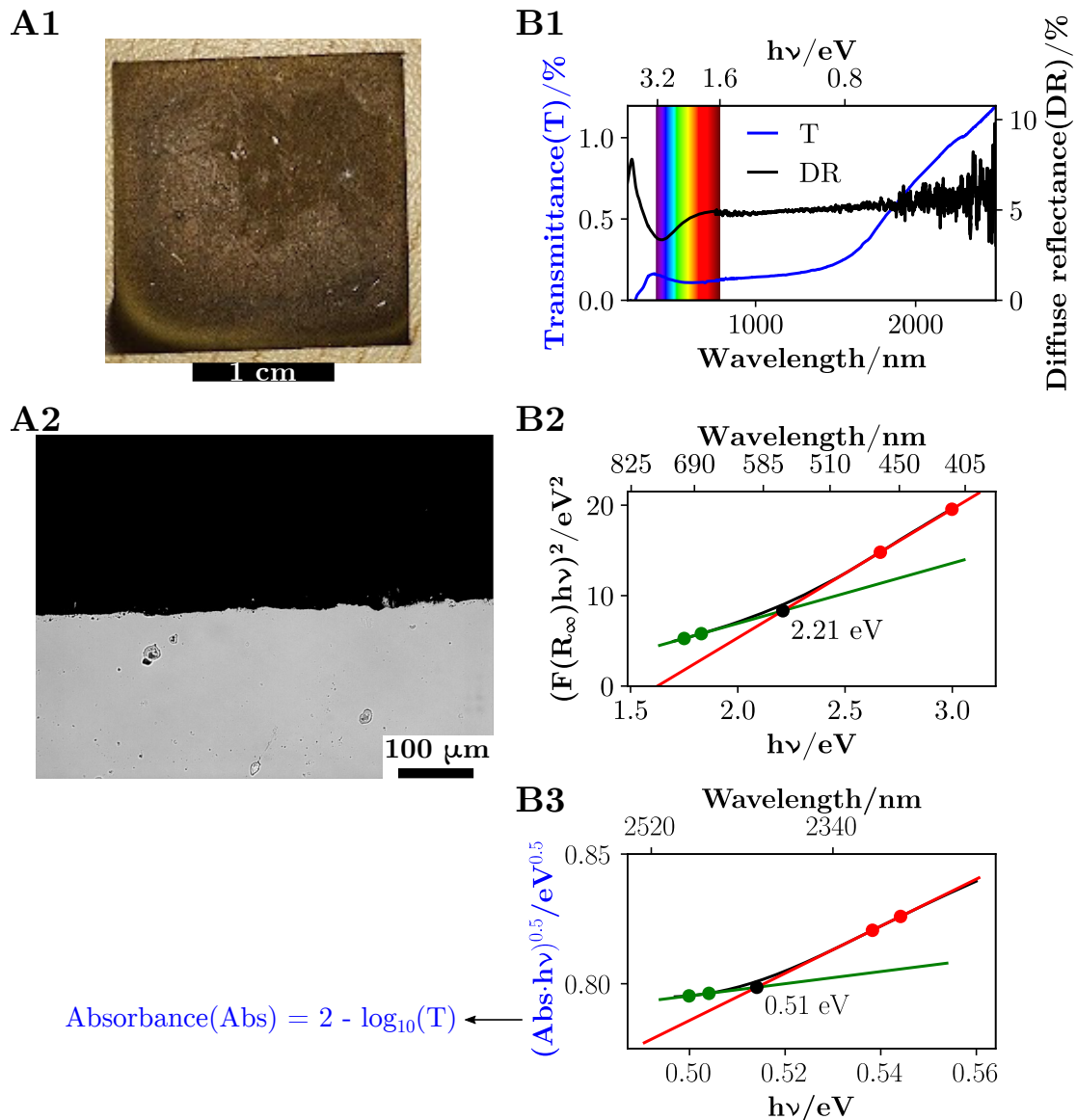


Figure 4.11: Photograph of the film of copper iron sulfide deposited by spray (A1), microscopy image (A2), transmittance and diffuse reflectance spectra (B1), and Tauc plots estimated from the diffuse reflectance spectrum (B2) and the transmittance spectrum (B3). The colored lines on the Tauc plot are the linear regressions used to estimate the band gap (black dot). The colored dots indicate the limits used to perform the regression. The scale bar is 1 cm in (A1) and 100  $\mu\text{m}$  in (A2).

The deposited film presented a heterogeneous texture (A1) with some color variation from dark brown to dark yellow and black, especially in the lower left corner, which resulted from the accumulation of ink at the overlapping zone of the perpendicular polyimide tapes. The yellow luster, similar to that of pyrite ( $\text{FeS}_2$ ) and also known as "fool's gold", is characteristic of  $\text{CuFeS}_2$ . No holes are visible in the microscope image (A2), indicating that the film is dense. Also, notice that the film's transmittance (B1) below 1500 nm is extremely small (below 0.5%), as well as the diffuse reflectance over the whole spectrum, indicating that the film absorbs the majority of



the light, as seen in Figure A.18 in the Appendix A, which contains the total reflectance and absorption of the film.

A value of 2.21 eV was determined from the diffuse reflectance spectrum using the Kubelka-Munk method. However, according to other reports, this absorption is in fact a surface plasmon absorption band, usually centered at 2.4 eV[359], resulting from the movement of the electrons in the conduction band that form a dipole when light passes and attenuates it.[360] A second band gap of indirect nature with a value of 0.51 eV was calculated from the absorbance spectrum, obtained from the transmittance spectrum, using the Tauc method. This lower band gap was determined at the limit of the sensor of the spectrophotometer and should only be considered qualitatively. Unfortunately, the synthesized powder from Section 3.3.1.1 was insufficient to measure the diffuse spectrum, and no comparison was possible.

The Raman spectrum acquired for this film is represented in Figure 4.12 (A), as well as the pictures taken to estimate the film's thickness (B).

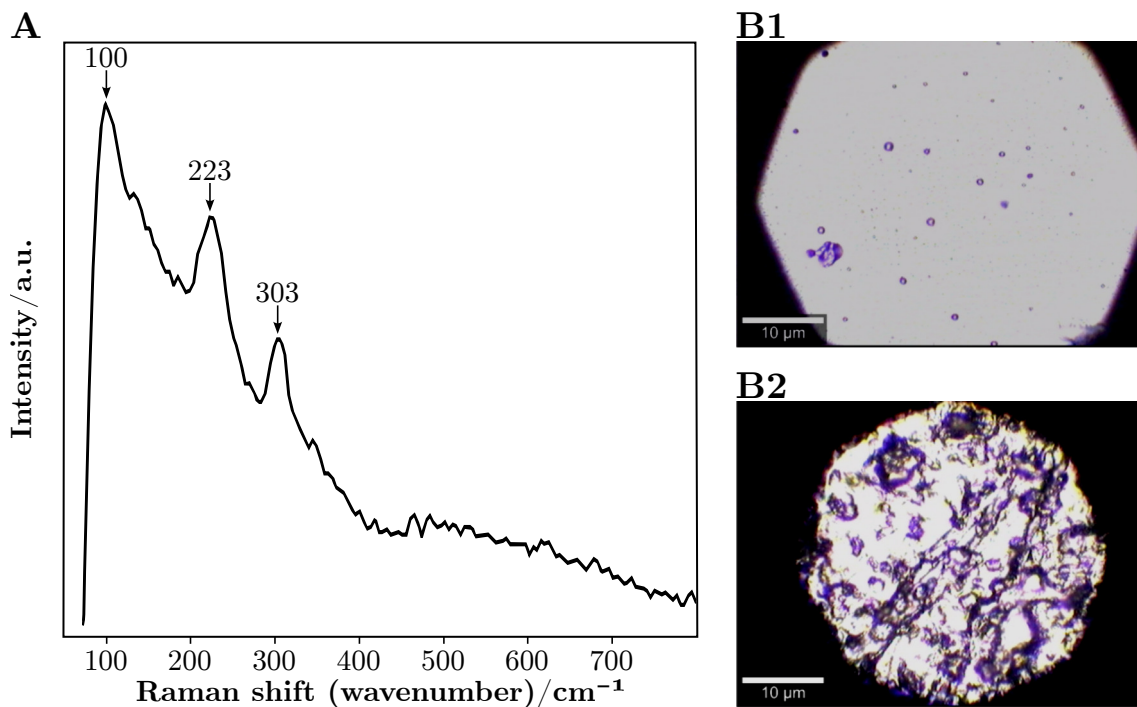


Figure 4.12: Raman spectrum (A) and two microscope images, one focused on the substrate's surface (B1) and another on the film's surface (B2), of the film obtained by spray from the copper iron sulfide ink. The scale bars are 10  $\mu\text{m}$  in (B1) and (B2).

In the obtained Raman spectrum, the only peak that matches the typical for the  $\text{CuFeS}_2$  is at  $303\text{ cm}^{-1}$  but the ones at lower wavenumbers do not belong to  $\text{CuFeS}_2$ , since it is flat in that region.[361] As pointed by Xi et al.[362]  $\text{CuFeS}_2$  can convert to hematite ( $\text{Fe}_2\text{O}_3$ ) when subjected to the heat produced from the laser. Since hematite is known to have a band gap of 2.1 eV[363], and the obtained band gap of the deposited film was 2.21 eV, the deposited  $\text{CuFeS}_2$  could have also been converted to hematite during the deposition, under the influence of the heat. The conductivity of the  $\sim 6\text{ }\mu\text{m}$  thick film was measured by applying two silver contacts, each approximately with a length 5 mm and both 1 mm apart, and was estimated to be  $1.7 \times 10^{-5}\text{ S/m}$ .

This value is considered low, according to the measurement obtained by Xie et al.[364] for a fully densified bulk  $\text{CuFeS}_2$ , sintered at  $550\text{ }^\circ\text{C}$ , with a conductivity of  $\sim 4 \times 10^3\text{ S/m}$ . The film deposited in this work was not annealed, which justifies the low conductivity. The measured Seebeck value was  $-223\text{ }\mu\text{V/K}$ , which is within the expected for this material ( $\sim 215\text{ }\mu\text{V/K}$ ).

A copper iron sulfide was successfully sprayed onto a glass substrate, producing a  $\sim 6\text{ }\mu\text{m}$  film with a heterogeneous texture and color, from black to dark yellow, a band gap of  $0.51\text{ eV}$  and a plasmonic band at  $2.21\text{ eV}$ , and a conductivity of  $1.7 \times 10^{-5}\text{ S/m}$  and a Seebeck value of  $-223\text{ }\mu\text{V/K}$ . The band at  $2.21\text{ eV}$  could also result from the hematite that was observed in the Raman spectrum of the film, resulting from the thermal degradation of  $\text{CuFeS}_2$ .

### 4.2.3 Resume

Unlike the slot-die cast deposition method, spray easily yielded dense films but with a large size distribution of particle aggregates. The spray method was therefore the chosen deposition technique.

As the zinc sulfide film revealed, the surface is not smooth due to the large size distribution of the deposited aggregates. Particles as small as 1 micrometer composed the overall film, but clumps with 50 to 80 micrometers and, in a smaller proportion, larger clumps with 200 to 400 micrometers could be seen. On the other materials, since they are black due to their band gap in the near-infrared region, it was impossible to see the aggregates' sizes. However, the deposition method was consistent between materials, and the aggregates sizes should be similar. Future analysis using a profilometer and SEM imaging should be performed to refine the spray method further and obtain smaller aggregates, decreasing light dispersion over the whole spectrum and increasing the transparency below the band gap. The band gaps of the powders matched those obtained from the deposited films at 200 °C, except for niobium sulfide, which probably converted to oxide. This was confirmed by Raman spectroscopy, which revealed that the composition was indeed  $\text{Nb}_2\text{O}_5$ , while for the others the sulfide was retained. The copper iron sulfide film also revealed to contain an iron oxide phase (hematite) which formed by thermal degradation of the sulfide. One attempted solution was to divide the argon flux into two: one route to the airbrush and another pointing at the film with a constant stream of argon to protect it from the ambient oxygen. However, even after attempting to decrease the flux from the protective curtain of argon, the deposited films were grossly heterogeneous. Therefore, a solvent with a lower boiling temperature and higher vapor pressure, such as chloroform or carbon disulfide, should be paired with a lower deposition temperature to prevent unwanted oxidation. The overall conductivities of the films were very low due to the low temperature used during the deposition, which did not permit the annealing of the grains. In future depositions, a piezoelectric device coupled to the airbrush's tip should be considered to produce ultrasounds that could break the droplets into extremely small droplets. These smaller droplets would result in a smoother, more transparent film, below the band gap, with less light dispersion. As for the thiol contamination seen in the zinc sulfide and niobium oxide films, instead of leaving the slurry dry by gravity for 1 hour, they should be left drying for a longer period of time.



## Conclusions and Future Perspectives

The initial proposal of this work was to develop a synthesis and deposition protocol, as well as obtain a library of metal sulfide nanoparticles, using readily available, abundant, and cheap elements, with the required band gaps to cover the full solar spectrum. To achieve this, a synthesis control was necessary by defining the synthesis parameters, such as the time, temperature, reagent choice, and concentration to achieve the desired material's size, morphology, phase, and optical properties. To prevent waste and achieve some degree of sustainability, the solvent's recovery, its reutilization in the following syntheses, and characterization of the obtained powders was desirable. The final step was to obtain a stable ink with the synthesized nanoparticles and deposit them as a film to evaluate their optical performance.

A systematic approach to synthesizing metal sulfide nanomaterials, using 1-dodecanethiol as a sulfur source, solvent, and stabilization agent was presented in this work. This alkyl thiol proved to be a simple mean to obtain the metal sulfide nanoparticles, due to its high boiling point and high temperature of decomposition. Throughout the majority of the syntheses performed, a sharp transition from a colored complex, formed between the thiol and the metal cation, to a black precipitate could be seen, signaling the formation of the metal sulfide, similarly to the hot-injection synthesis method. Some exceptions, such as the synthesis involving the zinc cation which resulted in a white precipitate, due to the large band gap of zinc sulfide, or the yellow precipitate obtained from the synthesis involving a precursor with indium. These transformations were registered through the recording of a video during the synthesis, which was later processed by a Python 3 script developed in this work and outputted a color profile containing the average color of the pixels from each of the video's frames. With this information, as well as the registered temperature, microwave power and pressure, it was possible to understand the various steps that occurred during the synthesis and achieve a better synthesis control. Some metal cations and some anions were prone to lead to the formation of electric arcs during the syntheses, such as those that belong to the periodic table's groups 5 (Nb and Ta), group 8 (Fe and Ru), group 9 (Co) and Cu from group 10. Regarding the anions, the nitrates and the chlorides usually provoked a large rise in pressure and eventually develop electric arcs. There were some cation and anion combinations that were safe to use, such as copper(I) iodide and silver(I) nitrate, which indicates that for every cation, there is an anion that allows the synthesis to proceed safely. Regarding the properties of the final product, the choice of the reagent did not have a significant impact. For example, the same mixture of two copper sulfides were obtained, regardless of the precursor chosen, with the exception of the triflate salt, which resulted in solely one of the copper sulfides. Of the two temperature control methods available in the microwave reactor, the automated mode achieved a higher reproducibility regarding the temperature profiles between syntheses. The constant power mode at a higher power input lead to completely different temperature profiles between replicas.

---

However, at a power of 20 W the temperature profiles were similar, it was possible to obtain some metal sulfides, and it was possible to see exothermic reactions occurring due to an abnormal increase in temperature. This effect was obscured by the automated temperature control that decreased the microwave power in those moments to maintain a steady temperature ramp. Light had an impact on the synthesis product when light-sensitive precursors were used. Silver salts yielded smaller particles in the presence of light, when compared to the material synthesized in the dark. Finally, the effect of the precursor concentration was determinant to obtain stable metal sulfide nanoparticle inks. The original synthesis protocol developed used a concentration of 1 mmol of precursor in 5 g of thiol, which led to the formation of a precipitate that did not easily suspend, especially after being cleaned and dried. A modification to the concentration, setting it to 0.1 mmol of precursor in 15 g of thiol, and to the cleaning procedure led to a stable colloid after the addition of isopropanol. Lower concentrations also allowed to capture the color of the complexes formed between the metal cation and 1-dodecanethiol, especially for the syntheses that resulted in the formation of a black material. Since the thiol is a poor microwave absorber, the majority of the syntheses required less energy input to achieve a higher temperature when higher concentrations of precursors were used, which are more efficient at absorbing the radiation. Using the formulated metal sulfide nanoparticle ink in slot die coating, where the isopropanol was added to the nanoparticle slurry and the mixture was submitted to ultrasounds for 5 minutes in an ultrasound bath, resulted in films in poor conditions, such as incomplete surface coverage. The ink formulation used was inadequate for the technique, which requires a thicker ink that prevents the formation of material islands. As an alternative to the slot-die coating deposition, tin sulfide, zinc sulfide, niobium sulfide and copper iron sulfide nanoparticles were deposited by spray, onto the preheated substrate, and micrometer thick films were obtained. Under the optical microscope, the films appeared to be percolating with no holes. However, after the deposition of the ink containing niobium sulfide, the film's exposure to ambient oxygen led to a complete and fast change of the film's color from black to white, indicating that the metal sulfide was not stable at a mild temperature. Throughout the deposition, the color of the film remained black, since the medium used to create the spray was an inert gas, which protected the material temporarily. Overall, the methods developed and the results obtained in this work establish a primary foundation for a general approach to synthesize practically any metal sulfide, including the more complex alloys containing multiple metals. A library of metal sulfides nanoparticles with diverse band gaps was obtained, with materials capable of light from the infrared to the ultraviolet. The metal elements used to synthesize the sulfides are readily available, abundant, and cheap, and in terms of sustainability, the reutilization of the solvent was successfully demonstrated. The formulated inks containing the fabricated nanomaterials were deposited by spray and the films obtained were deemed suitable to build or integrate them in devices in future work, as they retained their original properties.

## Research Impact

The following sections display a summary of the relevant articles published in peer-reviewed journals, oral presentations, and posters, ordered by year. Each item is followed by a brief explanation of my participation in the work.

### 6.1 Main Publications

- **David Sousa**, Luís Cerqueira Alves, Ana Marques, Guilherme Gaspar, João Carlos Lima, Isabel Ferreira, (2018). Facile Microwave-assisted Synthesis Manganese Doped Zinc Sulfide Nanoparticles. *Science Reports*, 8(15992). DOI: 10.1038/s41598-018-34268-z
  - Zinc sulfide nanoparticle synthesis, manganese doping control, characterizations, and article writing, excluding the particle-induced X-ray emission part.
- **David Sousa**, William Chiappim, Joaquim Pratas Leitão, João Carlos Lima, Isabel Ferreira, (2020). Microwave Synthesis of Silver Sulfide and Silver Nanoparticles: Light and Time Influence. *ACS Omega*, 5(22), 12877–12881. DOI: 10.1021/acsomega.0c00656
  - Silver sulfide light and time controlled nanoparticle synthesis and article writing, except the photoluminescence part.
- Beatriz Matos, Marta Martins, Antonio Cid Samamed, **David Sousa**, Isabel Ferreira, Mário Sousa Diniz, (2020). Toxicity evaluation of quantum dots (ZnS and CdS) singly and combined in Zebrafish (*Danio rerio*). *International Journal of Environmental Research and Public Health*, 17(1), 1–18. DOI: 10.3390/ijerph17010232
  - Fabrication and post-synthesis characterization of zinc sulfide and cadmium sulfide nanoparticles and writing of the corresponding experimental part.
- **David Sousa**, João Carlos Lima, Isabel Ferreira, (2020) Image Recording and Processing Chemical Synthesis: Method Description and Demonstration. *Chemistry–Methods*. DOI: 10.1002/cmt.d.202000043
  - Zinc sulfide and silver sulfide synthesis, python script development, examples processing, color profile analysis, and article writing.

### 6.2 Other Publications

- **David Sousa**, João Carlos Lima, Isabel Ferreira, (2017). Synthesis of Cadmium Selenide Quantum Dots, Using 2,2-Bipyridine as a Capping and Phase Transfer Agent. *ChemistryS-*

elect, 2(3), 1271–1274. DOI: 10.1002/slet.201601804

- Cadmium selenide nanoparticle synthesis and phase transfer process to 2,2-bipyridine, absorbance, emission, and transmission electron microscopy images analysis and article writing.
- Ana Filipa Cristovão, **David Sousa**, Filipe Silvestre, Inês Ropio, Ana Gaspar, Célia Henriques, Alexandre Velhinho, Ana Catarina Baptista, Miguel Faustino, Isabel Ferreira (2019). Customized tracheal design using 3D printing of a polymer hydrogel: influence of UV laser cross-linking on mechanical properties. *3D Printing in Medicine*, 5(1). DOI: 10.1186/s41205-019-0049-8
  - Participated in the preparation and optimization of the poly(ethylene glycol diacrylate) cross-linkable gel-like ink for posterior 3D printing.
- Ana Claudia Marques, Davide Miglietta, Guilherme Gaspar, Ana Catarina Baptista, Ana Gaspar, Patrícia Perdigão, Iris Soares, Catarina Bianchi, **David Sousa**, Bruno Miguel Morais Faustino, Vitor Sequeira Amaral, Teresa Santos, António Pereira Gonçalves, Rui Coelho da Silva, Fabrizio Giorgis, Isabel Ferreira (2019). Synthesis of thermoelectric magnesium-silicide pastes for 3D printing, electrospinning and low-pressure spray. *Materials for Renewable and Sustainable Energy*, 8(4). DOI: 10.1007/s40243-019-0159-7
  - Participated in the development of the magnesium-silicide paste ink for posterior 3D printing.
- Diogo Mendes, **David Sousa**, Ana Cláudia Cerdeira, Laura Cristina de Jesus Pereira, Ana Marques, João Murta-Pina, Anabela Pronto, Isabel Ferreira, (2021). Low-cost and high-performance 3D printed YBCO superconductors. *Ceramics International*, 47(1), 381-387. DOI: 10.1016/j.ceramint.2020.08.143
  - Participated on the development of both paste ink for posterior 3D printing.
- Harold Moreno Fernández, Marcel Himmerlich, Pedro Costa-Pinto, João Coroa, **David Sousa**, Adrienn Baris, Mauro Taborelli, (2021). The impact of H<sub>2</sub> and N<sub>2</sub> on the material properties and secondary electron yield of sputtered amorphous carbon films for anti-multipacting applications. *Applied Surface Science*, 542, 148552. DOI: j.apsusc.2020.148552
  - Acquisition of transmittance spectra, determination of the band gaps of the carbon films, and writing of the corresponding experimental part of the article.

### 6.3 Oral Presentation

- **David Sousa**, Luís Cerqueira Alves, Ana Marques, Guilherme Gaspar, João Carlos Lima, Isabel Ferreira. Down conversion on manganese doped zinc sulfide nanoparticles. Oral



presented at: MATERIAIS 2019 - XIX Congresso da Sociedade Portuguesa de Materiais and X International Symposium on Materials. Lisbon, PT **2019**.

## 6.4 Posters

- Diogo Mendes, **David Sousa**, João Murta-Pina, Anabela Pronto, Isabel Ferreira. Superconducting materials by 3D printing. Poster presented at: MATERIAIS 2019 - XIX Congresso da Sociedade Portuguesa de Materiais and X International Symposium on Materials. Lisbon, PT **2019**.
- **David Sousa**, João Carlos Lima, Isabel Ferreira. Recording Material Synthesis Images and Processing with a Script for Data Visualization. Poster presented at 6th ed. of Nanotech France 2021 International Conference and Exhibition. (Online) Paris, FR **2021**.



## Bibliography

- [1] A. Al-Ashouri, E. Köhnen, B. Li, A. Magomedov, H. Hempel, P. Caprioglio, J. A. Márquez, A. B. Morales Vilches, E. Kasparavicius, J. A. Smith, N. Phung, D. Menzel, M. Grischek, L. Kegelmann, D. Skroblin, C. Gollwitzer, T. Malinauskas, M. Jošt, G. Matič, B. Rech, R. Schlatmann, M. Topič, L. Korte, A. Abate, B. Stannowski, D. Neher, M. Stolterfoht, T. Unold, V. Getautis, and S. Albrecht, “Monolithic perovskite/silicon tandem solar cell with >29% efficiency by enhanced hole extraction,” *Science*, vol. 370, no. 6522, pp. 1300–1309, **2020**. DOI: 10.1126/science.abd4016.
- [2] O. Burkacky, M. de Jong, A. Mittal, and N. Verma, “Value creation: How can the semiconductor industry keep outperforming?” McKinsey & Company, Tech. Rep., 2021.
- [3] K Schwab, *The Fourth Industrial Revolution*. Geneva: World Economic Forum, **2016**, ISBN: 9781944835002.
- [4] “I. Experimental researches in electricity. —fifteenth series,” *Philosophical Transactions of the Royal Society of London*, vol. 129, pp. 1–12, **1839**. DOI: 10.1098/rstl.1839.0002.
- [5] G Busch, “Early history of the physics and chemistry of semiconductors—from doubts to fact in a hundred years,” *European Journal of Physics*, vol. 10, no. 4, pp. 254–264, **1989**. DOI: 10.1088/0143-0807/10/4/002.
- [6] C. E. Fritts, “On a new form of selenium cell, and some electrical discoveries made by its use,” *American Journal of Science*, vol. s3-26, no. 156, pp. 465–472, **1883**. DOI: 10.2475/ajs.s3-26.156.465.
- [7] J. Jeevanandam, A. Barhoum, Y. S. Chan, A. Dufresne, and M. K. Danquah, “Review on nanoparticles and nanostructured materials: History, sources, toxicity and regulations,” *Beilstein Journal of Nanotechnology*, vol. 9, no. 1, pp. 1050–1074, **2018**. DOI: 10.3762/bjnano.9.98.
- [8] F. T. Rabouw and C. de Mello Donega, “Excited-State Dynamics in Colloidal Semiconductor Nanocrystals,” *Topics in Current Chemistry*, vol. 374, no. 5, p. 58, **2016**. DOI: 10.1007/s41061-016-0060-0.
- [9] V. Guidi, B. Fabbri, A. Gaiardo, S. Gherardi, A. Giberti, C. Malagù, G. Zonta, and P. Bellutti, “Metal sulfides as a new class of sensing materials,” *Procedia Engineering*, vol. 120, pp. 138–141, **2015**. DOI: 10.1016/j.proeng.2015.08.586.
- [10] X. Rui, H. Tan, and Q. Yan, “Nanostructured metal sulfides for energy storage,” *Nanoscale*, vol. 6, no. 17, p. 9889, **2014**. DOI: 10.1039/C4NR03057E.
- [11] T. Yu, F. Li, C. Liu, S. Zhang, H. Xu, and G. Yang, “Understanding the role of lithium sulfide clusters in lithium-sulfur batteries,” *J. Mater. Chem. A*, vol. 5, no. 19, pp. 9293–9298, **2017**. DOI: 10.1039/C7TA01006K.
- [12] P. F. Smet, I. Moreels, Z. Hens, and D. Poelman, “Luminescence in sulfides: A rich history and a bright future,” *Materials*, vol. 3, no. 4, pp. 2834–2883, **2010**. DOI: 10.3390/ma3042834.
- [13] N. P. Dasgupta, X. Meng, J. W. Elam, and A. B. F. Martinson, “Atomic Layer Deposition of Metal Sulfide Materials,” *Accounts of Chemical Research*, vol. 48, no. 2, pp. 341–348, **2015**. DOI: 10.1021/ar500360d.
- [14] S. I. Sadovnikov, N. S. Kozhevnikova, and A. I. Gusev, “Optical properties of nanostructured lead sulfide films with a D03 cubic structure,” *Semiconductors*, vol. 45, no. 12, pp. 1559–1570, **2011**. DOI: 10.1134/S1063782611120116.

- [15] C. Xia, W. Wu, T. Yu, X. Xie, C. van Oversteeg, H. C. Gerritsen, and C. de Mello Donega, "Size-Dependent Band-Gap and Molar Absorption Coefficients of Colloidal CuInS<sub>2</sub> Quantum Dots," *ACS Nano*, vol. 12, no. 8, pp. 8350–8361, **2018**. DOI: 10.1021/acsnano.8b03641.
- [16] S. I. Sadovnikov, A. V. Ishchenko, and I. A. Weinstein, "Synthesis and optical properties of nanostructured ZnS and heteronanostructures based on zinc and silver sulfides," *Journal of Alloys and Compounds*, vol. 831, p. 154 846, **2020**. DOI: 10.1016/j.jallcom.2020.154846.
- [17] R. Woods-Robinson, Y. Han, H. Zhang, T. Ablekim, I. Khan, K. A. Persson, and A. Zakutayev, "Wide Band Gap Chalcogenide Semiconductors," *Chemical Reviews*, vol. 120, no. 9, pp. 4007–4055, **2020**. DOI: 10.1021/acs.chemrev.9b00600. arXiv: 1910.08153.
- [18] C. Battaglia, A. Cuevas, and S. De Wolf, "High-efficiency crystalline silicon solar cells: status and perspectives," *Energy Environ. Sci.*, vol. 9, no. 5, pp. 1552–1576, **2016**. DOI: 10.1039/C5EE03380B.
- [19] A. Blakers, N. Zin, K. R. McIntosh, and K. Fong, "High Efficiency Silicon Solar Cells," *Energy Procedia*, vol. 33, pp. 1–10, **2013**. DOI: 10.1016/j.egypro.2013.05.033.
- [20] A. W. Bett, S. P. Philipps, S. S. Essig, S. Heckelmann, R. Kellenbenz, V. Klinger, M. Niemeyer, D. Lackner, and F. Dimroth, "Overview about technology perspectives for high efficiency solar cells for space and terrestrial applications," *28th European Photovoltaic Solar Energy Conference and Exhibition*, vol. 0, pp. 1–6, **2013**. DOI: 10.4229/28thEUPVSEC2013-1AP.1.1.
- [21] A. P. Kirk, *Solar Photovoltaic Cells: Photons to Electricity*, 1st. Elsevier Science, **2014**, ISBN: 9780128026038.
- [22] H. Su, X. Lin, Y. Wang, X. Liu, Z. Qin, Q. Shi, Q. Han, Y. Zhang, and L. Han, "Stable perovskite solar cells with 23.12area over 1 cm<sup>2</sup> by an all-in-one strategy," *Science China Chemistry*, vol. 65, no. 7, pp. 1321–1329, **2022**. DOI: 10.1007/s11426-022-1244-y.
- [23] E. Kobayashi, R. Tsuji, D. Martineau, A. Hinsch, and S. Ito, "Light-induced performance increase of carbon-based perovskite solar module for 20-year stability," *Cell Reports Physical Science*, p. 100 648, **2021**. DOI: 10.1016/j.xcrp.2021.100648.
- [24] A. Urbina, "The balance between efficiency, stability and environmental impacts in perovskite solar cells: a review," *Journal of Physics: Energy*, vol. 2, no. 2, p. 022 001, **2020**. DOI: 10.1088/2515-7655/ab5eee.
- [25] S. Shen and Q. Wang, "Rational tuning the optical properties of metal sulfide nanocrystals and their applications," *Chemistry of Materials*, vol. 25, no. 8, pp. 1166–1178, **2013**. DOI: 10.1021/cm302482d.
- [26] G. V. Gibbs, D. F. Cox, K. M. Rosso, N. L. Ross, R. T. Downs, and M. A. Spackman, "Theoretical electron density distributions for Fe- and Cu-sulfide earth materials: A connection between bond length, bond critical point properties, local energy densities, and bonded interactions," *Journal of Physical Chemistry B*, vol. 111, no. 8, pp. 1923–1931, **2007**. DOI: 10.1021/jp065086i.
- [27] Z. Grzesik and K. Przybylski, "Sulfidation of metallic materials," *Developments in High Temperature Corrosion and Protection of Materials*, Cambridge (UK), England Boca Raton (USA): Woodhead Pub. and Maney Pub. on behalf of the Institute of Materials, Minerals & Mining CRC Press, **2008**, ch. 20, pp. 599–638, ISBN: 9781845692193. DOI: 10.1533/9781845694258.3.599.
- [28] W. Feng, W. Pang, Y. Xu, A. Guo, X. Gao, X. Qiu, and W. Chen, "Transition Metal Selenides for Electrocatalytic Hydrogen Evolution Reaction," *ChemElectroChem*, vol. 7, no. 1, pp. 31–54, **2020**. DOI: 10.1002/celec.201901623.

- [29] R. Yousefi, "Metal-Selenide Nanostructures: Growth and Properties," *Metal Chalcogenide Nanostructures for Renewable Energy Applications*, Hoboken, NJ, USA: John Wiley & Sons, Inc., **2014**, pp. 43–81. DOI: 10.1002/9781119008934.ch4.
- [30] P. Zhao, F. Yu, B. Wang, H. Zhao, C. Chen, D. Wang, P. Ying, Y. Wu, P. Li, B. Zhang, B. Liu, Z. Zhao, W. Hu, D. Yu, J. He, Z. Liu, B. Xu, and Y. Tian, "Porous bismuth antimony telluride alloys with excellent thermoelectric and mechanical properties," *Journal of Materials Chemistry A*, vol. 9, no. 8, pp. 4990–4999, **2021**. DOI: 10.1039/D0TA09795K.
- [31] M.-Y. Lee, D. I. Bilc, E. Symeou, Y.-C. Lin, I.-C. Liang, T. Kyratsi, and K.-F. Hsu, "Synthesis, crystal structure and thermoelectric properties of a new metal telluride Ba<sub>3</sub>Ag<sub>3</sub>InTe<sub>6</sub>," *Inorganic Chemistry Frontiers*, vol. 4, no. 9, pp. 1458–1464, **2017**. DOI: 10.1039/C7QI00210F.
- [32] M. Balys, E. Brodawka, A. Korzeniewska, J. Szczurowski, and K. Zarębska, "LCA and economic study on the local oxygen supply in Central Europe during the COVID-19 pandemic," *Science of The Total Environment*, vol. 786, p. 147401, **2021**. DOI: 10.1016/j.scitotenv.2021.147401.
- [33] *Sulfur Price and Market Analysis - ECHEMI*. [Online]. Available: <https://www.echemi.com/productsInformation/pd20160117132320976-sulfur.html> (visited on 2021).
- [34] *Top Quality Industrial Grade Yellow Powder Sulphur*. [Online]. Available: [https://www.alibaba.com/product-detail/Top-Quality-Industrial-Grade-Yellow-Powder\\_1947288914.html?spm=a2700.galleryofferlist.normal\\_offer.d\\_title.15426157a5ZQ3X](https://www.alibaba.com/product-detail/Top-Quality-Industrial-Grade-Yellow-Powder_1947288914.html?spm=a2700.galleryofferlist.normal_offer.d_title.15426157a5ZQ3X) (visited on 2021).
- [35] *Factory Price Sell High Purity Selenium Powder CAS 7782-49-2*. [Online]. Available: [https://www.alibaba.com/product-detail/Factory-Price-Sell-High-Purity-Selenium\\_1600334339511.html](https://www.alibaba.com/product-detail/Factory-Price-Sell-High-Purity-Selenium_1600334339511.html) (visited on 2021).
- [36] *Supplier High Quality for Factory Building Material Selenium Ingot*. [Online]. Available: <https://hdrfjs.en.made-in-china.com/product/XZzAsVCMMLUq/China-Supplier-High-Quality-for-Factory-Building-Material-Selenium-Ingot.html> (visited on 2021).
- [37] *Customized 0.5-2.0 Silver Grey And Round Partilces Tellurium Pellets/ Shots For Semiconductor*. [Online]. Available: [https://www.alibaba.com/product-detail/Customized-0-5-2-0-Silver\\_62426232685.html?spm=a2700.galleryofferlist.normal\\_offer.d\\_title.154d4d1e8ZMMRd](https://www.alibaba.com/product-detail/Customized-0-5-2-0-Silver_62426232685.html?spm=a2700.galleryofferlist.normal_offer.d_title.154d4d1e8ZMMRd) (visited on 2021).
- [38] W. contributors, *Prices of chemical elements*, **2021**. [Online]. Available: [https://en.wikipedia.org/w/index.php?title=Prices\\_of\\_chemical\\_elements&oldid=1026910770](https://en.wikipedia.org/w/index.php?title=Prices_of_chemical_elements&oldid=1026910770) (visited on 2021).
- [39] *The 90 natural elements that make up everything*, **2021**. [Online]. Available: <https://i2.wp.com/www.euchems.eu/wp-content/uploads/2021/11/Endangered-ElementsCarbon-Updated.png?ssl=1> (visited on 2021).
- [40] R. Kresse, U. Baudis, P. Jäger, H. H. Riechers, H. Wagner, J. Winkler, and H. U. Wolf, "Barium and Barium Compounds," *Ullmann's Encyclopedia of Industrial Chemistry*, Weinheim, Germany: Wiley-VCH Verlag GmbH & Co. KGaA, **2007**. DOI: 10.1002/14356007.a03\_325.pub2.
- [41] I. Sadeghi, K. Ye, M. Xu, Y. Li, J. M. LeBeau, and R. Jaramillo, "Making BaZrS<sub>3</sub> Chalcogenide Perovskite Thin Films by Molecular Beam Epitaxy," *Advanced Functional Materials*, vol. 31, no. 45, pp. 1–8, **2021**. DOI: 10.1002/adfm.202105563. arXiv: 2105.10258.
- [42] T. M. Project, "Materials Data on Ba<sub>2</sub>TiS<sub>4</sub> by Materials Project," DOI: 10.17188/1192766.
- [43] D. Zilevu and S. E. Creutz, "Shape-controlled synthesis of colloidal nanorods and nanoparticles of barium titanium sulfide," *Chemistry of Materials*, vol. 33, no. 13, pp. 5137–5146, **2021**. DOI: 10.1021/acs.chemmater.1c01193.

- [44] Y. T. Huang, S. R. Kavanagh, M. Righetto, M. Rusu, I. Levine, T. Unold, S. J. Zelewski, A. J. Sneyd, K. Zhang, L. Dai, A. J. Britton, J. Ye, J. Julin, M. Napari, Z. Zhang, J. Xiao, M. Laitinen, L. Torrente-Murciano, S. D. Stranks, A. Rao, L. M. Herz, D. O. Scanlon, A. Walsh, and R. L. Hoyer, "Strong absorption and ultrafast localisation in NaBiS<sub>2</sub> nanocrystals with slow charge-carrier recombination," *Nature communications*, vol. 13, no. 1, p. 4960, **2022**. DOI: 10.1038/s41467-022-32669-3.
- [45] T. Teranishi, "Magnetic and Electric Properties of Chalcopyrite," *Journal of the Physical Society of Japan*, vol. 16, no. 10, pp. 1881–1887, **1961**. DOI: 10.1143/JPSJ.16.1881.
- [46] I. G. Austin, C. H. L. Goodman, and A. E. Pengelly, "New Semiconductors with the Chalcopyrite Structure," *Journal of The Electrochemical Society*, vol. 103, no. 11, p. 609, **1956**. DOI: 10.1149/1.2430171.
- [47] J. L. Kaufman, J. Vinckevičiūtė, S. Krishna Kolli, J. Gabriel Goiri, and A. Van der Ven, "Understanding intercalation compounds for sodium-ion batteries and beyond," *Philosophical Transactions of the Royal Society A: Mathematical, Physical and Engineering Sciences*, vol. 377, no. 2152, p. 20190020, **2019**. DOI: 10.1098/rsta.2019.0020.
- [48] D. Mei, J. Jiang, F. Liang, S. Zhang, Y. Wu, C. Sun, D. Xue, and Z. Lin, "Design and synthesis of a nonlinear optical material BaAl<sub>4</sub>S<sub>7</sub> with a wide band gap inspired from SrB<sub>4</sub>O<sub>7</sub>," *Journal of Materials Chemistry C*, vol. 6, no. 11, pp. 2684–2689, **2018**. DOI: 10.1039/C7TC05693A.
- [49] A. Jabłoński, "Efficiency of Anti-Stokes Fluorescence in Dyes," *Nature*, vol. 131, pp. 839–840, **1933**. DOI: 10.1038/131839b0.
- [50] G. A. Jones and D. S. Bradshaw, "Resonance Energy Transfer: From Fundamental Theory to Recent Applications," *Frontiers in Physics*, vol. 7, no. JULY, pp. 1–19, **2019**. DOI: 10.3389/fphy.2019.00100.
- [51] D. L. Dexter, "A theory of sensitized luminescence in solids," *The Journal of Chemical Physics*, vol. 21, no. 5, pp. 836–850, **1953**. DOI: 10.1063/1.1699044.
- [52] S. S. Skourtis, C. Liu, P. Antoniou, A. M. Virshup, and D. N. Beratan, "Dexter Energy transfer pathways," *Proceedings of the National Academy of Sciences of the United States of America*, vol. 113, no. 29, pp. 8115–8120, **2016**. DOI: 10.1073/pnas.1517189113.
- [53] H. Seiler, M. Krynski, D. Zahn, S. Hammer, Y. W. Windsor, T. Vasileiadis, J. Pflaum, R. Ernstorfer, M. Rossi, and H. Schworer, "Nuclear dynamics of singlet exciton fission in pentacene single crystals," *Science Advances*, vol. 7, no. 26, pp. 1–10, **2021**. DOI: 10.1126/sciadv.abg0869.
- [54] G. G. Stokes, "On the Change of Refrangibility of Light," *Philosophical Transactions of the Royal Society of London*, vol. 142, pp. 463–562, **1852**.
- [55] M. A. R. B. Castanho, N. C. Santos, and L. M. S. Loura, "Separating the turbidity spectra of vesicles from the absorption spectra of membrane probes and other chromophores," *European Biophysics Journal*, vol. 26, no. 3, pp. 253–259, **1997**. DOI: 10.1007/s002490050078.
- [56] M. B. Smith and J. Michl, "Singlet Fission," *Chemical Reviews*, vol. 110, no. 11, pp. 6891–6936, **2010**. DOI: 10.1021/cr1002613.
- [57] C. Sutton, N. R. Tummala, D. Beljonne, and J. L. Brédas, "Singlet Fission in Rubrene Derivatives: Impact of Molecular Packing," *Chemistry of Materials*, vol. 29, no. 7, pp. 2777–2787, **2017**. DOI: 10.1021/acs.chemmater.6b04633.
- [58] J. Zhou, Q. Liu, W. Feng, Y. Sun, and F. Li, "Upconversion Luminescent Materials: Advances and Applications," *Chemical Reviews*, vol. 115, no. 1, pp. 395–465, **2015**. DOI: 10.1021/cr400478f.

- [59] K. Nesmerak, "Lanthanide/Actinide Toxicity," *Encyclopedia of Metalloproteins*, R. H. Kretsinger, V. N. Uversky, and E. A. Permyakov, Eds., New York, NY: Springer New York, **2013**, pp. 1098–1103, ISBN: 978-1-4614-1533-6. DOI: 10.1007/978-1-4614-1533-6\_151.
- [60] X. Wang, M. Yao, J. Li, K. Zhang, H. Zhu, and M. Zheng, "China's rare earths production forecasting and sustainable development policy Implications," *Sustainability (Switzerland)*, vol. 9, no. 6, **2017**. DOI: 10.3390/su9061003.
- [61] B. McLellan, G. Corder, A. Golev, and S. Ali, "Sustainability of the Rare Earths Industry," *Procedia Environmental Sciences*, vol. 20, pp. 280–287, **2014**. DOI: 10.1016/j.proenv.2014.03.035.
- [62] M. Mahboub, H. Maghsoudiganjeh, A. M. Pham, Z. Huang, and M. L. Tang, "Triplet Energy Transfer from PbS(Se) Nanocrystals to Rubrene: the Relationship between the Upconversion Quantum Yield and Size," *Advanced Functional Materials*, vol. 26, no. 33, pp. 6091–6097, **2016**. DOI: 10.1002/adfm.201505623.
- [63] N. Kiseleva, P. Nazari, C. Dee, D. Busko, B. S. Richards, M. Seitz, I. A. Howard, and A. Turshatov, "Lanthanide Sensitizers for Large Anti-Stokes Shift Near-Infrared-to-Visible Triplet-Triplet Annihilation Photon Upconversion," *The Journal of Physical Chemistry Letters*, vol. 11, no. 7, pp. 2477–2481, **2020**. DOI: 10.1021/acs.jpcclett.0c00221.
- [64] M. Montalti, A. Credi, L. Prodi, and M. T. Gandolfi, *Handbook of Photochemistry*, 3rd. Boca Raton: CRC Press, **2006**, ISBN: 9780429115387. DOI: 10.1201/9781420015195.
- [65] H. Liu, F. Yan, W. Li, C. S. Lee, B. Chu, Y. Chen, X. Li, L. Han, Z. Su, J. Zhu, X. Kong, L. Zhang, and Y. Luo, "Up-conversion luminescence of crystalline rubrene without any sensitizers," *Organic Electronics*, vol. 11, no. 5, pp. 946–950, **2010**. DOI: 10.1016/j.orgel.2010.01.018.
- [66] M. Wu, D. N. Congreve, M. W. B. Wilson, J. Jean, N. Geva, M. Welborn, T. Van Voorhis, V. Bulović, M. G. Bawendi, and M. A. Baldo, "Solid-state infrared-to-visible upconversion sensitized by colloidal nanocrystals," *Nature Photonics*, vol. 10, no. 1, pp. 31–34, **2015**. DOI: 10.1038/nphoton.2015.226.
- [67] E. Radiunas, S. Raišys, S. Juršėnas, A. Jozeliūnaitė, T. Javorskis, U. Šinkevičiūtė, E. Orentas, and K. Kazlauskas, "Understanding the limitations of NIR-to-visible photon up-conversion in phthalocyanine-sensitized rubrene systems," *Journal of Materials Chemistry C*, vol. 8, no. 16, pp. 5525–5534, **2020**. DOI: 10.1039/C9TC06031F.
- [68] Z. Huang, X. Li, M. Mahboub, K. M. Hanson, V. M. Nichols, H. Le, M. L. Tang, and C. J. Bardeen, "Hybrid Molecule-Nanocrystal Photon Upconversion Across the Visible and Near-Infrared," *Nano Letters*, vol. 15, no. 8, pp. 5552–5557, **2015**. DOI: 10.1021/acs.nanolett.5b02130.
- [69] F. Morgner, M. Bennemann, P. J. Cywiński, M. Kollosche, K. Górski, M. Pietraszkiewicz, A. Gefner, and H. G. Löhmannsröben, "Elastic FRET sensors for contactless pressure measurement," *RSC Advances*, vol. 7, no. 80, pp. 50 578–50 583, **2017**. DOI: 10.1039/c7ra06379b.
- [70] O. V. Oyelade, O. K. Oyewole, D. O. Oyewole, S. A. Adeniji, R. Ichwani, D. M. Sanni, and W. O. Soboyejo, "Pressure-Assisted Fabrication of Perovskite Solar Cells," *Scientific Reports*, vol. 10, no. 1, p. 7183, **2020**. DOI: 10.1038/s41598-020-64090-5.
- [71] S. Melle, O. G. Calderón, M. Laurenti, D. Mendez-Gonzalez, A. Egatz-Gómez, E. López-Cabarcos, E. Cabrera-Granado, E. Díaz, and J. Rubio-Retama, "Förster Resonance Energy Transfer Distance Dependence from Upconverting Nanoparticles to Quantum Dots," *Journal of Physical Chemistry C*, vol. 122, no. 32, pp. 18 751–18 758, **2018**. DOI: 10.1021/acs.jpcc.8b04908.

- [72] C. A. Clark, *Los Alamos-Based UbiQD Installs Quantum Dot Solar Window Pilots In Local Commercial Buildings*, **2021**. [Online]. Available: <https://ladailypost.com/los-alamos-based-ubiqd-installs-quantum-dot-solar-window-pilots-in-local-commercial-buildings/> (visited on 2021).
- [73] Z. Deng, L. Tong, M. Flores, S. Lin, J.-X. Cheng, H. Yan, and Y. Liu, "High-Quality Manganese-Doped Zinc Sulfide Quantum Rods with Tunable Dual-Color and Multiphoton Emissions," *Journal of the American Chemical Society*, vol. 133, no. 14, pp. 5389–5396, **2011**. DOI: 10.1021/ja110996c.
- [74] A. Akkari, M. Reghima, C. Guasch, and N. Kamoun-Turki, "Effect of copper doping on physical properties of nanocrystallized SnS zinc blend thin films grown by chemical bath deposition," *Journal of Materials Science*, vol. 47, no. 3, pp. 1365–1371, **2012**. DOI: 10.1007/s10853-011-5912-y.
- [75] Z. Hosseinpour, S. Hosseinpour, M. Maaza, and A. Scarpellini, "Co <sup>2+</sup> and Ho <sup>3+</sup> doped CuS nanocrystals with improved photocatalytic activity under visible light irradiation," *RSC Adv.*, vol. 6, no. 48, pp. 42 581–42 588, **2016**. DOI: 10.1039/C6RA03647C.
- [76] J.-L. Wu, F.-C. Chen, Y.-S. Hsiao, F.-C. Chien, P. Chen, C.-H. Kuo, M. H. Huang, and C.-S. Hsu, "Surface Plasmonic Effects of Metallic Nanoparticles on the Performance of Polymer Bulk Heterojunction Solar Cells," *ACS Nano*, vol. 5, no. 2, pp. 959–967, **2011**. DOI: 10.1021/nn102295p.
- [77] X. Zhang, X. Wu, A. Centeno, M. P. Ryan, N. M. Alford, D. J. Riley, and F. Xie, "Significant Broadband Photocurrent Enhancement by Au-CZTS Core-Shell Nanostructured Photocathodes," *Scientific Reports*, vol. 6, no. 1, p. 23 364, **2016**. DOI: 10.1038/srep23364.
- [78] S. Chandrasekaran, L. Yao, L. Deng, C. Bowen, Y. Zhang, S. Chen, Z. Lin, F. Peng, and P. Zhang, "Recent advances in metal sulfides: from controlled fabrication to electrocatalytic, photocatalytic and photoelectrochemical water splitting and beyond," *Chemical Society Reviews*, vol. 48, no. 15, pp. 4178–4280, **2019**. DOI: 10.1039/C8CS00664D.
- [79] R. W. Johnson, A. Hultqvist, and S. F. Bent, "A brief review of atomic layer deposition: From fundamentals to applications," *Materials Today*, vol. 17, no. 5, pp. 236–246, **2014**. DOI: 10.1016/j.mattod.2014.04.026.
- [80] Y. A. Kotov, "Electric explosion of wires as a method for preparation of nanopowders," *Journal of Nanoparticle Research*, vol. 5, no. 5-6, pp. 539–550, **2003**. DOI: 10.1023/B:NANO.0000006069.45073.0b.
- [81] P. Baláž, M. Achimovicová, M. Baláž, P. Billik, C. Z. Zara, J. M. Criado, F. Delogu, E. Dutková, E. Gaffet, F. J. Gotor, R. Kumar, I. Mitov, T. Rojac, M. Senna, A. Streletskii, and W. C. Krystyna, "Hallmarks of mechanochemistry: From nanoparticles to technology," *Chemical Society Reviews*, vol. 42, no. 18, pp. 7571–7637, **2013**. DOI: 10.1039/c3cs35468g.
- [82] J. J. Hinman and K. S. Suslick, "Nanostructured Materials Synthesis Using Ultrasound," *Topics in Current Chemistry*, vol. 375, no. 1, pp. 1–36, **2017**. DOI: 10.1007/s41061-016-0100-9.
- [83] V. Chikan and E. McLaurin, "Rapid Nanoparticle Synthesis by Magnetic and Microwave Heating," *Nanomaterials*, vol. 6, no. 5, p. 85, **2016**. DOI: 10.3390/nano6050085.
- [84] Y.-J. Zhu and F. Chen, "Microwave-Assisted Preparation of Inorganic Nanostructures in Liquid Phase," *Chemical Reviews*, vol. 114, no. 12, pp. 6462–6555, **2014**. DOI: 10.1021/cr400366s.
- [85] D. Stuerger, *Microwave-Material Interactions and Dielectric Properties, Key Ingredients for Mastery of Chemical Microwave Processes*. **2008**, vol. 1, pp. 1–61, ISBN: 3527314520. DOI: 10.1002/9783527619559.ch1.



- [86] L. Estel, M. Poux, N. Benamara, and I. Polaert, "Continuous flow-microwave reactor: Where are we?" *Chemical Engineering and Processing: Process Intensification*, vol. 113, pp. 56–64, **2017**. DOI: 10.1016/j.cep.2016.09.022.
- [87] S. Dąbrowska, T. Chudoba, J. Wojnarowicz, and W. Łojkowski, "Current trends in the development of microwave reactors for the synthesis of nanomaterials in laboratories and industries: A review," *Crystals*, vol. 8, no. 10, pp. 1–26, **2018**. DOI: 10.3390/cryst8100379.
- [88] C. Antonio, R. Deam, and A. Taube, "A Review of the Variable Frequency Microwave Technology in Material Processing," *Journal of Microwave Power and Electromagnetic Energy*, vol. 38, no. 1, pp. 75–87, **2003**. DOI: 10.1080/08327823.2003.11688488.
- [89] R. Widlar, "An exact expression for the thermal variation of the emitter base voltage of bi-polar transistors," *Proceedings of the IEEE*, vol. 55, no. 1, pp. 96–97, **1967**. DOI: 10.1109/PROC.1967.5396.
- [90] C. O. Kappe, "How to measure reaction temperature in microwave-heated transformations," *Chemical Society Reviews*, vol. 42, no. 12, pp. 4977–4990, **2013**. DOI: 10.1039/c3cs00010a.
- [91] Y. Xie, D. Kocaefer, C. Chen, and Y. Kocaefer, "Review of Research on Template Methods in Preparation of Nanomaterials," *Journal of Nanomaterials*, vol. 2016, pp. 1–10, **2016**. DOI: 10.1155/2016/2302595.
- [92] T. Kuzuya, Y. Tai, S. Yamamuro, and K. Sumiyama, "Synthesis of copper and zinc sulfide nanocrystals via thermolysis of the polymetallic thiolate cage," *Science and Technology of Advanced Materials*, vol. 6, no. 1, pp. 84–90, **2005**. DOI: 10.1016/j.stam.2004.08.005.
- [93] L. Chen and G. Li, "Functions of 1-Dodecanethiol in the Synthesis and Post-Treatment of Copper Sulfide Nanoparticles Relevant to Their Photocatalytic Applications," *ACS Applied Nano Materials*, vol. 1, no. 9, pp. 4587–4593, **2018**. DOI: 10.1021/acsnm.8b00893.
- [94] H. Fu, "Environment-Friendly and Earth-Abundant Colloidal Chalcogenide Nanocrystals for Photovoltaic Applications," *Journal of Materials Chemistry C*, **2017**. DOI: 10.1039/C7TC04952H.
- [95] C. Tian, Z. Kang, E. Wang, B. Mao, S. Li, Z. Su, and L. Xu, "'One-step' controllable synthesis of Ag and Ag<sub>2</sub>S nanocrystals on a large scale," *Nanotechnology*, vol. 17, no. 22, pp. 5681–5685, **2006**. DOI: 10.1088/0957-4484/17/22/024.
- [96] Jiang, Zeng, and Yu, "Thiol-Frozen Shape Evolution of Triangular Silver Nanoplates," *Langmuir*, vol. 23, no. 4, pp. 2218–2223, **2007**. DOI: 10.1021/la062797z.
- [97] R. Sun, Q. Wei, Q. Li, W. Luo, Q. An, J. Sheng, D. Wang, W. Chen, and L. Mai, "Vanadium Sulfide on Reduced Graphene Oxide Layer as a Promising Anode for Sodium Ion Battery," *ACS Applied Materials & Interfaces*, vol. 7, no. 37, pp. 20902–20908, **2015**. DOI: 10.1021/acami.5b06385.
- [98] N. A. Kalam, C. Sengottaiyan, R. Jayavel, K. Ariga, R. G. Shrestha, T. Subramani, S. Sankar, and L. K. Shrestha, "Vanadium sulfide/reduced graphene oxide composite with enhanced supercapacitance performance," *Journal of the Taiwan Institute of Chemical Engineers*, vol. 0, pp. 1–8, **2018**. DOI: 10.1016/j.jtice.2018.01.040.
- [99] A. L. Washington and G. F. Strouse, "Microwave synthesis of CdSe and CdTe nanocrystals in nonabsorbing alkanes," *Journal of the American Chemical Society*, vol. 130, no. 28, pp. 8916–8922, **2008**. DOI: 10.1021/ja711115r.
- [100] T. Trindade and P. O'Brien, "A single source approach to the synthesis of CdSe nanocrystallites," *Advanced Materials*, vol. 8, no. 2, pp. 161–163, **1996**. DOI: 10.1002/adma.19960080214.
- [101] I. Jen-La Plante, T. W. Zeid, P. Yang, and T. Mokari, "Synthesis of metal sulfide nanomaterials via thermal decomposition of single-source precursors," *Journal of Materials Chemistry*, vol. 20, no. 32, p. 6612, **2010**. DOI: 10.1039/c0jm00439a.

- [102] S. Shen, Y. Zhang, L. Peng, B. Xu, Y. Du, M. Deng, H. Xu, and Q. Wang, "Generalized synthesis of metal sulfide nanocrystals from single-source precursors: size, shape and chemical composition control and their properties," *CrystEngComm*, vol. 13, no. 14, p. 4572, **2011**. DOI: 10.1039/c0ce00982b.
- [103] J. C. Sarker and G. Hogarth, "Dithiocarbamate Complexes as Single Source Precursors to Nanoscale Binary, Ternary and Quaternary Metal Sulfides," *Chemical Reviews*, vol. 121, no. 10, pp. 6057–6123, **2021**. DOI: 10.1021/acs.chemrev.0c01183.
- [104] A. Tang, Y. Wang, H. Ye, C. Zhou, C. Yang, X. Li, H. Peng, F. Zhang, Y. Hou, and F. Teng, "Controllable synthesis of silver and silver sulfide nanocrystals via selective cleavage of chemical bonds," *Nanotechnology*, vol. 24, no. 35, **2013**. DOI: 10.1088/0957-4484/24/35/355602.
- [105] M. Mozammel, "Kinetics of Silver Dissolution in Nitric Acid from Ag-Au<sub>0</sub> : 04-Cu<sub>0</sub> : 10 and Ag-," *Journal of Mechanical Science and Technology*, vol. 22, no. 5, pp. 696–700, **2006**.
- [106] E. Berger, M. Bagheri, S. Asgari, J. Zhou, M. Kokkonen, P. Talebi, J. Luo, A. F. Nogueira, T. Watson, and S. G. Hashmi, "Recent developments in perovskite-based precursor inks for scalable architectures of perovskite solar cell technology," *Sustainable Energy & Fuels*, vol. 6, no. 12, pp. 2879–2900, **2022**. DOI: 10.1039/D2SE00162D.
- [107] M. Zeng and Y. Zhang, "Colloidal nanoparticle inks for printing functional devices: Emerging trends and future prospects," *Journal of Materials Chemistry A*, vol. 7, no. 41, pp. 23 301–23 336, **2019**. DOI: 10.1039/c9ta07552f.
- [108] H. T. Phan and A. J. Haes, "What Does Nanoparticle Stability Mean?" *The Journal of Physical Chemistry C*, vol. 123, no. 27, pp. 16 495–16 507, **2019**. DOI: 10.1021/acs.jpcc.9b00913.
- [109] R. Zwanzig, "Diffusion past an entropy barrier," *The Journal of Physical Chemistry*, vol. 96, no. 10, pp. 3926–3930, **1992**. DOI: 10.1021/j100189a004.
- [110] G. Collins, F. Davitt, C. O'Dwyer, and J. D. Holmes, "Comparing Thermal and Chemical Removal of Nanoparticle Stabilizing Ligands: Effect on Catalytic Activity and Stability," *ACS Applied Nano Materials*, vol. 1, no. 12, pp. 7129–7138, **2018**. DOI: 10.1021/acsanm.8b02019.
- [111] G. B. Shombe, M. D. Khan, C. Zequine, C. Zhao, R. K. Gupta, and N. Revaprasadu, "Direct solvent free synthesis of bare  $\alpha$ -NiS,  $\beta$ -NiS and  $\alpha$ - $\beta$ -NiS composite as excellent electrocatalysts: Effect of self-capping on supercapacitance and overall water splitting activity," *Scientific Reports*, vol. 10, no. 1, pp. 1–14, **2020**. DOI: 10.1038/s41598-020-59714-9.
- [112] R. C. Weast and J. G. Grasselli, Eds., *Handbook of Data on Organic Compounds* (Handbook of Data on Organic Compounds: Supplement), 2nd ed. Boca Raton, FL: CRC Press, Inc., **1989**, ISBN: 9780849304415.
- [113] Q. Guo, G. M. Ford, R. Agrawal, and H. W. Hillhouse, "Ink formulation and low-temperature incorporation of sodium to yield 12inks," *Progress in Photovoltaics: Research and Applications*, vol. 21, no. 1, pp. 64–71, **2013**. DOI: 10.1002/pip.2200.
- [114] D. Y. Santiesteban, D. S. Dumani, D. Profili, and S. Y. Emelianov, "Copper Sulfide Perfluorocarbon Nanodroplets as Clinically Relevant Photoacoustic/Ultrasound Imaging Agents," *Nano Letters*, vol. 17, no. 10, pp. 5984–5989, **2017**. DOI: 10.1021/acs.nanolett.7b02105.
- [115] W. Guo, T. A. Brown, and B. M. Fung, "Micelles and aggregates of fluorinated surfactants," *Journal of Physical Chemistry*, vol. 95, no. 4, pp. 1829–1836, **1991**. DOI: 10.1021/j100157a060.

- [116] L. Meng, T. Zeng, Y. Jin, Q. Xu, and X. Wang, "Surface-Modified Substrates for Quantum Dot Inks in Printed Electronics," *ACS Omega*, vol. 4, no. 2, pp. 4161–4168, **2019**. DOI: 10.1021/acsomega.9b00195.
- [117] C. J. Hibberd, E. Chassaing, W. Liu, D. B. Mitzi, D. Lincot, and A. N. Tiwari, "Non-vacuum methods for formation of Cu(In, Ga)(Se, S) 2 thin film photovoltaic absorbers," *Progress in Photovoltaics: Research and Applications*, vol. 18, no. 6, pp. 434–452, **2010**. DOI: 10.1002/pip.914.
- [118] N. Sahu, B. Parija, and S. Panigrahi, "Fundamental understanding and modeling of spin coating process: A review," *Indian Journal of Physics*, vol. 83, no. 4, pp. 493–502, **2009**. DOI: 10.1007/s12648-009-0009-z.
- [119] L. Landau and B. Levich, "Dragging of a Liquid by a Moving Plate," *Dynamics of Curved Fronts*, 1, vol. XVII, Elsevier, **1988**, pp. 141–153. DOI: 10.1016/B978-0-08-092523-3.50016-2.
- [120] N. Kapur, S. J. Abbott, E. D. Dolden, and P. H. Gaskell, "Predicting the Behavior of Screen Printing," *IEEE Transactions on Components, Packaging and Manufacturing Technology*, vol. 3, no. 3, pp. 508–515, **2013**. DOI: 10.1109/TCPMT.2012.2228743.
- [121] S.-J. Potts, C. Phillips, E. Jewell, B. Clifford, Y. C. Lau, and T. Claypole, "High-speed imaging the effect of snap-off distance and squeegee speed on the ink transfer mechanism of screen-printed carbon pastes," *Journal of Coatings Technology and Research*, vol. 17, no. 2, pp. 447–459, **2020**. DOI: 10.1007/s11998-019-00291-6.
- [122] S. Kooij, A. Astefanei, G. L. Corthals, and D. Bonn, "Size distributions of droplets produced by ultrasonic nebulizers," *Scientific Reports*, vol. 9, no. 1, p. 6128, **2019**. DOI: 10.1038/s41598-019-42599-8.
- [123] T. Kudo, K. Sekiguchi, K. Sankoda, N. Namiki, and S. Nii, "Effect of ultrasonic frequency on size distributions of nanosized mist generated by ultrasonic atomization," *Ultrasonics Sonochemistry*, vol. 37, pp. 16–22, **2017**. DOI: 10.1016/j.ultsonch.2016.12.019.
- [124] B. Derby, "Inkjet Printing of Functional and Structural Materials: Fluid Property Requirements, Feature Stability, and Resolution," *Annual Review of Materials Research*, vol. 40, no. 1, pp. 395–414, **2010**. DOI: 10.1146/annurev-matsci-070909-104502.
- [125] W. C. Liu and A. A. R. Watt, "Solvodynamic Printing As A High Resolution Printing Method," *Scientific Reports*, vol. 9, no. 1, p. 10766, **2019**. DOI: 10.1038/s41598-019-47105-8.
- [126] R. Søndergaard, M. Hösel, D. Angmo, T. T. Larsen-Olsen, and F. C. Krebs, "Roll-to-roll fabrication of polymer solar cells," *Materials Today*, vol. 15, no. 1-2, pp. 36–49, **2012**. DOI: 10.1016/S1369-7021(12)70019-6.
- [127] D. M. Sousa, J. Carlos Lima, and I. Ferreira, "Image Recording and Processing Chemical Synthesis: Method Description and Demonstration," *Chemistry-Methods*, **2020**. DOI: 10.1002/cmt.202000043.
- [128] A. Jain, S. P. Ong, G. Hautier, W. Chen, W. D. Richards, S. Dacek, S. Cholia, D. Gunter, D. Skinner, G. Ceder, and K. A. Persson, "Commentary: The Materials Project: A materials genome approach to accelerating materials innovation," *APL Materials*, vol. 1, no. 1, p. 011002, **2013**. DOI: 10.1063/1.4812323.
- [129] S. P. Ong, W. D. Richards, A. Jain, G. Hautier, M. Kocher, S. Cholia, D. Gunter, V. L. Chevrier, K. A. Persson, and G. Ceder, "Python Materials Genomics (pymatgen): A robust, open-source python library for materials analysis," *Computational Materials Science*, vol. 68, pp. 314–319, **2013**. DOI: 10.1016/j.commatsci.2012.10.028.
- [130] A. L. Patterson, "The scherrer formula for X-ray particle size determination," *Physical Review*, vol. 56, no. 10, pp. 978–982, **1939**. DOI: 10.1103/PhysRev.56.978. arXiv: arXiv:1011.1669v3.

- [131] P. Makuła, M. Pacia, and W. Macyk, "How To Correctly Determine the Band Gap Energy of Modified Semiconductor Photocatalysts Based on UV-Vis Spectra," *Journal of Physical Chemistry Letters*, vol. 9, no. 23, pp. 6814–6817, **2018**. DOI: 10.1021/acs.jpcclett.8b02892.
- [132] A. Escobedo-Morales, I. Ruiz-López, M. Ruiz-Peralta, L. Tepech-Carrillo, M. Sánchez-Cantú, and J. Moreno-Orea, "Automated method for the determination of the band gap energy of pure and mixed powder samples using diffuse reflectance spectroscopy," *Heliyon*, vol. 5, no. 4, e01505, **2019**. DOI: 10.1016/j.heliyon.2019.e01505.
- [133] X. Bian, Y. Gao, Q. Fu, S. Indris, Y. Ju, Y. Meng, F. Du, N. Bramnik, H. Ehrenberg, and Y. Wei, "A long cycle-life and high safety Na + /Mg 2+ hybrid-ion battery built by using a TiS<sub>2</sub> derived titanium sulfide cathode," *Journal of Materials Chemistry A*, vol. 5, no. 2, pp. 600–608, **2017**. DOI: 10.1039/C6TA08505A.
- [134] D. Y. Oh, Y. E. Choi, D. H. Kim, Y.-G. Lee, B.-S. Kim, J. Park, H. Sohn, and Y. S. Jung, "All-solid-state lithium-ion batteries with TiS<sub>2</sub> nanosheets and sulphide solid electrolytes," *Journal of Materials Chemistry A*, vol. 4, no. 26, pp. 10329–10335, **2016**. DOI: 10.1039/C6TA01628F.
- [135] R.-z. Zhang, C.-l. Wan, Y.-f. Wang, and K. Koumoto, "Titanium sulphene: two-dimensional confinement of electrons and phonons giving rise to improved thermoelectric performance," *Physical Chemistry Chemical Physics*, vol. 14, no. 45, p. 15641, **2012**. DOI: 10.1039/c2cp42949g.
- [136] X. Zhu, S. Chen, M. Zhang, L. Chen, Q. Wu, J. Zhao, Q. Jiang, Z. Zheng, and H. Zhang, "TiS<sub>2</sub>-based saturable absorber for ultrafast fiber lasers," *Photonics Research*, vol. 6, no. 10, p. C44, **2018**. DOI: 10.1364/PRJ.6.000C44.
- [137] H. P. Vaterlaus and F. Levy, "Phonons and free carriers in group IVB transition-metal dichalcogenides," *Journal of Physics C: Solid State Physics*, vol. 18, no. 11, pp. 2351–2359, **1985**. DOI: 10.1088/0022-3719/18/11/016.
- [138] A. L. Let, D. E. Mainwaring, C. J. Rix, and P. Murugaraj, "Thio sol-gel synthesis of titanium disulfide thin films and nanoparticles using titanium(IV) alkoxide precursors," *Journal of Physics and Chemistry of Solids*, vol. 68, no. 7, pp. 1428–1435, **2007**. DOI: 10.1016/j.jpcs.2007.03.001.
- [139] S. Jeong, D. Yoo, J.-t. Jang, M. Kim, and J. Cheon, "Well-Defined Colloidal 2-D Layered Transition-Metal Chalcogenide Nanocrystals via Generalized Synthetic Protocols," *Journal of the American Chemical Society*, vol. 134, no. 44, pp. 18233–18236, **2012**. DOI: 10.1021/ja3089845.
- [140] X. Chen, L. Liu, and F. Huang, "Black titanium dioxide (TiO<sub>2</sub>) nanomaterials," *Chemical Society Reviews*, vol. 44, no. 7, pp. 1861–1885, **2015**. DOI: 10.1039/c4cs00330f.
- [141] V. V. Plashnitsa, F. Vietmeyer, N. Petchsang, P. Tongying, T. H. Kosel, and M. Kuno, "Synthetic Strategy and Structural and Optical Characterization of Thin Highly Crystalline Titanium Disulfide Nanosheets," *The Journal of Physical Chemistry Letters*, vol. 3, no. 11, pp. 1554–1558, **2012**. DOI: 10.1021/jz300487p.
- [142] R. P. Abendroth, "A thermodynamic study of the titanium sulfides," Ph.D. dissertation, University of Missouri, **1957**.
- [143] Y. Shimazu, Y. Fujisawa, K. Arai, T. Iwabuchi, and K. Suzuki, "Synthesis and Characterization of Zirconium Disulfide Single Crystals and Thin-Film Transistors Based on Multilayer Zirconium Disulfide Flakes," *ChemNanoMat*, vol. 4, no. 10, pp. 1078–1082, **2018**. DOI: 10.1002/cnma.201800304.
- [144] J.-t. Jang, S. Jeong, J.-w. Seo, M.-C. Kim, E. Sim, Y. Oh, S. Nam, B. Park, and J. Cheon, "Ultrathin Zirconium Disulfide Nanodiscs," *Journal of the American Chemical Society*, vol. 133, no. 20, pp. 7636–7639, **2011**. DOI: 10.1021/ja200400n.

- [145] M. Moustafa, T. Zandt, C. Janowitz, and R. Manzke, "Growth and band gap determination of the  $\text{ZrS}_x\text{Se}_{2-x}$  single crys," *Physical Review B*, vol. 80, no. 3, p. 035 206, **2009**. DOI: 10.1103/PhysRevB.80.035206.
- [146] Z. Li, Y. Li, Y. Lin, M. Z. Alam, and Y. Wu, "Synthesizing  $\text{Ag}^+ : \text{MgS}$ ,  $\text{Ag}^+ : \text{Nb}_2\text{S}_5$ ,  $\text{Sm}^{3+} : \text{Y}_2\text{S}_3$ ,  $\text{Sm}^{3+} : \text{Er}_2\text{S}_3$ , and  $\text{Sm}^{3+} : \text{ZrS}_2$  Compound Nanoparticles for Multicolor Fluorescence Imaging of Biotissues," *ACS Omega*, vol. 5, no. 51, pp. 32 868–32 876, **2020**. DOI: 10.1021/acsomega.0c02788.
- [147] V. Q. Dang and K. Al-Ali, "The synthesis and investigation of the reversible conversion of layered  $\text{ZrS}_2$  and  $\text{ZrS}_3$ ," *New Journal of Chemistry*, vol. 44, no. 18, pp. 7583–7590, **2020**. DOI: 10.1039/C9NJ05631A.
- [148] J. Yin, F. Zhu, J. Lai, H. Chen, M. Zhang, J. Zhang, J. Wang, T. He, B. Zhang, J. Yuan, P. Yan, and S. Ruan, "Hafnium Sulfide Nanosheets for Ultrafast Photonic Device," *Advanced Optical Materials*, vol. 7, no. 5, p. 1 801 303, **2019**. DOI: 10.1002/adom.201801303.
- [149] K. Xu, Z. Wang, F. Wang, Y. Huang, F. Wang, L. Yin, C. Jiang, and J. He, "Ultrasensitive Phototransistors Based on Few-Layered  $\text{HfS}_2$ ," *Advanced Materials*, vol. 27, no. 47, pp. 7881–7887, **2015**. DOI: 10.1002/adma.201503864.
- [150] T. Kanazawa, T. Amemiya, A. Ishikawa, V. Upadhyaya, K. Tsuruta, T. Tanaka, and Y. Miyamoto, "Few-layer  $\text{HfS}_2$  transistors," *Scientific Reports*, vol. 6, no. 1, p. 22 277, **2016**. DOI: 10.1038/srep22277.
- [151] H. Kaur, S. Yadav, A. K. Srivastava, N. Singh, S. Rath, J. J. Schneider, O. P. Sinha, and R. Srivastava, "High-yield synthesis and liquid-exfoliation of two-dimensional belt-like hafnium disulphide," *Nano Research*, vol. 11, no. 1, pp. 343–353, **2018**. DOI: 10.1007/s12274-017-1636-x.
- [152] D. Wang, X. Zhang, G. Guo, S. Gao, X. Li, J. Meng, Z. Yin, H. Liu, M. Gao, L. Cheng, J. You, and R. Wang, "Large-Area Synthesis of Layered  $\text{HfS}_2(1-x)\text{Se}_x$  Alloys with Fully Tunable Chemical Compositions and Bandgaps," *Advanced Materials*, vol. 30, no. 44, p. 1 803 285, **2018**. DOI: 10.1002/adma.201803285.
- [153] M. D. Meganathan, T. Huang, H. Fang, J. Mao, and G. Sun, "Electrochemical impacts of sheet-like hafnium phosphide and hafnium disulfide catalysts bonded with reduced graphene oxide sheets for bifunctional oxygen reactions in alkaline electrolytes," *RSC Advances*, vol. 9, no. 5, pp. 2599–2607, **2019**. DOI: 10.1039/C8RA09598A.
- [154] Y.-Y. Liu, L. Xu, X.-T. Guo, T.-T. Lv, and H. Pang, "Vanadium sulfide based materials: synthesis, energy storage and conversion," *Journal of Materials Chemistry A*, vol. 8, no. 40, pp. 20 781–20 802, **2020**. DOI: 10.1039/D0TA07436E.
- [155] L. Li, Z. Li, A. Yoshimura, C. Sun, T. Wang, Y. Chen, Z. Chen, A. Littlejohn, Y. Xiang, P. Hundekar, S. F. Bartolucci, J. Shi, S.-F. Shi, V. Meunier, G.-C. Wang, and N. Koratkar, "Vanadium disulfide flakes with nanolayered titanium disulfide coating as cathode materials in lithium-ion batteries," *Nature Communications*, vol. 10, no. 1, p. 1764, **2019**. DOI: 10.1038/s41467-019-09400-w.
- [156] S. Dey, J. Lee, S. Britto, J. M. Stratford, E. N. Keyzer, M. T. Dunstan, G. Cibin, S. J. Cassidy, M. Elgaml, and C. P. Grey, "Exploring Cation-Anion Redox Processes in One-Dimensional Linear Chain Vanadium Tetrasulfide Rechargeable Magnesium Ion Cathodes," *Journal of the American Chemical Society*, vol. 142, no. 46, pp. 19 588–19 601, **2020**. DOI: 10.1021/jacs.0c08222.

- [157] L. Najafi, S. Bellani, R. Oropesa-Nuñez, B. Martín-García, M. Prato, V. Mazánek, D. Debellis, S. Lauciello, R. Brescia, Z. Sofer, and F. Bonaccorso, “Niobium disulphide (NbS<sub>2</sub>)-based (heterogeneous) electrocatalysts for an efficient hydrogen evolution reaction,” *Journal of Materials Chemistry A*, vol. 7, no. 44, pp. 25 593–25 608, **2019**. DOI: 10.1039/C9TA07210A.
- [158] J. H. Han, H. K. Kim, B. Baek, J. Han, H. S. Ahn, M. H. Baik, and J. Cheon, “Activation of the Basal Plane in Two Dimensional Transition Metal Chalcogenide Nanostructures,” *Journal of the American Chemical Society*, vol. 140, no. 42, pp. 13 663–13 671, **2018**. DOI: 10.1021/jacs.8b05477.
- [159] V. G. Tissen, M. R. Osorio, J. P. Brison, N. M. Nemes, M. García-Hernández, L. Cario, P. Rodière, S. Vieira, and H. Suderow, “Pressure dependence of superconducting critical temperature and upper critical field of 2H-NbS<sub>2</sub>,” *Physical Review B*, vol. 87, no. 13, p. 134 502, **2013**. DOI: 10.1103/PhysRevB.87.134502.
- [160] A. Niazi and A. K. Rastogi, “Low-temperature resistance minimum in non-superconducting 3R-Nb<sub>1+x</sub>S<sub>2</sub> and 3R-Ga<sub>x</sub>NbS<sub>2</sub>,” *Journal of Physics: Condensed Matter*, vol. 13, no. 31, pp. 6787–6796, **2001**. DOI: 10.1088/0953-8984/13/31/315.
- [161] M. A. Bloodgood, P. Wei, E. Aytan, K. N. Bozhilov, A. A. Balandin, and T. T. Salguero, “Monoclinic structures of niobium trisulfide,” *APL Materials*, vol. 6, no. 2, p. 026 602, **2018**. DOI: 10.1063/1.5005813.
- [162] J. G. McCullough and L. Meites, “The electroreduction of niobium(V) in hydrochloric acid solutions at mercury electrodes,” *Journal of Electroanalytical Chemistry and Interfacial Electrochemistry*, vol. 19, no. 1-2, pp. 111–123, **1968**. DOI: 10.1016/S0022-0728(68)80194-9.
- [163] M. Leroux, L. Cario, A. Bosak, and P. Rodière, “Traces of charge density waves in <math>\langle \text{NbS}\_2 \rangle</math>,” *Physical Review B*, vol. 97, no. 19, p. 195 140, **2018**. DOI: 10.1103/PhysRevB.97.195140.
- [164] L. Zhou, C. Sun, X. Li, L. Tang, W. Guo, L. Luo, M. Zhang, K. S. Teng, F. Qian, C. Lu, J. Liang, Y. Yao, and S. P. Lau, “Tantalum disulfide quantum dots: preparation, structure, and properties,” *Nanoscale Research Letters*, vol. 15, no. 1, p. 20, **2020**. DOI: 10.1186/s11671-020-3250-1.
- [165] C. Tsai, K. Chan, J. K. Nørskov, and F. Abild-Pedersen, “Theoretical insights into the hydrogen evolution activity of layered transition metal dichalcogenides,” *Surface Science*, vol. 640, pp. 133–140, **2015**. DOI: 10.1016/j.susc.2015.01.019.
- [166] M. Zhang, Y. He, D. Yan, H. Xu, A. Wang, Z. Chen, S. Wang, H. Luo, and K. Yan, “Multifunctional 2H-TaS<sub>2</sub> nanoflakes for efficient supercapacitors and electrocatalytic evolution of hydrogen and oxygen,” *Nanoscale*, vol. 11, no. 46, pp. 22 255–22 260, **2019**. DOI: 10.1039/C9NR07564J.
- [167] C. W. Dunnill, “Synthesis, Characterisation and Properties of Tantalum Based,” **2008**.
- [168] J. Luxa, V. Mazánek, M. Pumera, P. Lazar, D. Sedmidubský, M. Callisti, T. Polcar, and Z. Sofer, “2H→1T Phase Engineering of Layered Tantalum Disulfides in Electrocatalysis: Oxygen Reduction Reaction,” *Chemistry - A European Journal*, vol. 23, no. 33, pp. 8082–8091, **2017**. DOI: 10.1002/chem.201701494.
- [169] E. Ahmadi and R. O. Suzuki, “Tantalum Metal Production Through High-Efficiency Electrochemical Reduction of TaS<sub>2</sub> in Molten CaCl<sub>2</sub>,” *Journal of Sustainable Metallurgy*, vol. 7, no. 2, pp. 437–447, **2021**. DOI: 10.1007/s40831-021-00347-1.
- [170] W. Hussain, A. Badshah, R. A. Hussain, I. ud Din, M. A. Aleem, A. Bahadur, S. Iqbal, M. U. Farooq, and H. Ali, “Photocatalytic applications of Cr<sub>2</sub>S<sub>3</sub> synthesized from single and multi-source precursors,” *Materials Chemistry and Physics*, vol. 194, pp. 345–355, **2017**. DOI: 10.1016/j.matchemphys.2017.04.001.

- [171] S. Zhou, R. Wang, J. Han, D. Wang, H. Li, L. Gan, and T. Zhai, "Ultrathin Non-van der Waals Magnetic Rhombohedral Cr<sub>2</sub>S<sub>3</sub>: Space-Confined Chemical Vapor Deposition Synthesis and Raman Scattering Investigation," *Advanced Functional Materials*, vol. 29, no. 3, p. 1805880, **2019**. DOI: 10.1002/adfm.201805880.
- [172] S. Ebrahimi and B. Yarmand, "Optimized optical band gap energy and Urbach tail of Cr<sub>2</sub>S<sub>3</sub> thin films by Sn incorporation for optoelectronic applications," *Physica B: Condensed Matter*, vol. 593, p. 412292, **2020**. DOI: 10.1016/j.physb.2020.412292.
- [173] S. Kulkarni, S. Gharpure, U. K. Sur, and B. Ankamwar, "Hydrothermal biosynthesis of chromium sulphide nanoparticles using egg yolk and its catalytic activity in degradation of dyes," *Nano Express*, vol. 1, no. 1, p. 010019, **2020**. DOI: 10.1088/2632-959X/ab844c.
- [174] P. Semyannikov, I. Igumenov, S. Trubin, T. Chusova, and Z. Semenova, "Thermodynamics of chromium acetylacetonate sublimation," *Thermochimica Acta*, vol. 432, no. 1, pp. 91–98, **2005**. DOI: 10.1016/j.tca.2005.02.034.
- [175] J. D. Benck, T. R. Hellstern, J. Kibsgaard, P. Chakthranont, and T. F. Jaramillo, "Catalyzing the Hydrogen Evolution Reaction (HER) with Molybdenum Sulfide Nanomaterials," *ACS Catalysis*, vol. 4, no. 11, pp. 3957–3971, **2014**. DOI: 10.1021/cs500923c.
- [176] L. Rapoport, N. Fleischer, and R. Tenne, "Applications of WS<sub>2</sub>(MoS<sub>2</sub>) inorganic nanotubes and fullerene-like nanoparticles for solid lubrication and for structural nanocomposites," *Journal of Materials Chemistry*, vol. 15, no. 18, p. 1782, **2005**. DOI: 10.1039/b417488g.
- [177] B. Radisavljevic, A. Radenovic, J. Brivio, V. Giacometti, and A. Kis, "Single-layer MoS<sub>2</sub> transistors," *Nature Nanotechnology*, vol. 6, no. 3, pp. 147–150, **2011**. DOI: 10.1038/nnano.2010.279.
- [178] M. S. Javed, S. Dai, M. Wang, D. Guo, L. Chen, X. Wang, C. Hu, and Y. Xi, "High performance solid state flexible supercapacitor based on molybdenum sulfide hierarchical nanospheres," *Journal of Power Sources*, vol. 285, pp. 63–69, **2015**. DOI: 10.1016/j.jpowsour.2015.03.079.
- [179] N. Thi Xuyen and J.-M. Ting, "Hybridized 1T/2H MoS<sub>2</sub> Having Controlled 1T Concentrations and its use in Supercapacitors," *Chemistry - A European Journal*, vol. 23, no. 68, pp. 17348–17355, **2017**. DOI: 10.1002/chem.201703690.
- [180] D. Barrera, Q. Wang, Y.-J. Lee, L. Cheng, M. J. Kim, J. Kim, and J. W. P. Hsu, "Solution synthesis of few-layer 2H MX<sub>2</sub> (M = Mo, W; X = S, Se)," *Journal of Materials Chemistry C*, vol. 5, no. 11, pp. 2859–2864, **2017**. DOI: 10.1039/C6TC05097B.
- [181] G. Alonso, M. Del Valle, J. Cruz, A. Licea-Claverie, V. Petranovskii, and S. Fuentes, "Preparation of MoS<sub>2</sub> and WS<sub>2</sub> catalysts by in situ decomposition of ammonium thiosalts," *Catalysis Letters*, vol. 52, pp. 55–61, **1998**.
- [182] Z. Huang, C. Wang, Z. Chen, H. Meng, C. Lv, Z. Chen, R. Han, and C. Zhang, "Tungsten Sulfide Enhancing Solar-Driven Hydrogen Production from Silicon Nanowires," *ACS Applied Materials & Interfaces*, vol. 6, no. 13, pp. 10408–10414, **2014**. DOI: 10.1021/am501940x.
- [183] J. Wang, L. Yu, Z. Zhou, L. Zeng, and M. Wei, "Template-free synthesis of metallic WS<sub>2</sub> hollow microspheres as an anode for the sodium-ion battery," *Journal of Colloid and Interface Science*, vol. 557, pp. 722–728, **2019**. DOI: 10.1016/j.jcis.2019.09.078.
- [184] T.-W. Chen, U. Rajaji, S.-M. Chen, and R. Jothi Ramalingam, "A relative study on sonochemically synthesized mesoporous WS<sub>2</sub> nanorods & hydrothermally synthesized WS<sub>2</sub> nanoballs towards electrochemical sensing of psychoactive drug (Clonazepam)," *Ultrasonics Sonochemistry*, vol. 54, pp. 79–89, **2019**. DOI: 10.1016/j.ultsonch.2019.02.012.

- [185] H. Li, L. Zhang, and Y. Cao, "Synthesis of palladium-modified MnS photocatalysts with enhanced photocatalytic activity in the photoreduction of CO<sub>2</sub> to CH<sub>4</sub>," *Applied Surface Science*, vol. 541, p. 148 519, **2021**. DOI: 10.1016/j.apsusc.2020.148519.
- [186] S. Sambasivam, C. V. M. Gopi, H. M. Arbi, Y. A. Kumar, H.-J. Kim, S. A. Zahmi, and I. M. Obaidat, "Binder-free hierarchical core-shell-like CoMn<sub>2</sub>O<sub>4</sub>@MnS nanowire arrays on nickel foam as a battery-type electrode material for high-performance supercapacitors," *Journal of Energy Storage*, vol. 36, p. 102 377, **2021**. DOI: 10.1016/j.est.2021.102377.
- [187] G. Zhang, H. Xuan, R. Wang, Y. Guan, H. Li, X. Liang, P. Han, and Y. Wu, "Enhanced supercapacitive performance in Ni<sub>3</sub>S<sub>2</sub>/MnS composites via an ion-exchange process for supercapacitor applications," *Electrochimica Acta*, vol. 353, p. 136 517, **2020**. DOI: 10.1016/j.electacta.2020.136517.
- [188] K. Krishnasamy and K. Purushothaman, "Preparation and characterisation of MnS@Mn<sub>3</sub>O<sub>4</sub>/C nanoflakes for hybrid supercapacitor applications," *Materials Technology*, pp. 1–8, **2020**. DOI: 10.1080/10667857.2020.1810923.
- [189] G. Li, B. He, M. Zhou, G. Wang, N. Zhou, W. Xu, and Z. Hou, "Solvothermal Synthesis of Mesoporous Manganese Sulfide Nanoparticles Supported on Nitrogen and Sulfur Co-doped Graphene with Superior Lithium Storage Performance," *ChemElectroChem*, vol. 4, no. 1, pp. 81–89, **2017**. DOI: 10.1002/celec.201600327.
- [190] D. Hu, C. Zhu, Y. Yao, S. Liu, X. Meng, H. Yuan, Z. Chen, X. Jiang, Y. Li, and S. Zhu, "A facile ex situ strategy of  $\alpha$ -MnS nanoparticles anchored on holey graphene as high-performance anode for lithium-ion batteries," *Applied Surface Science*, vol. 542, p. 148 496, **2021**. DOI: 10.1016/j.apsusc.2020.148496.
- [191] A. M. Ferretti, S. Mondini, and A. Ponti, "Manganese Sulfide (MnS) Nanocrystals: Synthesis, Properties, and Applications," *Advances in Colloid Science*, IntechOpen, **2016**, ch. 6, p. 138. DOI: 10.5772/65092.
- [192] A. M. Ferretti, S. Mondini, and A. Ponti, "Manganese Sulfide (MnS) Nanocrystals: Synthesis, Properties, and Applications," *Advances in Colloid Science*, M. M. Rahman and A. M. Asiri, Eds., Rijeka: IntechOpen, **2016**, ch. 06. DOI: 10.5772/65092.
- [193] G. Xu, Y. L. Zhu, and X. L. Ma, "Cu<sub>2</sub>S nanowires and MnS/Cu<sub>2</sub>S nanojunctions derived from  $\gamma$ -MnS nanowires via selective cation-exchange reaction," *physica status solidi (a)*, vol. 208, no. 1, pp. 123–128, **2011**. DOI: 10.1002/pssa.201026124.
- [194] Y. Gong, J. Tang, and D. Zhao, "Application of iron sulfide particles for groundwater and soil remediation: A review," *Water Research*, vol. 89, pp. 309–320, **2016**. DOI: 10.1016/j.watres.2015.11.063.
- [195] B. T. Gadisa, R. Appiah-Ntiamoah, and H. Kim, "Amorphous iron sulfide nanowires as an efficient adsorbent for toxic dye effluents remediation," *Environmental Science and Pollution Research*, vol. 26, no. 3, pp. 2734–2746, **2019**. DOI: 10.1007/s11356-018-3811-3.
- [196] Y. Chen, W. Liang, Y. Li, Y. Wu, Y. Chen, W. Xiao, L. Zhao, J. Zhang, and H. Li, "Modification, application and reaction mechanisms of nano-sized iron sulfide particles for pollutant removal from soil and water: A review," *Chemical Engineering Journal*, vol. 362, pp. 144–159, **2019**. DOI: 10.1016/j.cej.2018.12.175.
- [197] S. Bhattacharjee, F. Habib, N. Darwish, and A. Shanableh, "Iron sulfide nanoparticles prepared using date seed extract: Green synthesis, characterization and potential application for removal of ciprofloxacin and chromium," *Powder Technology*, vol. 380, pp. 219–228, **2021**. DOI: 10.1016/j.powtec.2020.11.055.



- [198] Y.-C. Chen, J.-H. Shi, and Y.-K. Hsu, "Multifunctional FeS<sub>2</sub> in binder-independent configuration as high-performance supercapacitor electrode and non-enzymatic H<sub>2</sub>O<sub>2</sub> detector," *Applied Surface Science*, vol. 503, p. 144304, **2020**. DOI: 10.1016/j.apsusc.2019.144304.
- [199] J. G. Lozano, F. Dillon, A. J. Naylor, L. Y. Lee, C. Lippard, D. Johnstone, P. G. Bruce, and N. Grobert, "Single source precursor route to iron sulfide nanomaterials for energy storage," *Chemical Physics Letters*, vol. 739, p. 136993, **2020**. DOI: 10.1016/j.cplett.2019.136993.
- [200] E. J. Kim and B. Batchelor, "Synthesis and characterization of pyrite (FeS<sub>2</sub>) using microwave irradiation," *Materials Research Bulletin*, vol. 44, no. 7, pp. 1553–1558, **2009**. DOI: 10.1016/j.materresbull.2009.02.006.
- [201] J. M. Rhodes, C. A. Jones, L. B. Thal, and J. E. Macdonald, "Phase-Controlled Colloidal Syntheses of Iron Sulfide Nanocrystals via Sulfur Precursor Reactivity and Direct Pyrite Precipitation," *Chemistry of Materials*, vol. 29, no. 19, pp. 8521–8530, **2017**. DOI: 10.1021/acs.chemmater.7b03550.
- [202] Z. Xu, C. Du, H. Yang, J. Huang, X. Zhang, and J. Chen, "NiCoP@CoS tree-like core-shell nanoarrays on nickel foam as battery-type electrodes for supercapacitors," *Chemical Engineering Journal*, vol. 421, p. 127871, **2021**. DOI: 10.1016/j.cej.2020.127871.
- [203] X. Hu, S. Liu, Y. Wang, X. Huang, J. Jiang, H. Cong, H. Lin, and S. Han, "Hierarchical CuCo<sub>2</sub>O<sub>4</sub>@CoS-Cu/Co-MOF core-shell nanoflower derived from copper/cobalt bimetallic metal-organic frameworks for supercapacitors," *Journal of Colloid and Interface Science*, vol. 600, pp. 72–82, **2021**. DOI: 10.1016/j.jcis.2021.05.008.
- [204] A. Mohammadi Zardkhoshoui, B. Ameri, and S. Saeed Hosseiny Davarani, "α-MnS@Co<sub>3</sub>S<sub>4</sub> hollow nanospheres assembled from nanosheets for hybrid supercapacitors," *Chemical Engineering Journal*, vol. 422, p. 129953, **2021**. DOI: 10.1016/j.cej.2021.129953.
- [205] C. Wang, G. Sui, D. Guo, J. Li, L. Zhang, S. Li, J. Xin, D.-F. Chai, and W. Guo, "Structure-designed synthesis of hollow/porous cobalt sulfide/phosphide based materials for optimizing supercapacitor storage properties and hydrogen evolution reaction," *Journal of Colloid and Interface Science*, vol. 599, pp. 577–585, **2021**. DOI: 10.1016/j.jcis.2021.04.118.
- [206] Y. Sun, C. Li, S. Jiang, R. Xia, X. Wang, H. Bao, and M. Gao, "Comparative study on supercapacitive and oxygen evolution reaction applications of hollow nanostructured cobalt sulfides," *Nanotechnology*, vol. 32, no. 38, p. 385401, **2021**. DOI: 10.1088/1361-6528/ac09aa.
- [207] C. Li, Y. Zhao, X. Liu, P. Huo, Y. Yan, L. Wang, G. Liao, and C. Liu, "Interface engineering of Co<sub>9</sub>S<sub>8</sub>/CdIn<sub>2</sub>S<sub>4</sub> ohmic junction for efficient photocatalytic H<sub>2</sub> evolution under visible light," *Journal of Colloid and Interface Science*, vol. 600, pp. 794–803, **2021**. DOI: 10.1016/j.jcis.2021.05.084.
- [208] F. Srouji, M. Afzaal, J. Waters, and P. O'Brien, "Single-Source Routes to Cobalt Sulfide and Manganese Sulfide Thin Films," *Chemical Vapor Deposition*, vol. 11, no. 2, pp. 91–94, **2005**. DOI: 10.1002/cvde.200404185.
- [209] B. You, N. Jiang, M. Sheng, and Y. Sun, "Microwave vs. solvothermal synthesis of hollow cobalt sulfide nanoprisms for electrocatalytic hydrogen evolution and supercapacitors," *Chemical Communications*, vol. 51, no. 20, pp. 4252–4255, **2015**. DOI: 10.1039/C4CC09849H.
- [210] L. Yin, L. Wang, X. Liu, Y. Gai, L. Su, B. Qu, and L. Gong, "Ultra-Fast Microwave Synthesis of 3D Flower-Like Co<sub>9</sub>S<sub>8</sub> Hierarchical Architectures for High-Performance Supercapacitor Applications," *European Journal of Inorganic Chemistry*, vol. 2015, no. 14, pp. 2457–2462, **2015**. DOI: 10.1002/ejic.201500120.

- [211] K. Skrodzky, M. M. Antunes, X. Han, S. Santangelo, G. Scholz, A. A. Valente, N. Pinna, and P. A. Russo, "Niobium pentoxide nanomaterials with distorted structures as efficient acid catalysts," *Communications Chemistry*, vol. 2, no. 1, p. 129, **2019**. DOI: 10.1038/s42004-019-0231-3.
- [212] J. Li, M. Li, and Z. Jin, "0D Cd<sub>x</sub>Zn<sub>1-x</sub>S and amorphous Co<sub>9</sub>S<sub>8</sub> formed S-scheme heterojunction boosting photocatalytic hydrogen evolution," *Molecular Catalysis*, vol. 501, p. 111 378, **2021**. DOI: 10.1016/j.mcat.2020.111378.
- [213] C. Huang, A. Gao, F. Yi, Y. Wang, D. Shu, Y. Liang, Z. Zhu, J. Ling, and J. Hao, "Metal organic framework derived hollow NiS@C with S-vacancies to boost high-performance supercapacitors," *Chemical Engineering Journal*, vol. 419, p. 129 643, **2021**. DOI: 10.1016/j.cej.2021.129643.
- [214] K. Song, W. Li, R. Yang, Y. Zheng, X. Chen, X. Wang, G. Chen, and W. Lv, "Controlled preparation of Ni(OH)<sub>2</sub>/NiS nanosheet heterostructure as hybrid supercapacitor electrodes for high electrochemical performance," *Electrochimica Acta*, vol. 388, p. 138 663, **2021**. DOI: 10.1016/j.electacta.2021.138663.
- [215] Y. Yang, H. Zhu, H. Meng, W. Ma, C. Wang, F. Ma, and Z. Hu, "Metal-organic framework derived Co<sub>9</sub>S<sub>8</sub>/Ni<sub>3</sub>S<sub>2</sub> composites on Ni foam with enhanced electrochemical performance by one-step sulfuration strategy for supercapacitors electrode," *Colloids and Surfaces A: Physicochemical and Engineering Aspects*, vol. 623, p. 126 695, **2021**. DOI: 10.1016/j.colsurfa.2021.126695.
- [216] J. Yoo, I. H. Kwak, I. S. Kwon, K. Park, D. Kim, J. H. Lee, S. A. Lim, E. H. Cha, and J. Park, "Nickel sulfide nanocrystals for electrochemical and photoelectrochemical hydrogen generation," *Journal of Materials Chemistry C*, vol. 8, no. 9, pp. 3240–3247, **2020**. DOI: 10.1039/C9TC05703J.
- [217] X. Cao, R. Ding, Y. Zhang, Y. Cui, and K. Hong, "A heterojunction film of NiS<sub>2</sub> and MnS as an efficient counter electrode for dye-sensitized solar cells," *Materials Today Communications*, vol. 26, p. 102 160, **2021**. DOI: 10.1016/j.mtcomm.2021.102160.
- [218] R. Zhang, Z. Zhu, J. Lin, K. Zhang, N. Li, and C. Zhao, "Hydrolysis assisted in-situ growth of 3D hierarchical FeS/NiS/nickel foam electrode for overall water splitting," *Electrochimica Acta*, vol. 332, p. 135 534, **2020**. DOI: 10.1016/j.electacta.2019.135534.
- [219] L. Peng, X. Ji, H. Wan, Y. Ruan, K. Xu, C. Chen, L. Miao, and J. Jiang, "Nickel Sulfide Nanoparticles Synthesized by Microwave-assisted Method as Promising Supercapacitor Electrodes: An Experimental and Computational Study," *Electrochimica Acta*, vol. 182, pp. 361–367, **2015**. DOI: 10.1016/j.electacta.2015.09.024.
- [220] M. Salavati-Niasari, G. Banaiean-Monfared, H. Emadi, and M. Enhessari, "Synthesis and characterization of nickel sulfide nanoparticles via cyclic microwave radiation," *Comptes Rendus Chimie*, vol. 16, no. 10, pp. 929–936, **2013**. DOI: 10.1016/j.crci.2013.01.011.
- [221] A. B. Urgunde, A. R. Kumar, K. P. Shejale, R. K. Sharma, and R. Gupta, "Metal Wire Networks Functionalized with Nickel Alkanethiolate for Transparent and Enzymeless Glucose Sensors," *ACS Applied Nano Materials*, vol. 1, no. 10, pp. 5571–5580, **2018**. DOI: 10.1021/acsanm.8b01115.
- [222] P. Dutta, R. Mandal, S. Bhattacharyya, R. Dey, and R. S. Dhar, "Fabrication and characterization of copper based semiconducting materials for optoelectronic applications," *Microsystem Technologies*, **2021**. DOI: 10.1007/s00542-020-05145-5.
- [223] Y. Zhao, H. Pan, Y. Lou, X. Qiu, J. Zhu, and C. Burda, "Plasmonic Cu<sub>2-x</sub>S Nanocrystals: Optical and Structural Properties of Copper-Deficient Copper(I) Sulfides," *Journal of the American Chemical Society*, vol. 131, no. 12, pp. 4253–4261, **2009**. DOI: 10.1021/ja805655b.

- [224] I. K. Durga, S. S. Rao, A. E. Reddy, C. V. Gopi, and H.-J. Kim, "Achieving copper sulfide leaf like nanostructure electrode for high performance supercapacitor and quantum-dot sensitized solar cells," *Applied Surface Science*, vol. 435, pp. 666–675, **2018**. DOI: 10.1016/j.apsusc.2017.11.171.
- [225] D. A. Islam, A. Chakraborty, B. Bhattacharya, U. Sarkar, and H. Acharya, "Tailored synthesis of CuS nanodisks from a new macrocyclic precursor and their efficient catalytic properties on methylene blue dye degradation," *Journal of Nanoparticle Research*, vol. 18, no. 5, p. 114, **2016**. DOI: 10.1007/s11051-016-3417-y.
- [226] S. Zhang, W. Meng, L. Wang, L. Li, Y. Long, Y. Hei, L. Zhou, S. Wu, Z. Zheng, L. Luo, and F. Jiang, "Preparation of Nano-Copper Sulfide and Its Adsorption Properties for 17 $\alpha$ -Ethinyl Estradiol," *Nanoscale Research Letters*, vol. 15, no. 1, p. 48, **2020**. DOI: 10.1186/s11671-020-3274-6.
- [227] Y. Muddassir, S. Tahir, A. Ali, K. Mahmood, U. Ur Rehman, A. Ashfaq, A. Manzoor, and S. Ikram, "Morphology-dependent thermoelectric properties of mixed phases of copper sulfide (Cu<sub>2-x</sub>S) nanostructures synthesized by hydrothermal method," *Applied Physics A*, vol. 127, no. 6, p. 457, **2021**. DOI: 10.1007/s00339-021-04599-2.
- [228] P. V. Quintana-Ramirez, M. C. Arenas-Arrocena, J. Santos-Cruz, M. Vega-González, O. Martínez-Alvarez, V. M. Castaño-Meneses, L. S. Acosta-Torres, and J. de la Fuente-Hernández, "Growth evolution and phase transition from chalcocite to digenite in nanocrystalline copper sulfide: Morphological, optical and electrical properties," *Beilstein Journal of Nanotechnology*, vol. 5, pp. 1542–1552, **2014**. DOI: 10.3762/bjnano.5.166.
- [229] Y. Wang, X. Ai, D. Miller, P. Rice, T. Topuria, L. Krupp, A. Kellock, and Q. Song, "Two-phase microwave-assisted synthesis of Cu<sub>2</sub>S nanocrystals," *CrystEngComm*, vol. 14, no. 22, p. 7560, **2012**. DOI: 10.1039/c2ce25809a.
- [230] R. C. Smith, V. D. Reed, and W. E. Hill, "Oxidation Of Thiols By Copper(II)," *Phosphorus, Sulfur, and Silicon and the Related Elements*, vol. 90, no. 1-4, pp. 147–154, **1994**. DOI: 10.1080/10426509408016396.
- [231] J. Tian, R. Qiao, K. Xiong, W. Zhang, and L. Chen, "A bioinspired Au-Cu<sub>1.97</sub>S/Cu<sub>2</sub>S film with efficient low-angle-dependent and thermal-assisted photodetection properties," *iScience*, vol. 24, no. 3, p. 102167, **2021**. DOI: 10.1016/j.isci.2021.102167.
- [232] Y. Rodríguez-Lazcano, H. Martínez, M. Calixto-Rodríguez, and A. Núñez Rodríguez, "Properties of CuS thin films treated in air plasma," *Thin Solid Films*, vol. 517, no. 21, pp. 5951–5955, **2009**. DOI: 10.1016/j.tsf.2009.03.075.
- [233] C. Ding, Y. Huang, Z. Shen, and X. Chen, "Synthesis and Bioapplications of Ag<sub>2</sub>S Quantum Dots with Near-Infrared Fluorescence," *Advanced Materials*, p. 2007768, **2021**. DOI: 10.1002/adma.202007768.
- [234] Y. Shu, J. Gao, J. Chen, J. Yan, J. Sun, D. Jin, Q. Xu, and X. Hu, "A near-infrared fluorescent sensor based on the architecture of low-toxic Ag<sub>2</sub>S quantum dot and MnO<sub>2</sub> nanosheet for sensing glutathione in human serum sample," *Talanta*, vol. 221, p. 121475, **2021**. DOI: 10.1016/j.talanta.2020.121475.
- [235] L.-w. Liu, S.-y. Hu, Y.-p. Dou, T.-h. Liu, J.-q. Lin, and Y. Wang, "Nonlinear optical properties of near-infrared region Ag<sub>2</sub>S quantum dots pumped by nanosecond laser pulses," *Beilstein Journal of Nanotechnology*, vol. 6, pp. 1781–1787, **2015**. DOI: 10.3762/bjnano.6.182.
- [236] R. Zamiri, H. Abbastabar Ahangar, A. Zakaria, G. Zamiri, M. Shabani, B. Singh, and J. M. F. Ferreira, "The structural and optical constants of Ag<sub>2</sub>S semiconductor nanostructure in the Far-Infrared," *Chemistry Central Journal*, vol. 9, no. 1, p. 28, **2015**. DOI: 10.1186/s13065-015-0099-y.

- [237] W. Yang, L. Zhang, Y. Hu, Y. Zhong, H. B. Wu, and X. W. D. Lou, "Microwave-Assisted Synthesis of Porous Ag<sub>2</sub>S-Ag Hybrid Nanotubes with High Visible-Light Photocatalytic Activity," *Angewandte Chemie International Edition*, vol. 51, no. 46, pp. 11 501–11 504, **2012**. DOI: 10.1002/anie.201206715.
- [238] D. Kumar, Kavita, K. Singh, V. Verma, and H. S. Bhatti, "Microwave-assisted synthesis and characterization of silver nanowires by polyol process," *Applied Nanoscience*, vol. 5, no. 7, pp. 881–890, **2015**. DOI: 10.1007/s13204-014-0386-2.
- [239] S. I. Sadovnikov and E. Y. Gerasimov, "Direct TEM observation of the "acanthite  $\alpha$ -Ag<sub>2</sub>S-argentite  $\beta$ -Ag<sub>2</sub>S" phase transition in a silver sulfide nanoparticle," *Nanoscale Advances*, vol. 1, no. 4, pp. 1581–1588, **2019**. DOI: 10.1039/C8NA00347E.
- [240] R. M. Aoki, E. T. d. S. Torres, J. P. A. de Jesus, S. A. Lourenço, R. V. Fernandes, E. Laureto, and M. A. Toledo da Silva, "Application of heterostructured CdS/ZnS quantum dots as luminescence down-shifting layer in P3HT:PCBM solar cells," *Journal of Luminescence*, vol. 237, p. 118 178, **2021**. DOI: 10.1016/j.jlumin.2021.118178.
- [241] T. Kuzuya, Y. Tai, S. Yamamuro, and K. Sumiyama, "Synthesis of copper and zinc sulfide nanocrystals via thermolysis of the polymetallic thiolate cage," *Science and Technology of Advanced Materials*, vol. 6, no. 1, pp. 84–90, **2005**. DOI: 10.1016/j.stam.2004.08.005.
- [242] C.-H. Lu, B. Bhattacharjee, and S.-Y. Chen, "Microwave synthesis of manganese-ion-doped zinc sulfide nano-phosphors using a novel monomer," *Journal of Alloys and Compounds*, vol. 475, no. 1-2, pp. 116–121, **2009**. DOI: 10.1016/j.jallcom.2008.08.042.
- [243] P. V. Raleaooa, A. Roodt, G. G. Mhlongo, D. E. Motaung, and O. M. Ntwaeaborwa, "Analysis of the structure, particle morphology and photoluminescent properties of ZnS:Mn<sup>2+</sup> nanoparticulate phosphors," *Optik - International Journal for Light and Electron Optics*, vol. 153, pp. 31–42, **2018**. DOI: 10.1016/j.ijleo.2017.09.120.
- [244] Y. C. Cheng, C. Q. Jin, F. Gao, X. L. Wu, W. Zhong, S. H. Li, and P. K. Chu, "Raman scattering study of zinc blende and wurtzite ZnS," *Journal of Applied Physics*, vol. 106, no. 12, **2009**. DOI: 10.1063/1.3270401.
- [245] D. M. Sousa, L. C. Alves, A. Marques, G. Gaspar, J. C. Lima, and I. Ferreira, "Facile Microwave-assisted Synthesis Manganese Doped Zinc Sulfide Nanoparticles," *Scientific Reports*, vol. 8, no. 15992, **2018**. DOI: 10.1038/s41598-018-34268-z.
- [246] F. A. La Porta, J. Andrés, M. S. Li, J. R. Sambrano, J. A. Varela, and E. Longo, "Zinc blende versus wurtzite ZnS nanoparticles: control of the phase and optical properties by tetrabutylammonium hydroxide," *Phys. Chem. Chem. Phys.*, vol. 16, no. 37, pp. 20 127–20 137, **2014**. DOI: 10.1039/C4CP02611J.
- [247] F. A. La Porta, J. Andrés, M. S. Li, J. R. Sambrano, J. A. Varela, and E. Longo, "Zinc blende versus wurtzite ZnS nanoparticles: control of the phase and optical properties by tetrabutylammonium hydroxide," *Phys. Chem. Chem. Phys.*, vol. 16, no. 37, pp. 20 127–20 137, **2014**. DOI: 10.1039/C4CP02611J.
- [248] V. Gayou, B. Salazar Hernández, R. Delgado Macuil, G. Zavala, P. Santiago, and A. Oliva, "Structural Studies of ZnS Nanoparticles by High Resolution Transmission Electron Microscopy," *Journal of Nano Research*, vol. 9, pp. 125–132, **2010**. DOI: 10.4028/www.scientific.net/JNanoR.9.125.
- [249] J. Cao, J. Yang, Y. Zhang, L. Yang, Y. Wang, M. Wei, Y. Liu, M. Gao, X. Liu, and Z. Xie, "Optimized doping concentration of manganese in zinc sulfide nanoparticles for yellow-orange light emission," *Journal of Alloys and Compounds*, vol. 486, no. 1-2, pp. 890–894, **2009**. DOI: 10.1016/j.jallcom.2009.07.097.

- [250] A. H. Khan, V. Pinchetti, I. Tanghe, Z. Dang, B. Martín-García, Z. Hens, D. Van Thourhout, P. Geiregat, S. Brovelli, and I. Moreels, “Tunable and Efficient Red to Near-Infrared Photoluminescence by Synergistic Exploitation of Core and Surface Silver Doping of CdSe Nanoplatelets,” *Chemistry of Materials*, vol. 31, no. 4, pp. 1450–1459, **2019**. DOI: 10.1021/acs.chemmater.8b05334.
- [251] S. Ullah, A. Bouich, H. Ullah, B. Mari, and M. Mollar, “Comparative study of binary cadmium sulfide (CdS) and tin disulfide (SnS<sub>2</sub>) thin buffer layers,” *Solar Energy*, vol. 208, pp. 637–642, **2020**. DOI: 10.1016/j.solener.2020.08.036.
- [252] T. Chu, H. Wang, and L. Mao, “Hydrogen Evolution Under Visible Light on CdS Nano-Rod,” *Journal of Materials Engineering and Performance*, vol. 23, no. 10, pp. 3413–3417, **2014**. DOI: 10.1007/s11665-014-1128-z.
- [253] Y.-J. Yuan, D. Chen, Z.-T. Yu, and Z.-G. Zou, “Cadmium sulfide-based nanomaterials for photocatalytic hydrogen production,” *Journal of Materials Chemistry A*, vol. 6, no. 25, pp. 11 606–11 630, **2018**. DOI: 10.1039/C8TA00671G.
- [254] N. Venkatesh, K. Sabarish, G. Murugadoss, R. Thangamuthu, and P. Sakthivel, “Visible light-driven photocatalytic dye degradation under natural sunlight using Sn-doped CdS nanoparticles,” *Environmental Science and Pollution Research*, vol. 27, no. 34, pp. 43 212–43 222, **2020**. DOI: 10.1007/s11356-020-10268-3.
- [255] I. Devadoss, P. Sakthivel, and A. Krishnamoorthy, “Band gap tailoring and photoluminescence performance of CdS quantum dots for white LED applications: influence of Ba<sup>2+</sup> and Zn<sup>2+</sup> ions,” *Journal of Materials Science: Materials in Electronics*, vol. 32, no. 5, pp. 5729–5737, **2021**. DOI: 10.1007/s10854-021-05293-y.
- [256] G. Nabiyouni, E. Azizi, and N. Nasrollahi, “A Simple Microwave Method for Synthesis of CdS Nanoparticles,” *Journal of Cluster Science*, vol. 24, no. 4, pp. 1043–1055, **2013**. DOI: 10.1007/s10876-013-0596-x.
- [257] I. López and I. Gómez, “Microwave-Assisted Synthesis of Cadmium Sulfide Nanoparticles: Effect of Hydroxide Ion Concentration,” *MRS Proceedings*, vol. 1617, pp. 151–156, **2013**. DOI: 10.1557/opl.2013.1178.
- [258] G. Tai, J. Zhou, and W. Guo, “Inorganic salt-induced phase control and optical characterization of cadmium sulfide nanoparticles,” *Nanotechnology*, vol. 21, no. 17, p. 175 601, **2010**. DOI: 10.1088/0957-4484/21/17/175601.
- [259] R. E. Dickson and M. Z. Hu, “Chemical synthesis and optical characterization of regular and magic-sized CdS quantum dot nanocrystals using 1-dodecanethiol,” *Journal of Materials Research*, vol. 30, no. 7, pp. 890–895, **2015**. DOI: 10.1557/jmr.2015.57.
- [260] F. Horani and E. Lifshitz, “Unraveling the Growth Mechanism Forming Stable  $\gamma$ -In<sub>2</sub>S<sub>3</sub> and  $\beta$ -In<sub>2</sub>S<sub>3</sub> Colloidal Nanoplatelets,” *Chemistry of Materials*, vol. 31, no. 5, pp. 1784–1793, **2019**. DOI: 10.1021/acs.chemmater.9b00013.
- [261] Gunawan, A Haris, and W Septina, “Synthesis of indium sulfide photoanode, its characterization and application for degradation of methylene blue and methyl orange,” *IOP Conference Series: Materials Science and Engineering*, vol. 959, p. 012 021, **2020**. DOI: 10.1088/1757-899X/959/1/012021.
- [262] F. Jiang, C. Ozaki, Gunawan, T. Harada, Z. Tang, T. Minemoto, Y. Nose, and S. Ikeda, “Effect of Indium Doping on Surface Optoelectrical Properties of Cu<sub>2</sub>ZnSnS<sub>4</sub> Photoabsorber and Interfacial/Photovoltaic Performance of Cadmium Free In<sub>2</sub>S<sub>3</sub>/Cu<sub>2</sub>ZnSnS<sub>4</sub> Heterojunction Thin Film Solar Cell,” *Chemistry of Materials*, vol. 28, no. 10, pp. 3283–3291, **2016**. DOI: 10.1021/acs.chemmater.5b04984.

- [263] C. R. Patra, S. Patra, A. Gabashvili, Y. Mastai, Y. Kolytyn, A. Gedanken, V. Palchik, and M. A. Slifkin, "A Microwave Route for the Synthesis of Nanoflakes and Dendrites-Type  $\beta$ -In<sub>2</sub>S<sub>3</sub> and their Characterization," *Journal of Nanoscience and Nanotechnology*, vol. 6, no. 3, pp. 845–851, **2006**. DOI: 10.1166/jnn.2006.134.
- [264] J.-H. Park, T.-M. Chung, B. K. Park, and C. G. Kim, "Indium complexes with aminothiolate ligands as single precursors for indium chalcogenides," *Inorganica Chimica Acta*, vol. 505, p. 119 504, **2020**. DOI: 10.1016/j.ica.2020.119504.
- [265] T. S.S., T. A.V., S. L.V., M. L.N., M. E.V., and M. V.F., "Semiconductor Thin Films of In<sub>2</sub>S<sub>3</sub> for Solar Cells," *Universal Journal of Chemistry*, vol. 4, no. 2, pp. 74–77, **2016**. DOI: 10.13189/ujc.2016.040205.
- [266] S. Ghoshal, N. P. Kushwah, M. K. Pal, V. K. Jain, and M. Nethaji, "Tris(dithiocarboxylato)indium(III): Thermal studies and crystal structure of [In(S<sub>2</sub>Ctol)<sub>3</sub>]," *Journal of Chemical Sciences*, vol. 120, no. 3, pp. 305–308, **2008**. DOI: 10.1007/s12039-008-0052-x.
- [267] S. Kumar and T. T. John, "Highly photo-responsive In<sub>2</sub>S<sub>3</sub> thin film by sulfurizing indium layer," *Materials Chemistry and Physics*, vol. 286, p. 126 222, **2022**. DOI: 10.1016/j.matchemphys.2022.126222.
- [268] M. Hashemi, M. Minbashi, S. M. B. Ghorashi, and A. Ghobadi, "A modeling study on utilizing low temperature sprayed In<sub>2</sub>S<sub>3</sub> as the buffer layer of CuBaSn(S, Se) solar cells," *Scientific Reports*, vol. 11, no. 1, p. 20 038, **2021**. DOI: 10.1038/s41598-021-99012-6.
- [269] J. Tabernor, P. Christian, and P. O'Brien, "A general route to nanodimensional powders of indium chalcogenides," *Journal of Materials Chemistry*, vol. 16, no. 21, p. 2082, **2006**. DOI: 10.1039/b600921b.
- [270] X. Guo, H. Yue, S. Huang, X. Gao, Y. Ma, H. Chen, P. Wu, T. Zhang, and Z. Wang, "In<sub>2</sub>S<sub>3</sub> nanosheet arrays grown on the 3D graphene for sensitive detection of epinephrine in the presence of uric acid," *Journal of Materials Science: Materials in Electronics*, vol. 31, no. 4, pp. 3549–3556, **2020**. DOI: 10.1007/s10854-020-02903-z.
- [271] J. Singh and R. Soni, "Fabrication of nanostructured In<sub>2</sub>S<sub>3</sub> thin film with broad optical absorption for improved sunlight mediated photocatalysis application," *Optical Materials*, vol. 122, p. 111 748, **2021**. DOI: 10.1016/j.optmat.2021.111748.
- [272] R. K. Sharma, Y. N. Chouryal, S. Chaudhari, J. Saravanakumar, S. R. Dey, and P. Ghosh, "Adsorption-Driven Catalytic and Photocatalytic Activity of Phase Tuned In<sub>2</sub>S<sub>3</sub> Nanocrystals Synthesized via Ionic Liquids," *ACS Applied Materials & Interfaces*, vol. 9, no. 13, pp. 11 651–11 661, **2017**. DOI: 10.1021/acsami.7b01092.
- [273] G. Su, V. G. Hadjiev, P. E. Loya, J. Zhang, S. Lei, S. Maharjan, P. Dong, P. M. Ajayan, J. Lou, and H. Peng, "Chemical Vapor Deposition of Thin Crystals of Layered Semiconductor SnS<sub>2</sub> for Fast Photodetection Application," *Nano Letters*, vol. 15, no. 1, pp. 506–513, **2015**. DOI: 10.1021/nl503857r.
- [274] V. Brune, N. Raydan, A. Sutorius, F. Hartl, B. Purohit, S. Gahlot, P. Bargiela, L. Burel, M. Wilhelm, C. Hegemann, U. Atamtürk, S. Mathur, and S. Mishra, "Single source precursor route to nanometric tin chalcogenides," *Dalton Transactions*, vol. 50, no. 46, pp. 17 346–17 360, **2021**. DOI: 10.1039/D1DT02964A.
- [275] A. R. Garcia-Angelmo, M. Nair, and P. Nair, "Evolution of crystalline structure in SnS thin films prepared by chemical deposition," *Solid State Sciences*, vol. 30, pp. 26–35, **2014**. DOI: 10.1016/j.solidstatesciences.2014.02.002.
- [276] K. Ramakrishna Reddy, N. Koteswara Reddy, and R. Miles, "Photovoltaic properties of SnS based solar cells," *Solar Energy Materials and Solar Cells*, vol. 90, no. 18-19, pp. 3041–3046, **2006**. DOI: 10.1016/j.solmat.2006.06.012.

- [277] Q. Tan, L.-D. Zhao, J.-F. Li, C.-F. Wu, T.-R. Wei, Z.-B. Xing, and M. G. Kanatzidis, "Thermoelectrics with earth abundant elements: low thermal conductivity and high thermopower in doped SnS," *J. Mater. Chem. A*, vol. 2, no. 41, pp. 17 302–17 306, **2014**. DOI: 10.1039/C4TA04462B.
- [278] K. J. Norton, F. Alam, and D. J. Lewis, "A Review of the Synthesis, Properties, and Applications of Bulk and Two-Dimensional Tin (II) Sulfide (SnS)," *Applied Sciences*, vol. 11, no. 5, p. 2062, **2021**. DOI: 10.3390/app11052062.
- [279] C. R. Patra, A. Odani, V. G. Pol, D. Aurbach, and A. Gedanken, "Microwave-assisted synthesis of tin sulfide nanoflakes and their electrochemical performance as Li-inserting materials," *Journal of Solid State Electrochemistry*, vol. 11, no. 2, pp. 186–194, **2006**. DOI: 10.1007/s10008-005-0086-7.
- [280] J. Xia, X. Z. Li, X. Huang, N. Mao, D. D. Zhu, L. Wang, H. Xu, and X. M. Meng, "Physical vapor deposition synthesis of two-dimensional orthorhombic SnS flakes with strong angle/temperature-dependent Raman responses," *Nanoscale*, vol. 8, no. 4, pp. 2063–2070, **2016**. DOI: 10.1039/c5nr07675g.
- [281] J. M. Skelton, L. A. Burton, A. J. Jackson, F. Oba, S. C. Parker, and A. Walsh, "Lattice dynamics of the tin sulphides SnS<sub>2</sub>, SnS and Sn<sub>2</sub>S<sub>3</sub>: vibrational spectra and thermal transport," *Physical Chemistry Chemical Physics*, vol. 19, no. 19, pp. 12 452–12 465, **2017**. DOI: 10.1039/C7CP01680H.
- [282] O. Asif and A. C. Rastogi, "Tin Disulfide-Oxide (SnS<sub>2-x</sub>O<sub>x</sub>) as n-type Heterojunction Layer Processed by Chemical Bath Technique for Cd Free Fabrication of Compound Semiconductor Thin Film Solar Cells," *MRS Advances*, vol. 3, no. 56, pp. 3301–3306, **2018**. DOI: 10.1557/adv.2018.523.
- [283] T. O. Ajiboye and D. C. Onwudiwe, "Bismuth sulfide based compounds: Properties, synthesis and applications," *Results in Chemistry*, vol. 3, p. 100 151, **2021**. DOI: 10.1016/j.rechem.2021.100151.
- [284] J. Liu, X. Zheng, L. Yan, L. Zhou, G. Tian, W. Yin, L. Wang, Y. Liu, Z. Hu, Z. Gu, C. Chen, and Y. Zhao, "Bismuth Sulfide Nanorods as a Precision Nanomedicine for in Vivo Multimodal Imaging-Guided Photothermal Therapy of Tumor," *ACS Nano*, vol. 9, no. 1, pp. 696–707, **2015**. DOI: 10.1021/nn506137n.
- [285] L. Ma, Q. Zhao, Q. Zhang, M. Ding, J. Huang, X. Liu, Y. Liu, X. Wu, and X. Xu, "Controlled assembly of Bi<sub>2</sub>S<sub>3</sub> architectures as Schottky diode, supercapacitor electrodes and highly efficient photocatalysts," *RSC Adv.*, vol. 4, no. 78, pp. 41 636–41 641, **2014**. DOI: 10.1039/C4RA07169G.
- [286] H. Song, X. Zhan, D. Li, Y. Zhou, B. Yang, K. Zeng, J. Zhong, X. Miao, and J. Tang, "Rapid thermal evaporation of Bi<sub>2</sub>S<sub>3</sub> layer for thin film photovoltaics," *Solar Energy Materials and Solar Cells*, vol. 146, pp. 1–7, **2016**. DOI: 10.1016/j.solmat.2015.11.019.
- [287] S. Bera, S. Ghosh, and R. N. Basu, "Fabrication of Bi<sub>2</sub>S<sub>3</sub>/ZnO heterostructures: an excellent photocatalyst for visible-light-driven hydrogen generation and photoelectrochemical properties," *New Journal of Chemistry*, vol. 42, no. 1, pp. 541–554, **2018**. DOI: 10.1039/C7NJ03424E.
- [288] H. El-Kouch, L. E. Farh, J. Sayah, and A. Challioui, "Electronic and Optical Properties of TiS<sub>2</sub> Determined from Generalized Gradient Approximation Study," *Chinese Physics Letters*, vol. 32, no. 9, p. 096 102, **2015**. DOI: 10.1088/0256-307X/32/9/096102.
- [289] A. Oliva, "Formation of the band gap energy on CdS thin films growth by two different techniques," *Thin Solid Films*, vol. 391, no. 1, pp. 28–35, **2001**. DOI: 10.1016/S0040-6090(01)00830-6.

- [290] G. Zhang, D. Chen, N. Li, Q. Xu, H. Li, J. He, and J. Lu, "Construction of Hierarchical Hollow Co<sub>9</sub>S<sub>8</sub>/ZnIn<sub>2</sub>S<sub>4</sub> Tubular Heterostructures for Highly Efficient Solar Energy Conversion and Environmental Remediation," *Angewandte Chemie International Edition*, vol. 59, no. 21, pp. 8255–8261, **2020**. DOI: 10.1002/anie.202000503.
- [291] A. V. Naumov, V. N. Semenov, A. N. Lukin, and E. G. Goncharov, "Phase Composition of Copper Sulfide Films Produced from Copper Salt-Thiourea Complexes," *Inorganic Materials*, vol. 38, no. 3, pp. 271–273, **2002**. DOI: 10.1023/A:1014779018372.
- [292] F. Shao, Z. Tian, P. Qin, K. Bu, W. Zhao, L. Xu, D. Wang, and F. Huang, "2H-NbS<sub>2</sub> film as a novel counter electrode for meso-structured perovskite solar cells," *Scientific Reports*, vol. 8, no. 1, p. 7033, **2018**. DOI: 10.1038/s41598-018-25449-x.
- [293] S. Conejeros, B. Guster, P. Alemany, J.-P. Pouget, and E. Canadell, "Rich Polymorphism of Layered NbS<sub>3</sub>," *Chemistry of Materials*, vol. 33, no. 14, pp. 5449–5463, **2021**. DOI: 10.1021/acs.chemmater.1c01417.
- [294] R. Boughalmi, R. Rahmani, A. Boukhachem, B. Amrani, K. Driss-Khodja, and M. Amlouk, "Metallic behavior of NiS thin film under the structural, optical, electrical and ab initio investigation frameworks," *Materials Chemistry and Physics*, vol. 163, pp. 99–106, **2015**. DOI: 10.1016/j.matchemphys.2015.07.019.
- [295] T. Pillo, J. Hayoz, D. Naumović, H. Berger, L. Perfetti, L. Gavioli, A. Taleb-Ibrahimi, L. Schlapbach, and P. Aebi, "Fine structure in high-resolution photoemission spectra of quasi-two-dimensional 1T-TaS<sub>2</sub>," *Physical Review B*, vol. 64, no. 24, p. 245105, **2001**. DOI: 10.1103/PhysRevB.64.245105.
- [296] R. G. Pearson, "Hard and soft acids and bases, HSAB, part 1: Fundamental principles," *Journal of Chemical Education*, vol. 45, no. 9, p. 581, **1968**. DOI: 10.1021/ed045p581.
- [297] S. Roy, S. Sarkar, J. Pan, U. V. Waghmare, R. Dhanya, C. Narayana, and S. C. Peter, "Crystal Structure and Band Gap Engineering in Polyoxometalate-Based Inorganic-Organic Hybrids," *Inorganic Chemistry*, vol. 55, no. 7, pp. 3364–3377, **2016**. DOI: 10.1021/acs.inorgchem.5b02718.
- [298] O. Stroyuk, A. Raevskaya, and N. Gaponik, "Solar light harvesting with multinary metal chalcogenide nanocrystals," *Chemical Society Reviews*, vol. 47, no. 14, pp. 5354–5422, **2018**. DOI: 10.1039/C8CS00029H.
- [299] P. Baláž, M. Achimovičová, M. Baláž, K. Chen, O. Dobrozhan, E. Guilmeau, J. Hejtmánek, K. Knížek, L. Kubíčková, P. Levinský, V. Puchý, M. J. Reece, P. Varga, and R. Zhang, "Thermoelectric Cu-S-Based Materials Synthesized via a Scalable Mechanochemical Process," *ACS Sustainable Chemistry & Engineering*, vol. 9, no. 5, pp. 2003–2016, **2021**. DOI: 10.1021/acssuschemeng.0c05555.
- [300] Y. Wang, X. Li, Y. Zhang, X. He, and J. Zhao, "Ether based electrolyte improves the performance of CuFeS<sub>2</sub> spike-like nanorods as a novel anode for lithium storage," *Electrochimica Acta*, vol. 158, pp. 368–373, **2015**. DOI: 10.1016/j.electacta.2015.01.141.
- [301] Y. L. Mikhlin, Y. V. Tomashevich, I. P. Asanov, A. V. Okotrub, V. A. Varnek, and D. V. Vyalikh, "Spectroscopic and electrochemical characterization of the surface layers of chalcopyrite (CuFeS<sub>2</sub>) reacted in acidic solutions," *Applied Surface Science*, vol. 225, no. 1-4, pp. 395–409, **2004**. DOI: 10.1016/j.apsusc.2003.10.030.
- [302] M. Sandroni, K. D. Wegner, D. Aldakov, and P. Reiss, "Prospects of Chalcopyrite-Type Nanocrystals for Energy Applications," *ACS Energy Letters*, vol. 2, no. 5, pp. 1076–1088, **2017**. DOI: 10.1021/acsenerylett.7b00003.



- [303] B. Kumar, S. V. Singh, A. Chattopadhyay, S. Biring, and B. N. Pal, "Scalable Synthesis of a Sub-10 nm Chalcopyrite ( $\text{CuFeS}_2$ ) Nanocrystal by the Microwave-Assisted Synthesis Technique and Its Application in a Heavy-Metal-Free Broad-Band Photodetector," *ACS Omega*, vol. 5, no. 40, pp. 25 947–25 953, **2020**. DOI: 10.1021/acsomega.0c03336.
- [304] B. Karuppanan, J. L. Sturgeon, K. L. Bunker, K. E. Harris, R. Ganesan, and J. A. Aitken, "Low-temperature synthesis of micro- and nano-crystalline  $\text{CuFeS}_2$  polymorphs," *SN Applied Sciences*, vol. 2, no. 11, p. 1931, **2020**. DOI: 10.1007/s42452-020-03729-4.
- [305] Y. Vahidshad, S. M. Mirkazemi, M. N. Tahir, R. Ghasemzadeh, and W. Tremel, "Synthesis of  $\text{CuFeS}_2$  Nanoparticles by One-pot Facile Method," *J. Nanostruct.*, vol. 7, no. 4, pp. 284–291, **2017**.
- [306] S. M. Hosseinpour-Mashkani, K. Rao, and Z. Chamanzadeh, "Novel precursor in synthesis, characterization of  $\text{CuInS}_2$  via Microwave method," *International Conference on Nanoscience, Engineering and Technology (ICONSET 2011)*, IEEE, **2011**, pp. 653–655, ISBN: 978-1-4673-0074-2. DOI: 10.1109/ICONSET.2011.6167891.
- [307] Y. Zheng, Y. Zou, and J. Jiang., "Synthesis of Gd-doped  $\text{CuInS}_2$  quantum dots exhibiting photoluminescence and high longitudinal relaxivity," *Materials Letters*, vol. 168, pp. 86–89, **2016**. DOI: 10.1016/j.matlet.2016.01.032.
- [308] S. Shen, L. Li, Z. Wu, M. Sun, Z. Tang, and J. Yang, "In<sub>4</sub>SnS<sub>8</sub> ultrathin nanosheets: a ternary sulfide with fast adsorption-visible-light photocatalysis dual function," *RSC Advances*, vol. 7, no. 8, pp. 4555–4562, **2017**. DOI: 10.1039/C6RA27262B.
- [309] Y. Lei, G. Wang, L. Zhou, W. Hu, S. Song, W. Fan, and H. Zhang, "Cubic spinel  $\text{In}_4\text{SnS}_8$ : electrical transport properties and electrochemical hydrogen storage properties," *Dalton Transactions*, vol. 39, no. 30, p. 7021, **2010**. DOI: 10.1039/c0dt00060d.
- [310] Y. Lei, Y. Xing, W. Fan, S. Song, and H. Zhang, "Synthesis, characterization and optical property of flower-like indium tin sulfide nanostructures," *Dalton Transactions*, no. 9, p. 1620, **2009**. DOI: 10.1039/b814602k.
- [311] P. K. Nair, A. R. Garcia-Angelmo, and M. T. S. Nair, "Cubic and orthorhombic  $\text{SnS}$  thin-film absorbers for tin sulfide solar cells," *physica status solidi (a)*, vol. 213, no. 1, pp. 170–177, **2016**. DOI: 10.1002/pssa.201532426.
- [312] F. Göde and S. Ünlü, "Nickel doping effect on the structural and optical properties of indium sulfide thin films by SILAR," *Open Chemistry*, vol. 16, no. 1, pp. 757–762, **2018**. DOI: 10.1515/chem-2018-0089.
- [313] B. Kempken, V. Dzhagan, D. R. Zahn, M. J. Alcocer, I. Kriegel, F. Scotognella, J. Parisi, and J. Kolny-Olesiak, "Synthesis, optical properties, and photochemical activity of zinc-indium-sulfide nanoplates," *RSC Advances*, vol. 5, no. 109, pp. 89 577–89 585, **2015**. DOI: 10.1039/c5ra20570k.
- [314] Y. Chen, S. Hu, W. Liu, X. Chen, L. Wu, X. Wang, P. Liu, and Z. Li, "Controlled syntheses of cubic and hexagonal  $\text{ZnIn}_2\text{S}_4$  nanostructures with different visible-light photocatalytic performance," *Dalton Transactions*, vol. 40, no. 11, p. 2607, **2011**. DOI: 10.1039/c0dt01435d.
- [315] J. E. Saal, S. Kirklin, M. Aykol, B. Meredig, and C. Wolverton, "Materials Design and Discovery with High-Throughput Density Functional Theory: The Open Quantum Materials Database (OQMD)," *JOM*, vol. 65, no. 11, pp. 1501–1509, **2013**. DOI: 10.1007/s11837-013-0755-4.
- [316] S. Kirklin, J. E. Saal, B. Meredig, A. Thompson, J. W. Doak, M. Aykol, S. Rühl, and C. Wolverton, "The Open Quantum Materials Database (OQMD): assessing the accuracy of DFT formation energies," *npj Computational Materials*, vol. 1, no. 1, p. 15 010, **2015**. DOI: 10.1038/npjcompumats.2015.10.

- [317] Y. Oh, S. Bag, C. D. Malliakas, and M. G. Kanatzidis, "Selective surfaces: High-surface-area zinc tin sulfide chalcogels," *Chemistry of Materials*, vol. 23, no. 9, pp. 2447–2456, **2011**. DOI: 10.1021/cm2003462.
- [318] Z. Wei, Y. Lu, J. Zhao, S. Zhao, R. Wang, N. Fu, X. Li, L. Guan, and F. Teng, "Synthesis and Luminescent Modulation of ZnS Crystallite by a Hydrothermal Method," *ACS Omega*, vol. 3, no. 1, pp. 137–143, **2018**. DOI: 10.1021/acsomega.7b01574.
- [319] S. Hegde, P. Murahari, B. J. Fernandes, R. Venkatesh, and K. Ramesh, "Synthesis, thermal stability and structural transition of cubic SnS nanoparticles," *Journal of Alloys and Compounds*, vol. 820, p. 153116, **2020**. DOI: 10.1016/j.jallcom.2019.153116.
- [320] I. Y. Ahmet, M. Guc, Y. Sánchez, M. Neuschitzer, V. Izquierdo-Roca, E. Saucedo, and A. L. Johnson, "Evaluation of AA-CVD deposited phase pure polymorphs of SnS for thin films solar cells," *RSC Advances*, vol. 9, no. 26, pp. 14 899–14 909, **2019**. DOI: 10.1039/C9RA01938C.
- [321] R. E. Abutbul, E. Segev, L. Zeiri, V. Ezersky, G. Makov, and Y. Golan, "Synthesis and properties of nanocrystalline  $\pi$ -SnS—a new cubic phase of tin sulphide," *RSC Advances*, vol. 6, no. 7, pp. 5848–5855, **2016**. DOI: 10.1039/c5ra23092f.
- [322] X. Wei, H. Hui, C. Zhao, C. Deng, M. Han, Z. Yu, A. Sheng, P. Roy, A. Chen, J. Lin, D. F. Watson, Y.-Y. Sun, T. Thomay, S. Yang, Q. Jia, S. Zhang, and H. Zeng, "Realization of BaZrS<sub>3</sub> chalcogenide perovskite thin films for optoelectronics," *Nano Energy*, vol. 68, p. 104317, **2020**. DOI: 10.1016/j.nanoen.2019.104317.
- [323] J. M. Polfus, T. Norby, and R. Bredesen, "Protons in Oxysulfides, Oxysulfates, and Sulfides: A First-Principles Study of La<sub>2</sub>O<sub>2</sub>S, La<sub>2</sub>O<sub>2</sub>SO<sub>4</sub>, SrZrS<sub>3</sub>, and BaZrS<sub>3</sub>," *The Journal of Physical Chemistry C*, vol. 119, no. 42, pp. 23 875–23 882, **2015**. DOI: 10.1021/acs.jpcc.5b08278.
- [324] M. Surendran, H. Chen, B. Zhao, A. S. Thind, S. Singh, T. Orvis, H. Zhao, J.-K. Han, H. Htoon, M. Kawasaki, R. Mishra, and J. Ravichandran, "Epitaxial Thin Films of a Chalcogenide Perovskite," *Chemistry of Materials*, vol. 33, no. 18, pp. 7457–7464, **2021**. DOI: 10.1021/acs.chemmater.1c02202.
- [325] C. Comparotto, P. Ström, O. Donzel-Gargand, T. Kubart, and J. J. S. Scragg, "Synthesis of BaZrS<sub>3</sub> Perovskite Thin Films at a Moderate Temperature on Conductive Substrates," *ACS Applied Energy Materials*, vol. 5, no. 5, pp. 6335–6343, **2022**. DOI: 10.1021/acsaem.2c00704.
- [326] T. Nitta, K. Nagase, and S. Hayakawa, "Formation, Microstructure, and Properties of Barium Zirconium Sulfide Ceramics," *Journal of the American Ceramic Society*, vol. 53, no. 11, pp. 601–604, **1970**. DOI: 10.1111/j.1151-2916.1970.tb15981.x.
- [327] Y. Wang, N. Sato, K. Yamada, and T. Fujino, "Synthesis of BaZrS<sub>3</sub> in the presence of excess sulfur," *Journal of Alloys and Compounds*, vol. 311, no. 2, pp. 214–223, **2000**. DOI: 10.1016/S0925-8388(00)01134-8.
- [328] V. K. Ravi, S. H. Yu, P. K. Rajput, C. Nayak, D. Bhattacharyya, D. S. Chung, and A. Nag, "Colloidal BaZrS<sub>3</sub> chalcogenide perovskite nanocrystals for thin film device fabrication," *Nanoscale*, vol. 13, no. 3, pp. 1616–1623, **2021**. DOI: 10.1039/D0NR08078K.
- [329] D. Coucouvanis, A. Hadjikyriacou, R. Lester, and M. G. Kanatzidis, "Zirconium-Sulfur Chemistry. Synthesis and Structural Characterization of the Zr<sub>3</sub>S<sub>3</sub>(tBuS)<sub>2</sub>(BH<sub>4</sub>)<sub>4</sub>(THF)<sub>2</sub>, Zr<sub>6</sub>S<sub>6</sub>(tBuS)<sub>4</sub>(BH<sub>4</sub>)<sub>8</sub>(THF)<sub>2</sub>, Zr<sub>3</sub>(S)(tBuS)<sub>10</sub>, and (Mg(THF)<sub>6</sub>)[Zr<sub>2</sub>(SPh)<sub>7.2</sub>(CH<sub>2</sub>Ph)<sub>1.8</sub>]<sub>2</sub>.cntdot.3THF Clusters. Activation and Cleavage of the C-S bond in Zircon," *Inorganic Chemistry*, vol. 33, no. 17, pp. 3645–3655, **1994**. DOI: 10.1021/ic00095a006.
- [330] K. Ramasamy, P. S. Shinde, N. Naghibolashrafi, S. Pan, and A. Gupta, "Nanocrystals of CuMSnS<sub>4</sub> (M = In or Ga) for solar energy conversion applications," *Chemical Communications*, vol. 54, no. 83, pp. 11 757–11 760, **2018**. DOI: 10.1039/C8CC06644B.

- [331] T. Hong, Z. Liu, W. Yan, J. Liu, and X. Zhang, "Inorganic-organic solar cells based on quaternary sulfide as absorber materials," *Physical Chemistry Chemical Physics*, vol. 17, no. 46, pp. 30 993–30 998, **2015**. DOI: 10.1039/C5CP05742F.
- [332] A. Raevskaya, O. Rozovik, A. Novikova, O. Selyshchev, O. Stroyuk, V. Dzhagan, I. Goryacheva, N. Gaponik, D. R. T. Zahn, and A. Eychmüller, "Luminescence and photo-electrochemical properties of size-selected aqueous copper-doped Ag-In-S quantum dots," *RSC Advances*, vol. 8, no. 14, pp. 7550–7557, **2018**. DOI: 10.1039/C8RA00257F.
- [333] U. Dasgupta, S. K. Saha, and A. J. Pal, "Fully-depleted pn-junction solar cells based on layers of Cu<sub>2</sub>ZnSnS<sub>4</sub> (CZTS) and copper-diffused AgInS<sub>2</sub> ternary nanocrystals," *Solar Energy Materials and Solar Cells*, vol. 124, pp. 79–85, **2014**. DOI: 10.1016/j.solmat.2014.01.041.
- [334] R. N. Bukke and J. Jang, "Gel-based precursors for the high-performance of n-channel GaInSnZnO and p-channel CuGaSnSO thin-film transistors," *RSC Advances*, vol. 11, no. 54, pp. 34 392–34 401, **2021**. DOI: 10.1039/D1RA04787F.
- [335] N. On, B. K. Kim, Y. Kim, E. H. Kim, J. H. Lim, H. Hosono, J. Kim, H. Yang, and J. K. Jeong, "Boosting carrier mobility and stability in indium-zinc-tin oxide thin-film transistors through controlled crystallization," *Scientific Reports*, vol. 10, no. 1, p. 18 868, **2020**. DOI: 10.1038/s41598-020-76046-w.
- [336] I.-H. Baek, J. J. Pyeon, S. H. Han, G.-Y. Lee, B. J. Choi, J. H. Han, T.-M. Chung, C. S. Hwang, and S. K. Kim, "High-Performance Thin-Film Transistors of Quaternary Indium-Zinc-Tin Oxide Films Grown by Atomic Layer Deposition," *ACS Applied Materials & Interfaces*, vol. 11, no. 16, pp. 14 892–14 901, **2019**. DOI: 10.1021/acsami.9b03331.
- [337] W. Chen, B. Gutmann, and C. O. Kappe, "Characterization of Microwave-Induced Electric Discharge Phenomena in Metal-Solvent Mixtures," *ChemistryOpen*, vol. 1, no. 1, pp. 39–48, **2012**. DOI: 10.1002/open.201100013.
- [338] T. T. Chen, J. E. Dutrizac, K. E. Haque, W. Wyslouzil, and S. Kashyap, "The Relative Transparency of Minerals to Microwave Radiation," *Canadian Metallurgical Quarterly*, vol. 23, no. 3, pp. 349–351, **1984**. DOI: 10.1179/cm.1984.23.3.349.
- [339] Y. Zhao, Y. Zhang, H. Zhu, G. C. Hadjipanayis, and J. Q. Xiao, "Low-Temperature Synthesis of Hexagonal (Wurtzite) ZnS Nanocrystals," *Journal of the American Chemical Society*, vol. 126, no. 22, pp. 6874–6875, **2004**. DOI: 10.1021/ja048650g.
- [340] S. S. Chetty, S. Praneetha, A. Vadivel Murugan, K. Govarthanan, and R. S. Verma, "Microwave-Assisted Synthesis of Quasi-Pyramidal CuInS<sub>2</sub>-ZnS Nanocrystals for Enhanced Near-Infrared Targeted Fluorescent Imaging of Subcutaneous Melanoma," *Advanced Biosystems*, vol. 3, no. 1, p. 1 800 127, **2019**. DOI: 10.1002/adbi.201800127.
- [341] D. Magalhães Sousa, W. Chiappim, J. P. Leitão, J. C. Lima, and I. Ferreira, "Microwave Synthesis of Silver Sulfide and Silver Nanoparticles: Light and Time Influence," *ACS Omega*, vol. 5, no. 22, pp. 12 877–12 881, **2020**. DOI: 10.1021/acsomega.0c00656.
- [342] M. M. Cortese-Krott, B. O. Fernandez, M. Kelm, A. R. Butler, and M. Feelisch, "On the chemical biology of the nitrite/sulfide interaction," *Nitric Oxide - Biology and Chemistry*, vol. 46, pp. 14–24, **2015**. DOI: 10.1016/j.niox.2014.12.009.
- [343] A. Dejam, P. Kleinbongard, T. Rassaf, S. Hamada, P. Gharini, J. Rodriguez, M. Feelisch, and M. Kelm, "Thiols enhance NO formation from nitrate photolysis," *Free Radical Biology and Medicine*, vol. 35, no. 12, pp. 1551–1559, **2003**. DOI: 10.1016/j.freeradbiomed.2003.09.009.

- [344] A. B. Seabra, N. Manosalva, B. de Araujo Lima, M. T. Pelegriño, M. Brocchi, O. Rubilar, and N. Duran, "Antibacterial activity of nitric oxide releasing silver nanoparticles," *Journal of Physics: Conference Series*, vol. 838, p. 012031, **2017**. DOI: 10.1088/1742-6596/838/1/012031.
- [345] Y. Cao, W. Geng, R. Shi, L. Shang, G. I. Waterhouse, L. Liu, L. Z. Wu, C. H. Tung, Y. Yin, and T. Zhang, "Thiolate-Mediated Photoinduced Synthesis of Ultrafine Ag<sub>2</sub>S Quantum Dots from Silver Nanoparticles," *Angewandte Chemie - International Edition*, vol. 55, no. 48, pp. 14952–14957, **2016**. DOI: 10.1002/anie.201608019.
- [346] C. Wang, K. Tang, Q. Yang, C. An, B. Hai, G. Shen, and Y. Qian, "Blue-light emission of nanocrystalline CaS and SrS synthesized via a solvothermal route," *Chemical Physics Letters*, vol. 351, no. 5-6, pp. 385–390, **2002**. DOI: 10.1016/S0009-2614(01)01413-0.
- [347] B. Matos, M. Martins, A. C. Samamed, D. Sousa, I. Ferreira, and M. S. Diniz, "Toxicity evaluation of quantum dots (ZnS and CdS) singly and combined in Zebrafish (*Danio rerio*)," *International Journal of Environmental Research and Public Health*, vol. 17, no. 1, pp. 1–18, **2020**. DOI: 10.3390/ijerph17010232.
- [348] K. Aso, A. Hayashi, and M. Tatsumisago, "Synthesis of Needlelike and Platelike SnS Active Materials in High-Boiling Solvents and Their Application to All-Solid-State Lithium Secondary Batteries," *Crystal Growth & Design*, vol. 11, no. 9, pp. 3900–3904, **2011**. DOI: 10.1021/cg200459t.
- [349] T.-T. Xuan, J.-Q. Liu, C.-Y. Yu, R.-J. Xie, and H.-L. Li, "Facile Synthesis of Cadmium-Free Zn-In-S:Ag/ZnS Nanocrystals for Bio-Imaging," *Scientific Reports*, vol. 6, no. 1, p. 24459, **2016**. DOI: 10.1038/srep24459.
- [350] A. Tang, S. Qu, K. Li, Y. Hou, F. Teng, J. Cao, Y. Wang, and Z. Wang, "One-pot synthesis and self-assembly of colloidal copper(I) sulfide nanocrystals," *Nanotechnology*, vol. 21, no. 28, p. 285602, **2010**. DOI: 10.1088/0957-4484/21/28/285602.
- [351] C. Xiong, M. Liu, X. Zhu, and A. Tang, "A General One-Pot Approach to Synthesize Binary and Ternary Metal Sulfide Nanocrystals," *Nanoscale Research Letters*, vol. 14, no. 1, p. 19, **2019**. DOI: 10.1186/s11671-019-2856-7.
- [352] G. Murtaza, S. Alderhami, Y. T. Alharbi, U. Zulfiqar, M. Hossin, A. M. Alanazi, L. Almanqur, E. U. Onche, S. P. Venkateswaran, and D. J. Lewis, "Scalable and Universal Route for the Deposition of Binary, Ternary, and Quaternary Metal Sulfide Materials from Molecular Precursors," *ACS Applied Energy Materials*, vol. 3, no. 2, pp. 1952–1961, **2020**. DOI: 10.1021/acsaem.9b02359.
- [353] E. Güneri, F. Göde, B. Boyarbay, and C. Gümüş, "Structural and optical studies of chemically deposited Sn<sub>2</sub>S<sub>3</sub> thin films," *Materials Research Bulletin*, vol. 47, no. 11, pp. 3738–3742, **2012**. DOI: 10.1016/j.materresbull.2012.06.031.
- [354] T. S. Reddy, M. C. Santhosh Kumar, and S. Shaji, "Deposition rate dependant formation and properties of Sn<sub>2</sub>S<sub>3</sub> and SnS thin films by co-evaporation," *Materials Research Express*, vol. 4, no. 4, p. 046404, **2017**. DOI: 10.1088/2053-1591/aa6b71.
- [355] U. P. Gawai, U. P. Deshpande, and B. N. Dole, "A study on the synthesis, longitudinal optical phonon-plasmon coupling and electronic structure of Al doped ZnS nanorods," *RSC Advances*, vol. 7, no. 20, pp. 12382–12390, **2017**. DOI: 10.1039/C6RA28180J.
- [356] A. Derbali, A. Attaf, H. Saidi, H. Benamra, M. Nouadji, M. Aida, N. Attaf, and H. Ezzaouia, "Investigation of structural, optical and electrical properties of ZnS thin films prepared by ultrasonic spray technique for photovoltaic applications," *Optik*, vol. 154, pp. 286–293, **2018**. DOI: 10.1016/j.ijleo.2017.10.034.

- [357] G. C. Leindecker, A. K. Alves, and C. P. Bergmann, "Synthesis of niobium oxide fibers by electrospinning and characterization of their morphology and optical properties," *Ceramics International*, vol. 40, no. 10, pp. 16 195–16 200, **2014**. DOI: 10.1016/j.ceramint.2014.07.054.
- [358] E. T. Salim, J. A. Saimon, M. K. Abood, and M. A. Fakhri, "Electrical conductivity inversion for Nb<sub>2</sub>O<sub>5</sub> nanostructure thin films at different temperatures," *Materials Research Express*, vol. 6, no. 12, p. 126 459, **2020**. DOI: 10.1088/2053-1591/ab771c.
- [359] A. Cheruvathoor Poullose, G. Zoppellaro, I. Konidakis, E. Serpetzoglou, E. Stratakis, O. Tomanec, M. Beller, A. Bakandritsos, and R. Zbořil, "Fast and selective reduction of nitroarenes under visible light with an earth-abundant plasmonic photocatalyst," *Nature Nanotechnology*, vol. 17, no. 5, pp. 485–492, **2022**. DOI: 10.1038/s41565-022-01087-3.
- [360] A. Slistan-Grijalva, R. Herrera-Urbina, J. Rivas-Silva, M. Ávalos-Borja, F. Castellón-Barraza, and A. Posada-Amarillas, "Classical theoretical characterization of the surface plasmon absorption band for silver spherical nanoparticles suspended in water and ethylene glycol," *Physica E: Low-dimensional Systems and Nanostructures*, vol. 27, no. 1-2, pp. 104–112, **2005**. DOI: 10.1016/j.physe.2004.10.014.
- [361] G. Urbano, I. Lázaro, I. Rodríguez, J. L. Reyes, R. Larios, and R. Cruz, "Electrochemical and spectroscopic study of interfacial interactions between chalcopyrite and typical flotation process reagents," *International Journal of Minerals, Metallurgy, and Materials*, vol. 23, no. 2, pp. 127–136, **2016**. DOI: 10.1007/s12613-016-1219-y.
- [362] Xi, Zhang, Luan, Du, Li, Liang, Lian, and Yan, "Micro-Raman Study of Thermal Transformations of Sulfide and Oxysalt Minerals Based on the Heat Induced by Laser," *Minerals*, vol. 9, no. 12, p. 751, **2019**. DOI: 10.3390/min9120751.
- [363] C. Xia, Y. Jia, M. Tao, and Q. Zhang, "Tuning the band gap of hematite  $\alpha$ -Fe<sub>2</sub>O<sub>3</sub> by sulfur doping," *Physics Letters A*, vol. 377, no. 31-33, pp. 1943–1947, **2013**. DOI: 10.1016/j.physleta.2013.05.026.
- [364] H. Xie, X. Su, T. P. Bailey, C. Zhang, W. Liu, C. Uher, X. Tang, and M. G. Kanatzidis, "Anomalous Large Seebeck Coefficient of CuFeS<sub>2</sub> Derives from Large Asymmetry in the Energy Dependence of Carrier Relaxation Time," *Chemistry of Materials*, vol. 32, no. 6, pp. 2639–2646, **2020**. DOI: 10.1021/acs.chemmater.0c00388.
- [365] A. Waag, F. Fischer, K. Schüll, T. Baron, H.-J. Lugauer, T. Litz, U. Zehnder, W. Ossau, T. Gerhard, M. Keim, G. Reuscher, and G. Landwehr, "Laser diodes based on beryllium-chalcogenides," *Applied Physics Letters*, vol. 70, no. 3, pp. 280–282, **1997**. DOI: 10.1063/1.118422.
- [366] N. Gong, C. Deng, L. Wu, B. Wan, Z. Wang, Z. Li, H. Gou, and F. Gao, "Predicted semiconducting beryllium sulfides in 3D and 2D configurations: Insights from first-principles calculations," *Journal of Alloys and Compounds*, vol. 781, pp. 371–377, **2019**. DOI: 10.1016/j.jallcom.2018.11.374.
- [367] K. A. Walsh, *Beryllium Chemistry and Processing*, E. E. Vidal, A. Goldberg, E. N.C. Dalder, D. L. Olson, and B. Mishra, Eds. ASM International, **2009**, ISBN: 9780871707215.
- [368] Y.-H. Lai, W.-Y. Cheung, S.-K. Lok, G. K. L. Wong, S.-K. Ho, K.-W. Tam, and I.-K. Sou, "Rocksalt MgS solar blind ultra-violet detectors," *AIP Advances*, vol. 2, no. 1, p. 012 149, **2012**. DOI: 10.1063/1.3690124.
- [369] H. M. and M. Fichtner, "Magnesium Sulphide as Anode Material for Lithium-Ion Batteries," *Electrochimica Acta*, vol. 169, pp. 180–185, **2015**. DOI: 10.1016/j.electacta.2015.04.086.
- [370] Y. Xu and X. Xiao, "Accelerated microwave synthesis of magnesium sulfide with the pre-heating medium of graphite," *Journal of Materials Research*, vol. 10, no. 2, pp. 334–338, **1995**. DOI: 10.1557/JMR.1995.0334.

- [371] S. Sharif, K. Shahzad Ahmad, M. S. Akhtar, R. Farhat Mehmood, M. K. Alamgir, and M. Azad Malik, "In situ synthesis and deposition of un-doped and doped magnesium sulfide thin films by green technique," *Optik*, vol. 182, pp. 739–744, **2019**. DOI: 10.1016/j.ijleo.2018.12.108.
- [372] L. Konczewicz, P. Bigenwald, T. Cloitre, M. Chibane, R. Ricou, P. Testud, O. Briot, and R. Aulombard, "MOVPE growth of zincblende magnesium sulphide," *Journal of Crystal Growth*, vol. 159, no. 1-4, pp. 117–120, **1996**. DOI: 10.1016/0022-0248(95)00832-2.
- [373] S. P. Delaney, M. J. Nethercott, C. J. Mays, N. T. Winkquist, D. Arthur, J. L. Calahan, M. Sethi, D. S. Pardue, J. Kim, G. Amidon, and E. J. Munson, "Characterization of Synthesized and Commercial Forms of Magnesium Stearate Using Differential Scanning Calorimetry, Thermogravimetric Analysis, Powder X-Ray Diffraction, and Solid-State NMR Spectroscopy," *Journal of Pharmaceutical Sciences*, vol. 106, no. 1, pp. 338–347, **2017**. DOI: 10.1016/j.xphs.2016.10.004.
- [374] Y. Nishiwaki, T. Matsunaga, and M. Kumasaki, "Stabilization effects of carboxylate on pyrotechnic compositions including Mg powder in water," *Journal of Thermal Analysis and Calorimetry*, vol. 137, no. 5, pp. 1493–1498, **2019**. DOI: 10.1007/s10973-019-08069-z.
- [375] X. Song, S. Sun, D. Zhang, J. Wang, and J. Yu, "Synthesis and characterization of magnesium hydroxide by batch reaction crystallization," *Frontiers of Chemical Science and Engineering*, vol. 5, no. 4, pp. 416–421, **2011**. DOI: 10.1007/s11705-011-1125-9.
- [376] S. P. Delaney, M. J. Nethercott, C. J. Mays, N. T. Winkquist, D. Arthur, J. L. Calahan, M. Sethi, D. S. Pardue, J. Kim, G. Amidon, and E. J. Munson, "Characterization of Synthesized and Commercial Forms of Magnesium Stearate Using Differential Scanning Calorimetry, Thermogravimetric Analysis, Powder X-Ray Diffraction, and Solid-State NMR Spectroscopy," *Journal of Pharmaceutical Sciences*, vol. 106, no. 1, pp. 338–347, **2016**. DOI: 10.1016/j.xphs.2016.10.004.
- [377] A. R. Putranti, E. Hendradi, and R. Primaharinastiti, "EFFECTIVITY AND PHYSICO-CHEMICAL STABILITY OF NANOSTRUCTURED LIPID CARRIER COENZYME Q10 IN DIFFERENT RATIO of LIPID ALFA CETYL PALMITATE AND ALPHA TOCOPHERYL ACETATE AS CARRIER," *Asian Journal of Pharmaceutical and Clinical Research*, vol. 10, no. 2, p. 146, **2017**. DOI: 10.22159/ajpcr.2017.v10i2.14835.
- [378] S. Aydoğan, M. Erdemoğlu, A. Aras, G. Uçar, and A. Özkan, "Dissolution kinetics of celestite (SrSO<sub>4</sub>) in HCl solution with BaCl<sub>2</sub>," *Hydrometallurgy*, vol. 84, no. 3-4, pp. 239–246, **2006**. DOI: 10.1016/j.hydromet.2006.06.001.
- [379] A. B. Parmentier, J. J. Joos, P. F. Smet, and D. Poelman, "Luminescence of ytterbium in CaS and SrS," *Journal of Luminescence*, vol. 154, pp. 445–451, **2014**. DOI: 10.1016/j.jlumin.2014.05.033.
- [380] S.-S. Sun, "A new blue emitting TFEL phosphor: SrS : Cu," *Displays*, vol. 19, no. 4, pp. 145–149, **1999**. DOI: 10.1016/S0141-9382(98)00044-4.
- [381] L. Lu, X. Zhang, Z. Bai, X. Wang, X. Mi, and Q. Liu, "Synthesis of infrared up-conversion material SrS: Eu, Sm," *Advanced Powder Technology*, vol. 17, no. 2, pp. 181–187, **2006**. DOI: 10.1163/156855206775992300.
- [382] A. Obut, "Direct conversion of celestine to SrS by microwave heating," *Minerals Engineering*, vol. 20, pp. 1320–1322, **2007**. DOI: 10.1016/j.mineng.2007.06.005.
- [383] A. Jain, G. Hautier, S. Ong, C. Moore, C. Fischer, K. Persson, and G. Ceder, "Formation enthalpies by mixing GGA and GGA + U calculations," *Physical Review B*, vol. 84, no. 4, p. 45115, **2011**. DOI: 10.1103/PhysRevB.84.045115.

- [384] K. Maeda, N. Kawaida, R. Tsudome, K. Sakai, and T. Ikari, "X-ray and photoluminescence properties of Sm 3+ doped barium sulfide," *physica status solidi c*, vol. 9, no. 12, pp. 2271–2274, **2012**. DOI: 10.1002/pssc.201200321.
- [385] D. Zagorac, K. Doll, J. Zagorac, D. Jordanov, and B. Matović, "Barium Sulfide under Pressure: Discovery of Metastable Polymorphs and Investigation of Electronic Properties on ab Initio Level," *Inorganic Chemistry*, vol. 56, no. 17, pp. 10644–10654, **2017**. DOI: 10.1021/acs.inorgchem.7b01617.
- [386] G. Chen, J. Chen, and J. Peng, "Homogeneous precipitation synthesis of BaCO<sub>3</sub> powders with a needle-like morphology," *Green Processing and Synthesis*, vol. 7, no. 3, pp. 225–230, **2018**. DOI: 10.1515/gps-2016-0231.
- [387] G. S. Ahluwalia, "Management of Unwanted Hair," *Cosmetics Applications of Laser & Light-Based Systems*, Elsevier, **2009**, pp. 239–252. DOI: 10.1016/B978-0-8155-1572-2.50015-4.
- [388] W. Zhang, Y. Zhou, J. Zhu, and Y. Pan, "New Clean Process for Barium Sulfide Preparation by Barite Reduction with Elemental Sulfur," *Industrial & Engineering Chemistry Research*, vol. 53, no. 14, pp. 5646–5651, **2014**. DOI: 10.1021/ie4042356.
- [389] S. Singh, A. Vij, S. Lochab, R. Kumar, and N. Singh, "Synthesis and characterization of bismuth doped barium sulphide nanoparticles," *Materials Research Bulletin*, vol. 45, no. 5, pp. 523–526, **2010**. DOI: 10.1016/j.materresbull.2010.02.007.
- [390] J. P. Dismukes and J. G. White, "The Preparation, Properties, and Crystal Structures of Some Scandium Sulfides in the Range Sc<sub>2</sub>S<sub>3</sub>-ScS," *Inorganic Chemistry*, vol. 3, no. 9, pp. 1220–1228, **1964**. DOI: 10.1021/ic50019a004.
- [391] H. Nakamura and A. Kasahara, "Electrical Conductivity of Solid Scandium Sulfide," *Journal of the Japan Institute of Metals*, vol. 50, no. 11, pp. 974–978, **1986**. DOI: 10.2320/jinstmet1952.50.11\_974.
- [392] H. Nakamura, Y. Ogawa, and A. Kasahara, "Electrical Conductivity of IIa and IIIa Metal Sulfides in Solid," *Journal of the Japan Institute of Metals*, vol. 58, no. 5, pp. 519–525, **1994**. DOI: 10.2320/jinstmet1952.58.5\_519.
- [393] W. WENJING, H. DONGBO, L. PENG, G. ZHENG, K. FANAO, and Z. QIHE, "Formation and photodissociation of scandium-sulfide clusters," *Acta Chimica Sinica*, vol. 56, no. 7, pp. 675–681, **1998**.
- [394] T. Kaneko, Y. Yashima, E. Ahmadi, S. Natsui, and R. O. Suzuki, "Synthesis of Sc sulfides by CS<sub>2</sub> sulfurization," *Journal of Solid State Chemistry*, vol. 285, p. 121268, **2020**. DOI: 10.1016/j.jssc.2020.121268.
- [395] H. Nakamura, Y. Ogawa, and K. Gunji, "P-Type and N-Type Semiconductivities of Solid Yttrium Sulfide," *Transactions of the Japan Institute of Metals*, vol. 25, no. 10, pp. 698–702, **1984**. DOI: 10.2320/matertrans1960.25.698.
- [396] S. Liu, R. Ma, R. Jiang, and F. Luo, "Synthesis and Structure of Hydrated Yttrium Carbonate, Y<sub>2</sub>(CO<sub>3</sub>)<sub>3</sub>·3.279H<sub>2</sub>O," *Synthesis and Reactivity in Inorganic and Metal-Organic Chemistry*, vol. 30, no. 2, pp. 271–279, **2000**. DOI: 10.1080/00945710009351762.
- [397] H. Pushpalatha, T. Ghogare, N. Vibhu, P. Bagwade, R. Bulakhe, I. In, and C. Lokhande, "Characterization of soft chemically deposited yttrium sulfide (Y<sub>2</sub>S<sub>3</sub>) thin films," *Materials Today: Proceedings*, vol. 59, pp. 1236–1241, **2022**. DOI: 10.1016/j.matpr.2022.04.464.
- [398] J. Smajic, S. Wee, F. R. F. Simoes, M. N. Hedhili, N. Wehbe, E. Abou-Hamad, and P. M. F. J. Costa, "Capacity Retention Analysis in Aluminum-Sulfur Batteries," *ACS Applied Energy Materials*, vol. 3, no. 7, pp. 6805–6814, **2020**. DOI: 10.1021/acsaem.0c00921.

- [399] H. Senoh, T. Takeuchi, H. Kageyama, H. Sakaebe, M. Yao, K. Nakanishi, T. Ohta, T. Sakai, and K. Yasuda, "Electrochemical characteristics of aluminum sulfide for use in lithium secondary batteries," *Journal of Power Sources*, vol. 195, no. 24, pp. 8327–8330, **2010**. DOI: 10.1016/j.jpowsour.2010.06.079.
- [400] T. Leisegang, F. Meutzner, M. Zschornak, W. Münchgesang, R. Schmid, T. Nestler, R. A. Eremin, A. A. Kabanov, V. A. Blatov, and D. C. Meyer, "The Aluminum-Ion Battery: A Sustainable and Seminal Concept?" *Frontiers in Chemistry*, vol. 7, **2019**. DOI: 10.3389/fchem.2019.00268.
- [401] R. J. Wehmschulte and P. P. Power, "Low-Temperature Synthesis of Aluminum Sulfide as the Solvate  $\text{Al}_4\text{S}_6(\text{NMe}_3)_4$  in Hydrocarbon Solution," *Journal of the American Chemical Society*, vol. 119, no. 40, pp. 9566–9567, **1997**. DOI: 10.1021/ja972111c.
- [402] Y. XIAO, D. V. D. PLAS, J. SOONS, S. LANS, A. V. SANDWIJK, and M. REUTER, "SULFIDATION OF  $\text{Al}_2\text{O}_3$  WITH  $\text{CS}_2$  GAS FOR COMPACT ALUMINIUM PRODUCTION PROCESS," *Canadian Metallurgical Quarterly*, vol. 43, no. 2, pp. 283–292, **2004**. DOI: 10.1179/cmq.2004.43.2.283.
- [403] H. Zheng, B. Chen, L. Shi, F. Zhang, Z. Zhao, Y. Liu, L. Huang, B. Zou, and Y. Wang, "Stable blue-emissive aluminum acetylacetonate nanocrystals with high quantum yield of over 80UV-pumped white light-emitting diodes," *Nanophotonics*, vol. 9, no. 6, pp. 1509–1518, **2020**. DOI: 10.1515/nanoph-2020-0142.
- [404] S. Daniel and D. M. Hoffman, "Synthesis and Structures of Aluminum Alkanethiolate Complexes," *Inorganic Chemistry*, vol. 41, no. 15, pp. 3843–3849, **2002**. DOI: 10.1021/ic011257g.
- [405] P. Wang, M. Liu, F. Mo, Z. Long, F. Fang, D. Sun, Y.-n. Zhou, and Y. Song, "Exploring the sodium ion storage mechanism of gallium sulfide ( $\text{Ga}_2\text{S}_3$ ): a combined experimental and theoretical approach," *Nanoscale*, vol. 11, no. 7, pp. 3208–3215, **2019**. DOI: 10.1039/C8NR09356C.
- [406] Z. M. Hu, G. T. Fei, and L. D. Zhang, "Synthesis and tunable emission of  $\text{Ga}_2\text{S}_3$  quantum dots," *Materials Letters*, vol. 239, pp. 17–20, **2019**. DOI: 10.1016/j.matlet.2018.12.046.
- [407] A. Seral-Ascaso, S. Metel, A. Pokle, C. Backes, C. J. Zhang, H. C. Nerl, K. Rode, N. C. Berner, C. Downing, N. McEvoy, E. Muñoz, A. Harvey, Z. Gholamvand, G. S. Duesberg, J. N. Coleman, and V. Nicolosi, "Long-chain amine-templated synthesis of gallium sulfide and gallium selenide nanotubes," *Nanoscale*, vol. 8, no. 22, pp. 11 698–11 706, **2016**. DOI: 10.1039/C6NR01663D.
- [408] K. Ramalingam, G. Sivagurunathan, and C. Rizzoli, "Synthesis and characterization of gallium(III) dithiocarbamates as suitable nano-gallium(III) sulfide precursors," *Main Group Metal Chemistry*, **2015**. DOI: 10.1515/mgmc-2015-0019.
- [409] P. A. G. O'Hare, "Thermochemistry of silicon-containing materials," *Pure and Applied Chemistry*, vol. 71, no. 7, pp. 1243–1248, **2007**. DOI: 10.1351/pac199971071243.
- [410] C. Chen, X. Zhang, L. Krishna, C. Kendrick, S.-L. Shang, E. Toberer, Z.-K. Liu, A. Tamboli, and J. M. Redwing, "Synthesis, characterization and chemical stability of silicon dichalcogenides,  $\text{Si}(\text{Se S1-})_2$ ," *Journal of Crystal Growth*, vol. 452, pp. 151–157, **2016**. DOI: 10.1016/j.jcrysgro.2015.12.005.
- [411] R. Piekos and W. Wojnowski, "Untersuchungen über die Alkoholyse des  $\text{SiS}_2$ . II. Darstellung von Trialkoxysilanthiolen und Tetraalkoxycyclodisilthianen aus den tertiären Alkoholen," *Zeitschrift für anorganische und allgemeine Chemie*, vol. 318, no. 3-4, pp. 212–216, **1962**. DOI: 10.1002/zaac.19623180310.



- [412] R. O. Suzuki, Y. Yashima, T. Kaneko, E. Ahmadi, T. Kikuchi, T. Watanabe, and G. Nogami, "Synthesis of Silicon Sulfide by Using CS<sub>2</sub> Gas," *Metallurgical and Materials Transactions B*, vol. 52, no. 3, pp. 1379–1391, **2021**. DOI: 10.1007/s11663-021-02103-y.
- [413] M.-X. Xie, J.-W. Zhang, Y. Zhang, H.-R. Wu, Y.-P. Wang, W.-H. Wang, and G.-Q. Shao, "Synthesis and Growth Mechanism of SiS<sub>2</sub> Rods," *ACS Omega*, vol. 7, no. 26, pp. 22 500–22 510, **2022**. DOI: 10.1021/acsomega.2c01725.
- [414] C. Chen, X. Zhang, L. Krishna, C. Kendrick, S.-L. Shang, E. Toberer, Z.-K. Liu, A. Tamboli, and J. M. Redwing, "Synthesis, characterization and chemical stability of silicon dichalcogenides, Si(Se S1-)<sub>2</sub>," *Journal of Crystal Growth*, vol. 452, pp. 151–157, **2016**. DOI: 10.1016/j.jcrysgro.2015.12.005.
- [415] E. Sutter, B. Zhang, M. Sun, and P. Sutter, "Few-Layer to Multilayer Germanium(II) Sulfide: Synthesis, Structure, Stability, and Optoelectronics," *ACS Nano*, vol. 13, no. 8, pp. 9352–9362, **2019**. DOI: 10.1021/acsnano.9b03986.
- [416] B. Wang, W. Du, Y. Yang, Y. Zhang, Q. Zhang, X. Rui, H. Geng, and C. C. Li, "Two-Dimensional Germanium Sulfide Nanosheets as an Ultra-Stable and High Capacity Anode for Lithium Ion Batteries," *Chemistry - A European Journal*, vol. 26, no. 29, pp. 6554–6560, **2020**. DOI: 10.1002/chem.201904116.
- [417] A. Y. Shah, G. Kedarnath, A. Tyagi, C. A. Betty, V. K. Jain, and B. Vishwanadh, "Germanium Xanthates: Versatile Precursors for Photo Responsive Germanium Sulfide Nanostructures," *ChemistrySelect*, vol. 2, no. 17, pp. 4598–4604, **2017**. DOI: 10.1002/slct.201700486.
- [418] P. Ardalan, Y. Sun, P. Pianetta, C. B. Musgrave, and S. F. Bent, "Reaction Mechanism, Bonding, and Thermal Stability of 1-Alkanethiols Self-Assembled on Halogenated Ge Surfaces," *Langmuir*, vol. 26, no. 11, pp. 8419–8429, **2010**. DOI: 10.1021/la904864c.
- [419] P. Kitschke, T. Ruffer, H. Lang, A. A. Auer, and M. Mehring, "Chiral Spirocyclic Germanium Thiolates - An Evaluation of Their Suitability for Twin Polymerization based on A Combined Experimental and Theoretical Study," *ChemistrySelect*, vol. 1, no. 6, pp. 1184–1191, **2016**. DOI: 10.1002/slct.201600314.



## Auxiliary Data

This appendix contains a collection of data, figures and tables regarding the binary and multinary metal sulfide nanoparticle syntheses and their input parameters, ink depositions, and the auxiliary Python 3 scripts used in combination with the scripts found in Appendix B. Finally, a table with the reagents used in this work is presented at the end (Table A.1).

### A.1 Binary Metal Sulfides

#### A.1.1 Group 2: Be, Mg, Sr, Ba

##### A.1.1.1 Beryllium

The temperatures required to synthesize the sulfides from the alkaline groups are usually several hundreds of degrees Celsius with the added drawback of the oxides being more stable, relative to the sulfides. Beryllium sulfide is a highly reactive ionic metal sulfide. However, it is a promising wide band gap semiconductor that can find applications when alloyed in blue emitting lasers.[365] Some predicted phases of  $\text{BeS}_2$  could also be interesting given their predicted wide band gaps.[366] No publications regarding the current uses of unalloyed  $\text{BeS}$  were found in the literature, as well as no reports on the synthesis of  $\text{BeS}$  with the exception of the reaction between beryllium metal and hydrogen sulfide gas at  $900\text{ }^\circ\text{C}$ .[367]

The synthesis of beryllium sulfide was attempted starting from beryllium oxide ( $\text{BeO}$ ). The color, temperature, and pressure profiles, and the resulting powder's XRD pattern can be found in Figure A.1.

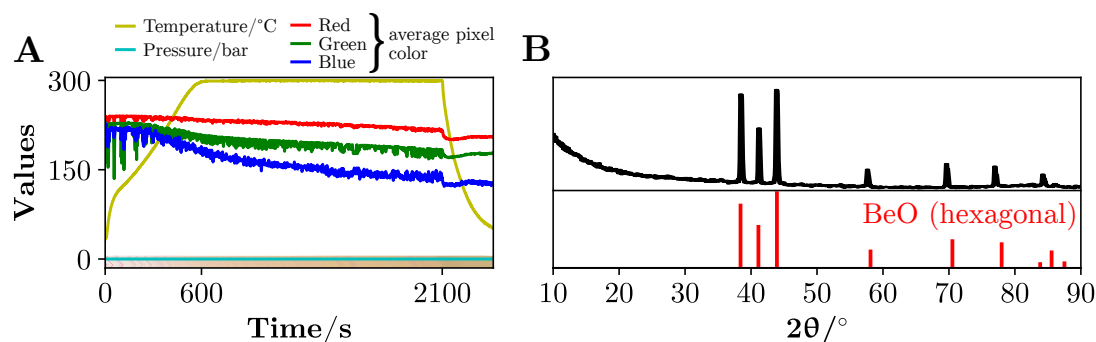


Figure A.1: Color, temperature and pressure profiles (A) of the synthesis attempt, starting from  $\text{BeO}$ , to obtain a beryllium sulfide and the XRD pattern (B) of the obtained product. The reference pattern of the hexagonal phase of  $\text{BeO}$  was taken from Materials Project[128][129] with the respective IDs: mp-2542.

There are no color changes in the color profile (A), with the exception of a slight darkening of the yellow suspension. The noise in the color profile is from a defect in the camera hardware. The

reaction did not yield a beryllium sulfide, since the XRD pattern (B) corresponds to the reagent, BeO. In future synthesis, a more reactive reagent should be used such as BeB<sub>2</sub> or BeH.

**Synthesis** Following the protocol guidelines from Section 3.1.1, 1 mmol (25 mg) of beryllium(II) oxide was added to an Anton Paar G30 proprietary reaction vial, with a polytetrafluoroethylene-covered Cowie stirring magnets with a size of 10 mm by 3 mm. Then the vial was filled with 5 g of 1-dodecanethiol. The mixture was then purged for 15 minutes by bubbling with industrial-grade nitrogen gas. The vial was capped with the proprietary polytetrafluoroethylene-covered silicon sealing cap and immediately inserted into the Anton Paar Monowave 400 microwave reactor's cavity. Under constant steering at 1200 RPM, the temperature was raised to 300 °C in 10 minutes, kept for 25 minutes, followed by an automated cooling procedure to 50 °C. The suspension was then divided into three 2 mL microcentrifuge tubes, centrifuged at 9000 RPM (9146 *g*), the supernatant discarded, followed by the addition of ethanol up to the 2 mL mark. Next, with a vortex, the tubes were shaken until all of the material was resuspended, and the suspensions were centrifuged again. This process was repeated two more times. After discarding the supernatant, the pellet was vacuum dried for 1 h by perforating the microcentrifuge cap with a needle to create a hole for the air and solvent to pass.

#### A.1.1.2 Magnesium

Magnesium sulfide is a reactive compound that upon contact with hot water forms magnesium hydroxide and with oxygen forms the oxide. Depending on the structure, rocksalt, zincblende and wurtzite, the sulfide's band gap is estimated to be, respectively, 2.66 eV, 3.46 eV and 3.5 eV, and can be used in ultra-violet photodetectors.[368] As anode in lithium batteries, the resulting voltage is 0.5 V and the theoretical specific capacity is 951 mAh/g.[369]

The only attempt to produce MgS by microwave irradiation was performed in 1995 by Yu and Xiao[370], by mixing Mg, S and graphite, which permitted achieving very high temperatures. Others have fabricated thin films of MgS by physical vapor deposition (PVD)[371] and by a technique similar to chemical vapor deposition (CVD)[372]. The only hydrothermal synthesis found in the literature, although is done at a relative mild temperature of 120 °C, the mixture of reagents required is complex, with 13 substances, and contains various toxic or hazardous substances such as methacrylic anhydride and terephthalamide - which is probably incorrectly written as terephthalimidazole.[146]

Synthesis of MgS was attempted starting from 1-dodecanethiol and a mixture of magnesium stearate and palmitate, technical grade from Sigma-Aldrich with 65% stearate and 25% palmitate. It is presumed that the remainder 10% of the reagent is the water from the salt's hydration. The amount of reagent used was assuming that the powder was composed of 100% of magnesium stearate, which has a molar mass of 591.27 g/mol while the palmitate has a molar mass of 535.1 g/mol. Since the structures of both molecules are very similar, it was assumed that the effect would be negligible on the synthesis.

The synthesis of magnesium sulfide was attempted starting from magnesium stearate. The color,

temperature, and pressure profiles can be found in Figure A.2.

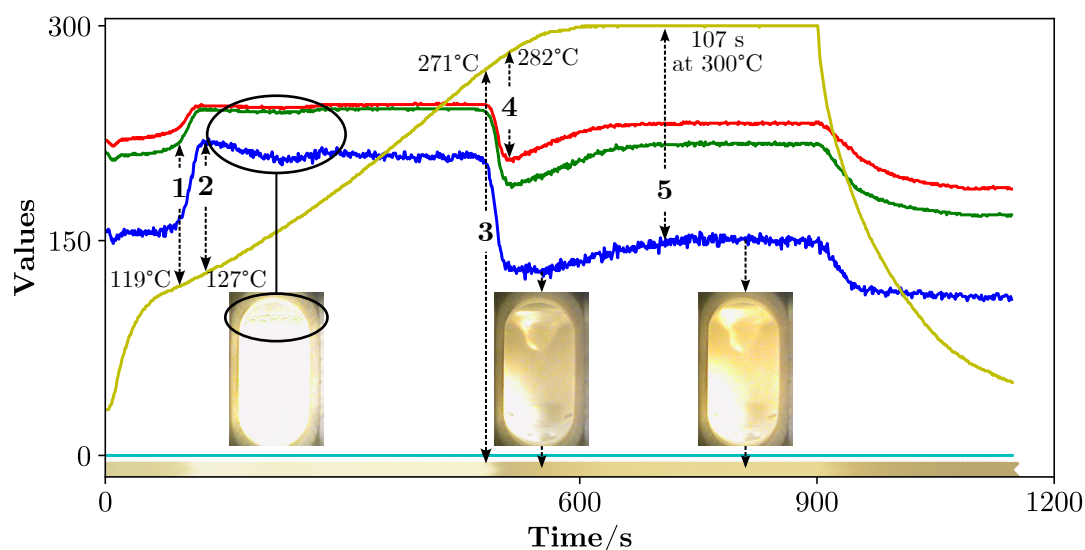


Figure A.2: Color, temperature and pressure profiles of the synthesis attempt to obtain MgS starting from magnesium stearate and three pictures of the vial at different synthesis times. Five moments were also marked to denote distinct events.

Two color changes are observed in the color profile. The first corresponds to the melting and partial dissolution of the reagent at 119 °C. The mixture boil continuously and then subsided, signaling the dehydration of the salts, which occurs around 120 °C[373].

The second transition occurs at 271 °C with a sharp color transition where the suspension no longer reflects light and becomes fully translucent. This is attributed to the complete dissolution of the reagents. The color then gradually changes to a brighter yellow, probably linked to the formation of a complex.

The majority of the diffraction peaks found in the XRD pattern in Figure A.3 belong to the reagent itself, hydrates of magnesium stearate[374] and magnesium palmitate, as well as magnesium hydroxide[375]. On the inset, which is a zoom in the region from  $2\theta$  of 25° to 40°, a very small diffraction band can be seen right before where  $2\theta$  is equal to 35°, but the signal is insufficient to be attributed to MgS. Near the peaks corresponding to the stearate and palmitate, at a  $2\theta$  of 23.75°, is a peak that matches the most intense peak from cetyl palmitate ester. Since 1-dodecanethiol is slightly acidic and a mild reducer, part of the palmitate could have been converted to the alcohol which then reacted with another palmitate to form the ester. The residual water could have been sequestered by the magnesium ions, forming the hydroxide.

Starting from a mixture of magnesium palmitate and stearate, and a temperature of 300 °C was not enough to produce detectable MgS. Yu and Xiao[370] assumed that their mixture of Mg, S and graphite powders under microwave irradiation reached temperatures higher than 1000 °C. Using an automated microwave reactor with a maximum allowed temperature of 300 °C restricts the synthesis of MgS, starting from 1-dodecanethiol, to more reactive magnesium reagents such as magnesium alkoxides.

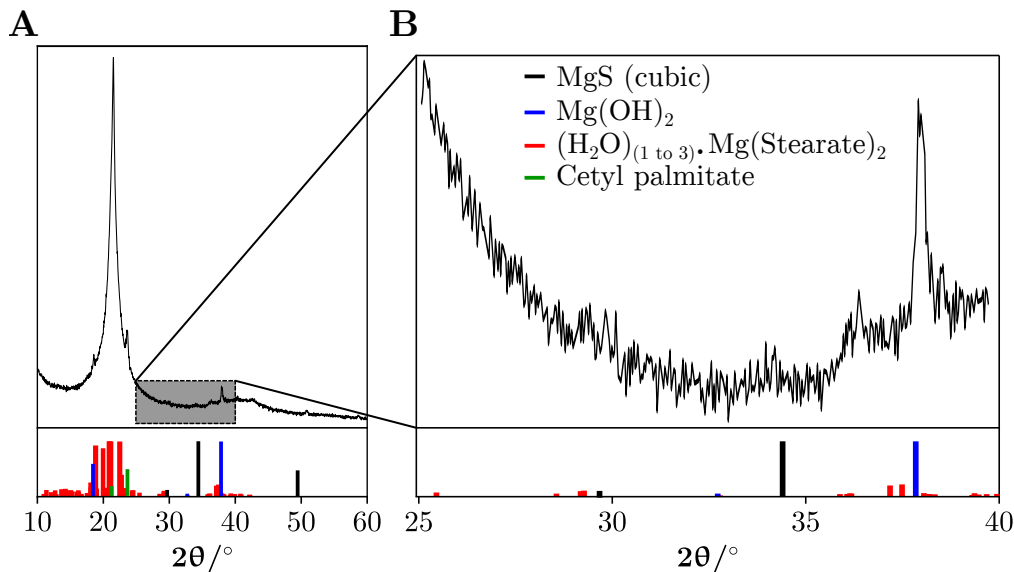


Figure A.3: X-ray diffraction pattern of the resulting powder from the synthesis attempt to obtain MgS (A) and an amplification of the pattern (B). The reference pattern of MgS, was adapted [369],  $\text{Mg}(\text{OH})_2$  from [375], a group of magnesium stearates (disordered monohydrate, anhydrate, ordered monohydrate, dihydrate, and trihydrate) from [376] and cetyl palmitate from [377].

**Synthesis** Following the protocol guidelines from Section 3.1.1, 1 mmol (591 mg) of magnesium(II) stearate and palmitate mixture was added to an Anton Paar G30 proprietary reaction vial, with a polytetrafluoroethylene-covered Cowie stirring magnets with a size of 10 mm by 3 mm. Then the vial was filled with 5 g of 1-dodecanethiol. The mixture was then purged for 15 minutes by bubbling with industrial-grade nitrogen gas. The vial was capped with the proprietary polytetrafluoroethylene-covered silicon sealing cap and immediately inserted into the Anton Paar Monowave 400 microwave reactor's cavity. Under constant steering at 1200 RPM, the temperature was raised to 300 °C in 10 minutes, kept for 5 minutes, followed by an automated cooling procedure to 50 °C. The suspension was then divided into three 2 mL microcentrifuge tubes, centrifuged at 9000 RPM (9146 *g*), the supernatant discarded, followed by the addition of ethanol up to the 2 mL mark. Next, with a vortex, the tubes were shaken until all of the material was resuspended, and the suspensions were centrifuged again. This process was repeated two more times. After discarding the supernatant, the pellet was vacuum dried for 1 h by perforating the microcentrifuge cap with a needle to create a hole for the air and solvent to pass.

### A.1.1.3 Strontium

Strontium sulfides, like other sulfides from alkaline earth group 2 of the periodic table, is more reactive towards acids, such as hydrogen chloride, and salts, such as sodium carbonate, etc. In fact, it can be used as a source of other strontium salts.[378] In terms of uses as a semiconductor, with a wide band gap of around 4.6 eV[379] it is adequate host for other elements such as Cu, Ag or Yb. The Cu or Ag doped SrS materials emit in the blue region (480 nm / 2.58 eV)[380], or in the red region (950 nm / 1.31 eV)[379] when doped with Yb, and are adequate for light emitting devices. The SrS host can also incorporate Eu and Sm leading to an upconverter material, capable

of emitting red light (600 nm / 2.07 eV) upon irradiation with infrared light from a laser (980 nm / 1.27 eV).[381]

Strontium sulfide has been previously synthesized in the oven at around 1100 °C for 1 hour, starting from strontium(II) carbonate, ammonia and sulfur.[381] A solvothermal route was developed by Wang et al.[346], starting from  $\text{SrCl}_2 \cdot 6\text{H}_2\text{O}$  and sulfur but using an amine base (ethylenediamine) as a solvent, to guarantee the reaction to proceed forward to the formation of the sulfide. The sulfide can also be obtained by roasting with charcoal as a reducer in a microwave oven.[382] No microwave-assisted solvothermal synthesis was found in the literature.

The synthesis of strontium sulfide was attempted starting from strontium(II) chloride ( $\text{SrCl}_2$ ). The color, temperature, and pressure profiles, and the resulting powder's XRD pattern can be found in Figure A.4.

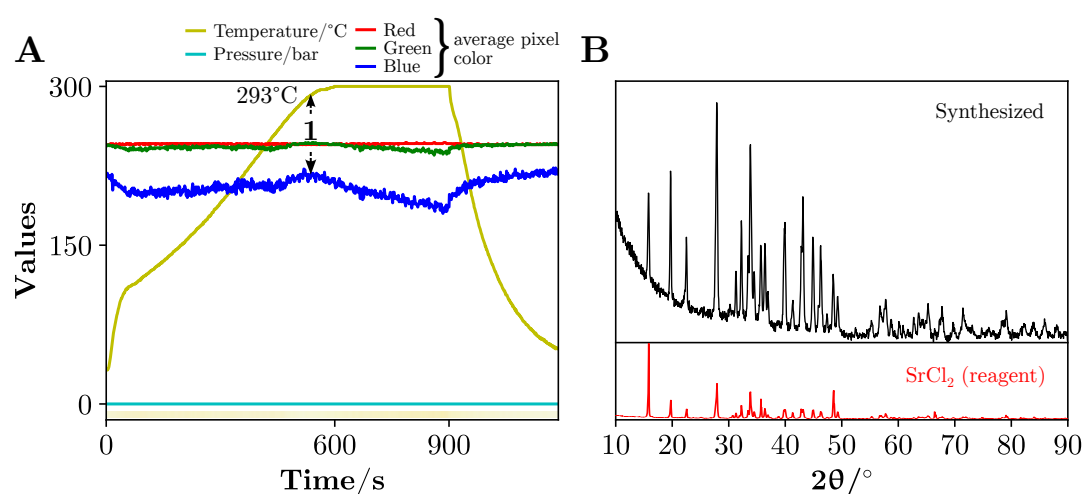


Figure A.4: Color, temperature and pressure profiles (A) and XRD pattern (B) of the synthesis starting from  $\text{SrCl}_2$ . One moment was marked as (1) in the color profile.

As stated before, strontium sulfide is usually the starting precursor for other strontium salts. As predicted by the Materials Project Reaction Calculator[383], the enthalpy of reaction between  $\text{SrS}$  and  $\text{HCl}$  resulting in  $\text{SrCl}_2$  and  $\text{H}_2\text{S}$ , which is presumed to form upon the deprotonation of the thiol, is  $-152 \text{ kJ mol}^{-1}$ . Comparatively, the enthalpy of reaction between  $\text{CuS}$  and  $\text{HCl}$  resulting in  $\text{CuCl}_2$  and  $\text{H}_2\text{S}$  is  $44 \text{ kJ mol}^{-1}$ , which is positive and indicates that the reaction should not occur. The color transformation (1) at 293 °C seen in (A) is therefore not attributed to the formation of the sulfide, but to a change in the reagent's structure. The XRD pattern (B) of the resulting powder has the same peaks as the reagent, but with different relative intensities. Future synthesis should be attempted starting from strontium isopropoxide, since  $\text{SnS}$  is not expected to react with the byproduct isopropanol and alkoxides are usually more reactive.

**Synthesis** Following the protocol guidelines from Section 3.1.1, 1 mmol (159 mg) of strontium(II) chloride was added to an Anton Paar G30 proprietary reaction vial, with a polytetrafluoroethylene-covered Cowie stirring magnets with a size of 10 mm by 3 mm. Then the vial was filled with 5 g of 1-dodecanethiol. The mixture was then purged for 15 minutes by bubbling with industrial-grade

nitrogen gas. The vial was capped with the proprietary polytetrafluoroethylene-covered silicon sealing cap and immediately inserted into the Anton Paar Monowave 400 microwave reactor's cavity. Under constant steering at 1200 RPM, the temperature was raised to 300 °C in 10 minutes, kept for 5 minutes, followed by an automated cooling procedure to 50 °C. The suspension was then divided into three 2 mL microcentrifuge tubes, centrifuged at 9000 RPM (9146 *g*), the supernatant discarded, followed by the addition of ethanol up to the 2 mL mark. Next, with a vortex, the tubes were shaken until all of the material was resuspended, and the suspensions were centrifuged again. This process was repeated two more times. After discarding the supernatant, the pellet was vacuum dried for 1 h by perforating the microcentrifuge cap with a needle to create a hole for the air and solvent to pass.

#### A.1.1.4 Barium

Barium sulfide (BaS), like its group 2 counterparts, is an excellent dopant host, such as Sm, and has a wide band gap of 3.81 eV.[384] As Zagorac et al. reviewed[385], it is a source to fabricate other barium salts[386], it is used as a fire retardant and in luminescent inks, and since it is the material with the largest ration between the ions' radius, it is regarded as a promising material for electronics and optical devices. It is also found in other atypical areas, namely in depilatory creams.[387]

Zhang et al. have synthesized BaS previously by a solid-state reaction between BaSO<sub>4</sub> and elemental sulfur at a high temperature of ~1200 °C.[388] Bismuth doped BaS has also been synthesized in a similar matter by heating BaSO<sub>4</sub> and elemental carbon to 1000 °C for 2 hours.[389] No solvothermal synthesis was found in the literature.

The synthesis of barium sulfide was attempted starting from barium(II) triflate. The color, temperature, and pressure profiles can be found in Figure A.5.

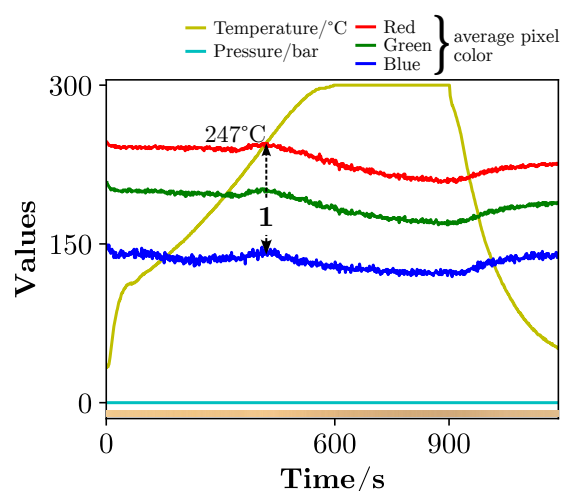


Figure A.5: Color, temperature and pressure profiles of the synthesis starting from barium(II) triflate. One moment was marked as (1) in the color profile.

The only color transformation (1) seen in the color profile (A), that began at 247 °C, is probably just a change in geometry of the reagent, as was seen in the synthesis involving SrCl<sub>2</sub> (Section A.1.1.3).



In future syntheses, since the barium(II) nitrate will probably provoke the development of electric arcs (Section 3.3.1.6), barium(II) isopropoxide is a better candidate as a precursor.

**Synthesis** Following the protocol guidelines from Section 3.1.1, 1 mmol (435 mg) of barium(II) triflate was added to an Anton Paar G30 proprietary reaction vial, with a polytetrafluoroethylene-covered Cowie stirring magnets with a size of 10 mm by 3 mm. Then the vial was filled with 5 g of 1-dodecanethiol. The mixture was then purged for 15 minutes by bubbling with industrial-grade nitrogen gas. The vial was capped with the proprietary polytetrafluoroethylene-covered silicon sealing cap and immediately inserted into the Anton Paar Monowave 400 microwave reactor's cavity. Under constant steering at 1200 RPM, the temperature was raised to 300 °C in 10 minutes, kept for 5 minutes, followed by an automated cooling procedure to 50 °C. The suspension was then divided into three 2 mL microcentrifuge tubes, centrifuged at 9000 RPM (9146 *g*), the supernatant discarded. After the addition of the ethanol, the powder dissolved completely in it. Since barium sulfide is highly insoluble in alcohols, especially in ethanolBaSInsolubleAlcohol, the obtained powder was probably the reagent itself.

## A.1.2 Group 3: Sc, Y

### A.1.2.1 Scandium

Literature regarding scandium sulfides is scarce. Most of the work was published in the 20th century, involving the sulfides' synthesis and characterization[390]–[392]. The ionic conductivity of  $\text{Sc}_2\text{S}_3$ [392] could make this material a promising candidate for energy storage devices.

One of the first attempts to synthesize scandium sulfides,  $\text{ScS}$  and  $\text{Sc}_2\text{S}_3$ , was in 1964 by Dismukes and White, by heating Sc and S at high temperatures. Later, in 1998,  $\text{Sc}_2\text{S}_3$  was synthesized by Wenjing et al.[393] using laser ablation. Recently, Kaneko et al.[394] have synthesized  $\text{Sc}_2\text{S}_3$  at 1200 °C, starting from  $\text{Sc}_2\text{O}_3$  in the presence of  $\text{CS}_2$  gas for 2 h.

The synthesis of scandium sulfide was attempted starting from scandium(III) acetate hydrate. The color, temperature, and pressure profiles, and the resulting powder's XRD pattern and TEM images can be found in Figure A.6.

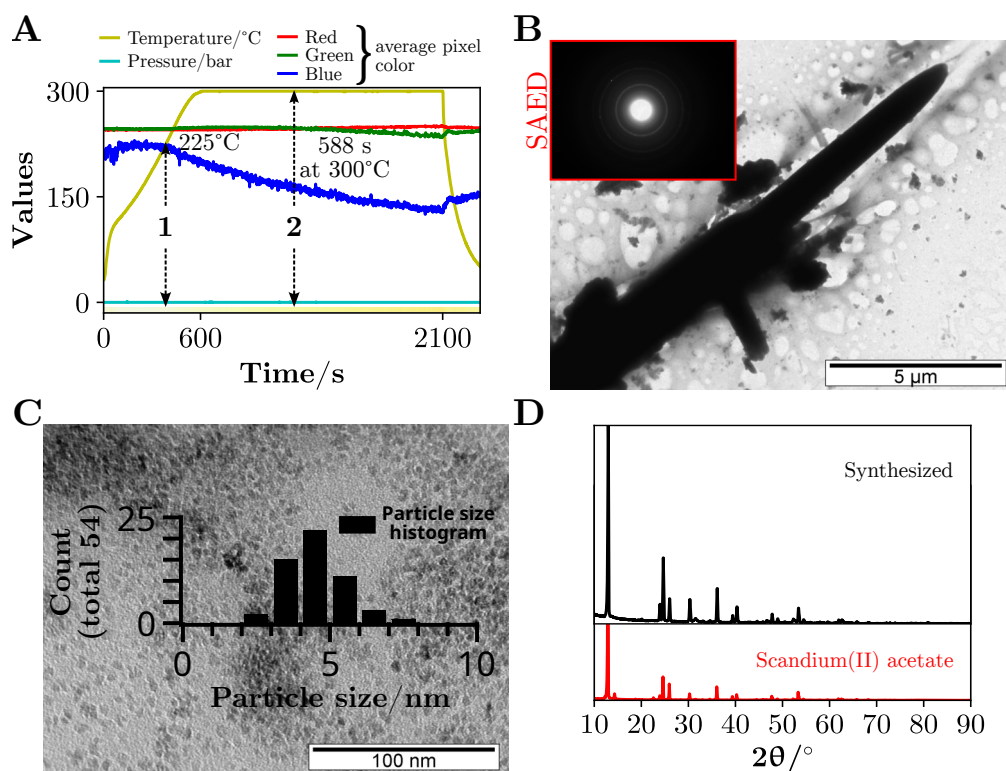


Figure A.6: Color, temperature and pressure profiles (A) of the syntheses starting from scandium(III) acetate hydrate, TEM images (B), with a SAED pattern as an inset, another TEM image (C), with the particle size histogram, and the XRD patterns (D) of the synthesized powder and the reagent. Two events are marked as (1) and (2) in the profiles. The scale bar is 5 μm in (B) and 100 nm in (C).

The color profile (A) presents two color changes, one at 225 °C (1) where the blue channel decreases until the end of the synthesis, followed by another event where the green channel starts to decrease 588 seconds after the synthesis reached 300 °C (2). After washing the resulting powder with ethanol, the TEM image (B) reveals large crystals with more than 10 micrometers. The SAED pattern could not be matched with any pattern found in the literature regarding scandium

sulfides and no pattern was found for scandium acetate. In the background it possible to see some smaller particles. Those particles, shown in TEM image (C), are very small and have a particle size distribution centered around 4 nm to 5 nm. The peaks from the XRD pattern (D) of the synthesized powder coincide with the reagent scandium(II) acetate. Using the current method, it was not possible to obtain scandium sulfide.

**Synthesis** Following the protocol guidelines from Section 3.1.1, 1 mmol (222 mg) of scandium(III) acetate hydrate was added to an Anton Paar G30 proprietary reaction vial, with a polytetrafluoroethylene-covered Cowie stirring magnets with a size of 10 mm by 3 mm. Then the vial was filled with 5 g of 1-dodecanethiol. The mixture was then purged for 15 minutes by bubbling with industrial-grade nitrogen gas. The vial was capped with the proprietary polytetrafluoroethylene-covered silicon sealing cap and immediately inserted into the Anton Paar Monowave 400 microwave reactor's cavity. Under constant steering at 1200 RPM, the temperature was raised to 300 °C in 10 minutes, kept for 25 minutes, followed by an automated cooling procedure to 50 °C. The suspension was then divided into three 2 mL microcentrifuge tubes, centrifuged at 9000 RPM (9146 *g*), the supernatant discarded, followed by the addition of ethanol up to the 2 mL mark. Next, with a vortex, the tubes were shaken until all of the material was resuspended, and the suspensions were centrifuged again. This process was repeated two more times. After discarding the supernatant, the pellet was vacuum dried for 1 h by perforating the microcentrifuge cap with a needle to create a hole for the air and solvent to pass.

#### A.1.2.2 Yttrium

There are almost no reports regarding the synthesis of yttrium sulfide and its properties in optoelectronics, energy storage, or thermoelectrics. However, one article from 1984[395] states that it is possible to synthesize  $Y_2S_3$  in a glove box. By reacting yttrium metal with sulfur 900 °C, they obtained a yellow powder with an estimated band gap of 2.8 eV and an n-type conductivity under low sulfur vapor pressure and p-type under high.

In the same article published regarding the hydrothermal synthesis of MgS, the synthesis of  $Y_2S_3$  is also reported, performed at a temperature of 180 °C for two h.[146]

The synthesis of yttrium sulfide was attempted starting from yttrium(III) carbonate. The color, temperature, and pressure profiles, and the resulting powder's XRD pattern can be found in Figure A.7.

The synthesis starts with no visible change in the color profile (A) until a temperature of 267 °C (1) is reached, where the suspension becomes darker and browner. During the remainder of the synthesis, no other changes can be seen in the profiles. As per the XRD pattern (B), yttrium sulfide was not obtained since the resulting powder pattern corresponds to the reagent itself, according to the reference pattern from [396], and most probably the dehydrated form. It is unclear if the only peak that could belong to  $Y_2S_3$  (marked as with a #) is, in fact, from the sulfide or an unidentified compound. More reactive yttrium precursors should be used in future synthesis.

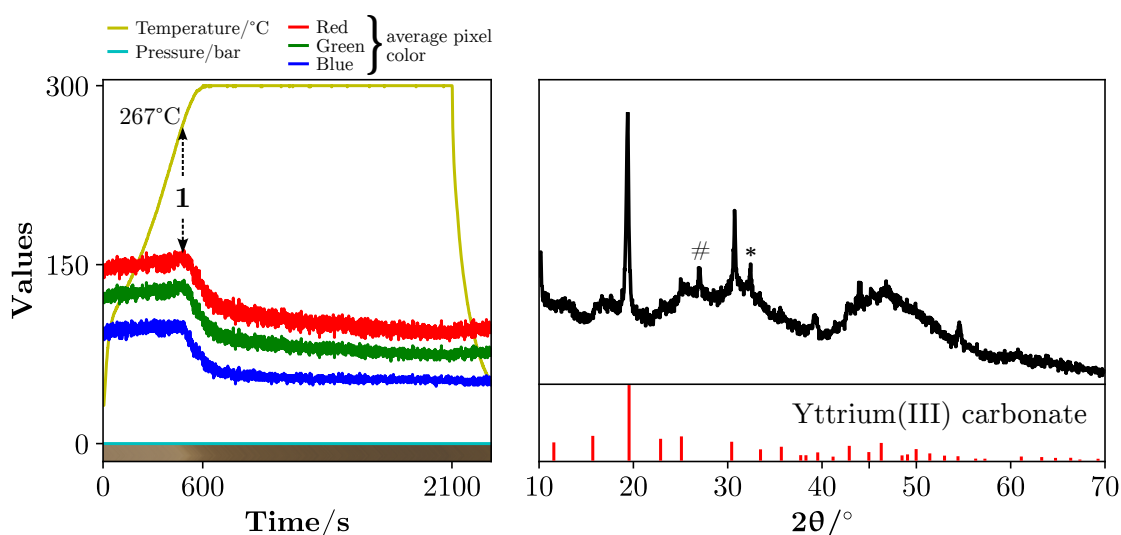


Figure A.7: Color, temperature, and pressure profiles (A) of the syntheses starting from yttrium(III) carbonate and the XRD pattern from the obtained powder (B). An event is marked as (1) in the profiles. The reference pattern of yttrium(III) carbonate was adapted from [396]. The # corresponds to a possible  $Y_2S_3$  peak according to reference [397], and \* could not be identified.

**Synthesis** Following the protocol guidelines from Section 3.1.1, 1 mmol (358 mg) of yttrium(III) carbonate was added to an Anton Paar G30 proprietary reaction vial with a polytetrafluoroethylene-covered Cowie stirring magnets with a size of 10 mm by 3 mm. Then the vial was filled with 5 g of 1-dodecanethiol. The mixture was then purged for 15 minutes by bubbling with industrial-grade nitrogen gas. The vial was capped with the proprietary polytetrafluoroethylene-covered silicon sealing cap and immediately inserted into the Anton Paar Monowave 400 microwave reactor's cavity. Under constant steering at 1200 RPM, the temperature was raised to 300 °C in 10 minutes, kept for 25 minutes, followed by an automated cooling procedure to 50 °C. The suspension was then divided into three 2 mL microcentrifuge tubes, centrifuged at 9000 RPM (9146 *g*), the supernatant discarded, and ethanol added to the 2 mL mark. Next, with a vortex, the tubes were shaken until all of the material was resuspended, and the suspensions were centrifuged again. This process was repeated two more times. After discarding the supernatant, the pellet was vacuum dried for 1 h by perforating the microcentrifuge cap with a needle to create a hole for the air and solvent to pass.

### A.1.3 Group 4: Ti, Zr, Hf

#### A.1.3.1 Titanium

**Synthesis** Following the protocol guidelines from Section 3.1.1, 1 mmol (284 mg) of titanium(IV) isopropoxide was added to an Anton Paar G30 proprietary reaction vial with a polytetrafluoroethylene-covered Cowie stirring magnets with a size of 10 mm by 3 mm. Then the vial was filled with 5 g of 1-dodecanethiol. The mixture was then purged for 15 minutes by bubbling with industrial-grade nitrogen gas. The vial was capped with the proprietary polytetrafluoroethylene-covered silicon sealing cap and immediately inserted into the Anton Paar Monowave 400 microwave reactor's cavity. Under constant steering at 1200 RPM, the temperature was raised to 300 °C in 10 minutes, kept for 5 minutes, followed by an automated cooling procedure to 50 °C. The suspension was then divided into three 2 mL microcentrifuge tubes, centrifuged at 9000 RPM (9146 *g*), the supernatant discarded, and ethanol added to the 2 mL mark. Next, with a vortex, the tubes were shaken until all of the material was resuspended, and the suspensions were centrifuged again. This process was repeated two more times. After discarding the supernatant, the pellet was vacuum dried for 1 h by perforating the microcentrifuge cap with a needle to create a hole for the air and solvent to pass.

#### A.1.3.2 Zirconium

**Synthesis** Following the protocol guidelines from Section 3.1.1, 1 mmol (233 mg) of zirconium(IV) chloride was added to an Anton Paar G30 proprietary reaction vial with a polytetrafluoroethylene-covered Cowie stirring magnets with a size of 10 mm by 3 mm. Then the vial was filled with 5 g of 1-dodecanethiol. The mixture was then purged for 15 minutes by bubbling with industrial-grade nitrogen gas. The vial was capped with the proprietary polytetrafluoroethylene-covered silicon sealing cap and immediately inserted into the Anton Paar Monowave 400 microwave reactor's cavity. Under constant steering at 1200 RPM, the temperature was raised to 300 °C in 10 minutes, kept for 5 minutes, followed by an automated cooling procedure to 50 °C. The suspension was then divided into three 2 mL microcentrifuge tubes, centrifuged at 9000 RPM (9146 *g*), the supernatant discarded, and ethanol added to the 2 mL mark. Next, with a vortex, the tubes were shaken until all of the material was resuspended, and the suspensions were centrifuged again. This process was repeated two more times. After discarding the supernatant, the pellet was vacuum dried for 1 h by perforating the microcentrifuge cap with a needle to create a hole for the air and solvent to pass.

#### A.1.3.3 Hafnium

**Synthesis** Following the protocol guidelines from Section 3.1.1, 1 mmol (320 mg) of hafnium(IV) chloride was added to an Anton Paar G30 proprietary reaction vial with a polytetrafluoroethylene-

covered Cowie stirring magnets with a size of 10 mm by 3 mm. Then the vial was filled with 5 g of 1-dodecanethiol. The mixture was then purged for 15 minutes by bubbling with industrial-grade nitrogen gas. The vial was capped with the proprietary polytetrafluoroethylene-covered silicon sealing cap and immediately inserted into the Anton Paar Monowave 400 microwave reactor's cavity. Under constant steering at 1200 RPM, the temperature was raised to 300 °C in 10 minutes, kept for 5 minutes, followed by an automated cooling procedure to 50 °C. The suspension was then divided into three 2 mL microcentrifuge tubes, centrifuged at 9000 RPM (9146 *g*), the supernatant discarded, and ethanol added to the 2 mL mark. Next, with a vortex, the tubes were shaken until all of the material was resuspended, and the suspensions were centrifuged again. This process was repeated two more times. After discarding the supernatant, the pellet was vacuum dried for 1 h by perforating the microcentrifuge cap with a needle to create a hole for the air and solvent to pass.

## A.1.4 Group 5: V, Nb, Ta

### A.1.4.1 Vanadium

Following the protocol guidelines from Section 3.1.1, 1 mmol (166 mg) of vanadium(IV) oxide **or** 1 mmol (242 mg) of vanadium(V) triisopropoxide oxide was added to an Anton Paar G30 proprietary reaction vial with a polytetrafluoroethylene-covered Cowie stirring magnets with a size of 10 mm by 3 mm. Then the vial was filled with 5 g of 1-dodecanethiol. The mixture was then purged for 15 minutes by bubbling with industrial-grade nitrogen gas. The vial was capped with the proprietary polytetrafluoroethylene-covered silicon sealing cap and immediately inserted into the Anton Paar Monowave 400 microwave reactor's cavity. Under constant steering at 1200 RPM, the temperature was raised to 300 °C in 10 minutes, kept for 5 minutes, followed by an automated cooling procedure to 50 °C. The suspension was then divided into three 2 mL microcentrifuge tubes, centrifuged at 9000 RPM (9146 *g*), the supernatant discarded, and ethanol added to the 2 mL mark. Next, with a vortex, the tubes were shaken until all of the material was resuspended, and the suspensions were centrifuged again. This process was repeated two more times. After discarding the supernatant, the pellet was vacuum dried for 1 h by perforating the microcentrifuge cap with a needle to create a hole for the air and solvent to pass.

### A.1.4.2 Niobium

Following the protocol guidelines from Section 3.1.1, 1 mmol (270 mg) of niobium(V) chloride was added to an Anton Paar G30 proprietary reaction vial with a polytetrafluoroethylene-covered Cowie stirring magnets with a size of 10 mm by 3 mm. Then the vial was filled with 5 g of 1-dodecanethiol. The mixture was then purged for 15 minutes by bubbling with industrial-grade nitrogen gas. The vial was capped with the proprietary polytetrafluoroethylene-covered silicon sealing cap and immediately inserted into the Anton Paar Monowave 400 microwave reactor's cavity. Under constant steering at 1200 RPM, the temperature was raised to 300 °C in 10 minutes, kept for 5 minutes, followed by an automated cooling procedure to 50 °C. The suspension was then divided into three 2 mL microcentrifuge tubes, centrifuged at 9000 RPM (9146 *g*), the supernatant discarded, and ethanol added to the 2 mL mark. Next, with a vortex, the tubes were shaken until all of the material was resuspended, and the suspensions were centrifuged again. This process was repeated two more times. After discarding the supernatant, the pellet was vacuum dried for 1 h by perforating the microcentrifuge cap with a needle to create a hole for the air and solvent to pass.

### A.1.4.3 Tantalum

Following the protocol guidelines from Section 3.1.1, 1 mmol (358 mg) of tantalum(V) chloride was added to an Anton Paar G30 proprietary reaction vial with a polytetrafluoroethylene-covered Cowie stirring magnets with a size of 10 mm by 3 mm. Then the vial was filled with 5 g of 1-dodecanethiol. The mixture was then purged for 15 minutes by bubbling with industrial-grade nitrogen gas. The vial was capped with the proprietary polytetrafluoroethylene-covered silicon

sealing cap and immediately inserted into the Anton Paar Monowave 400 microwave reactor's cavity. Under constant steering at 1200 RPM, the temperature was raised to 300 °C in 10 minutes, kept for 5 minutes, in the temperature control mode. The power was set to 20 W in the constant power mode synthesis. The constant power mode had to be interrupted by turning off the equipment, as soon as the electric arcs developed, since the microwave reactor's software stopped responding. The reactor was turned on immediately after and the boot procedure automatically cooled the vial to 30 °C. The temperature mode was also interrupted due to the electric arcs but via the software. The automated cooling procedure began until a temperature of 30 °C was reached. Both suspensions were then divided into three 2 mL microcentrifuge tubes, centrifuged at 9000 RPM (9146 *g*), the supernatant discarded, and ethanol added to the 2 mL mark. Next, with a vortex, the tubes were shaken until all of the material was resuspended, and the suspensions were centrifuged again. This process was repeated two more times. After discarding the supernatant, the pellets were vacuum dried for 1 h by perforating the microcentrifuge cap with a needle to create a hole for the air and solvent to pass.



### A.1.5 Group 6: Cr, Mo, W

#### A.1.5.1 Chromium

Following the protocol guidelines from Section 3.1.1, 1 mmol (349 mg) of chromium(III) acetylacetonate **or** 1 mmol (266 mg) of chromium(III) chloride hexahydrate were added to an Anton Paar G30 proprietary reaction vial with a polytetrafluoroethylene-covered Cowie stirring magnets with a size of 10 mm by 3 mm. Then the vial was filled with 5 g of 1-dodecanethiol. The mixture was then purged for 15 minutes by bubbling with industrial-grade nitrogen gas. The vial was capped with the proprietary polytetrafluoroethylene-covered silicon sealing cap and immediately inserted into the Anton Paar Monowave 400 microwave reactor's cavity. Under constant steering at 1200 RPM, the temperature was raised to 300 °C in 10 minutes, kept for 25 minutes in the acetylacetonate case, **or** 5 minutes in the synthesis performed with the chloride, followed by an automated cooling procedure to 50 °C. The suspension was then divided into three 2 mL microcentrifuge tubes, centrifuged at 9000 RPM (9146 *g*), the supernatant discarded, and ethanol added to the 2 mL mark. Next, with a vortex, the tubes were shaken until all of the material was resuspended, and the suspensions were centrifuged again. This process was repeated two more times. After discarding the supernatant, the pellet was vacuum dried for 1 h by perforating the microcentrifuge cap with a needle to create a hole for the air and solvent to pass.

#### A.1.5.2 Molybdenum

Following the protocol guidelines from Section 3.1.1, 1 mmol (128 mg) of molybdenum(IV) oxide **or** 1 mmol (273 mg) of Molybdenum(V) chloride were added to an Anton Paar G30 proprietary reaction vial with a polytetrafluoroethylene-covered Cowie stirring magnets with a size of 10 mm by 3 mm. Then the vial was filled with 5 g of 1-dodecanethiol. The mixture was then purged for 15 minutes by bubbling with industrial-grade nitrogen gas. The vial was capped with the proprietary polytetrafluoroethylene-covered silicon sealing cap and immediately inserted into the Anton Paar Monowave 400 microwave reactor's cavity. Under constant steering at 1200 RPM, the temperature was raised to 300 °C in 10 minutes, kept for 5 minutes in the oxide case, **or** 25 minutes in the synthesis performed with the chloride, followed by an automated cooling procedure to 50 °C. The suspension was then divided into three 2 mL microcentrifuge tubes, centrifuged at 9000 RPM (9146 *g*), the supernatant discarded, and ethanol added to the 2 mL mark. Next, with a vortex, the tubes were shaken until all of the material was resuspended, and the suspensions were centrifuged again. This process was repeated two more times. After discarding the supernatant, the pellet was vacuum dried for 1 h by perforating the microcentrifuge cap with a needle to create a hole for the air and solvent to pass.

#### A.1.5.3 Tungsten

Following the protocol guidelines from Section 3.1.1, 1 mmol (216 mg) of tungsten(IV) oxide **or** 1 mmol (397 mg) of Tungsten(VI) chloride were added to an Anton Paar G30 proprietary reaction vial with a polytetrafluoroethylene-covered Cowie stirring magnets with a size of 10 mm

by 3 mm. Then the vial was filled with 5 g of 1-dodecanethiol. The mixture was then purged for 15 minutes by bubbling with industrial-grade nitrogen gas. The vial was capped with the proprietary polytetrafluoroethylene-covered silicon sealing cap and immediately inserted into the Anton Paar Monowave 400 microwave reactor's cavity. Under constant steering at 1200 RPM, the temperature was raised to 300 °C in 10 minutes in both syntheses, kept for 5 minutes, followed by an automated cooling procedure to 50 °C. The suspension was then divided into three 2 mL microcentrifuge tubes, centrifuged at 9000 RPM (9146 *g*), the supernatant discarded, and ethanol added to the 2 mL mark. Next, with a vortex, the tubes were shaken until all of the material was resuspended, and the suspensions were centrifuged again. This process was repeated two more times. After discarding the supernatant, the pellet was vacuum dried for 1 h by perforating the microcentrifuge cap with a needle to create a hole for the air and solvent to pass.

## A.1.6 Group 7: Mn

### A.1.6.1 Manganese

Following the protocol guidelines from Section 3.1.1, 1 mmol (245 mg) of manganese(II)acetate tetrahydrate was added to an Anton Paar G30 proprietary reaction vial with a polytetrafluoroethylene-covered Cowie stirring magnets with a size of 10 mm by 3 mm. Then the vial was filled with 5 g of 1-dodecanethiol. The mixture was then purged for 15 minutes by bubbling with industrial-grade nitrogen gas. The vial was capped with the proprietary polytetrafluoroethylene-covered silicon sealing cap and immediately inserted into the Anton Paar Monowave 400 microwave reactor's cavity. Under constant steering at 1200 RPM, the temperature was raised to 300 °C in 10 minutes, kept for 5 minutes, followed by an automated cooling procedure to 50 °C. The suspension was then divided into three 2 mL microcentrifuge tubes, centrifuged at 9000 RPM (9146 *g*), the supernatant discarded, and ethanol added to the 2 mL mark. Next, with a vortex, the tubes were shaken until all of the material was resuspended, and the suspensions were centrifuged again. This process was repeated two more times. After discarding the supernatant, the pellet was vacuum dried for 1 h by perforating the microcentrifuge cap with a needle to create a hole for the air and solvent to pass.

### A.1.7 Group 8: Fe

#### A.1.7.1 Iron

Following the protocol guidelines from Section 3.1.1, 1 mmol (270 mg) of iron(III) chloride hexahydrate, **or** 1 mmol (278 mg) of iron(II) sulfate heptahydrate, **or** 1 mmol (353 mg) of iron(III) acetylacetonate were added to an Anton Paar G30 proprietary reaction vial with a polytetrafluoroethylene-covered Cowie stirring magnets with a size of 10 mm by 3 mm. Then the vial was filled with 5 g of 1-dodecanethiol. The mixture was then purged for 15 minutes by bubbling with industrial-grade nitrogen gas. The vial was capped with the proprietary polytetrafluoroethylene-covered silicon sealing cap and immediately inserted into the Anton Paar Monowave 400 microwave reactor's cavity. Under constant steering at 1200 RPM, the temperature was raised to 300 °C in 10 minutes in both syntheses, kept for 5 minutes, followed by an automated cooling procedure to 50 °C. The suspension was then divided into three 2 mL microcentrifuge tubes, centrifuged at 9000 RPM (9146 *g*), the supernatant discarded, and ethanol added to the 2 mL mark. Next, with a vortex, the tubes were shaken until all of the material was resuspended, and the suspensions were centrifuged again. This process was repeated two more times. After discarding the supernatant, the pellet was vacuum dried for 1 h by perforating the microcentrifuge cap with a needle to create a hole for the air and solvent to pass.

## A.1.8 Group 9: Co

### A.1.8.1 Cobalt

Following the protocol guidelines from Section 3.1.1, 1 mmol (238 mg) of cobalt(II) chloride hexahydrate was added to an Anton Paar G30 proprietary reaction vial with a polytetrafluoroethylene-covered Cowie stirring magnets with a size of 10 mm by 3 mm. Then the vial was filled with 5 g of 1-dodecanethiol. The mixture was then purged for 15 minutes by bubbling with industrial-grade nitrogen gas. The vial was capped with the proprietary polytetrafluoroethylene-covered silicon sealing cap and immediately inserted into the Anton Paar Monowave 400 microwave reactor's cavity. Under constant steering at 1200 RPM, the temperature was raised to 300 °C in 10 minutes, kept for 5 minutes, followed by an automated cooling procedure to 50 °C. The suspension was then divided into three 2 mL microcentrifuge tubes, centrifuged at 9000 RPM (9146 *g*), the supernatant discarded, and ethanol added to the 2 mL mark. Next, with a vortex, the tubes were shaken until all of the material was resuspended, and the suspensions were centrifuged again. This process was repeated two more times. After discarding the supernatant, the pellet was vacuum dried for 1 h by perforating the microcentrifuge cap with a needle to create a hole for the air and solvent to pass.

## A.1.9 Group 10: Ni

### A.1.9.1 Nickel

Following the protocol guidelines from Section 3.1.1, 1 mmol (249 mg) of nickel(II) acetate tetrahydrate was added to an Anton Paar G30 proprietary reaction vial with a polytetrafluoroethylene-covered Cowie stirring magnets with a size of 10 mm by 3 mm. Then the vial was filled with 5 g of 1-dodecanethiol. The mixture was then purged for 15 minutes by bubbling with industrial-grade nitrogen gas. The vial was capped with the proprietary polytetrafluoroethylene-covered silicon sealing cap and immediately inserted into the Anton Paar Monowave 400 microwave reactor's cavity. Under constant steering at 1200 RPM, the temperature was raised to 300 °C in 10 minutes, kept for 5 minutes, followed by an automated cooling procedure to 50 °C. The suspension was then divided into three 2 mL microcentrifuge tubes, centrifuged at 9000 RPM (9146 *g*), the supernatant discarded, and ethanol added to the 2 mL mark. Next, with a vortex, the tubes were shaken until all of the material was resuspended, and the suspensions were centrifuged again. This process was repeated two more times. After discarding the supernatant, the pellet was vacuum dried for 1 h by perforating the microcentrifuge cap with a needle to create a hole for the air and solvent to pass.

## A.1.10 Group 11: Cu, Ag

### A.1.10.1 Copper

Following the protocol guidelines from Section 3.1.1, 1 mmol (80 mg) of copper(II) oxide **or** 1 mmol (143 mg) of copper(I) oxide was added to an Anton Paar G30 proprietary reaction vial with a polytetrafluoroethylene-covered Cowie stirring magnets with a size of 10 mm by 3 mm. Then the vial was filled with 5 g of 1-dodecanethiol. The mixture was then purged for 15 minutes by bubbling with industrial-grade nitrogen gas. The vial was capped with the proprietary polytetrafluoroethylene-covered silicon sealing cap and immediately inserted into the Anton Paar Monowave 400 microwave reactor's cavity. Under constant steering at 1200 RPM, the temperature was raised to 300 °C in 10 minutes, kept for 5 minutes, followed by an automated cooling procedure to 50 °C. The suspension was then divided into three 2 mL microcentrifuge tubes, centrifuged at 9000 RPM (9146 *g*), the supernatant discarded, and ethanol added to the 2 mL mark. Next, with a vortex, the tubes were shaken until all of the material was resuspended, and the suspensions were centrifuged again. This process was repeated two more times. After discarding the supernatant, the pellet was vacuum dried for 1 h by perforating the microcentrifuge cap with a needle to create a hole for the air and solvent to pass.

### A.1.10.2 Silver

Following the protocol guidelines from Section 3.1.1, 1 mmol (170 mg) of silver(I) nitrate was added to an Anton Paar G30 proprietary reaction vial with a polytetrafluoroethylene-covered Cowie stirring magnets with a size of 10 mm by 3 mm. Then the vial was filled with 5 g of 1-dodecanethiol. The mixture was then purged for 15 minutes by bubbling with industrial-grade nitrogen gas. The vial was capped with the proprietary polytetrafluoroethylene-covered silicon sealing cap and immediately inserted into the Anton Paar Monowave 400 microwave reactor's cavity. Under constant steering at 1200 RPM, the temperature was raised to 300 °C in 10 minutes, kept for 5 minutes, followed by an automated cooling procedure to 50 °C. The suspension was then divided into three 2 mL microcentrifuge tubes, centrifuged at 9000 RPM (9146 *g*), the supernatant discarded, and ethanol added to the 2 mL mark. Next, with a vortex, the tubes were shaken until all of the material was resuspended, and the suspensions were centrifuged again. This process was repeated two more times. After discarding the supernatant, the pellet was vacuum dried for 1 h by perforating the microcentrifuge cap with a needle to create a hole for the air and solvent to pass.

### A.1.11 Group 12: Zn, Cd

#### A.1.11.1 Zinc

Following the protocol guidelines from Section 3.1.1, 1 mmol (220 mg) of zinc(II) acetate dihydrate was added to an Anton Paar G30 proprietary reaction vial with a polytetrafluoroethylene-covered Cowie stirring magnets with a size of 10 mm by 3 mm. Then the vial was filled with 5 g of 1-dodecanethiol. The mixture was then purged for 15 minutes by bubbling with industrial-grade nitrogen gas. The vial was capped with the proprietary polytetrafluoroethylene-covered silicon sealing cap and immediately inserted into the Anton Paar Monowave 400 microwave reactor's cavity. Under constant steering at 1200 RPM, the temperature was raised to 300 °C in 10 minutes, kept for 5 minutes, followed by an automated cooling procedure to 50 °C. The suspension was then divided into three 2 mL microcentrifuge tubes, centrifuged at 9000 RPM (9146 *g*), the supernatant discarded, and ethanol added to the 2 mL mark. Next, with a vortex, the tubes were shaken until all of the material was resuspended, and the suspensions were centrifuged again. This process was repeated two more times. After discarding the supernatant, the pellet was vacuum dried for 1 h by perforating the microcentrifuge cap with a needle to create a hole for the air and solvent to pass.

#### A.1.11.2 Cadmium

Following the protocol guidelines from Section 3.1.1, 1 mmol (267 mg) of cadmium(II) acetate dihydrate was added to an Anton Paar G30 proprietary reaction vial with a polytetrafluoroethylene-covered Cowie stirring magnets with a size of 10 mm by 3 mm. Then the vial was filled with 5 g of 1-dodecanethiol. The mixture was then purged for 15 minutes by bubbling with industrial-grade nitrogen gas. The vial was capped with the proprietary polytetrafluoroethylene-covered silicon sealing cap and immediately inserted into the Anton Paar Monowave 400 microwave reactor's cavity. Under constant steering at 1200 RPM, the temperature was raised to 300 °C in 10 minutes, kept for 25 minutes, followed by an automated cooling procedure to 50 °C. The suspension was then divided into three 2 mL microcentrifuge tubes, centrifuged at 9000 RPM (9146 *g*), the supernatant discarded, and ethanol added to the 2 mL mark. Next, with a vortex, the tubes were shaken until all of the material was resuspended, and the suspensions were centrifuged again. This process was repeated two more times. After discarding the supernatant, the pellet was vacuum dried for 1 h by perforating the microcentrifuge cap with a needle to create a hole for the air and solvent to pass.



### A.1.12 Group 13: Al, Ga, In

#### A.1.12.1 Aluminum

Aluminum is one of the most abundant, cheap and available elements. One of the sulfides (hexagonal  $\text{Al}_2\text{S}_3$ ) is wide band gap 4.1 eV  $\text{Al}_2\text{S}_3$  Hexag Bandgap. This aluminum sulfide can also be found in Al-S batteries' cathodes [398], [399] and can one day surpass the commercial lithium batteries, since the estimated volumetric capacity is 4 times higher. [400] Solvothermal synthesis of a cluster of this material was achieved in 1997 by Wehmschulte and Power, where  $(\text{CH}_3)_{33}\text{N} \cdot \text{AlH}_3$  and  $\text{S}(\text{Si}(\text{CH}_3)_3)_2$  were heated to 95 °C in toluene. [401] The classic method to obtain aluminum sulfide is by the simple reaction between the metal and sulfur at around 200 °C. However, this is inadequate for a microwave-assisted synthesis, due to the presence of a metal, and it also leads to an uncontrollable particle size distribution. Other  $\text{Al}_2\text{S}_3$  synthesis methods consist on the reaction of  $\text{CS}_2$  with  $\text{Al}_2\text{O}_3$  at very high temperatures (850 °C). [402] No other solvothermal synthesis of  $\text{Al}_2\text{S}_3$  was found in the literature.

The synthesis of aluminum sulfide was attempted starting from aluminum(III) acetylacetonate. The color, temperature, and pressure profiles, and a TEM image can be found in Figure A.8.

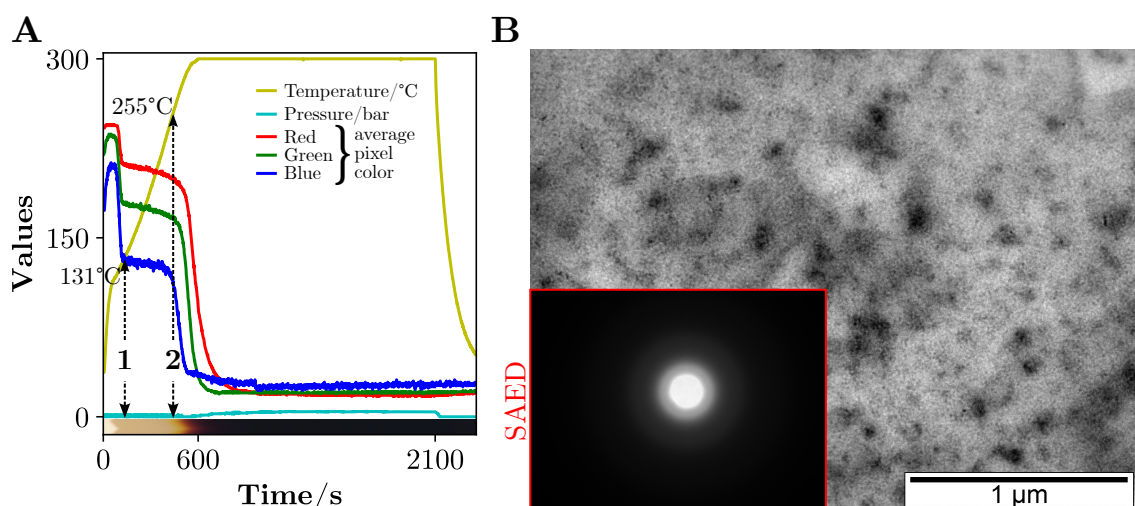


Figure A.8: Color, temperature and pressure profiles (A) and TEM image (B), with a SAED pattern as an inset, of the syntheses starting from aluminum(III) acetylacetonate. Two events were marked in the profiles with (1) and (2). The scale bar is 1  $\mu\text{m}$  in (B).

The beginning of the synthesis starts with the dissolution of the reagent in the thiol, finishing at around 131 °C (1). At a higher temperature 255 °C (2), the solution abruptly becomes darker and pressure starts to rise, followed by no further significant changes. Even after centrifugation a powder could not be collected. The TEM image in (B) shows some aggregates of very small particles. It was not possible to zoom-in further as the objects could not be focused. The SAED pattern shows that the material was amorphous. The obtained mixture had a deep orange/yellow color and under the sun's light it emitted a faint yellow light. The absorbance and emission spectra of the mixture in chloroform were measured and are shown in Figure A.9.

The absorbance spectrum reveals various absorption bands, typical of the aluminum complexes

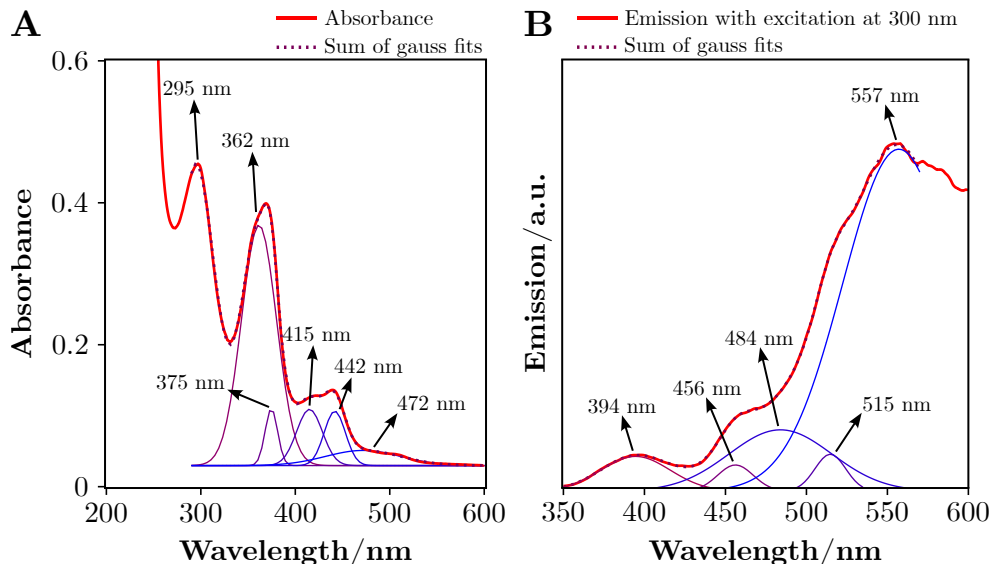


Figure A.9: Absorbance (A) and emission (B) spectra of a few drops in chloroform of the obtained mixture from the synthesis starting from aluminum(III) acetylacetonate and 1-dodecanethiol. The emission was collected while exciting with 300 nm light. A optical filter of 320 nm was used to filter the excitation light. Gaussian fits were adjusted to the absorbance and the emission spectrum and the individual centers are presented.

such as the aluminum(III) acetylacetonate that has three absorption bands at 355 nm, 375 nm, and 395 nm.[403] The emission spectrum also reveals several emission peaks but the most intense is the one centered in the yellow region of the visible spectrum at 557 nm. The aluminum(III) acetylacetonate complex obtained by Hong et al.[403] emits at 409 nm, 435 nm, and 460 nm, with a quantum efficiency of 0.8. Therefore, the addition of a thiol to the acetylacetonate leads to a red-shift of the emission of the resulting complex. There is no information in the literature regarding this aluminum-acetylacetonate-thiol complex emission but the most similar colored complex to the one obtained in this work was presented by Daniel and Hoffman[404]. They obtained thick pale yellow liquid by reacting 2-propanethiol ( $\text{HSCH}(\text{CH}_3)_2$ ) with a mixture of  $\text{AlCl}_3$  and  $\text{LiAlH}_4$ , which formed the complex  $[\text{Al}(\text{SCH}(\text{CH}_3)_2)_3]_2$  but it was not characterized optically. Absorbing ultraviolet light and converting it to yellow light is still a promising property, even if the product obtained is not a solid metal sulfide. Doping zinc sulfide with manganese, as explored in Section 3.2.9.1, to obtain the same downconversion is technically more challenging since the synthesis involving aluminum yields directly the solution containing the complex, which does not require any cleaning procedure. An ink can also be easily obtained by adding a solvent, such as chloroform, and deposit on a surface. Aluminum is also cheaper, more abundant and available than zinc. Hong et al.[403] aluminum(III) acetylacetonate complex's target was to obtain a white-emitting device that was composed of three layers, containing the later complex and two more with  $\text{CuInS}_2$ . The sulfides were responsible for emitting the green, yellow, and red part of the white light, which was produced from downconverting the light from a ultraviolet led that illuminated the three films. Since the thiol complex obtained here does not use the rare element indium and it emits the part of the spectrum that is missing to achieve white light, it

would be interesting to fabricate a two-layer device, containing aluminum(III) acetylacetonate as the blue emitter in one layer and the aluminum(III) acetylacetonate thiol in another layer to cover the green to red region.

Nonetheless, since the target was to obtain an aluminum sulfide, future synthesis should be attempted using different precursors, such as  $\text{AlCl}_3$  and  $\text{AlI}_3$ .

**Synthesis** Following the protocol guidelines from Section 3.1.1, 1 mmol (324 mg) of aluminum(III) acetylacetonate was added to an Anton Paar G30 proprietary reaction vial, with a polytetrafluoroethylene-covered Cowie stirring magnets with a size of 10 mm by 3 mm. Then the vial was filled with 5 g of 1-dodecanethiol. The mixture was then purged for 15 minutes by bubbling with industrial-grade nitrogen gas. The vial was capped with the proprietary polytetrafluoroethylene-covered silicon sealing cap and immediately inserted into the Anton Paar Monowave 400 microwave reactor's cavity. Under constant steering at 1200 RPM, the temperature was raised to 300 °C in 10 minutes, kept for 25 minutes, followed by an automated cooling procedure to 50 °C. The solution was used as is, without further cleaning.

#### A.1.12.2 Gallium

Gallium sulfide,  $\text{Ga}_2\text{S}_3$ , can serve as an anode in batteries, with the predicted benefit of generating liquid Ga to help in the process of the electrode's self-healing.[405] Quantum dots of this material are also promising in regard to photonic applications, due to its tunable blue to yellow emission and high quantum yield of 0.26.[406]

Previously,  $\text{GaS}_x$  has been synthesized by Seral-Ascaso et al.[407], starting from gallium(III) acetylacetonate, sulfur and hexadecylamine and dodecylamine as solvents at 200 °C for 144 hours, where a white precipitate formed. Another group synthesized a new single gallium sulfide precursor, tris(cyclohexylmethyldithiocarbamate) gallium(III), and used to fabricate  $\text{Ga}_2\text{S}_3$  nanotubes at the much lower temperature of 65 °C, for 45 minutes, in chloroform with diethylenetriamine.[408] The synthesis of gallium sulfide was attempted starting from gallium(III) isopropoxide. The color, temperature, and pressure profiles can be found in Figure A.10.

As soon the reagent was added to 1-dodecanethiol, the mixture became yellow; the same color observed by Seral-Ascaso et al. with the acetylacetonate. The color changes over the whole duration of the synthesis are very small. Overall, the values of the three color channels decrease pressure increases over time. The blue channel decreases faster at 233 °C, above the 220 °C that Seral-Ascaso et al. reported as the temperature where the white precipitate redissolved. Since the suspension is remained yellow, the reaction of the isopropoxide with 1-dodecanethiol is different from the acetylacetonate with sulfur in amines. The previous color change is followed by the red and green channel at 280 °C with a simultaneous higher rate of increasing pressure. The three color channels and pressure then stabilize until the end of the synthesis. The increase in pressure could be explained by the evaporation of the isopropanol that was released upon the formation of the gallium thiolate complex. The remainder events cannot be explained without data from XRD and TEM analysis. It was not possible to extract a pellet from the suspension,

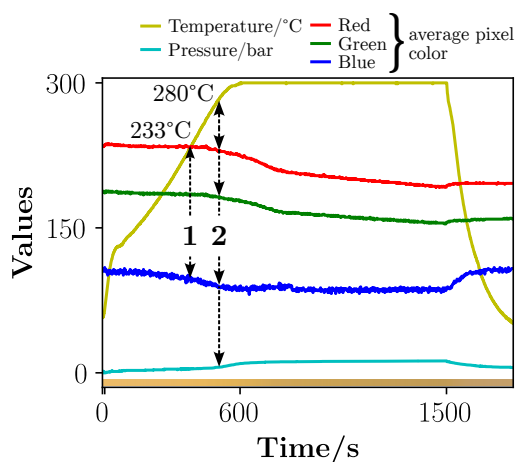


Figure A.10: Color, temperature and pressure profiles of the syntheses starting from gallium(III) isopropoxide. Two events were marked with (1) and (2).

through centrifugation of the as synthesized product. The isopropoxide is not a viable precursor for this method and in future synthesis other precursors should be used, such as gallium(III) acetylacetonate.

**Synthesis** Following the protocol guidelines from Section 3.1.1, 1 mmol (247 mg) of gallium(III) isopropoxide was added to an Anton Paar G30 proprietary reaction vial, with a polytetrafluoroethylene-covered Cowie stirring magnets with a size of 10 mm by 3 mm. Then the vial was filled with 5 g of 1-dodecanethiol. The mixture was then purged for 15 minutes by bubbling with industrial-grade nitrogen gas. The vial was capped with the proprietary polytetrafluoroethylene-covered silicon sealing cap and immediately inserted into the Anton Paar Monowave 400 microwave reactor's cavity. Under constant steering at 1200 RPM, the temperature was raised to 300 °C in 10 minutes, kept for 15 minutes, followed by an automated cooling procedure to 50 °C. The suspension was then divided into three 2 mL microcentrifuge tubes, centrifuged at 9000 RPM (9146 *g*), the supernatant discarded, followed by the addition of ethanol up to the 2 mL mark. Next, with a vortex, the tubes were shaken until all of the material was resuspended, and the suspensions were centrifuged again. This process was repeated two more times. After discarding the supernatant, the pellet was vacuum dried for 1 h by perforating the microcentrifuge cap with a needle to create a hole for the air and solvent to pass.

### A.1.12.3 Indium

Following the protocol guidelines from Section 3.1.1, 1 mmol (221 mg) of indium(III) chloride was added to an Anton Paar G30 proprietary reaction vial with a polytetrafluoroethylene-covered Cowie stirring magnets with a size of 10 mm by 3 mm. Then the vial was filled with 5 g of 1-dodecanethiol. The mixture was then purged for 15 minutes by bubbling with industrial-grade nitrogen gas. The vial was capped with the proprietary polytetrafluoroethylene-covered silicon sealing cap and immediately inserted into the Anton Paar Monowave 400 microwave reactor's cavity. Under constant steering at 1200 RPM, the temperature was raised to 300 °C in 10 minutes,

**or** 215 °C in 7 minutes and 10 seconds, both kept for 25 minutes, followed by an automated cooling procedure to 50 °C. The suspension was then divided into three 2 mL microcentrifuge tubes, centrifuged at 9000 RPM (9146 *g*), the supernatant discarded, and ethanol added to the 2 mL mark. Next, with a vortex, the tubes were shaken until all of the material was resuspended, and the suspensions were centrifuged again. This process was repeated two more times. After discarding the supernatant, the pellet was vacuum dried for 1 h by perforating the microcentrifuge cap with a needle to create a hole for the air and solvent to pass.

### A.1.13 Group 14: Si, Ge, Sn

#### A.1.13.1 Silicon

Reports on silicon sulfide are scarce. Silicon sulfide  $\text{SiS}_2$  is a very unstable compound that easily reacts with oxygen[409], water[410] and even alcohols[411]. Its band gap is not reported in the literature but a recent work regarding the synthesis of the sulfide, reported that they obtained white needles, which implies a relatively high band gap.[412]

Obtaining  $\text{SiS}_2$  is not trivial, given its reactivity towards alcohols, but, nonetheless, the synthesis was attempted starting from tetramethoxysilane (commonly known as tetramethyl orthosilicate or TMOS), with the expectation that the resulting methanol side-product would have less contact with the silicon sulfide, due to the lower solubility of methanol in 1-dodecanethiol, when compared to ethanol.

The synthesis of silicon sulfide was attempted starting from tetramethoxysilane. The color, temperature, and pressure profiles and a TEM image can be found in Figure A.11.

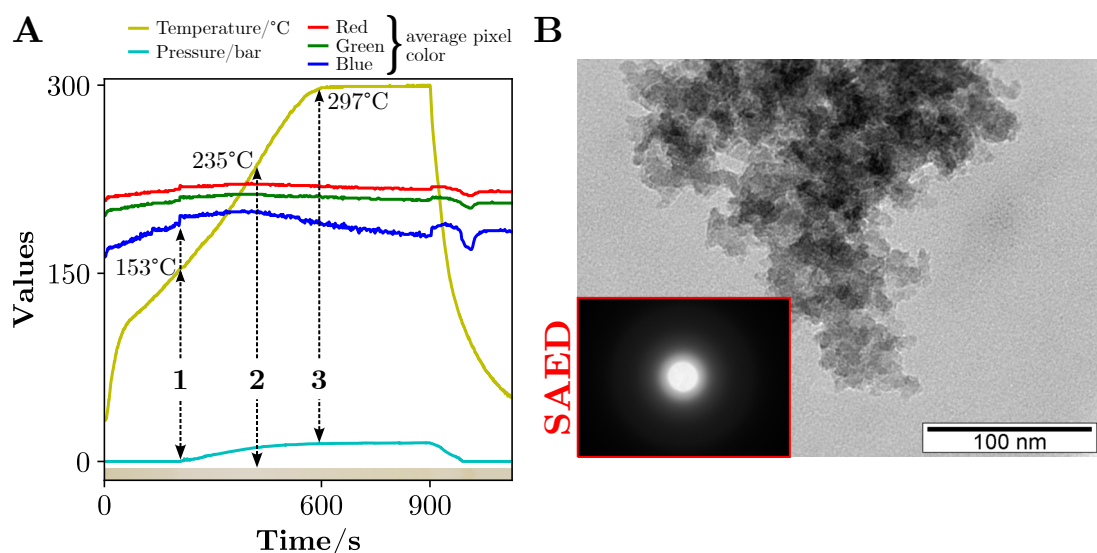


Figure A.11: Color, temperature and pressure profiles (A) of the syntheses starting from tetramethoxysilane and a TEM image with a SAED pattern as an inset (B). Distinct moments were marked from (1) to (3) in the color profile. The scale bar is 100 nm in (B).

At first glance, there appears to be no significant color change over the course of the synthesis, starting from tetramethoxysilane and 1-dodecanethiol. The color profile in Figure A.11 (A) shows a pressure rise at 150 °C, accompanied by a small decrease in the blue channel which raises at 200 °C and starts decreasing again at 275 °C. One of these transformations could be the responsible for the formation of the particles seen in the TEM images (B), with particles around ~9 nm. The selected area electron diffraction (SAED) pattern reveals that the material seen in the TEM image is in an amorphous phase. Silicon disulfide is known to require very high temperatures to be obtained. Its solid state synthesis and characterization has very recently been published[413], where the authors managed to obtain rods of  $\text{SiS}_2$  at 800 °C starting from Si and S. There are currently no reports on the solvothermal synthesis of  $\text{SiS}_2$ . Chen et al.[414]

also synthesized  $\text{SiS}_2$  at a high temperature. They described it as a white powder but in the picture shown it appears to be white to yellow. The powder was characterized optically and they estimated a band gap of around 3.0 eV, which indicates that the powder is indeed less white and more yellow (complementary of purple). Since in Figure A.11 (A) at 235 °C the suspension starts to become gradually more yellow. Assuming that it is the sulfide that is forming, future synthesis should extend the time to obtain a higher yield and, perhaps, a more crystalline powder.

**Synthesis** Following the protocol guidelines from Section 3.1.1, 1 mmol (152 mg) of tetramethoxysilane was added to an Anton Paar G30 proprietary reaction vial, with a polytetrafluoroethylene-covered Cowie stirring magnets with a size of 10 mm by 3 mm. Then the vial was filled with 5 g of 1-dodecanethiol. The mixture was then purged for 15 minutes by bubbling with industrial-grade nitrogen gas. The vial was capped with the proprietary polytetrafluoroethylene-covered silicon sealing cap and immediately inserted into the Anton Paar Monowave 400 microwave reactor's cavity. Under constant steering at 1200 RPM, the temperature was raised to 300 °C in 10 minutes, kept for 5 minutes, followed by an automated cooling procedure to 50 °C. The suspension was then divided into three 2 mL microcentrifuge tubes, centrifuged at 9000 RPM (9146 *g*), the supernatant discarded, followed by the addition of ethanol up to the 2 mL mark. Next, with a vortex, the tubes were shaken until all of the material was resuspended, and the suspensions were centrifuged again. This process was repeated two more times. After discarding the supernatant, the pellet was vacuum dried for 1 h by perforating the microcentrifuge cap with a needle to create a hole for the air and solvent to pass.

#### A.1.13.2 Germanium

Germanium sulfide has two phases,  $\text{GeS}_2$ , with practically no literature regarding both synthesis and properties, and  $\text{GeS}$ , which has been used in optoelectronics, remaining stable in air if protected by a  $\text{GeO}$  shell[415], and as an anode in lithium batteries[416].

Germanium sulfide has been previously synthesized from single precursors germanium xanthates.[417] They obtained the orthorhombic phase of  $\text{GeS}$  by thermolysis of the xanthates in oleic acid at 345 °C for 45 minutes.

The synthesis of germanium sulfide was attempted starting from germanium(IV) iodide. The color, temperature, and pressure profiles can be found in Figure A.12.

The color profile reveals three changes. The first is suspension/dissolution of the reagent in the thiol, practically at room temperature. The mixture darkens as the temperature rises until 207 °C (1) where the color stabilizes. According to Ardalan et al.[418], germanium thiolates are stable up to 150 °C but decompose into a sulfide at 350 °C. Another germanium thiolate related article shows that the decomposition of the germanium thiolate complex they synthesized begins around 280 °C[419]. Indeed, at 290 °C the mixture begins to darken again and pressure starts to rise, keeping this behavior until the end of the synthesis. Since  $\text{GeS}$  is black, with a band gap of 1.6 eV[417], the dark suspension could be composed of the sulfide. Although no pellet was obtainable for further powder analysis after centrifugation, future synthesis should be prolonged at 300 °C

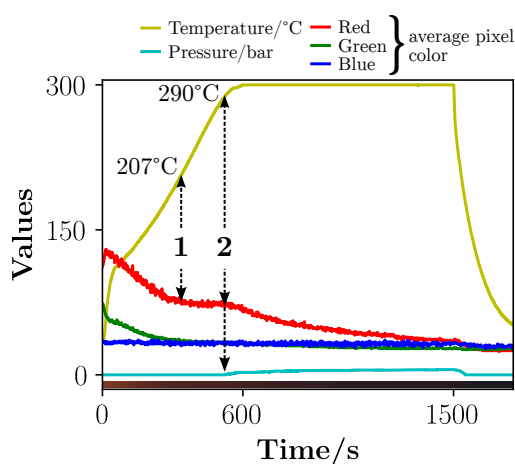


Figure A.12: Color, temperature and pressure profiles of the syntheses starting from  $\text{GeI}_4$ . Distinct moments were marked from (1) to (3) in the color profile.

to attempt to obtain a precipitate.

**Synthesis** Following the protocol guidelines from Section 3.1.1, 1 mmol (580 mg) of germanium(IV) iodide was added to an Anton Paar G30 proprietary reaction vial, with a polytetrafluoroethylene-covered Cowie stirring magnets with a size of 10 mm by 3 mm. Then the vial was filled with 5 g of 1-dodecanethiol. The mixture was then purged for 15 minutes by bubbling with industrial-grade nitrogen gas. The vial was capped with the proprietary polytetrafluoroethylene-covered silicon sealing cap and immediately inserted into the Anton Paar Monowave 400 microwave reactor's cavity. Under constant steering at 1200 RPM, the temperature was raised to 300 °C in 10 minutes, kept for 15 minutes, followed by an automated cooling procedure to 50 °C. The suspension was then divided into three 2 mL microcentrifuge tubes, centrifuged at 9000 RPM (9146 *g*), the supernatant discarded, followed by the addition of ethanol up to the 2 mL mark. Next, with a vortex, the tubes were shaken until all of the material was resuspended, and the suspensions were centrifuged again. This process was repeated two more times. After discarding the supernatant, the pellet was vacuum dried for 1 h by perforating the microcentrifuge cap with a needle to create a hole for the air and solvent to pass.

### A.1.13.3 Tin

Following the protocol guidelines from Section 3.1.1, 1 mmol (405 mg) of tin(II) 2-ethylhexanoate was added to an Anton Paar G30 proprietary reaction vial with a polytetrafluoroethylene-covered Cowie stirring magnets with a size of 10 mm by 3 mm. Then the vial was filled with 5 g of 1-dodecanethiol. The mixture was then purged for 15 minutes by bubbling with industrial-grade nitrogen gas. The vial was capped with the proprietary polytetrafluoroethylene-covered silicon sealing cap and immediately inserted into the Anton Paar Monowave 400 microwave reactor's cavity. Under constant steering at 1200 RPM, the temperature was raised to 300 °C in 10 minutes, kept for 5 minutes, followed by an automated cooling procedure to 50 °C. The suspension was then divided into three 2 mL microcentrifuge tubes, centrifuged at 9000 RPM (9146 *g*), the



supernatant discarded, and ethanol added to the 2 mL mark. Next, with a vortex, the tubes were shaken until all of the material was resuspended, and the suspensions were centrifuged again. This process was repeated two more times. After discarding the supernatant, the pellet was vacuum dried for 1 h by perforating the microcentrifuge cap with a needle to create a hole for the air and solvent to pass.

### A.1.14 Group 15: Bi

#### A.1.14.1 Bismuth

The D-spacing plot calculated from the SAED pattern of the powder obtained from the synthesis starting from bismuth(III) nitrate pentahydrate is shown in Figure A.13.

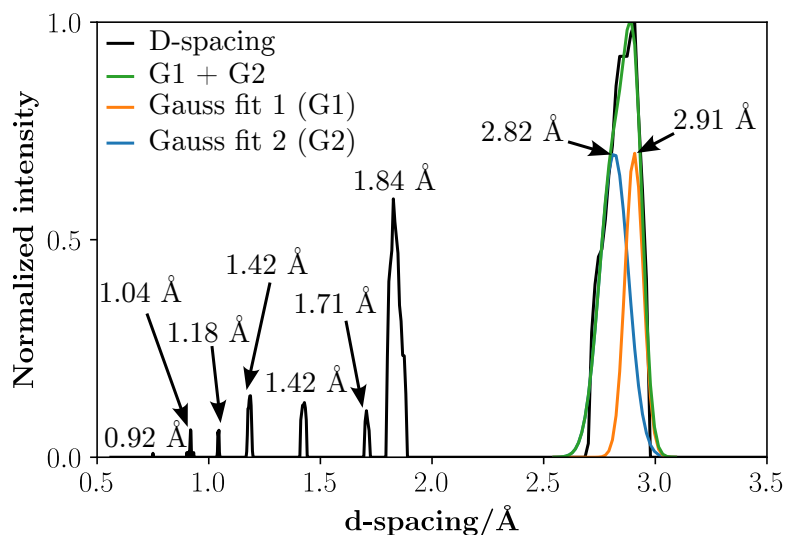


Figure A.13: D-spacing plot calculated from the SAED pattern obtained from the synthesis starting from bismuth(III) nitrate pentahydrate, according to the procedure found in Section B.4. The black and white threshold of the SAED pattern was first adjusted before performing the calculation. Two Gaussian fits were adjusted to the largest peak at the largest d-spacing.

**Synthesis** Following the protocol guidelines from Section 3.1.1, 1 mmol (485 mg) of bismuth(III) nitrate pentahydrate was added to an Anton Paar G30 proprietary reaction vial with a polytetrafluoroethylene-covered Cowie stirring magnets with a size of 10 mm by 3 mm. Then the vial was filled with 5 g of 1-dodecanethiol. The mixture was then purged for 15 minutes by bubbling with industrial-grade nitrogen gas. The vial was capped with the proprietary polytetrafluoroethylene-covered silicon sealing cap and immediately inserted into the Anton Paar Monowave 400 microwave reactor's cavity. Under constant steering at 1200 RPM, the temperature was raised to 300 °C in 10 minutes, kept for 5 minutes, followed by an automated cooling procedure to 50 °C. The suspension was then divided into three 2 mL microcentrifuge tubes, centrifuged at 9000 RPM (9146 *g*), the supernatant discarded, followed by the addition of chloroform up to the 2 mL mark. Next, with a vortex, the tubes were shaken until all of the material was resuspended, and the suspensions were centrifuged again. This process was repeated two more times. After discarding the supernatant, the pellet was vacuum dried for 1 h by perforating the microcentrifuge cap with a needle to create a hole for the air and solvent to pass.

## A.2 Multinary Metal Sulfides

### A.2.1 Ternary

#### A.2.1.1 Cu, Fe

**Synthesis** Following the protocol guidelines from Section 3.1.1, 1 mmol (191 mg) of copper(I) iodide and 1 mmol (353 mg) of iron(III) acetylacetonate were added to an Anton Paar G30 proprietary reaction vial with a polytetrafluoroethylene-covered Cowie stirring magnets with a size of 10 mm by 3 mm. Then the vial was filled with 5 g of 1-dodecanethiol. The mixture was then purged for 15 minutes by bubbling with industrial-grade nitrogen gas. The vial was capped with the proprietary polytetrafluoroethylene-covered silicon sealing cap and immediately inserted into the Anton Paar Monowave 400 microwave reactor's cavity. Under constant steering at 1200 RPM, the temperature was raised to 300 °C in 10 minutes, kept for 25 minutes, followed by an automated cooling procedure to 50 °C. The suspension was then divided into three 2 mL microcentrifuge tubes, centrifuged at 9000 RPM (9146 *g*), the supernatant discarded, and ethanol added to the 2 mL mark. Next, with a vortex, the tubes were shaken until all of the material was resuspended, and the suspensions were centrifuged again. This process was repeated two more times. After discarding the supernatant, the pellet was vacuum dried for 1 h by perforating the microcentrifuge cap with a needle to create a hole for the air and solvent to pass.

#### A.2.1.2 Cu, In

**Synthesis** Following the protocol guidelines from Section 3.1.1, 1 mmol (191 mg) of copper(I) iodide and 1 mmol (221 mg) of indium(III) chloride were added to an Anton Paar G30 proprietary reaction vial with a polytetrafluoroethylene-covered Cowie stirring magnets with a size of 10 mm by 3 mm. Then the vial was filled with 5 g of 1-dodecanethiol. The mixture was then purged for 15 minutes by bubbling with industrial-grade nitrogen gas. The vial was capped with the proprietary polytetrafluoroethylene-covered silicon sealing cap and immediately inserted into the Anton Paar Monowave 400 microwave reactor's cavity. Under constant steering at 1200 RPM, the temperature was raised to 300 °C in 10 minutes, kept for 5 minutes, followed by an automated cooling procedure to 50 °C. The suspension was then divided into three 2 mL microcentrifuge tubes, centrifuged at 9000 RPM (9146 *g*), the supernatant discarded, followed by the addition of ethanol or chloroform up to the 2 mL mark. Next, with a vortex, the tubes were shaken until all of the material was resuspended, and the suspensions were centrifuged again. This process was repeated two more times. After discarding the supernatant, the pellet was vacuum dried for 1 h by perforating the microcentrifuge cap with a needle to create a hole for the air and solvent to pass.

#### A.2.1.3 In, Sn

**Synthesis** Following the protocol guidelines from Section 3.1.1, 1 mmol (221 mg) of indium(III) chloride and 1 mmol (405 mg) of tin(II) 2-ethylhexanoate were added to an Anton Paar G30 proprietary reaction vial with a polytetrafluoroethylene-covered Cowie stirring magnets with a size of 10 mm by 3 mm. Then the vial was filled with 5 g of 1-dodecanethiol. The mixture was then purged for 15 minutes by bubbling with industrial-grade nitrogen gas. The vial was capped with the proprietary polytetrafluoroethylene-covered silicon sealing cap and immediately inserted into the Anton Paar Monowave 400 microwave reactor's cavity. Under constant steering at 1200 RPM, the temperature was raised to 300 °C in 10 minutes, kept for 5 minutes, followed by an automated cooling procedure to 50 °C. The suspension was then divided into three 2 mL microcentrifuge tubes, centrifuged at 9000 RPM (9146 *g*), the supernatant discarded, and ethanol added to the 2 mL mark. Next, with a vortex, the tubes were shaken until all of the material was resuspended, and the suspensions were centrifuged again. This process was repeated two more times. After discarding the supernatant, the pellet was vacuum dried for 1 h by perforating the microcentrifuge cap with a needle to create a hole for the air and solvent to pass.

#### A.2.1.4 Zn, In

**Synthesis** Following the protocol guidelines from Section 3.1.1, 1 mmol (220 mg) of zinc(II) acetate dihydrate and 1 mmol (221 mg) of indium(III) chloride were added to an Anton Paar G30 proprietary reaction vial with a polytetrafluoroethylene-covered Cowie stirring magnets with a size of 10 mm by 3 mm. Then the vial was filled with 5 g of 1-dodecanethiol. The mixture was then purged for 15 minutes by bubbling with industrial-grade nitrogen gas. The vial was capped with the proprietary polytetrafluoroethylene-covered silicon sealing cap and immediately inserted into the Anton Paar Monowave 400 microwave reactor's cavity. Under constant steering at 1200 RPM, the temperature was raised to 300 °C in 10 minutes, followed by an automated cooling procedure to 50 °C. The suspension was then divided into three 2 mL microcentrifuge tubes, centrifuged at 9000 RPM (9146 *g*), the supernatant discarded, and ethanol added to the 2 mL mark. Next, with a vortex, the tubes were shaken until all of the material was resuspended, and the suspensions were centrifuged again. This process was repeated two more times. After discarding the supernatant, the pellet was vacuum dried for 1 h by perforating the microcentrifuge cap with a needle to create a hole for the air and solvent to pass.

#### A.2.1.5 Zn, Sn

**Synthesis** Following the protocol guidelines from Section 3.1.1, 1 mmol (220 mg) of zinc(II) acetate dihydrate and 1 mmol (405 mg) of tin(II) 2-ethylhexanoate were added to an Anton Paar G30 proprietary reaction vial with a polytetrafluoroethylene-covered Cowie stirring magnets with a size of 10 mm by 3 mm. Then the vial was filled with 5 g of 1-dodecanethiol. The mixture was then purged for 15 minutes by bubbling with industrial-grade nitrogen gas. The vial was capped with the proprietary polytetrafluoroethylene-covered silicon sealing cap and immediately

inserted into the Anton Paar Monowave 400 microwave reactor's cavity. Under constant steering at 1200 RPM, the temperature was raised to 300 °C in 10 minutes, followed by an automated cooling procedure to 50 °C. The suspension was then divided into three 2 mL microcentrifuge tubes, centrifuged at 9000 RPM (9146 *g*), the supernatant discarded, and ethanol added to the 2 mL mark. Next, with a vortex, the tubes were shaken until all of the material was resuspended, and the suspensions were centrifuged again. This process was repeated two more times. After discarding the supernatant, the pellet was vacuum dried for 1 h by perforating the microcentrifuge cap with a needle to create a hole for the air and solvent to pass.

#### A.2.1.6 Ba, Zr

**Synthesis** Following the protocol guidelines from Section 3.1.1, 1 mmol (261 mg) of barium(II) nitrate **and** 1 mmol (233 mg) of zirconium(IV) chloride, **or** 1 mmol (435 mg) of barium(II) triflate **or** 1 mmol (233 mg) of zirconium(IV) chloride were added to an Anton Paar G30 proprietary reaction vial with a polytetrafluoroethylene-covered Cowie stirring magnets with a size of 10 mm by 3 mm. Then the vial was filled with 5 g of 1-dodecanethiol. The mixture was then purged for 15 minutes by bubbling with industrial-grade nitrogen gas. The vial was capped with the proprietary polytetrafluoroethylene-covered silicon sealing cap and immediately inserted into the Anton Paar Monowave 400 microwave reactor's cavity. Under constant steering at 1200 RPM, the temperature was raised to 300 °C in 10 minutes, kept for 25 minutes, followed by an automated cooling procedure to 50 °C. The suspension was then divided into three 2 mL microcentrifuge tubes, centrifuged at 9000 RPM (9146 *g*), the supernatant discarded, and ethanol added to the 2 mL mark. Next, with a vortex, the tubes were shaken until all of the material was resuspended, and the suspensions were centrifuged again. This process was repeated two more times. After discarding the supernatant, the pellet was vacuum dried for 1 h by perforating the microcentrifuge cap with a needle to create a hole for the air and solvent to pass.

## A.2.2 Quaternary

### A.2.2.1 Cu, In, Sn

**Synthesis** Following the protocol guidelines from Section 3.1.1, 2 mmol (382 mg) of copper(I) iodide, 1 mmol (221 mg) of indium(III) chloride, and 1 mmol (405 mg) of tin(II) 2-ethylhexanoate were added to an Anton Paar G30 proprietary reaction vial with a polytetrafluoroethylene-covered Cowie stirring magnets with a size of 10 mm by 3 mm. Then the vial was filled with 5 g of 1-dodecanethiol. The mixture was then purged for 15 minutes by bubbling with industrial-grade nitrogen gas. The vial was capped with the proprietary polytetrafluoroethylene-covered silicon sealing cap and immediately inserted into the Anton Paar Monowave 400 microwave reactor's cavity. Under constant steering at 1200 RPM, the temperature was raised to 300 °C in 10 minutes and kept for 25 minutes **or** the temperature was raised as fast as possible to 150 °C and then slowly raised to 225 °C in 90 minutes. Both were cooled by an automated cooling procedure to 50 °C. The suspension was then divided into three 2 mL microcentrifuge tubes, centrifuged at 9000 RPM (9146 *g*), the supernatant discarded, and ethanol added to the 2 mL mark. Next, with a vortex, the tubes were shaken until all of the material was resuspended, and the suspensions were centrifuged again. This process was repeated two more times. After discarding the supernatant, the pellet was vacuum dried for 1 h by perforating the microcentrifuge cap with a needle to create a hole for the air and solvent to pass.

### A.2.2.2 Cu, Ag, In

**Synthesis** Following the protocol guidelines from Section 3.1.1, 1 mmol (191 mg) of copper(I) iodide, 1 mmol (170 mg) of silver(I) nitrate, and 1 mmol (221 mg) of indium(III) chloride were added to an Anton Paar G30 proprietary reaction vial with a polytetrafluoroethylene-covered Cowie stirring magnets with a size of 10 mm by 3 mm. Then the vial was filled with 5 g of 1-dodecanethiol. The mixture was then purged for 15 minutes by bubbling with industrial-grade nitrogen gas. The vial was capped with the proprietary polytetrafluoroethylene-covered silicon sealing cap and immediately inserted into the Anton Paar Monowave 400 microwave reactor's cavity. Under constant steering at 1200 RPM, the temperature was raised to 300 °C in 10 minutes, kept for 25 minutes. This was followed by an automated cooling procedure to 50 °C. The suspension was then divided into three 2 mL microcentrifuge tubes, centrifuged at 9000 RPM (9146 *g*), the supernatant discarded, and ethanol added to the 2 mL mark. Next, with a vortex, the tubes were shaken until all of the material was resuspended, and the suspensions were centrifuged again. This process was repeated two more times. After discarding the supernatant, the pellet was vacuum dried for 1 h by perforating the microcentrifuge cap with a needle to create a hole for the air and solvent to pass.

### A.2.2.3 Zn, In, Sn

The color, temperature, and pressure profiles, and the stacked plots of the temperature and red color profiles of two replica syntheses to attempt to produce the alloy between the elements Zn, Sn, In are shown in Figure A.14

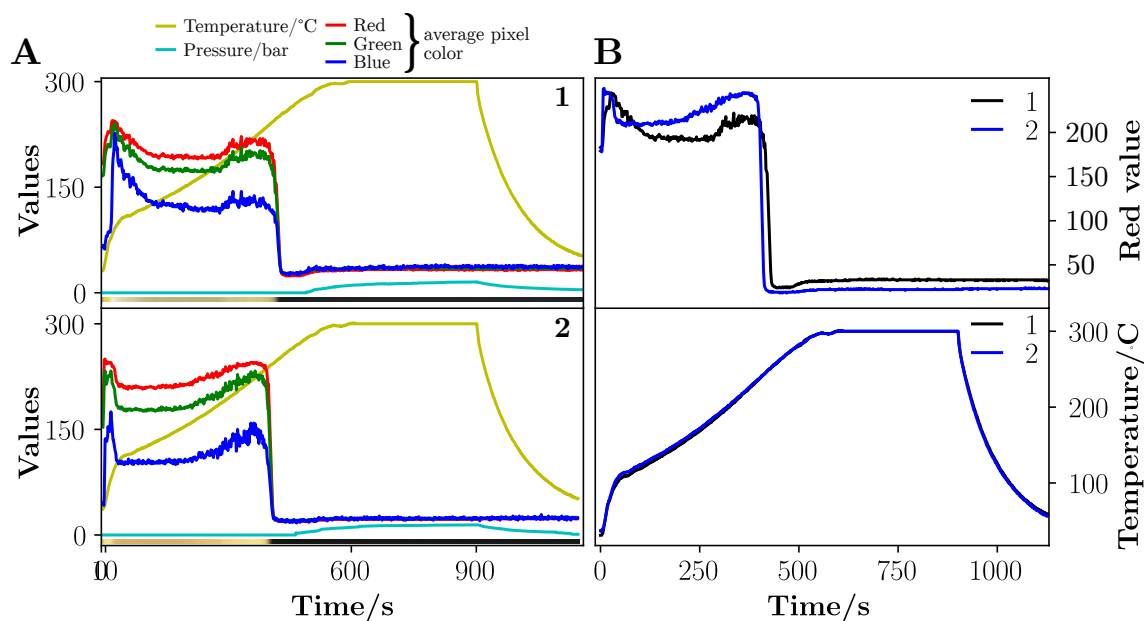


Figure A.14: Color, temperature, and pressure profiles (A) and stacked temperature and red color profiles (B) of two replica syntheses, 1 and 2, to attempt to produce the alloy between the elements Zn, Sn, In.

The color, temperature, and pressure profiles, and the Raman spectra and XRD patterns of two sequential syntheses to attempt to produce core-shell structures with the elements Zn, Sn, In are shown in Figure A.14

**Synthesis** Following the protocol guidelines from Section 3.1.1, 1 mmol (220 mg) of zinc(II) acetate dihydrate, 1 mmol (221 mg) of indium(III) chloride, and 1 mmol (405 mg) of tin(II) 2-ethylhexanoate were added to an Anton Paar G30 proprietary reaction vial with a polytetrafluoroethylene-covered Cowie stirring magnets with a size of 10 mm by 3 mm. Then the vial was filled with 5 g of 1-dodecanethiol. The mixture was then purged for 15 minutes by bubbling with industrial-grade nitrogen gas. The vial was capped with the proprietary polytetrafluoroethylene-covered silicon sealing cap and immediately inserted into the Anton Paar Monowave 400 microwave reactor's cavity. Under constant steering at 1200 RPM, the temperature was raised to 300 °C in 10 minutes, kept for 5 minutes. This was followed by an automated cooling procedure to 50 °C. The suspension was then divided into three 2 mL microcentrifuge tubes, centrifuged at 9000 RPM (9146 *g*), the supernatant discarded, and ethanol added to the 2 mL mark. Next, with a vortex, the tubes were shaken until all of the material was resuspended, and the suspensions were centrifuged again. This process was repeated two more times. After discarding the supernatant, the pellet was vacuum dried for 1 h by perforating the microcentrifuge cap with a needle to create a hole for the air and solvent to pass.

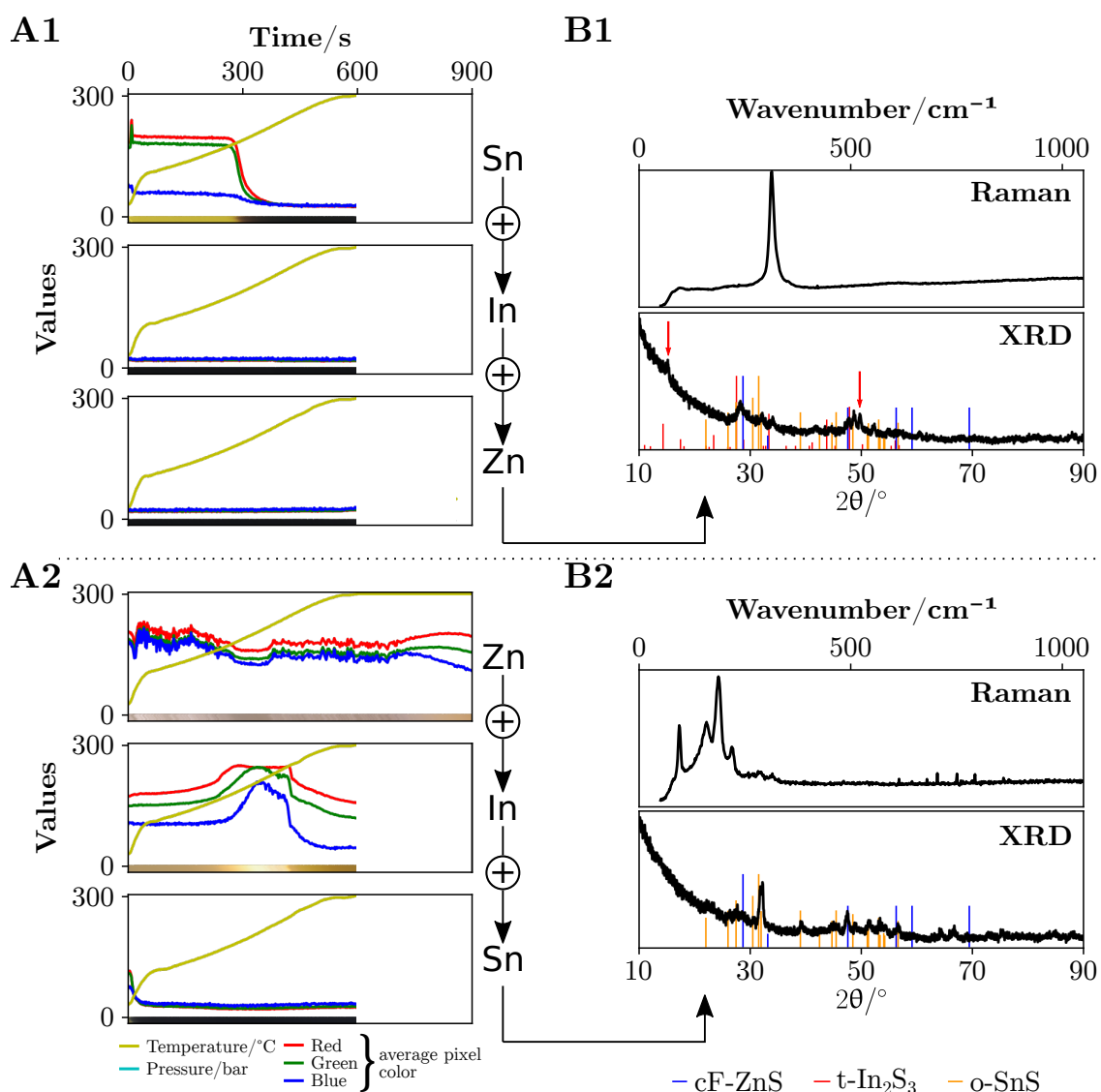


Figure A.15: Color, temperature, and pressure profiles of two sequential syntheses, according to the ordered addition of precursors: Sn → In → Zn (A1) and Zn → In → Sn (A2), and their resulting powders' Raman spectra and XRD patterns, respectively (B1) and (B2).

**Sequential Synthesis (Sn → In → Zn)** Following the protocol guidelines from Section 3.1.1, 1 mmol (405 mg) of tin(II) 2-ethylhexanoate was added to an Anton Paar G30 proprietary reaction vial with a polytetrafluoroethylene-covered Cowie stirring magnets with a size of 10 mm by 3 mm. Then the vial was filled with 5 g of 1-dodecanethiol. The mixture was then purged for 15 minutes by bubbling with industrial-grade nitrogen gas. The vial was capped with the proprietary polytetrafluoroethylene-covered silicon sealing cap and immediately inserted into the Anton Paar Monowave 400 microwave reactor's cavity. Under constant steering at 1200 RPM, the temperature was raised to 300 °C in 10 minutes, kept for 5 minutes. This was followed by an automated cooling procedure to 50 °C. Then, 1 mmol (221 mg) of indium(III) chloride was added to the vial and the same synthesis procedure followed. Again, the synthesis procedure was repeated with the addition of 1 mmol (220 mg) of zinc(II) acetate dihydrate. After the automated cooling procedure cooled the vial to 50 °C, the suspension was then divided into three 2 mL



microcentrifuge tubes, centrifuged at 9000 RPM (9146 *g*), the supernatant discarded, and ethanol added to the 2 mL mark. Next, with a vortex, the tubes were shaken until all of the material was resuspended, and the suspensions were centrifuged again. This process was repeated two more times. After discarding the supernatant, the pellet was vacuum dried for 1 h by perforating the microcentrifuge cap with a needle to create a hole for the air and solvent to pass.

**Sequential Synthesis (Zn → In → Sn)** Following the protocol guidelines from Section 3.1.1, 1 mmol (220 mg) of zinc(II) acetate dihydrate was added to an Anton Paar G30 proprietary reaction vial with a polytetrafluoroethylene-covered Cowie stirring magnets with a size of 10 mm by 3 mm. Then the vial was filled with 5 g of 1-dodecanethiol. The mixture was then purged for 15 minutes by bubbling with industrial-grade nitrogen gas. The vial was capped with the proprietary polytetrafluoroethylene-covered silicon sealing cap and immediately inserted into the Anton Paar Monowave 400 microwave reactor's cavity. Under constant steering at 1200 RPM, the temperature was raised to 300 °C in 10 minutes, kept for 5 minutes. This was followed by an automated cooling procedure to 50 °C. Then, 1 mmol (221 mg) of indium(III) chloride was added to the vial and the same synthesis procedure followed. Again, the synthesis procedure was repeated with the addition of 1 mmol (405 mg) of tin(II) 2-ethylhexanoate. After the automated cooling procedure cooled the vial to 50 °C, the suspension was then divided into three 2 mL microcentrifuge tubes, centrifuged at 9000 RPM (9146 *g*), the supernatant discarded, and ethanol added to the 2 mL mark. Next, with a vortex, the tubes were shaken until all of the material was resuspended, and the suspensions were centrifuged again. This process was repeated two more times. After discarding the supernatant, the pellet was vacuum dried for 1 h by perforating the microcentrifuge cap with a needle to create a hole for the air and solvent to pass.

### A.3 Input Parameters and Impact on the Synthesis

#### Electric Arcs

Figure A.16 (inorganic anions) and Figure A.17 (organic anions) include all the syntheses attempted using different precursors with the color-coded information if electric arcs developed during the synthesis.

		Group													
		2	3	4	5	6	7	8	9	10	11	12	13	14	15
Period	2	Be	Chlorides Cation: Ni <sup>2+</sup> ↑ Electric arcs? (background color): NO (blue), YES (red)											B	C
	3	Mg												Al	Si
	4	Ca	Sc	Ti	V	Cr <sup>1+</sup>	Mn	Fe <sup>3+</sup>	Co <sup>2+</sup>	Ni	Cu	Zn <sup>2+</sup>	Ga	Ge	
	5	Sr <sup>2+</sup>	Y	Zr <sup>4+</sup>	Nb <sup>5+</sup>	Mo <sup>5+</sup>	Tc	Ru <sup>3+</sup>	Rh	Pd	Ag	Cd	In <sup>3+</sup>	Sn <sup>2+</sup>	
	6	Ba	La	Hf <sup>4+</sup>	Ta <sup>5+</sup>	W <sup>6+</sup>	Re	Os	Ir	Pt	Au	Hg	Tl	Pb	
			Oxides												
2	Be <sup>2+</sup>												B	C	
3	Mg												Al	Si	
4	Ca	Sc	Ti	V <sup>1+</sup>	Cr	Mn	Fe	Co	Ni	Cu <sup>2+</sup> / Cu <sup>1+</sup>	Zn	Ga	Ge		
5	Sr	Y	Zr	Nb	Mo <sup>1+</sup>	Tc	Ru	Rh	Pd	Ag <sup>+</sup>	Cd	In	Sn <sup>1+</sup>		
6	Ba	La	Hf	Ta	W <sup>4+</sup>	Re	Os	Ir	Pt	Au	Hg	Tl	Pb		
		Nitrates													
2	Be												B	C	
3	Mg												Al	Si	
4	Ca	Sc	Ti	V	Cr	Mn	Fe	Co	Ni	Cu <sup>2+</sup>	Zn	Ga	Ge		
5	Sr	Y	Zr	Nb	Mo	Tc	Ru	Rh	Pd	Ag <sup>+</sup>	Cd	In	Sn		
6	Ba <sup>2+</sup>	La	Hf	Ta	W	Re	Os	Ir	Pt	Au	Hg	Tl	Pb	Bi <sup>2+</sup>	

Figure A.16: Segments of periodic tables showing which precursors developed electric arcs during the synthesis, marked by the element background; red - formed electric arcs, blue - no arcs. Each segment belongs to an anion: chlorides, oxides, or nitrates.

		Group													
		2	3	4	5	6	7	8	9	10	11	12	13	14	
Period	2	Be	Acetates											B	C
	3	Mg												Al	Si
	4	Ca	Sc <sup>3+</sup>	Ti	V	Cr	Mn <sup>2+</sup>	Fe	Co	Ni <sup>2+</sup>	Cu	Zn <sup>2+</sup>	Ga	Ge	
	5	Sr	Y	Zr	Nb	Mo	Tc	Ru	Rh	Pd	Ag	Cd <sup>2+</sup>	In	Sn	
	6	Ba	La	Hf	Ta	W	Re	Os	Ir	Pt	Au	Hg	Tl	Pb	
			<div style="display: flex; justify-content: space-around; align-items: center;"> <div style="border: 1px solid black; padding: 5px;">           Cation  <math>\uparrow</math>  <math>\text{Ni}^{2+}</math> </div> <div style="border: 1px solid black; padding: 5px;">           Electric arcs?            (background color)  <div style="display: flex; justify-content: space-around;"> <span style="background-color: blue; color: white; padding: 2px;">NO</span> <span style="background-color: red; color: white; padding: 2px;">YES</span> </div> </div> </div>												
Period	2	Be	Acetylacetonates											B	
	3	Mg												Al <sup>3+</sup>	Si
	4	Ca	Sc	Ti	V	Cr <sup>3+</sup>	Mn	Fe <sup>3+</sup>	Co <sup>3+</sup>	Ni	Cu <sup>2+</sup>	Zn <sup>2+</sup>	Ga	Ge	
	5	Sr	Y	Zr	Nb	Mo	Tc	Ru	Rh	Pd	Ag	Cd	In	Sn	
	6	Ba	La	Hf	Ta	W	Re	Os	Ir	Pt	Au	Hg	Tl	Pb	
			Other organic anions*												
Period	2	Be	Other organic anions*											B	
	3	Mg <sup>2+</sup> <small>Stearate</small>												Al	Si <sup>4+</sup> <small>Trimethylolpropane</small>
	4	Ca	Sc	Ti <sup>4+</sup> <small>Propionate</small>	V <sup>5+</sup> <small>Propionate</small>	Cr	Mn	Fe	Co	Ni	Cu	Zn <sup>2+</sup> <small>Stearate</small>	Ga <sup>3+</sup> <small>Propionate</small>	Ge	
	5	Sr	Y <sup>3+</sup> <small>Carbonate</small>	Zr <sup>4+</sup> <small>Propionate</small>	Nb	Mo	Tc	Ru	Rh	Pd	Ag	Cd	In	Sn <sup>2+</sup> <small>Propionate</small>	
	6	Ba	La	Hf	Ta	W	Re	Os	Ir	Pt	Au	Hg	Tl	Pb	

Figure A.17: Segments of periodic tables showing which precursors developed electric arcs during the synthesis, marked by the element background; red - formed electric arcs, blue - no arcs. Each segment belongs to an anion: acetates, acetylacetonates, or others. \* Other organic anions such as alkoxides, stearates, etc, as described per element. In the case of iron acetylacetonate, the amount of precursor used was 0.1 mmol and 15 g of thiol. The remainder were 1 mmol to 5 g.

## Concentration

**Synthesis** Following the protocol guidelines from Section 3.1.1, 0.1 mmol (41 mg) of tin(II) 2-ethylhexanoate was added to an Anton Paar G30 proprietary reaction vial with a polytetrafluoroethylene-covered Cowie stirring magnets with a size of 10 mm by 3 mm. Then the vial was filled with 15 g of 1-dodecanethiol. The mixture was then purged for 15 minutes by bubbling with industrial-grade nitrogen gas. The vial was capped with the proprietary polytetrafluoroethylene-covered silicon sealing cap and immediately inserted into the Anton Paar Monowave 400 microwave reactor's

cavity. Under constant steering at 1200 RPM, the temperature was raised to 300 °C in 10 minutes, followed by an automated cooling procedure to 50 °C. The suspension was then transferred to a 50 mL Falcon conical centrifuge tube, centrifuged at 9000 RPM (9146 *g*) and the supernatant was discarded. The tube was then left upside-down, with the cap facing a surface, for 1 hour.

## Reagents

**Synthesis** Following the protocol guidelines from Section 3.1.1, one of the precursors was added to an Anton Paar G30 proprietary reaction vial, with polytetrafluoroethylene-covered Cowie stirring magnets with a size of 10 mm by 3 mm. Then the vial was filled with 5 g of 1-dodecanethiol. The mixture was then purged for 15 minutes by bubbling with industrial-grade nitrogen gas. The vial was capped with the proprietary polytetrafluoroethylene-covered silicon sealing cap and immediately inserted into the Anton Paar Monowave 400 microwave reactor's cavity. Under constant steering at 1200 RPM, the temperature was raised to 300 °C in 10 minutes, kept for 5 minutes, followed by an automated cooling procedure to 50 °C. The suspension was then divided into three 2 mL microcentrifuge tubes, centrifuged at 9000 RPM (9146 *g*), the supernatant discarded, and ethanol added to the 2 mL mark. Next, with a vortex, the tubes were shaken until all of the material was resuspended, and the suspensions were centrifuged again. This process was repeated two more times. After discarding the supernatant, the pellet was vacuum dried for 1 h by perforating the microcentrifuge cap with a needle to create a hole for the air and solvent to pass.

## A.4 Metal Sulfide Nanoparticle Inks

### A.4.1 Tin Sulfide Film

**Synthesis, Ink Formulation, and Deposition** Following the protocol guidelines from Section 3.1.1, 0.1 mmol (41 mg) of tin(II) 2-ethylhexanoate was added to an Anton Paar G30 proprietary reaction vial with a polytetrafluoroethylene-covered Cowie stirring magnets with a size of 10 mm by 3 mm. Then the vial was filled with 15 g of 1-dodecanethiol. The mixture was then purged for 15 minutes by bubbling with industrial-grade nitrogen gas. The vial was capped with the proprietary polytetrafluoroethylene-covered silicon sealing cap and immediately inserted into the Anton Paar Monowave 400 microwave reactor's cavity. Under constant steering at 1200 RPM, the temperature was raised to 300 °C in 10 minutes, followed by an automated cooling procedure to 50 °C. The suspension was then transferred to a 50 mL Falcon conical centrifuge tube, centrifuged at 9000 RPM (9146 *g*), and the supernatant was discarded. The tube was left upside-down, with the cap facing a surface, for 1 hour. To obtain the ink, 7.86 g (10 mL) of isopropanol was added, and the suspension was treated with ultrasounds in a bath for 5 minutes. The suspension was transferred to the airbrush's ink deposit. Following the setup found in Figure 4.4, with a complete turn instead of a quarter and a spray time of 20 seconds, the ink volume was depleted after 22 spray cycles.

### A.4.2 Zinc Sulfide Film

**Synthesis, Ink Formulation, and Deposition** Following the protocol guidelines from Section 3.1.1, 0.1 mmol (22 mg) of zinc(II) acetate dihydrate was added to an Anton Paar G30 proprietary reaction vial with a polytetrafluoroethylene-covered Cowie stirring magnets with a size of 10 mm by 3 mm. Then the vial was filled with 15 g of 1-dodecanethiol. The mixture was then purged for 15 minutes by bubbling with industrial-grade nitrogen gas. The vial was capped with the proprietary polytetrafluoroethylene-covered silicon sealing cap and immediately inserted into the Anton Paar Monowave 400 microwave reactor's cavity. Under constant steering at 1200 RPM, the temperature was raised to 300 °C in 10 minutes, followed by an automated cooling procedure to 50 °C. The suspension was then transferred to a 50 mL Falcon conical centrifuge tube, centrifuged at 9000 RPM (9146 *g*), and the supernatant was discarded. The tube was left upside-down, with the cap facing a surface, for 1 hour. To obtain the ink, 7.86 g (10 mL) of isopropanol was added, and the suspension was treated with ultrasounds in a bath for 5 minutes. The suspension was transferred to the airbrush's ink deposit. Following the setup found in Figure 4.4, with a complete turn instead of a quarter, the ink volume was depleted after 30 spray cycles.

### A.4.3 Niobium Sulfide Film

**Synthesis, Ink Formulation, and Deposition** Following the protocol guidelines from Section 3.1.1, 0.1 mmol (27 mg) of niobium(V) chloride was added to an Anton Paar G30 proprietary reaction vial with a polytetrafluoroethylene-covered Cowie stirring magnets with a size of 10 mm by 3 mm. Then the vial was filled with 15 g of 1-dodecanethiol. The mixture was then purged for 15 minutes by bubbling with industrial-grade nitrogen gas. The vial was capped with the proprietary polytetrafluoroethylene-covered silicon sealing cap and immediately inserted into the Anton Paar Monowave 400 microwave reactor's cavity. Under constant steering at 1200 RPM, the temperature was raised to 300 °C in 10 minutes, followed by an automated cooling procedure to 50 °C. The suspension was then transferred to a 50 mL Falcon conical centrifuge tube, centrifuged at 9000 RPM (9146 *g*), and the supernatant was discarded. The tube was left upside-down, with the cap facing a surface, for 1 hour. To obtain the ink, 7.86 g (10 mL) of isopropanol was added, and the suspension was treated with ultrasounds in a bath for 5 minutes. The suspension was transferred to the airbrush's ink deposit, and the ink volume was depleted after 44 spray cycles.

#### A.4.4 Copper Iron Sulfide Film

The total reflectance and absorption spectra of the copper iron sulfide film deposited by spray is shown in Figure A.18.

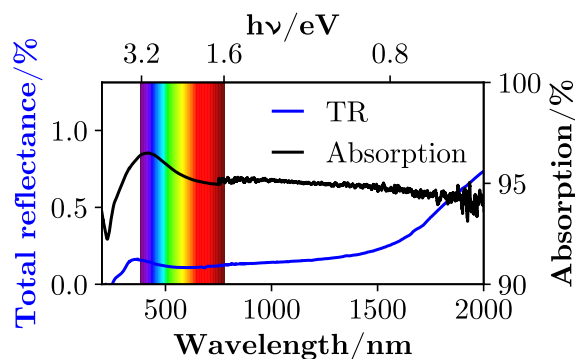


Figure A.18: Total reflectance spectra (TR) and absorption spectrum of the copper iron sulfide film deposited by spray.

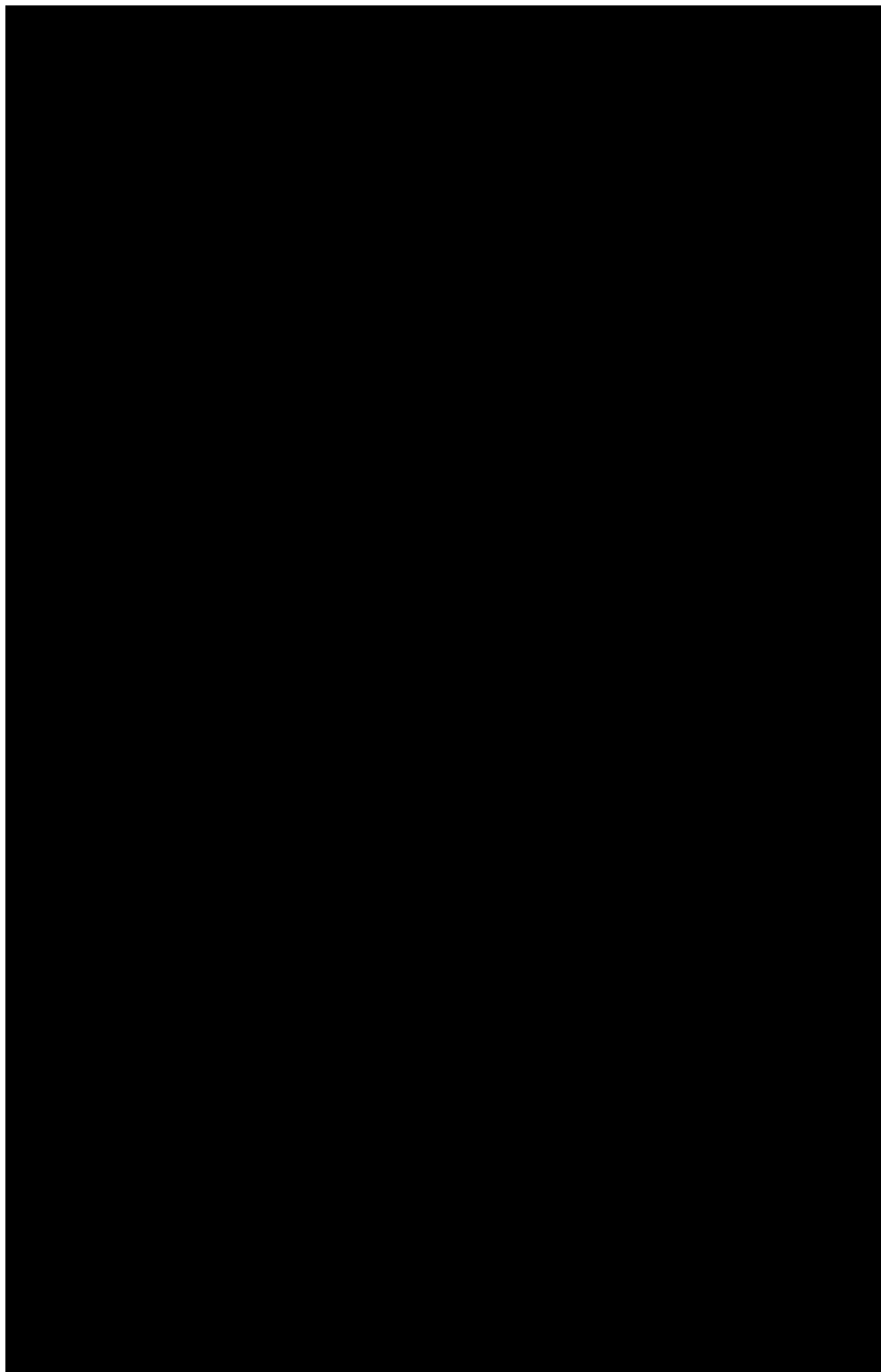
**Synthesis, Ink Formulation, and Deposition** Following the protocol guidelines from Section 3.1.1, 0.1 mmol (19 mg) of copper(I) iodide and 0.1 mmol (35 mg) of iron(III) acetylacetonate were added to an Anton Paar G30 proprietary reaction vial with a polytetrafluoroethylene-covered Cowie stirring magnets with a size of 10 mm by 3 mm. Then the vial was filled with 15 g of 1-dodecanethiol. The mixture was then purged for 15 minutes by bubbling with industrial-grade nitrogen gas. The vial was capped with the proprietary polytetrafluoroethylene-covered silicon sealing cap and immediately inserted into the Anton Paar Monowave 400 microwave reactor's cavity. Under constant steering at 1200 RPM, the temperature was raised to 300 °C in 10 minutes, followed by an automated cooling procedure to 50 °C. The suspension was then transferred to a 50 mL Falcon conical centrifuge tube, centrifuged at 9000 RPM (9146 *g*), and the supernatant was discarded. The tube was left upside-down, with the cap facing a surface, for 1 hour. To obtain the ink, 7.86 g (10 mL) of isopropanol was added, and the suspension was treated with ultrasounds in a bath for 5 minutes. The suspension was transferred to the airbrush's ink deposit, and the ink volume was depleted after 45 spray cycles.



## A.5 Reagents

The following table contains the reagents and solvents used in this work, as well as their brand and purity.

Table A.1: Reagents and solvents name, brand, and purity.





## Python Scripts

This appendix contains the scripts used and described in this work. These scripts can also be found or will be made available soon in my GitHub repository at <https://github.com/DavidMSou/Scientific-Tools>. After the publication of this document, the scripts will have suffered some modifications but I will make an effort to keep them as compatible with their current version as possible. The code herein is not easy to copy and paste, due to the way PDF files are built. The reader is advised to download the Python scripts from the GitHub page.

### B.1 Interpolation

The Python 3 script "Interpolation.py" was used to interpolate data, such as the diffuse reflectance spectrum, to be able to have more points without changing the spectrum shape. It does so by adding an intermediate point in-between each two consecutive points, using a simple linear regression. The content of the script is displayed below.

---

```
# -*- coding: utf-8 -*-

try:
    import cupy as np_i
    cupy = True
except:
    import numpy as np_i
    cupy = False
import pandas as pd

def interpolator_halves(x, y, split_halves : int = 5, clipboard = True):
    c = 0
    while c <= split_halves-1:
        print(c)
        if c == 0:
            y_i = y.astype("float64")
            x_i = x.astype("float64")
        y_0 = []
        if c == 0 and len(y.shape) == 2:
            y_t = [(y_i[i+1][0]+y_i[i][0])/2 for i in range(len(y_i)-1)]
```

---

```

else:
    y_t = [(y_i[i+1]+y_i[i])/2 for i in range(len(y_i)-1)]
    for i in range(len(y_t)):
        y_0.append(y_i[i][0] if type(y_i[i]) != np_i.float64 else y_i
            [i])
        y_0.append(y_t[i][0] if type(y_0[i]) != np_i.float64 else y_t
            [i])
    y_i = y_0

x_0 = []
if c == 0 and len(x.shape) == 2:
    x_t = [(x_i[i+1][0]+x_i[i][0])/2 for i in range(len(x_i)-1)]
else:
    x_t = [(x_i[i+1]+x_i[i])/2 for i in range(len(x_i)-1)]
    for i in range(len(x_t)):
        x_0.append(x_i[i][0] if type(x_i[i]) != np_i.float64 else x_i
            [i])
        x_0.append(x_t[i][0] if type(x_0[i]) != np_i.float64 else x_t
            [i])
    x_i = x_0
    c += 1

interp_y = y_i
target_x = x_i
if clipboard:
    pd.DataFrame(np_i.array([target_x, interp_y]).get()).to_clipboard
        (excel=True, index=False, header=None)

y = np_i.append(y, np_i.zeros(len(target_x)-len(x)) + np_i.nan).
    ravel().tolist()
x = np_i.append(x, np_i.zeros(len(target_x)-len(x)) + np_i.nan).
    ravel().tolist()

return pd.DataFrame(np_i.array([target_x, interp_y, x, y]).T.get(),
    columns=["Interpolated X", "Interpolated Y", "X", "Y"])

```

---

## B.2 Band Gap Determination

The Python 3 script "Spectra.py" was used for the determination of the band gap of the powders synthesized in this work, using either the diffuse reflectance or the transmittance spectra. The content of the script is displayed below.

---

```
# -*- coding: utf-8 -*-

import pandas as pd
from matplotlib import pyplot as plt
import numpy as np
import cupy as cp
import scipy.stats as stats
from operator import itemgetter
import math
from sys import path as syspath
from os import path as ospath
syspath.append(ospath.abspath('../Interpolation'))
from Interpolation import interpolator_halves

params = {'mathtext.default': 'regular',
          'axes.linewidth': 0.8,
          'font.size': 10.95/0.75,
          'axes.labelweight': 'bold',
          'mathtext.fontset': 'cm',
          'font.family': 'serif',
          'font.serif': 'Computer Modern Roman',
          'text.usetex': True,
          'text.latex.preamble': r"\usepackage{textgreek}"
        }

plt.rcParams.update(params)

bandgaps = None # Global variable to guarantee that the user has the result available in
                # case the function was not attributed to a variable when executed
def bandgap_diffuse_reflectance(csv : str, kubelka = True, optical_path
    : int = 0, interpolate : int = 0, dif_points : int = 100,
    dif_smooth_window : int = 20, dif_smooth_window_iter : int = 1,
    data_smooth_window : int = 1, data_smooth_window_iter : int = 2,
    upper_range : int = 100, lower_range : int = 100, initial_plot_limits
    : list = [[None, None], [None, None]], final_plot_limits : list = [[
```

```
None, None], [None, None]], slope : bool = True, axis_width = 59,
axis_height = 49, nm_spacer : int = 10):
```

```
# Too add: description of arguments
```

```
data_smooth_window = data_smooth_window if data_smooth_window%2 == 0
    else data_smooth_window+1
dif_smooth_window = dif_smooth_window if dif_smooth_window%2 == 0
    else dif_smooth_window+1
```

```
global bandgaps
```

```
bandgaps = []
```

```
def find_nearest(array, value):
    array = np.asarray(array)
    idx = np.nanargmin((np.abs(array - value)))
    return array[idx], idx
```

```
### Adapted from https://stackoverflow.com/questions/9148927/matplotlib-extended-
line-over-2-control-points, by krouk
```

```
def drawLine2P(x,y,xlims,color):
    xrange = np.arange(xlims[0],xlims[1],0.01)
    A = np.vstack([x, np.ones(len(x))]).T
    k, b = np.linalg.lstsq(A, y, rcond=None)[0]
    plt.plot(xrange, k*xrange + b, color)
```

```
def findIntersection(x1,y1,x2,y2,x3,y3,x4,y4):
    px = ( (x1*y2-y1*x2)*(x3-x4)-(x1-x2)*(x3*y4-y3*x4) ) / ( (x1-x2)
        *(y3-y4)-(y1-y2)*(x3-x4) )
    py = ( (x1*y2-y1*x2)*(y3-y4)-(y1-y2)*(x3*y4-y3*x4) ) / ( (x1-x2)
        *(y3-y4)-(y1-y2)*(x3-x4) )
    return [px, py]
```

```
# Import data from csv file
```

```
data = pd.read_csv(csv, header=None)
data = data[pd.to_numeric(data[data.columns[0]], errors='coerce').
    notnull()].astype(float)
nm = data[0].values
dr = data[1].values/100
```

```
if interpolate > 0:
    interp = interpolator_halves(nm, dr, interpolate, False)
    nm = interp["Interpolated X"].to_numpy()
    dr = interp["Interpolated Y"].to_numpy()

ev = 1240/nm
evd = ev
evi = ev
del data # Memory management

# Tauc transformations for direct (dt) and indirect (it) plots
dt = (((1-dr)**2/(2*dr))*evd)**2 if kubelka else (((2 - np.log10(100*
    dr))/(optical_path if optical_path else 1))*evd)**2
it = (((1-dr)**2/(2*dr))*evi)**0.5 if kubelka else (((2 - np.log10
    (100*dr))/(optical_path if optical_path else 1))*evi)**0.5

if data_smooth_window > 1:
    for i in range(data_smooth_window_iter):
        cumsum_vec = np.cumsum(np.concatenate(([dt[0]]*int(
            data_smooth_window/2), dt,[dt[-1]]*int(data_smooth_window
            /2))))
        dt = (cumsum_vec[data_smooth_window:] - cumsum_vec[:-
            data_smooth_window]) / data_smooth_window
        cumsum_vec = np.cumsum(np.concatenate(([it[0]]*int(
            data_smooth_window/2), it,[it[-1]]*int(data_smooth_window
            /2))))
        it = (cumsum_vec[data_smooth_window:] - cumsum_vec[:-
            data_smooth_window]) / data_smooth_window

# Show the user the plots to help pin point the upper and lower slopes
plt.plot(evd, dt, "k")
plt.xlim(initial_plot_limits[0])
plt.ylim(initial_plot_limits[1])
plt.title("Direct")
plt.show()
plt.plot(evi, it, "k")
plt.xlim(initial_plot_limits[0])
plt.ylim(initial_plot_limits[1])
plt.title("Indirect")
```

```

plt.show()

# Slice the data to make the script faster by asking the user for the range where the band
  gap is
udrange = float(input("Where is the upper limit of the range to
  determine the direct bandgap? (value in eV and do not enter any
  value or text if to use the full higher energy spectrum)\n")) or
  np.max(evd))
ldrange = float(input("Where is the lower limit of the range to
  determine the direct bandgap? (value in eV and do not enter any
  value or text if to use the full lower energy spectrum)\n")) or np
  .min(evd))
uirange = float(input("Where is the upper limit of the range to
  determine the indirect bandgap? (value in eV and do not enter any
  value or text if to use the full higher energy spectrum)\n")) or
  np.max(evi))
lirange = float(input("Where is the lower limit of the range to
  determine the indirect bandgap? (value in eV and do not enter any
  value or text if to use the full lower energy spectrum)\n")) or
  np.min(evd))

if udrange != None:
    dt = dt[:find_nearest(ev,udrange)[1]]
    evd = evd[:find_nearest(ev,udrange)[1]]
if ldrange != None:
    dt = dt[find_nearest(evd,ldrange)[1]:]
    evd = evd[find_nearest(evd,ldrange)[1]:]
if uirange != None:
    it = it[:find_nearest(ev,uirange)[1]]
    evi = evi[:find_nearest(ev,uirange)[1]]
if lirange != None:
    it = it[find_nearest(evi,lirange)[1]:]
    evi = evi[find_nearest(evi,lirange)[1]:]

normdifd = (np.diff(dt)-np.min(np.diff(dt)))/(np.max(np.diff(dt))-np
  .min(np.diff(dt)))
if data_smooth_window > 1:
    for i in range(dif_smooth_window_iter):
        cumsum_vec = np.cumsum(np.concatenate([[normdifd[0]]*int(

```



```

        dif_smooth_window/2), normdifd, [normdifd[-1]]*int(
        dif_smooth_window/2)))
    normdifd = (cumsum_vec[dif_smooth_window:] - cumsum_vec[:-
        dif_smooth_window]) / dif_smooth_window
plt.plot(evd, (dt-np.min(dt))/(np.max(dt)-np.min(dt)), "k")
plt.plot(evd[1:], normdifd, "r", alpha=0.3)
plt.title("Direct")
plt.gca().xaxis.set_major_locator(plt.MultipleLocator(0.1))
plt.gca().xaxis.grid(True)
plt.show()
plt.plot(evi, (it-np.min(it))/(np.max(it)-np.min(it)), "k")
normdifi = (np.diff(it)-np.min(np.diff(it)))/(np.max(np.diff(it))-np
    .min(np.diff(it)))
if data_smooth_window > 1:
    cumsum_vec = np.cumsum(np.concatenate(([normdifi[0]]*int(
        dif_smooth_window/2), normdifi, [normdifi[-1]]*int(
        dif_smooth_window/2))))
    normdifi = (cumsum_vec[dif_smooth_window:] - cumsum_vec[:-
        dif_smooth_window]) / dif_smooth_window
plt.plot(evi[1:], normdifi, "r", alpha=0.3)
plt.title("Indirect")
plt.gca().xaxis.set_major_locator(plt.MultipleLocator(0.1))
plt.gca().xaxis.grid(True)
plt.show()

# Ask user where the upper and lower slopes to obtain the bandgap are
udb = float(input("Where is the upper slope to determine the direct
    bandgap?\nWarning: please choose a value away from too much noise
    . (value in eV and 0 if to skip)\n") or 0)
if udb != 0:
    udb_v = find_nearest(evd, udb)
    udb_i = udb_v[1] if udb_v[1] < len(dt)-30 else len(dt)-30
    udb_v = udb_v[0]
    ldb = float(input("Where is the lower slope to determine the
        direct bandgap? (value in eV and it's the flat line to serve
        as baseline')\n"))
    ldb_v = find_nearest(evd, ldb)
    ldb_i = ldb_v[1] if ldb_v[1] > 30 else 30
    ldb_v = ldb_v[0]
else:
```

```

    udb = None
    ldb = None

uib = float(input("Where is the upper slope to determine the
    indirect bandgap?\nWarning: please choose a value away from too
    much noise. (value in eV and 0 if to skip)\n") or 0)
if uib != 0:
    uib_v = find_nearest(evi, uib)
    uib_i = uib_v[1] if uib_v[1] <= len(it)-31 else len(it)-31
    uib_v = uib_v[0]
    lib = float(input("Where is the lower slope to determine the
        indirect bandgap? (value in eV and it's the flat line to serve
        as baseline')\n"))
    lib_v = find_nearest(evi, lib)
    lib_i = lib_v[1] if lib_v[1] >= 30 else 30
    lib_v = lib_v[0]
else:
    uib = None
    lib = None

# Define a function to plot the spectrum and the linear fits and calculate the intersection
# between the two fits
def plotter(array_pair, index_l, index_u, title, d_or_i, plot=True,
    xlims = [0, 10], nm_spacer = 10, final_plot_limits = [[None, None
], [None, None]]):
    ev = d_or_i[0]
    d_or_i = d_or_i[1]
    evl0 = ev[array_pair[0][index_l][1][0] if array_pair[0][index_l
][1][0] < len(ev) else len(ev)-1]
    evl1 = ev[array_pair[0][index_l][1][1] if array_pair[0][index_l
][1][1] < len(ev) else len(ev)-1]
    dl0 = d_or_i[array_pair[0][index_l][1][0] if array_pair[0][
index_l][1][0] < len(d_or_i) else len(d_or_i)-1]
    dl1 = d_or_i[array_pair[0][index_l][1][1] if array_pair[0][
index_l][1][1] < len(d_or_i) else len(d_or_i)-1]
    evu0 = ev[array_pair[1][index_u][1][0] if array_pair[1][index_l
][1][0] < len(ev) else len(ev)-1]
    evu1 = ev[array_pair[1][index_u][1][1] if array_pair[1][index_l
][1][1] < len(ev) else len(ev)-1]
    du0 = d_or_i[array_pair[1][index_u][1][0] if array_pair[1][

```

```

index_l][1][0] < len(d_or_i) else len(d_or_i)-1]
du1 = d_or_i[array_pair[1][index_u][1][1] if array_pair[1][
index_l][1][1] < len(d_or_i) else len(d_or_i)-1]
bandgap = findIntersection(ev_l0,d_l0,ev_l1,d_l1,ev_u0,du0,ev_u1,du1)
if plot:
    h = ((-0.212+axis_height)/25.4)/0.75
    figsize=[((-0.212+axis_width)/25.4)/0.75,
             h+(15/25.4)/0.75] # [W, H]
    ws = 1/0.4
    figsize = [ws*figsize[0], figsize[1]]
    fig = plt.figure(figsize=(figsize[0], figsize[1]))

    wscale = 1/ws
    hscale = h/figsize[1]
    wpos = (15/25.4)/(figsize[0])
    hpos = (15/25.4)/(figsize[1])
    ax = fig.add_axes([wpos,hpos,
                      wscale,hscale])
    ax.plot(ev, d_or_i, "k", zorder=0)
    ax.scatter((ev_l0,ev_l1), (d_l0,d_l1), c="g", zorder=1)
    ax.scatter((ev_u0,ev_u1), (du0,du1), c="r", zorder=1)
    ax.text(ev_l0, d_l0, str(int(ev_l0*100)/100), horizontalalignment
            ='right')
    ax.text(ev_l1, d_l1, str(int(ev_l1*100)/100), horizontalalignment
            ='right')
    ax.text(ev_u0, du0, str(int(ev_u0*100)/100), horizontalalignment
            ='right')
    ax.text(ev_u1, du1, str(int(ev_u1*100)/100), horizontalalignment
            ='right')
    ax.text(1.05*np.min(ev), np.max(d_or_i), "Points upper: " +
            str(array_pair[1][0][1][1]-array_pair[1][0][1][0]),
            horizontalalignment='left')
    ax.text(1.05*np.min(ev), 0.88*np.max(d_or_i), "Points lower: "
            + str(array_pair[0][0][1][1]-array_pair[0][0][1][0]),
            horizontalalignment='left')
    drawLine2P((ev_l0,ev_l1), (d_l0,d_l1), ax.get_xlim(), "g")
    drawLine2P((ev_u0,ev_u1), (du0,du1), ax.get_xlim(), "r")
    ax.scatter(bandgap[0], bandgap[1], c="k", zorder=10)
    ax.text(bandgap[0]+1.059/50.7*(ax.get_xlim()[1]-ax.get_xlim()
            [0]),

```

```

        bandgap[1]-1.059/26.9*(ax.get_ylim()[1]-ax.get_ylim()
            [0]),
        str(round(bandgap[0],2))+ " eV",
        horizontalalignment='left', verticalalignment='top')
if final_plot_limits != [[None, None], [None, None]]:
    ax.set_xlim(final_plot_limits[0])
    ax.set_ylim(final_plot_limits[1])
else:
    ax.set_ylim((0, np.max(d_or_i)*1.1))
ax.set_title(title)
if kubelka:
    label = "("+"F(R$_{\infty}$)"+"r"$\text{h}\text{t}\text{e}\text{x}\text{t}\text{n}\text{u}$"^(+"2$" if
        title == "Direct" else "{0.5}$")+"/"+"eV"+"$"^(+"2$" if
        title == "Direct" else "{0.5}$")
else:
    label = ("(Abs$_{\cdot}$" if optical_path == 0 else r"(\
        textalpha$_{\cdot}$"")+r"$\text{h}\text{t}\text{e}\text{x}\text{t}\text{n}\text{u}$"^(+"2$" if title == "
        Direct" else "{0.5}$")+("/(" if optical_path else "/")+
        "eV"+"($_{\cdot}$cm$^{-1}$)" if optical_path else "")+"$
        ^"+"2$" if title == "Direct" else "{0.5}$")
ax.set_ylabel(r"$\text{t}\text{b}\text{f}\{"+label+"}$")
ax.set_xlabel(r"$\text{t}\text{b}\text{f}\{"+r"$\text{h}\text{t}\text{e}\text{x}\text{t}\text{n}\text{u}/\text{eV}"+"$")

# Adapted from https://stackoverflow.com/questions/10514315/how-to-add-a-
# second-x-axis-in-matplotlib, by Hooked:
limev = np.array(list(range(int(ax.get_xlim()[0]*1000), int(ax
    .get_xlim()[1]*1000))))/1000
new_tick_locations_ev = [limev[i] for i in range(len(limev))
    if round(1240/limev[i],0)%nm_spacer == 0]
new_tick_locations_nm = [int(round(1240/limev[i],0)) for i in
    range(len(limev)) if round(1240/limev[i],0)%nm_spacer ==
    0]
new_tick_locations_ev = new_tick_locations_ev[:int(len(
    new_tick_locations_ev)/len(ax.get_xticks()))+2]
new_tick_locations_nm = new_tick_locations_nm[:int(len(
    new_tick_locations_nm)/len(ax.get_xticks()))+2]
ax2 = ax.twinx()
ax2.set_xlim(ax.get_xlim())
ax2.set_xticks(new_tick_locations_ev)
ax2.set_xticklabels([str(i) for i in new_tick_locations_nm])

```

```
ax2.set_xlabel(r"\textbf{"+"Wavelength/nm"+"}")

return bandgap[0], (evl0,dl0,evl1,dl1,evu0,du0,evu1,du1)

# Use the plotter function to calculate all the band gaps and scores (pearson product * (
# upper) or / (lower) by the slope) starting from the chosen points
# For the upper slope, the nearest highest slope is determined first. Data should not have a
# high amount of noise at the slope
direct = None
if udb != None and udb != 0:
    udb_i = find_nearest(normdifd, np.max(normdifd))[1]+1
    du = []
    print("\nDirect upper slope fitting all points starting from "+
          str(int(evd[udb_i]*1000)/1000)+" eV:")
    ut = upper_range
    for i in range(udb_i+5, udb_i+ut):
        inverse = udb_i-(ut*2 if udb_i-ut*2 >= 0 else 0)
        du.append([((stats.pearsonr(evd[j:i], dt[j:i])[0]))
                  *(stats.linregress(evd[j:i], dt[j:i])[0] if slope
                    else 1)
                  *math.log((abs(i-j)**0.075)*evd[j], 1000*evd[j])
                  ,(j, i)) for j in range(udb_i-5, inverse, -1) ])
        printProgressBar(i-(udb_i), ut)
    du = [item for sublist in du for item in sublist]
    du = sorted(du, key=itemgetter(0), reverse=True)

    dl = []
    print("\nDirect lower slope fitting all points starting from "+
          str(int(ldb*1000)/1000)+" eV:")
    lt = lower_range
    for i in range(ldb_i+5, ldb_i+lt):
        inverse = ldb_i-(lt if ldb_i-lt >= 0 else 0)
        dl.append([(stats.pearsonr(evd[j:i], dt[j:i])[0]
                  /stats.linregress(evd[j:i], dt[j:i])[0]
                  *math.log((abs(i-j)**0.075)*evd[j], 1000*evd[j])
                  ,(j, i)) for j in range(ldb_i-5, inverse, -1) ])
        printProgressBar(i-(ldb_i), lt)
    dl = [item for sublist in dl for item in sublist]
    dl = sorted(dl, key=itemgetter(0), reverse=True)
```

```

# After ordering the list of all the fits, by the pearson products, create a list of
# intersections from the best 50 pearson products of the upper and lower slopes,
# generating 2500 combinations and then calculate the average band gap and its
# standard deviation
bgd = plotter((dl, du), 0, 0, "Direct", (evd, dt), True, (np.min(
    evd), np.max(evd)), nm_spacer, final_plot_limits)
bgds = []
print("\nMatching the best 50 scores between upper and lower fits
for the direct tauc:")
for i in range(50):
    for j in range(50):
        bgds.append(plotter((dl, du), i, j, "Doesn't matter", (evd
            , dt), False, nm_spacer)[0])
        printProgressBar((i+1)*(j+1), 50*50)
bgds = [np.average(bgds), np.std(bgds)]
direct = ([bgd, [du[0], dl[0]]], bgds)
bandgaps = [direct, None]

# Same as before but for the indirect band gap
indirect = None
if uib != None and uib != 0:
    uib_i = find_nearest(normdifi, np.max(normdifi))[1]+1
    iu = []
    print("\nIndirect upper slope fitting all points starting from "+
        str(int(uib*1000)/1000)+" eV:")
    ut = upper_range
    for i in range(uib_i+15, uib_i+1+50):
        inverse = uib_i-(ut*2 if uib_i-ut*2 >= 0 else 0)
        iu.append([(((stats.pearsonr(evi[j:i], it[j:i])[0]))
            *(stats.linregress(evi[j:i], it[j:i])[0] if slope
                else 1)
            *math.log((abs(i-j)**0.075)*evi[j], 1000*evi[j])
            , (j, i)) for j in range(uib_i-5, inverse, -1) ])
        printProgressBar(i-(uib_i+1), 50)
    iu = [item for sublist in iu for item in sublist]
    iu = sorted(iu, key=itemgetter(0), reverse=True)

    il = []
    print("\nIndirect lower slope fitting all points starting from "+

```

```
    str(int(lib*1000)/1000)+" eV:")
lt = lower_range
for i in range(lib_i+15, lib_i+1+200):
    inverse = lib_i-(lt if lib_i-lt >= 0 else 0)
    il.append([(stats.pearsonr(evi[j:i], it[j:i])[0]
                /stats.linregress(evi[j:i], it[j:i])[0]
                *math.log((abs(i-j)**0.075)*evi[j], 1000*evi[j])
                ,(j, i)) for j in range(lib_i-5, inverse, -1) ])
    printProgressBar(i-(lib_i+1), 200)
il = [item for sublist in il for item in sublist]
il = sorted(il, key=itemgetter(0), reverse=True)

bgi = plotter((il, iu), 0, 0, "Indirect", (evi, it), True, (np.
    min(evd), np.max(evd)), nm_spacer, final_plot_limits)
bgis = []
print("\nMatching the best 50 scores between upper and lower fits
    for the indirect tauc:")
for i in range(50):
    for j in range(50):
        bgis.append(plotter((il, iu), i, j, "Doesn't matter", (evi
            , it), False, nm_spacer)[0])
        printProgressBar((i+1)*(j+1), 50*50)
bgis = [np.average(bgis), np.std(bgis)]
indirect = ([bgi, [iu[0], il[0]]], bgis)
bandgaps = [direct, indirect]

print("Bandgaps = [(Best fit, (Best fir intersection coordinates)),
    Best fit paramters[Upper(Score, (Indexes)), Lower(Score, (Indexes
    ))], [Average, standard deviation]]")

return direct, indirect
```

```
def plotter_spec(transmittance_file : str, difreflectance_file : str,
    xlim = [200, 2000], spacer = 0.05, show_spectrum_colors = 2,
    axis_width=50.7, axis_height=26.9):
```

```

data = pd.read_csv(transmittance_file, header=None)
data = data[pd.to_numeric(data[data.columns[0]], errors='coerce').
    notnull()].astype(float)
x1 = data[0].values
y1 = data[1].values

data = pd.read_csv(difreflectance_file, header=None)
data = data[pd.to_numeric(data[data.columns[0]], errors='coerce').
    notnull()].astype(float)
x2 = data[0].values
y2 = data[1].values

h = ((-0.212+axis_height)/25.4)/0.75
figsize=[((-0.212+axis_width)/25.4)/0.75,
    h+(15/25.4)/0.75] # [W, H]
ws = 1/0.4
figsize = [ws*figsize[0], figsize[1]]
fig = plt.figure(figsize=(figsize[0], figsize[1]))

wscale = 1/ws
hscale = h/figsize[1]
wpos = (15/25.4)/(figsize[0])
hpos = (15/25.4)/(figsize[1])
ax = fig.add_axes([wpos,hpos,
    wscale,hscale])

ax.set_xlim(xlim)

### Adapted from https://scipython.com/book/chapter-7-matplotlib/examples/a-
    depiction-of-the-electromagnetic-spectrum/
for i in range(380, 780, show_spectrum_colors):
    c = wavelength_to_rgb(i)
    ax.axvspan(i-show_spectrum_colors/2, i+show_spectrum_colors/2,
        facecolor=c[:3], ec='none', alpha=0.75)
###

a1, = ax.plot(x1, y1, "b", zorder=2, label="T")
ax2 = ax.twinx()
a2, = ax2.plot(x2, y2, "k", zorder=2, label="DR")

```



```
ax.set_ylim((0, np.max(y1)*1.1))
ax2.set_ylim((0, np.max(y2)*1.1))
ax.set_ylabel(r"\textbf{"+"Transmittance(T)/%"+"}")
ax2.set_ylabel(r"\textbf{"+"Diffuse reflectance(DR)/%"+"}")
ax.set_xlabel(r"\textbf{"+"Wavelength/nm"+"}")
ax.yaxis.label.set_color('blue')

### Adapted from https://stackoverflow.com/questions/10514315/how-to-add-a-second-x-axis-in-matplotlib, by Hooked:
limnm = np.array(list(range(int(ax.get_xlim()[0]), int(ax.get_xlim()[1]))))
new_tick_locations_nm = [limnm[i] for i in range(len(limnm)) if
    round(1240/limnm[i],2)%spacer == 0]
new_tick_locations_ev = [round(1240/limnm[i],2) for i in range(len(limnm)) if
    round(1240/limnm[i],2)%spacer == 0]
new_tick_locations_nm = new_tick_locations_nm[::int(len(new_tick_locations_nm)/len(ax.get_xticks()))]
new_tick_locations_ev = new_tick_locations_ev[::int(len(new_tick_locations_ev)/len(ax.get_xticks()))]
while len(new_tick_locations_ev) != len(set(new_tick_locations_ev)):
    i = 0
    c = len(new_tick_locations_ev)
    while i < c:
        if new_tick_locations_ev[i] in new_tick_locations_ev[i+1:]:
            del(new_tick_locations_ev[i])
            del(new_tick_locations_nm[i])
            c = len(new_tick_locations_ev)
        i += 1
ax3 = ax.twinx()
ax3.set_xlim(ax.get_xlim())
ax3.set_xticks(new_tick_locations_nm)
ax3.set_xticklabels([str(i) for i in new_tick_locations_ev])
ax3.set_xlabel(r"\textbf{"+r"h\textnu/eV"+"}")
ax.legend((a1, a2), (a1.get_label(), a2.get_label()), loc='best',
    frameon=False, handlelength=1)
return (x1, y1), (x2, y2)

###
```

### Adapted from <https://www.codedrome.com/exploring-the-visible-spectrum-in-python/>

```
def wavelength_to_rgb(nm):

    gamma = 0.8
    max_intensity = 255
    factor = 0

    rgb = {"R": 0, "G": 0, "B": 0}

    if 380 <= nm <= 439:
        rgb["R"] = -(nm - 440) / (440 - 380)
        rgb["G"] = 0.0
        rgb["B"] = 1.0
    elif 440 <= nm <= 489:
        rgb["R"] = 0.0
        rgb["G"] = (nm - 440) / (490 - 440)
        rgb["B"] = 1.0
    elif 490 <= nm <= 509:
        rgb["R"] = 0.0
        rgb["G"] = 1.0
        rgb["B"] = -(nm - 510) / (510 - 490)
    elif 510 <= nm <= 579:
        rgb["R"] = (nm - 510) / (580 - 510)
        rgb["G"] = 1.0
        rgb["B"] = 0.0
    elif 580 <= nm <= 644:
        rgb["R"] = 1.0
        rgb["G"] = -(nm - 645) / (645 - 580)
        rgb["B"] = 0.0
    elif 645 <= nm <= 780:
        rgb["R"] = 1.0
        rgb["G"] = 0.0
        rgb["B"] = 0.0

    if 380 <= nm <= 419:
        factor = 0.3 + 0.7 * (nm - 380) / (420 - 380)
    elif 420 <= nm <= 700:
        factor = 1.0
    elif 701 <= nm <= 780:
        factor = 0.3 + 0.7 * (780 - nm) / (780 - 700)
```

```
if rgb["R"] > 0:
    rgb["R"] = int(max_intensity * ((rgb["R"] * factor) ** gamma))
else:
    rgb["R"] = 0

if rgb["G"] > 0:
    rgb["G"] = int(max_intensity * ((rgb["G"] * factor) ** gamma))
else:
    rgb["G"] = 0

if rgb["B"] > 0:
    rgb["B"] = int(max_intensity * ((rgb["B"] * factor) ** gamma))
else:
    rgb["B"] = 0

return (rgb["R"]/255, rgb["G"]/255, rgb["B"]/255)
###
```

```
def printProgressBar (iteration, total, prefix = '', suffix = '',
    decimals = 1, length = 10, fill = 'X', printEnd = "\r"):
    percent = ("{0:." + str(decimals) + "f}").format(100 * ((iteration
        +1) / float(total)))
    filledLength = int(length * (iteration+1) // total) + 1
    bar = fill * filledLength + '-' * ((length) - filledLength)
    print('\r%s |%s| %s%% %s | %s/%s' % (prefix, bar, percent, suffix,
        str(iteration+1), str(total)), end = printEnd)
    return None
```

---

## B.3 X-ray Diffraction Pattern Identification

The Python 3 script "X-ray Diffraction.py" was used for accessing The Materials Project Database calculated XRD diffraction patterns and plot them against the experimental data obtained from the powders synthesized in this work. The content of the script is displayed below.

---

```

# -*- coding: utf-8 -*-

import numpy as np
import pandas as pd
import os
import time
from matplotlib import pyplot as plt
from operator import itemgetter
from bs4 import BeautifulSoup
from requests import get
from json import loads
# conda install -c conda-forge pymatgen
# or
# pip install pymatgen
from pymatgen.ext.matproj import MPRester
from pymatgen.analysis.diffraction.xrd import XRDCalculator
import gc # Required to clean the patterns variable if the user does not want to accumulate
          (stack) patterns

params = {'mathtext.default': 'regular',
          'axes.linewidth': 0.8,
          'font.size': 10.95/0.75,
          'axes.labelweight': 'bold',
          'mathtext.fontset': 'cm',
          'font.family': 'serif',
          'font.serif': 'Computer Modern Roman',
          'text.usetex': True,
          'text.latex.preamble': r"\usepackage{textgreek}"
        }
plt.rcParams.update(params)

##### Put your own Materials #####
##### Project API key in #####

```

```
api_key = MPRester("ADD YOUR KEY HERE")
#####

# Global variable to capture the results, in case the user forgets to attribute the function result
to a variable:
patterns = ["Material id", "Formula", "Spacegroup", "Crystal system", "
X-ray diffraction pattern", "Band gap/eV", "Final energy/eV", "
Density (atomic)", "Density/(g/cm3)", "Metal's atomic weight/(g/mol)"
]]

def XRD_PLOTTER(data_list : list, material_id_list = None,
element_criteria = ["Fe", "S"], criteria_add = {'nsites': {'$lt':
1000000}, "theoretical": False}, data_labels : list = [], selected =
1, xlim = [10,90], stretch_references = True, mark_references = False
, mark_thresh = 10, stack_patterns = False, axis_width = 70,
axis_height = 20):
    """
    Description
    -----
    Searches materialsproject database for reference patterns containing a set of elements and
    plots them against the user data.

    Parameters
    -----
    data_list : list
        List of data with the following example format: [[x1, y1], [x2, y2], ...].
        XRDAalysis.py supplies a read_csv definition for CENIMAT (NOVA School of
        Science and Technology) XRD patterns. If a file is used, it will automatically
        assume read_csv is to be used on it.
    material_id_list : list
        List of material_id_list. Leave as None if you prefer to generate a list of IDs based
        on the following arguments. It can also be generated with the following example,
        which yields the materials sorted based on formation_energy_per_atom from the
        lowest value (negative) to the highest:
        entries = entries_chemsys(['In', 'Sn', 'S'])
        energy_per_atom = [a["formation_energy_per_atom"] for a in entries if a["
        nelements"] > 1]
        material_ids = [a["material_id"] for a in entries if a["nelements"] > 1]
```

```
material_id_list = [x for _,x in sorted(zip(energy_per_atom, material_ids),
reverse=False)]
```

or/and using the argument elements.

Otherwise, use the x-ray diffraction patterns from JSON files from materialsproject; list of files.

element\_criteria : list

List of elements to generate a list of "material\_id" that includes X-ray diffraction patterns.

criteria\_add : dict

Dictionary to be concatenated to the query criteria. Choose criteria\_add = {}, for no additional criteria.

data\_labels : list

List of the data labels. Must match the size of the list data\_list.

selected : int

Selected data to plot on top of the references. Example: selected = 1, will select the first data pair from data\_list to be plotted and compared with the references.

xlim : list

Limits for the x axis (2 theta).

stretch\_references : bool

Defines if the bars from the references stretch all the way to the top of the sample pattern.

mark\_references : bool

The plotted bars from the references that were imported from materialsproject database will color the selected plot for each value.

mark\_thresh : int

The colorizing of the selected plot based on the references values is extended to the sides with this argument.

Returns

-----

None. However, since the variable patterns is global, it will append any result it finds to patterns.

Example

-----

```
XRD_PLOTTER(['E:/Work/PhD/Data/Particles/Bi/Bi(NO3)3-DDCT-mwave-185-6
min10s/XRD/DJ.csv'], [], ["Bi"], criteria_add = {'nsites': {'$lt': 10000}},
data_labels = ["Bi(NO3)3-DDCT-mwave-185-6min10s"])
"""
```

```
dif = (xlim[1] - xlim[0])*1.05
```

```
if material_id_list == None or material_id_list == []:
    material_id_list = []

global patterns

if (not stack_patterns and len(patterns) > 1) or len(patterns) == 0:
    del(patterns)
    try:
        gc.garbage = []
    except:
        pass
    patterns = ["Material id", "Formula", "Spacegroup", "Crystal
                system", "X-ray diffraction pattern", "Band gap/eV", "Final
                energy/eV", "Density (atomic)", "Density/(g/cm3)", "Metal's
                atomic weight/(g/mol)"]

if element_criteria != None and type(element_criteria) is list:
    criteria = dict({"elements":{"$all":element_criteria},"nelements"
                    :len(element_criteria)}, **criteria_add if criteria_add !=
                    None else {})
    properties = ["material_id", "pretty_formula", "spacegroup", u"
                  final_energy", "density_atomic", "density"]
    data = api_key.query(criteria=criteria, properties=properties)
    for i in data:
        material_id_list.append([i["material_id"], i["pretty_formula"
                                ], i["spacegroup"]["crystal_system"], i[u"final_energy"],
                                i["density_atomic"], i["density"]])
material_id_list = [i[0] for i in sorted(material_id_list, key=
    itemgetter(1, 2))]

data_color = [0.5*(i/len(data_list)) if (i != 0 and i != len(
    data_list)-1)
              else 0 if i == 0
              else 0.5 if i == len(data_list)-1
              else None
              for i in range(len(data_list))]

material_id_color = [0.5*(i/len(material_id_list)) if (i != 0 and i
```

```

!= len(material_id_list)-1)
        else 0 if i == 0
        else 0.5 if i == len(material_id_list)-1
        else None
        for i in range(len(material_id_list))]

h = ((-0.212+axis_height)/25.4)/0.75
h0 = (len(material_id_list)+len(data_list))
figsize=[((-0.212+axis_width)/25.4)/0.75,
          h0*h+(15/25.4)/0.75] # [W, H]
ws = 1/0.4
figsize = [ws*figsize[0], figsize[1]]
fig = plt.figure(figsize=(figsize[0], figsize[1]))

wscale = 1/ws
hscale = h/figsize[1]
#1/(h0+2*(15/25.4)/0.75)
axs = []
for i in range(h0):
    wpos = (15/25.4)/(figsize[0])
    hpos = (15/25.4)/(figsize[1])+i*hscale
    ax = fig.add_axes([wpos,hpos,
                      wscale,hscale])
    ax.set_yticks([])
    ax.set_xticks([]) if i != 0 else ax.set_xticks([i*10 for i in
        range(int(xlim[0]/10), int(xlim[1]/10)+1)])
    ax.set_xlim(xlim)
    ax.set_ylim([0,1])
    if i == 0:
        ax.set_xlabel('2\straighttheta/^\circ$')
    axs.append(ax)

for i in range(len(data_list)):
    try:
        if os.path.isfile(data_list[i]):
            data_list[i] = read_csv(data_list[i])
    except:
        print("Error while reading csv file: "+str(data_list[i]))
    y = normalize(data_list[i][1])

```



```
    axs[i].plot(data_list[i][0], normalize(data_list[i][1]), color=[
        data_color[i], data_color[i], data_color[i]])
    axs[i].annotate(text = data_labels[i],
                    xy = (dif, 0.5),
                    ha="right")
    axs[selected-1].annotate(text = "(Selected)",
                             xy = (dif, 0.35),
                             ha="right")

sx = data_list[selected-1][0]
sy = normalize(data_list[selected-1][1])

annotate_x = xlim[1]*1.02
annotate_position = "left"
if len(material_id_list) > 0:
    for m in range(len(material_id_list)):
        if m == 0:
            printProgressBar(0, len(material_id_list))
        mm = m + len(data_list)
        if ".json" not in material_id_list[m]:
            calc = XRDCalculator()
            connect = 0
            tries = 1
            while connect == 0 and tries < 5:
                try:
                    l = api_key.query(criteria={"material_id":
                        material_id_list[m]}, properties=["
                        pretty_formula", "spacegroup", "band_gap", "tags
                        ", u"final_energy", "density_atomic", "density"
                    ])[0]
                    structure = api_key.get_structure_by_material_id(
                        material_id_list[m])
                    formula = l["pretty_formula"]
                    spacegroup = l["spacegroup"]["symbol"]
                    crystal = l["spacegroup"]["crystal_system"]
                    energy = l[u"final_energy"]
                    density_atomic = l["density_atomic"]
```

```

density = l["density"]
pattern = calc.get_pattern(structure)
tags = l["tags"]
x = [pattern.x[i] for i in range(len(pattern.x)) if
     pattern.x[i] <= xlim[1] and pattern.x[i] >=
     xlim[0]]
y = [pattern.y[i] for i in range(len(pattern.x)) if
     pattern.x[i] <= xlim[1] and pattern.x[i] >=
     xlim[0]]
y = normalize(y)
plt.rcParams.update({'font.size': 7/0.75})
if stretch_references:
    axs[mm].bar(x, np.ones(len(y))-y*0.5, bottom = y
               *0.5,
               #color=[material_id_color[m],
               material_id_color[m], material_id_color[m]],

               color=[0.99, 0, 0, 0.15],
               width = 0.5)
if mark_references:
    if selected != None:
        colors = np.zeros(len(sx))
        for i in x:
            if min(sx[mark_thresh:]) < i < max(sx[:
            len(sx)-mark_thresh-1]):
                for j in range(len(sx)):
                    if sx[int(max(j-mark_thresh, 0))]
                    <= i <= sx[int(min(j+
                    mark_thresh, len(sx)-1))]:
                        size = len(colors[int(max(j-
                        mark_thresh, 0)):int(min(j+
                        mark_thresh, len(sx)))+1])
                        colors[int(max(j-mark_thresh,
                        0)):int(min(j+mark_thresh,
                        len(sx)))+1] = np.ones(size
                        )
        colors = [[i-0.02 if i == 1 else 0,0,0] for
                  i in colors]
        axs[mm].scatter(sx, sy*0.5+0.5, c=colors, s
                        =1, zorder=1)

```

```
axs[mm].plot(sx,sy*0.5+0.5, "k", zorder=0)
axs[mm].bar(x, y*0.5, bottom = 0,
            #color=[material_id_color[m], material_id_color[m],
            material_id_color[m]],
            color=[0.99, 0, 0, 1],
            width = 0.5)
axs[mm].annotate(text = material_id_list[m],
                 xy = (annotate_x, 0.90),
                 ha=annotate_position,
                 annotation_clip=False)
axs[mm].annotate(text = "".join(["$_"+i+"$" if i.
isdigit() else i for i in formula]),
                 xy = (annotate_x, 0.80),
                 ha=annotate_position,
                 annotation_clip=False)
axs[mm].annotate(text = spacegroup,
                 xy = (annotate_x, 0.70),
                 ha=annotate_position,
                 annotation_clip=False)
axs[mm].annotate(text = crystal,
                 xy = (annotate_x, 0.60),
                 ha=annotate_position,
                 annotation_clip=False)
axs[mm].annotate(text = "Band gap: "+ str(int(1["
band_gap"]*100)/100),
                 xy = (annotate_x, 0.50),
                 ha=annotate_position,
                 annotation_clip=False)
plt.rcParams.update({'font.size': 6/0.75})
for i in range(0, len(tags)):
    axs[mm].annotate(text = tags[i],
                    xy = (annotate_x, 0.42-0.5*i
                        *0.15),
                    ha=annotate_position,
                    annotation_clip=False)
plt.rcParams.update({'font.size': 10.9/0.75})
if material_id_list[m] not in [z[0] for z in
patterns]:
    patterns.append([material_id_list[m], formula,
                    spacegroup, crystal, np.array((x, y)).T, 1["
```

```

        band_gap"], energy, density_atomic, density,
        metal_atomic_weight(formula)])
    connect = 1
except Exception as e:
    print("Connection error. Might not being able to
        find the material with the id: " +
        material_id_list[m])
    print(e)
    tries += 1
    time.sleep(1)
else:
    id_mp = os.path.basename(material_id_list[m]).split("_")
        [0]
    url = "https://materialsproject.org/materials/"+id_mp
    title = [t.get_text() for t in BeautifulSoup(get(url).text
        , 'html.parser').find_all('title')][0]
    formula = title.split(" ")[2]
    spacegroup = title.split(" ")[4][:−1]
    pattern = XRD_JSON(material_id_list[m])
    y = [0 if pattern[0][i] < xlim[0] or pattern[0][i] > xlim
        [1] else pattern[1][i] for i in range(len(pattern[0]))]
    y = normalize(y)
    plt.bar(pattern[0], y, bottom = m, color=[
        material_id_color[m], material_id_color[m],
        material_id_color[m]], width = 0.5)
    plt.annotate(text = id_mp,
        xy = (dif, (m+1) − 0.15),
        ha="right")
    plt.annotate(text = "".join(["$_"+i+"$" if i.isdigit()
        else i for i in formula]),
        xy = (dif, (m+1) − 0.30),
        ha="right")
    plt.annotate(text = spacegroup, xy = (dif, (m+1) − 0.45),
        ha="right")
    patterns.append([material_id_list[m], formula, spacegroup,
        np.array((x, y)).T, None])

printProgressBar(m+1, len(material_id_list))

```

```
def grab_information(element_criteria = ["Fe", "S"], criteria_add = {'
nsites': {'$lt': 1000000}, "theoretical": False}, xlim = [10, 90]):
    """
    Description
    -----
    Same as XRD_PLOTTER but simply fetches the patterns from materialsproject without
    plotting anything.
    """

    criteria = dict({"elements":{"$all":element_criteria},"nelements":
        len(element_criteria)}, **criteria_add if criteria_add != None
        else {}))
    properties = ["material_id", "pretty_formula", "spacegroup", u"
        final_energy", "density_atomic", "density"]
    global patterns
    material_id_list = []
    data = api_key.query(criteria=criteria, properties=properties)
    for i in data:
        material_id_list.append([i["material_id"], i["pretty_formula"], i
            ["spacegroup"]["crystal_system"], i[u"final_energy"], i["
            density_atomic"], i["density"]])
    material_id_list = [i[0] for i in sorted(material_id_list, key=
        itemgetter(1, 2))]
    for m in range(len(material_id_list)):
        calc = XRDCalculator()
        connect = 0
        tries = 1
        while connect == 0 and tries < 5:
            try:
                l = api_key.query(criteria={"material_id":
                    material_id_list[m]}, properties=["pretty_formula", "
                    spacegroup", "band_gap", "tags", u"final_energy", "
                    density_atomic", "density"])[0]
                structure = api_key.get_structure_by_material_id(
                    material_id_list[m])
                formula = l["pretty_formula"]
                spacegroup = l["spacegroup"]["symbol"]
                crystal = l["spacegroup"]["crystal_system"]
                energy = l[u"final_energy"]
```

```

density_atomic = l["density_atomic"]
density = l["density"]
pattern = calc.get_pattern(structure)
x = [pattern.x[i] for i in range(len(pattern.x)) if
     pattern.x[i] <= xlim[1] and pattern.x[i] >= xlim[0]]
y = [pattern.y[i] for i in range(len(pattern.x)) if
     pattern.x[i] <= xlim[1] and pattern.x[i] >= xlim[0]]
y = normalize(y)
if material_id_list[m] not in [z[0] for z in patterns]:
    patterns.append([material_id_list[m], formula,
                    spacegroup, crystal, np.array((x, y)).T, l["
                    band_gap"], energy, density_atomic, density,
                    metal_atomic_weight(formula)])
connect = 1
printProgressBar(m+1, len(material_id_list))
except Exception as e:
    print("Connection error. Might not being able to find the
          material with the id: " + material_id_list[m])
    print(e)
    tries += 1
    time.sleep(1)

```

*# Auxiliary functions:*

```

def XRD_JSON(file, data_only = True):
    with open(file, 'r') as outfile:
        dic = loads(outfile.read())
    if data_only:
        return [i[2] for i in dic["pattern"]], [i[0] for i in dic["
            pattern"]]
    else:
        return dic

def read_csv(file_name : str, skip : str = '[Scan points]'):
    with open(file_name, "r") as f_in:
        lines = [line for line in f_in.readlines() if line != []]
    # with open(file_name, "w") as f_in:
    # f_in.writelines(lines)
    # f_in.close()

```

```

skiprows = [i for i in range(len(lines)) if skip in lines[i]][0]+1
data = pd.read_csv(file_name, skiprows=skiprows)
x = np.array(data["Angle"])
y = np.array(data["Intensity"])
return (x, y)

def metal_atomic_weight(formula : str):
    d = {'Ag': 107.868, 'Al': 26.98154, 'As': 74.9216, 'Au': 196.9665, 'B': 10.81, 'Ba': 137.33, 'Be': 9.01218, 'Bi': 208.9804, 'Ca': 40.08, 'Cd': 112.41, 'Ce': 140.12, 'Co': 58.9332, 'Cr': 51.996, 'Cs': 132.9054, 'Cu': 63.546, 'Dy': 162.5, 'Er': 167.26, 'Eu': 151.96, 'Fe': 55.847, 'Ga': 69.72, 'Gd': 157.25, 'Ge': 72.59, 'Hf': 178.49, 'Ho': 164.9304, 'In': 114.82, 'Ir': 192.22, 'K': 39.0983, 'La': 138.9055, 'Li': 6.941, 'Lu': 174.967, 'Mg': 24.305, 'Mn': 54.938, 'Mo': 95.94, 'Na': 22.98977, 'Nb': 92.9064, 'Nd': 144.24, 'Ni': 58.7, 'Os': 190.2, 'Pb': 207.2, 'Pd': 106.4, 'Pr': 140.9077, 'Pt': 195.09, 'Rb': 85.4678, 'Re': 186.207, 'Rh': 102.9055, 'Ru': 101.07, 'Sb': 121.75, 'Sc': 44.9559, 'Si': 28.0855, 'Sm': 150.4, 'Sn': 118.69, 'Sr': 87.62, 'Ta': 180.9479, 'Tb': 158.9254, 'Te': 127.6, 'Ti': 47.9, 'Tl': 204.37, 'Tm': 168.9342, 'V': 50.9415, 'W': 183.85, 'Y': 88.9059, 'Yb': 173.04, 'Zn': 65.38, 'Zr': 91.22}
    try:
        return sum([d[x] for x in d.keys() if x in formula])
    except:
        return None

def normalize(array, between = [0,1]):
    return between[0]+(between[1] - between[0])*(array-np.min(array))/(np.max(array)-np.min(array))

def printProgressBar (iteration, total, prefix = '', suffix = '', decimals = 1, length = 10, fill = 'X', printEnd = "\r"):
    percent = ("{0:." + str(decimals) + "f}").format(100 * ((iteration) / float(total)))
    filledLength = int(length * iteration // total) + 1
    bar = fill * filledLength + '-' * ((length) - filledLength)
    print('\r%s |%s| %s%% %s | %s/%s' % (prefix, bar, percent, suffix, iteration, total), end=printEnd)

```

```
    str(iteration), str(total)), end = printEnd)  
return None
```

---



## B.4 Selected Area Electron Diffraction Pattern Identification

The Python 3 script "Selected Area Electron Diffraction.py" was used to process the data obtained from a selected area electron diffraction pattern. The content of the script is displayed below.

---

```
# -*- coding: utf-8 -*-

try:
    import cupy as cu
    import numpy as np
    cupy = True
except:
    import numpy as cu, np
    cupy = False
import pandas as pd
import matplotlib.pyplot as plt

# Image (1376x1032), 875 pixel radius.

params = {'mathtext.default': 'regular',
          'axes.linewidth': 0.8,
          'font.size': 10.95/0.75,
          'axes.labelweight': 'bold',
          'mathtext.fontset': 'cm',
          'font.family': 'serif',
          'font.serif': 'Computer Modern Roman',
          'text.usetex': True,
          'text.latex.preamble': r"\usepackage{textgreek}"
          }
plt.rcParams.update(params)

def get_data(csv : str = None):
    if csv == None:
        data = pd.read_clipboard(header=None,
                                index_col=0,
                                names=[str(i-1) if i != 0 else "X" for i in
                                       range(0, 361)]).fillna(0)
    else:
        data = pd.read_csv(csv, delimiter=",",
                           header=None,
```

```

        index_col=0,
        names=[str(i-1) if i != 0 else "X" for i in
                range(0,361)].fillna(0)
    return data

def plot_data(data, Rau = None, dau002 = 2.039, plot = "d-space"):
    # plot: "map", "angle", "d-space"
    # Hitachi H-8100: Rau = 241
    if Rau == None and (plot == "map" or plot == "angle"):
        print("Please calibrate first to set a value of Rau instead of
              None.")
    Y = Rau*dau002/cu.array(data["X"]) if Rau != None else cu.array(data
        ["X"])
    X = cu.array(range(0, len(list(data.columns))-1))
    if plot == "map":
        x, y = cu.meshgrid(X, Y)
        z = np.array(data[list(data.columns)[1:]])
        fig, ax = plt.subplots()
        z = z[:-1, :-1]
        z_min, z_max = -np.abs(z).max(), np.abs(z).max()
        c = ax.pcolormesh(x.get() if cupy else x, y.get() if cupy else y,
            z, cmap='RdGy', vmin=z_min, vmax=z_max)
        ax.set_xlim([0,360])
        ax.set_ylim([0,10])
        ax.set_xlabel(r"\textbf{"+r"\straighttheta/\$^{\circ}\$"+}")
        ax.set_ylabel(r"\textbf{"+r"d-spacing/\AA"+}")
        return (x,y,z,c)
    if plot == "angle":
        fig, ax = plt.subplots()
        ax.plot(X.get() if cupy else X, data[data.columns[1:]].mean(axis
            =0), "k")
        ax.set_xlabel(r"\textbf{"+r"\straighttheta/\$^{\circ}\$"+}")
        ax.set_ylabel(r"\textbf{"+r"d-spacing/\AA"+}")
        #ax.set_xlim([0,100])
        #ax.set_ylim([0,10])
        return (X,data[data.columns[1:]].mean(axis=0))
    if plot == "d-space":
        d = [cu.sum(i[1:]) for i in data.values]
        d = (d-np.min(d))/(np.max(d)-np.min(d))

```

```
fig, ax = plt.subplots()
ax.set_xlabel(r"\textbf{"+(r"d-spacing/\AA" if Rau != None else "
    Distance/pixel")+}")
ax.set_ylabel(r"\textbf{"+r"Normalized intensity"+}")
ax.set_yticks([0, 0.5, 1])
ax.set_ylim([0, 1])
ax.set_xlim([0, 10])
ax.plot(Y.get() if cupy else Y, d, "k")
return (Y.get() if cupy else Y, np.array(d))
```

---

## B.5 Auxiliary Python 3 Scripts

This section was dedicated to supplying any additional information or auxiliary scripts to the ones used in this work. Most of these scripts were written for personal use and not with public use in mind. As such, an effort to make them readily available in my GitHub page will be attempted during and after the conclusion of this work.

### Is the Metal, Oxide, or Sulfide of a Group of Elements predicted to exist?

The Python 3 script below uses the code available in the "X-Ray Diffraction.py" from my GitHub repository at <https://github.com/DavidMSou/Scientific-Tools>. It check if for a given set of elements, for example ["Zn", "Sn", "In"], the metal alloy, the oxide or the sulfide is predicted. For the latter example, neither the metal, the oxide or the sulfide are predicted to exist.

---

```

from itertools import product, permutations

elements_synth = ["Li", "Be", "Na", "Mg", "Al", "Si", "K", "Ca", "Sc", "Ti", "V", "
    Cr", "Mn", "Fe", "Co", "Ni", "Cu", "Zn", "Ga", "Sr", "Y", "Zr", "Nb", "Mo", "Ag", "
    Cd", "In", "Sn", "Ba", "Hf", "Ta", "W", "Bi"]

ternary = []
for e1 in range(len(elements_synth)):
    temp = elements_synth.copy()
    del(temp[e1])
    print(len(elements_synth), len(temp))
    for e2 in range(len(temp)):
        if [elements_synth[e1], temp[e2]] in ternary or [temp[e2],
            elements_synth[e1]] in ternary:
            pass
        else:
            ternary.append([elements_synth[e1], temp[e2]])

quaternary = []
for e1 in range(len(elements_synth)):
    temp = elements_synth.copy()
    temp.remove(elements_synth[e1])
    for e2 in range(len(temp)):
        temp2 = elements_synth.copy()
        temp2.remove(elements_synth[e1])
        temp2.remove(temp[e2])
        for e3 in range(len(temp2)):

```

```
        if [elements_synth[e1], temp2[e3], temp[e2]] in quaternary or
            [elements_synth[e1], temp[e2], temp2[e3]] in quaternary
        or [temp[e2], elements_synth[e1], temp2[e3]] in quaternary
        or [temp2[e3], elements_synth[e1], temp[e2]] in
            quaternary or [temp[e2], temp2[e3], elements_synth[e1]] in
            quaternary or [temp2[e3], temp[e2], elements_synth[e1]]
        in quaternary:
            pass
        else:
            quaternary.append([elements_synth[e1], temp[e2], temp2[e3]
                               ])

d = []
all = ternary+quaternary
count = 0
for i in all:
    o = None
    s = None
    e = grab_information(element_criteria=i+"O", criteria_add={},
                        interrupt=i, stack_patterns = False)
    if e == 1:
        o = True
    else:
        o = False
    e = grab_information(element_criteria=i+"S", criteria_add={},
                        interrupt=i, stack_patterns = False)
    if e == 1:
        s = True
    else:
        s = False
    e = grab_information(element_criteria=i, criteria_add={}, interrupt=
                        i, stack_patterns = False)
    if e == 1:
        m = True
    else:
        m = False
    d.append([i, m, o, s])

dictionary = {"Metal, no oxide, no sulfide": [0, [], 0], "Metal, oxide, no
sulfide": [0, []], "Metal, oxide, sulfide": [0, []], "Metal, no oxide,
```

```
sulfide": [0,[]], "No metal, no oxide, no sulfide": [0,[]], "No metal
, oxide, no sulfide": [0,[]], "No metal, no oxide, sulfide": [0,[]],
"No metal, oxide, sulfide": [0,[]]}
```

```
for i in d:
for j in product(["True", "False"], repeat = 3):
    if str(i[1]) == j[0] and str(i[2]) == j[1] and str(i[3]) == j[2]:
        Metal = ("No m" if j[0] == "False" else "M")+etal, "
        Oxide = ("no " if j[1] == "False" else "")+oxide, "
        Sulfide = ("no " if j[2] == "False" else "")+sulfide"
        phrase = Metal+Oxide+Sulfide
        dictionary[phrase][0] += 1
        dictionary[phrase][1] += [i[0]]
for k,v in dictionary.items():
    dictionary[k][0] = dictionary[k][0]/len(d)
```

*#Searching newly created dictionary for the existence  
#of a metal alloy, oxide or sulfide of ["Zn", "In", "Sn"]:*

```
for k,v in dictionary.items():
    for i in dictionary[k][1]:
        for j in list(permutations(["Zn", "In", "Sn"], 3)):
            if list(j) == i:
                print(k)
```

*#As per the output "No metal, no oxide, no sulfide",  
#none of the three are predicted.*

---



